ISSN 2434-9488

KURNS Progress Report 2020

KURNS
Institute for Integrated Radiation and Nuclear Science,
Kyoto University

KURNS Progress Report 2020

APRIL 2020 – MARCH 2021

Published by
Institute for Integrated Radiation and Nuclear Science,
Kyoto University,
Kumatori-cho, Sennan-gun, Osaka 590-0494, Japan

Preface for the KURNS Progress Report 2020

It is our pleasure to announce that the KURNS Progress Report 2020 has been published. This report contains all of the accomplishments of research and related activities at the Institute for Integrated Radiation and Nuclear Science, Kyoto University (KURNS) during the fiscal year 2020 (hereafter called as FY2020). A large number of research subjects has been enrolled also in FY2020, which covers various fields of nuclear science and technology, material science, radiation life science and radiation medical science. It means that our institute continues to play a distinctive role as a Joint Usage/Research Center, promoting an extensive range of studies from fundamental to applied research with research reactors and accelerators.

In FY2020, our activity was drastically restricted due to the COVIT-19 pandemic. During the 1st period of a state of emergency issued for Osaka prefecture (from April 17 to May 21, 2020), all the activity related to the preparation for the operation of the joint research facilities including KUR and KUCA was suspended, therefore the operation time for these facilities decreased significantly. Note that the activity on the safety management was still continued under the corresponding period. In FY 2020, KUR was operated for 570 hours and KUCA was for 152 hours. In total, we accepted 2,560 man-day researchers and students for using research facilities and for attending scientific meetings. Because of the operation time reduction, some of the research subjects were carried forward to FY2021.

We strive for safe and stable operations for nationwide use, making it our primary mission to provide scientists the opportunity to conduct research and education. We are happy to dedicate our support to enable users conduct significant interdisciplinary research at KURNS.

Kumatori, July 12, 2021
Ken Nakajima
Director, KURNS

CONTENTS

5. Geochemistry and Environmental Science

7. Neutron Capture Therapy

I. ANNUAL SUMMARY OF EXPERIMENTAL RESEARCH ACTIVITIES

I-1. PROJECT RESEARCHES

Project 1

PR1 Analyzing Tumor Microenvironment and Exploiting its Characteristics in Search of Optimizing Cancer Therapy Including Neutron Capture Therapy

Shin-ichiro Masunaga, M.D., Ph.D.

Particle Radiation Biology, Division of Radiation Life Science, Institute for Integrated Radiation and Nuclear Science, Kyoto University

BACKGROUNDS AND PURPOSES: Human solid tumors contain moderately large fractions of quiescent (Q) tumor cells that are out of the cell cycle and stop cell division, but are viable compared with established experimental animal tumor cell lines. The presence of Q cells is probably due, in part, to hypoxia and the depletion of nutrition in the tumor core, which is another consequence of poor vascular supply. As a result, Q cells are viable and clonogenic, but stop cell division. In general, radiation and many DNA-damaging chemotherapeutic agents kill proliferating (P) tumor cells more efficiently than Q tumor cells, resulting in many clonogenic Q cells remaining following radiotherapy or chemotherapy. Therefore, it is harder to control Q tumor cells than to control P tumor cells, and many post-radiotherapy recurrent tumors result partly from the regrowth of Q tumor cells that could not be killed by radiotherapy. Similarly, sufficient doses of drugs cannot be distributed into Q tumor cells mainly due to heterogeneous and poor vascularity within solid tumors. Thus, one of the major causes of post-chemotherapy recurrent tumors is an insufficient dose distribution into the Q cell fractions.

With regard to boron neutron capture therapy (BNCT), with ^{10}B-compounds, boronophenylalanine-^{10}B (BPA) increased the sensitivity of the total cells to a greater extent than mercaptoundecahydrododecaborate-^{10}B (BSH). However, the sensitivity of Q cells treated with BPA was lower than that in BSH-treated Q cells. The difference in the sensitivity between the total and Q cells was greater with ^{10}B-compounds, especially with BPA. These findings concerning the difference in sensitivity, including other recovery and reoxygenation following neutron irradiation after ^{10}B-compound administration were mainly based on the fact that it is difficult to deliver a therapeutic amount of ^{10}B from ^{10}B-carriers throughout the target tumors, especially into intratumor hypoxic cells with low uptake capacities.

Hypoxia is suggested to enhance metastasis by increasing genetic instability. Acute, but not chronic, hypoxia was reported to increase the number of macroscopic metastases in mouse lungs. We recently reported the significance of the injection of an acute hypoxia-releasing agent, nicotinamide, into tumor- bearing mice as a combined treatment with γ-ray irradiation in terms of repressing lung metastasis. As the delivered total dose increased with irradiation, the number of macroscopic lung metastases decreased reflecting the decrease in the number of clonogenically viable tumor cells in the primary tumor. The metastasis-repressing effect achieved through a reduction in the number of clonogenic tumor cells by irradiation is much greater than that achieved by releasing tumor cells from acute hypoxia. On the other hand, more ^{10}B from BPA than from BSH could be distributed into the acute hypoxia-rich total tumor cell population, resulting in a greater decrease in the number of highly clonogenic P tumor cells with BPA-BNCT than with BSH-BNCT and with neutron beam irradiation only. BPA-BNCT rather than BSH-BNCT has some potential to decrease the number of lung metastases, and an acute hypoxia-releasing treatment such as the administration of nicotinamide, bevacizumab, wortmannin or thalidomide may be promising for reducing numbers of lung metastases. Consequently, BPA-BNCT in combination with the treatment using these agents may show a little more potential to reduce the number of metastases. Now, it has been elucidated that control of the chronic hypoxia-rich Q cell population in the primary solid tumor has the potential to impact the control of local tumors as a whole, and that control of the acute hypoxia-rich total tumor cell population in the primary solid tumor has the potential to impact the control of lung metastases.

The aim of this research project is focused on clarifying and analyzing the characteristics of intratumor microenvironment including hypoxia within malignant solid tumors and optimizing cancer therapeutic modalities, especially radiotherapy including BNCT in the use of newly-developed ^{10}B-carriers based on the revealed findings on intratumor microenvironmental characteristics.

RESEARCH SUBJECTS:

The collaborators and allotted research subjects (ARS) were organized as follows;

ARS-1 (R2P1-1)*: Optimization of Radiation Therapy Including BNCT in terms of the Effect on a Specific Cell Fraction within a Solid Tumor and the Suppressing Effect of Distant Metastasis. (S. Masunaga,*et al.*)

ARS-2 (R2P1-2): Development of Hypoxic Micro-environment-Oriented ^{10}B-Carriers. (H. Nagasawa, *et al.*)

ARS-3 (R2P1-3)*: Search and Functional Analysis of Novel Genes that Activate HIF-1, and Development into Local Tumor Control. (H. Harada, *et al.*)

ARS-4 (R2P1-4)*: Radiochemical Analysis of Cell Lethality Mechanism in Neutron Capture Reaction. (R. Hirayama, *et al.*)

ARS-5 (R2P1-5)*: Development of Neutron Capture Therapy Using Cell-Membrane Fluidity Recognition Type Novel Boron Hybrid Liposome. (S. Kasaoka, *et al.*)

ARS-6 (R2P1-6): Drug Delivery System Aimed at Adaptation to Neutron Capture Therapy for Melanoma. (T. Nagasaki, *et al.*)

ARS-7 (R2P1-7)*: Molecular Design, Synthesis and Functional Evaluation of Hypoxic Cytotoxin Including Boron. (Y. Uto, *et al.*)

ARS-8 (R2P1-8)*: Bystander Effect on Malignant Trait of Tumor Cells by Irradiation. (H. Yasui, *et al.*)

ARS-9 (R2P1-9): Analysis of the Response of Malignant Tumor to BNCT. (M. Masutani, *et al.*)

ARS-10 (R2P1-10)*: Cell Survival Test by Neutron Capture Reaction Using Boron Compound and Inhibitory Effect on Tumor Growth. (K. Nakai, *et al.*)

ARS-11 (R2P1-11)*: Multilateral Approach Toward Realization of Next Generation Boron Neutron Capture Therapy. (Y. Matsumoto, *et al.*)

ARS-12 (R2P1-12): Analysis of Radiosensitization Effect through Targeting Intratumoral Environmental. (Y. Sanada, *et al.*)

(*There were no allocated time for experiments using reactor facilities during their operation periods of FY 2020, partially due to the impact of measures to prevent the spread of new coronavirus infection.)

PR1-1

Significance of combination with both continuous administration of hypoxic cytotoxin, tirapazamine and mild temperature hyperthermia in BNCT in terms of local tumor control and lung metastatic potential

S. Masunaga[1], Y. Sakurai[2], H. Tanaka[2], T. Takata[2], M. Suzuki[3], Y. Sanada[1], K. Tano[1], N. Kondo[3], T. Watanabe[3], S. Takeno[3], A. Maruhashi[2] and K. Ono[4]

[1]Particle Radiation Biology, [2]Prticle Radiation Medical Physics and [3]Particle Radiation Oncology Center, Division of Radiation Life Science, Institute for Integrated Radiation and Nuclear Science, Kyoto University.
[4]Kansai BNCT Medical Center, Osaka Medical College.

INTRODUCTION: To evaluate the usefulness of combined treatment with both continuous administration of a hypoxic cytotoxin, tirapazamine (TPZ) and mild temperature hyperthermia (MTH) in boron neutron capture thrrapy (BNCT) in terms of local tumor response and lung metastatic potential, referring to the response of intratumor quiescent (Q) cells.

MATERIALS AND METHODS: B16-BL6 melanoma tumor-bearing C57BL/6 mice were continuously given 5-bromo-2'-deoxyuridine (BrdU) to label all proliferating (P) cells. The tumors received reactor thermal neutron beam irradiation following the administration of a ^{10}B-carrier (L-para-boronophenylalanine-^{10}B (BPA) or sodium mercaptoundecahydrododecaborate-^{10}B (BSH)) after single intraperitoneal injection of an acute hypoxia-releasing agent (nicotinamide), mild temperature hyperthermia (MTH, 40 °C for 60 min), 24h continuous subcutaneous infusion of TPZ or combined treatment with both TPZ and MTH. Immediately after irradiation, cells from some tumors were isolated and incubated with a cytokinesis blocker. The responses of the Q and total (= P + Q) tumor cell populations were assessed based on the frequency of micronuclei using immunofluorescence staining for BrdU. In other tumor-bearing mice, 17 days after irradiation, macroscopic lung metastases were enumerated.

RESULTS: BPA-BNCT increased the sensitivity of the total tumor cell population more than BSH-BNCT. However, the sensitivity of Q cells treated with BPA was lower than that of BSH-treated Q cells. With or without a ^{10}B–carrier, combination with continuously administered TPZ with or without MTH enhanced the sensitivity of the both total and Q cells, especially Q cells. Even without irradiation, nicotinamide treatment decreased the number of lung metastases. With irradiation, BPA-BNCT, especially in combination with combined treatment with both TPZ and MTH as well as nicotinamide treatment, showed the potential to reduce the number more than BSH-BNCT.

CONCLUSION: BSH-BNCT combined with TPZ with or without MTH improved local tumor control, while BPA-BNCT in combination with both TPZ and MTH as well as nicotinamide is thought to reduce the number of lung metastases. It was elucidated that control of the chronic hypoxia-rich Q cell population in the primary solid tumor has the potential to impact the control of local tumors as a whole and that control of the acute hypoxia-rich total tumor cell population in the primary solid tumor has the potential to impact the control of lung metastases [1,2].

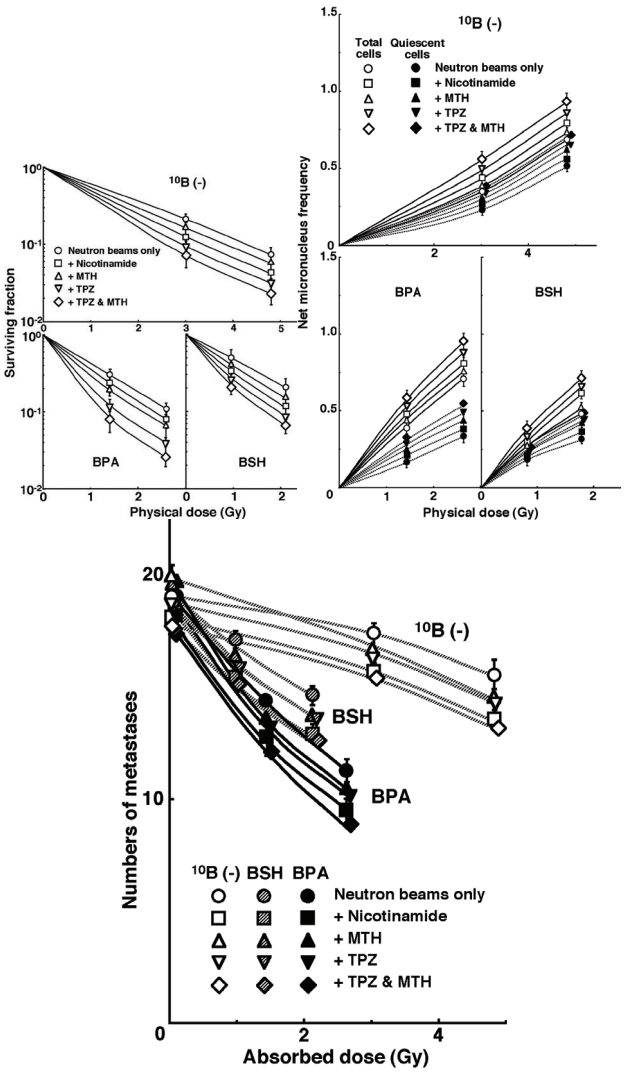

REFERENCES:

[1] Masunaga S. *et al., Int J Radiat Biol* **95**(2019) 1708–1717.

[2] Masunaga S. *et al., J Radiat Res* **61**(2020) 876–885.

R2P1-1

PR1-2 Development of Amino Acid Derivatives Containing ^{10}B-Clusters for BNCT

A. Matsushita[1], S. Kusanagi[1], M. Tsuji[1], Y. Sanada[2], T. Hirayama[1], S. Masunaga[2], and H. Nagasawa[1]

[1] *Laboratory of Medicinal & Pharmaceutical Chemistry, Gifu Pharmaceutical University*

[2] *KURNS*

INTRODUCTION: Malignant tumor cells exhibit metabolic alterations that have been recognized as one of the hallmarks of cancer. Proliferating cancer cells increase their uptake of glutamine for energy metabolism, leading to glutamine addiction. Glutamine is transported into cells through ASCT2, and the imported glutamine can be used or exchanged through the L-type amino acid transporter (LAT1 or SLC7A5) for hydrophobic or aromatic amino acids such as isoleucine, valine, methionine, tryptophan, and phenylalanine. It is known that these transporters are overexpressed in a variety of tumor cells. Focusing on this characteristic of malignant tumor "glutamine addiction," we have designed, synthesized, and evaluated boron cluster-containing amino acid derivatives to develop boron carriers that can efficiently accumulate ^{10}B atoms in tumors via amino acid transporters that are highly expressed in tumors.

EXPERIMENTS AND RESULTS: Since carborane ($C_2B_{10}H_{12}$) is hydrophobic and has three-dimensional aromaticity, we designed and synthesized various amino acid derivatives possessing carborane as a hydrophobic pharmacophore (Fig. 1). They were efficiently obtained from the corresponding amino acid alkynes and decaborane in a short step using our microwave-assisted reaction [1]. The obtained compounds and L-boronophenylalanine

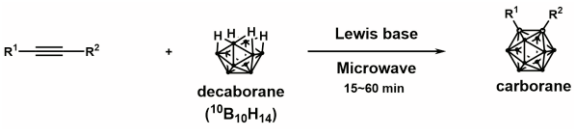

	R_1	R_2
BC-1	H	
BC-2	H	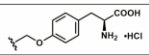
BC-3	Ph	
BC-4	H	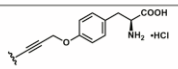

Fig. 1. Structures of new boron carriers synthesized from corresponding alkynes and decaborane by micro-wave assisted reaction.

(BPA) were administered to T98G cells at 10 μg ^{10}B/mL and treated for 20 hours, after which the collected cells were dissolved in nitric acid to be measured the boron concentration by ICP-AES. As a result, intracellular boron uptake was highest in BC-2, with a very high value of about 185 ng ^{10}B/10^6 cells, which is more than 10 times higher than BPA (Fig. 2).

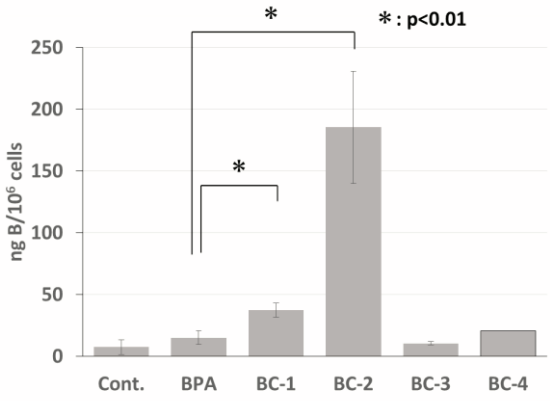

Fig. 2. Uptake of boron carriers in T98G cells.

Next, to evaluate neutron sensitizing ability of the compounds, T98G cells were treated with 10 μg ^{10}B/mL boron carriers for 20 h. Then the cells were washed with PBS, suspended in serum containing medium and aliquoted into Teflon tubes for irradiation. Cells were irradiated using the neutron beam at the Heavy Water Facility of the Kyoto University Research Reactor (KUR) operated at 1 MW power output. The survival rates of the irradiated cells were determined using conventional colony assays. The D_{10} of BNCT was calculated from survival curve shown in Fig 3.

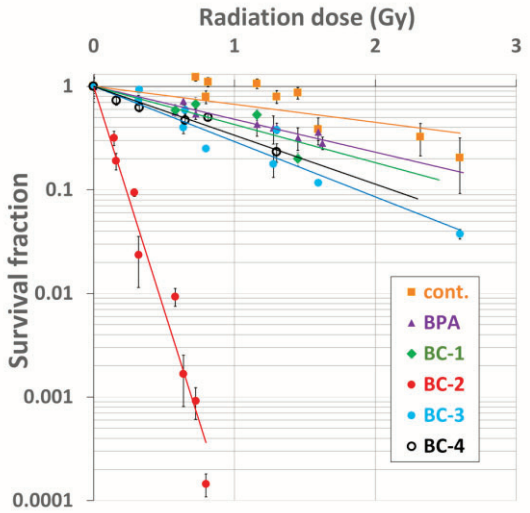

Fig. 3. Survival curves after irradiation on T98G with mew boron carries.

BC-2 showed the highest enhancement of the cell killing effect of thermal neutrons on T98G cells, with a D_{10} of 0.23 Gy and an enhancement ratio of 24.8. These results suggest that BC-2 is a promising candidate for a new boron carrier. We will investigate the mechanism of cellular uptake and the biodistribution of BC-2.

REFERENCES:

[1] S. Kimura *et al.,* Bioorg. Med. Chem., **19**(2011), 1721-1728.

PR1-3 Proteolysis of a Histone Acetyl Reader Protein Induces Chemoresistance of Cancer Cells under Hypoxia by Inhibiting Cell Cycle Progression in S Phase

T. Haitani[1,2,3], M. Kobayashi[1,2], S. Koyasu[1,2,3], S. Akamatsu[4], O. Ogawa[4], and H. Harada[1,2]

[1]*Laboratory of Cancer Cell Biology, Graduate School of Biostudies, Kyoto University*

[2]*Department of Genome Dynamics, Radiation Biology Center, Graduate School of Biostudies, Kyoto University*

[3]*Research Center for Advanced Science and Technology, The University of Tokyo*

[4]*Department of Urology, Graduate School of Medicine, Kyoto University*

INTRODUCTION: Cancer cells acquire resistance to conventional chemotherapy in hypoxic regions of solid tumors [1,2], which is suggested to be at least partly due to reduction of their proliferative activity. However, mo-lecular mechanisms behind it have not been fully eluci-dated.

EXPERIMENTS: We performed both basic studies using cultured cells and tumor-bearing mice and clinical immunohistochemical analyses and found the importance of active proteolysis of a histone acetylation reader protein in the chemoresistance of cancer cells under hypoxic conditions.

RESULTS: We identified the histone acetylation reader protein as a target of proteasomal degradation under hypoxic conditions. Moreover, we found that inactivation of an O_2/Fe^{2+}/α-ketoglutarate-dependent dioxygenase triggered the degradation of the histone acetylation reader protein by the proteasome system upon hypoxia. The proteolysis was observed in hypoxia-inducible factor 1β (HIF-1β) knockout cells as well as their parental cells, suggesting HIFs'-independency. Consistently, the expression levels of the histone acetylation reader protein were markedly lower in perinecrotic hypoxic regions in both xenografted and clinical tumor tissues. The proteolysis of the histone acetylation reader protein was accompanied by a decrease in the amount of acetylated histone H4 and inhibited cell cycle progression from the early to late S phase under hypoxia. The S phase retardation caused cancer cell chemoresistance, which was blocked by the overexpression of the histone acetylation reader protein.

CONCLUSIONS: Degradation of the histone acetylation reader protein induces chemoresistance of cancer cells under hypoxia through heterochromatinization and the subsequent S phase retardation; therefore, inhibition of the proteolysis is expected to be a strategy to overcome chemoresistance of hypoxic tumor cells.

REFERENCES:

[1] S. Kizaka-Kondoh *et al.*, Tumor hypoxia: a target for selective cancer therapy. Cancer Sci, **94** (2003) 1021-1028.

[2] S. Kizaka-Kondoh *et al*. The HIF-1-active microenvironment: an environmental target for cancer therapy. Adv Drug Deliv Rev, **61** (2009) 623-632.

[3] H. Harada. Hypoxia-inducible factor 1-mediated characteristic features of cancer cells for tumor radio-resistance. J Radiat Res. **57** (2016) 99-105.

[4] S. Koyasu, M. Kobayashi, Y. Goto, M. Hiraoka, H. Harada. Regulatory mechanisms of hypoxia-inducible factor 1 activity: Two decades of knowledge. Cancer Sci. 109 (2018) 560-571.

[5] A. Nagao, M. Kobayashi, S. Koyasu, C.C.T. Chow, H. Harada. HIF-1-dependent reprogramming of glucose metabolic pathway of cancer cells and its therapeutic significance. Int J Mol Sci. 20 (2019) 238.

PR1-4 Cancer-Targeting Hyaluronic Acid/Carboranyl Pyrene Complex for Boron Neutron Capture Therapy

K. Yamana[1], R. Kawasaki[1], Y. Sanada[2], S. Masunaga[2], M. Suzuki[2], Y. Sakurai[2], A. Tabata[3], K. Bando[3], K. Yoshikawa[3], K. Sugikawa[1], T. Nagasaki[3], and A. Ikeda[1]
[1]Program of Applied Chemistry, Graduate School of Advanced Science and Technology, Hiroshima University
[2]Institute for Integrated Radiation and Nuclear Science, Kyoto University
[3]Department of Applied Chemistry and Bioengineering, Graduate School of Engineering, Osaka City University

INTRODUCTION: With minimal invasiveness and spatiotemporal therapeutic effects, boron neutron capture therapy (BNCT) is one of the most robust candidates for the treatment of cancer. In this therapy, destruction of cancer cells is achieved by the energy of particle beam generated by nuclear reaction between boron (^{10}B) and thermal neutrons, that is boron neutron capture reaction [1]. Moreover, the effective range of the energy is corresponding to the size of single cells, suggesting BNCT can eliminate cancer cells without affecting healthy cells if boron agents can be delivered to cancer cells with high specificity. For these points of views, success of BNCT is highly dependent on the selective and efficient delivery of boron agents to tumor cells. Currently, two types of boron agents, L-boronophenylalanine (L-BPA) and sodium boronocaptate (BSH) are clinically available. However, several issues such as water-solubility, tumor selectivity, tumor accumulation, and retention capacity in bloodstream are remaining in delivery with these two boron agents. Therefore, development of platforms for boron delivery has been desired to exploit therapeutic efficacy of BNCT. In this study, we developed the complex of pyrene substituted carborane (CBP-H) with sodium hyaluronate (HA) as cancer cell targeted boron agents for BNCT (Fig. 1). HA enabled to solubilize hydrophobic carboranes and strong fluorescence properties derived from aggregation induced emission (AIE) are powerful means to visualize subcellular distribution of boron agents [2]. The excellent deliverability of the HA/CBP-H complex through CD44 [3] that is overexpressed on cancer cells enabled to boost the efficacy of BNCT.

RESULTS and DISCUSSION: The complex of CBP-H with HA was prepared by high-speed vibration milling method as previously reported [4]. The formation of the CBP-H/HA complex was confirmed by measuring UV-Vis absorption spectra and fluorescence spectra. Current systems enabled to dissolved hydrophobic carborane derivatives at most 730 μM (boron concentration, 7300 ppm). Moreover, the UV-Vis absorption spectra of CBP-H got broadened after complexation with HA, suggesting the CBP-H encapsulated with HA forms self-aggregate. In addition, the complex exhibited strong AIE properties that is powerful means to visualize the subcellular distribution of CBP-H. Hydrodynamic diameter of the complex

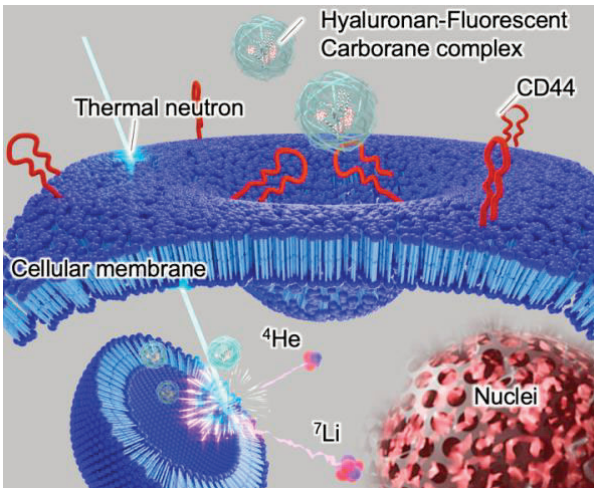

Fig. 1 Schematic illustration of BNCT using the complex of fluorescent carborane with hyaluronic acid.

obtained was estimated to be 200 nm with relatively narrow dispersity (PDI, 0.12). The size of complexes corresponds to passive tumor targeting, enhanced permeable and retention effect (EPR effect).

We evaluated the efficacy of BNCT in affecting cell viability of HA/CBP-H complex against murine colon cancer cell lines (colon26). After 24 h co-incubation with HA/CBP-H, colon26 cells were treated with thermal neutron irradiation with a fluence (6.3×10^{11} n·cm^{-2}). No apparent cytotoxicity was found in the absence of thermal neutron irradiation, suggesting current system is appropriate as a boron agent for BNCT. On the other hand, thermal neutron irradiation induced cytotoxicity against colon 26 treated with HA/CBP-H complex. Moreover, the IC_{50} value of HA/CBP-H complex is 0.074 ppm, which is slightly lower than that of clinically available boron agent, L-BPA/fructose complex (0.080 ppm). The competitive inhibition assay using free HA revealed cellular uptake mechanism of current system is dominantly relying on CD44-mediated endocytosis, as we expected. Furthermore, we successfully visualized the delivered CBP-H from their strong fluorescent properties and large part of CBP-H was distributed in lysosomes.

In conclusion, we developed cancer-targeting fluorescent carborane/hyaluronic acid complex as a boron agent for BNCT. Current system enabled to visualize the subcellular distribution of boron agents and exhibited excellent therapeutic efficacy of BNCT. These results suggest that our system has a promising potential as a boron agent for BNCT.

REFERENCES:

[1] J. A. Coderre, G. M. Morris, *Radiat. Res*. **7**, 1511. (1999).
[2] J. Ochi, K. Tanaka, Y. Chujo, *Angew. Chem. Int. Ed.*, **59**, 9841. (2020).
[3] M. Zöller, *Nat. Rev. Cancer*, **11**, 254. (2011).
[4] R. Kawasaki, K. Yamana, R. Shimada, K. Sugikawa, A. Ikeda, *ACS Omega*, **6**, 3209. (2021).

PR1-5 An evaluation of stratified mouse model and the response of tumor cells to BNCT

S. Imamichi[1,2,3,4], L. Chen[2,3], Y. Tong[3], A. Takahira[3], T. Onodera[2,3], Y. Sasaki[2,3], M. Ihara[2,3], Y. Sanada[4], M. Suzuki[4], S. Masunaga[4] and M. Masutani[1,2,3]

1 Division of Boron Neutron Capture Therapy, EPOC, National Cancer Center

2 Lab. of Collaborative Research, Division of Cell Signaling, Research Institute, National Cancer Center

3 Dept. of Molecular and Genomic Biomedicine, Center for Bioinformatics and Molecular Medicine, Nagasaki University Graduate School of Biomedical Sciences

4 Institute for Integrated Radiation and Nuclear Science, Kyoto University

INTRODUCTION: Boron neutron capture therapy (BNCT) is based on nuclear reactions and the reaction occurs between thermal neutron and boron-10. Generated alpha particle and lithium nuclei in a short length causes cancer cell killing. For the clinical trials, boron compounds such as ^{10}B-boronophenylalanine (BPA) have been used. Accelerator-based BNCT systems have been developed recently. Therefore, accurate assessment of the extent of cell and DNA damages by boron neutron capture reaction (BNCR) is important to improve BNCT. However, it is difficult to measure or calculate the irradiated dose. This is because that the neutron beam is attenuated in objects and delivered dose by BNCT is affected by various factors including boron uptake and neutron dose. We previously observed extensive DNA damage such as γ-H2AX foci, and an increased poly(ADP-ribose) level in the rat lymphosarcoma model[1]. We also performed comprehensive analysis of proteome for human squamous carcinoma SAS cells after BNCR treatment[2]. These results suggested that the changes in the particular protein levels may be involved in the early response of BNCT. In this study, we tried to evaluate the deliverd doses to beam-depth direction in mice stratified in three layers. We also investigated the dynamics of genes and proteins after BNCR or neutron beam irradiation in comparison with the γ-ray irradiation.

EXPERIMENTS: We used human squamous cell line SAS, C57BL/6J male mice of 5 weeks old. For BNCR experiment, ^{10}B-BPA fructose complex (BPA) was used as a boron compound, and neutron irradiations at KUR reactor was operated at 1 MW. Three mice were positioned in three layers (stratified model) or in a single layer against irradiation port. The local irradiations to the mouse hind legs were also performed at the same time. Local irradiations to mouse legs were operated using ^{6}LiF containing thermal neutron shield. BPA were administrated to all mice approximately 30 min before irradiation and added to vials of cell suspension at least 60 min before the irradiation. We used gold foil activation analysis for the measurement of thermal neutron fluences and thermoluminescence dosimeter (TLD) for the measurement of the γ-ray doses including secondary γ-ray. Total physical dose calculation was carried out using the flux-to-dose conversion factor by the sum of the absorbed doses resulting from ^{1}H(n, γ)^{2}D, ^{14}N(n, p)^{14}C, and ^{10}B(n, α)^{7}Li reactions, as previously described. To analyze the acute cellular responses, cell culture supernatants were filtrated and analyzed 6 and 24 hrs after irradiation. RNA and proteins were also isolated and RNA expression levels were examined using real-time PCR and protein levels were analyzed by ELISA.

RESULTS:

Table 1. Irradiated doses at stratified positions (three layers) of mice (cart, irradiation room)).

Irradiation time [min]	Position	Thermal neutron fluence [/cm^2]	Thermal neutron [Gy]	Epi-thermal neutron [Gy]	Fast neutron [Gy]	Gamma-ray [Gy]	Physical dose [Gy]
60	Closest	3.5E+12	0.47	0.050	0.35	0.21	1.1
	Center	1.7E+12	0.22	0.024	0.17	0.27	0.68
	Farthest	8.7E+11	0.12	0.013	0.09	0.23	0.44

Table 2. Delivered doses for local irradiation of mouse legs (cart, irradiation room).

Irradiation time [min]	Thermal neutron fluence [/cm^2]	Thermal neutron dose [Gy]	Epi-thermal neutron dose [Gy]	Fast neutron dose [Gy]	Gamma-ray dose [Gy]	Physical dose [Gy]
60	4.8E+12	0.63	0.068	0.47	0.7	1.9
60	5.2E+12	0.70	0.075	0.52	0.67	2.0

Table 3. Irradiated doses of mice (single layer, E-4 rail port).

	Irradiation time [min]	Sample	Thermal neutron [/cm^2]	Thermal neutron [Gy]	Epi-thermal neutron [Gy]	Fast neutron [Gy]	Gamma-ray [Gy]	Total dose [Gy]
1	50	Top	4.6E+12	0.62	0.07	0.47	1.0	2.1
		Center	4.7E+12	0.63	0.07	0.47	1.0	2.2
		Bottom	4.7E+12	0.63	0.07	0.47	1.0	2.2
2	50	Top	4.6E+12	0.61	0.07	0.46	1.3	2.4
		Center	4.9E+12	0.66	0.07	0.49	1.3	2.5
		Bottom	4.8E+12	0.65	0.07	0.48	1.3	2.5

The measurement of thermal neutron fluence and doses for stratified mice model (three layers) and local irradiation to legs were performed twice, respectively, and the average data are shown in Tables 1 and 2. For the stratified positions, the physical doses between the two mice, closest and farthest from the irradiation port, showed approximately 2-fold difference. Depending on the distance from the irradiation port, delivered thermal neutron doses decreased thereby allowing the evaluation of biological effects on beam-depth direction. Irradiation data of 3 mice set in a single layer to rail port showed similar doses at the irradiated surface of mice (Table 3).

We also observed that *HMGB1* mRNA level in culture supernatant increased depending on the increase in doses 24 hrs after neutron beam irradiation with BPA. The results suggest a potential role of HMGB1 as a biomarker for evaluation of BNCT response.

REFERENCES:

[1] M. Masutani et al., Appl. Rad. Iso., 104 (2014) 104-108.

[2] A. Sato et al., Appl. Rad. Iso., 106 (2015) 213-219.

PR1-6 Attempts to sensitize tumor cells by exploiting the tumor microenvironment

Y. Sanada, T. Takata, Y. Sakurai, H. Tanaka and S. Masunaga

Institute for Integrated Radiation and Nuclear Science, Kyoto University

INTRODUCTION: Hypoxia and glucose deprivation have been suggested to play important roles in resistance to radiation [1]. Attempts to sensitize tumor cells by exploiting the tumor microenvironment have been studied. A major mediator of the cellular hypoxic response, hypoxia inducible factor 1 (HIF-1), is a potential target for cancer therapy, because it transcriptionally regulates a number of genes, including those involved in glucose metabolism, angiogenesis and resistance to chemotherapy and radiation therapy [2]. We previously reported that the disruption of Hif-1α enhanced the sensitivity of murine squamous cell carcinoma (SCC VII) cells to gamma-ray [3]. We have investigated whether the disruption of Hif-1α affects the sensitivity of SCC VII cells to the boron neutron capture reaction (BNCR). Previous studies reported that HIF-1 is likely involved in DNA damage and DNA repair. We have found that Hif-1α-deficient SCC VII cells exhibit higher amount of DNA damage than SCC-VII cells. The intracellular ^{10}B levels in Hif-1α-deficient cells was higher than SCC-VII cells. In the present study, we investigated SLC7A5 expression profiles in SCC VII cells. Unfortunately, antibodies against mouse SLC7A5 protein in SCC VII cells were not available. Therefore, we established SCC VII cells expressing SLC7A5-6xHis proteins.

EXPERIMENTS: In order to establish SCC VII cells expressing SLC7A5-6xHis proteins, a targeting vector was generated. SCC VII cells were transfected with this targeting vector and treated with G418 for selection. A CreER expression vector was used for recombination between loxP sites. G418-senstitive clone (SCC VII -S7A5-H) was isolated and used for analysis of SLC7A5 expression profiles.
SCC VII-S7A5-H and SCC VII-S7A5-H-Hif-1α-deficient cells were grown under hypoxic conditions. SLC7A5 expression profiles were analyzed by Western blotting.

RESULTS: We examined whether SLC7A5 protein levels were affected under hypoxic conditions and the disruption of HIF-1α. SLC7A5-6×His protein levels decreased after 4 h and then increased near to the base level. HIF-1α protein levels continued to be elevated. If Hif-1α gene was disrupted, SLC7A5-6×His protein levels were not significantly decreased under hypoxia.

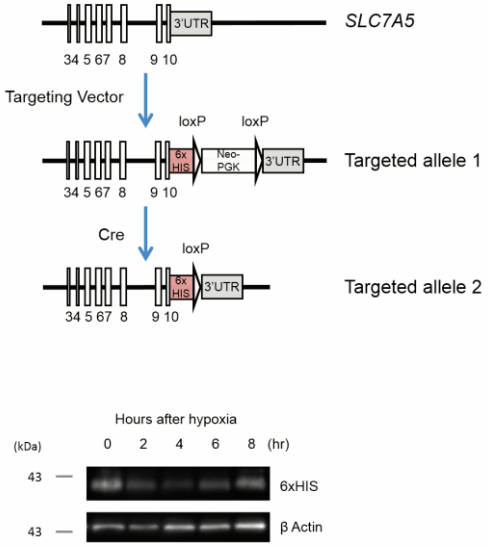

Fig. 1. (Top) Generation of SCC VII cells expressing SLC7A5-6xHis proteins. (Bottom) Effects of hypoxia on the expression of SLC7A5-6xHis protein levels in SCC VII. β Actin was used as a loading control.

REFERENCES:

[1] S. Masunaga et al., Int. J. Rad. Biol. 92 (2016) 187–194.
[2] Z. Luo et al., Neuropharmacology. 89 (2015) 168–174.
[3] Y. Sanada et al., Int. J. Rad. Biol. 94 (2018) 88-96.

I-1. PROJECT RESEARCHES

Project 2

PR2 Project Research on Advances in Isotope-Specific Studies Using Muti-Element Mössbauer Spectroscopy

M. Seto

Institute for Integrated Radiation and Nuclear Science, Kyoto University

OBJECTIVES AND PERFORMED RESEARCH SUBJECTS:

The main objectives of this project research are the investigation of the fundamental properties of new materials and the development of the advanced experimental methods for multi-element Mössbauer spectroscopy. One of the most unique features of the Mössbauer spectroscopy is to extract element-specific or isotope-specific information. Since the Mössbauer resonance line is extremely narrow, hyperfine interactions are well resolved and give us the information on the surrounding electronic states and magnetism. Therefore, promotion of the variety of Mössbauer isotope provides more useful and valuable methods for modern precise materials science of complex systems, such as biological substances, multi-layer films, and complicated-structured matter.

In this project research, each group performed their research by specifying a certain isotope:

- ^{57}Fe in P2-1, P2-2, P2-3 and P2-4
- ^{119}Sn and ^{151}Eu in P2-5
- ^{197}Au in P2-6
- ^{119}Sn and ^{197}Au in P2-7
- Development for other isotopes in P2-8

Due to the influence of COVID-19, a part of planned researches had not been performed. Main subjects from these researches are as follows:

P2-1 Peak intensity of quadrupole doublet of cordierite by single crystal Mössbauer microspectroscopy (K. Shinoda *et al.*)

P2-2 Low-temperature behavior of Mössbauer spectra for Fe_2O_3-Al_2O_3 solid solution (S. Takai *et al.*)

P2-3 Characterization of steel microstructure using Mössbauer spectroscopy (G. Miyamoto *et al.*)

P2-4 Mössbauer study of diluted iron nanoparticles (R. Masuda *et al.*)

P2-5 Research on magnetism in novel Kondo lattice II (Y. Kamihara *et al.*)

P2-7 ^{119}Sn Mössbauer study of absorbed Sn on metallic oxide (Y. Kobayashi *et al.*)

P2-8 Development of Single-Line Compounds for ^{166}Er Mössbauer Spectroscopy (S. Kitao *et al.*)

MAIN RESULTS AND CONTENTS OF THIS REPORT:

K. Shinoda *et al.* (P2-1) have developed the Mössbauer microspectrometer to characterize the electric field gradient tensor from the anisotropic intensity ratios of quadrupole doublets. Thin sections of cordierite ($(Mg,Fe)_2Si_5Al_4O_{18}$) with a hexagonal crystal structure and that with a orthorhombic structure are compared by using the ^{57}Fe-Mössbauer microspectrometer. The results showed the electric field gradient were similar in both cordierites. The results suggest that the second neighboring atoms give little effect to the electric field gradient.

S. Takai *et al.* (P2-2) studied low-temperature behavior of Fe_2O_3-Al_2O_3 solid solutions. Although the anomalous behavior was found in heat capacity at around 4K, the Mössbauer spectra did not show any drastic change. Therefore, the anomalous behavior in heat capacity is supposed not to be due to the change in the magnetic structure.

G. Miyamoto *et al.* (P2-3) investigated the transformation-induced-plasticity (TRIP) steels, which have high strength and high ductility using metastable retained austenite. The ^{57}Fe-Mössbauer study was performed to understand the microstructures of carbide precipitation and carbon enrichment behavior. The Mössbauer spectra of the specimen with 180-min heat treatment showed a decomposition of fcc phase and the existence of cementite or eta-carbide.

R. Masuda *et al.* (P2-4) studied the iron nanoparticle sample prepared by the laser ablation method. The Mössbauer spectra of diluted iron nanoparticles sealed in the ionic solvent were successfully measured. The spectra confirmed its Fe^{3+} property with a size distribution of the nanoparticles.

Y. Kamihara *et al.* (P2-5) investigated a novel compound of $EuSn_2As_2$. The ^{119}Sn- and ^{151}Eu-Mössbauer study have been performed to reveal its magnetic property. Both of Sn and Eu spectra showed the magnetic splitting at 4.2K and the distributions of the internal magnetic fields were obtained from the refined analyses.

Y. Kobayashi *et al.* (P2-7) studied the adsorbed Sn on metallic oxides by ^{119}Sn-Mössbauer spectroscopy. The spectrum of the adsorbed Sn on δ-MnO_2 was similar to that of SnO_2. That implies the electronic structure of the adsorbed Sn is close to SnO_2.

S. Kitao *et al.* (P2-8) performed some improvements for the source preparation in several less-common Mössbauer spectroscopy. As for ^{166}Er-Mössbauer spectroscopy, a single-line source, $Ho_{0.4}Y_{0.6}H_2$ and a single-line absorber, ErH_2 was successfully synthesized. This source and the absorber are useful for various researches for Er Mössbauer spectroscopy even in low temperatures.

PR2-1 Peak intensity of quadrupole doublet of cordierite by single crystal Mössbauer microspectros-copy

K. Shinoda[1], Y. Kobayashi[2]

[1]*Department of Geosciences, Graduate School of Science, Osaka City University*
[2]*Institute for Integrated Radiation and Nuclear Science, Kyoto University*

INTRODUCTION: Cordierite ($(Mg,Fe)_2Si_5Al_4O_{18}$) is a rock-forming mineral which belongs to cyclosilicate. The crystal structure of cordierite is characterized by honeycomb rings. The honeycomb rings of cordierite consist of four SiO_4 and two AlO_4 tetrahedra. Governed by the Al-avoidance rule, two Al ions occupy opposite sites in the honeycomb rings, resultantly, Si and Al ions are ordered in tetrahedral site. Ordered cordierite belongs to the orthorhombic crystal system. In cordierite which crystallized at high temperature, Si and Al ions are arranged in disorder state. As the result, the disordered cordierite belongs to hexagonal crystal system. In the crystal structure of cordierite, Fe ion occupies a octahedral site which is surrounded by three tetrahedral sites including Si and Al. Five Si and four Al occupy the added nine tetrahedral site in the unit cell of cordierite. Since nine Si and Al are arranged in the ordered state in the orthorhombic cordierite, Si and Al around the octahedral site are also ordered. On the other hand, Si and Al around the octahedral site disordered in the hexagonal cordierite. Mössbauer spectra of cordierite show quadrupole doublet.

Intensities of component peaks in a quadrupole doublet of a thin section as a single crystal are asymmetric and vary depending on the angle between the direction of incident γ-rays and the crystallographic orientation of the thin section. Intensity of quadrupole doublet (I^h / I^{total}) means a ratio between area of the peak of the higher energy (I^h) and total area of the doublet ($I^{total}= I^h + I^l$) (sum of I^h and area of the lower energy (I^l)). The intensity of component peaks of a ^{57}Fe Mössbauer doublet is related to an electronic field gradient (EFG) tensor of the site containing Fe^{2+} (Zimmermann, 1975 and 1983). Electric gradient is in inverse proportion to the cube of distance between the Mössbauer nuclei and the neighboring atoms. How far is electric gradient at Mössbauer nuclei influenced by the neighboring atoms?

In hexagonal and orthorhombic cordierite, the first neighboring atoms are commonly oxygens. However, the second neighboring atoms in the orthorhombic cordierite are expected to be different from those of hexagonal cordierite. To compare quadrupole doublet of cordierite, Mössbauer spectra of hexagonal and orthorhombic cordierite were measured. In this study, single crystals of natural cordierite were used for this study. In the crystal, black and white crystals coexist. The black crystal shows hexagonal X-ray diffraction pattern, and the white crystal shows orthorhombic X-ray diffraction pattern. Crystallographically oriented thin sections perpendicular to *c** was prepared by measuring X-ray diffraction patterns by using X-ray precession camera. Mössbauer spectra of thin section of single crystal of cordierite were measured under γ-ray parallel to the *c**-axis.

EXPERIMENTS and RESULTS: Mössbauer measurements were carried out in transmission mode on a constant acceleration spectrometer with an Si-PIN semiconductor detector (XR-100CR, AMPTEK Inc.) and multi-channel analyzer of 1024 channels. A 3.7GBq ^{57}Co/Rh of 4mmϕ in diameter was used as γ-ray source. An ^{57}Fe-enriched iron foil was used as velocity calibrant. The two symmetric spectra were folded and velocity range was ±5mm/s. Thickness corrections of raw spectra were not done.

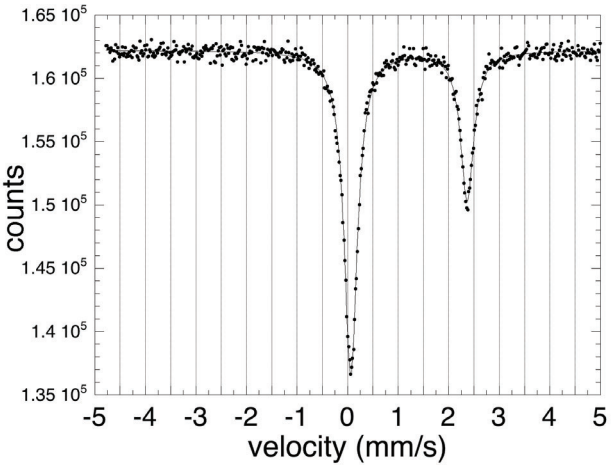

Fig.1 Mössbauer spectrum of hexagonal cordierite measured under γ-ray parallel to the *c**-axis.

Fig.1. Mössbauer spectrum of hexagonal cordierite measured under γ-ray parallel to the *c**-axis. Isomer shift, Q-splitting, line width and intensity of quadruploe doublet were 1.21, 2.30, 0.32 mm/s and 0.31, respectively. Orthorhombic cordierite shows quite resemble spectrum to the hexagonal cordierite The Mössbauer parameters were also the same values. The results suggest that the second neighboring atoms give little effect to electric gradient at Mössabauer nuclei.

REFERENCES

[1] Zimmermann, R. (1983) Advances in Mössbauer spectroscopy (Thosar, B.V. Ed.). pp.273-315, Elsevier Scientific Publishing Co. Amsterdam.
[2] Zimmermann, R. (1975) Nucl. Instr. and Meth. **128**, 537-543

PR2-2 Low-Temperature Behavior of Mössbauer Spectra for Fe_2O_3-Al_2O_3 Solid Solution

S. Takai[1], T. Yabutsuka[1], F. Song[1], T. Yao[2], S. Kitao[3], M. Seto[3]

[1]*Graduate School of Energy Science, Kyoto University*
[2]*Kyoto University*
[3]*Institute for Integrated Radiation and Nuclear Science, Kyoto University*

INTRODUCTION: It is well known that solid solution range of Fe_2O_3-Al_2O_3 system is much restricted due to the lattice parameter mismatch, while α-Fe_2O_3 and α-Al_2O_3 possess the isostructure of corundum-type [1]. In recent years, we have reported the formation of corundum-type structured solid solution for Fe_2O_3–Al_2O_3 system by means of mechanochemical method through the whole compositional range. Since the most of composition has been newly prepared by this method, we have investigated these solid solutions by means of EXAFS, Mössbauer spectroscopy, magnetic susceptibility, or heat capacity measurement as well as neutron diffraction.

In the previous study (30121), we have carried out Mössbauer spectroscopy on $(Fe_2O_3)_{1-x}(Al_2O_3)_x$ solid solutions at room temperature and it is revealed that the spectra varies from sextet peaks at x = 0 into almost doublet at x = 0.50. This indicates that substitution of non-magnetic aluminum ions allows the change in magnetic properties from weak ferromagnetism to paramagnetic state by the dilution of spin interactions. In the last year (31P8-3), we have measured the low temperature Mössbauer spectra down to 10 K, where variation from doublet into sextet spectra is observed with decreasing temperature for x = 0.5 of $(Fe_2O_3)_{1-x}(Al_2O_3)_x$ system.

On the other hand, heat capacity measurement showed the anomalous behavior at 4 – 5 K as shown in Fig. 1. Since no additional information in this region has been obtained, we have carried out Mössbauer spectroscopy in the liquid helium temperature.

EXPERIMENTS: Stoichiometric mixture of γ-Fe_2O_3 and γ-Al_2O_3 reagents were put into a silicon nitride milling pod with 10 milling balls. In the present study, the compositions were selected as x = 0.50 for $(Fe_2O_3)_{1-x}(Al_2O_3)_x$ system. Mechanical alloying has been carried out using a planetary ball milling machine operated at 800 rpm for 240 min. The crystalline phase of the obtained sample was confirmed by X-ray diffraction.

For the measurement of Mössbauer spectroscopy, ^{57}Co in Rh was employed as the γ-ray source. Doppler velocity scale has been calibrated by using Fe foil. The Mössbauer spectra have been measured at various temperatures using a liquid He cryostat.

RESULTS: The Mössbauer spectra measured at various temperatures are represented in Fig. 2. It is consistent with the previous measurement that the profile showing doublet at 300 K changes into sextet below 40 K. As for the data collected at 4.2 K, drastic change in profile is not observed from 10 K. Then the heat capacity anomaly observed at low temperature is supposed not to be accompanied by significant change in magnetic structure. Further investigation should be made to explain the anomalous heat capacity behavior.

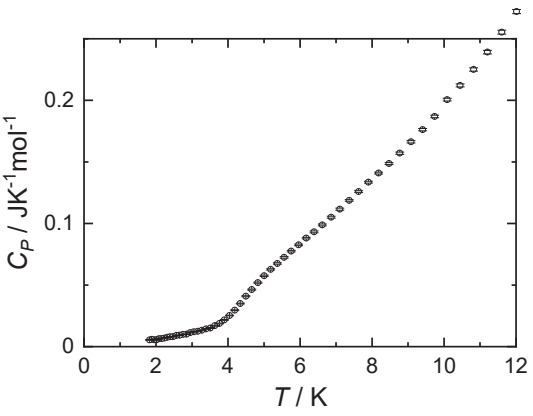

Fig. 1 Heat capacities of $(Fe_2O_3)_{0.5}(Al_2O_3)_{0.5}$.

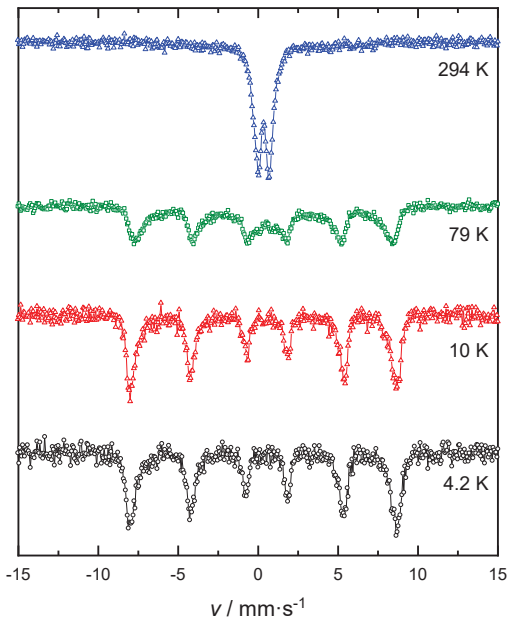

Fig. 2 Temperature dependence of Mössbauer spectra for $(Fe_2O_3)_{0.5}(Al_2O_3)_{0.5}$.

REFERENCES:

[1] A. Muan et al., *J. Am. Ceram. Soc.*, 39 (1956) 207-214.
[2] S. Takai et al., *Solid State Ionics*, 313 (2017) 1-6.

PR2-3 Characterization of steel microstructure using Mössbauer spectroscopy

G. Miyamoto, M. Watanabe[1], Y. Kobayashi[2], T. Furuhara

Institute for Materials Research, Tohoku University,
[1] Graduate School of Materials Science and Engineering, Tohoku University.
[2]Insitute for Integrated Radiation and Nuclear Science, Kyoto University

INTRODUCTION: TRIP steels with high strength and high ductility using metastable retained austenite have been developed and commercialized in order to improve both fuel efficiency and crash safety of automobiles. Understanding the stability of austenite is a key factor for improving the properties of TRIP steels.

In TRIP steels, the austenite is stabilized by enriching the carbon in the austenite through phase transformation during heat treatment. On the other hand, if the heat treatment conditions are inappropriate, carbides may form and inhibit the carbon enrichment [1, 2]. Therefore, a quantitative understanding of carbide precipitation and carbon enrichment behavior in austenite is important for microstructure control of TRIP steels.

Since the Mössbauer spectrum is sensitive to the energy levels of Fe atoms, it has the potential to identify and quantify the amount of austenite and carbide types in steel. Therefore, the purpose of this study is to investigate the amount of austenite and carbide precipitation behavior in TRIP steel using Mössbauer measurements.

EXPERIMENTS: Fe-2Mn-1.5Si-0.4C TRIP steel heat treated at various temperature and conditions were used. Thin foils of about 20μm in thickness were prepared from the heat-treated specimen and Mössbauer measurement is performed on the thin foil at room temperature to identify and quantify the amount of austenite and carbides. In order to elucidate the faint signal from the small amount of austenite or carbide, Mössbauer measurements were carried out for12-13 days, that is four to five times longer than normal measurement.

RESULTS: Fig. 1 shows Mössbauer spectra taken from the TRIP steels heat-treated at 400°C for 30 min and 180 min. Both spectra consist of six bcc peaks and one fcc peak. Intensity of bcc peak after 180 min is much weaker than that for 30 min, indicating decomposition of fcc phase after 180 min treatment. Volume fraction of fcc phase for 30 min and 180 min estimated from Mössbauer are 19.3% and 4.1%, respectively, and they are in good agreement with those fractions estimated from XRD measurements, 22.2 % and 5.2 %.

Fig. 2 compares magnified Mössbauer spectra with fitted ones, where only bcc and fcc phases are considered in the fitting. Fitted curve reproduces measurement quite well in the 30 min specimen, that indicates the specimen contains only bcc and fcc phases. On the other hand, fitting and measurement deviates significantly in 180 min specimen as indicated by red arrows and this discrepancy is considered to be the presence of other phase, namely iron carbide. Preliminary fitting assuming one of the cementite and eta-carbides cannot explain this discrepancy but fitting assuming both cementite and eta-carbide gives better agreement. Therefore, simultaneous precipitation of cementite or eta-carbide may occur 180 min heat treatment.

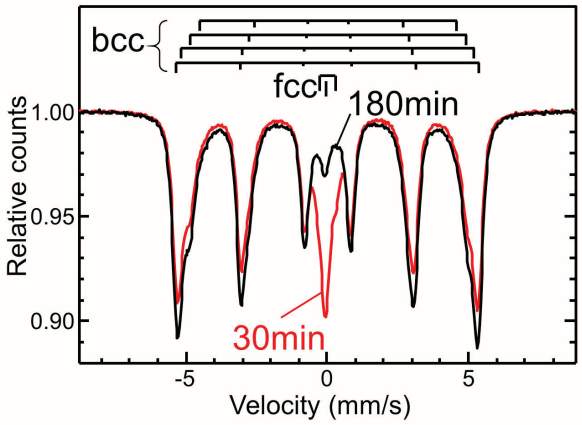

Fig. 1 Mössbauer spectra taken from the TRIP steel transformed at 400°C for 30 min and 180 min respectively.

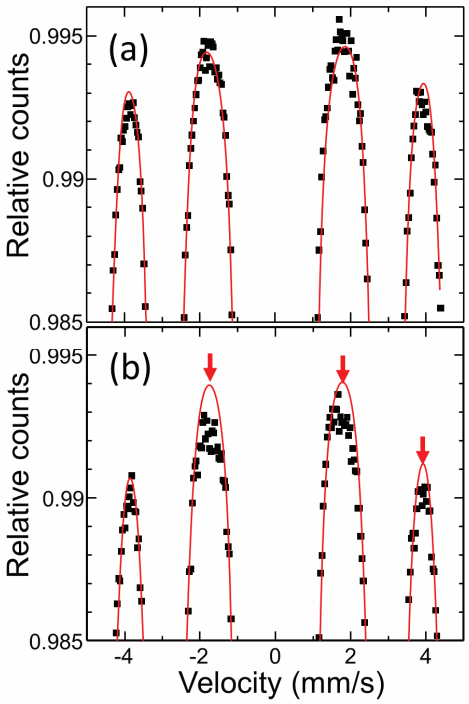

Fig. 2 Magnified Mössbauer spectra taken from the TRIP steel transformed at 400°C for (a) 30 min and (b)180 min. Red curves are fitted one assuming only bcc and fcc phases.

REFERENCES:

[1]Y Xia *et al.,* Acta Mater., **91**(2015), 10-18.
[2]H. Wu *et al.,* Acta Mater., **149**(2018), 68-77.

PR2-4

Mössbauer study of Diluted Iron Nanoparticles

R. Masuda, S. Kitao[1], Y. Kobayashi[1], M. Saito[1], M. Kurokuzu[1], H. Tajima[2]

Graduate School of Science and Technology, Hirosaki University
[1]Institute for Integrated Radiation and Nuclear Science
[2]Graduate School of Science, Kyoto University

INTRODUCTION: Recently, a laser ablation method has been developed. A bulk metal in a solution is locally evaporated by laser ablation to produce nanoparticles through a cooling process of the agglomeration of the evaporated metal in the solution. The nanoparticles produced by this method are easy to handle in air because of the protection by the solution, but they do not have a coating different to the nanoparticles synthesized by the conventional chemical reduction method. It has been pointed out that they may show high reactivity with appropriate isolation, due to the loss of the "protection" by the coating materials.

This catalytic property is attributed to electronic states such as valence. However, the nanoparticles prepared by the laser ablation method are protected by the solvent and the solvent also disturbs various measurement methods to evaluate the electronic states. Therefore, the aim of this work is to elucidate the electronic structure of the Fe nanoparticles prepared by this method by Mössbauer spectroscopy using gamma-rays with high penetrating power.

EXPERIMENTS: The iron nanoparticle sample was prepared by the laser ablation method using an ^{57}Fe-enriched iron foil. The nanoparticles are sealed in ionic liquid. It was cooled down to around 4 K in a refrigerator cryostat to solidify the liquid and to enhance the recoilless fraction of the sample. The Mössbauer spectra was measured using ^{57}Co/Rh radioactive gamma-ray source in KURNS. The velocity scale was calibrated by another ^{57}Fe enriched iron foil.

RESULTS: The Mössbauer spectra measured in 17 days are shown in Fig. 1. Although the concentration of the nanoparticles was considerably less than 100 ppm, the analyzable Mössbauer spectra was successfully obtained. The spectrum showed at least two sites and thus we evaluated it by a two-site model: the non-magnetic doublet and magnetic sextet. The evaluated parameters are summarized in Table I. It is known that the nanoparticle sample sometimes show this type of two-site spectrum due to the magnetic relaxation; when the size of the nanoparticles is not unified and has some distribution, the relatively big nanoparticles show the magnetic sextet, although the relatively small nanoparticles show the non-magnetic doublet, due to the superparamagnetism. In that case, the isomer shifts of the two sites should be identical. The results of our spectrum agree with this condition and thus it is reasonable for us to analyze our spectrum on the basis of two-site model reflecting the size distribution and magnetic relaxation. In fact, the line width of magnetic site is considerably wider than that of the non-magnetic site; this difference is due to the distribution of magnetic hyperfine field, which reflects the size distribution [1.2].

Mössbauer parameters in Table. I shows the electronic states of the nanoparticles is rather Fe^{3+} state than the metallic state. The large internal magnetic field over 50 T is similar to oxides, such as hematite and magnetite. In addition, in literature [2], superparamagnetization effect is seen in the Mössbauer spectra of hematite nanoparticles with the size of typically 10 nm. This size agrees with the size distribution of this nanoparticles evaluated by the electronic microscope; the average and standard deviation of the size was 7.1 nm and 3.5 nm, respectively. This agreement also supports the Fe^{3+} state of the nanoparticles in our sample.

In summary, the Mössbauer spectrum of the very diluted iron nanoparticles synthesized by laser ablation method was successfully measured in situation condition. The spectrum reflects the size distribution of the nanoparticles and shows that the iron was in Fe^{3+} state.

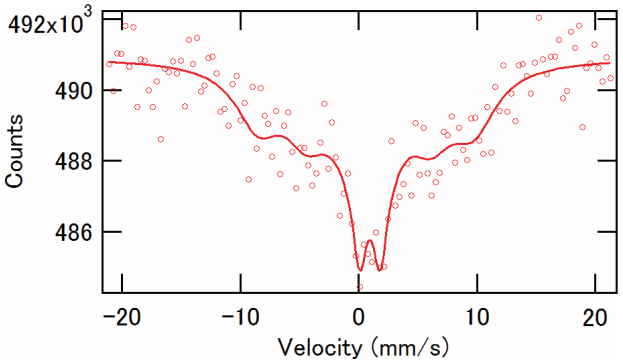

Fig. 1. Mössbauer spectrum of the diluted Fe nanoparticles at 4 K.

Table I. Evaluated parameters of the Mössbauer spectrum.

Site	Non-magnetic	Magnetic
Area ratio	1 (fixed)	5±1
Center shift (mm/s)	0.9±0.1	0.7±0.3
Quadrupole shift (mm/s)	1.7±0.2	0.3±0.4
Internal magnetic field	-	56±2
Line width (mm.s)	1.4±0.4	5±1

REFERENCES:

[1] S. Morup: J. Magn. Magn. Mater. 37 (1983) 39-50.
[2] P. Gütlich, et al., Mössbauer spectroscopy and transition metal chemistry: fundamentals and applications (Springer, Berlin, 2011).

PR2-5 **Research on magnetism in a novel Kondo Lattice II**

Y. Kamihara, R. Sakagami, S. Kitao[1], and M. Seto[1]

Department of Applied Physics and Physico-Informatics , Faculty of Science and Technology, Keio University
[1]Institute for Integrated Radiation and Nuclear Science, Kyoto University

INTRODUCTION: The compounds with a 1:2:2 compositional ratio (so-called "122 compounds") are attractive for thermoelectric materials. Several researchers have defined these materials as "so-called" Zintle phase, although definitions of the Zintle phase are controversial or variety group of concepts by many researchers. $EuSn_2As_2$ is a "so-called" Zintle phase. [1] In 2018, we succeed to make a high quality polycrystalline samples of $EuSn_2As_2$ using a new synthesis technique. [2] In 2020, thermoelectric properties of $EuSn_2As_2$ are demonstrated. [3] Theoretical magnetic phase of Eu sub lattice are calculated as ferromagnetic along to (*a*, *b*) axis and antiferromagnetic along to *c* axis. These magnetic phase are due to *s-f* interaction between Eu 4f electrons via itinerant electrons. A Neel temperature of the Eu sublattice, which has been measured for single crystalline sample, is about 24 K.
In the polycrystalline sample, the Eu sublattice exhibits ferromagnetic phase with spontaneous magnetic moments ~5 μ_B at 2 K under finite magnetic fields. The spontaneous magnetic moments are smaller than those of theoretical Eu^{2+} ions with spontaneous magnetic moments ~7 μ_B. A possible mechanism, which should be origin for the difference between experimental and theoretical magnetic moments of Eu^{2+}, is controversial. In this report, we demonstrate element-specific distributed internal magnetic fields for the polycrystalline $EuSn_2As_2$.

EXPERIMENTS: According to our previous report, polycrystalline samples of $EuSn_2As_2$ were prepared from Eu ingots and Sn-As pellets via a liquid phase reaction in carbon crucibles within evacuated silica tubes. [2] X-ray diffraction measurements at room temperature (RT) were performed in order to characterize the crystallographic phases of powdered sample of as-grown $EuSn_2As_2$ and the crystallographic orientation of small single crystalline $EuSn_2As_2$, which are picked up from the powdered ingot. In this research, we had measured ^{151}Eu and ^{119}Sn Mössbauer spectra for polycrystalline $EuSn_2As_2$ using conventional optical setting. Both of ^{151}Eu and ^{119}Sn Mössbauer spectra demonstrates magnetic splitting at 4.2 K. The experimental spectra had been reported in 2020. [4] The spectra were fitted to Lorenzian line shapes using the MossWinn [5] Program.

RESULTS: Assuming distributed internal magnetic field ($B_{int} = \mu_0 H$), refined internal magnetic field distribution (W) are obtained for both spectra. Figure 1 and Figure 2 show the W of internal B_{int} for ^{151}Eu and ^{119}Sn Mössbauer spectra (MS) at temperature = 4.2 K respectively. [6]

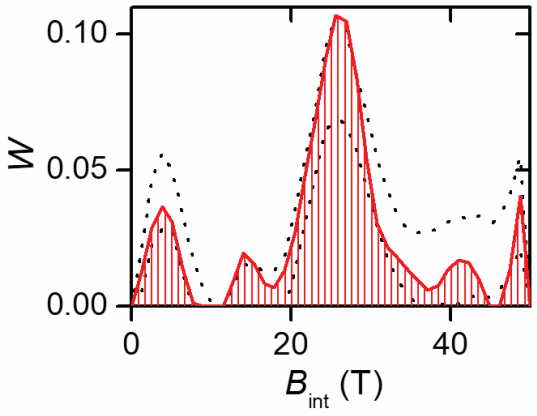

Fig. 1. Distribution (W) of internal magnetic field ($B_{int} = \mu_0 H$) based on the ^{151}Eu Mössbauer spectroscopy (MS) of polycrystalline $EuSn_2As_2$. [6]

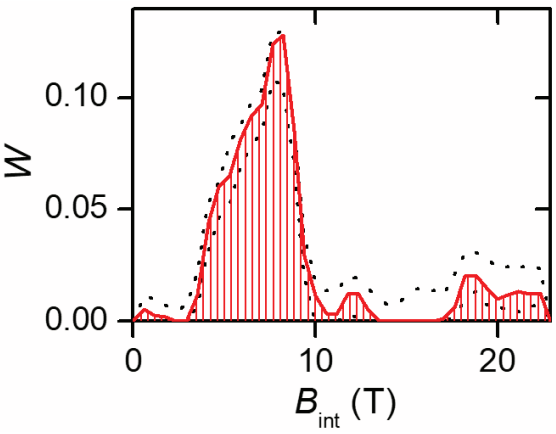

Fig. 2. Distribution (W) of internal magnetic field ($B_{int} = \mu_0 H$) based on the ^{119}Sn Mössbauer spectroscopy (MS) of polycrystalline $EuSn_2As_2$. [6]

REFERENCES:

[1] M. Q. Arguilla, *et al.*, Inorg. Chem. Front. 4, 378 (2017).
[2] R. Sakagami, *et al.*, Mater. Sci. Tech. Jpn. 55, 72 (2018) in Japanese.
[3] R. Sakagami, *et al.*, J. J. Appl. Phys. 60, 035511 (2021).
[4] Y. Kamihara, *et al.*, KURNS Progress Report 2019, PR8-6 (2020).
URL:https://www.rri.kyoto-u.ac.jp/PUB/report/PR/ProgRep2019/PR8.pdf
[5] Z. Klencsar: Mosswinn Program, Budapest, 2001 [http://www.mosswinn.com/].
[6] R. Sakagami, *et al.*, "Magnetic splitting of a Mössbauer spectra of ^{151}Eu and ^{119}Sn of rhombohedral crystal Kondo lattice system $EuSn_2As_2$", The Physical Society of Japan, 2020 Autumn Meeting online (10 Sept. 2020) in Japanese.

PR2-6

Recoil-free fraction in ^{197}Au Mössbauer Spectroscopy for precursor of supported gold cluster catalysts

H. Ohashi, T. Sai, Y. Umetsu, H. Murayama[1], M. Takaki[1], T. Ishida[2], D. Kawamoto[3], Y. Kobayashi[4], S. Kitao[4]

Faculty of Symbiotic Systems Science, Fukushima University
[1]Faculty of Sciences, Kyushu University
[2]Department of Applied Chemistry for Environment, Tokyo Metropolitan University
[3]Faculty of Sciences, Okayama University of Science
[4]Institute for Integrated Radiation and Nuclear Science, Kyoto University

INTRODUCTION:

Though sulfide deposition-precipitation (SDP) method was a kind of new DP method, it was a very unique method and different from DP on several points such as preparation pH. However, until now, the structure of gold sulfide as a precursor synthesized by the SDP method was unknown.

On the other hand, Mössbauer effect (recoilless nuclear resonance) is the phenomenon of resonant absorption of γ-radiation, emitted at the radioactive decay of a nucleus in a radioactive material, which act as absorber. This method is widely used in material research that contains iron (^{57}Fe) and tin (^{119}Sn), which are easy to obtain radioactive isotopes that are radiation sources. However, ^{197}Au Mössbauer spectroscopy has not been widely used because radiation source, ^{197}Pt has short half-life.

The purpose of this study was to analyze the state of gold valence and Au-S bond on gold sulfide synthesized by a similar method of SDP using ^{197}Au Mössbauer spectroscopy.

EXPERIMENTS:

The gold sulfide (Au_2S_x) and activated carbon supported gold sulfide were synthesized by the similar SDP method already reported[1]. Samples obtained were characterized by X-ray Absorption Fine Structure (XAFS) and ^{197}Au Mössbauer spectroscopy. Au L_3 edge XAFS spectra were measured at Kyushu University Beamline (SAGA-LS/BL06). ^{197}Au Mössbauer spectra were measured at Kyoto University Research Institute of Nuclear Science. The ^{197}Pt isotope ($T_{1/2}$ = 18.3 h), γ-ray source feeding the 77.3 keV Mössbauer transition of ^{197}Au, was prepared by neutron irradiation of isotopically enriched ^{196}Pt metal at the Kyoto University Reactor. The measurement temperature was 14 - 20 K, and the measurement was performed by the transmission method.

RESULTS:

The ^{197}Au Mössbauer spectra for the Au_2S_x and activated carbon supported gold sulfide were showed in Fig.1. It showed that the Mössbauer spectrum of Au_2S_x consisted of doublets in shape. Based on the value of IS-QS derived from the synthesized Au_2S_x and $Na_3[Au(S_2O_3)_2]$, the chemical state of gold in Au_2S_x was estimated to be monovalent (Au(I)). Shown in Fig.1 (a), the spectrum of activated carbon supported gold sulfide did not appear when accumulating over 2,500,000 γ-ray-counts. Since XANES spectrum of the sample were similar to that of Au_2S_x, chemical state of gold in the sample was estimated to be Au_2S_x. These results suggested that recoil-free fraction of the sample was quite small, which were exceptionally rare phenomenon. We are going to discuss the details on the fraction.

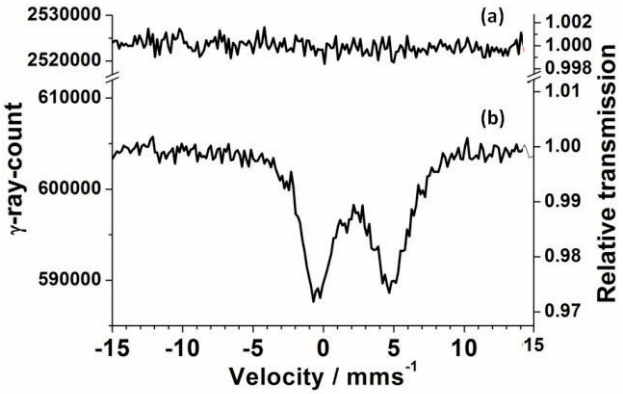

Fig.1.^{197}Au Mössbauer spectra for activated carbon supported Au_2S_x (a) and Au_2S_x (b) prepared by similar SDP method.

REFERENCE:

[1] H. Ohashi *et al.*, "Method for dispersing and immobilizing gold fine particles and material obtained thereby", Patent No. 5010522.

PR2-7 ^{119}Sn Mössbauer Study of Absorbed Sn on Metallic Oxide

Yasuhiro KOBAYASHI, Daisuke KAWAMOTO[1], Shinji KITAO and Makoto SETO

Institute for Integrated Radiation and Nuclear Science, Kyoto University
[1]Faculty of Science, Okayama University of Science

Due to the influence of COVID-19, only some of the submitted projects could be conducted.

INTRODUCTION

There are various compounds and ions in the hydrosphere. Besides, many compounds exist in a state of being attached or adsorbed on the surface of a substance. Sn is one of the ions with many valences, and it forms a variety of compounds in nature. Mössbauer measurements for adsorbed Sn on various metal oxides were performed to investigate the details of the chemical state in nature. It is also important to investigate various adsorptions for the development of new catalysts.

^{119}Sn is the second most measured Mössbauer nucleus after ^{57}Fe. The Mössbauer nuclear transition of ^{119}Sn is a transition between nuclear spins 1/2 and 3/2, and the information from the obtained Mössbauer parameters is almost the same as ^{57}Fe. Due to the similar parameters of the hyperfine structure, the same equipment as the ^{57}Fe Mössbauer measurement can be used for the ^{119}Sn. On the other hand, the change in isomer shift due to the difference in valence is large, so it is a powerful tool for Sn valence evaluation. On ^{119}Sn Mössbauer spectra, the half-width of the peak is wider than Fe, so resolution is inferior.

EXPERIMENTS

^{119}Sn Mössbauer spectroscopy was measured with a conventional Mössbauer device. The radiation source was ^{119m}Sn with a half-life of 293.1 days, and the radiation source matrix is $CaSnO_3$. A 75 μm thick Pd foil was used as a filter to remove 26 keV fluorescent X-rays from the γ-ray source. A Xe proportional counter was used for the detector. The velocity scale was calibrated by replacing the γ-ray source and measuring the ^{57}Fe Mössbauer spectrum of α-Fe with the same spectrometer. The zero-velocity position is the peak position of $BaSnO_3$. This is a commonly used reference position for Sn Mössbauer measurements.

RESULTS

Figure 1 shows the ^{119}Sn Mössbauer spectrum of the compounds SnO and SnO2, and the lowermost is the Mössbauer spectrum of adsorbed Sn on δ-MnO_2. There are impurity components in the SnO spectrum that are thought to be due to the deterioration of the sample. The position of the center of gravity of the spectra differs greatly between SnO and SnO_2. This shift (isomer shift) is a parameter that reflects the difference in the valence of Sn. The Sn adsorbed on δ-MnO_2 has a peak at the same position as SnO_2, indicating that the Sn atoms are Sn^{4+}. The spectrum of absorbed Sn does not show wide splitting, such as the spectrum of SnO. This splitting (quadrupole splitting) reflects the symmetry around the Sn atom, and the smaller splitting means the higher symmetry. Since the splitting of the adsorbed-Sn sample is small, it is considered that the Sn atoms are not isolated and adsorbed on the surface but are adsorbed in an environment close to that of a compound such as SnO_2. Details of the spectra and comparison with other conditions will be made in the future.

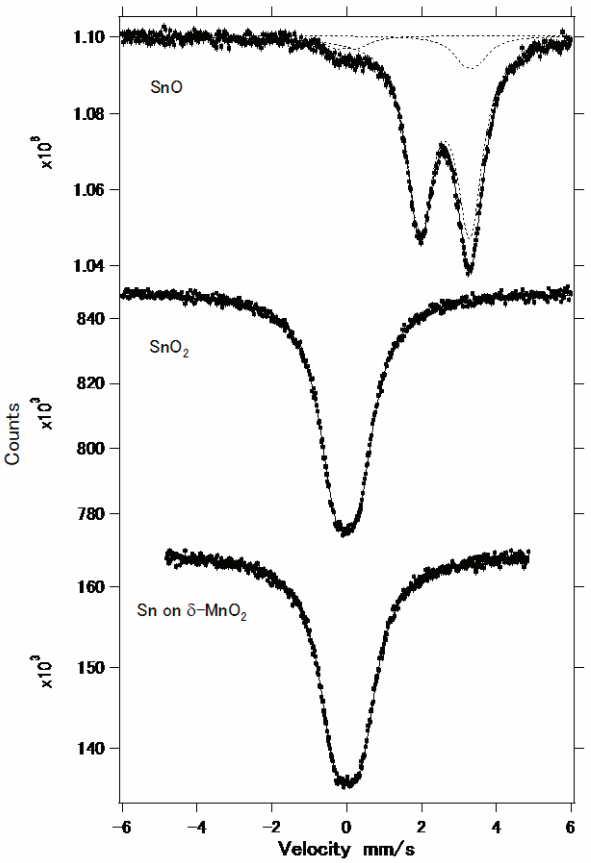

Fig. 1 ^{119}Sn Mössbauer spectra of SnO, SnO_2 and absorbed Sn on δ-MnO_2.

PR2-8 Development of Single-Line Compounds for ^{166}Er Mössbauer Spectroscopy

S. Kitao[1], M. Kobayashi[1], T. Kubota[1], M. Kurokuzu[1], H. Tajima[2], and M. Seto[1]

[1]*Institute for Integrated Radiation and Nuclear Science, Kyoto University*
[2]*Graduate School of Science, Kyoto University*

INTRODUCTION:

The Mössbauer spectroscopy is a powerful method for various investigations of electronic states, magnetic properties, chemical properties, and so on. One of remarkable features is that this method can extract the information of specific isotope. Although about one hundred of Mössbauer energy levels are known, recent Mössbauer activities are quite limited to ^{57}Fe and ^{119}Sn, whose sources are commercially available. In order to promote studies for other less-common Mössbauer isotopes, we have been developing short-lived Mössbauer sources by neutron irradiation at Kyoto University Reactor (KUR). Moreover, some short-lived isotopes can be complementarily produced by high-energy γ-ray irradiation using the electron linear accelerator (KURNS-LINAC). We have already developed preparation methods of the Mössbauer sources for various isotopes (source nuclides in parentheses): ^{61}Ni(^{61}Co), ^{125}Te(^{125m}Te), ^{129}I(^{129}Te,^{129m}Te), ^{161}Dy(^{161}Tb), ^{166}Er(^{166}Ho), ^{169}Tm(^{169}Er), ^{170}Yb(^{170}Tm), ^{197}Au(^{197}Pt), etc. Among these researches, an improvement of ^{166}Er Mössbauer spectroscopy is described in this report.

The 80.6keV level of ^{166}Er is the most useful for Er Mössbauer spectroscopy. Since the natural abundance of ^{165}Ho is 100 %, ^{166}Ho with a half-life of 26.8 hours can be obtained as the Mössbauer source without by-product nuclides even by neutron irradiation of natural Ho. As for the source material, we had used $HoAl_2$, by arc-melting method from Ho and Al. Several ^{166}Er experiments have already been performed using $HoAl_2$ at KUR[1]. However, since $HoAl_2$ has a Curie temperature of about 25 K[2,3], the source temperature had to be kept above 40 K to avoid line broadening by magnetic splitting. To overcome this disadvantage, rare-earth dihydrides can be used as single-line compounds at the temperatures down to 4 K[4].

EXPERIMENTS AND RESULTS:

In this study, we have synthesized rare-earth dihydrides for ^{166}Er Mössbauer experiments, $Ho_{0.4}Y_{0.6}H_2$ as the source and ErH_2 as the absorber. The synthesis procedure is basically similar to that in ref. 4. We used TiH_2 instead of H_2 gas bombe for the H_2 gas source[5]. Since the TiH_2 decomposes by heating and generates H_2 gas, this method is convenient and safer for the H_2 gas handling. The $Ho_{0.4}Y_{0.6}$ was prepared by the arc-melting method from Ho and Y metals. The $Ho_{0.4}Y_{0.6}$, doubly-rapped with Ti and Ta foils, was evacuated in quartz tubes in an electric furnace. The pelletized powder of TiH_2, rapped with Ti foil, is separately evacuated in quartz tubes in another electric furnace. Two tubes are connected by a tube through a liquid N_2 trap with a valve. The valve was open and the evacuation was stopped when the hydridation proceeded. The furnace for the $Ho_{0.4}Y_{0.6}$ was kept at 850 °C before and during the hydridation. The temperature of the furnace for the TiH_2 was changed from about 400 to 800 °C to control the pressure of decomposed H_2. After the hydridation, the quartz tube of $Ho_{0.4}Y_{0.6}H_2$ was quenched into the water. The ErH_2 is prepared similarly using Er metal. The obtained $Ho_{0.4}Y_{0.6}H_2$ was sealed into coin-shaped polyethylene container using polystyrene resin. Typical irradiation condition for the $Ho_{0.4}Y_{0.6}H_2$ containing 20 mg Ho was 15-min irradiation using the pneumatic tube in 1 MW operation of KUR to obtain 140 MBq of ^{166}Ho. The observed Mössbauer spectrum of ErH_2 using ^{166}Ho source in $Ho_{0.4}Y_{0.6}H_2$ at the temperature of 18 K is shown in Fig. 1. Since the recoilless fraction of Er compounds is low at high temperature, the sample and the source were necessary to be cooled. The gamma-rays with the energy of 80.6 keV have been measured by a $CeBr_3$ scintillation detector. The obtained spectrum successfully showed a single-line shape, indicating both the $Ho_{0.4}Y_{0.6}H_2$ source and the ErH_2 absorber has a single-line shape. This source and absorber are useful for various application in Er Mössbauer studies even for the low temperatures. Moreover, the preparation method of rare-earth dihydrides is applicable to synthesize a single-line source or absorber for other rare-earth Mössbauer spectroscopies.

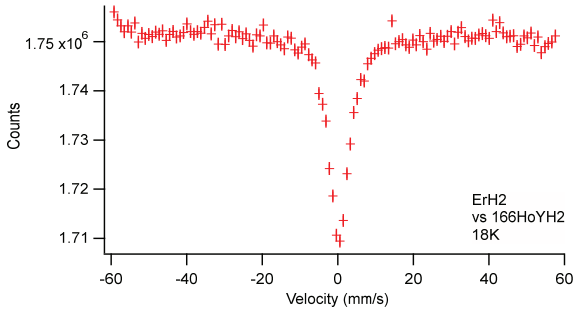

Fig. 1. ^{166}Er-Mössbauer spectrum of ErH_2 at 18 K using ^{166}Ho source in $Ho_{0.4}Y_{0.6}H_2$.

REFERENCES:

[1] S. Nakamura, H. Yokota, S. Kitao, Y. Kobayashi, M. Saito, R. Masuda, M. Seto, Hyperfine Interact. **240**, 75 (2019).
[2] E. Munck, D. Quitmann, S. Hufner, Z. Naturforsch. **21A**, 847 (1966).
[3] E. Munck, D. Quitmann, S. Hufner, Phys. Lett. **24B**, 392 (1967).
[4] J. Stöhr and J. D. Cashion, Phys. Rev. B **12**, 4805 (1975).
[5] D. B. Prowse, A. Vas and J. D. Cashion, J. Phys. D: Appl. Phys. **6**, 646 (1973).

I-1. PROJECT RESEARCHES

Project 4

PR4 The effect of boron neutron capture therapy on normal tissues

M. Suzuki

Institute for Integrated Radiation and Nuclear Science, Kyoto University

In this research project, five research projects were included. One research projects (P4-4 could not be conducted due to delay of begging of KUR by COVID-19).

The effect of normal tissues including lung, liver, brain, and bone were investigated in this study. Details of each project is referred to the following contents.

P4-1: "**The effect of boron neutron capture therapy (BNCT) on normal lung in mice**."

The effect of thermal neutron beam at KUR on normal lung was analyzed with reference to the survival. The mice were sorted into four treatment groups, 40-min, 50-min, 60-min, and 70-min irradiation groups. In each group, six to seven mice were irradiated. In 70-min irradiation group, all the three mice died within 10 days. In 60-min irradiation group, six mice died within an observation period of 12 days, and three mice survive within an observation period of 380 to 540 days. In 50-min irradiation groups, five mice died, and two mice survived within an observation period of 451 to 570 days. In 40-min irradiation groups, two mice died, and five mice survived within an observation period of 465 to 577 days.

P4-2: "**Clarification of the normal cell fractionation as a trigger for radiation-induced liver injury**."

The objective of our study is to clarify the mechanism of radiation-induced liver injury.

We used the following boron cluster-sugar chain-conjugated albumin.

- Asialo-N-glycan-HSA-^{10}B
- Mannose-N-glycan-HSA-^{10}B
- Hybrid-N-glycan-HSA-^{10}B

The sugar chains recognize the normal tissue components, hepatocytes, and non-parenchymal cells. We analyzed boron spatial distribution using autoradiography technique.

P4-3: "**The Effect of Boron Neutron Capture Therapy to Normal Bones in Mice."**

Cognitive impairment and radiation brain necrosis are late adverse effects after radiation therapy against brain or head and neck tumors. Biological effect of Boron Neutron Capture therapy (BNCT) on central nervous system is unknown. To avoid those late adverse effects,

We investigate the biological effects of BNCT on neuronal cells and brain blood vessels. We used human iPSC-derived Neural stem/progenitor cell (NSPC) lines and blood-brain barrier (BBB) model composed of rat brain capillary endothelial cells, pericytes, and astrocytes.

In neuronal cells, early apoptosis was not detected after 24 hours after BNCT. Frequency of Necrosis occurrence did not increase with increasing BPA concentration.

P4-5: "**The Effect of Boron Neutron Capture Therapy to Normal Bones in Mice."**

In this project, we have performed X-ray or neutron irradiation to normal tibial bone in mice with and without boronophenylalanine (BPA) and determined the compound biological effectiveness (CBE) factor for BPA as the biological endpoint of the tibial bending strength.

PR4-1 The effect of boron neutron capture therapy (BNCT) on normal lung in mice

M. Suzuki, Y. Tamari
Institute for Integrated Radiation and Nuclear Science Kyoto University

INTRODUCTION: An accelerator-based boron neutron capture therapy (BNCT) system and boronophenylalanine (BPA)-based new drug were approved by the Ministry of Health, Labour and Welfare of Japan for the treatment of locally unresectable recurrent or unresectable advanced head and neck cancer in March 2020. Since BNCT will be carried out at the medical institute, the accessibility of BNCT will improve dramatically and much greater patients will be treated with accelerator-BNCT compared with reactor-BNCT. One of the drawbacks of BNCT is that thermal neutrons necessary for tumor control cannot be delivered to the deep portion of the tumor which is located at > 6 cm in depth from the skin surface. For BNCT to be recognized as effective treatment modality for malignant tumors, to expand indication of BNCT is very important. We have investigated the possibility of BNCT for malignant tumors in body trunk such as liver and lung cancers. In these body trunk tumors, multiple lung metastatic tumor is good candidate for new application. Since the lung contains air, thermal neutron is delivered to the lung tissues in deep portion. In BNCT for multiple lung tumors, whole lung is irradiated with boron thermal neutron capture irradiation. We have investigated the compound biological effectiveness (CBE) factor for normal lung tissues. The CBE factors depend on the biological or clinical endpoint. The CBE factor for normal lung tissue had been reported at 2.3 from the Massachusetts Institute of Technology (MIT) group. In MIT study, the biological endpoint for the CBE factor was the occurrence of lung fibrosis. In our study, the clinical endpoint for the CBE was the death. We have already reported the survival fraction following whole thorax irradiation with X-ray irradiation. In 2020, the effect of thermal neutron beam at KUR on normal lung was investigated.

EXPERIMENTS: Ten- to twelve-week-old female C3H/He mice were used. Since, in this experiment, a large amount of thermal neutrons was needed to cause equivalent biological effect with X-ray irradiation, the irradiations were carried out at the 5MW reactor power. The mice were anesthetized by intraperitoneal injection of three types of mixed anesthesia (MMB), consists of medetomidine, midazolam, and butorphanol. The three or four mice were fixed in the acryl box and the body except for the thorax were shielded with LiF plate. The mice were sorted into four treatment groups, 40-min, 50-min, 60 min, and 70-min irradiation groups. In 40-min, 50-min, and 60-min irradiation group, seven to ten mice were treated. In 70-min irradiation group, three mice were irradiated. The acryl box containing mice were irradiated with thermal neutron beam at the thermal neutron flux of 7.5E+09 n/cm^2/s which was measured by analysis of activation of gold foil attached to the surface of the box. Survival curves have been investigated for each treatment groups.

RESULTS: In 60-min and 70-min irradiation group, six mice (40%) and three mice (100%) died within an observation period of 12 days due to acute side effects. Figure 1 shows the survival curve of each group treated with thermal neutron beam irradiation.

The physical dose by 70-min thermal neutron beam irradiation was 11.0 Gy which consists of hydrogen and nitrogen dose (5.9 Gy) and gamma-ray dose (4.9 Gy).

Fig 1.

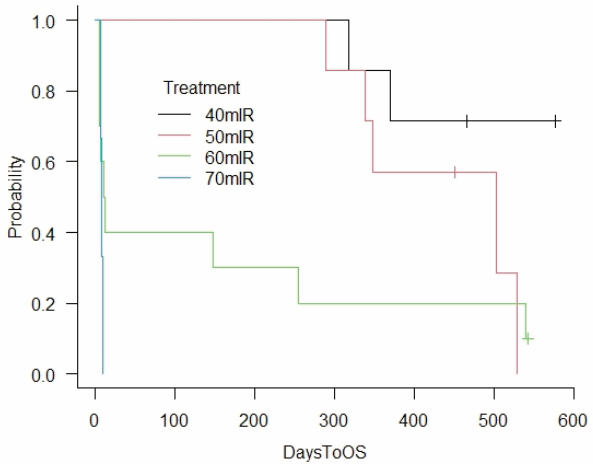

Fig 2.

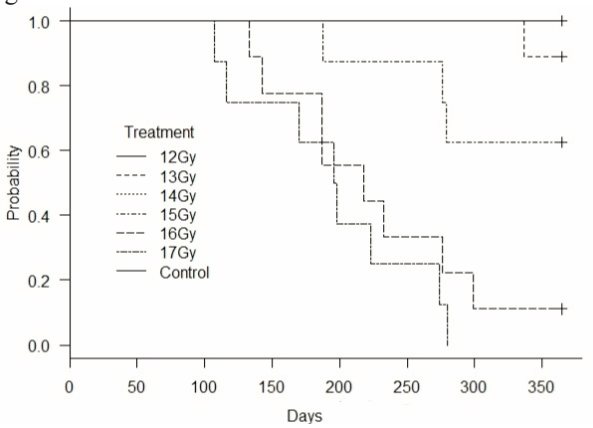

Discussion: Figure.2 shows the survival for X-ray treatment groups which was already reported. In this experiment, the physical dose causing acute fatal side effect by thermal neutron beam irradiation was revealed to be 11.0 Gy. The relative biological effectiveness (RBE) of high linear energy transfer (LET) component in thermal neutron beam is estimated to be greater than 2.0 as the endpoint of acute fatal effect in whole thoracic irradiation.

To investigate the acute side effects following whole thoracic irradiation, we plan to conduct histopathologic studies.

PR4-2 Clarification of the normal cell fractionation as a trigger for radiation-induced liver injury

S. Takeno[1], M. Suzuki[2]

[1]*Graduate School of Science, Kyoto University*
[2]*Institute for Integrated Radiation and Nuclear Science, Kyoto University*

INTRODUCTION:

Even though radiation-induced liver injury is one of the fatal adverse events in radiation therapy, normal cell fractionation, which causes radiation-induced liver injury, is still not clear. We have developed a boron compound that is distributed in different cell fractions of the liver [1,2]. By distributing the drug in each cell fraction and irradiating it with neutrons, it is possible to destroy the cell fraction specifically. The objective of our study is to clarify the mechanism of radiation-induced liver injury using the drugs.

EXPERIMENTS:

In this experiment, we examined the distribution of the drugs in liver using autoradiography. We used the following drugs:

- Asialo-N-glycan-HSA-10B (distributes in hepatocytes)
- Mannose-N-glycan-HSA-10B (distributes in sinusoids)
- Hybrid-N-glycan-HSA-10B

We applied each drug to C57BL or BALB/c mice Intravenously, and sacrificed and resected livers from them 1.5 hour later. Liver tissue sections was put into CR-39 (solid state nuclear track detector) and irradiated with thermal neutrons. Then we analyzed boron spatial distribution using autoradiography technique described in our previous study [3].

RESULTS:

The distribution of each boron compound in liver is shown in Fig. 1. According to this result, the drug distribution of Asialo-N-glycan-HSA-10B in liver tissue seems to show hepatocyte predominance trend. However, the distributions of other drugs were not clear due to the lack of fluence in neutron irradiation (because this is simply a preliminary study). To clarify the drug distribution trend of all the drugs, we need to conduct re-examination with enough fluence.

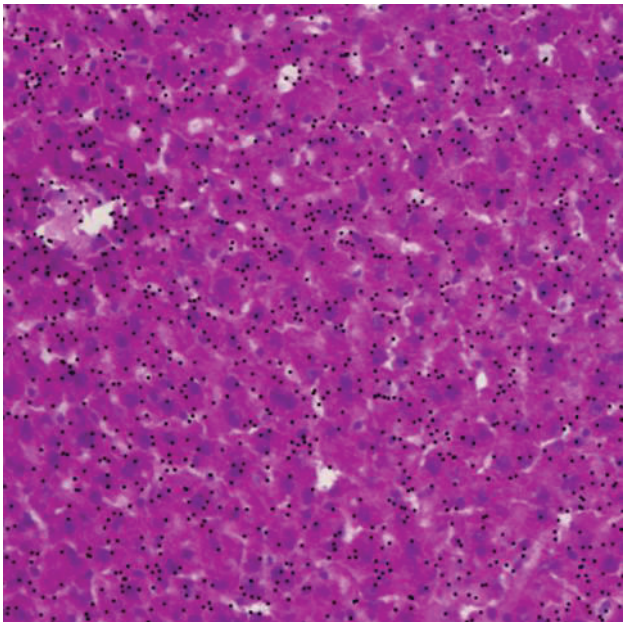

Fig. 1 Micro-distribution of Asialo-N-glycan-HAS-10B in liver tissue section.

REFERENCES:

[1] Kikuchi S, Kanoh D, Sato S, Sakurai Y, Suzuki M, Nakamura H. Maleimide-functionalized closo-dodecaborate albumin conjugates (MID-AC): Unique ligation at cysteine and lysine residues enables efficient boron delivery to tumor for neutron capture therapy. J Control Release 2016;237:160–7. https://doi.org/10.1016/j.jconrel.2016.07.017.

[2] Ogura A, Tahara T, Nozaki S, Morimoto K, Kizuka Y, Kitazume S, et al. Visualizing Trimming Dependence of Biodistribution and Kinetics with Homo-and Heterogeneous N-Glycoclusters on Fluorescent Albumin. Sci Rep 2016;6. https://doi.org/10.1038/srep21797.

[3] Takeno S, Tanaka H, Watanabe T, Mizowaki T, Suzuki M. Quantitative autoradiography in boron neutron capture therapy considering the particle ranges in the samples. Phys Medica 2021;82:306–20. https://doi.org/10.1016/j.ejmp.2021.02.012.

PR4-3 The biological effect on neurons and brain blood vessels induced by Boron Neutron Capture Therapy

N. Kondo[1], Y. Sakurai[1], T. Takata[1], Y. Kanemura[2], N. Takai[3], and M. Suzuki[1]

[1] Institute for Integrated Radiation and Nuclear Science, Kyoto University (KURNS)
[2]Department of Biomedical Research and Innovation Research, National Hospital Organization Osaka National Hospital
[3]Department of Pharmaceutical Sciences, Nagasaki International University

INTRODUCTION: Cognitive impairment and radiation brain necrosis are late adverse effects after radiation therapy against brain or head and neck tumors. Biological effect of Boron Neutron Capture therapy (BNCT) on central nervous system is unknown. To avoid those late adverse effects, we, first of all, investigate the biological effects of BNCT on neuronal cells and brain blood vessels.

EXPERIMENTS:

Cell culture

We used human iPSC-derived Neural stem/progenitor cell (NSPC) lines [1]. We differentiated these iPSC derived NSPCs and seeded into laminin-coated 8 well chambers and T25 flasks. Cells were sealed and transferred from the Osaka national hospital to KURNS the day before irradiation kept at 24 °C in the box and cultured at 37 °C CO_2 incubator after transfer.

We used blood-brain barrier (BBB) model [2] composed of rat brain capillary endothelial cells, pericytes, and astrocytes. This model can form tight junctions between endothelial cells which is the feature of BBB function.

Treatment of L-p-Boronophenylalanine (BPA)

We treated cells with medium containing BPA at the concentration of 5-45 ppm for 2 h. The BPA was formulated and its concentration was measured as previously described [3].

Thermal Neutron Irradiation

We irradiated thermal neutron irradiation to 1) the neuronal cells with sealing for 30 minutes with 1 MW power or 2) the blood cells (endothelial cells and pericytes) for 10 min with 5 MW power at room temperature by D_2O facility.

Cell death assay

We stained the neuronal cells in 8 well chamber 24 hour after irradiation with Hoechst 33342, Annexin V-FITC and Propidium Iodide Solution following the manufacture's protocol (nacalai tesque, Japan) and captured them by the microscope [Keyence BZ9000].

Measurement of transendothelial electrical resistance (TEER)

TEER, which reflects in culture conditions the flux of mainly sodium ions through cell layers, was measured by Epithelial-volt-ohm meter (Millipore) and Endohm-6 chamber electrodes (World Precision Instruments, USA). TEER of coated, but cell-free filters was subtracted from measured TEER values of the models shown as Ohm x 0.33 cm^2.

RESULTS:

As shown in table 1, in neuronal cells, early apoptosis was not detected after 24 hours after BNCT. Frequency of Necrosis occurrence didn't increase with increasing BPA concentration.

BNCT	control	0 ppm	5 ppm	20 ppm	45 ppm
Early apoptosis(%)	0.00	0.00	0.00	0.00	0.00
Necrosis(%)	0.54	1.20	2.09	1.62	1.30

Table. 1. Occurrence frequency (%) of apoptosis and necrosis 24 hours after BNCT in neuronal cells.

And as shown in figure 2, TEER decreased with increasing BPA concentration 10 days after BNCT.

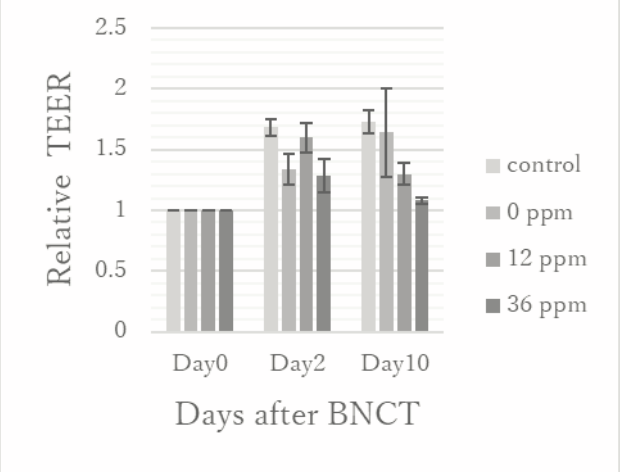

Fig. 2. Change of TEER after BNCT in BBB model

****

REFERENCES:

[1] Fukusumi *et al*. (2018), Peer J, DOI 10.7717/peerj.4187

[2]S.Nakagawa *et al*. Cell Mol Neurobiol 27(2007) 687–694. DOI 10.1007/s10571-007-9195-4

[3] N. Kondo *et al.* Radiat. Environ. Biophys. 55 (2016) 89–94.

PR4-4 The Effect of Boron Neutron Capture Therapy to Normal Bones in Mice

R. Iwasaki, R. Yoshikawa[1], T. Mori, Y. Sakurai[2], M. Suzuki[2] and K. Ono[3]

Faculty of Applied Biological Sciences, Gifu University
[1]United Graduate School of Veterinary Sciences, Gifu University
[2]Institute for Integrated Radiation and Nuclear Science, Kyoto University
[3]Kansai BNCT Medical Center, Osaka Medical College

INTRODUCTION: Primary malignant bone tumors have been mainly treated with preoperative chemotherapy followed by surgery. Wide or radical margins including limb amputation are required for local control. Although surgical techniques named limb-salvage therapy become a mainstay of treatment to avoid the limb amputation, complications such as postoperative infection, fracture, or local recurrence often occurred.

Although primary bone tumors have been generally considered as radio-resistant, radiation therapy has been used for the purpose of the functional and cosmetic status of patients. When a large single dose of photon radiation therapy is delivered to achieve the effective tumor control, clinically relevant late effects in the surrounding normal tissues include skin ulceration, neuropathy, and fracture.

Boron neutron capture therapy (BNCT), a tumor cell - selective particle radiation therapy, is considered to be effective for the tumors without any late effects to the normal bone. However, an appropriate BNCT dose irradiated safely to the normal bone, that is evaluated using experiment animals, is not determined. To elucidate the compound biological effectiveness (CBE) factor in normal bone is necessary to calculate the accurate radiation dose for performing BNCT.

In this project, we have performed X-ray or neutron irradiation to normal bone in mice and determined the CBE factor by evaluating the influence on their bone strengths.

EXPERIMENTS: Female eight-week-old C3H/He mice were used for the study (n = 6 in each group). As boron compound, p-boronophenylalanine (BPA) was prepared at a dose of 25 mg/ml. Irradiation was performed using X-ray and neutron at Gifu University and Kyoto University Reactor, respectively.

X-ray irradiation On the next day after X-ray irradiation to the right hind limb at a top-up dose of 24 Gy, mice were additionally irradiated at a dose of 4, 8, 12, 16, and 20 Gy.

Neutron irradiation On the next day after X-ray irradiation of 24 Gy, neutron irradiation was carried out as follows; neutron beam only (for 60, 90, and 120 min), neutron beam for 60 min after subcutaneously injected into mice at doses of 125, 250, and 500 mg/kg of BPA. Based on a preliminary study of the biodistribution of BPA, irradiation was performed between 30 and 90 min after the injection.

Bone strength analyses Tibias were collected at 12 weeks post-irradiation. Subsequently, they were mechanically tested by three-point bending to determine the bone strength. Tests were performed at HAMRI CO., LTD.

RESULTS: Figures 1−3 show the changes of the tibial bending strength after 12 weeks from the irradiation. The value of the horizontal axis in each figure represents the irradiation dose except for the top-up dose, based on the tissue ^{10}B concentration obtained from our previous study.

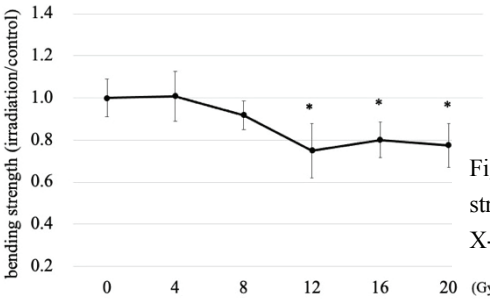

Fig.1. Tibial strength change by X-ray irradiation.

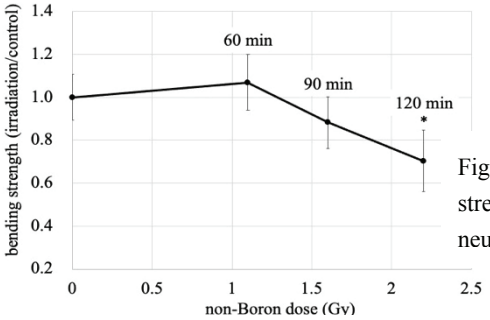

Fig. 2. Tibial strength change by neutron irradiation.

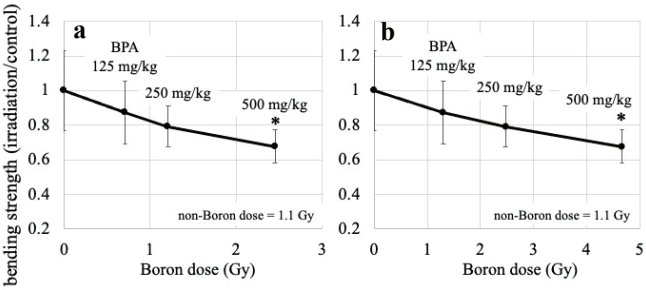

Fig. 3. Tibial strength changes by 60 min-neutron irradiation with BPA administration. Boron doses are calculated based on the ^{10}B concentration in bone (a) and blood (b), respectively.

According to the two inclinations of the straight line, that is, bone strength-X-ray dose line (Fig. 1) and bone strength-boron dose line (Fig. 3), the CBE factor for normal bone using BPA was determined as follows:

CBE factor	notes
4.09	using ^{10}B concentration in whole bone
2.15	using ^{10}B concentration in blood distributed in bone

CONCLUSION: The CBE factor for normal bone was elucidated when decrease in bone strength was set as the biological endpoint by analyzing the tibial bending strength. Further investigation such as identifying the ^{10}B distribution in normal bone using the alpha autoradiography or analyzing the changes of bone construction using the micro-CT will contribute the understanding the influence of BNCT on normal bone.

I-1. PROJECT RESEARCHES

Project 5

PR5 Preclinical studies on gadolinium neutron capture therapy

M. Suzuki

Institute for Integrated Radiation and Nuclear Science, Kyoto University

In this research project, nine research projects were included. Details of each project is referred to the following contents.

P5-1: Investigation of cell killing effect by auger electrons emitted during gadolinium neutron capture therapy (Gd-NCT)

We investigated the cell killing effect by auger electrons in Gd-NCT with micronucleus assay in which cytochalasin B was used to inhibit cell division to yield binucleated cells. Although the cause is unclear, CB did not work in the experiment.

We will retry the experiment next year.

P5-2: Development of Nano Carriers Installed with Gd (III)-Thiacalixarene Complex for Gd-NCT

In this study, Gd in a form of 1),2), 3) free Gd3TCAS2, 4) Gd3TCAS2bound to Alb, and 5) Gd-DTPA complex were tested in this study. The cell killing effect was assayed with colony formation assay. the effectiveness of new Gd-loaded nanoparticle was tested in vivo study. Since this study was carried out as preliminary study, only one mouse was used. The GdXX-NCT showed a little growth inhibition compared with that of thermal neutron irradiation. The difference in CUF among 1–5) was too subtle to evaluate the effectiveness in the cell killing ability.

P5-3: Gadolinium neutron capture therapy as new treatment for head and neck cancer.

In this study.the authors have developed gadolinium-loaded chitosan nanoparticles (Gd-nanoCPs). This nanoparticulate device is composed of Gd-iethylenetriaminepentaacetic acid (Gd-DTPA) which is a Gd-based MRI contrast agent and chitosan which is a naturally abounded polysaccharide material having bio-degradable, biocompatible and bioadhesive characteristics.

The Gd-NCT using Gd-nanoCPs yielded remarkable tumor (SCCVII) growth suppression compared with irradiation control group. The Gd-NCT using Gd-nanoCPs could be a promising therapeutic option for head and neck cancer.

P5-5: Preparation of functional molecules with Hoechst unit.

In this study, we attempted to construct the molecular system to take the complex into cell nucleus by using Hoechst molecules. Since the Hoechst group has high DNA−binding function and accumulates in the cell nucleus,1,2 it was expected that this molecule act as a courier molecule to deliver drugs into the nucleus.

Experiments using F-Hoechst shows that the unit take functional molecules into cell nucleus.

P5-6: Development of Gadolinium-loaded mesoporous silica-based nanoparticles and application to cancer radiotherapy.

We carried out preliminary evaluation of Gd-MSN or Gd-BMPO using the chicken chorioallantoic membrane (CAM) model that was established by transplanting human ovarian cancer cells.

Preliminary investigation of tumor growth inhibition efficacy Gd-BPMO in the CAM model showed that the tumor growth was significantly inhibited when Gd-BPMO was injected compared to no injection or empty BPMO.

P5-7: Evaluation of Antitumor effectivity by Gd-neutron capture therapy using Gd_2O_3 incorporated nanomicelle.

A Gd_2O_3incorporated nanomicellewas synthesized and the effect of NCT was evaluated with Human Pancreas Adenocarcinoma cell line (AsPC-1) bearing mice.

From the results in this time, we confirmed the anti-tumor effect of Gd_2O_3 incorporated nanomicelle.

P5-8: Development of 10B-enriched GdBO3nanoparticles for neutron capture therapy of cancer.

^{10}B-enriched $GdBO_3$ nanoparticles (NPs) was prepared from Gd_2O_3 and $^{10}B(OH)_3$. After the $Gd^{10}BO_3$ NP was coated by silica (SiO_2), the resulting $Gd^{10}BO_3@SiO_2$ was functionalized with polyglycerol (PG) to give $Gd^{10}BO_3@SiO_2$-PG. The tumor size of BNCT increased at the similar rate to that of the hot control. This indicates the $Gd^{10}BO_3@SiO_2$-PG works as neither BNCT nor Gd-NCT agents.

P5-9: Study about neutron capture therapy using polymeric drug delivery systems chelating Gd.

We recently synthesized functional polymers for chelating Gd, and their size can be easily controlled by fine-tuning the composition. For this purpose, in this fiscal year, we tried to set up the experimental condition for neutron irradiation to subcutaneous tumor models using a prototype of the polymeric drug.

The low-molecular drug and polymeric drug exhibited considerable anti-tumor efficacy, suggesting the successful neutron capture therapy and the appropriate irradiation condition.

P5-10: In vivo dose-dependent administration study in mice of Gd-EDTMP: gadolinium neutron capture therapy formulation for bone metastasis.

We conducted an in vivo administration study in mice to investigate the distribution and safety of Gd-EDTMP, and conducted a basic study focusing on the dose-dependency. The distribution of ^{157}Gd in the tissue was imaged by laser ablation inductively coupled plasma mass spectrometry (LA-ICP-MS). The results of semi-quantitative analysis by LA-ICP-MS show that Gd was distributed in the part of femur bone in the order of sub per-cent.

PR5-1 Investigation of cell killing effect by auger electrons emitted during gadolinium neutron capture therapy (Gd-NCT)

M. Suzuki, H. Tanaka
Institute for Integrated Radiation and Nuclear Science Kyoto University

INTRODUCTION: An accelerator-based boron neutron capture therapy (BNCT) system and boronophenylalanine (BPA)-based new drug were approved by the Ministry of Health, Labour and Welfare of Japan for the treatment of locally unresectable recurrent or unresectable advanced head and neck cancer in March 2020. Since BNCT will be carried out at the medical institute, the accessibility of BNCT will improve dramatically.

The isotope of gadolinium-157 (^{157}Gd) has the highest thermal neutron capture cross-section about 254,000 barn which is about 66 times higher compared with that of boron-10 (^{10}B). The gadolinium neutron capture reaction is as follows, ^{157}Gd+n = ^{158}Gd+gannma-ray+internal conversion elections +Auger electrons. Among the byproducts, Auger electrons is categorized as a high linear energy transfer radiation which can induce double strand brake of DNA. Since the range of the Auger electron is the order of a few nanometers, cell killing effect by the electron is evoked at when ^{157}Gd is incorporated into the target such as DNA. Combination therapy with BNCT and Gd-NCT may help to raise the radiation dose for the deep portion of the tumors. To investigate the cell killing effect by Auger electron, irradiation by other byproducts yielded by ^{157}Gd neutron capture reaction should be eliminated as much as possible from the site of the reaction. In the case of irradiation to the cell incorporating ^{157}Gd compound which are suspended liquid, the cells are irradiated with gamma-ray (range is >100 μm) which are emitted from surrounding the cells. To eliminate the irradiation by gamma-ray as much as possible, the irradiation system as follows is effective; the cells adhered to the well of the microplate which stands upright are irradiated with thermal neutrons.

In 2020, feasibility of the irradiation system was confirmed. We investigated the cell killing effect by auger electrons in Gd-NCT using this irradiation system. The cell killing effect was assayed by micronucleus assay.

EXPERIMENTS: The V79 cells were maintained in E-MEM supplemented with L-glutamine and 10% fetal bovine serum (FBS). The 1,000 cells per well were seeded in the 96-well microplates. The ^{157}Gd containing medium was adjusted using a contrast media for magnetic resonance imaging (OMNISCAN®). The ^{157}Gd containing medium at a concentration of 100, 1,000 and 5,000 ppm were replaced at 24h before irradiation with thermal neutron. The microplate was sealed with sterilized seat and kept standing upright. The microplate was irradiated with thermal neutron beam at the flux of $1x10^9$ n/cm^2/s^{-1} for 30 minutes. After the irradiation, the each well was rinsed twice with phosphate buffered saline and replaced with cytochalasin B (CB) containing medium (2μg/ml). Since CB inhibits cell division, micronuclei (MN) derived from chromosome damage are detected in binucleated cells. After 48 h incubation, the cells were fixed with Carnoy's solution and their nucleus and micronucleus were stained with propinium iodine. To estimate the cell killing effect by Gd-NCT, function of normal nuclear division was calculated by dividing binucleated cells without MN by binucleated cells.

RESULTS: The figure 1 shows the binucleated cells with micronucleus. However, almost all the cells were mononuclear cells (Fig.2). Although the cause is unclear, CB did not work in this experiment.

Fig.1

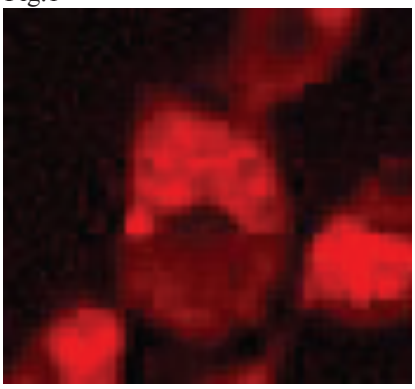

Fig.2

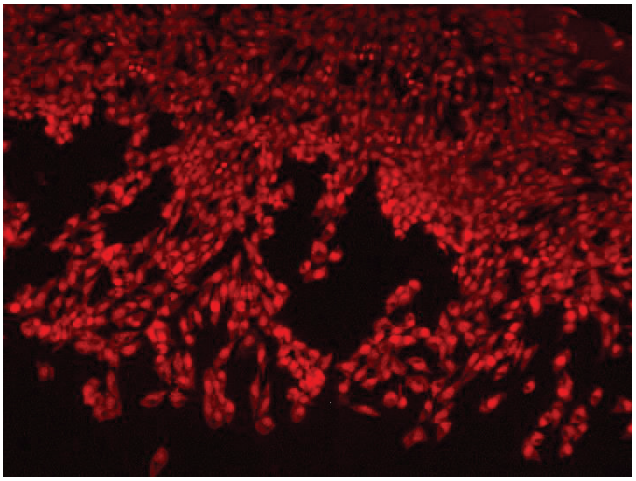

We will conduct this experiment again.

PR5-2 Development of Nano Carriers Installed with Gd(III)-Thiacalixarene Complex for Gd-NCT

N. Iki[1], M. Komiya[1], T. Yamatoya[1], T. Nagasaki[2], and M. Suzuki[3]

[1]*Graduate School of Environmental Studies, Tohoku University*

[2] *Graduate School of Engineering, Osaka City University*

[3]*KURNS*

INTRODUCTION: Owing to a large thermal neutron capture cross section and total kinetic energy of $^{157}Gd(n,\gamma)^{158}Gd$ larger than that of $^{10}B(n,\alpha)^{7}Li$, gadolinium attracts growing attention as an alternative to boron in neutron capture therapy [1]. Because free gadolinium ($Gd(OH_2)_9$) has toxicity, a safe carrier of Gd to tumor not to release free Gd is required. We recently found that thiacalix[4]arene-*p*-tetrasulfonate (TCAS) self-assembled three lanthanide (Ln) cores including Gd to form a sandwich-type complex, Ln_3TCAS_2 (Fig. 1) [2], the characteristic features of which are high kinetic stability, luminescence signal [3], and ^1H relaxation arising from the Ln center [4]. Nano-sized particles are frequently used as a drug carrier toward tumor by enhanced permeability and retention (EPR) effect. This year, we shifted from a silica nano-particle (SiNP, 61.6 ± 3.8 nm in diameter) containing Gd_3TCAS_2 [5] to albumin NP (AlbNP) as a carrier for Gd-NCT. Here we report the ability to kill cancer cells upon neutron irradiation by comparison with the cases of Gd_3TCAS_2, BSA-Gd_3TCAS_2 complex, Gd-DTPA, and PBS control.

EXPERIMENTS: *Preparation of AlbNP installed with Gd.* The trinuclear complex Gd_3TCAS_2 was prepared as reported elsewhere [2]. The AlbNP was prepared by a method reported [6]. Briefly, BSA solution was added MeOH or EtOH, followed by addition of glutaraldehyde to obtain the particle containing solution. This was mixed with Gd_3TCAS_2 to afford Gd_3TCAS_2-installed AlbNP (denoted as 1) Gd_3TCAS_2-AlbNP(MeOH) and 2) Gd_3TCAS_2-AlbNP(EtOH), respectively).

Cell experiments. MCF-7 cells were seeded in a 6-well plate at a cell concentration of 1.0×10^5 cells/mL and incubated for 24 h. After supernatant was removed, RPMI medium and solution containing Gd in a form of 1), 2), 3) free Gd_3TCAS_2, 4) Gd_3TCAS_2 bound to Alb, and 5) Gd-DTPA complex were added to each well and incubated for 24 hr. After washing with PBS, the cells were detached from the well and transferred to tubes to be irradiated with thermal neutron (8.6×10^{12} n/cm^2) for 40 min.

Assay. To the wells containing 2 mL of RPMI medium in 6-well plates, irradiated cells were seeded at the concentration of 1,000 cells/well. After incubation for 14 days, the colony was stained with crystalviolet.

RESULTS:

The concentration of Gd in the medium to incubate MCF-7 was set to be 24.3 μM for 1, 3–5) and 15.4 for 2). The colony formation units (CFU) normalized with one for no irradiation is shown in Fig. 2. As can be seen, there seems appreciable difference between CFU for 6) control and samples 1–5) containing Gd, suggesting that the gamma ray, internal conversion electron, and/or Auger electron emitted from Gd killed fraction of MCF-7 cells. However, the difference in CUF among 1–5) was too subtle to evaluate the effectiveness in the cell killing ability. Elucidation of the efficiency in the Gd-delivery and the region in the cell where the Gd-agent is delivered are now underway.

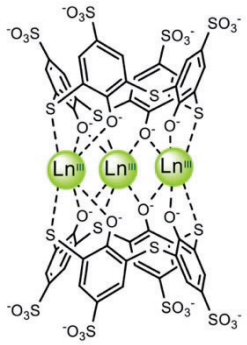

Fig. 1 Structure of Ln_3TCAS_2 complex.

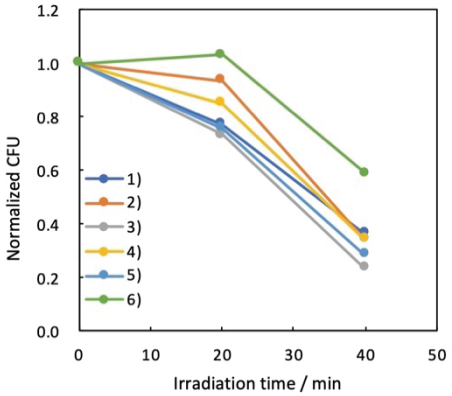

Fig. 2 Dependence of time of neutron irradiation on the colony formation rate for Gd-agents 1–5) and control 6) (n = 3).

REFERENCES:

[1] M. Takagaki *et al*., Future Application of Boron and Gadolinium Neutron Capture Thrapy, in *Boron Science*, Ed N. S. Hosmane (CRC Press) (2012) 243.

[2] N. Iki *et al.*, *Eur. J. Inorg. Chem.,* **2016** (2016) 5020-5027.

[3] R. Karashimada *et al.*, *Chem. Commun*. **52** (2016) 3139-3142.

[4] N. Iki et al., *Inorg. Chem.* **55** (2016) 4000-4005.

[5] T. Yamatoya et al, 31P11-8, p. 105, *KURNS Progress Report 2019*.

[6] C. Weber, C. Coester, J. Kreuter, K. Langer, *Int. J. Pharm*., 194 (2000) 91–102.

PR5-3 Gadolinium neutron capture therapy as new treatment for head and neck cancer

T. Andoh[1], T. Fujimoto[2], M. Suzuki[3], T. Takata[4], Y. Sakurai[4] and H. Ichikawa[1].

1Faculty of Pharmaceutical Sciences, Kobe Gakuin University, Japan.
2Department of Orthopaedic Surgery, Hyogo Cancer Center, Japan.
3Particle Radiation Oncology Research Center, Institute for Integrated Radiation and Nuclear Science, Kyoto University, Japan.
4 Division of Radiation Life Science, Institute for Integrated Radiation and Nuclear Science, Kyoto University, Japan

INTRODUCTION: Neutron-capture therapy using nonradioactive ^{157}Gd (Gd-NCT) is currently under development as a potential radiation therapy for cancer. Unlike boron neutron capture therapy (BNCT), which uses ^{10}B, ^{157}Gd has several potential advantages. γ-rays have long range (. 100 μm) emitted by ^{157}Gd (n, γ) ^{158}Gd reaction, so that considerable tumor-killing effects can be expected to a bulky tumor i.e, head and neck cancer. As a nanoparticulate device for the controlled delivery of Gd in NCT, the authors have developed gadolinium-loaded chitosan nanoparticles (Gd-nanoCPs). This nanoparticulate device is composed of Gd-iethylenetriaminepentaacetic acid (Gd-DTPA) which is a Gd-based MRI contrast agent and chitosan which is a naturally abounded polysaccharide material having biodegradable, biocompatible and bioadhesive characteristics. In the present study, we investigate the *in vivo* antitumor effects after NCT with intratumoral injected nanoparticulate formulations.

EXPERIMENTS: Gd-nanoCPs was prepared by using chitosan with molecular weights of 10 k and Gd-DTPA through the previously developed w/o emulsion-droplet coalescence technique [1]. Mean particle size and zeta potential of the resultant Gd-nanoCPs were measured by Zetasizer® (Malvern Instruments Ltd, UK) in water at 25ºC. Gd content in Gd-nanoCPs was determined by inductively coupled plasma atomic emission spectrometry (ICP-AES, SPS3100, Hitachi High-Tech Science Corporation, Japan) followed by incineration of each sample. In the NCT trial, male SCC-VII bearing C3H/HeN mice were used. The mice were divided into NCT group and HOT control group. Gd-nanoCPs incorporating 1.2 mg of natural Gd were injected intratumorally twice (2.4 mg Gd/kg) to the mice. The tumors in the left hind legs were exposed to thermal neutron irradiation at the Institute for Integrated Radiation and Nuclear Science, Kyoto University. For determining the tumor volume, two bisecting diameters of the tumor were measured with a slide caliper, and calculation with the longest and shortest length of the tumor in millimeters (mm). The tumor-growth suppressing effect was assessed by the ratio of tumor volume before and after neutron irradiation.

RESULTS: The mean particle diameter, Gd content and zeta potential of Gd-nanoCPs were 165 nm, 22% and +23 mV, respectively. Before injection, the Gd-nanoCPs was condensed to 6000 μg Gd/mL with a centrifuge. In the NCT trial, eight hours after the last administration, thermal neutron was irradiated to tumor region of the mice. Remarkable tumor-growth was observed in HOT control groups, while the NCT groups showed a suppression of tumor growth (Fig. 1). The decrease in tumor volume was similar to that observed in our previous study using a subcutaneously transplanted melanoma-bearing mouse model [2]. These results have relations that Gd-nanoCPs exhibited a good cell affinity to SCC-VII cells which seems to our previous studies using melanoma cells [3]. Therefore, a Gd-NCT using Gd-nanoCPs could be a promising therapeutic option for head and neck cancer.

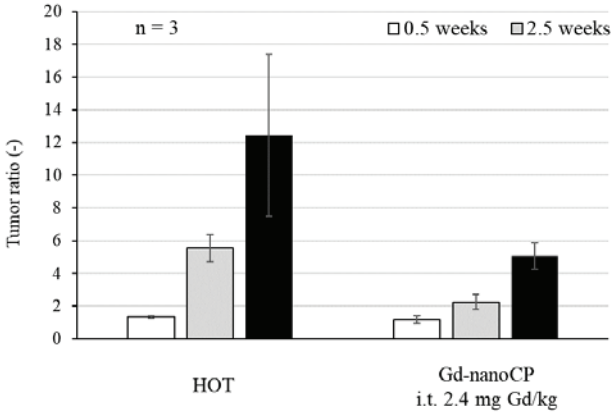

Fig. 1. Tumor volumes after thermal neutron beam irradiation of NCT and HOT control groups.

REFERENCES:

[1] H. Tokumitsu et al., Pharm. Res., 16, 1830–1835 (1999).
[2] H. Ichikawa et al., Appl. Radiat. Isot., 88, 109-113 (2014).
[3] T. Andoh et al., Appl. Radiat. Isot., 164, 109270 (2020).

PR5-4 Preparation of functional molecules with Hoechst unit

K. Tanabe[1], M. Suzuki[2], T. Nishihara[1] and M. Mizutani[1]

[1]*Department of Chemistry and Biological Science, College of Science and Engineering, Aoyama Gakuin University*

[2]*Integrated Radiation and Nuclear Science, Kyoto University*

INTRODUCTION:

Neutron capture therapy (NCT) is an effective medical cure for treatment of tumor tissue. This therapy is based on the accumulation of neutron capture agents at the target tumor to which thermal neutrons are irradiated. NCT is valuable because the thermal neutrons with low energy showed negligible damage to normal tissue in which neutron-capturing agents were not accumulated. This technique thus provides a solution to the major problem of radiation therapy; the radiation led to a damage of normal tissue. Thus, the techniques for the accumulation of NCT agents in the diseased tissues and cells is important to prevent side-effect of radiation.

Gadolinium (^{157}Gd)-based NCT (Gd-NCT) has recognized as a useful cancer treatment approach. To obtain success with ^{157}Gd-NCT, we designed a novel Gd complex which had neutron capturing properties in cell nucleus, because target DNA was accommodated in the cell nucleus. In this study, we attempted to construct the molecular system to take the complex into cell nucleus by using Hoechst molecules. Since the Hoechst group has high DNA−binding function and accumulates in the cell nucleus,[1,2] it was expected that this molecule act as a courier molecule to deliver drugs into the nucleus. Herein, we estimated the modification procedure of Hoechst molecules by Huisgen cycloaddition reaction and conducted cellular experiments to evaluate their properties in living cells.

EXPERIMENTS:

Preparation of modified Hoechst unit for Huisgen reaction. The Hoechst skeleton was synthesized as follows. Diaminobenzene derivative 1 was coupled with benzaldehyde 2 to give desired A-Hoechst (Figure 1A).

Huisgen cycloaddition reaction between A-Hoechst and fluorophore. A-Hoechst (1.0 mg, 2.2 μmol) was added to the solution of fluorescein with azide unit (0.5 mg, 2.1 μmol) in DMF-H_2O. Then, $CuSO_4$, TBTA and sodium ascorbate were added to the solution. The resulting mixture was stirred for 20 h at ambient temperature. After the reaction, the mixture was extracted with ethyl acetate. The organic layer was washed with brine, dried over $MgSO_4$, filtered and concentrated in vacuo. The crude product was purified by silica gel column chromatography to give fluorescein derivative with Hoechst unit (F-Hoechst).

Cellular experiments using fluorophore-labeled Hoechst derivative (F-Hoechst). A549 cells were seeded in 96 well plates at a density of 5000 cells/well in DMEM and allowed to grow at 37 ˚C for 24 hours. The cells were incubated with 30 μM F-Hoechst in DMEM (DMSO 1%) for 1 h. After the cells were washed with phosphate buffered salts (PBS), the cells were subjected to laser scanning confocal microscope to investigate the cellular uptake of F-Hoechst.

RESULTS:

Initially, we conducted the Huisgen reaction of A-Hoechst. In this experiment, we employed fluorescein as a phantom drug for easy tracking in the cells, and conducted the cycloaddition reaction. The reaction was proceeded at ambient temperature in the presence of catalytic $CuSO_4$ and ascorbic acid. Efficiently, the triazole ring formation occurred, and fluorophore with Hoechst unit (F-Hoechst) was formed.

We next conducted cellular experiments using F-Hoechst. A549 cells were incubated with F-Hoechst for 1 h, and then subjected microscopy. As shown in Figure 1B, we observed strong fluorescence of F-Hoechst from cell nucleus. Thus, Hoechst unit efficiently take functional molecules into cell nucleus.

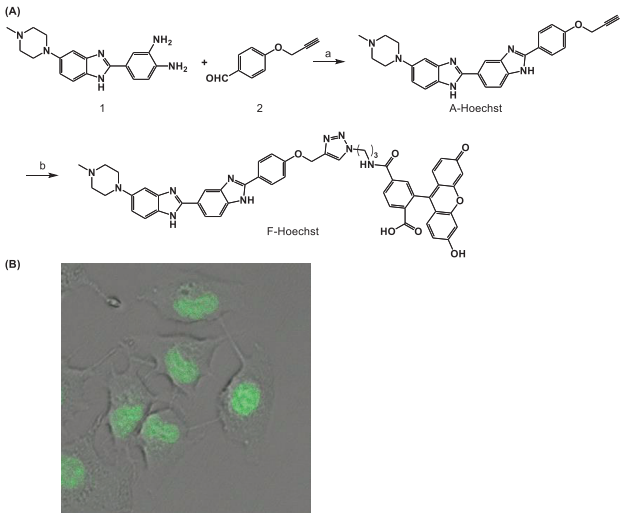

Figure 1. (A) Synthesis of A-Hoechst and F-Hoecsht. (a) $Na_2S_2O_5$, EtOH, H_2O, 55% (b) $CuSO_4$, TPTA, Sodium ascorbate, DMF, H_2O, 86%. (B) Confocal fluorescence microscopy imaging of living A549 cells incubated with F-Hoechst (Ex. 488 nm).

REFERENCES:

[1] K. Tanabe *et al.*, *Chem.Bio.Chem.* **19** (2018), 956–962.

R2P5-5

PR5-5 Development of Gadolinium-loaded mesoporous silica-based nanoparticles and application to cancer radiotherapy

F. Tamanoi[1], K. Matsumoto[1] and M. Suzuki[2]

[1]*Institute for Advanced Study*
Institute for Integrated Cell-Materials Sciences, Kyoto University
[2]*Institute for Integrated Radiation and Nuclear Science, Kyoto University*

INTRODUCTION: Boron phenylalanine (BPA) has been developed as useful boron compound which is available for boron neutron capture therapy (BNCT). We have developed two types of mesoporous silica-based nanoparticles that are loaded with BPA and found that the BPA-loaded nanoparticles have ability of improving the BNCT efficacy [1]. We have also developed mesoporous silica-based nanoparticles loaded with gadolinium instead of boron. We assumed this Gd-MSN or Gd-BPMO could be applied to gadolinium neutron capture therapy (GNCT). These nanoparticles have a large surface area where Gd can be attached for GNCT application. We carried out preliminary evaluation of these gadolinium nanoparticles using the chicken chorioallantoic membrane (CAM) model that was established by transplanting human ovarian cancer cells.

EXPERIMENTS:
Mesoporous silica nanoparticles (MSN) were synthesized by sol-gel synthesis of TEOS. BPMO nanoparticles were synthesized by sol-gel synthesis of two precursors, bis[3-(triethoxysilyl) propyl] tetrasulfide and 1, 2-bis(triethoxysilyl) ethane. This resulted in the incorporation of tetrasulfide bonds into the framework of the nanoparticles. These nanoparticles were surface modified with an amino group. Gadolinium diethylenetriamine penta-acetic acid (DTPA) was then mixed with amine-modified BPMO to couple Gd on the nanoparticles by electrostatic interaction between positively charged $NH3^+$ and negatively charged COO^- of DTPA. The synthesized nanoparticles were characterized by using SEM and EDX-TEM. The amount of Gd attached on the nanoparticles was examined by ICP-AES, and Gd content was determined.

CAM model was established by transplanting human ovarian cancer cells OVAR8 on the CAM in fertilized chicken eggs. After intravenously injection of Gd-loaded nanoparticles the eggs were placed at the center of emerging neutron beam. Eggs were irradiated with thermal neutron for 1 h at an operating power of 1MW. After the irradiation, eggs were incubated for 3 days at 37℃ with 65% humidity. Tumors were then cut out to evaluate the tumor size.

RESULTS: Nanoparticles synthesized had approximately 80-100 nm of diameter and homogenous shapes examined by SEM and TEM microscopy. After coupling of Gd, we detected that the amount of Gd coupled with the nanoparticles by ICP. Gd occupied 2.6% of the weight of Gd-BPMO nanoparticle.

Preliminary investigation of tumor growth inhibition efficacy Gd-BPMO in the CAM model showed that the tumor growth was significantly inhibited when Gd-BPMO was injected compared to no injection or empty BPMO. Tumor weight after the injection of Gd-BPMO followed by neutron irradiation and incubation was 27% of that compared with no injection of empty nanoparticle injection. Free Gd was 75% of the no injection control.

Further experiments on the biodistribution of Gd-BPMO are planned.

REFERENCES:
[1] Tamanoi, F. *et al*., Int. J. Mol. Sci. **22**, 2251 (2021).

PR5-6

Evaluation of Antitumor effectivity by Gd-neutron capture therapy using Gd_2O_3 incorporated nanomicelle

H. Xuan[1], H. Yanagie[2,3,4], M. Yanagawa[5], Y. Sakurai[3,4], K. Mouri[3,4], H. Cabral[1], Y. Sakurai[6], H. Tanaka[6], M. Suzuki[6], S. Masunaga[6], and H. Takahashi[1,2,3]

[1]Dept of Bioengineering, School of Engineering, Univ of Tokyo, [2]Institute of Engineering Innovation, School of Engineering, Univ of Tokyo, [3]Cooperative Unit of Medicine & Engineering, Univ of Tokyo Hospital, [4]Niigata Univ of Pharmacy & Applied Life Sciences, [5]Obihiro Univ of Agriculture and Veterinary Medicine, [6]Institute for Integrated Radiation & Nuclear Science, Kyoto Univ

INTRODUCTION

In the previous research, we developed a series of polymers containing gadolinium for neutron capture therapy (Gd-NCT) [1,2,3,4]. Gd-NCT is a noninvasive therapy for treating tumors with secondary particle (Auger electron and photon) released after neutron capture reaction. Compared with boron, which has been research many times, gadolinium-157 has higher thermal neutron cross section (66 times more than boron). Therefore, less amount of gadolinium can receive same effect with boron. Besides, because the compound of gadolinium is a kind of contrast agent used for MRI, a suitable Gd compound can be expected to achieve diagnostic treatment.

However, due to the strong toxicity, low molecular weight and poor selectivity of Gd compound, a carrier, for example, nanomicelle should be introduced to solve these problems. And gadolinium oxide (Gd_2O_3) is more stable than gadolinium ion and higher tumor intention time can be expected.

In this time, a Gd_2O_3 incorporated nanomicelle was synthesized and the effect of NCT was evaluated with Human Pancreas Adenocarcinoma cell line (AsPC-1) bearing mice.

EXPERIMENTS

Female Balb/c nude mice were used to prepare AsPC-1 bearing model. Tumor cells were subcutaneously injected into the right leg of the mouse. After two weeks for tumor growth, the mouse injected Gd_2O_3 incorporated nanomicelle and Gd-DTPA (a Gd chelate without nanomicelle) received neutron irradiation (2.0×10^{12} n/cm^2) for 1h. The tumor size was measured by a caliper and the tumor volume was calculated using the equation, $V = (a \times b^2) / 2$, where a and b are the major and minor axes of the tumor.

RESULTS

Anti-tumor ability was evaluated by tumor growth speed. The slower tumor increased, the better anti-tumor effect was confirmed. From the Fig. 1, the mice injected Gd_2O_3 incorporated nanomicelle and received neutron irradiation showed the best anti-tumor effect. Therefore, the better anti-tumor effect of Gd_2O_3-nanomicelle than other samples was improved. Among irradiation group, the mice injected Gd-DTPA showed higher tumor growth speed than mice without injection. It can be considered as the introduction of extraneous materials like Gd-DTPA. Another point should be noticed is that the mice only received neutron irradiation also showed the anti-tumor effect. The reason was most likely considered as the gamma ray mixed with neutron beam. Because gamma has the ability to kill tumor cells, all irradiation group showed anti-tumor effect. Besides, no acute toxicities were recognized among all groups injected samples.

From the results of histologic analysis, no abnormal change in the liver, the kidney, the heart, and the lung were found one month after Gd-NCT treatment.

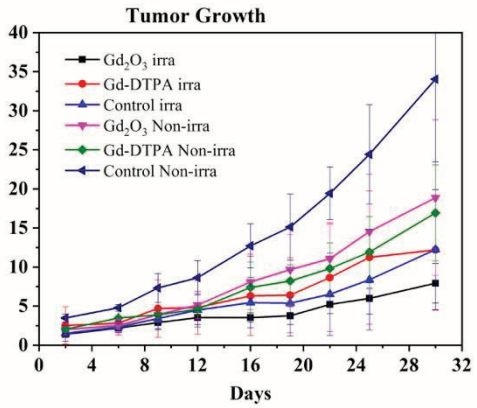

Fig 1. Tumor growth suppression in the group of Gd_2O_3 incorporated nanomicelle and bare Gd-DTPA

In the next works, due to the hollow structure of nanomicelle, we are considering the introduction of anti-tumor drugs to improve the tumor killing ability. What's more, we will check the expression of integrin receptors in many cancer cells lines and we hope to check that if the cell absorbs Gd_2O_3-nanomicelle through endocytosis. The mechanism of cytotoxicity on Gd-NCT is also very important consider the clinical application in the future. Therefore, it will be evaluated with apoptosis, autophagy, senescence etc.

In a word, from the results in this time, we confirmed the anti-tumor effect of Gd_2O_3 incorporated nanomicelle. But there are still some points should be solved and improved.

REFERENCES:

[1] Dewi N et al., Biomed & Pharmacother (2013) **67**:451-7.

[2] Dewi N et al., J Can.Res.Clin.Oncol. (2016) **142**(4):767-75.

[3] Mi P, et al.: J Cont. Release (2014) **174**:63-71.

[4] Qin C, et al., Chem Nano Mat. (2020) **6**:1-9.

R2P5-7

PR5-7 Development of ^{10}B-enriched $GdBO_3$ nanoparticles for neutron capture therapy of cancer

Li Zhao[1], Heon Gyu Kang[2], Masahiro Nishikawa[2], Minoru Suzuki[3] and Komatsu Naoki[2]

[1] *School for Radiological and Interdisciplinary Sciences (RAD-X) and Collaborative Innovation Center of Radiation Medicine of Jiangsu Higher Education Institutions, Soochow University, P. R. China*
[2] *Graduate School of Human and Environmental Studies, Kyoto University*
[3] *Institute for Integrated Radiation and Nuclear Science, Kyoto University*

INTRODUCTION: Gadolinium neutron capture therapy (GdNCT) has been attracting increasing interest together with boron neutron capture therapy (BNCT). Herein, we combined the two NCTs by synthesizing nanoparticle including both Gd and B.

EXPERIMENTS: ^{10}B-enriched $GdBO_3$ nanoparticles (NPs) was prepared from Gd_2O_3 and $^{10}B(OH)_3$. After the $Gd^{10}BO_3$ NP was coated by silica (SiO_2), the resulting $Gd^{10}BO_3@SiO_2$ was functionalized with polyglycerol (PG) to give $Gd^{10}BO_3@SiO_2$-PG. The product was characterized by X ray diffraction, FTIR spectroscopy and transmission electron microscopy (TEM). The size and thickness of the core ($Gd^{10}BO_3$ NP) and the SiO_2 layer were determined to be 120 and 40 nm, respectively, by TEM. After PG functionalization, $Gd^{10}BO_3@SiO_2$-PG showed very good dispersibility (>2 mg/mL) both in water and saline. The hydrodynamic size and the zeta potential of $Gd^{10}BO_3@SiO_2$-PG were 242 nm and –16.8 mV.

For in vivo experiments using tumor mice, we injected $Gd^{10}BO_3@SiO_2$-PG in phosphate buffer saline (17 mg mL^{-1}, 200 μL) from the tail vein. After 24 h, anesthesia was injected and the mice were fixed in holding plastic tool. Neutron was irradiated to the mice tumor (1 MW for 50 min). Then, tumor size was monitored and compared with the results of the control experiments.

RESULTS: As shown in Figure 1, the tumor size of BNCT increased at the similar rate to that of the hot control. This indicates the $Gd^{10}BO_3@SiO_2$-PG works as neither BNCT nor GdNCT agents. We need to do pharmacokinetics to confirm if the NP accumulates in tumor. We also have to optimize the experimental procedure for neutron irradiation, especially, the timing when we irradiate neutron after the injection of the $Gd^{10}BO_3@SiO_2$-PG.

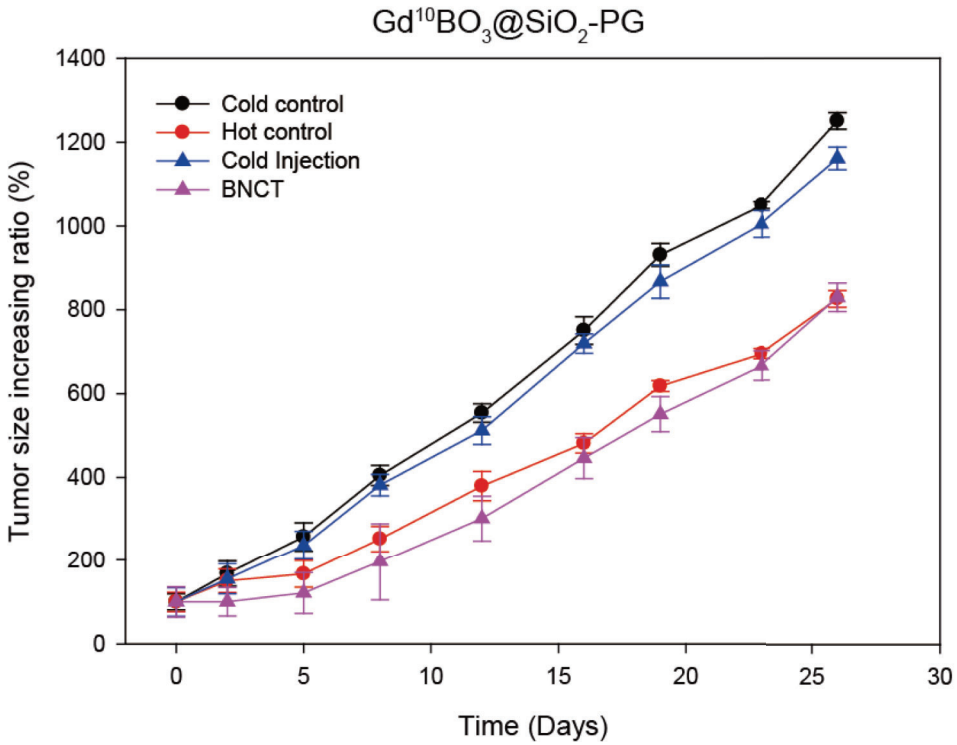

Figure 1 Time coarse of tumor size (%) as compared with the size on day 0 (100%). Cold control: no injection and no neutron irradiation. Hot control: no injection with neutron irradiation. Cold injection: no neutron irradiation with injection. BNCT: injection of $Gd^{10}BO_3@SiO_2$-PG with neutron irradiation.

PR5-8 Study about neutron capture therapy using polymeric drug delivery systems chelating Gd

Y. Miura[1], T. Nomoto[1], K. Konarita[1], Y. Sakurai[2], M. Suzuki[2], N. Nishiyama[1]

[1]*Institute of Innovative Research, Tokyo Institute of Technology*
[2]*Institute for Integrated Radiation and Nuclear Science, Kyoto University*

INTRODUCTION: ^{157}Gd has the high neutron capture cross section and can generate Auger electrons and γ-rays upon thermal neutron irradiation. Thus, Gd has been expected to be a promising atom in neutron capture therapy. We previously synthesized the inorganic-organic hybrid nanoparticle encapsulating Gd and demonstrated strong antitumor efficiency in subcutaneous tumor models [1]. However, the tumor accumulation level of Gd and ultimate antitumor efficiency was not always well correlated [2]. Thus, it is important to quantitatively investigate the intratumoral distribution and tumor accumulation level of Gd and study the correlation between such pharmacokinetic parameters and therapeutic effect.

We recently synthesized functional polymers for chelating Gd, and their size can be easily controlled by fine-tuning the composition. Using these polymers, we will comprehensively investigate the biodistribution and therapeutic efficacy in neutron capture therapy. For this purpose, in this fiscal year, we tried to set up the experimental condition for neutron irradiation to subcutaneous tumor models using a prototype of the polymeric drug.

EXPERIMENTS: BALB/c mice bearing subcutaneous CT26 tumors were prepared by subcutaneous injection of the cell suspension. The polymeric drug or the low-molecular drug as a control were intravenously injected to the mouse, and the thermal neutrons were irradiated to the tumor using KUR at 5 MW for 10 min. The tumor volume (V) was calculated using the following equation:

$$V = 1/2 \times a \times b^2$$

where a and b denote major and minor axes of a tumor, respectively.

RESULTS: As shown in Fig. 1, the low-molecular drug and polymeric drug exhibited considerable antitumor efficacy, suggesting the successful neutron capture therapy and the appropriate irradiation condition. In the next fiscal year, we will correlate the therapeutic efficacy with the tumor accumulation level of Gd.

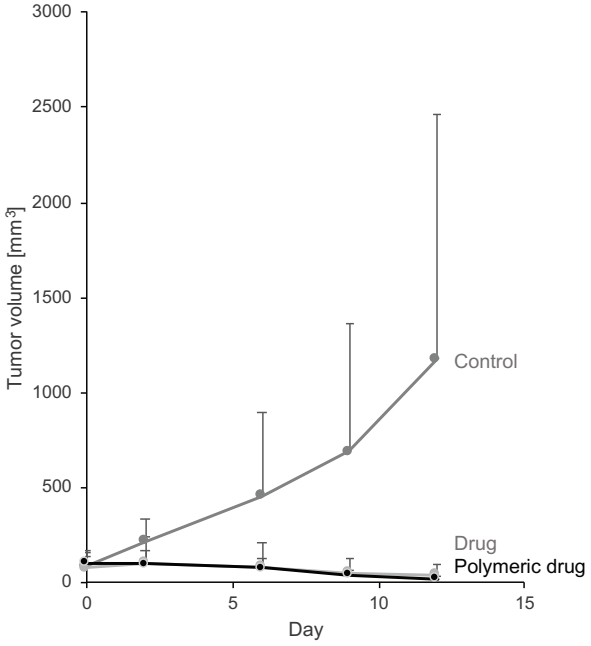

Fig. 1. Antitumor efficacy to subcutaneous CT26 tumor models.

REFERENCES:

[1] P. Mi *et al.*, ACS Nano, **9** (2015) 5913-5921.
[2] N. Dewi *et al.*, J. Cancer Res. Clin. Oncol., **142** (2016) 767-775.

PR5-9 In vivo dose-dependent administration study in mice of Gd-EDTMP: gadolinium neutron capture therapy formulation for bone metastasis

T. Matsukawa[1], M. Suzuki[2], A. Shinohara[1,3], K. Kajino[1], K. Yokoyama[1,4]

[1] *Juntendo University Faculty of Medicine*
[2] *Institute for Integrated Radiation and Nuclear Science, Kyoto University*
[3] *Research Institute for Cultural Studies, Seisen University*
[4] *International University of Health and Welfare*

INTRODUCTION: To develop the next generation of cancer radiotherapy, we evaluated tissue distribution and effects of thermal neutron irradiation on tumor animal models of tetra (methylene phosphonic acid) chelate of Gd (Gd-EDTMP), a neutron capture therapy formulation containing gadolinium. On the other hand, based on findings from previous MRI contrast media studies, Gd formulation are known to cause skin fibrosis called nephrogenic systemic fibrosis (NSF) and calcification of rhabdomyosarcoma and tendons in rare cases. Therefore, in the present study, we conducted an in vivo administration study in mice to investigate the distribution and safety of Gd-EDTMP, and conducted a basic study focusing on the dose-dependency. The distribution of ^{157}Gd in the tissue was imaged by laser ablation inductively coupled plasma mass spectrometry (LA-ICP-MS).

EXPERIMENTS: Gd-EDTMP solutions were prepared from gadolinium chloride and EDTMP. BALB/cAJcl female mice (5 weeks old) were acclimated for 1 week and then intraperitoneally administered a single dose of phosphate-buffered saline solution of Gd-EDTMP (1 mg-Gd/ml) at 5, 10, and 20 mg/kg body weight (n=2 or 3). The mice were fed and watered ad libitum until 21 days post-dose, and their general condition was monitored. Body weight was measured every 2 days until 6 days post-dose, and then every 3-5 days. Cardiac blood sampling was performed under pentobarbital anesthesia on the 21st day of administration. After euthanasia, bones and muscles of the lower limbs were collected to observe Gd distribution. The ^{157}Gd concentrations in blood and left femur were measured by inductively coupled plasma mass spectrometry (ICP-MS, Agilent 8800) after acid digestion by microwave. The right frmur was cut into thin sections every 5 μm using the Kawamoto method, a non-demineralized frozen section preparation method, and the ^{157}Gd distribution was determined by LA-ICP-MS[1]. The invasion of the tumor into the bone was assessed by micrographs of H.E. stained sections of the femur and tibia.

RESULTS and DISCUSSION: No clear toxicity was observed in the dose range of the present study, although a slight weight loss was observed immediately after administration. There were no behavioral changes suggestive of NSF. These results suggest that the Gd-EDTMP formulation is applicable to neutron capture therapy for bone tumors.

Although the blood Gd concentrations were higher in the 20 mg/kg group, no clear dose-dependence was observed in blood. The blood Gd concentration was lower than 50 μg/L (50 ppb), suggesting that most of the administered Gd-EDTMP was distributed promptly in the bone and the Gd amount circulating in the blood was small.

From the result of Gd concentration by conventional ICP-MS analysis, a linear dose dependence of ^{157}Gd distribution to bone was observed. The ^{157}Gd concentration in the whole femur was enriched, about 80 mg/kg in the 20 mg/kg dose group. The results of semi-quantitative analysis by LA-ICP-MS show that Gd was distributed in the part of femur bone in the order of sub per-cent. It was found that a single intraperitoneal administration of Gd-EDTMP resulted in high dose distribution to the bone as the target of this formulation. In general, neutron capture therapy is expected to be effective if the concentration of the neutron capture element in the target tumor is on the order of parts per million (ppm). By limiting the application to bone tumors, Gd-EDTMP might be used sufficiently for neutron capture therapy.

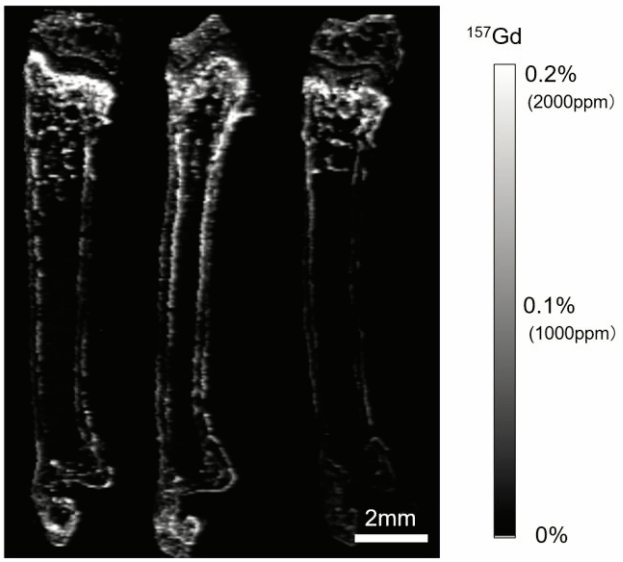

Fig. 1. Semi-quantitative ^{157}Gd imaging of mice femurs 21days after injection of Gd-EDTMP (20mg/kg).

REFERENCES:

[1] A. Kubota *et al.*, Juntendo Medical Journal., **65** (2019): 461-467.

R2P5-10

I-1. PROJECT RESEARCHES

Project 6

PR6 Enhancement of research methods for material irradiation and defect analysis

A. Kinomura

Institute for Integrated Radiation and Nuclear Science, Kyoto University

OBJECTIVES: Irradiation facilities of high-energy particles for neutrons (Material Controlled irradiation Facility), ions (e.g., Heavy ion irradiation facility) and electrons (Temperature-controlled irradiation facilities of KUR-LINAC) have been extensively developed at the Institute for Integrated Radiation and Nuclear Science. The developed facilities have been in operation and opened for joint research projects. One of the objectives of this project is to further improve or optimize irradiation facilities for advanced irradiation experiments.

As characterization techniques for irradiated materials, a slow positron-beam system and a focused ion beam system have been developed and introduced, respectively, in addition to previous characterization facilities such as an electron microscope, an electron-spin-resonance spectrometer, a bulk positron annihilation spectrometer and a thermal desorption spectrometer. Another objective is to introduce new techniques or reconsider analytical methods of previously used characterization techniques.

Based on these two objectives, we expect the enhancement of previous studies and the attraction of new users for the joint research program.

The allotted research subjects (ARS) and co-researchers are listed below. The titles of research subjects are taken from the individual reports.

ARS-1:
Study to improve transport and measurement performance of a slow positron beamline (A. Kinomura et al.)
ARS-2:
Doping effect of Re, Mo, Ta on electron irradiation induced defects in W (T. Toyama et al.)
ARS-3:
Change in the Positron Annihilation Lifetime of Electron-irradiated F82H by Hydrogen Charging 2 (K. Sato et al.)
ARS-4:
Gamma-ray induced light emission from GaN single crystal wafer (T. Nakamura et al.)
ARS-5:
Irradiation technique for study on corrosion resistance of fusion divertor materials to liquid metal during irradiation (M. Akiyoshi et al.)
ARS-6:
Change of free volume in hydrogenated DLC film by the irradiation of soft X X-rays (K. Kanda et al.)
ARS-7
Positron annihilation spectroscopy on diamond-like carbon films (S. Nakao et al.)

RESULTS:

In ARS-1, the brightness enhancement system of the KUR slow positron beamline was evaluated and the brightness enhancement values of 5.6 - 8.5 were obtained from phosphor screen images of microchannel plates. The actual samples were measured by positron annihilation lifetime spectroscopy using the KUR slow positron beam.

In ARS-2, electron-irradiation to W or W-5%Re (in weight %) was performed. After electron irradiation, the average lifetime increased, showing positron trapping to vacancy type defects. In contrast, the average lifetime for W 5%Re remained relatively short compared with the other alloys, suggesting that the formation of irradiation induced defects was suppressed.

In ARS-3, positron lifetimes of the number of hydrogen atoms trapped at vacancy clusters in electron-irradiated F82H were estimated and compared with the results of positron annihilation lifetime spectroscopy. The decrease in the positron lifetime per additional hydrogen atom is approximately 5 ps for 4 hydrogen atoms or less, and approximately 2 ps for 5 hydrogen atoms or more. However, the positron lifetime is almost constant when V5 contains 7 and 8 hydrogen atoms.

In ARS-4, as-grown and gamma-ray irradiated GaN single crystal wafers irradiated at room temperature with gamma-rays of a cobalt-60 source. One end of the optical fiber cable was set on the front face of the GaN placed near the Co source and was led to the analysis room with the spectrometer. The emission characteristics of as-grown GaN and gamma-irradiated GaN were compared.

In ARS-5, irradiation techniques for study on corrosion resistance of fusion divertor materials to liquid metal during irradiation have been developed in this research subject. However, the planned experiments were not performed this year due the limitation of the sample preparation period.

In ARS-6, The irradiation of soft X-rays to the H H-DLC film was carried out at BL06 of the NewSUBARU synchrotron facility. In Doppeler broadening measurements of the irradiated samples, the W parameter decreased linearly with increasing of the S parameter. This indicate indicated that the same types of positron trapping sites are present.

In ARS-7, positron annihilation spectroscopy were performed for type-IV (a-C:H) and type-VI (PLC) films deposited by plasma-based ion implantation (PBII). The S-parameters of carbon layer significantly decrease to ~0.47 for both a-C:H and PLC films after annealed at 800oC. However, a-C:H films only indicate the decrease in S-parameters at shallower region of the films.

SUMMARY: Several new irradiation (electron-beam and gamma-rays) and analytical (slow beam and conventional positron measurements) techniques for verious materials have been developed and demonstrated for the objectives of this project. Such studies may enhance developments of new techniques and materials in various scientific fields.

PR6-1 Study to improve transport and measurement performance of a slow positron beamline

A. Kinomura, N. Oshima[1], A. Uedono[2] and A. Yabuuchi

Institute for Integrated Radiation and Nuclear Science, Kyoto University
[1]National Institute of Advanced Industrial Science and Technology (AIST)
[2]University of Tsukuba

INTRODUCTION: Positron annihilation spectroscopy is an important analytical method to detect vacancy-type defects and vacant spaces of materials. Energy-variable mono-energetic positron beams (slow positron beams) are essential to perform depth-dependent positron annihilation spectroscopy of surface layers such as ion-implanted layers or thin films formed on substrates. Intense positron sources are necessary to obtain slow positron beams for practical use. In general, positron sources based on pair creation can provide higher intensity than radioisotope-based positron sources. A positron source using pair-creation by gamma-rays from a nuclear reactor have been developed by using Kyoto University research Reactor (KUR) to obtain a slow positron beam for materials analysis. In the KUR slow positron beamline, the source size (converter and moderator assembly) is approximately 30 mm in diameter. For typical sample sizes of materials analysis ($\leq$10 mm), it is necessary to reduce beam sizes efficiently while keeping beam intensity as high as possible. For this purpose, a brightness enhancement system have been developed for the KUR slow positron beamline [1]. In addition, measurement systems for positron annihilation lifetime spectroscopy have been optimized in this study.

EXPERIMENTS: The brightness enhancement system of the KUR slow positron beam system has been evaluated in terms of the spot size and the beam intensity. A single-crystalline Ni thin film annealed in vacuum at 750 °C for 1h was used as a re-moderator of the brightness enhancement system. The Ni re-moderator film was cleaned by thermally excited hydrogen atoms after installation in vacuum to remove contamination during handling in air.

The spot sizes and the intensities of the brightness enhanced beams was checked for previously obtained experimental data. In particular, the data sets of the spot images were carefully investigated again by appropriate data treatments. Brightness values were recalculated from the obtained spot sizes as well as the previously measured beam intensities

RESULTS: Beam-spot images were obtained by phosphor screens on microchannel plates (MCP's). The brightness enhancement system was optimized by observing the spot images on the MCP screen positioned at the focal point of the lens. The beam profiles at individual MCP screens were taken using a digital single-lens reflex camera with a CMOS CCD (charge coupled device) image sensor as digital photographs. To avoid unnecessary data processing in the camera, a RAW-mode (a raw-data mode without data processing) was selected for this experiment. Parameters of image acquisition were appropriately selected to keep the linearity of the combination of the MCP and the image sensor (CCD).

Figure 1 shows the normalized horizontal (x-direction) and vertical (y-direction) intensity profiles of the beam spots before and after the brightness enhancement. The distribution in the beam spot were different for horizontal and vertical directions as shown in fig. 1. One of the reasons is that the beam shape at the entrance of the beamline is not circular. We believe that the original beam (i.e., circular beam) extracted from the source was cut several times by the walls of vacuum ducts during beam transportation. We evaluated spot size as a full-width at half-maximum (FWHM) value for horizontal and vertical directions.

The brightness enhancement experiments were performed at acceleration energies of 5.0 – 6.5 keV. The original beam size of ~10 mm was focused to ~1.5 mm. Calculated demagnification factors were approximately 1/6.4 – 1/7.4. The efficiencies of the re-moderator were measured to be 2.3 – 3.8% by gamma-ray intensities measured from the MCPs placed before and after the brightness enhancement system. Based on these measured values, the brightness enhancement values were calculated to be 5.6 - 8.5.

The performance of the positron pulsing system was confirmed last year [2] and the actual samples have been successfully measured by positron annihilation lifetime spectroscopy.

In summary, transport and measurement performance of the KUR slow positron system was evaluated with a positron beam during the KUR operation. The brightness enhancement system and positron pulsing system were confirmed to be effective.

REFERENCES:

[1] Y. Kuzuya et al. J. Phys. Conf. Series 791 (2017) 012012.
[2] M. Nakajima et al. Rev. Sci. Instrum. 91 (2020) 125109.

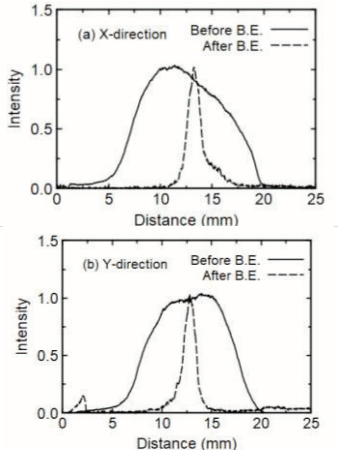

Fig. 1 Beam spot profiles for x and y directions, respectively, before and after brightness enhancement.

PR6-2 Doping effect of Re, Mo, Ta on electron-irradiation induced defects in W

T. Toyama[1], Y. Hatano[2], T. Suzudo[1], C. Zhao[1], K. Inoue[1], A. Yabuuchi[3], A. Kinomura[3], Y. Nagai[1]

[1]*Institute for Materials Research, Tohoku University*
[2]*Organization for Promotion of Research, University of Toyama*
[3]*Institute for Integrated Radiation and Nuclear Science, Kyoto University*

INTRODUCTION: Development of the plasma-facing materials for fusion reactors is in progress over the world. Tungsten (W) is a primary candidate material due to its high melting point, high sputtering resistance to energetic particles, and the very low solubility of hydrogen isotopes which is a notable advantage in reducing tritium (T) retention. However, recent studies have reported that neutron-irradiation and ion-irradiation cause significant enhancement of hydrogen isotope retention in W, due to hydrogen trapping at irradiation-induced defects such as vacancies, vacancy clusters, and dislocation loops. Recently it was found that the addition of rhenium (Re) to W drastically reduces the hydrogen isotope accumulation [1]. As a mechanism for this, quantum chemical calculation has been performed [2]; it is suggested that Re is strongly bound to interstitial atoms, so that recombination of interstitial atoms and vacancies is promoted, and the formation of vacancy-type defects that become hydrogen capture sites is suppressed. However, no experimental studies on this have been obtained. In this study, we performed electron-irradiation to introduce only a simple Frenkel pair to W or W-Re alloy. The effect of Re addition on the defect formation is investigated by the positron annihilation method. In addition, the effect of Mo and Ta is investigated.

EXPERIMENTS: Electron-irradiation to pure W, W-5%Re (in weight %), W-1.5%Mo, and W-5%Ta was performed at LINAC at KUR at 8 MeV, at temperature of < 100 ℃ to the fluence of ~4E+23 e^-/m^2. Positron annihilation measurements (lifetime measurement and coincidence Doppler broadening measurement) were performed. Three-dimensional atom probe (3D-AP) observation was also performed.

RESULTS: Figure 1 shows results of average positron lifetime before and after electron-irradiation for the samples. In pure W, the average lifetime was about 120 ps before electron-irradiation, which is close to the value in W bulk. After electron-irradiation, the average lifetime increased, showing positron trapping to vacancy-type defects induced by electron-irradiation. In W-1.5%Mo and W-5%Ta alloys, the trends were almost similar to that for pure W, indicating that the effect of these elements on the formation of irradiation-induced defects are not significant. In contrast, the average lifetime for W-5%Re remained relatively short compared with the other alloys, suggesting that the formation of irradiation-induced defects was suppressed. The possible candidate for positron trapping site for W-5%Re after irradiation could be dislocations in which positron life-time value may be shorter than mono-vacancy. Other candidate could be vacancy-Re complexes, however, positron lifetime value at vacancy-Re complex might be almost same as at mono-vacancy in W because Re and W are the "neighborhood" in the periodic table. Figure 2 shows the atom maps of Re obtained by 3D-AP. It was revealed that no Re clusters were formed after electron-irradiation. The kinetics of the irradiation-induced defects, i.e. interstitials and vacancies in W-Re alloy is now being simulated with quantum chemical calculation, which would make a direct comparison with the present results to understand the dynamic behavior of defects and solutes under irradiation.

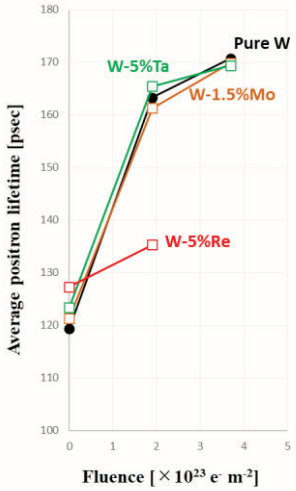

Fig. 1. Average positron lifetime before and after electron-irradiation.

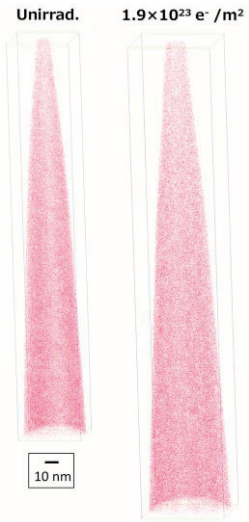

Fig. 2. Atom maps of Re for W-5%Re alloy before and after electron-irradiation.

REFERENCES:

[1] Y. Hatano et al., Nucl. Mater. Energy 9 (2016) 93.
[2] T. Suzudo, A. Hasegawa, Sci. Rep. 6 (2016) 36738.

PR6-3 Change in the Positron Annihilation Lifetime of Electron-irradiated F82H by Hydrogen Charging 2

K. Sato, M. Hirabaru, Y. Kondo, M. Ohta, Q. Xu[1], A. Yabuuchi[1], A. Kinomura[1]

Graduate School of Science and Engineering, Kagoshima University
[1]Institute for Integrated Radiation and Nuclear Science, Kyoto University

INTRODUCTION: The structural materials of spallation neutron sources (SNS) cause more serious irradiation damage than fission reactors due to high-energy protons or spallation neutrons and the formation of extremely larger amount of gas atoms by nuclear transmutation [1, 2]. Therefore, irradiation resistance is required. Reduced activation ferritic/martensitic steel F82H, one of the candidates for fusion reactor structural materials, has good thermal and mechanical properties [3]. Using this steel, many researchers have investigated the effect of He or H on its microstructural evolution [4−6]. The increase in hydrogen retention caused by the interaction with defects has an influence on the mechanical properties of structural materials [7, 8]. Vacancy-type defects are detected well by positron annihilation spectroscopy (PAS). Sato et al. determined the change in the positron annihilation lifetime (PAL) through experiments and simulations [9]. Comparison and estimation of the number of hydrogen atoms trapped at single vacancies in electron-irradiated tungsten by PAS were performed [9]. In this study, to estimate the quantity of hydrogen atoms trapped at vacancy clusters in electron-irradiated F82H, we calculated the PAL of vacancy clusters containing the hydrogen atoms in Fe.

CALCULATION METHODS: The Schrödinger equation of a positron wave function was calculated using the method developed by Puska and Nieminen [10]. The electron density was constructed by the superposition of the atomic wave function provided by Herman and Skillman [11] for core electrons (1s, 2s, 2p, 3s, and 3p), and was obtained using the VASP code [12, 13] for valence electrons (3d, and 4s). The same simulation method as in previous works [9, 14] was used in this study. For the same number of hydrogen atoms trapped at V_5, all configurations were calculated by VASP to obtain the total energy of the model lattice. The PAL was calculated using the configuration with the lowest total energy.

RESULTS: Table 1 shows the calculated PAL of V_5H_n complexes in Fe. The PAL decreases with increasing number of hydrogen atoms. The decrease in the PAL per additional hydrogen atom is approximately 5 ps for 4 hydrogen atoms or less, and approximately 2 ps for 5 hydrogen atoms or more. However, the PAL is almost constant when V_5 contains 7 and 8 hydrogen atoms. This trend agrees with those in previous studies [9, 15]. The number of hydrogen atoms trapped at vacancy clusters during hydrogen charging was estimated using the same method as in [9]. When we theoretically estimated the number of hydrogen atoms trapped at vacancy clusters under cathodic electrolysis hydrogen charging according to Oriani's local equilibrium theory, the value was 14.1. On the other hand, compared between the calculated and experimental results, each V_5 contains 4 hydrogen atoms. This value is much lower than the theoretical value mentioned above. Since samples are kept at ambient temperature for 5 minutes after hydrogen charging, we also discussed whether hydrogen atoms can be de-trapped during 5 minutes. The difference between experimental results and theory cannot be explained by the annealing at ambient temperature.

Table 1. Calculated PAL of V_5H_n complexes vs the number of hydrogen atoms trapped at V_5 (n) in Fe.

Number of hydrogen atoms trapped at V_5.	Positron annihilation lifetime (ps)
0	247
1	242
2	239
3	234
4	228
5	226
6	224
7	222
8	222
10	218
12	214
14	208

REFERENCES:

[1] Y. Dai, G.S. Bauer, J. Nucl. Mater. 296 (2001) 43.
[2] Y. Dai et al., J. Nucl. Mater. 343 (2005) 33.
[3] M. Tamura et al., J. Nucl. Mater. 141−143 (1986) 1067.
[4] X. Jia, Y. Dai, J. Nucl. Mater. 318 (2003) 207.
[5] Z. Tong, Y. Dai, J. Nucl. Mater. 385 (2009) 258.
[6] Z. Tong, Y. Dai, T J. Nucl. Mater. 398 (2010) 43.
[7] H.K. Birnbaum, P. Sofronis, Mater. Sci. Eng. A 176 (1994) 191.
[8] M. Nagumo et al., Metall. Mater. Trans. A 32 (2001) 339.
[9] K. Sato et al., J. Nucl. Mater. 496 (2017) 9.
[10] M.J. Puska, R.M. Nieminen, J. Phys. F 13 (1983) 333.
[11] F. Herman, S. Skillman, Atomic Structure Calculations, Prentice Hall, Inc., Englewood Cliffs, New Jersey, 1963.
[12] G. Kresse, J. Hafner, Phys. Rev. B 47 (1993) 558.
[13] G. Kresse, J. Furthmüller, Phys. Rev. B 54 (1996) 11169.
[14] K. Sato, et al., Phys. Rev. B 75 (2007) 094109.
[15] B.L. Shivachev et al., J. Nucl. Mater. 306 (2002) 105.

PR6-4 Gamma-ray induced light emission from GaN single crystal wafer

T. Nakamura[1], T. Nishimura[1], K. Kuriyama[1], Atsushi Kinomura[2]
[1]Research Center of Ion Beam Technology, Hosei University, Koganei, Tokyo 184-8584, Japan
[2]Institute for Integrated Radiation and Nuclear Science, Kyoto University, Kumatori, Osaka 590-0494, Japan

INTRODUCTION: Emission characteristics for native and radiation induced defects of wide-gap semiconductors such as GaN have been studied by cathode-luminescence using an electron beam and photoluminescence using a UV laser. The possibility in luminescence excited by gamma rays for GaN is an interesting issue. This is because GaN can be used as an application for a gamma ray detector. Furthermore, examining the defects caused by various radiations on GaN is important when assuming its use under the space environment. In our previous study [1, 2], we reported that the energy levels relating to nitrogen vacancy (VN) and gallium vacancy (VGa) were induced by neutron and proton irradiated GaN. The neutron irradiation has been used as the neutron transmutation doping into semiconductors such as GaAs [3], GaP [4], and GaN [5]. We have also reported that the high resistive ZnO bulk single crystals became low resistive due to the Zn interstitials induced by gamma irradiation [6]. Therefore, to survey the radiation effect of gamma ray alone is meaningful.

EXPERIMENTS: As-grown and gamma-ray irradiated GaN single crystal wafers with thicknesses of 250 ~ 750 nm were used for the present study. The crystals were irradiated at room temperature with gamma-rays of 1.17 and 1.33 MeV from a cobalt-60 source of Institute for Integrated Radiation and Nuclear Science, Kyoto University. One end of the optical fiber cable was set on the front face of GaN placed near the Co source and was led to the analysis room with the spectrometer. Part of as-grown GaN was pre-irradiated with an absorption dose rate of 1.771 KGy/h. Total gamma-ray dose for the present study was 990 kGy. The emission characteristics of as-grown GaN and gamma-irradiated GaN were compared. Finally, we compared the photo emission induced by gamma rays with the photoluminescence using a He-Cd laser.

RESULTS: Figures 1(a) and 1(b) show the absorption dose rate dependence of the gamma-ray induced photo emission spectra and the absorption dose rate dependence of the integrated emission intensity, respectively. The film thickness of as-grown GaN single crystal wafer used for the measurement is 250 nm. The integrated intensity on the vertical axis is the integrated value of the entire measurement wavelength range of the emission spectrum. As the absorbed dose rate of gamma rays increases, the emission intensity increases, and the integrated emission intensity increases almost in proportion to the absorption dose rate of gamma-ray. However, the emission peak position near 600 nm did not change due to the difference in absorbed dose rate. The possible excitation mechanism in gamma-ray induced light emission is Compton electrons produced by gamma-ray irradiation.

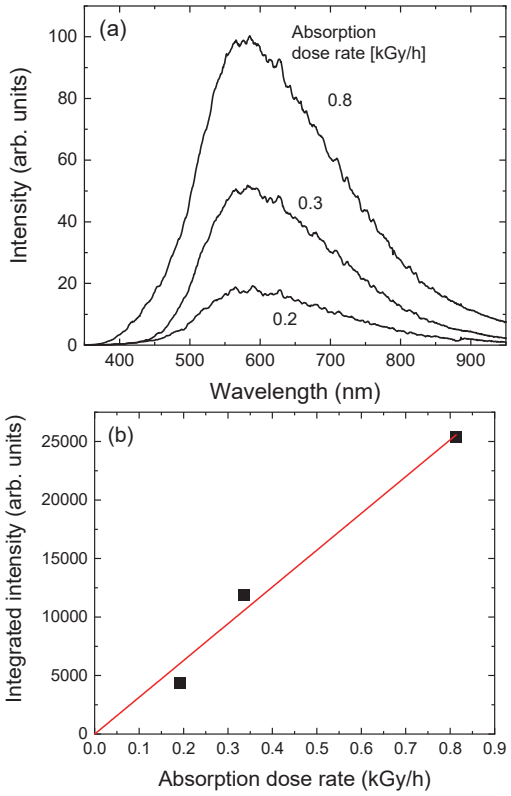

Fig. 1. (a) Absorption dose rate dependence of the gamma-ray induced photo emission spectra from the as-grown GaN single crystal wafer. (b) Absorption dose rate dependence of the integrated emission intensity for the as-grown GaN single crystal wafer.

Part of this research was published in Applied Physics Letters 118, 032106 (2021).

REFERENCES:

[1] K. Kuriyama, M. Ooi, A. Onoue, K. Kushida, M. Okada and Q. Xu, Appl. Phys. Lett. **88** (2006) 132109.
[2] T. Nakamura, N. Nishikata, K. Kamioka, K. Kuriyama and K. Kushida, Nucl. Instrum, Method Phys. Res. B **371** (2016) 251.
[3] M. Satoh, K. Kuriyama and T. Kawakubo, J. Appl. Phys. **67** (1990) 3542.
[4] K, Kuriyama, Y. Miyamoto, T. Koyama, O. Ogawa and M. Okada, J. Appl. Phys. **86** (1999) 2352
[5] K. Kuriyama, T. Tokumasu, J. Takahashi, H. Kondo and M. Okada, Appl. Phys. Lett. **80** (2002) 3328.
[6] J. Tashiro, Y. Torita, T. Nishimura, K. Kuriyama, K. Kushida, Q. Xu and A. Kinomura, Solid State Commun. **292** (2019) 24.

PR6-5 Change of free volume in hydrogenated DLC film by the irradiation of soft X-rays

K. Kanda, F. Hori[1], A. Yabuuchi[2] and A. Kinomura[2]

Laboratory of Advanced Science and Technology for Industry, University of Hyogo
[1]Department of Materials Science, Osaka Prefecture University
[2]Institute for Integrated Radiation and Nuclear Science, Kyoto University

INTRODUCTION: Diamond-like carbon (DLC) film generally has a very strong tolerance of soft X-ray irradiation. However, highly hydrogenated DLC (H-DLC) film with a hydrogen content greater than 40 at.% was reported to be modified by the irradiation of soft X-rays [1]. Soft X-ray irradiation against H-DLC film decreases the film volume and hydrogen content and increases hardness. The density of the H-DLC film was reported to increase dramatically from 1.25 g/cm^3 before irradiation to 1.40 g/cm^3 after the irradiation of soft X-rays with 200 mA·h. However, how the free volume in DLC films is changed by soft X-ray irradiation has not been investigated at all. In this study, we observed the dependence of the free volume in the H-DLC film on the dose of soft X-ray irradiation by Positron lifetime spectroscopy (PAS) measurement using a slow positron beam, and discussed the structural change of the H-DLC film caused by hydrogen desorption upon soft X-ray irradiation.

EXPERIMENTS: H-DLC film was deposited on Si wafers by using an amplitude-modulated radio-frequency plasma-enhanced chemical vapor deposition method. (Nippon ITF Co.) The desired film thickness was 200-nm-thick. The hydrogen content of H-DLC film was estimated to be ≈50 at.%.

The irradiation of soft X-rays to the H-DLC film was carried out at BL06 of the NewSUBARU synchrotron facility [2]. The synchrotron radiation (SR) at the BL06 sample stage had a continuous spectrum from infrared to soft X-rays, lower than 1 keV. An SR dose [mA·h] is derived from the product of the ring current [mA] and exposure time [h].

Positron lifetime spectroscopy (PAS) measurement was performed at the slow positron beam system (B-1) at Kyoto University research Reactor (KUR). Doppler broadening profiles of annihilation γ-rays were obtained using a Ge detector for each positron energy. The low and high momentum parts of spectra were characterized by the *S* and *W* parameters. *S* and *W* parameters as a function of energy were measured in the range of 0 - 30 keV. Positron annihilation lifetime spectroscopy (PALS) was performed at an energy of 2 keV, corresponding to the DLC film on Si. A Kapton (polyimide) film was measured before and after measurements of the DLC samples as a control sample. Obtained lifetime spectra were analyzed by the PALSfit code assuming one-lifetime component.

RESULTS: Figure 1 shows the SR dose-dependence of positron annihilation lifetime. The positron annihilation lifetime of the H-DLC film before irradiation was 0.41 ns and it increased to ≈0.44 ns rapidly at an SR dose of less than 500 mA·h. However, at an SR dose above 500 mA·h, the positron annihilation lifetime was approximately constant at ≈0.44. An increase in positron annihilation lifetime indicates an expansion of free volume in H-DLC film. That is to say, the desorption of hydrogen caused by the irradiation of soft X-rays increases the film density but increases the volume of the voids.

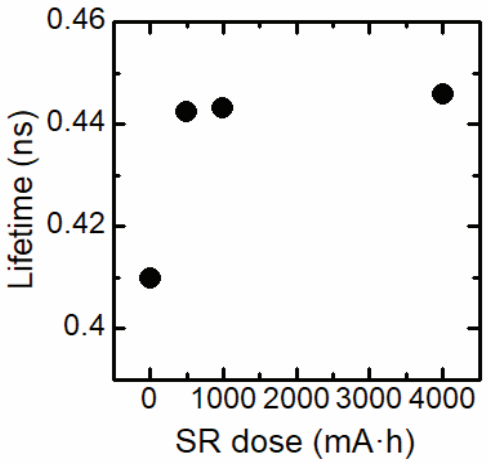

Fig. 1 The SR dose-dependence of positron annihilation life-time.

The *W* parameters were plotted as a function of the *S* parameter in Fig. 2. The *W* parameter decreased linearly with increasing of the *S* parameter. This indicated that the same types of positron trapping sites are present. In other words, different types of vacancies were not created by the desorption of hydrogen due to the SR irradiation.

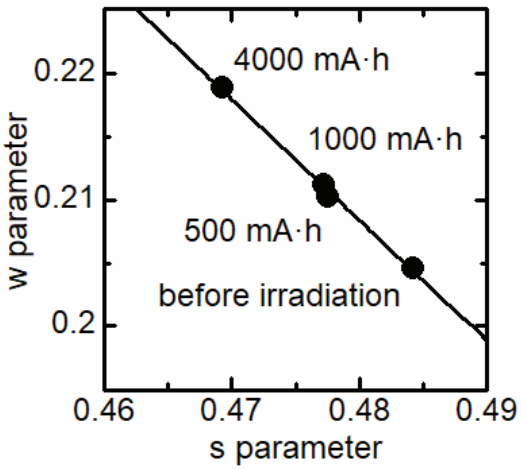

Fig. 2 The core annihilation parameter W versus the valence parameter S, in H-DLC films before and after SR irradiation.

REFERENCES:

[1] K. Kanda *et al*., Sen. Mater., 29 (2017) 817-826.
[2] J. Taniguchi *et al*., Jpn. J. Appl. Phys., **41** (2002) 4304-4306.

PR6-6 Positron annihilation spectroscopy on diamond-like carbon films

S. Nakao, X. Qu[1], A. Yabuuchi[1] and A. Kinomura[1]

Structure Materials Research Institute, National Institute of Advanced Industrial Science and Technology
[1]Institute for Integrated Radiation and Nuclear Science, Kyoto University

INTRODUCTION: Diamond-like carbon (DLC) films have attracted much attention because of their excellent mechanical properties. However, the properties strongly depend on the microstructure of the films which is varied by the deposition conditions and methods. Recently, DLC or carbon films are categorized from type I to VI, which includes graphite-like carbon (GLC) and polymer-like carbon (PLC).
The thermal stability of the films is of importance for practical applications. However, the thermal stability is not always enough at high temperature. It is considered that the degradation of the properties should be caused by the changes of the microstructure at high temperature. The structural changes may be related to hydrogen (H) desorption and creation of defects at high temperature. Many studies have been carried out on the thermal stability of DLC films. However, the principal phenomena, such as defect behavior, are not always clear. Therefore, to make clear the behavior of defects is necessary for every type of DLC films (type I to VI) because of different microstructure and hydrogen content. The positron annihilation spectroscopy (PAS) is one of the useful methods to clarify the defect behavior of materials. The aim of this study is to examine the relationship between the thermal stability and the behavior of defects in several types of DLC films by PAS and thermal desorption (TDS) method.
In a previous report [1,2], the films of type I, III, IV, V and VI were examined by TDS measurement from room temperature (RT) to 800°C and it was found that H desorption clearly started at ~600ºC for a-C:H (type IV) films and at ~400°C for PLC (type VI) films. The results suggested that defects may be created due to H desorption by annealing and the behavior may play important role for the durability of the films. Several types of DLC and carbon films were also examined by PAS measurement [3,4]. The results showed that the situation of the defect in the type III – V films may be similar among as-grown films. However, the changes of S-parameters by thermal annealing might be slightly different depending on preparation conditions, such as source gases. In this study, a-C:H and PLC films are annealed every 200ºC up to 800ºC and examined by PAS measurement.

EXPERIMENTS: Samples for PAS measurement were type IV (a-C:H) and VI (PLC) films which were deposited by plasma-based ion implantation (PBII) under the different conditions. The details on the PBII system were reported elsewhere [5]. Si wafer was used as substrate. The S-parameter was obtained at different positron energies ranging from 0 to 30 keV.

RESULTS: Figure 1 shows the change in S-parameter against positron energy obtained from the PAS spectra of the samples, (a) a-C:H and (b) PLC films, at different annealing temperature. The S-parameters of ~0.49 at less than 5keV and ~0.52 at higher energies correspond to carbon film layer and Si substrate, respectively. The S-parameters of carbon layer significantly decrease to ~0.47 for both a-C:H and PLC films after annealed at 800ºC. However, a-C:H films only indicate the decrease in S-parameters at shallower region of the films. These results suggest that a-C:H films are thermally more stable than PLC films.

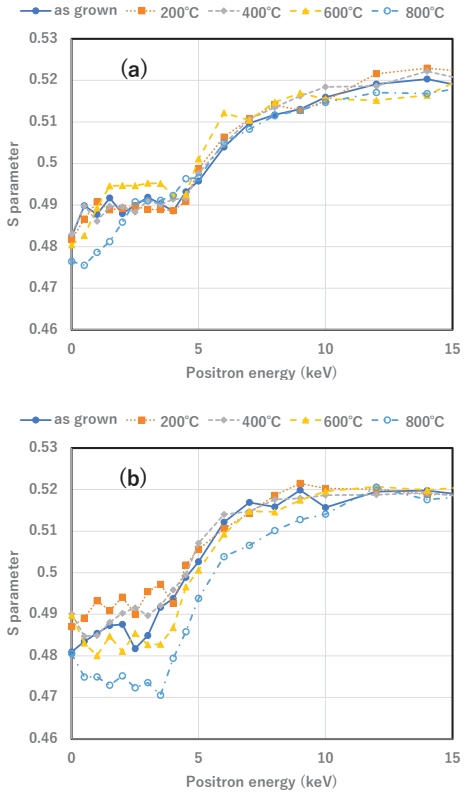

Fig.1. The change in S-parameters against positron energy of (a) a-C:H and (b) PLC films at different annealing temperature.

REFERENCES:
[1] S. Nakao et al., KURRI Progress Report 2016, 28P12-8 (2016) 57.
[2] S. Nakao et al., KURRI Progress Report 2017, 29P6-8 (2017) 32.
[3] S. Nakao et al., KURRI Progress Report 2018, 30P1-8 (2018) 11.
[4] S. Nakao et al., KURRI Progress Report 2019, 31P12-7 (2019) 114.
[5] S. Miyagawa *et al.*, Surf. Coat. Technol., **156** (2002) 322-327.

I-1. PROJECT RESEARCHES

Project 7

PR7 Chemical and electronic properties of Actinide compounds and their applications

T. Yamamura[1], Y. Haga[2], H. Amitsuka[3], T. Suzuki[4], K. Shirasaki[5], M. Nogami[6], M. Abe[7], H. Shishido[8], M. Nakase[9], H. Nakai[10]

[1]*KURNS, Kyoto University*
[2]*Advanced Science Research Center, JAEA*
[3]*Graduate School of Science, Hokkaido University*
[4] *Nagaoka University of Technology*
[5]*Institute for Materials Research, Tohoku University*
[6]*Graduate school of Electronic Eng., Kindai University*
[7]*Department of Chemistry, Tokyo Metropolitan University*
[8]*Graduate School of Engineering, Tohoku University*
[9]*Lab. for Adv. Nuclear Energy, Tokyo Inst. of Tech.*
[10]*Faculty of Science and Engineering, Kindai University*

INTRODUCTION:

Actinide compounds shows a unique chemical and electronic nature due to the partial and insufficient shield of 5f orbital electrons as inner transition elements. We have a deep interest in the aspect of the electronic properties of the actinide compounds and formed the group consisting of three major fields: (1) inorganic and coordination chemistry, (2) electronic properties and (3) theoretical chemistry and its users. These studies will be also useful for application research area such as the handling of the 1F debris and developments of nuclear medicines.

Such research environments to handle actinides elements are extremely difficult to build in ordinary university institutes. The hot laboratory of the KURNS offers unique opportunities for the above-mentioned characteristic research activities.

EXPERIMENTS:

The second fiscal year of the project has been devoted to the setting up the experimental environment and initial test experiments. Each of research fields has made their progress as followings:

(1) T. Suzuki *et al.* has the investigated adsorption behaviors of actinides on polyvinylpolypyrrolidone (PVPP) in nitric acid and hydrochloric acid solutions. The adsorption behaviors were evaluated through measurements of the distribution coefficient.

(2) Y. Haga *et al*. has synthesized the novel uranium intermetallic compound $U_2Pt_6Ga_{15}$. The single-crystalline samples of this compound have been investigated by the measurements of crystallographic, thermodynamic, and transport properties.

(3) M. Nakase *et al.* has studied properties of Phthalocyanine (Pc) as a ligand for an effective extraction of U. First, they built an electrical furnace for purifications of complex materials. A test operation of the furnace was performed by using a Pc-Zn complex they synthesized.

(4) T. Yamamura *et al.* has studied the hydrothermal synthesis of actinide compounds for the U-Zr, U-Fe, and U-Si systems as the simulating-debris compounds. The conditions were (2) 150ºC for 8 h, and (1) 450ºC for 30 min, and an addition of acetaldehyde as organic additive. The characterization was carried out by using XRD.

RESULTS:

(1) From the distribution coefficients measured for uranyl ions on PVPP, T. Suzuki *et al.* confirmed that only actinides adsorb on PVPP and can separate the actinides form other elements such as alkaline earth elements. They concluded that the hexavalent actinide is adsorbed on PVPP both in the nitric acid solution and in the hydrochloric acid solution. They also revealed that the tetravalent actinide is not adsorbed on PVPP in the hydrochloric acid solution but adsorbed in the nitric acid solution.

(2) A newly synthesized compound $U_2Pt_6Al_{15}$ crystallizes in a layered structure of honeycomb planes with an interlayer disorder. The average crystal structure belongs to the hexagonal space group. This compound was revealed to show a magnetic phase transition at approximately 25 K. The relatively sharp transition implicated by the magnetic susceptibility measurement the magnetic ordering is considered to be dominated by the in-plane correlations.

(3) The electric furnace for sublimation purifications (Fig. 1) has been built in the Hot Laboratory of KURNS. The test heating of the ZnPc yielded some impurities out of the crude product, indicating a sign for the purification. Currently the equipment is still being adjusted, and this setup will be fixed and systematic test is planned.

Fig. 1. Building the electric furnace for the sublimation purification method.

(4) Not only the very moderate hydrothermal condition (1), but also relatively severe condition (2), produced the diffractograms based on the UO_2, independent from the metals coexisted. The result agrees well with our previous result without coexisting other metal ions [1]. The atmosphere is indicative of being reductive enough to transfer U(VI) to U(IV). An coexistence of other anions could result in the formation of new salt compounds such as silicates and phospites [2-3]. The conditions are to be improved in future studies.

REFERENCES:

[1] C. Tabata, K. Shirasaki, M. Konaka, Dexin Li, N. Sakai, T. Yamamura, Now in preparation for submission.
[2] E.M. Villa, et al., Inorg. Chem., 52 (2013) 965.
[3] P. Estevenon, et al., Dalton Trans., 49 (2020) 6434.

PR7-1 Antiferromagnetism in uranium intermetallic compound with structural modulation

Y. Haga[1], C. Tabata[2] and Y. Matsumoto[3]

[1]*Advanced Science Research Center, JAEA*
[2]*Institute for Integrated Radiation and Nuclear Science, Kyoto University*
[3]*Faculty of Science, Toyama University*

INTRODUCTION: Uranium ternary compounds having the chemical composition close to 2:6:15 are investigated. The detailed crystal structure investigation suggests the honeycomb arrangement of uranium atoms with the stacking modulation. [1,2] Among them, a new analogue $U_2Pt_6Ga_{15}$ has been successfully synthesized and magnetic property measurements identified the antiferromagnetic ordering.

EXPERIMENTS: The single crystal sample was grown by the gallium flux technique. Electron microprobe analysis ensured the homogeneity of the composition. The crystallographic parameters were determined by the single-crystal X-ray diffraction. The existence of streak scattering elongated along the *c*-axis suggests the stacking modulation as reported for the uranium [1] and rare earth analogues. Electrical resistivity, magnetization and specific heat as a function of temperature between 2 K and room temperature were measured to identify the magnetic phase transition.

RESULTS: Figure 1 shows the temperature dependence of magnetic susceptibility with magnetic field applied along the principal directions of the hexagonal lattice, *a* and *c*-directions. A significant magnetic anisotropy with the magnetic easy axis along the *c* is observed. Paramagnetic behavior is observed between about 25 K and 60 K for the field along the *c*-axis. The paramagnetic effective moment is estimated as 3 μ_B/U, suggesting that uranium atoms carry magnetic moments. With lowering temperature, a peak appears in susceptibility, and, subsequently, a sudden drop is observed at 25.4 K. Susceptibility further decreases down to the lowest temperature of the measurement. On the other hand, susceptibility with the field along the *a*-axis is smaller and less temperature dependent, even below the susceptibility anomaly at 25.4 K. These observations are consistent with the occurrence of an antiferromagnetic ordering at the Néel temperature T_N = 25.4 K with the ordered moment along the *c*-axis. Electrical resistivity and specific heat measurements (not shown) also detected an anomaly related to the antiferromagnetic transition. Considering the stacking disorder mentioned above, such a relatively sharp phase transition seems unlikely, because of the modulated magnetic interaction due to partially disordered atomic arrangements. The present observation therefore suggests that the magnetic interaction within the honeycomb layer is dominant and (disordered) interlayer interaction plays only a secondary role.

It should be noted that there is an unusual behavior of magnetic susceptibility just above T_N. A broad maximum appears at 27 K. Such anomaly is not seen in ordinary antiferromagnets. However, in uranium and other correlated magnets show similar anomalies in the paramagnetic state. To clarify the origin of the anomaly, we measured field dependence of magnetization in detail. It turned out that the position of the broad anomaly changes with magnetic field in exactly the same manner as that of T_N. On the contrary, the maximum appearing in the correlated magnets has different field dependence in general. It is therefore likely that the susceptibility maximum in $U_2Pt_6Ga_{15}$ is related to antiferromagnetism rather than the electronic correlation, namely, the structural modulation probably modulates magnetic interaction between the honeycomb layers leading to a distribution of the T_N resulting in relatively broad anomaly above the main antiferromagnetic transition.

To conclude this report, we found a new uranium intermetallic antiferromagnet with honeycomb arrangements. Considering the relatively sharp transition, antiferromagnetism within the honeycomb layer is likely. Further investigation on the magnetic structure and magnetic interaction are needed to clarify the magnetic characteristics.

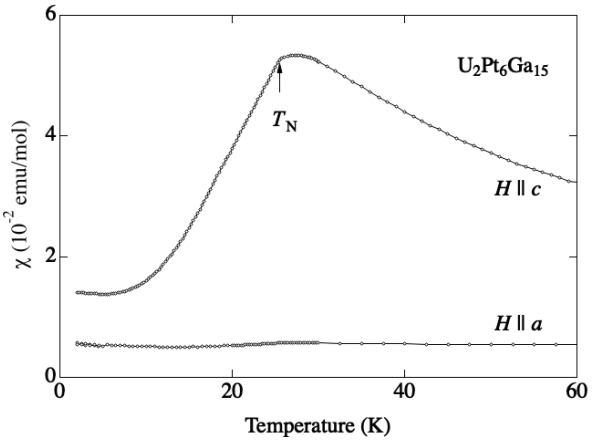

Fig. 1. Temperature dependence of magnetic susceptibility measured on a single crystal sample of $U_2Pt_6Ga_{15}$.

REFERENCES:

[1] Y. Haga *et al.*, JPS Conf. Proc., **29** (2020) 013003.
[2] Y. Matsumoto *et al.*, to be published in J. Phys. Soc. Jpn.

PR7-2 Adsortpion Chracterization of Actinide Chemical Species on Solid Adsorbents

T. Suzuki[1], F. H. Ikhwan[1], R. Murayama[1], S. Fukutani[2] and T. Yamamura[2]

[1]Department of Nuclear System Safety Engineering, Ngaoka University of Technology
[2]Institute for Integrated Radiation and Nuclear Science, Kyoto University

INTRODUCTION: The accurate and precise analyses of actinides and many kinds of fission products in the spent fuels and/or nuclear debris are important issue for nuclear fuel management and the radioactive waste management. The separation or removal of the actinides is required before the above analyses. In addition, recently, the supply of α-nuclides for α-therapy is becoming increasingly important. Increase. For the purpose, the actinides separation from the decay series is required. In this year, the adsorption behaviors of actinides on polyvinylpolypyrrolidone (PVPP) were investigated in nitric acid and hydrochloric acid solutions. We use the uranyl ion as a representative of the hexavalent actinide ions, and the thorium ion as representative of the tetravalent actinide ions.

EXPERIMENTS: We used the commercially available type PVPP (Alfa Aesar). The uranyl ion was used in ICP-MS standard solution (XSTC-289, SPEX). The other ions including thorium ion were used in XSTC-311. The adsorption behaviors were estimated by using distribution coefficient, Kd [mL/g]. The Kds were obtained by batch experiment. The adsorption behaviors of alkali metal ions, alkaline earth ions, several transition metal ions such as Cr, Ni, Fe, Ag, etc. were also investigated.

RESULTS: The distribution coefficients of uranyl ion are shown in Fig.1. The uranyl ion in nitric acid solution is adsorbed on PVPP under the wide range of concentration. While in hydrochloric acid solution, the distribution coefficient increases with the concentration. In the case of thorium ion, the adsorption on PVPP was not observed in the hydrochloric acid solution, but was observed in the nitric acid solution as shown in Fig. 2. The distribution coefficient was confirmed to increase with the concentration of nitric acid. From results of distribution coefficients of uranyl ion and thorium ion, we concluded that the uranium and thorium can be separated in the both case of nitric acid and hydrochloric acid. It was not observed the adsorption of other elements on PVPP in nitric acid solution. While in hydrochloric acid solution, the slight adsorptions of iron and silver were observed. From these obtain data, we confirmed that we make only actinides adsorb on PVPP and can separate the actinides form other elements such as alkaline earth elements. In conclusion, the hexavalent actinide is adsorbed on PVPP both in the nitric acid solution and in the hydrochloric acid solution, and the tetravalent actinide is not adsorbed on PVPP in the hydrochloric acid solution but adsorbed on PVPP in the nitric acid solution.

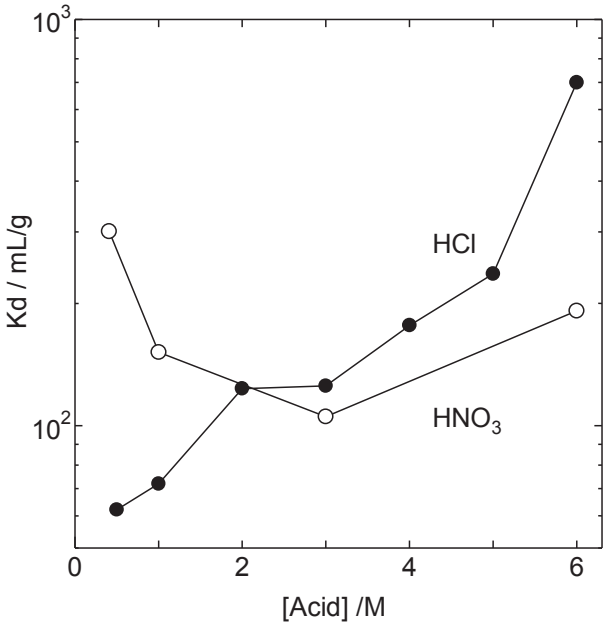

Fig. 1. Adsorption behaviors of uranyl ion on PVPP in nitric acid solution and hydrochloric acid solution.

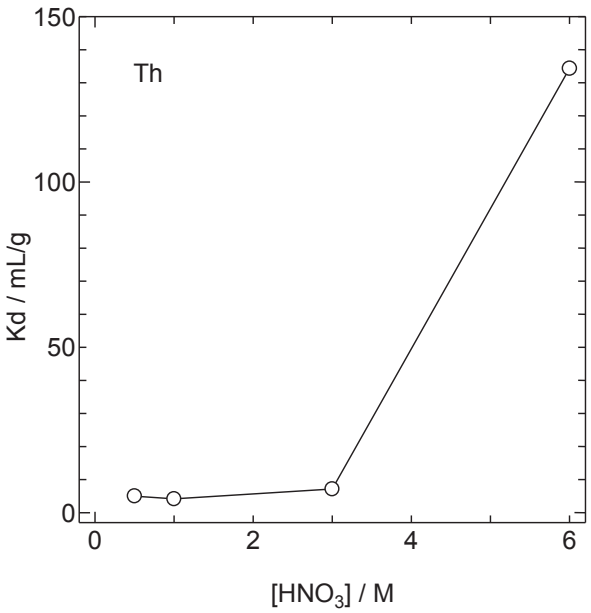

Fig. 2. Adsorption behaviors of thorium ion on PVPP in nitric acid solution.

PR7-3 Synthesis of nobel phthaloyanine derivatives and effect of substitutent on recognition of light actinide and chemical property-2

M. Nakase[1], M. Harigai[1], C. Tabata[2], T. Yamamura[2]

[1]*Institute of Innovative Research, Tokyo Institute of Technology*
[2]*Institute for Integrated Radiation and Nuclear Science, Kyoto University*

INTRODUCTION:

In Th fuel cycle, effective separation of U from Th and other fission products in spent Th fuels is needed. To enable that, thorium–uranium extraction (THOREX) process, similar to the plutonium–uranium redox extraction (PUREX) process, has been studied[1]. In the THOREX process, UO_2^{2+} is extracted by tri-*n*-butyl phosphate (TBP) with the aid of $Al(NO_3)_3$. Some of the other ligand which consisted of C, H, O, N atoms (CHON principle) such as monoamide is recently reported for U/Th separation [2]. In this study, Phthalocyanine (Pc) was selected as the main structure of the ligand which also satisfy the CHON principle. To make the solubility of Pc in organic solvent higher, the Pc derivatives with substituent modification is ongoing. The Pc-metal complex in organic solvent itself is also interesting to investigate. In FY2020, some Pc complexes were synthesized. To obtain the complex with actinide, the purification technique with minimized waste production is highly desirable. Therefore, some of the purification technique is tested, and sublimination setup was equipped in the control area.

EXPERIMENTS AND RESULTS:

Synthesis of Pc was done at Tokyo Tech as shown in **Figure 1**. By ^{1}H-NMR measurement, successful synthesis of the desired products was confirmed but small amount of impurity was detected.

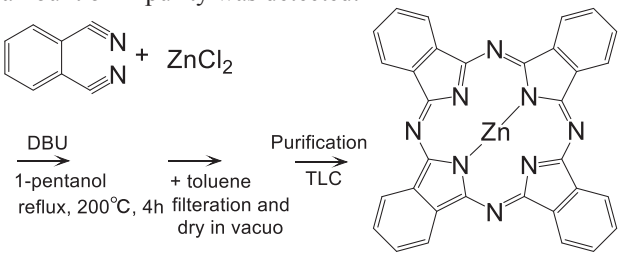

Figure 1 Synthetic scheme of Pc-Zn complex

To purify the product, recrystallization was firstly tested. As well known, the Pc-derivatives are not soluble into most of the solvents, hence, suitable noble solvent was not determined. In small scale, recrystallization seems to be well proceeded, but the purification was not successful once the scale becomes large. In FY2020, some of the purification methods were tested as shown in **Figure 2**. When the chromatography was implemented, the green product did not move much, indicating huge amount of organic solution is needed. The thin-layered chromatography also gave green product but this method is not suitable for the large-scale synthesis. The soxlet extraction is convenient method to efficiently remove impurity. In our test, sometimes it is difficult to keep the product in the cylindrical filter equipped in the center position. The final attempt was sublimination method. This method was done intensively by T.Yamamura et al.,for Pc-U or -Th complexes purification. The quartz tube was sealed and the tungsten wire was equipped inside the tube with changing the pitch. Currently the equipment is still adjusting but in FY2021, this setup will be fixed and systematic test will be done.

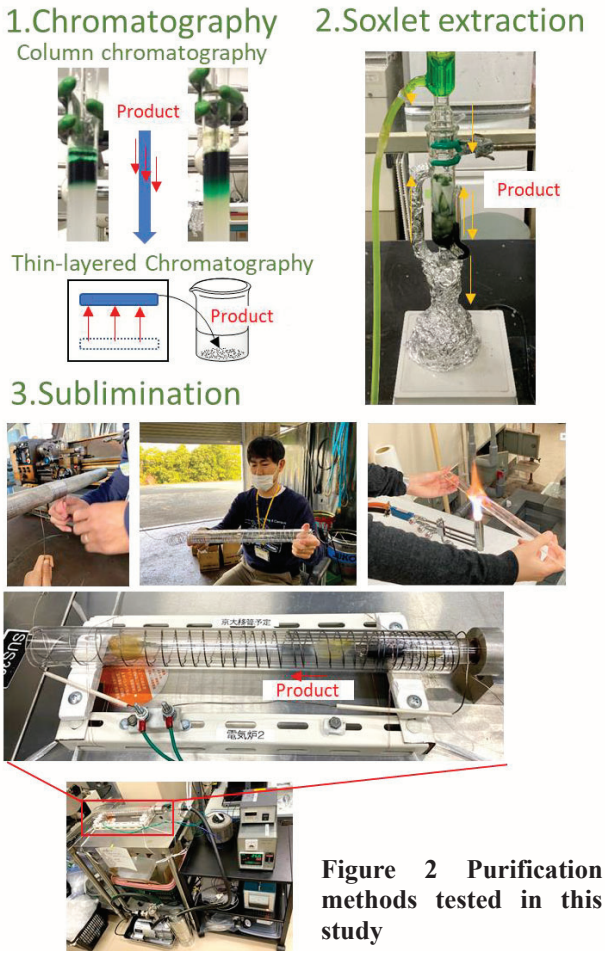

Figure 2 Purification methods tested in this study

CONCLUSIONS and FUTURE PLAN:

Purification of Pc-metal complexes were surveyed and some insight for waste minimization was obtained. The plan in FY2021 is listed;

1. Synthesis and purification of Pc derivatives with long alkyl chain to increase solubility in organic phase.
2. Upgrade the purification method.
3. Implement solvent extraction experiment
4. Survey of the synthetic scheme of Pc derivatives to make the Pc *N*,*O*-hybrid donor ligand

REFERENCES:

[1] R.H.Rainey and J.G.Moore, *Nucl Sci Eng*, 10(4), 367–371, 1961.
[2] P.N.Pathak, *Solv Ext Ion Exch*, 20(3), 293–311, 2002.

PR7-4 Hydrothermal synthesis of actinide mixed oxides for basic debris research

T. Yamamura[1], C. Tabata[1], M. Nakase[2], K. Shirasaki[3]
[1]*KURNS, Kyoto University*
[2]*Lab. for Adv. Nuclear Energy, Tokyo Inst. of Tech.*
[3]*Institute for Materials Research, Tohoku University*

INTRODUCTION: The Fukushima Daiichi Power Plant (1F) of Tokyo Electric Power Company, Incorporated (TEPCO) is characterized not only by the core meltdown but also by the formation of debris containing not only fuels and claddings but also containment vessels, concrete structures, and seawater salts. The composition of the debris is considered to be U-Zr-Fe(Ni,Cr)-Si-O-B-C-FP. Materials with different elemental compositions, structures, and electronic states are considered to be generated locally through cooling processes such as crystallization and amorphization as oxide or metallic phases.
From the standpoint of actinide science, the study on the physical and chemical mechanisms on their aging will contribute to the improvement of reliability in the storage of 1F molten debris. According to the knowledge of materials science, such micro-material and structural changes at grain boundaries and within grains due to lattice damage should be reflected in macroscopic properties such as shape and mechanical properties.
Specifically, we have found that the lattice parameter in the $(U,Th)O_2$ and $(U,Np)O_2$ system follows the Vegard's law, which decreases linearly with Np content, and that Na exists in a lattice position with good symmetry in the $(U,Na)O_2$ system by ^{23}Na NMR [1].
In this study, we investigated in the extension of our hydrothermal method to the U-Zr, U-Fe-Ni-Cr, U-Fe-Si, and U-B systems. For the study in the first year, we have carried out the hydrothermal experiments for the U-Zr, U-Fe, and U-Si systems.

EXPERIMENTS: We have developed techniques for hydrothermal synthesis by fabricating an ultra-small cell which can be used under the condition of 500ºC-25 MPa. Uranium was initially used as hexavalent nitrate or chloride, but electrolytically reduced tetravalent was also used. In the hydrothermal synthesis, the salts and organic complexes of each element are added and dissolved to produce a homogeneous reaction, which may be closer to the actual condition of the simulated debris.
Hydrothermal experiments for the U-Zr, U-Fe, and U-Si systems were carried out by using $UO_2(NO_3)_2$ and $Fe(NO_3)_3$ as starting materials, zirconium nitrate dihydrate, sodium metasilicate dihydrate, (1) 150ºC for 8 h, and (2) 450ºC for 30 min, and an addition of acetaldehyde as organic additive, etc. The slurry was centrifuged and the solid phase was collected. The slurry was centrifuged, the solid phase was collected, dried, and XRD was obtained. The slurry was centrifuged and the solid phase was collected.

RESULTS: Not only the very moderate hydrothermal condition (1), but also relatively severe condition (2), produced the diffractograms based on the UO_2 as shown in Fig. 1, independent from the metals coexisted. The result agrees well with our previous result without coexisting other metal ions [1]. The atmosphere is indicative of being reductive enough to transfer U(VI) to U(IV). An coexistence of other anions could result in the formation of new salt compounds such as silicates and phospites [2-3].

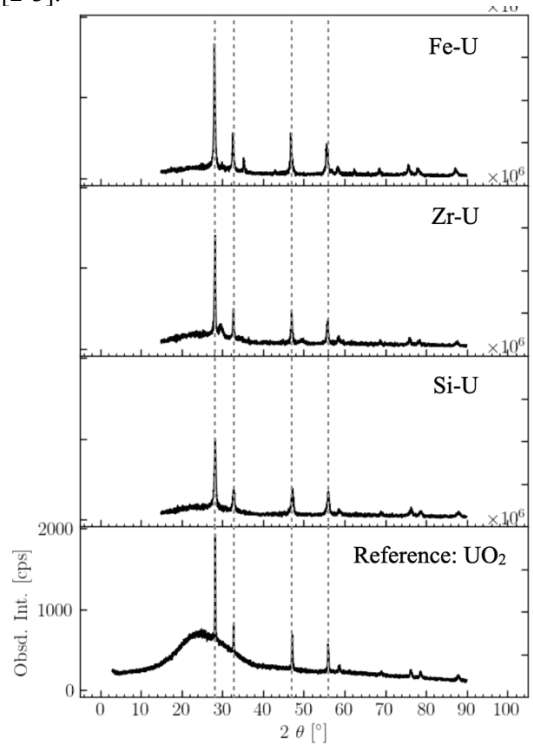

Fig. 1. X-ray diffractograms for samples obtained after hydrothermal synthesis at 450ºC for 30 min. Starting materials are described in text.

By referring to recent researches by other researchers, hydrothermal synthesis of actinide compounds is challenging in some compounds. The phosphite salts of actinides(IV) are not extensively studied, but by using organic templates, some compounds with rare structures have been prepared [2]. On the other hand, the hydrothermal synthesis of silicates of rare earths and actinides such as $ThSiO_4$ and $USiO_4$ has been widely studied, but the synthesis was not reproducible. Eventually, the synthesis of $PuSiO_4$ has been done including calcination at 1350°C after pellet formation [3]. Thus, various developments could be necessary for hydrothermal synthesis of uranium salts.
The conditions are to be improved in future studies.

REFERENCES:
[1] C. Tabata, K. Shirasaki, M. Konaka, Dexin Li, N. Sakai, T. Yamamura, Now in preparation for submission.
[2] E.M. Villa, et al., Inorg. Chem., 52 (2013) 965.
[3] P. Estevenon, et al., Dalton Trans., 49 (2020) 6434.

I-1. PROJECT RESEARCHES

Project 8

PR8 Development on Neutron Imaging Application

Y. Saito

Institute for Integrated Radiation and Nuclear Science, Kyoto University

1. Objectives and Allotted Research Subjects: Neutron imaging provides valuable information which cannot be obtained from an optical or X-ray imaging. The purpose of this project is to develop the imaging method itself and also the experimental environment for expanding the application area of the neutron imaging. The allotted research subjects are as follows:

ARS-1: Measurements of Multiphase Dynamics by Neutron Radiography (Y. Saito et al.)
ARS-2: Void Fraction Measurement of Refrigerant Two-Phase Flows in Cross-Flow Parallel Mini-Channel Evaporator (H. Asano et al.)
ARS-3: Visualization of Transient Change of Refrigerant Distribution in Activated Carbon Particle Layer (H. Asano et al.)
ARS-4: Neutron radiography measurements of the mixing behavior of reactant streams during hydrothermal synthesis (S. Takami et al.)
ARS-5: Quantatively Visualization of a Microchannel Heat Exchanger under Non-uniformly Heated Condition (H. Umekawa et al.)
ARS-6: Frost Deposition Distribution Estimated by X-ray and Neutron Cooperative Imaging (R. Matsumoto et al.)
ARS-7: 3D Imaging of Plant roots (U. Matsushima et al.)
ARS-8: Analysis of vapor pressure in fire spalling of high-strength concrete (M. Kanematsu et al.)
ARS-9: Measurement of coolant inside a flat laminate vapor chamber in the vertical posture with Neutron Radiography (K. Mizuta et al.)
ARS-10: Visualization of Organic Materials for Development of Industrial Applications (M. Kitaguchi et al.)
ARS-11: Visualization of Excimer cluster tracers by using Neutrons (Y. Tsuji et al.)
ARS-12: Development of Neutron Imaging Techniques and Its Application (T. Sakai et al.)
ARS-13: Dynamic Visualization of Hydrogen Accumulation Behavior in Metallic Materials via Neutron Imaging (K. Shimizu et al.)
ARS-14: In-situ Lithium diffusion behavior in NASICON-Type Structured Lithium Ion Conductive Composite by Means of Neutron Radiography (S. Takai et al.)

2. Main results and the contents of this report: To develop neutron imaging, our imaging system was developed so that high-speed imaging could be per-formed at thermal neutron flux of 10^7 n/cm^{2}s. Such improved system was shared with all of the project members and valuable results were obtained as follows:

ARS-1 improved the above-mentioned high-speed imaging system at the B4 port. The spatial and temporal resolution of the system was tested. Then, the present system was applied to investigate the effect of motion blur in the observation of rapidly moving object and to visualize particle motions dropped in a molten glass.
ARS-2 applied to neutron imaging to refrigerant two-phase flows in a cross-flow parallel mini-channel evaporator. HFC-134a and FC3283 were used as the refrigerant. From the measurement results, the effect of rib in the mini-channel was clarified in the two-dimensional void fraction distributions. It indicates that the offset rib is not effective.
ARS-3 applied neutron imaging to measurements of refrigerant distribution in activated carbon, which is strongly related to the performance of adsorption refrigerator. Liquid ethanol was used as the refrigerant. Transient change of the refrigerant in the activated carbon particle layer.
ARS-4 applied neutron imaging to the flow visualization of mixing behavior of reactant streams during hydrothermal synthesis. Water and Aqueous solution of GD(CH3C)3 was fed into T-junction tube using high pressure pumps, simultaneously. Due to the attenuation of neutron in Gd in the aqueous solutions, the mixing behavior was clearly visualized.
ARS-5 applied the neutron imaging to boiling two-phase flow in a microchannel heat exchanger under non-uniformly heated conditions. The effect of heat flux distributions on the heat transfer was estimated.
ARS-6 applied neutron imaging to frosting behavior in cooling heat exchange system. Simultaneous Xray and neutron imaging was performed to clarify the 3D frost deposition at the B4 port.
ARS-8 applied neutron imaging to analysis of vapor pressure in fire spalling of high-strength concrete. Measuring moisture transfer inside concrete quantitatively, how vapor pressure inside concrete affect spalling was considered.
ARS-9 applied neutron imaging to measurements of coolant distribution in a flat laminate vapor chamber. Experiments were performed at the E2 port. Measurement results indicate that the liquid thickness depends mainly on the inner structure of the vapor chamber rather than its outer size and shape.
ARS-13 performed dynamic visualization of hydrogen accumulation behavior in metallic materials. However, the contrast of image was not enough. Probably the absolute value of the hydrostatic stress was relatively low, or the size of the formed hydrostatic stress field was much smaller that the spatial resolution of the detector system.
ARS-14 applied to in-situ Lithium diffusion behavior in NASICON-Type structured Lithium Ion conductive composite. From measurement results, it indicates that the material should be changed.

PR8-1 Measurements of multiphase flow dynamics using neutron radiography

Y. Saito, D. Ito and N. Odaira

Institute for Integrated Radiation and Nuclear Science, Kyoto University

INTRODUCTION: Neutron radiography (NRG) is a powerful tool for multiphase flow visualization. Especially, it is possible to observe the flow at high temperature and pressure conditions using NRG. In this work, our neutron imaging system was improved to observe the dynamic two-phase flows. With the improved system, particle motions in a high temperature molten glass was visualized.

IMPROVEMENT OF HIGH-SPEED NEUTRON IMAGING SYSTEM: A high-speed neutron imaging system for flow visualization has been developed at the B-4 supermirror neutron guide facility [1] of the Institute for Integrated Radiation and Nuclear Science, Kyoto University. Using the system with an optical image intensifier, a frame rate of 10,000 fps could be achieved. However, the spatial resolution was deteriorated (~1 mm) due to the highly intensification of the optical light emitted from the scintillator. The current work focuses on the improvement of the spatial resolution in high-speed neutron imaging. So, a neutron image intensifier was applied instead of the optical image intensifier and neutron scintillator, as shown in Fig. 1. As a result, the spatial resolution was improved although the frame rate decreases to few hundred fps. This system is suitable for relatively slow phenomena. In the high-speed neutron imaging, the imaging system which is appropriate to research target should be selected and used.

VISUALIZATION OF PARTICLE BEHAVIOR IN MOLTEN GLASS: Neutron imaging experiments were conducted at the B-4 port of the Kyoto University Research Reactor. Soda-lime glass beads were filled in a zirconia melting pot and heated by an electric heating furnace. Figure 2 shows the neutron transmission images of glass melting process and the temperature change in the furnace. At the beginning of the heating, the temperature is lower than the melting point and the apparent volume was large due to the existing void among the glass beads. When the temperature increases around 1,000 ° C, the glass starts to melt and the apparent volume of the glass decreases gradually. Finally, the glass melts completely. As shown in Fig.2, the visualization of molten glass in the furnace can be performed above 1,000 ° C by using the neutron imaging. Then, a tungsten sphere with 10 mm in diameter was dropped into the molten glass in the melting pot. Figure 3 shows the neutron transmission images of the falling sphere in the molten glass. The sphere was clearly observed by neutron transmission imaging. The molten glass has very high viscosity, therefore, the particle motion in the glass is relatively slow. From these images, the velocity could be estimated. The relation between the fluid temperature and the viscosity was evaluated for high temperature molten glass. However, the obtained images have still some noises. The post image processing method would be important for more accurate analysis like a particle size estimation.

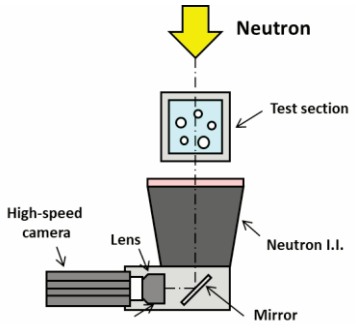

Fig. 1 Neutron imaging system with neutron image intensifier.

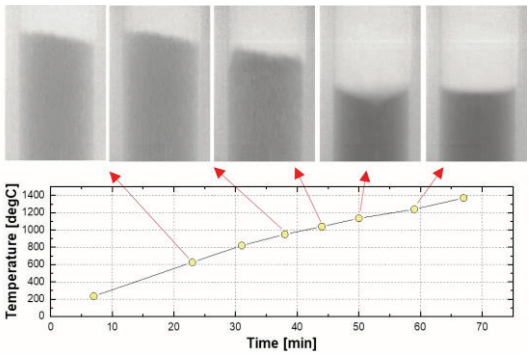

Fig. 2 Melting process of soda-lime glass.

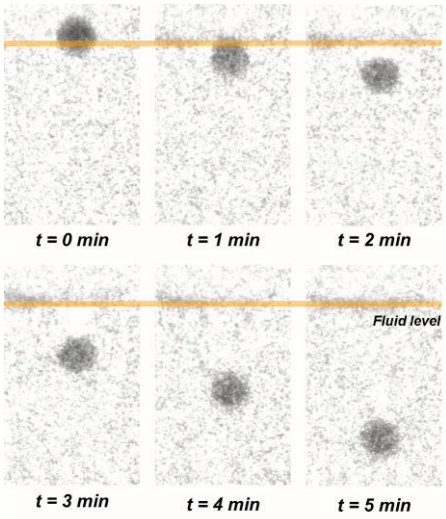

Fig. 3 Neutron transmission images of falling sphere in molten glass at 1200 ° C.

REFERENCES:

[1] Y. Saito, *et al*., Nucl. Instr. Meth. Phys. Res., A, **651** (2011) 36-41

PR8-2 Void Fraction Measurement of Refrigerant Two-Phase Flows in Cross-Flow Parallel Mini-Channel Evaporator

H. Asano, H. Murakawa, S. Inoue, K. Sugimoto, D. Ito[1], Y. Saito[1]

Department of Mechanical Engineering, Kobe University
[1] Institute for Integrated Radiation and Nuclear Science, Kyoto University

INTRODUCTION: Mini-channel compact heat exchangers are attracting attention because of the compactness and reduction in temperature difference between fluids leading to the improvement of the efficiency. Since smaller diameter leads to not only larger heat transfer area density but also larger pressure loss, micro channel heat exchanger has many parallel channels. In the case that the heat exchanger is used for an evaporator, refrigerant flow distribution often causes a deterioration in the heat transfer performance. Especially, when the refrigerant flow is heated by a heating medium flowing in channels with cross-flow arrangement as shown in Fig. 1, non-uniform heat flux might cause the maldistribution of refrigerant flows. In this study, boiling flow behaviors in a single layer microchannel heat exchanger made of stainless steel had been visualized by neutron radiography at B4 port. Void fraction distributions had been measured from the radiographs.

EXPERIMENTS: The tested heat exchanger was manufactured by diffusion bonding of thin stainless-steel plates, and consists of single-layer refrigerant and heating medium parallel channels. The channel cross-section and flow arrangement are shown in Fig. 1 and 2, respectively. HFC-134a and FC3283 were used as the refrigerant and the heating medium, respectively. Each channel has semi- circular cross-section. The heat exchanger was placed in a vertical plane to form vertically upward boiling flows of the refrigerant. The details of the channel patterns are shown in KURNS Progress Report 2019. Radiographs were recorded by a cooled CCD camera with the exposure time of 30 seconds and the pixel size of 88 μm/pixel.

RESULTS: Void fraction was measured for each pixel of visualized images. In gas-liquid two-phase flows in a small diameter non-circular channel, liquid would be accumulated in corners by surface tension. So, volumetric cross-sectional average void fractions were calculated. The distributions for the test sections with the straight, perforated-rib, and offset-rib channels are shown in Fig. 3 (a) to (c), respectively. The horizontal distribution of the void fraction for each test section are also shown in Fig. 4. It can be clearly observed that the void fraction on the right side close to the heating medium inlet was higher than the left side due to the larger temperature difference. The inhomogeneous distribution could be improved by perforation to the ribs. The offset rib was not effective.

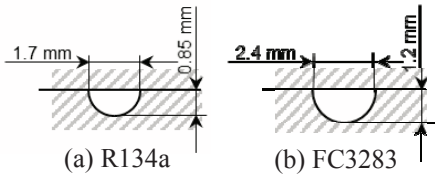

(a) R134a (b) FC3283

Fig.1 Channel cross-section

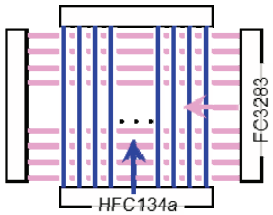

Fig. 2 Channel arrangement

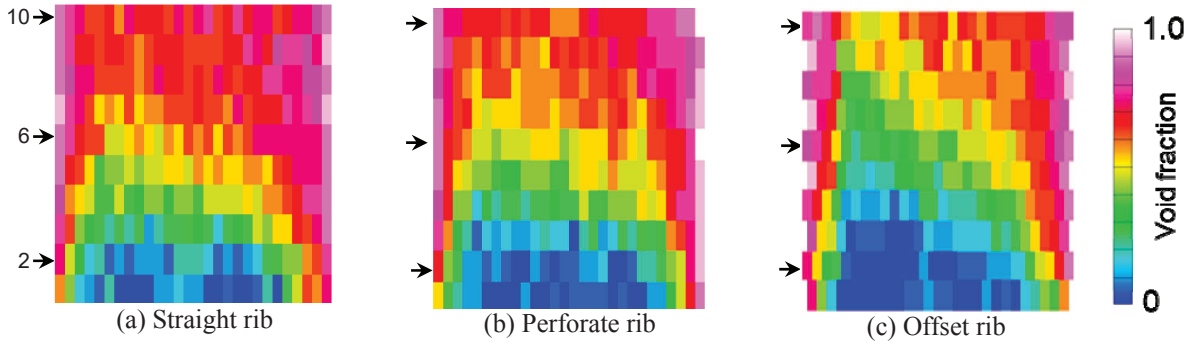

(a) Straight rib (b) Perforate rib (c) Offset rib

Fig. 3 Volumetric average void fraction distribution.

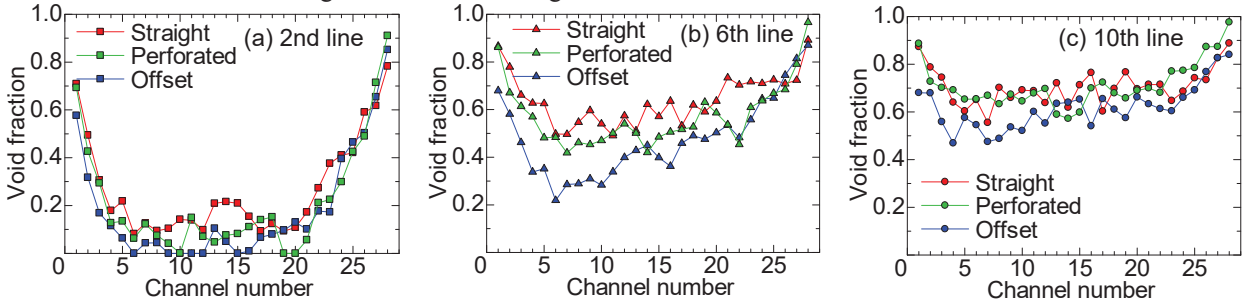

Fig. 4 Effect of the channel pattern on horizontal void fraction distribution.

PR8-3 Visualization of Transient Change of Refrigerant Distribution in Activated Carbon Particle Layer

H. Asano, H. Murakawa, K. Sugimoto, D. Ito[1], Y. Saito[1]

Department of Mechanical Engineering, Kobe University
[1] Institute for Integrated Radiation and Nuclear Science, Kyoto University

INTRODUCTION: Adsorption refrigerator is one of the efficient tools for waste heat recovery because the refrigerator can be driven by heat at relatively low temperature. Refrigerant vapor from an evaporator at low pressure is adsorbed in an adsorbent particle layer in an adsorber. In order to keep vapor adsorption rate and evaporation pressure, a batch process is applied using two or more adsorbers. The adsorbers alternate between the drying process by heating and the adsorption process with cooling. Adsorption amount of refrigerant increases with decreasing the adsorbent temperature for a setting refrigerant pressure. However, in the adsorption process, the adsorbent is heated by adsorption heat which is equivalent to the enthalpy difference between vapor and liquid of refrigerant. So, quick removal of the adsorption heat from the adsorbent is required to enhance the adsorption. Metallic fins are often used for higher heat diffusion. Since the installed metallic fins lead to the increase in heat capacity of the adsorber, fin placement should be optimized. Although it is required to understand the distribution of adsorption amount in adsorption process, it is difficult to measure it, and only the change of total amount has been measured. In this study, the distribution of adsorption amount in an adsorbent particle layer in a cylindrical cell was visualized by neutron radiography at the E2 port.

EXPERIMENTS: Activated carbon and ethanol were used as the combination of adsorbent and refrigerant. The mean particle diameter and specific surface area of the activated carbon were 86 μm and 3170 m^2/g, respectively. Activated carbon was installed in a cylindrical cell with thin stainless-steel wall and the inner diameter of 21 mm. The depth of the adsorbent layer was about 20 mm. The installed amount of dry activated carbon was 1.8 g. The bottom of the cell was brazed on a brass plate whose temperature was maintained by cooling water. The cell was connected to a liquid ethanol reservoir immersed in a temperature-controlled water. The configuration of the cell is shown in Fig. 1. An aluminum pin with the diameter of 3 mm and the height of 20 mm was placed at the center of the cell.
The mass attenuation coefficient of liquid ethanol was 3.86 cm^2/g [1]. Radiographs on a scintillation converter were recorded by a cooled CCD camera with the exposure time of 10 seconds and the pixel size of 42.8 μm/pixel. The surface temperatures of the bottom plate and ethanol reservoir were maintained at 19.5°C and 20°C during the adsorption process, respectively.

RESULTS: Transient change in original radiographs from the dry condition in adsorption process are shown in Fig. 2 (a) to (g). The image becomes darker by increasing the adsorption amount. It can be seen that the adsorption was progressing from the surface of the adsorbent layer. The effect of the aluminum pin was little. Although it was expected that the adsorption amount would be larger near the heat transfer surface, i.e., near the bottom of the adsorbent layer because of the lower temperature, the adsorption amount was higher near the surface of the adsorbent layer. Two reasons are cited. The first is the change in porosity. The height of the layer was seemed to become lower by the adsorption. Increase in vapor flow resistance due to the decrease in porosity might disturb the supply of vapor into the layer. The second is an existence of inert gas. If the inert gas was involved, the concentration might become higher in the layer. The inert gas might disturb the adsorption. The temperature profile is required to consider the phenomena.

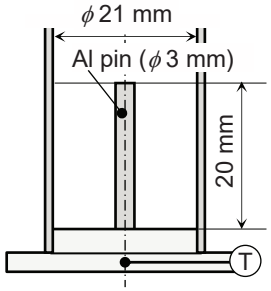

Fig. 1 Test cell

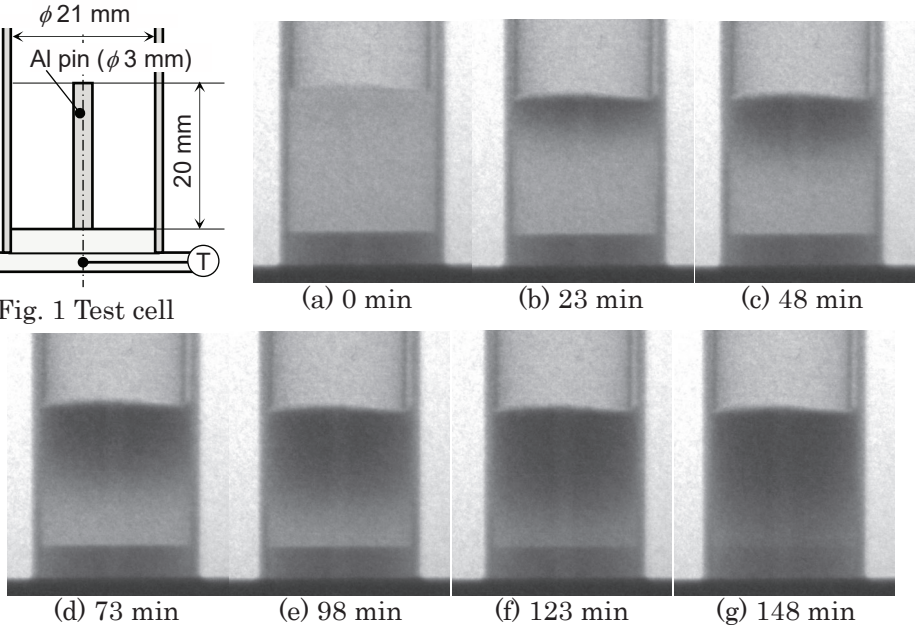
(a) 0 min (b) 23 min (c) 48 min
(d) 73 min (e) 98 min (f) 123 min (g) 148 min
Fig. 2 Transient change in adsorption process.

REFERENCE:
[1] H. Asano, K. Murata, N. Takenaka and Y. Saito, " Visualization and measurement of adsorption/ desorption process of ethanol in activated carbon adsorber", Physics Procedia, **69** (2015) 503-508.

PR8-4 Neutron radiography measurements of the mixing behavior of reactant streams during hydrothermal synthesis

S. Takami, K. Sato, M. Kubo[1], T. Tsukada[1],
K. Sugimoto[2], N. Odaira[3], D. Ito[3], Y. Saito[3]

Graduate School of Engineering, Nagoya University
[1] Graduate School of Engineering, Tohoku University
[2] Graduate School of Engineering, Kobe University
[3] Institute for Integrated Radiation and Nuclear Science, Kyoto University

INTRODUCTION: We have performed the neutron radiography measurements of the mixing behavior of cold and supercritical water in a tubular flow reactor to elucidate the effects of mixing on the supercritical hydrothermal synthesis [1-4]. In the previous measurements, the density and temperature of water at the mixing point were visualized, which suggested the mixing behavior of the two streams. However, the temperature of the streams can be also affected by the heat conduction through the tube wall. Therefore, the experiments that directly show the mass transport should be performed. Here, in this experiment, we performed the neutron radiography measurements of the mixing behavior of the aqueous solution of $Gd(CH_3COO)_3$ with heated water and observed the distribution of Gd^{3+} ions at the mixing point.

EXPERIMENTS: Fig. 1 shows the schematics of the experimental apparatus. A stream of water was fed using a high-pressure pump and heated by an external heater. Simultaneously, the aqueous solution of $Gd(CH_3COO)_3$ (0.025~0.2 M) was fed using another high-pressure pump. The two streams were mixed at the mixing point to initiate the hydrothermal reaction. The inner diameter of the tubes at the mixing point was 2.3 mm. Toward this mixing point, a neutron beam was irradiated and radiography images were obtained using ^{6}LiF/ZnS scintillator screen.

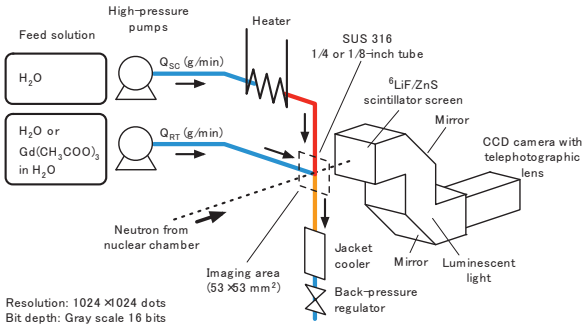

Fig. 1 Schematics of the experimental apparatus.

RESULTS: First of all, we mixed the aqueous solution of $Gd(CH_3COO)_3$ with the stream of water at room temperature. Figure 2a shows the radiography image of the solution that contained Gd^{3+} ions. As we noticed, the darker area existed in the side and the lower tubes. These areas corresponded to the streams that contained Gd^{3+} ions. By subtracting the absorption profile by water, the distribution of Gd^{3+} ions was obtained (Fig. 2b). This image confirmed that the reactant solution was fed from the side tube and went downward on the right-side wall in the lower tube after mixing. This image also showed that the Gd^{3+} ion can be used as the tracer ion to study the mixing behavior in the tubular flow reactor.

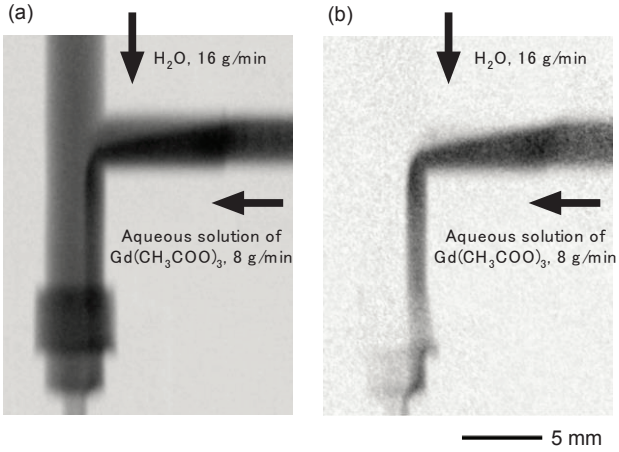

Figure 2 Neutron radiography images of the mixing point showing the absorption by (a) solution and (b) Gd^{3+} ions.

We then performed similar mixing experiments at higher temperatures. Figure 3 shows a snapshot of the neutron radiography measurement during the hydrothermal synthesis of $Gd(OH)_3$ from $Gd(CH_3COO)_3$ aqueous solution. The heated water with smaller density penetrated the upper part of the side tube. The Gd^{3+} solution went through the lower part and mixed with the heated water. The absorption by Gd^{3+} directly indicated the flow of reactant solution. However, as we continued the experiments, the blocking by produced $Gd(OH)_3$ occurred and we could not obtain the neutron radiography images at the steady-state conditions.

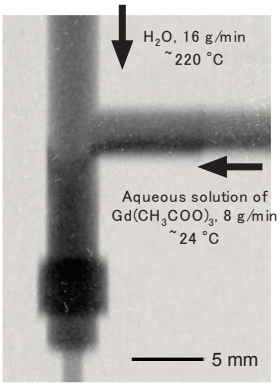

Figure 3 The neutron radiography image of the mixing point during hydrothermal synthesis.

CONCLUSION: By using the aqueous solution of Ga^{3+} ions, the mixing behavior of the reactant solution was directly visualized using neutron radiography. However, the measurement at the steady-state conditions was not successful this time due to plugging.

REFERENCES:

[1] S. Takami *et al.*, J. Supercrit. Fluids, **63** (2012) 46-51.
[2] K. Sugioka *et al.*, AIChE J., **60** (2014) 1168-1175.
[3] S. Takami *et al.,* Phys. Proc., **69** (2015) 564-569.
[4] K. Sugioka *et al.*, J. Supercrit. Fluids, **109** (2016) 43-50.

PR8-5 Quantatively Visualization of a Microchannel Heat Exchanger under Non-uniformly Heated Condition

H. Umekawa[1], T. Ami[1], H. Sakai[1], R. Funakura, Y. Saito[2] and D. Ito[2]

[1]*Department of Mechanical Engineering, Kansai University*
[2]*Institute for Integrated radiation and Nuclear Science, Kyoto University*

INTRODUCTION: Microchannel heat exchanger has several advantages against the conventional fin-tube heat exchanger, thus recently it has been used as the heat exchanger of air-conditioning unit. But this microchannel heat exchanger is consisted from a lot of parallel microchannels, thus it would easily cause the flow oscillation, such as pressure drop oscillation and density wave oscillation. Moreover, the heat transfer coefficient of air at the front edge of heat exchanger plate takes larger value than that of the tail edge owing to the development of thermal boundary layer. and it cause the nonuniform heat flux condition.

In this series of investigation, the effect of heat flux distribution on the heat transfer and flow characteristics have been estimated by using single plate micro channel heat exchanger.

In this report estimation results of a void fraction of microchannel heat exchanger under non-uniform heating by using neutron radiography are briefly introduced.

EXPERIMENTS: Experiments of the visualization were carried out using the B-4 beam line in KUR (1 MW). The schematic diagram of experimental apparatus is shown in Fig.1. The working fluid used in this study was Methanol (99.5% purity), which has low viscosity similar with actual refrigerant (R32) and enough attenuation coefficient for visualization. The experimental apparatus is consisted of a reserve tank, a pump and a test section. Test section is an actual aluminum microchannel heat exchanger of the air-conditioning unit, and it was heated by Joule heating by using two nichrome foils attached to the plate surface with electrical insulation of Kapton film. These nichrome foil heaters could be heated independently, and which achieved the non-uniform heating condition.

RESULTS: Fig. 2 shows the void fraction profile under certain heating condition. All results was obtained with same exit thermal equilibrium quality (x_{exave}=0.188), but (a) was heated by uniform heat flux, and the heat flux ratio (q_L:q_H) of (b) is 1:2 and ratio of (c) is 1:4, respectively. Histograms of void fraction at the high heat flux side of Fig.2 are drawn in Fig 3. As shown in these Figures, influences of the heat flux distribution on the void fraction profile is clearly obtained quantitatively. In this stage, the void fraction profile is obtained as time average image, but quantitatively data of the flow oscillation will be obtained by using dynamic image in next step.

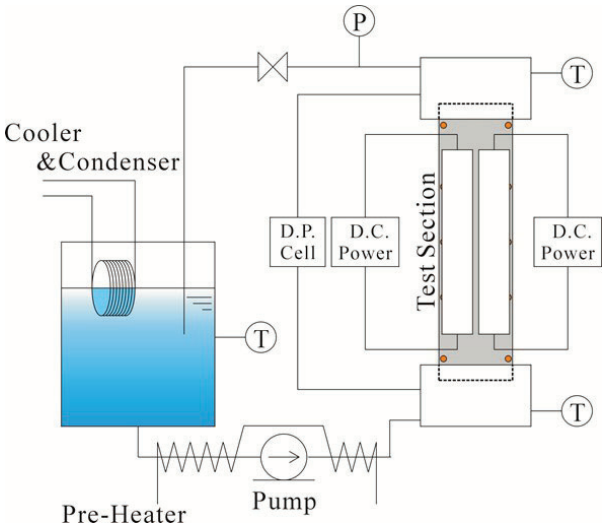

Fig.1 Schematic diagram of experimental apparatus.

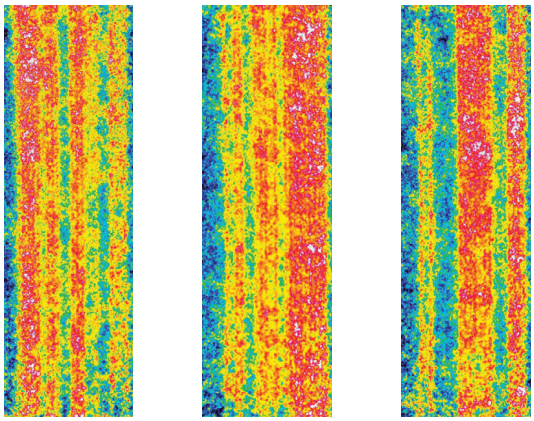

a.Uniform b. 1∶2 c. 1∶4

Fig.2 Example of the visualization results of void fraction xeqave=0.188

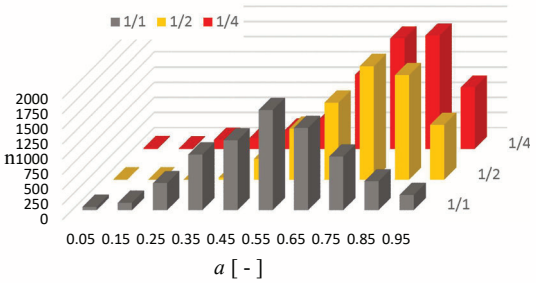

Fig.3 Histogram of void fraction at high heat flux side in Fig.2.

PR8-6 Frost Deposition Distribution Estimated by X-ray and Neutron Cooperative Imaging

R. Matsumoto[1], R. Kuroda[2], T. Makihara[2], H. Ikishima[1], T. Shirai[1], D. Ito[3], N. Odaira[3] and Y. Saito[3]

[1]*Faculty of Engineering Science, Kansai University*
[2]*Graduate School of Science and Engineering, Kansai University*
[3]*Institute for Integrated Radiation and Nuclear Science, Kyoto University*

INTRODUCTION: Recently, heat pumps have been proposed as an effective air conditioning system of heating operation for electric vehicles (EV), because of the inability to use the engine heat as in the conventional vehicles. However, during the heating operation, frosting occurs on the outdoor heat exchanger of the air conditioning system. The frost formation causes a serious energy loss on the battery of EV due to the heat transfer performance degradation by increasing the thermal resistance. In addition, the corrugated fin heat exchanger which is mainly used as an automotive heat exchanger, has a more complicated structure than conventional one, so it is difficult to capture the frosting situation. In this study, the three dimensional distribution of the frost deposition on the corrugated fin heat exchanger were estimated by X-ray and neutron cooperative imaging.

EXPERIMENTAL PROCUDURE: Fig.1 shows the schematic view of the experimental setup. The frost deposition between the fins is measured by irradiating X-ray parallel to the fins of the heat exchanger. The heat exchanger is made of aluminum. Thus, the frost deposition inside of the heat exchanger can be measured by irradiating neutron beam perpendicularly to the fins though the heat exchanger. Cooled humid air adjusted to the flow velocity 1 m/sec is supplied to the test section. The test section consists of the styrofoam block duct and the corrugated fin heat exchanger. The heat exchanger was cooled by circulating the -27 ºC fluorinert. The frost deposition on the heat exchanger was observed by CCD camera (Princeton Inst., 16-bit, 1024×1024 pixels and 512×512 pixels) with image intensifier (Toshiba Electron Tubes & Dev., E5877CS-P1K and E5830NE-P4K) in every 1 min for 20 min frosting duration. Exposure time is 0.5sec for X-ray and 1.7sec for neutron beam.

RESULTS: Fig.2 shows the front view of the corrugated fin heat exchanger. The corrugated fin heat exchanger consists of flat tubes and the brazed corrugated louver fins. The coolant flows in the parallel flat tubes and the humid air flows in the small fin channels formed by the corrugated louver fins. Fig.3 shows the frost deposition distributions on the heat exchanger. X-ray images show the frost formation observed from the front view of the heat exchanger. On the X-ray images, frost was formed uniformly on the fins. The neutron images show the frost deposition inside of the heat exchanger. The main flow direction is left to right on the neutron images in Fig.3. At 100 sec, the frost formed in the upstream side of the fin channels. At 1200 sec, the frost deposits on the fin front, which induces the heat transfer problems by the air side pressure loss. This results shows the frost deposition distribution in the corrugated fin heat exchanger clearly by X-ray and neutron cooperative imaging.

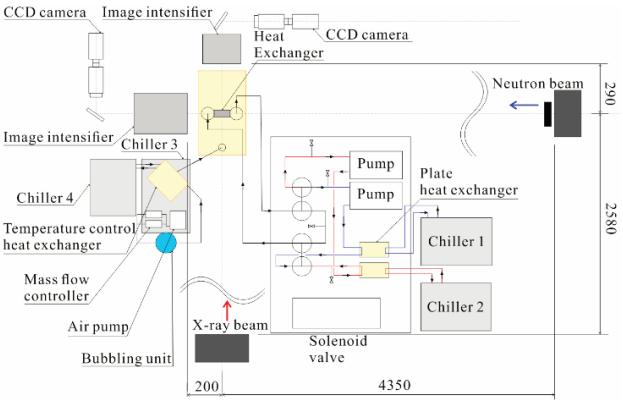

Fig.1 Schematic view of the experimental setup

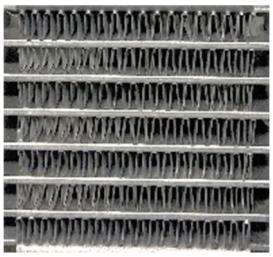

Fig.2 Front view of the corrugated fin heat exchanger

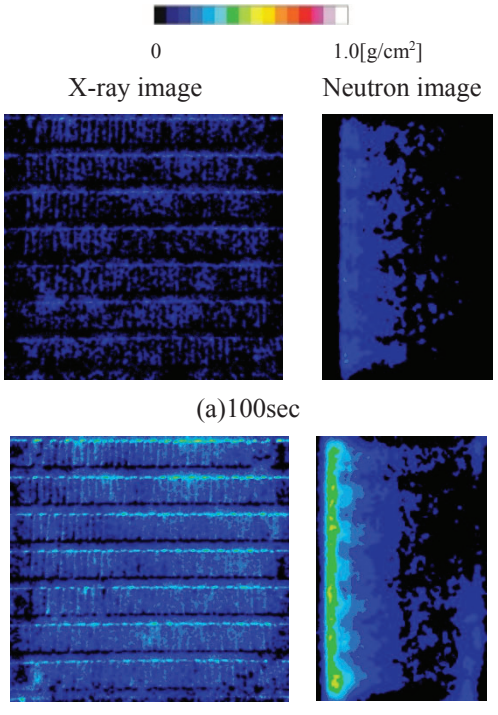

(a)100sec

(b)1200sec

Fig.3 Forst deposition distributions observed by X-ray and neutron radiography.

PR8-7 Analysis of vapor pressure in fire spalling of high-strength concrete

Y. Nishio[1], M. Kanematsu[1], A. Miyabe[1], K. Kobayashi[1], A. Yang[1], H. Fumino[1], N.Odaira[2], D. Ito[2], Y. Saito[2]

[1] Department of Architecture, Tokyo University of Science
[2] The Institute for Integrated radiation and nuclear science joint-use research, Kyoto University

INTRODUCTION: Fire spalling with High-strength concrete was a well-known phenomenon, and thermal stress and water vapor pressure in concrete have considered to be the main causes of spalling. To capture detailed moisture movement in concrete under fire is important to clarify the mechanism of spalling [1]. In this study, we investigated the relationship between spalling phenomena and moisture transfer under heating by using neutron radiography. Measuring moisture transfer inside concrete quantitatively, how vapor pressure inside concrete affect spalling was considered.

EXPERIMENTS: Concrete specimens (70×100×30 mm^3) with W / B of 18% were prepared. In some of them, a single rebar (D10, 120mm) with a thermocouple was embedded at 20mm from the heating surface. Adjusting water content before heating, specimens with three different water content (named as "dry", "air" and "sat" respectively) were prepared. The initial relative humidity (RH) of those were 25%, 75% and 100% respectively. In this experiment, the specimens were heated at the bottom surface with quartz heater. Neutron radiography was performed at the B-4 port of KUR. Setup for the experiment is shown in Fig.1. Apart from NR measurement, temperatures in specimen were measured by thermocouples installed in holes with 1.2 mm diameter at the position of 10, 20, 30 and 50 mm from the heating surface.

RESULTS: Using relationships between values measured by neutron radiography and paste volume ratio to concrete (Vp) with different RH (0, 25, 80 and 100%) shown in Fig. 2 and Fig. 3, water amount in concrete specimen during heating was calculated quantitatively. Fig. 4 shows calculated RH inside concrete at each water content for each distance from heating surface just before spalling. Temperatures at 2 and 5 mm from the surface in Fig. 4 were analytical values calculated by measured values. Fig. 5 shows vapor pressure distribution just before spalling calculated by the result of Fig. 4. From the figure, the vapor pressure in "air" is higher than that in "sat" or "dry", and the observed maximum value is about 1.8Mpa. This is about the same value reported in the past researches.

REFERENCES:

[1] JCI, (2017). "Committee Reports:JCI-TC-154A"

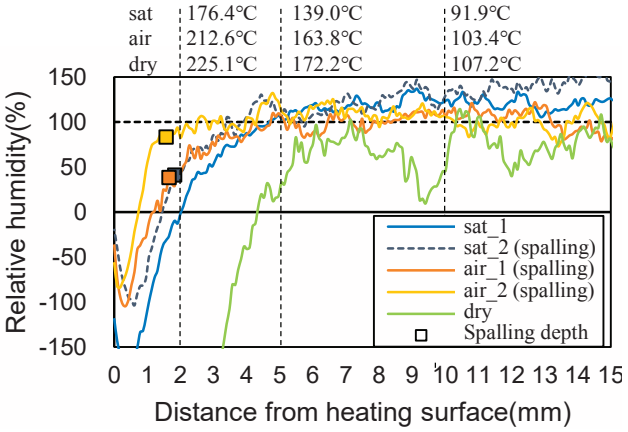

Fig. 4. Moisture content distribution from heating surface immediately before spalling.

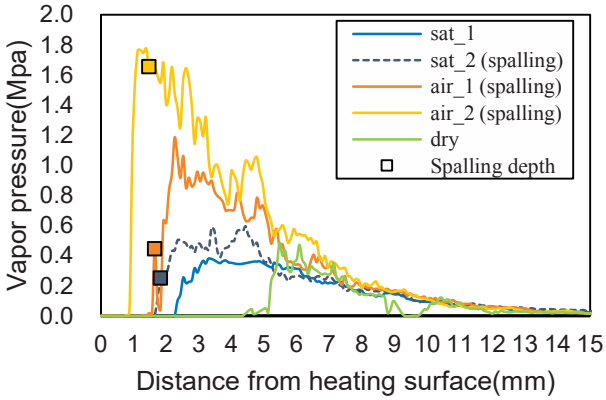

Fig. 5. Vapor pressure distribution from heating surface immediately before spalling.

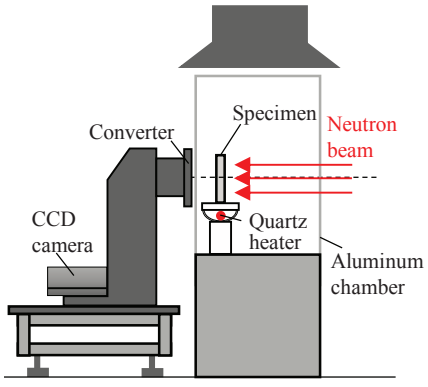

Fig. 1. Outline of Experimental setup.

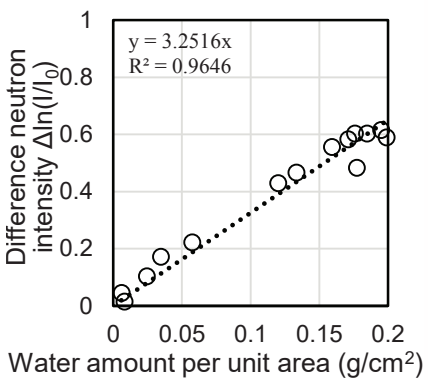

Fig. 2. Relationship between differential intensity and water amount.

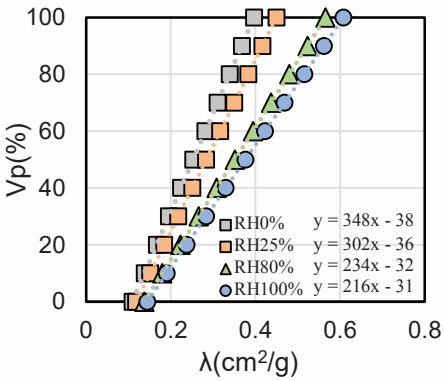

Fig. 3. Relationship between paste volume and absorption coefficient.

PR8-8 Measurement of coolant inside a flat laminate vapor chamber in the vertical posture with Neutron Radiography

K. Mizuta, Y. Saito [1], D. Ito [1]

Faculty of Engineering, Kagoshima University
[1]Institute for Integrated Radiation and Nuclear Science, Kyoto University

INTRODUCTION: Recently, cooling of electronic devices has been crucial than ever because size of such devices is rapidly shrinking though the power input to the devices is almost the same or even getting larger, which leads to the rapid increase in power density. This trend makes it difficult to achieve adequate heat exhausting ability especially at the heat receiving region of such heat exhausting system. Thus, various types of vapor chambers are getting more attention than ever with a hope for solving such problems by their higher heat spreading ability than conventional methods such as copper heat spreader. In the practical use of vapor chambers, postural influence on thermal performance of vapor chambers is very important, because the change in the thermal performance of vapor chamber with posture, if it occurs, may restrict the performance of the electronic devices not to exceed its limit of junction temperature. A flat laminate vapor chamber called FGHP (Fine Grid Heat Pipe) is one of the most promising candidates to solve such thermal problems, with the highest heat spreading ability concerning the overall heat transfer coefficient based on heat source area [1]. Our previous study shows that the effect of gravity on the coolant distribution of FGHP is negligible [2].

In this study, we investigated the gravitational effects on the coolant distribution in the FGHP by using neutron radiography at the Kyoto University Research Reactor (KUR) for various types of FGHP.

EXPERIMENTS: Experiment was conducted at the E-2 port of the KUR, where the thermal neutron flux at the sample position was about 3×10^5 cm^2s at 5 MW operation. Test samples of FGHP were disc shaped, diameters were 40, 80 mm, respectively and the thickness of ether samples were 2 mm. Inner structure of both sample was almost the same as the test samples utilized in our previous study[2]. The test samples were set vertically, which means that its bottom and top plate was placed parallel to the gravitational direction. Figure 1 shows the experimental setup. A CCD camera (BU-53LN, BITRAN Co. Ltd.) was utilized, which has 4008×2672 pixels and ^{6}LiFZnS (50 μm thickness) was used as a scintillator screen. The spatial resolution was 9.0 μm/pixel at the present system setup, however, the effective spatial resolution was about 50 μm/pixel due to the scintillator screen characteristics. Neutron imaging of the sample was performed at the 1 MW operation mode of the KUR and the exposure time was 300 s. Neutron images of the sample were utilized to calculate liquid thickness in the FGHP. The effect of gravity on the coolant distribution was evaluated by the calculated liquid thickness in the wick area at different four positions. The liquid thickness was evaluated by the same scheme as in our previous study[2].

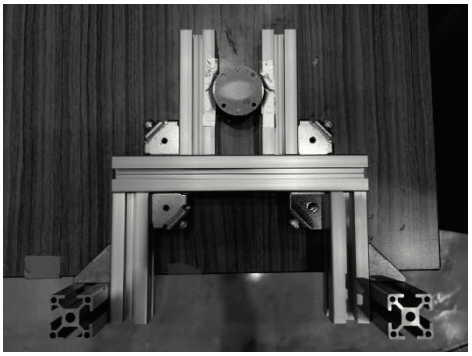

(a) ϕ = 40 mm

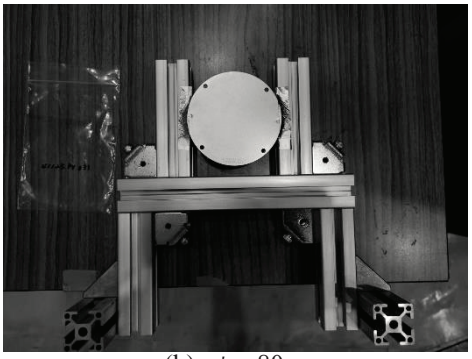

(b) ϕ = 80 mm

Fig. 1 FGHP test samples.

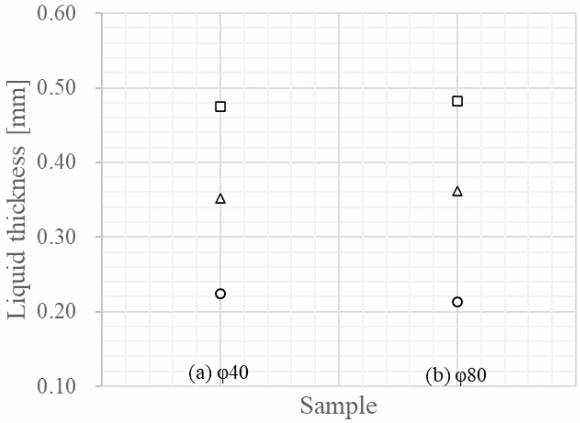

Fig. 2 Liquid thickness for both samples.
(○:top, □:bottom, △:horizontal average)

RESULTS: Evaluated liquid thickness of both samples were shown in Fig. 2. Figure 2 shows that liquid thickness at various positions were almost same regardless of the diameter of FGHP test sample, and the liquid thickness was also almost the same as those in our previous work of 65 mm square sample [2]. This fact means that the liquid thickness depends mainly on the inner structure of FGHP rather than its outer size and shape.

REFERENCES:

[1] Mizuta, K., et al., Applied thermal management, **104** (2016) 461-471.
[2] Mizuta, K., el al., Physics Procedia, **69** (2015) 556-563

R2P8-9

PR8-9 Quantitative Study of the Image Quality for Neutron Imaging

M. Kitaguchi, K. Hirota[1], H. M. Shimizu[1], D Ito[2], and Y. Saitoh[2]

KMI, *Nagoya University*

[1]*Graduate School of Science, Nagoya University*
[2]*Institute for Integrated Radiation and Nuclear Science, Kyoto University*

INTRODUCTION: Mechanical and industrial products such as automobiles and aircraft are progressing with higher performance and higher accuracy in Japan. One of the demands at the development site of these state-of-the-art products is a visualization of the state of organic materials (oil film, grease, electrolyte, etc.) existing between metals, which can not be seen directly by our eyes. Neutron imaging is one of the solutions to observe the dynamic state of the organic materials (shape, properties, thickness distribution) and its dynamic change. We have started to obtain of the imaging of automobile parts as an example in KUR E2 port. We are also proceeding with the quantitative evaluation of the CCD output image.

In order to expand the evaluation technique to wide range of applications, the quality of image should be studied systematically. The quality should be estimated by using the information of neutron flux, the upstream optics, the performance of detector system, and their arrangement. In the case of visible light optics, the performance of optical system is qualified by using the 'modulation transfer function (MTF)' (Figure 1). The MTF for visible light optics can be calculated precisely by simulations. On the other hand, the systematic qualification for neutron imaging has not been standardized. Because of the large volume of the source, the divergence of the rays, and the finite resolution of the detector system, the performance of the whole system of neutron imaging can not be written as a simple combination of MTF for each subsystem. The general formula to qualify the whole system should be established even for the case of low-intensity compact neutron source.

EXPERIMENTS AND RESULTS: For the demonstration, the transmission images of a standard indicator were taken with various conditions of the distance between the sample and the detector. Figure 2 shows the change of the contrast according to the distance. We can also find that the contrast depends on the measurement time because of the statistical uncertainty with low flux of neutrons.

The E2 port as an optical source is not a pinhole but a spread area. This means that the MTF of each component, for example, source, beamline, and detector, can not be extracted simply. We are going to combine more measurements under various conditions to understand the quality of image quantitatively.

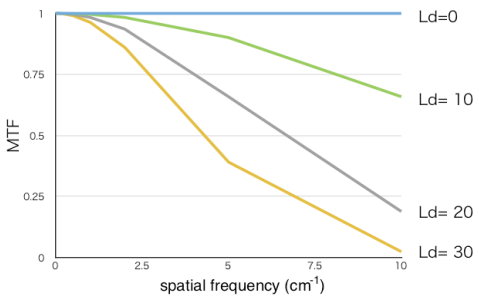

Figure 1: Typical shape of MTF according to the distance between sample and detector for a simple pinhole system.

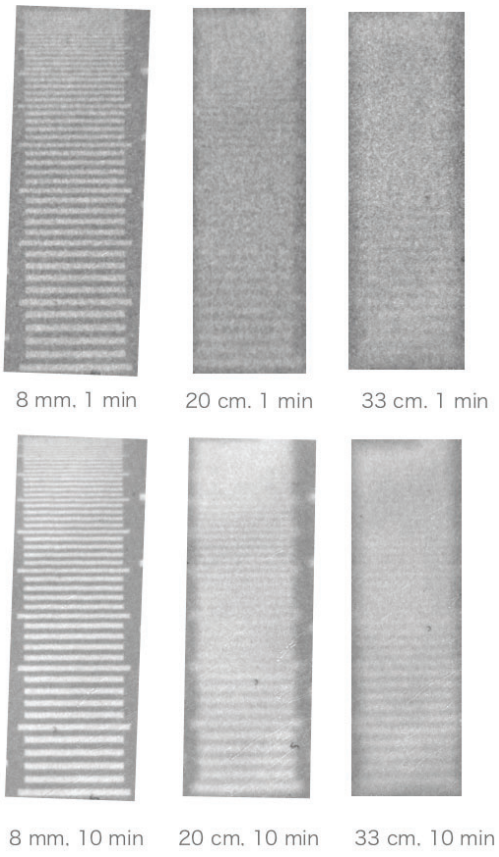

Figure 2: The transmission image of a standard indicator with various conditions. Not only the distance between sample and detector but also the measurement time affect the quality of image.

PR8-10 Dynamic Visualization of Hydrogen Accumulation Behavior in Metallic Materials via Neutron Imaging

K. Shimizu[1], H. Toda[2], K. Hirayama[2], H. Fujihara[2], D. Ito[3], Y. Saito[3]

[1]*Department of Physical Science and Materials Engineering, Iwate University*
[2]*Department of Mechanical Engineering, Faculty of Engineering, Kyushu university*
[3]*Institute for Integrated Radiation and Nuclear Science, Kyoto University*

INTRODUCTION: It is widely recognized that hydrogen in metallic materials degrades the mechanical properties of the materials. Various hydrogen embrittlement mechanisms, such as HELP, HEDE and HESIV have been proposed to date [1], but there is still no comprehensive interpretation. However, for each mechanism, it is consistent that hydrogen trapping and the resulting localization of hydrogen to defects and microstructures are the dominant factors of hydrogen embrittlement [2]. To understand the hydrogen embrittlement, it is necessary to visualize the hydrogen distribution and to elucidate its evolutionary behavior over time. In this study, hydrogen in a metal was visualized by neutron radiography and tomography, and hydrogen accumulation under stress was assessed. Several palladium specimens with different hydrogen contents were prepared and a notch was introduced. It has been demonstrated that hydrogen content can be analyzed by neutron tomography, and the possibility of evaluating hydrogen accumulation under stress is discussed.

EXPERIMENTS: Palladium specimens with hydrogen contents of 0 at%, 10 at% were prepared for neutron imaging. Hydrogen content was controlled by high temperature hydrogen exposure. Neutron radiography was performed on the KUR B-4 port [3]. The imaging system consists of a ^{6}LiF:ZnS visible light converter and a cooled CCD detector. The exposure time was set to 5 min at a thermal power of 1 MW in the research reactor.

RESULTS: Fig. 1 shows pure Pd and Pd-23%Ag alloys visualized at the B-4 port of KUR. Charged hydrogen concentrations are 0% and 10%. In both alloys, the contrast of neutron transmission images is darkened due to hydrogen charging. The difference in hydrogen concentration of 10% can be clearly visualized by static observation in B-4 port. After static imaging, the Pd specimen with 10% hydrogen concentration shown in Fig. 1(b) was subjected to tensile loading by a test-jig and was observed continuously. Fig. 2 shows the neutron transmission images of unloading, the first loading, and the second loading, indicating that the notch introduced in Pd was opened by monotonic tensile loading. The stress state of notch-tip becomes triaxial and forms a hydrostatic stress field in tension by tensile loading. We expected to see a dark contrast in the neutron transmission image due to the accumulation of hydrogen in this hydrostatic stress field before the present experiment, but this was not observed in Fig. 2. The reason for this is that the absolute value of the hydrostatic stress is low, or the size of the formed hydrostatic stress field is much smaller than the spatial resolution of this imaging. This hydrogen accumulation behavior will be investigated deeply in the future work.

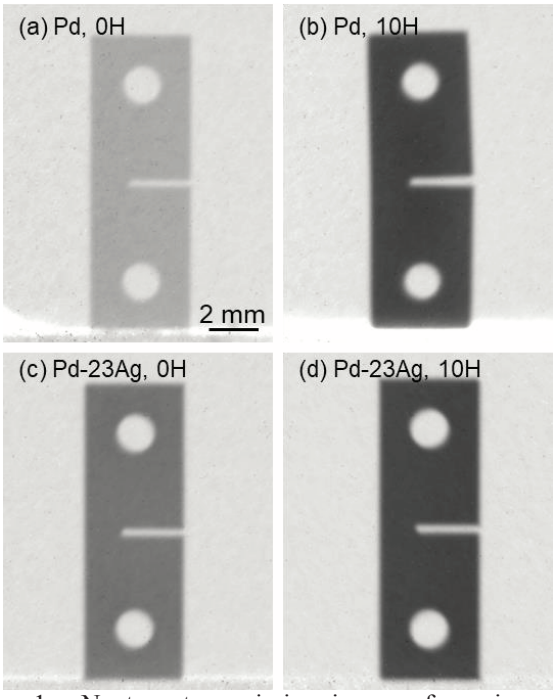

Fig. 1. Neutron transmission image of specimens visualized at B-4 port. (a) and (b) are pure Pd with 0% and 10% hydrogen concentration, respectively. (c) and (d) are Pd-23%Ag alloys with 0% and 10% hydrogen concentration, respectively.

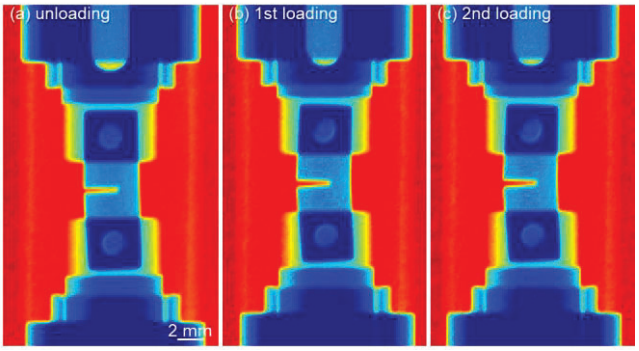

Fig. 2. Neutron transmission image of the specimen captured at (a) unloading, (b) after 1st loading, and (c) after 2nd loading. The contrast of these neutron transmission image is shown in color scale.

REFERENCES:

[1] I. M. Robertson *et al.*, Metall. Mater. Trans. A 46 (2015) 1085-1103.
[2] Z. Zhang *et al.*, Acta. Mater. 113 (2016) 272–283.
[3] Y. Saito *et al.*, J. Jpn. Soc. Precis. Eng. 79 (2013) 822–825.

PR8-11 *In-situ* Lithium diffusion behavior in NASICON-Type Structured Lithium Ion Conductive Composite by Means of Neutron Radiography

S. Takai[1], F. Song[1], H. Chen[1], K. Ota[1], T. Yamamoto[1], T. Yabutsuka[1], T. Yao[2], D. Saito[3], Y. Saito[3]

[1]*Graduate School of Energy Science, Kyoto University*
[2]*Kyoto University*
[3]*Institute for Integrated Radiation and Nuclear Science, Kyoto University*

INTRODUCTION: Heterogenous doping effect, originally observed in halide solid state electrolytes, is proven to be favourable in oxide solid-state electrolytes by Onishi and Song *et. al.* [1,2]. Heterogenous doping is to disperse insulative particles in Li^+ ion conductors and create space charge layers at the vicinity of the insulative particles, which eventually improves the overall ionic conductivity of solid-state electrolyte [3]. Such dispersion system is referred as composite solid-state electrolytes.
In this work, an electrolysis apparatus was built and utilised to electrolyse ^{N}Li LATP / ^{7}Li LATP diffusion couple, where N and 7 is the abbreviation of natural and 7 of isotopes. By applying a galvanostatic current across this diffusion couple at elevated temperature, the ^{6}Li in ^{N}Li LATP can be driven and diffuse towards and through ^{7}Li LATP. The process of ^{6}Li diffusion can be observed *in-situ* by the transmissive neutron beam in KUR (B4 port), owing to the significant difference in absorption cross-section in neutron beam between ^{6}Li and ^{7}Li.

EXPERIMENTS: ^{7}Li and ^{N}Li $Li_{1.3}Al_{0.3}Ti_{1.7}(PO_4)_3$ pellets were synthesised by solid-state reaction method. ^{N}Li Li_2TiO_3 and Mn_2O_3 pellets were also produced by sintering from precursor. The surfaces of LATP were polished to ensure the flatness and mirror finish. During neutron radiography, the LATP, LTO pellets were assembled as the configuration shown in Fig. 2. The assembly was heated to 300 °C while subjected to 0.25 μA of DC current to lead the solid-state electrolysis. After the electrolysis was started, the entire apparatus was subjected to direct neutron beam for 45 minutes at B4 port of KUR (reactor power output was 1MW). Neutron radiography images were taken by the CCD camera (5 min exposure) every 15 minutes.

RESULTS: As shown in Fig. 2, the neutron radiography images from t = 0 to 75 minutes show no change in contrast in the ^{7}Li LATP section, indicating that the electrolysis was insufficient to drive the diffusion of ^{6}Li from ^{N}Li LATP towards ^{7}Li LATP. This is due to the significantly suppressed DC current (0.25 μA) during the electrolysis. Owing to high resistance of LTO pellets, higher DC current can cause an overpotential across the assembly, which might decompose the LTO and subsequently block the current entirely. Furthermore, the large thickness of the pellets is also impeding the current. To improve the issues, materials other than LTO and Mn_2O_3 should be employed to serve as Li^+ reservoir and receiver, such that the assembly can allow higher DC current (around 45 mA to drive sufficient $^{6}Li^+$ migration). And the thickness of the pellets should also be reduced to bring down the over-all resistance of the assembly.

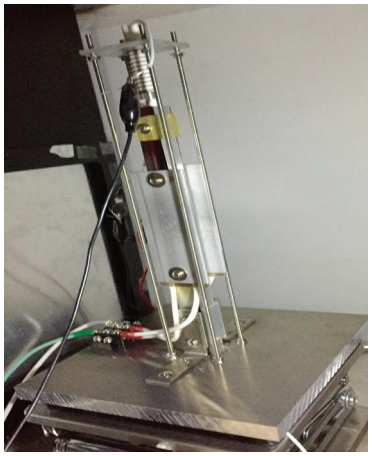

Figure 1 Photo of the apparatus.

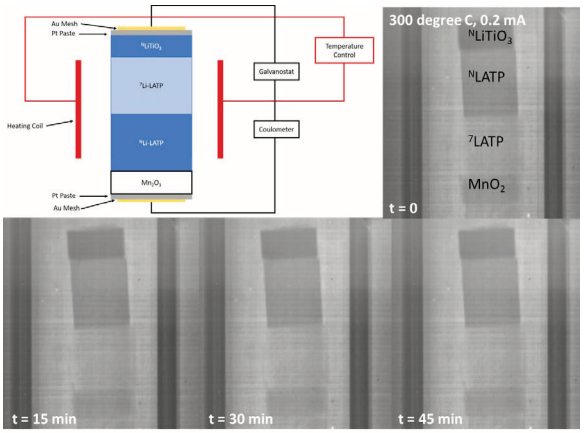

Figure 2 Scheme of the configuration of the solid-state electrolysis set-up and neutron radiography images at *t* = 0, 15, 30 and 45 minutes at 300 °C.

REFERENCES:

[1] H. Onishi *et al*. *Electrochemistry*. 84 (2016) 967.
[2] F. Song *et. al. J. Alloys Compds*. 853(2021)157089.
[3] C. C Liang. *J. Electrochemical Soc*. 120 (1973) 1289.

I-1. PROJECT RESEARCHES

Project 9

PR9 Advancement of integrated system for dose estimation in BNCT

Y. Sakurai

Institute for Integrated Radiation and Nuclear Science, Kyoto University

BACKGROUNDS AND PURPOSES:

There are a number of subjects, which should be improved for the further advance and generalization of boron neutron capture therapy (BNCT). In the viewpoints of medical physics and engineering, the advance for dose estimation is one of the important subjects. The purposes of this project research are the advance for various dose estimation methods, and the establishment of an integrated system for dose estimation in BNCT.

In the first year of this research project, 2020, the advancement for the respective dose estimation methods were forwarded mainly using Heavy Water Neutron Irradiation Facility (HWNIF) and E-3 Neutron Guide Tube (E-3) at KUR. In addition, the integrated system was considered for the simultaneous usage of several dose estimation methods.

RESEARCH SUBJECTS:

The collaboration and allotted research subjects (ARS) were organized as follows;

ARS-1 (R2P9-1): Establishment of characterization estimation method in BNCT irradiation field using Bonner sphere and ionization chamber (IV). (Y. Sakurai, S. Shiraishi, N. Matsubayashi, A. Sasaki, Y. Kakimoto, T. Naito, H. Matsunaga, T. Nakamura, R. Narita, M. Nojiri, H. Kato, T. Takata, H. Tanaka)

ARS-2 (R2P9-2): Study on new type of neutron spectrometer for BNCT. (K. Watanabe, A. Ishikawa, A. Uritani, S. Yoshihashi, A. Yamazaki, Y. Sakurai)

ARS-3 (R2P9-3): Response characteristic measurements of lithium-glass scintillators used in the BSS for the intense neutron beams. (A. Masuda, T. Matsumoto, H. Tanaka, D. Ito, H. Harano, Y. Sakurai, T. Takata)

ARS-5 (R2P9-5): Neutron measurement by using the self-activation of iodine-added liquid scintillators. (A. Nohtomi, Y. Kanzaki, G. Wakabayashi, Y. Sakurai, T. Takata)

ARS-6 (R2P9-6): Development of absolute epi-thermal and fast neutron flux intensity detectors for BNCT (I. Murata, K. Aoki, Y. Miyaji, D. Hatano, S. Kusaka, H. Tanaka, Y. Sakurai, T. Takada)

ARS-8 (R2P9-8): Study for microdosimetry using silicon-on-insulator microdosimeter in the BNCT irradiation field (IV). (Y. Sakurai, N. Ko, T. Takata, H. Tanaka, T. L. Tran, J. Davis, S. Guatelli, A. Rozenfeld, N. Kondo, M. Suzuki)

ARS-9 (R2P9-9): Measurement of thermal neutrons and gamma rays in BNCT beam with polymer gel detector. (K. Tanaka, Y. Sakurai, T. Kajimoto, A. Mitsuyasu, S. Hayashi, Hiroki Tanaka, T. Takata, G. Bengua, S. Endo)

ARS-10 (R2P9-10): Development of two dimensional neutron detector in BNCT irradiation field. (H. Tanaka, T. Takata, Y. Sakurai, S. Uno)

ARS-11 (R2P9-11): Study of neutron fluence and gamma ray distribution measuring using thermoluminescence slabs. (K. Shinsho, R. Oh, M. Tanaka, S. Yanagisawa, H. Tanaka, T. Takata1, G. Wakabayashi, Y. Koba)

ARS-13 (R2P9-13): Development and evaluation of 3D gel dosimeter for the measurement of dose distribution in BNCT. (S. Hayashi, Y. Kakimoto, T. Takata, M. Suzuki, Y. Sakurai)

ARS-14 (R2P9-14): Establishment of beam-quality estimation method in BNCT irradiation field using dual phantom technique (IV). (Y. Sakurai, N. Kondo, T. Takata, H. Tanaka, M. Suzuki)

ARS-15 (R2P9-15): Development of a prompt gamma-ray imaging detector using an 8 x 8 arrayed $LaBr_3$(Ce) scintillator for BNCT. (K. Okazaki, T. Takata, Y. Sakurai, H. Tanaka)

ARS-16 (R2P9-16): Development of fiber-reading radiation monitoring system with an optical fiber and red-emitting scintillator at the ^{60}Co radiation facility. (S. Kurosawa, H. Tanaka, S. Kodama, Y. Kurashima, A. Yamaji)

ARS-17 (R2P9-17): Establishment of the imaging technology of 478 keV prompt gamma-rays of boron-neutron capture reaction and the measurement of the intensity of the neutron field. (S. Komura, T. Mizumoto, Y. Sakurai, T. Takata, T. Tanimori, A. Takada)

ARS-18 (R2P9-18): Feasibility study for quality assurance and control for irradiation field in BNCT. (S. Nakamura, M. Takemori, K. Iijima, S. Imamichi, H. Nakayama, T. Chiba, M. Masutani, Y. Sakurai, H. Tanaka, T. Takata, M. Suzuki, H. Igaki, H. Okamoto)

ARS-19 (R2P9-19): Evaluation of thermal neutron irradiation field for semiconductor device irradiation. (H. Tanaka, T. Takata, N. Matsubayashi, Y. Sakurai)

ARS-20 (R2P9-20): Optimization of bolus shape for boron neutron capture therapy - examination using simple shaped phantom for experimental verification -. (T. Takata, H. Tanaka, A. Sasaki1, Y. Sakurai, M. Suzuki)

ARS-23 (R2P9-23): Verification of the annealing capability of boric acid-infused PVA-GTA-I gel dosimeter. (H. Yasuda, JE. Taño, CAB. Gonzales, Y. Sakurai)

ARS-24 (R2P9-24): Establishment of quantitative measurement of boron concentration distribution in vivo by imaging of prompt gamma rays. (S. Komura, T. Mizumoto, T. Mitani, Y. Sakurai, N. Kondo, M. Suzuki, T. Takata, T. Tanimori, A. Takada)

ARS-4, ARS-12, ARS-21 and ARS-22 could not be performed because of the influence of COVID-19 infection. For ARS-7, the submission of the report was suspended because of the reason for the patent application. So, the reports for these subjects are not appeared.

PR9-1 Establishment of characterization estimation method in BNCT irradiation field using Bonner sphere and ionization chamber (IV)

Y. Sakurai, S. Shiraishi[1], N. Matsubayashi[1], A. Sasaki[1], Y. Kakimoto[1], T. Naito[1], H. Matsunaga[1], T. Nakamura[1], R. Narita[1], M. Nojiri[1], H. Kato[1], T. Takata and H. Tanaka

Institute for Integrated Radiation and Nuclear Science, Kyoto University
[1]Graduate School of Engineering, Kyoto University

INTRODUCTION: Development in accelerator-based irradiation systems for BNCT is underway. In the near future, BNCT using these newly developed systems may be carried out at multiple facilities across the world. Considering this situation, it is important that the estimations for dose quantity and quality are performed consistently among several irradiation fields, and that the equivalency of BNCT is guaranteed, within and across BNCT systems. Then, we are establishing QA/QC system for BNCT.

As part of the QA/QC system, we are developing estimation method for neutron energy spectrum using Bonner sphere [1]. For our spectrometer using Bonner sphere, liquid such as pure water and/or boric acid solution is used as the moderator. A multi-layer concentric-sphere case with several sphere shells is prepared. The moderator and its diameter are changeable without entering the irradiation room, by the remote supply and drainage of liquid moderator in the several layers. For the detector, activation foils are remotely changed, or online measurement is performed using SOF detector, etc.

MATERIALS AND METHODS: In the neutron energy spectrometry by Bonner-sphere, the combinations of the moderator material and diameter should be previously decided and prepared. Of course, the more information can be obtained as the more moderators and detectors are prepared. However, the information number from those measured data is less than the combination number, because of the overlapped regions among the combinations. The selection is important, in which the more information number is obtained for the combination number.

The combination of moderator and detector is decided, for that the response functions cannot be approximated by the linear functions of the other response functions. The accuracy and precision for the spectrometry can be higher, because the independent information can be obtained from the measurement by the respective combinations. We were developed the selection method, High Independence Selection (HIS) [2].

On the assumption of the application in the standard epi-thermal neutron irradiation mode of Heavy Water Neutron Irradiation Facility (HWNIF), the combination of the moderators for boron-10 concentration and diameter was optimized by HIS. Based on this optimization, a prototype of RBS was made. Some experiments were performed for the characteristic verification of the prototype RBS at HWNIF.

RESULTS: The configuration of the RBS was decided as follows. A five-layer concentric spherical acrylic shell is used as a container. Each acrylic wall is 1 mm in thickness. The moderator injection part is 9 mm in thickness for each layer. Pure water and 0.14-wt% boric acid water for boron-10 were used as liquid moderators. LiCaF scintillation detector and gold wire were used as the detectors. Figure 1 shows the combination of moderator injection patterns for RBS, used in the experiments.

In both cases of LiCaF scintillation detector and gold wire, the measured values were larger than the calculated values. The concentration of boric acid was assumed to be 0.14 wt% in the calculation, but the actual concentration was 0.12 wt%. This is considered to be one of the reasons for the disagreement. The other possible reasons are the differences in sizes between the actually prepared spectrometer, field size, beam directionality, etc..

Figure 2 shows the comparison between the nominal spectrum and unfolded spectrum. Unfolding was performed by GRAVEL using the response function of each Bonner sphere corrected by multiplying the ratio for measured/calculated values. The nominal spectrum of the epi-thermal neutron irradiation mode was input as an initial guess. The spectrum obtained by the unfolding reproduced the nominal spectrum relatively well, but the absolute value was overestimated about two times.

CONCLUSION: We have plan to perform (1) simulation with boric acid concentration set to 0.12 wt%, and (2) preparation of a Bonner sphere spectrometer including the remote mechanism for the supply and drainage of the liquid moderators.

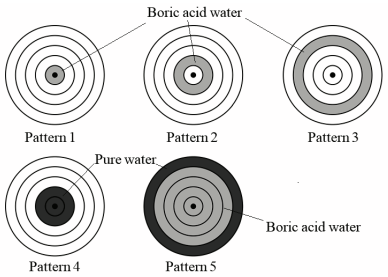

Fig. 1. The used combination for RBS.

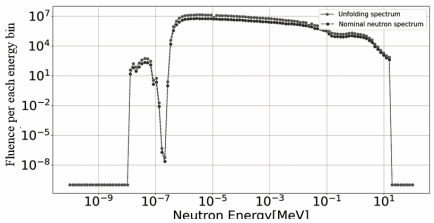

Fig. 2. Comparison between the nominal spectrum and the unfolded spectrum.

REFERENCES:

[1] S. Shiraishi *et al.*, Appl. Radiat. Isot. **163** (2020) 109213.
[2] H. Ueda, Doctoral Thesis (2016).

Study on New Type of Neutron Spctrometer for BNCT

K. Watababe, A. Ishikawa, A. Uritani, S. Yoshihashi, A. Yamazaki and Y. Sakurai[1]

Graduate School of Engineering, Nagoya University
[1] Institute for Integrated Radiation and Nuclear Science, Kyoto University

INTRODUCTION: Boron neutron capture therapy (BNCT) is a combined modality of radiotherapy and chemotherapy for cancer treatment. In the BNCT, a boron-containing agent is injected in patient's blood and concentrated into tumor cells. And then, the patient is irradiated with neutrons externally and $^{10}B(n,a)$ reactions are induced in tumor cells. Recently, an accelerator-driven neutron source has actively been developed instead of nuclear reactors, owing to its simplicity of management. In commissioning phase of the facilities, characterization of the irradiation field, such as neutron intensity, the neutron energy spectrum and gamma-ray components, should be characterized in order to assure designed ones.

We are developing a new neutron energy spectrometer using the optical fiber type neutron detector. The conventional technique for neutron spectrometry is the Bonner sphere method. Generally, energy response in epithermal region in moderation based neutron spectrometers is not sufficient. In order to improve the energy response, the number of detectors with different responses should be increased. In our proposed system, the thermal neutron flux profile in a liquid moderator is measured by the optical fiber type neutron detector. So far, in order to realize the optical fiber type neutron detector showing a neutron peak in the pulse height spectrum, bright neutron scintillators, such as Eu:$LiCaAlF_6$ or LiF/Eu:CaF_2 eutectics, have been used [1]. Recently, we attempted to replace them with the faster Li glass scintillator. Using an optical fiber with high numerical aperture, we successfully demonstrated the optical fiber type neutron detector showing a neutron peak by using the Li glass scintillator [2]. In this study, we evaluated gamma-ray sensitivity of the optical fiber type neutron detector using the Li glass scintillator.

EXPERIMENTS: We fabricated the optical fiber type neutron detectors using Li glass scintillator. A small piece of the Li glass scintillator was mounted at a tip of the optical fiber. The scintillator was coated with a reflector powder and then covered with a heat shrinking tube for light shielding.

First of all, we evaluated the neutron response at the E3 port in the Kyoto University Reactor. In this experiment, signal pulse height spectra for $^6Li(n,t)$ reactions were obtained. And then, the same detectors were irradiated with gamma-rays at Co-60 gamma-ray irradiation facility in Nagoya University to evaluate the gamma-ray sensitivity. Figure 1 shows photographs of thermal neutron and Co-60 gamma-ray irradiation experiments.

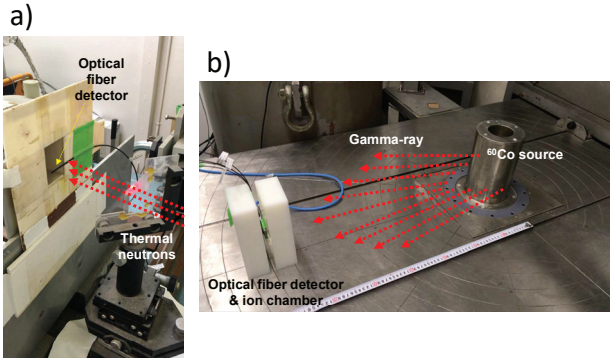

Fig. 1 Experimental setup. a) E3 port in KUR for thermal neutron irradiation. b) Co-60 gamma-ray irradiation facility in Nagoya University.

RESULTS: Figure 2 shows signal pulse height spectra obtained when the optical fiber type neutron detector using a Li glass scintillator of 18 μg was irradiated with thermal neutrons and Co-60 gamma-rays. The fabricated optical fiber type neutron detector shows a clear neutron peak. When irradiating with Co-60 gamma-rays, signals with slightly lower pulse heights compared with a neutron peak were recorded. In order t define the gamma-ray sensitivity of the detector, we have to determine the discrimination level for neutron events. When setting the discrimination level at a valley in the pulse height spectrum, the gamma-ray sensitivity was evaluated to be 4 cps at 1.9 Gy/h irradiation, which is higher dose rate compared with expected BNCT irradiation fields. This gamma-ray sensitivity is sufficiently low because the counting rate of the detector in typical BNCT irradiation field is expected to be more than 10^3 cps.

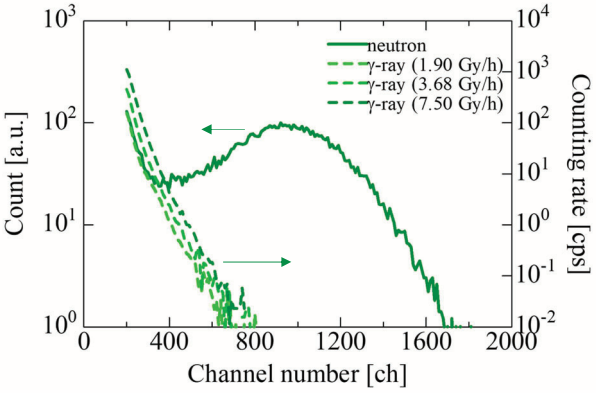

Fig. 2 Signal pulse height spectra obtained when the optical fiber type neutron detector using a Li glass scintillator of 18 μg was irradiated with thermal neutrons and Co-60 gamma-rays.

REFERENCES:

[1] K. Watanabe *et al.*, Nuclear Instruments and Methods in Physics Research Section A , **802**, 1 (2015).
[2] A. Ishikawa *et al.*, Sensors and Materials, **32**, 1489-1495 (2020).

PR9-3 Response characteristic measurements of lithium-glass scintillators used in the BSS for the intense neutron beams

A. Masuda, T. Matsumoto, H. Tanaka[1], D. Ito[1], H. Harano, Y. Sakurai[1] and T. Takata[1]

National Metrology Institute of Japan, National Institute of Advanced Industrial Science and Technology
[1]Institute for Integrated Radiation and Nuclear Science, Kyoto University

INTRODUCTION: Characteristics of the intense neutron beam should be evaluated to ensure the performance and safety of boron neutron capture therapy (BNCT). The Bonner unfolding method is commonly used when the time-of-flight method is not suitable for the moderated neutron source. Although the Bonner unfolding method has been successfully applied to measure weak beams at a BNCT facility[1], direct measurements of the therapy-level intense neutron beams are required. A new Bonner sphere spectrometer (BSS) using a pair of lithium-glass scintillators coupled with current-integration-operated PMTs has been developed to measure the BNCT beams[2]. Characteristics of the lithium-glass scintillators should be evaluated in detail for the practical use.

EXPERIMENTS: Directional-dependent response characteristics of the pair of lithium-glass scintillators are focused in this study. The well-collimated thermal neutron beam of the B-4 beam hole of the KUR[3] was used to evaluate the directional dependency precisely. The pair of the lithium-glass scintillators of GS20 (95% ^{6}Li, 10 mm in diameter and 2 mm in thickness) and GS30 (99.99% ^{7}Li, 10 mm in diameter and 2 mm in thickness) was set and irradiated by the thermal neutron beams from the four different directions as shown in Fig. 1. The effect of the γ-ray induced signal was corrected by the difference between the GS20 and GS30[4]. The same measurements using the standard mixed neutron irradiation mode were also carried out in the heavy water irradiation facility of the KUR[5] to simulate the actual therapy environment.

RESULTS: Relative efficiency to the direction (1) is shown in Fig. 2. Output variation of the reactor for each measurement was corrected using a fission chamber. A significant directional dependency was observed for the well-collimated thermal neutron beam. Decreasing of efficiency in the side irradiations is considered to be due to the effect of the absorption by the scintillator. Difference between the (2) and (3) can be explainable by effects on the subtraction of γ-ray induced signal. On contrast, the directional dependency was not so much observed in the heavy water irradiation facility. Since the irradiation room is not large, room-scattered low-energy neutrons seems to be dominant for the detector.

The results have shown that the efficiency of the detector has strong directional dependency and it should be considered when it is used in the actual treatment rooms of BNCT. Although the directional dependency can be negligible when used in the large moderator spheres of the BSS, it might be problematic when used with small spheres or without spheres.

The characteristics of the detector will be investigated more, and it will be utilized to improve the measurements and analysis of the BSS measurement in BNCT facilities.

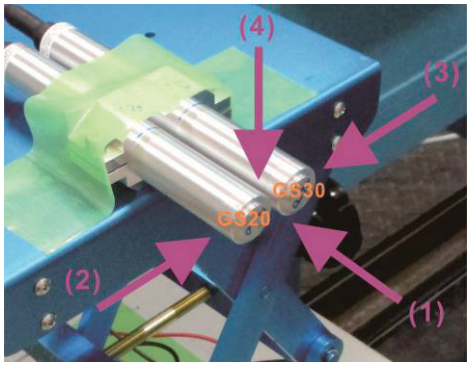

Fig. 1. The pair of GS20 and GS30 scintillators irradiated by the for directions: (1) top, (2) GS20 side, (3) GS30 side and (4) equivalently side.

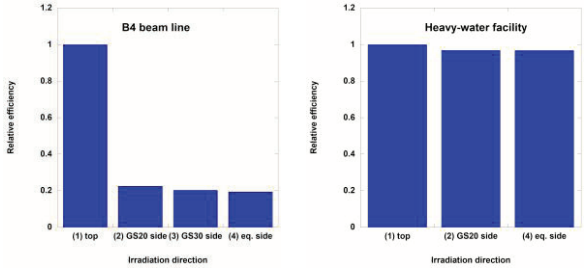

Fig. 2. Directional dependency of output from the pair of the lithium-glass scintillators.

REFERENCES:

[1] A. Masuda et al., Appl. Radiat. Isot., 127 (2017) 47-51.
[2] A. Masuda et al., 2018 IEEE NSS/MIC Proceedings (2019) 10.1109/NSSMIC.2018.8824697.
[3] Y. Saito et al., Nucl. Instr. Meth. Phys. Res. A, 651 (2011).
[4] T. Matsumoto et al., Radiat. Prot. Dosim., 188 (2019) 117-122.
[5] Y. Sakurai and T. Koyabashi, Nucl. Instr. Meth. Phys. Res. A, 453 (2000).

This study is supported by Grant-in-Aid for Scientific Research, Japan Society for the Promotion of Science (JSPS KAKENHI Grant Number 19K12638).

PR9-4 Neutron measurement by using the self-activation of iodine-added liquid scintillators

A. Nohtomi, Y. Kanzaki, G.Wakabayashi[1], Y.Sakurai[2] and T.Takata[2]

Graduate School of Medicine, Kyushu University
[1] Atomic Energy Research Institute, Kindai University
[2] Institute for Integrated Radiation and Nuclear Science, Kyoto University

INTRODUCTION: In our previous report, applicability of iodine-added plastic scintillator was studied at rather intense neutron field like BNCT at one of KUR irradiation facility [1]. In the study, thermal neutron was successfully detected by using the self-activation of iodine which was added to plastic scintillators. As with iodine-containing inorganic scintillators, NaI and CsI [2,3], the method is highly sensitive even for short time irradiation. On the other hand, the tuning of sensitivity is possible for this method. In addition, another benefit of this method is no production of byproduct activity, ^{24}Na and ^{134m}Cs. In the present work, applicability of iodine-added liquid scintillator was studied for comparison with the iodine-added plastic scintillator.

EXPERIMENTS: Iodine-added liquid scintillator was prepared by adding iodobenzen (C_6H_5I) to commercially available liquid scintillator (Insta-Gel Plus, Perkin Elmer). 20 ml polyethylene vials were used as the container of liquid scintillator. The surface of polyethylene vial was covered with Teflon tape as scintillation reflector (Fig.1). The concentration of iodobenzene in liquid scintillator was adjusted to be 1 wt% and 0.1 wt%. Two liquid scintillators were irradiated at Rail Device of the Heavy Water Neutron Irradiation Facility with OO-0000F mode (1MW) [4]. Those scintillator vials were put at the Bismuth Surface (thermal neutron flux : ~10^9 n/cm^2/s) during 10 seconds for 1 wt% scintillator and 100 seconds for 0.1 wt% one. After the termination of each irradiation, the output signal of scintillators was read out by PMT and MCA every one minute continuously.

Fig. 1. Appearance of iodine-added liquid scintillator.

RESULTS: Figure 2 shows decay curves of count rate observed by the iodine-added liquid scintillators after the termination of irradiation. In addition to ^{128}I decaying components with half-life of 25 min, small amount of unknown decaying components with half-life of 900 min are seen for both 1 wt% and 0.1 wt% scintillators. The count rate for 1 wt% at the termination of irradiation is 1.09 x 10^6 cpm and that for 0.1 wt% is 1.02 x 10^6 cpm.

$$1\text{wt\%}: 1.09\times10^6\times(1/2)^{\frac{x}{25}}+270\times(1/2)^{\frac{x}{900}}+230$$

$$0.1\text{wt\%}: 1.02\times10^6\times(1/2)^{\frac{x}{25}}+3000\times(1/2)^{\frac{x}{900}}+300$$

Because the irradiation time of neutrons is very shorter than the half life of ^{128}I (25 min), total amount of ^{128}I activity generation is approximately proportional to the product of the neutron irradiation time and the total number of ^{127}I atom existing in the scintillators. Therefore, it is consistent that the initial count rate (cpm) for 1 wt% scintillator after 10 seconds irradiation is almost equivalent to that for 0.1 wt% scintillator after 100 seconds irradiation (~1 x 10^6 cpm).

We could confirm that the unknown component was ^{24}Na by the gamma-ray spectroscopy using HPGe. It has been found that such small amount of contamination of ^{23}Na in liquid scintillator is not desirable for the application of iodine-added liquid scintillator to intense BNCT neutron field.

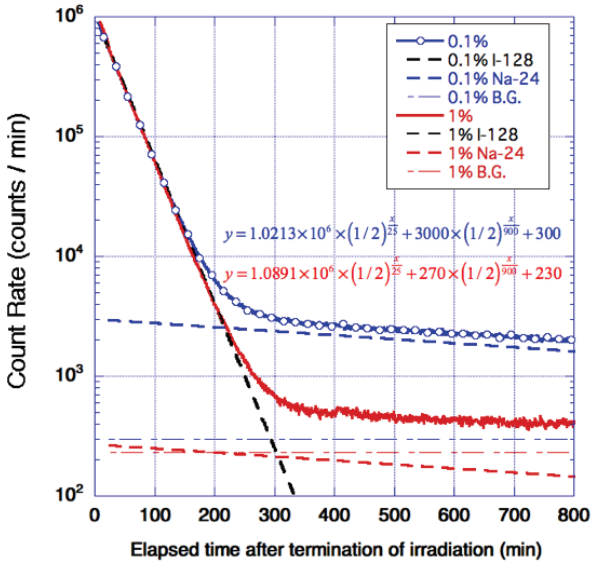

Fig. 2. Decay curves of count rate observed by the iodine-added liquid scintillators.

ACKNOWLEDGEMENT: This work was supported by JSPS KAKENHI Grant Number JP19K08202.
Mr. N. Sakamoto and Mr. H. Maeda of Kyushu University are deeply appreciated for their preparation of iodine-added liquid scintillators.

REFERENCES:

[1] A. Nohtomi *et al.*, KURRI progress report 2019.
[2] G. Wakabsyashi *et al.*, Radiol. Phys. Technol., **8** (2015) 125-134.
[3] A. Nohtomi *et al.*, JPS Conf. Proc., **24** (2019) 011041.
[4] Y. Sakurai and T. Kobayashi, Nucl. Instr. and Meth., **A453** (2000) 569-5.

PR9-5

Development of Absolute Epi-thermal and Fast Neutron Flux Intensity Detectors for BNCT

I. Murata, K. Aoki, Y. Miyaji, D. Hatano, S. Kusaka, H. Tanaka[1], Y. Sakurai[1], T. Takada[1]

Graduate School of Engineering, Osaka University
[1]Institute for Integrated Radiation and Nuclear Science, Kyoto University

INTRODUCTION: BNCT is a promising cancer therapy which can kill tumor cells while suppressing exposure dose to normal tissues. Normally, the neutron field of BNCT, which is produced by a nuclear reactor or an accelerator, has an energy distribution spreading within thermal, epi-thermal and fast neutron regions. Because epi-thermal neutrons are generally used for BNCT, we must measure the epi-thermal neutron flux intensity to evaluate the therapeutic effect and patient's exposure dose. In addition, we also have to evaluate the exposure dose of the fast neutrons that may be harmful to the human body. However, it is quite difficult to know such intensities directly and accurately, because there is no suitable neutron spectrometer and no activation material covering epi-thermal or fast neutrons separately. The objective of this work is hence to develop new detectors to precisely measure the absolute integral flux intensities of epi-thermal (0.5 eV ~ 10 keV) and fast neutrons (10 keV ~ 1 MeV).

EXPERIMENTAL METHODS: Epi-thermal neutron detector was designed to reduce sensitivities to thermal and fast neutrons by using cadmium and polyethylene. Fast neutron detector reduces sensitivities to thermal and epi-thermal neutrons by using cadmium, B_4C and polyethylene. We performed numerical simulations by MCNP5 and $^{71}Ga(n, \gamma)^{72}Ga$ reaction was determined to use as an activation reaction. In order to test the performance of the epi-thermal and fast neutron detectors, verification experiments were conducted at KUR, Kyoto University.

RESULTS and DISCUSSION: Figure 1 shows the design result of the epi-thermal neutron detector. Figure 2 and 3 are sensitivities of epi-thermal and fast neutron detectors, respectively. Epi-thermal neutron detector still has a small but non-negligible sensitive to fast neutrons as

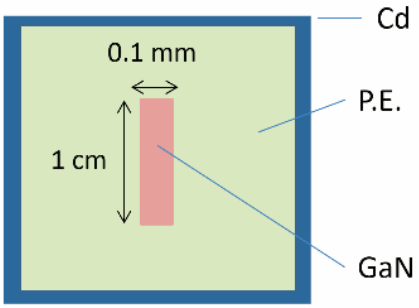

Fig. 1. Calculation model of epi-thermal neutron detector.

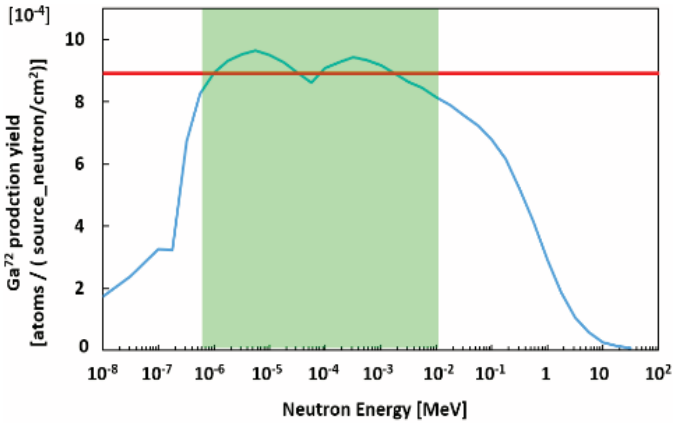

Fig. 2. Sensitivity of epi-thermal neutron detector.

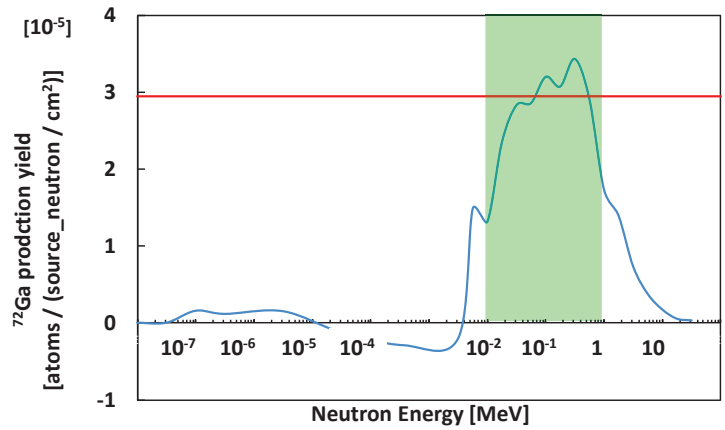

Fig. 3. Sensitivity of fast neutron detector.

in Fig. 2. The experimental results thus show a slight overestimation in the epi-thermal neutron flux intensity, i.e., C/E = 0.61. Similarly, since fast neutron detector has a little sensitivity to thermal and epi-thermal neutron, a considerable overestimation, C/E = 0.28, was observed. This is mainly because the real spectrum has a peak in the epi-thermal energy region.

PR9-6 Characterization of Active Neutron Detector for Boron Neutron Capture Therapy

M. Takada, S. Endo[1], H. Tanaka[2], T. Nunomiya[3], K. Aoyama[3], T. Nakamura[3]

Department of Applied Physics, National Defense Academy of Japan
[1]Graduate School of Engineering, Hiroshima University
[2]Institute for Integrated Radiation and Nuclear Science, Kyoto University
[3]Fuji Electric Co. Ltd.

INTRODUCTION: Boron Neutron Capture Therapy (BNCT) is a binary radiotherapy method developed to treat patients with certain malignant tumors. BNCT has been widely used at nuclear reactors. Currently, several accelerator-based BNCT facilities are being developed and clinical trials are conducted. Intensity of neutron beam produced from the neutron accelerator could be varied with time due to instability of the accelerator condition and the neutron target degression. Now, thermal neutron flux is measured before and after the neutron irradiation using offline gold activation method. However, real-time neutron beam measurement is required during the neutron irradiation.

The active neutron detector, which composes of thin silicon sensor and ultra thin LiF neutron converter with around 0.1μm thickness, measures the BNCT neutron beam over $1x10^9$ (cm^{-2} s^{-1}), separately from high dose-rate gamma rays around 500 mGy/h [1-3]. The detection efficiency of the real-time neutron detector for thermal neutron was experimentally obtained. Neutron responses for a wide range of neutron converter thickness have been measured and simulated. Neutron detectors have been developed to measure epithermal and fast neutrons produced from the neutron target.

These neutron detectors will be applied to monitor the target neutrons during the BNCT treatments by installing the neutron detector near the neutron target. There, photon dose rates are dramatically increased than that at the neutron irradiation position. It is difficult to separate neutron events from photons under high-dose-rate photon fields because of interruption by pile-up signals. A neutron detector was tried to improve the separation property of neutron and photon events by acquiring larger particle energies of summing both triton and alpha partilces produced by the $^6Li(n,t)^4He$ reaction.

EXPERIMENTS: The neutron measurements were performed at the heavy water irradiation facility of research reactor of KURNS. Two thin silicon sensors were faced each other and an ultra thin LiF neutron converter, evaporated on a thin Mylar film, is inserted between them. Summed both signals from the two Si sensors were fed to a pre-amplifier outside of the irradiation room, and then, acquired using fast digital pulse-shaping processor. The thermal neutron beam fluxes and cadmium ratios are changed by opening a Cd aperture slit at an upward of the irradiation location. Channel number of multi-channel analyzer was converted to particle energies by measuring alpha sources at our university before the neutron irradiation.

RESULTS: Figure.1 shows the pulse heights of thermal neutrons measured using the Si neutron detector, normalized with the neutron fluences. Here, the neutron fluences are referred from the previous evaluation values. Three main peaks are observed in the plot, (A)-(C). The peak (A) is created by detecting both alpha particles and tritons. Tritons are transmitted through the thin film and loss their energies, however, alpha particles loss no energy in the film. The peak (B) is created by detecting alpha particles without any energy loss and tritons transmitted through the film. Neutron peak is split due to different particle energy losses in the film. These split peaks are resolved by evaporating the LiF on the Si sensor, directly and removing the film. Unfortunately, the creation of peak (C) has never been understood. Events (D) and (E) are observed due to detection of pile-up signals and mainly electrons produced by gamma rays, respectively.

During the neutron irradiation, the neutron peaks show constant particle energy and no peak shift was observed. Until now, neutron damage on Si sensor has never been measured. Up to $6.5x10^8$ (cm^{-2} s^{-1}) neutron flux, linearity of count rates was obtained. BNCT neutron beam was measured directly, using the compact neutron detector. We will measure thermal neutron fluxes under high photon-dose-rates environments.

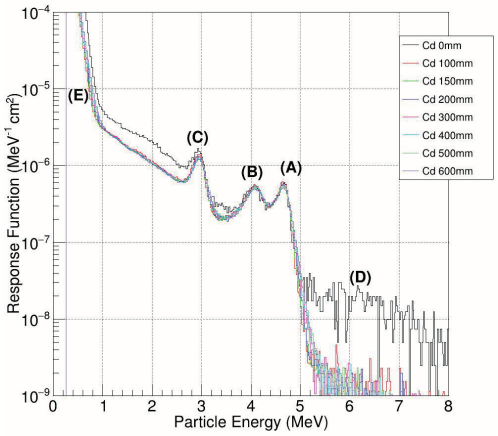

Figure 1. Pulse heights of neutron detector, which is consisted of thin Si sensor and ultra-thin LiF neutron converter, measuring BNCT neutron beam. Thermal neutron fluxes were changed by opening the Cd aperture window.

REFERENCES:

[1] M. Takada *et al.*, Radiat. Meas., 99, 33-54 (2017).
[2] M. Takada *et al.*, Appl. Radiat. Isotopes (submitted).
[3] M. Takada *et al.*, Radiat. Meas. 137 (2020) 106381.

PR9-7 Study for microdosimetry using silicon-on-insulator microdosimeter in the BNCT irradiation field (IV)

Y. Sakurai, N. Ko[1], T. Takata, H. Tanaka, T. L. Tran[1], J. Davis[1], S. Guatelli[1], A. Rozenfeld[1], N. Kondo and M. Suzuki

Institute for Integrated Radiation and Nuclear Science, Kyoto University
[1]Kansai BNCT Medical Center, Osaka Medical College
[2]Centre for Medical Radiation Physics, University of Wollongong

INTRODUCTION: Research and development into several types of accelerator-based irradiation systems for boron neutron capture therapy (BNCT) is underway [1,2]. In the near future, BNCT using these newly developed irradiation systems may be carried out at multiple facilities across the world. In contrast to conventional radiotherapy, the types of radiation present in BNCT consists of many distinct radiation components, each having a different biological weighting factor.
Microdosimetry is an effective dosimetry technique in a mixed radiation environment. Using this technique, it is possible to derive the relative contributions of different radiation modalities. The feasibility study of a novel 3D mesa bridge silicon-on-insulator microdosimeter (SIM) in BNCT [3], developed by University of Wollongong (UOW).
In 2020, a new-type silicon microdosimeter and its application for boron neutron capture therapy (BNCT) were investigated by Monte Carlo simulation.
MATERIALS AND METHODS: Two detector configurations were investigated, based on the current 3D mushroom microdosimeter. The first structure consists of a cylindrical p+ core electrode through the center of the SV with n+ ring electrode wrapped around the outside of the SV. The second structure consists of a cylindrical n+ core electrode through the center of the SV with p+ ring electrode wrapped around the outside of the SV. Each SV has a diameter and height of 10 μm and the pitch between each individual SV is 40 μm to reduce cross talk between neighboring row of detectors. A total of 2500 individual SVs were connected in an array with odd and even detector row readout channels.
PHITS was used for this study. The T-deposit tally, which scores dose and event-by-event deposition energy distribution was used to calculate the energy deposited inside the SV of the mushroom microdosimeter. The microdosimetric spectrum (frequency mean and dose mean lineal energy distribution) were calculated by dividing the deposited energy by the average chord length of the SV.
The neutron response of the new-type detector were investigated using the neutron source for the mixed neutron irradiation mode of Heavy Water Neutron Irradiation Facility installed in Kyoto University Reactor (KUR-HWNIF) [4].
RESULTS: The ion track of 1.47 MeV alpha particles produced inside the p+ region is shown in Figure 1. It was found the total flux inside the SV was higher for the p+ core through the center. This was due to the fact some of the alpha particles escaped from the p+ ring.
The number of alpha particles depositing it's full energy (1.47 MeV) was also found to be higher with the p+ core design, shown in Figure 2. The range of 1.47 MeV alpha particles inside silicon is approximately 5 μm. Most of the alpha particles generated inside the p+ core will deposit all its energy inside the SV. However, the alpha particles generated inside the p+ ring will only deposit a portion of its energy inside the SV before escaping.
CINCLUSION: It was found that the absorbed dose was approximately 2.5 times more with the p+ core design. The dose to the surrounding PMMA was much less with the p+ core.

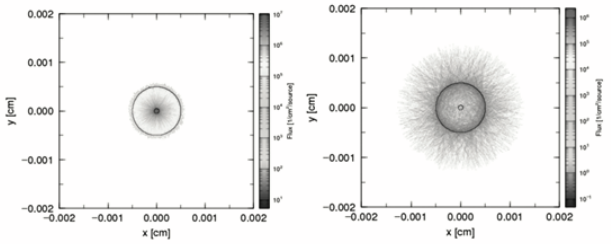

Fig. 1. Ion track of 1.47 MeV alpha particles inside a single SV. Left) p+ core through the centre of the SV. Right) p+ ring around the outside of SV.

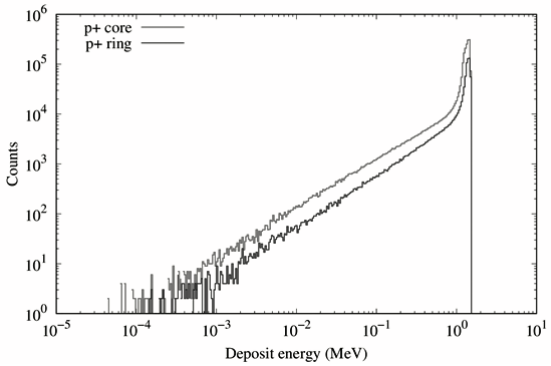

Fig. 2. Deposit energy of 1.47 MeV alpha particles inside the SV for p+ core and p+ ring.

REFERENCES:
[1] H. Tanaka *et al*., Nucl. Instr. Meth. B **267** (2009) 1970-1977.
[2] H. Kumada *et al*., Appl. Radiat. Isot. **88** (2014) 211-215.
[3] L. T. Tran *et al*., IEEE Trans. Nucl. Sci. **62** (2015) 3027-3033.
[4] Y. Sakurai and T. Kobayashi, Nucl. Instr. Meth. A **453** (2000) 569-596.

R2P9-8

PR9-8 Measurement of thermal neutrons and gamma rays in BNCT beam with polymer gel detector

Kenichi Tanaka, Yoshinori Sakurai[1], Tsuyoshi Kajimoto, Aruma Mitsuyasu[1], Shin-ichiro Hayashi[2], Hiroki Tanaka[1], Takushi Takata[1], Gerard Bengua[3], Satoru Endo

Graduate School of Advanced Science and Engineering, Hiroshima University
[1]Institute for Integrated Radiation and Nuclear Science,, Kyoto University
[2]Faculty of Health Sciences, Hiroshima International University
[3]Auckland City Hospital

INTRODUCTION: For the quality assurance of spatial beam component distribution, this study investigates the use of the MAGAT polymer gel detector. The trial to measure thermal neutrons and gamma rays are reported.

EXPERIMENTS: In the experiments for the present study, the MAGAT-type gel detector was infused with LiCl, where the naturally abundant isotope ^{6}Li was used. The ^{6}Li concentrations were set at 0 and 100 ppm. The dimension of the gel detector was 60 × 60 × 60 mm^3. The gel detector was encased in a box made of 5 mm thick acrylic acid resin. The box was set inside a 200 × 200 × 200 mm^3 acrylic acid resin phantom, to simulate a human head in a brain tumor treatment.
The irradiation was performed with the standard epithermal neutron irradiation mode of KUR-HWNIF [1] at 1 MW. The beam size was set to about 120 × 120 mm^2 using the collimator. The irradiation was performed for 110 minutes for 0 ppm and 30 minutes for 100 ppm. The nominal value of the flux at the center of the collimator aperture was 7.07 × 10^6 cm^{-2}s^{-1} and 1.25 × 10^7 cm^{-2}s^{-1} for thermal neutrons and gamma rays, respectively.
The response of the MAGAT to dose was measured. The irradiation was performed by using Co gamma rays irradiation facility at Hiroshima University. The transverse relaxation rate (R_2) was determined using a 0.3T MRI scanner (AIRIS Ⅱ comfort, Hitachi Medical Corp.) with a standards head coil.
The fluence ϕ_j of each component was determined using the following model;

$$S = \begin{pmatrix} S_1 k_1 \\ S_2 k_2 \end{pmatrix} = \begin{pmatrix} a_{11} & a_{12} \\ a_{21} & a_{22} \end{pmatrix} \begin{pmatrix} \Phi_1 \\ \Phi_2 \end{pmatrix} = A \cdot \Phi \qquad (1),$$

$$\Phi = A^{-1} \cdot S \qquad (2),$$

where a_{ij} denotes the sensitivity of the ith gel for the component j, and where k_i denotes the conversion factor from the signal intensity to the absorbed dose. The sensitivity a_{ij} was estimated using the PHITS simulation [2] of the irradiation condition at KUR-HWNIF. Assuming that the signal intensity is proportional to the energy deposition, the ratio of the energy deposition to the beam component fluence at the gel detector regions of 5 × 5 × 5 mm^3 along the central axis was computed and assigned as a representative of a_{ij}. The conversion factor k_i from the signal intensity to the absorbed dose was measured for the irradiation with ^{60}Co gamma rays in Hiroshima University [3].

RESULTS: The response of the gel detector to ^{60}Co gamma rays is shown in Fig. 1. The slopes of the regression lines are 7.8 and 7.1 s^{-1}Gy^{-1}. These correspond to $1/k_i$ in equation (1). Though the signal intensity for KUR irradiation is not shonw here. The estimated fluence is hown in figure 2. The standard deviation is about 2% for gold activation, 10% for TLD. The fluence distribution measured by the gel detector agrees to within 5% to 10% of other estimates. This suggests the potential usability of polymer gel detector in spatial measurement of fluence in BNCT beam.

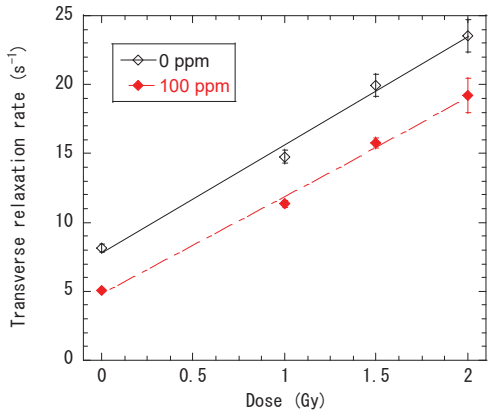

Fig. 1 Response of the gel detector to ^{60}Co gamma rays.

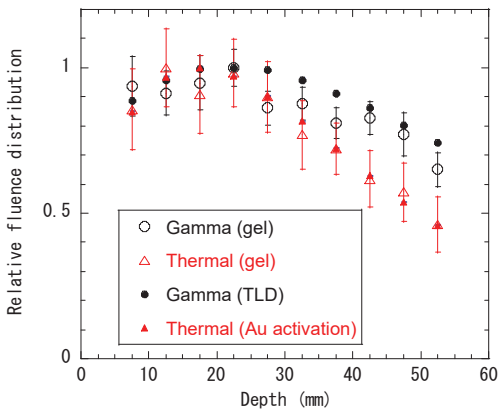

Fig. 2 Relative distribution of fluence estimated.

REFERENCES:

[1] Sakurai Y and Kobayashi T Nucl. Instr. Meth. A453 569-596 (2000).
[2] Sato T *et al.*, J. Nucl., Sci. Technol. 50 913-923 (2013).
[3] Murakata A, Endo S, *et al.*, J. Radiat. Res. 51 198-203 (2010).

PR9-9 Development of two dimensional neutron detector in BNCT irradiation field

H. Tanaka[1], T. Takushi[1], Y. Sakurai[1], S. Uno[2]

[1]Institute for Integrated Radiation and Nuclear Science, Kyoto University
[2] High Energy Accelerator Research Organization

INTRODUCTION:

Boron neutron capture therapy is a radiotherapy that uses alpha rays and lithium nuclei emitted by the reaction of boron-10 and thermal neutrons. Since the accelerator BNCT[1][2] has been covered by insurance, it has been desired to improve the quality assurance method. In particular, since there is no system that can measure the thermal neutron distribution in two dimensions in real time, we are considering the application of a gas electron multiplier (GEM) detector [3] in this study.

While proceeding with the property test at the KUR heavy water neutron irradiation facility, the two-dimensional distribution was measured by the gold activation method in order to evaluate the validity of the thermal neutron distribution obtained by a GEM detector.

EXPERIMENTS:

The gold film was irradiated under the condition of a collimator diameter of 12 cm in the mixed mode of the KUR heavy water irradiation facility. The size of the gold film was 10 cm square, and it was installed covering a quarter of the collimator.

After irradiation for 15 minutes, the activated gold film was placed on an imaging plate (IP) and exposed. A small gold foil with a thickness of 50 μm was installed at positions 42 mm from the center of irradiation, and used as a reference foil for standardizing the thermal neutron flux.

After irradiation, the saturated radioactivity of gold foil was measured by a germanium detector, and thermal neutrons were evaluated. The photo-stimulated luminescence (PSL) value of an IP at the same point was normalized by the thermal neutron flux.

RESULTS:

Fig. 1 shows the result of the two-dimensional distribution of PSL values. The fig. 2 shows the result of the thermal neutron flux normalizing the PSL value in the r-axis direction.

It was confirmed that the collimator was able to shield about two digits. In the future, a GEM detector will be installed directly under the collimator to compare the thermal neutron distribution.

CONCLUSION:

Two-dimensional thermal neutron distribution was measured by the combination between a gold film and an IP. This method is not able to detect thermal neutron in real time. And the procedure is time consuming. However, position resolution is good because it is depended on an IP position resolution around 50 μm. In this time, two-dimensional thermal neutron distribution was evaluated to compare with the experiment results of a GEM detector.

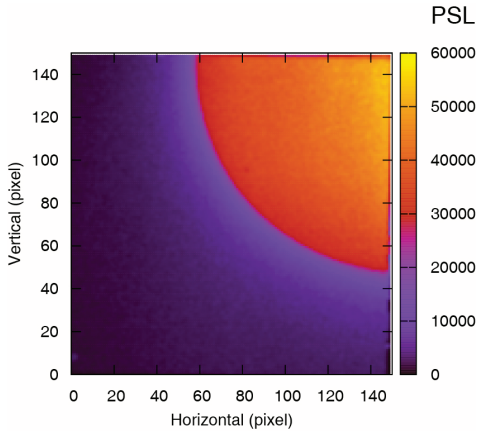

Fig. 1. The photo-stimulated luminescence (PSL) distribution exposed with activated gold film.

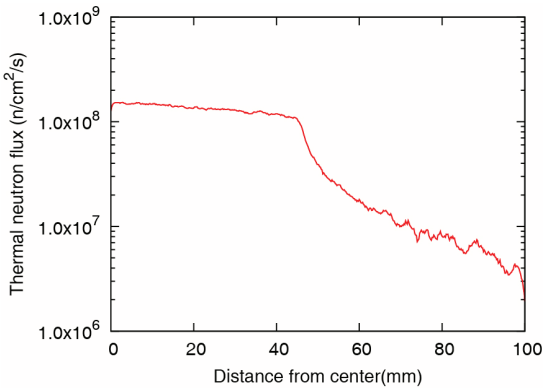

Fig. 2. Normalized thermal neutron distribution.

REFERENCES :

[1] Hirose, K., Konno, A., Hiratsuka, J., Yoshimoto, S., Kato, T., Ono, K., Otsuki, N., Hatazawa, J., Tanaka, H., Takayama, K., Wada, H., Suzuki, M., Sato, M., Yamaguchi, H., Seto, I., Ueki, Y., Iketani, S., Imai, S., Nakamura, T., Ono, T., Endo, H., Azami, Y., Kikuchi, Y., Murakami, M., Takai, Y. Boron neutron capture therapy using cyclotron-based epithermal neutron source and borofalan (10B) for recurrent or locally advanced head and neck cancer (JHN002): An open-label phase II trial, (2021) Radiotherapy and Oncology, 155, pp. 182-187.

[2]Tanaka, H., Sakurai, Y., Suzuki, M., Masunaga, S., Mitsumoto, T., Fujita, K., Kashino, G., Kinashi, Y., Liu, Y., Takada, M., Ono, K., Maruhashi, A. Experimental verification of beam characteristics for cyclotron-based epithermal neutron source (C-BENS) (2011), Applied Radiation and Isotopes, 69 (12), pp. 1642-1645.

[3] Uno, S., Uchida, T., Sekimoto, M., Murakami, T., Miyama, K., Shoji, M., Nakano, E., Koike, T., Morita, K., Satoh, H., Kamiyama, T., Kiyanagi, Y.,Two-dimensional Neutron Detector with GEM and its Applications (2012), Physics Procedia, 26, pp. 142-152.

PR9-10 Study of Neutron Fluence and Gamma ray Distribution Measuring using Thermoluminescence Slabs

K. Shinsho, R. Oh, M. Tanaka, S. Yanagisawa, H. Tanaka[1], T.Takata[1], G. Wakabayashi[2], Y. Koba[3]

Graduate School of Human Health Science, Tokyo Metropolitan University

[1] Institute for Integrated Radiation and Nuclear Science, Kyoto University

[2] Graduate school of Science and Engineering Research, Kindai University

[3]Center for Radiation Protection Knowledge, QST-NIRS

INTRODUCTION: Boron Neutron Capture Therapy (BNCT) is one of the radiation therapies using neutrons and ^{10}B drugs which are attracted to tumors. BNCT is expected to be next-generation cancer therapy which will improve the QOL of patient because it can irradiate a cancer cell at the molecular level selectively. However, dosimetry techniques in mixed neutron-gamma fields have not been established yet. Therefore, we focused on reusable two-dimensional thermoluminescence dosimeter (2D-TLD). The 2D-TLD which we used is thermoluminescence (TL) phosphor Cr doped Al_2O_3 ceramic plate (2-D Al_2O_3: Cr TLD).[1] 2-D Al_2O_3: Cr TLD that can acquire radiation images with high spatial resolution. In addition, it has high solidity and can be used under water. We are investigating neutron imaging using 2-D Al_2O_3: Cr TLD and Cd neutron-gamma ray converter technique in mixed neutron-gamma fields. Furthermore, we are conducting research on γ-ray imaging in mixed fields using TL characteristics of BeO ceramic plates. And then, we have found that the Cd neutron-gamma ray converter lets the sensitivity of the neutron increase selectively, and we can acquire theneutron images easily without dis-crimination of gamma ray. In this study, the thermal neu-tron fluence distribution was measured using a large-area 2-D Al_2O_3: Cr TLD with Cd converter, and the γ-ray measurement using BeO ceramic plates was performed in mixed neutron-gamma field.

EXPERIMENTS: Low melting point Al_2O_3 of Chibaceramic MFG Co. LTD., which was composed of Al_2O_3 > 99.5 wt% was used for measurements of thermal neutron fluence distribution. The bulk density of the plates was 3.7g·cm^{-1}. The dimensions used for the glow curve measurements were 10 × 10 × 0.7 mm^3 and 80 × 80 × 0.7 mm^3. The concentration of Cr_2O_3 in the present study was 0.05 wt%. BeO ceramic plates（Thermalox995) of Materion Corporation, which was composed of BeO > 99.5 wt %, Si 0.186 wt%, Mg 0.092 wt%, was used for γ-ray measurement in mixed neutron-gamma field. The bulk density of the plates was 3.02 g·cm^{-1}. The dimensions used for the glow curve measurements were 10 × 10 × 1.0 mm^3. The assumed irradiation fields are the mixed irradiation mode in KUR-HWNIF, with a power of 1MW. The glow curves were recorded from room temperature up to 400 °C at a heating rate of 0.1 °C·s^{-1}. The 2-D TL measurement system consists of a CMOS camera, 80×80 mm^2 heater, and a dark box. After expo-sure, the TL slabs were heated to 400 ℃ for 5 min. The TL images were captured using a CMOS camera equipped with a thermal cut filter.

RESULTS: Figure 1 shows the relationship between the neutron reaction rate of Cd in KUR and the TL amount of Al_2O_3: Cr. From Fig.1, it became clear that the neutron reaction rate and the amount of TL are represented by quadratic functions. Since the nuclear reaction cross section of Cd to neutrons is constant, it was suggested that by measuring the TL amount of Al_2O_3: Cr, it may be possible to investigate the presence or absence of changes in the neutron energy spectrum during periodic inspections. Figure 2 shows arrangement of TL slabs irradiation arrangement for both TL imaging and the TL image of the slab. It was shown that high spatial resolution thermal neutron distribution measurement is possible.In γ-ray measurement in mixed neutron-gamma field using BeO ceramic plates, the results of the BeO ceramic plate showed good agreement with the TLD (UD-170LS) of Panasonic Corporation.

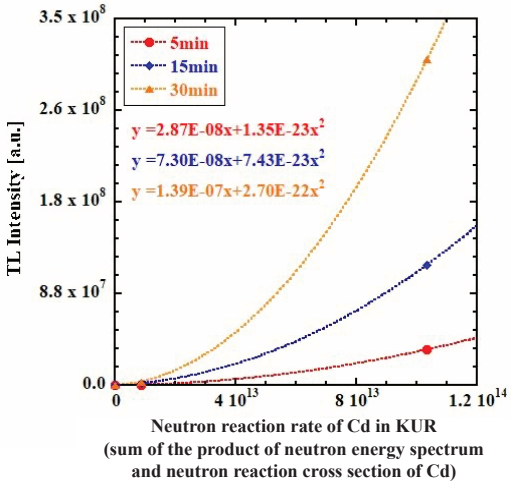

Fig.1 relationship between the neutron reaction rate of Cd in KUR and the TL amount of Al_2O_3: Cr.

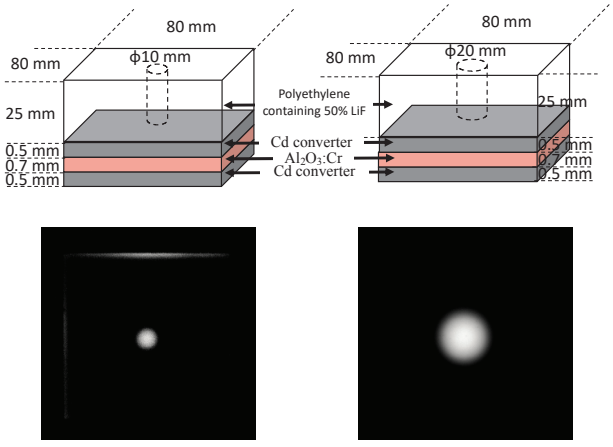

Fig.2 Upper: Arrangement of TL slabs (Al_2O_3: Cr using Cd converter) irradiation arrangement for TL imaging. Lower: TL image of the slab.

REFERENCES: [1]K. Shinsho et al., Sensors and Mate-rials., 30 (2018) 1591-1598.

R2P9-11

PR9-11 Development and evaluation of 3D gel dosimeter for the measurement of dose distribution in BNCT

S. Hayashi, Y. Kakimoto[1], T. Takata[2], M. Suzuki[2] and Y. Sakurai[2]

Department of Clinical Radiology, Hiroshima International University
[1]Graduate School of Engineering, Kyoto University
[2]Institute for Integrated Radiation and Nuclear Science, Kyoto University

INTRODUCTION: Irradiation field for boron neutron capture therapy (BNCT) is the mixed field of thermal neutrons, epi-thermal neutrons, fast neutrons, and gamma rays, so the discrimination estimation is necessary for each dose component in the irradiation field characterization. The point-wise estimation using activation foil, thermo-luminescent dosimeter (TLD), ionization chamber, etc., is mainly performed at present, but two-dimensional (2D) estimation is also needed. As part of the advancement in characterization for BNCT irradiation field, a study was performed for the 2D component-discrimination estimation using a radiochromic gel dosimeter base on polyvinyl alcohol - glutaraldehyde - iodide (PVA-GTA-I) [1].

MATERIALS AND METHODS: Three-layered planer gel dosimeter was prepared, as shown in Figure 1 (left). Each planar gel dosimeter was 10 cm in width, 10 cm in length and 0.3 cm in thickness. The first layer (Gel-1) was a PVA-GTA-I gel dosimeter containing boric acid ($B(OH)_3$) of natural abundance for boron-10 or lithium sulphate (Li_2SO_4) of enrichment for lithium-6 as the sensitizers for thermal neutrons. The second layer (Gel-2) was a normal PVA-GTA-I gel dosimeter without the sensitizers. The third layer (Gel-3) was a PVA-GTA-I gel dosimeter consisting of heavy water instead of light water. For fast neutrons, the recoiled protons or deuterons due to the elastic scatter of hydrogen or deuterium mainly contribute to dose. For thermal neutrons, the nuclear reactions of boron-10 or lithium-6 mainly contribute to dose.
The response characteristic for gamma rays was estimated using Co-60 gamma-Ray Irradiation Facility. The response characteristic for neutrons was estimated by the irradiation experiments using three irradiation modes for thermal, epi-thermal, and mixed neutrons at Heavy Water Neutron Irradiation Facility (HWNIF) of KUR [2], and by the simulation calculation using Particle and Heavy Ion Transport-code-System (PHITS) [3].

The verification experiment for 2D component-discrimination estimation was performed using the mixed neutron irradiation mode of KUR-HWNIF. The size of the collimator aperture was 12 cm in diameter, and the three-layered planer gel dosimeter was placed at the collimator exit to hang on the aperture edge (*e.g.*, Figure 1 (right)).

The irradiated gel dosimeters were scanned using a scanner and the transmission images were obtained. The transmission images were analyzed using a Python program, the net optical density (net OD) was calculated from the analogue digital conversion (ADC) values, and the response characteristic was estimated.

RESULTS AND DISCUSSION: From the response characteristic experiment for gamma rays, the high linearity was confirmed between the response and dose from 0 to 20 Gy. From the response characteristic experiment for neutrons, the response curve to dose-weighted linear energy transfer (LET) was obtained. Using this response curve, the correction factors regarding LET-dependency for the recoiled protons, recoiled deuterons and the thermal neutron reactions with boron-10 and lithium-6, were obtained.

From the verification experiment for 2D component-discrimination estimation, the 2D dose distributions were obtained. It was confirmed that the 2D distribution for thermal neutrons were relatively in close agreement with the estimated result by activation method using gold thin film. The absolute value by the gel dosimeter was almost two times larger compared with the activation method. It is thought that the components scattered in the gel dosimeter contributed additionally. For gamma rays, the 2D dose distribution was in good agreement with the estimated result by TLD.

CONCLUSION: The feasibility for the 2D component-discrimination estimation using the three-layered planer gel dosimeter was confirmed. In future, the sensitivity improvement and thickness reduction of this gel dosimeter will be studied. Also, the dependency for LET will be precisely estimated.

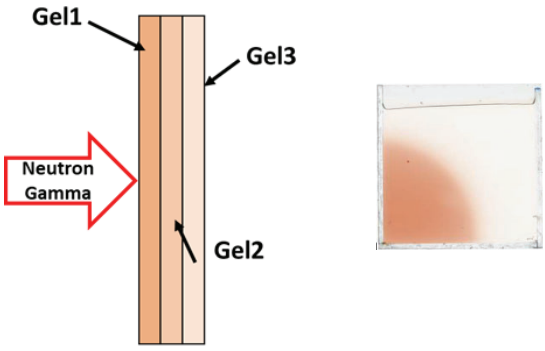

Figure 1 (left) Schematic of three-layered planer gel dosimeter. (right) An irradiated gel sample.

REFERENCES:

[1] S. Hayashi *et al.*, J. Phys.: Conf. Ser. (accepted) (2021).
[2] Y. Sakurai and T. Kobayashi, Nucl. Instr. Meth. A **453** (2000) 569-596.
[3] T. Sato *et al.*, J. Nucl. Sci. Technol. **50** (2011) 913-923.

R2P9-13

PR9-12 Establishment of beam-quality estimation method in BNCT irradiation field using dual phantom technique (IV)

Y. Sakurai, N. Kondo, T. Takata, H. Tanaka and M. Suzuki

Institute for Integrated Radiation and Nuclear Science, Kyoto University

INTRODUCTION: Development in several types of accelerator-based irradiation systems for boron neutron capture therapy (BNCT) is underway. Many of these systems are nearing or have started clinical trials. Before the start of treatment with BNCT, the relative biological effectiveness (RBE) for the fast neutrons (over 10 keV) incident to the irradiation field must be estimated.

Measurements of RBE are typically performed by biological experiments with a phantom. Although the dose deposition due to secondary gamma rays is dominant, the relative contributions of thermal neutrons and fast neutrons are virtually equivalent under typical irradiation conditions in a water and/or acrylic phantom. Uniform contributions to the dose deposited from thermal and fast neutrons are based in part on relatively inaccurate dose information for fast neutrons.

The aim of this study is the establishment of accurate beam-quality estimation method mainly for fast neutrons by using two phantoms made of different materials, in which the dose components can be separated according to differences in the interaction cross-sections. The fundamental study of a "dual phantom technique" for measuring the fast neutron component of dose is reported [1].

In 2020, verification experiments for the dual phantom technique were performed using Heavy Water Neutron Irradiation Facility installed in Kyoto University Reactor (KUR-HWNIF) as in the previous year. Biological experiments were performed using the solid phantoms, which were made based on the simulation results.

MATERIALS AND METHODS: One of the dual solid phantoms was made of polyethylene with natural lithium fluoride for 30 weight percent (LiF-polyethylene phantom), and the other phantom was made of polyethylene with 95%-enriched lithium-6 fluoride for 30 weight percent (^{6}LiF-polyethylene phantom).

Vials containing one kind of human brain cell, such as U87ΔEGFR, were placed at the surface, 2-cm depth, 5-cm depth and 8-cm depth in the phantoms on the center axis of the beam line. Cell growth assay was performed for the irradiated cells.

The neutron flux and gamma-ray dose rate were measured using activation foils and thermo-luminescent dosimeter, respectively. The depth dose distributions for the thermal neutron, fast neutron and gamma-ray components were determined based on the simulation calculation results normalized referring to the measured values.

Figure 1 shows a photograph of the experimental setup. The epi-thermal neutron irradiation mode was used.

RESULTS: Figure 2 shows the depth distributions of the cell survival for the BPA administration group, BPA(+), and the non-administration group, BPA(-), in the LiF-polyethylene phantom. For BPA(+) group, the concentration of boron-10 was 25 ppm. The difference for the cell survival was shown between BPA(+) group and BPA(-) group. Due to the neutrons thermalized in this phantom, the cell survival for BPA(+) group was lower than that for BPA(-) group.

Figure 3 shows the depth distributions of the cell survival in the ^{6}LiF-polyethylene phantom. In this phantom, most of the thermalized neutrons were absorbed by ^{6}LiF. So, the cell-survival distributions for BPA(+) group and BPA(-) group were almost the same.

CONCLUSION: The assay results will be more analyzed in association with the data of the depth dose distribution for the thermal neutrons, fast neutrons and gamma-rays.

ACKNOWLEDGMENT: This work was supported by JSPS KAKENHI Grant Number JP 16H05237.

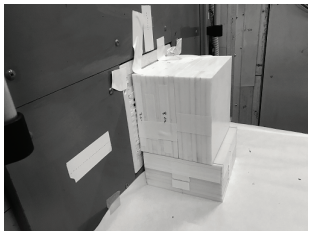

Fig. 1. A photograph of the experimental setup.

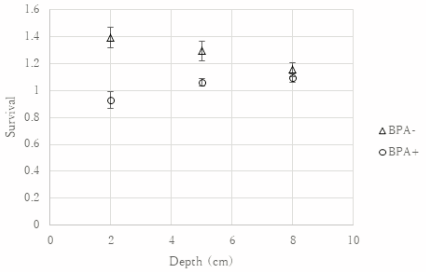

Fig. 2. Depth distributions for the cell survival in the LiF-poly phantom.

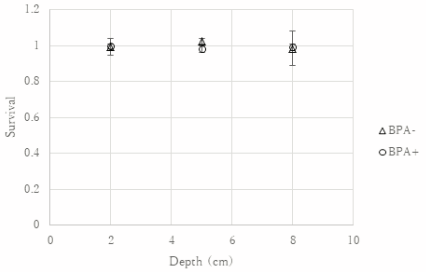

Fig. 3. Depth distributions for the cell survival in the ^{6}LiF-poly phantom.

REFERENCES:

[1] Y. Sakurai *et al*., Med. Phys. **42** (2015) 6651-6657.

R2P9-14

PR9-13

Development of a prompt gamma-ray imaging detector using an 8 x 8 arrayed $LaBr_3$(Ce) scintillator for BNCT

K. Okazaki[1], T. Takushi[1], Y. Sakurai[1], H. Tanaka[1]

[1]*Institute for Integrated Radiation and Nuclear Science, Kyoto University*

INTRODUCTION: New boron compounds have been investigated with small animal studies for improving boron neutron capture therapy (BNCT). To evaluate the boron dose, the ^{10}B concentration in animal body is needed. Usually, the information on ^{10}B concentration in the animal body has been evaluated using a high-purity germanium detector with prompt gamma-ray analysis[1] or the induced coupled plasma. However, these methods can not measure ^{10}B concentration in real time. A real-time detector has been developed to obtain the information on ^{10}B concentration in basic research of BNCT. An 8 x 8 arrayed $LaBr_3$(Ce) scintillator and Multi Pixel Photon Counter (MPPC) were used to acquire information on ^{10}B concentration by measuring prompt gamma rays emitted from the reaction between thermal neutrons and ^{10}B. This detector system needs the energy resolution of 6.5 % for 511 keV gamma-ray to discriminate between prompt gamma rays of 478 keV and annihilation gamma rays of 511 keV as background events. This report presents the characteristics about energy resolution of this detector system.

EXPERIMENTS: This detector system consists of an 8 x 8 arrayed $LaBr_3$(Ce) scintillator, an 8 x 8 arrayed MPPC, 64 channels amplifiers-shapers, and 64 channels analog digital convertors. The size of each scintillator was 5 mm x 5 mm x 10 mm and the light yield was 63 photons/keV. There were reflectors made from $BaSO_4$ between scintillator pixels. The effective active area of one channel of the MPPC was 6 mm x 6 mm, and the MPPC had 14400 pixels in total. The scintillator was placed in front of the MPPC. Energy calibration were performed using common isotopes (^{22}Na, ^{57}Co, ^{133}Ba, and ^{137}Cs). In order to confirm the characteristics of this system, particle and heavy ion transport code system (PHITS) was used.

RESULTS: Fig. 1 shows the relationship between ADC channels and gamma-ray energy. Theoretically, saturation ADC channel would be corresponding to around 230 keV. Furthermore, we calculated events that Compton scattering occurred in one pixel of the scintillator and entered other pixels. The events were 26.5 % of total events with PHITS. In the experiment data, the events those were deposited energy in two or three pixels were corresponding to the Compton scattering. The events were 26.9 % of total events in the experiment. The gamma-ray spectra with an ^{22}Na were broadened because summed signals from two or three pixels of the MPPC were large because of the distribution of deposit energy without the saturation. This came from Compton scattering. After the spectrum was calibrated, the energy resolution for 511 keV peak was 5.0 % as shown in Fig. 2.

CONCLUSION: The developed prompt gamma-ray imaging detector measured gamma-ray spectra; however, gamma-ray spectra obtained from raw data had broadened peaks. We corrected events caused by Compton scattering because the MPPC acquired higher ADC channels. As a result, after this detector system was calibrated, it had about 5.0 % energy resolution for 511 keV peak. This is sufficient to discriminate between 478 and 511 keV gamma rays.

Acknowledgements
This study was partially supported by JSPS KAKENHI Grant Number JP25282155 and 16H03193.

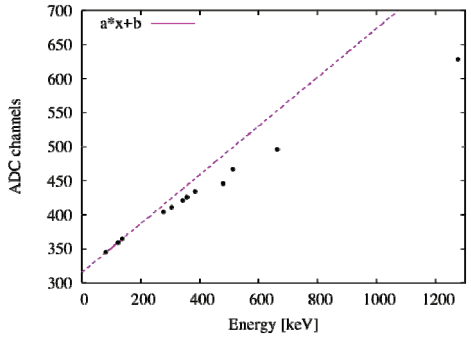

Fig. 1. Relationship between ADC channels and gamma ray energy.

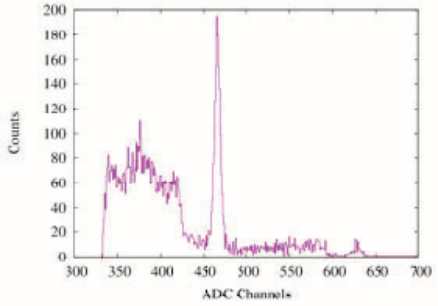

Fig. 2. Gamma-ray spectrum at the center of the MPPC after the correction of Compton scattering events.

REFERENCES :
[1]T. Kobayashi, Y. Sakurai, M. Ishikawa: Real-time absorbed dose estimation system for BNCT by PG-SPECT, Frontiers in Neutron Capture Therapy, pp 641-645.

R2P9-15

PR9-14 **Development of Fiber-reading Radiation Monitoring System with an Optical Fiber and Red-emitting Scintillator at the ^{60}Co Radiation Facility**

S. Kurosawa[1,2], H. Tanaka[3], S. Kodama[2,] Y. Kurashima, Akihiro Yamaji

[1]New Industry Creation Hatchery Center, Tohoku University
[2] Institute for Materials Research Tohoku University
[3] Institute for Integrated Radiation and Nuclear Science, Kyoto University

INTRODUCTION: Decommissioning reactors at the nuclear power plant with safety is a big issue in Japan, and a real-time dose-rate monitor in the extremely high radiation dose condition is required for the above application. We have developed this monitor consisting of a scintillator, optical fiber and CCD spectrometer, and last year we succeeded in demonstrating the monitor in the ^{60}Co radiation facility of the Institute for Integrated Radiation and Nuclear Science, Kyoto University, using Cs_2HfI_6 (CHI) scintillator with an emission band of around 700 nm [1].

CHI has other attractive points such as high light output (over 60,000 photons/MeV), high effective-atomic number (over 60) and no afterglow (less than 1% within 1s), while this material cannot be applied to alpha-ray detection due to the package for the hygroscopic nature[1,2]. Thus, we demonstrated the monitor using novel materials with red/infrared emission and without hygroscopic nature in the ^{60}Co radiation facility.

Since the size of the scintillation sample should be small as well as a few mm^3 due to the fiber diameter and space limitation in the power plant, so that a high effective atomic number is required. One of the candidate materials is Yb-doped $La_2Hf_2O_7$ (Yb:LHO), because this atomic number is 64. Moreover, Yb-doped samples are expected to show an infrared sharp peak around 970 nm originating from Yb^{3+} of 4f-4f transition. Although Yb:LHO has a high melting point of over 2400C, we grew this crystal by the Core-Heating (CH) method we have developed as a novel crystal-growth technique in 2020[3].

EXPERIMENTS: We fabricated a Yb:LHO sample grown by the CH method, and scintillation properties such as transmittance spectrum and emission spectrum excited by UV and X-ray photons.

The demonstration was performed at the ^{60}Co Gamma-ray Irradiation Facility with an activity of ~100 TBq, and the gamma-ray air dose rates at certain points on the experimental apparatus were estimated based on the absorbed gamma-ray doses for water measured by Sato et al.[4]. The monitor and set up at this time were the same as that in last year; an optical fiber (S.600/600B, Fujikura) had a length of 20 m and a pure SiO2core diameter of 600 ± 30μm using an optical grease. The scintillation light was transmitted through the fiber and measured with a CCD spectrometer (Blue-UVNb, StellarNet).

RESULTS: We succeeded in growing the transparent Yb:LHO sample for the first time by the CH method as shown in Fig. 1, even the high-melting point material, and its transmittance was ~50% at 870 nm. The sharp emission peak was observed at 974 nm excited by X-rays and UV photons, while CHI had broad emission peak at around 700nm. The noises were generated in the onptical fiber had mainly photons below 600 nm, and some noises have remained even at 700 nm, still.

Figure 2 shows the sicintillation intensities with the CCD at several dose-rate positions for Yb:LHO and Cr:α-Al_2O_3 as the reference sample. The intensity of Yb:LHO had lower intensity (1% of CHI) than those of Cr:α-Al_2O_3 (10% of CHI), and dose-rate dynamic range was narrow than the others. Nevertheless, Yb:LHO had a good Signal-to-Noise ratio (S/N) by 5 – 100 times than the others had, depending on noise condition (dose-rate condition for the optical fiber). This good S/N is due to small noise at ~970 nm and sharp peak, and the wavvelenth sensitive detector is effective to remove the noise. We succeeded in development of the novel material, Yb:LSO, with good S/N for the dose monitor.

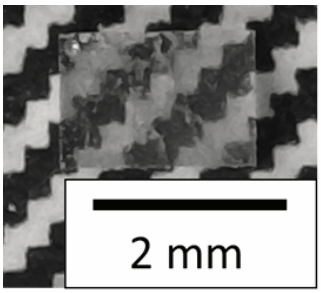

Fig. 1. Pphotograph of the Yb:LHO sample after cut and polishing.

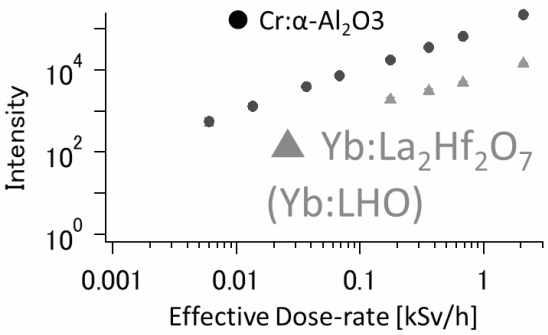

Fig. 2. The scintillation signal intensity of CHI cement and ruby cement specimens, respectively, as a function of effective dose rate.

REFERENCES:

[1]S Kodama et al., Appl. Phys. Express, **13** (2020) 047002.
[2]S. Kodama et al., Radiat. Meas., **124**, (2019) 54.
[3]N. Sato et al., (2008), [www.rri.kyoto-u.ac.jp/gamma/doseratesheet.pdf]
[4]Y. Kurashima *et al.*, Cryst. Growth Des., **21** (2021) 572–578.

R2P9-16

PR9-15 Establishment of the Imaging Technology of 478 keV Prompt Gamma-rays of Boron-neutron Capture Reaction and the Measurement of the Intensity of the Neutron Field

S. Komura, T. Mizumoto, Y. Sakurai[1], T. Takata[1], T. Tanimori[2] and A. Takada[2]

Fukushima SiC Applied Engineering Inc.
[1]Institute for Integrated Radiation and Nuclear Science, Kyoto University
[2]Graduate School of Science, Kyoto University

INTRODUCTION: Boron neutron capture therapy (BNCT) is one of the promising cancer treatment methods. However, a good method for real-time monitoring of therapeutic effects during BNCT is not yet available. The main reason is that it is difficult to accurately know the concentration of boron-containing drugs in tumor tissue and healthy tissue. If we can image the 478 keV prompt gamma rays emitted from the $^{10}B(n,\alpha)^{7}Li$ reaction occurring in the patient's body, we can confirm the concentration of these drugs in each site. Although detectors such as SPECT cameras and Compton cameras have been proposed to obtain images of the 478 keV prompt gamma rays, each of them has its own weaknesses and is not yet ready for practical use [1].

To overcome this situation, we have been developing an advanced Compton camera, the Electron Tracking Compton Camera (ETCC), which can uniquely determine the direction of arrival of sub-MeV/MeV gamma rays for each event by measuring information on the recoil direction of electrons. An ETCC is a complex detector with two sub-detectors: a time projection chamber TPC (Compton scatterer and recoil electron detector) and a scintillation camera (scattered gamma-ray absorber). In our previous studies, we demonstrated that our ETCC provides high contrast images of 478 keV prompt gamma rays emitted from a large water phantom with a ^{10}B concentration of 2000 ppm using E-3 Neutron Guide Tube (E-3) at Kyoto University Reactor (KUR) [2]. In the present study, two experiments were performed to confirm the performance of our ETCC under more realistic conditions.

EXPERIMENTS AND RESULTS:

Exp. 1: We performed prompt gamma-ray imaging studies using a boron-containing solution in a 4.5 mm diameter tube that simulates a small tumor tissue. The experimental setup is shown in Fig. 1. The tube was placed just above the ETCC and was irradiated with thermal neutrons at E-3 at the 1-MW operation. The ETCC measured the prompt gamma rays emitted from the solution during the irradiation time and reconstructed a back-projection image. As a result, high quality images with a spatial resolution of less than 1 cm were obtained. This experiment was conducted on four tubes with different ^{10}B concentrations (0, 500, 1000, 2000 ppm) to investigate the relationship between ^{10}B concentration and image brightness. These results are currently being analyzed.

Exp. 2: We also carried out performance tests in a BNCT environment, a strong gamma-ray environment where conventional Compton cameras are disturbed by random coincidence noise, using Heavy Water Neutron Irradiation Facility of KUR at the 1-MW operation. As shown in Fig. 2., a 10-cm cubic solution with a ^{10}B concentration of 230 ppm was placed in the irradiation room. The prompt gamma rays emitted from the solution and passing through the cylindrical hole in the ceiling entered the ETCC. The obtained image precisely shows the position of the solution even in the huge background radiation environment. This experiment was performed twice by changing the position of the solution.

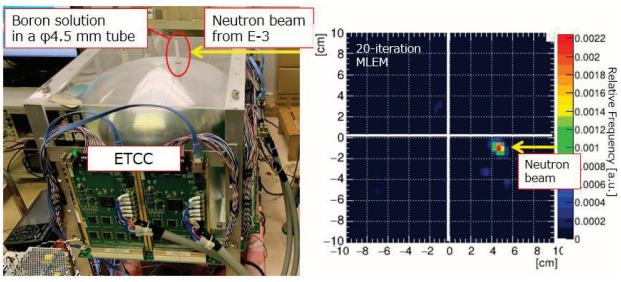

Fig. 1. Photograph and obtained image of 478 keV prompt gamma rays from ^{10}B 500 ppm tube

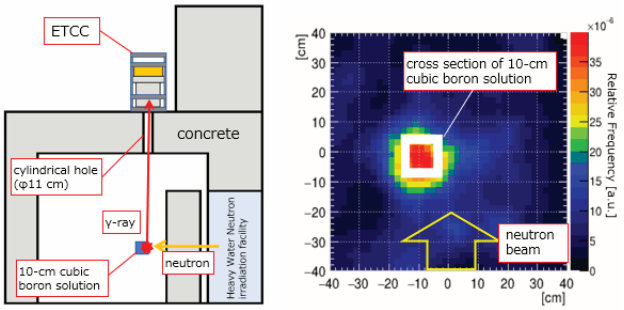

Fig. 2. Schematic view and obtained image of 478 keV prompt gamma rays from 10-cm cubic boron solution

REFERENCES:

[1] T. Mizumoto, KURNS Progress Report 2018 (2019).
[2] T. Mizumoto, KURNS Progress Report 2019 (2020).

PR9-16 Feasibility study for quality assurance and control for irradiation field in BNCT

S. Nakamura[1,2], M. Takemori[1,3], K. Iijima[1], S. Imamichi[4], H. Nakayama[1,3], T. Chiba[1,3], M. Masutani[5], Y. Sakurai[6], H. Tanaka[6], T. Takata[6], M. Suzuki[6], H. Igaki[7] and H. Okamoto[1,2]

[1]*Department of Medical Physics, National Cancer Center Hospital.*
[2]*Devisoin of Research & Development for Boron Neutron Capture Therapy, National Cancer Center Exploratory Oncology Research & Clinical Trial Center.*
[3]*Department of Radiological Science, Graduate School of Human Health Sciences, Tokyo Metropolitan University.*
[4]*Devision of Cellular Signaling, National Cancer Center Research Institute.*
[5]*Department of Molecular and Genomic Biomedicine, Graduate School of Biomedical Sciences, Nagasaki University.*
[6]*Institute for Integrated Radiation and Nuclear Science, Kyoto University*
[7]*Department of Radiation Oncology, National Cancer Center Hospital*

INTRODUCTION: In boron neutron capture therapy (BNCT), the neutron irradiation to the patient is performed after a sufficient accumulation of ^{10}B to tumor cells because the treatment efficacy is based on the ^{10}B(n,α)^{7}Li reaction. It is important for the radiation therapy that the delivered dose is verified as a quality assurance before the treatment. However, it is a difficult for the existing detector that the three dimensional dose distribution is measured in BNCT with considering a non-uniformity of ^{10}B on the actual patient. Thus, this study focuses on the gel-dosimeter for the three dimensional dosimetry in BNCT. There are some reasons. First, the gel-dosimeter can mix a few ^{10}B with keeping the dose response. Second, the gel-dosimeter is generally used for the three dimensional dosimeter. Third, the gel-dosimeter is not expensive, and the quality assurance using the gel-dosimeter may not affect the medical costs in BNCT. Therefore, this study aims to evaluate the dose response dependence of the gel-dosimeter which contains a certain boron-10 density in BNCT.

EXPERIMENTS: The experiment was performed in the Heavy Water Neutron Irradiation Facility (Kyoto University Reactor, KUR). The KUR was operated at a power of 1 MW. The neutrons were delivered to the gel-dosimeter which composed of water, PVA, KI, KCl, Gellan gum, Fructose, and boron solutions. The boron-10 density of the gel-dosimeter was 0, 25, 50, and 75 ppm. The irradiation time was set to 0, 5, 10, 20, 30 min in each gel-dosimeter. After the neutron irradiation, the dose response in each gel-dosimeter was read by an optical scanner. The dose response dependence in each gel-dosimeter was evaluated. In our previous experiment, the mixing time for the gel-dosimeter was 15 min, and the dose response in each gel-dosimeter then had variations. Thus, the mixing time for this experiment was set to 60 min.

RESULTS: Figure 1 (a) shows the dose response of the gel-dosimeter for each boron-10 density in this experiment. Additionally, Fig. 1 (b) shows it derived from our previous study. As shown in Fig. 1, in this experiment, the dose responses against the irradiation time was better than those in our previous study.

Discussion and Conclusion: This study investigated that the gel-dosimeter has a sufficient sensitivity for the reaction of ^{10}B(n,α)^{7}Li in BNCT although the boron-10 density expects very low (25 ppm, etc…). According to fig. 1, the dose response in the gel-dosimeter increased with the boron-10 density and the irradiation time, and it seems that the dose response can evaluate the actual dose delivered to the gel-dosimeter. Although linearity of the dose response was not better in our previous study, it is improved in this study. It relates to a creating method of the gel-dosimeter. In this experiment, the mixing time is longer than that in our previous study. Therefore, we are able to fix the creating method for the gel-dosimeter. We will try to measure three dimensional dose with using the gel-dosimeter in the future work.

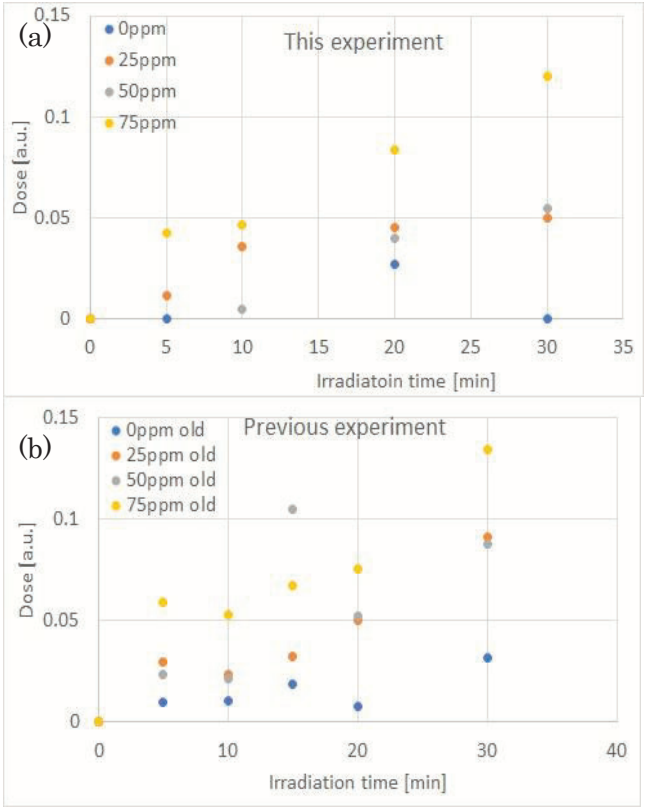

Fig. 1. Dose response dependence in the gel-dosimeter. (a): This experiment, (b): our previous study

PR9-17 Evaluation of thermal neutron irradiation field for semiconductor device irradiation

H. Tanaka[1], T. Takushi[1], N. Matsubayashi[1] , Y. Sakurai[1]

[1]*Institute for Integrated Radiation and Nuclear Science, Kyoto University*

INTRODUCTION: At the BNCT irradiation field, electronic devices with semiconductor such as neutron monitors, patient monitor cameras, and implantable pacemakers may be irradiated. If a semiconductor device contains a nuclide having a large capture cross-section with respect to thermal neutrons, charged particles are generated in the semiconductor device when irradiated with thermal neutrons. The charged particle generates an electron-hole pair in its trajectory, and this charge becomes a noise current in the semiconductor device. There is a concern that the semiconductor device may malfunction due to this electric current. In addition, semiconductor devices are becoming finer year by year, and the signal current is becoming smaller. That is, it tends to be more sensitive to noise. To date, there are few data on semiconductor damage to thermal neutrons. In this study, we evaluated the thermal neutron irradiation field necessary for investigating the effects of thermal neutrons on a semiconductor device.

EXPERIMENTS: The heavy water neutron irradiation facility (HWNIF) slows down the fast neutrons generated in the reactor core to thermal neutron energy with heavy water and aluminum. In order to evaluate the effect of thermal neutrons on semiconductor devices, an irradiation field that changes only the thermal neutron flux without changing the epithermal and fast neutrons is required. The HWNIF is equipped with a aperture changeable cadmium filter behind the heavy water moderator. It is possible to change the thermal neutron flux. Further, the semiconductor device is installed on the substrate, and in order to observe the semiconductor error in real time, it is necessary to install a measuring instrument on a large career. The thermal neutron flux on the bismuth surface using an irradiation rail have been reported [1], however the combination of a large career and a collimator has not been evaluated. Here, the thermal neutron flux at the outlet of the collimator in diameter of 300 mm x 300 mm was evaluated using the gold activation method.

RESULTS: Fig. 1 showed the result of the thermal neutron flux at the center of the collimator outlet when the aperture size of cadmium filter was changed. Fig.2 showed the cadmium ratio. The thermal neutron flux at the position of the bismuth surface without a collimator was reported as 1 x 10^9 (n/ cm^2/s) for a 600 mm cadmium filter opening. However, thermal neutron flux with collimator was about 60%. Since it was far from the bismuth surface and was collimated. In addition, the cadmium ratio tended to increase because hydrogen was contained in the material of the collimator.

CONCLUSION: In the HWNIF, the relationship between the aperture size of cadmium filter and the thermal neutron flux was derived in the irradiation field combining a large career and a collimator. In the future, we plan to irradiate semiconductor devices based on this information.

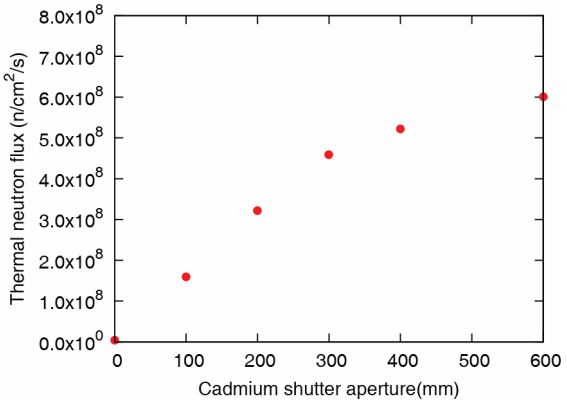

Fig. 1. Relationship between thermal neutron flux at reactor power of 1MW and the aperture size of cadmium filter.

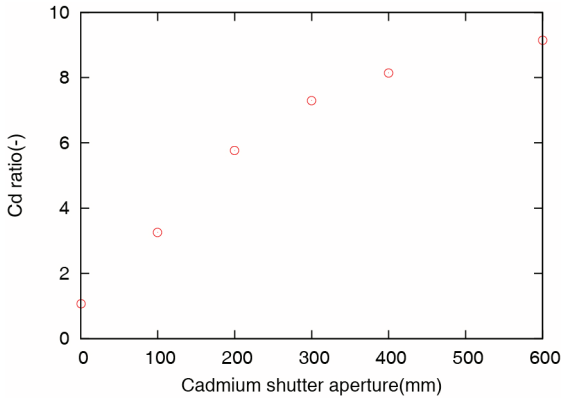

Fig. 2. Relationship between the cadmium ratio and the aperture size of cadmium filter.

REFERENCES :

[1] Yoshinori Sakurai, Tooru Kobayashi, Characteristics of the KUR heavy water neutron irradiation facility as a neutron irradiation field with variable energy spectra, Nucl. Instr. and Meth. A, 453 (2000), p. 569-596.

PR9-18 Optimization of Bolus Shape for Boron Neutron Capture Therapy — Examination Using Simple Shaped Phantom for Experimental Verification —

T. Takata, H. Tanaka, A. Sasaki[1], Y. Sakurai and M. Suzuki

Institute for Integrated Radiation and Nuclear Science, Kyoto University
[1]Graduate School of Engineering, Kyoto University

INTRODUCTION: In Boron Neutron Capture Therapy (BNCT), epithermal neutron beam has been utilized to treat a deep-seated tumor due to its high penetration ability based on thermalization within a patient body. However, thermal neutron buildup causes dose deficiency in a case where a tumor extends to a vicinity of patient surface. In such a case, a bolus consisting of a hydrogen-rich material has been utilized to improve the dose distribution. In present clinical BNCT, a bolus with a uniform thickness and a simple shape has been adopted. Aiming to increase a tumor dose more aggressively, the authors have studied an optimizing method of the bolus shape. A calculation of the bolus optimization using a simple shaped phantom was conducted prior to an experimental verification, and the result is described in this report.

MATERIALS AND METHODS: The optimization was performed according to the method previously reported by the authors [1]. A cylinder phantom assuming a head-and-neck case with a parotid gland cancer was used in this calculation. The detailed calculation procedure was as follows.

Phantom geometry modelling: A cylindrical water phantom with the height of 20 cm and diameter of 20 cm was modeled for the calculation (Fig. 1). A spherical volume with 4-cm diameter of which the center was located at 2-cm depth from the side surface of the cylinder, was defined as a planning target volume (PTV), assuming a parotid gland cancer extended to a subcutaneous region. In addition, a tubular volume with 3-cm diameter along the center axis of the cylinder was defined as an organ at risk (OAR), assuming a mucosal tissue of oral cavity and pharynx. These structures were prepared as a voxel model for the following transport simulation.

Neutron and photon transport calculation: The transport calculations were performed by using a Monte Carlo transport calculation module, SeraMC, implemented in SERA; the treatment planning system for BNCT [2]. An epithermal neutron beam of KUR heavy water neutron irradiation facility with an aperture of 12-cm diameter was assumed in the calculations [3]. The phantom was placed in contact with the aperture so that the beam entered the phantom from its side and passed through the center of the PTV. The results of the transport calculation were analyzed by using a dose evaluation module of SERA.

Bolus formation: A bolus forming area was limited within a surface area in a 5-cm distance from the beam incident point. Control points of bolus thickness were assigned to the representative voxels in the area by using a 1.5 × 1.5 × 1.5 cm^3 mesh-grid down sampling method for reduction of the calculation time. A bolus region was generated in the geometry by using an inverse-distance weighted interpolation of the thicknesses assigned to each of control points.

Optimization calculation: An objective function was defined as the ratio of the minimum PTV dose to the maximum OAR dose. The bolus thicknesses at the control points were adjusted to maximize the dose ratio by using a steepest gradient descent method.

RESULTS: The control points were assigned to 37 surface voxels by using the method described above. The iterative calculation was stared from bolus thicknesses of zero at all control points. The optimization result is shown in Fig.1 and Fig. 2. Increase and convergence in the dose ratio with increase in number of iterations were confirmed as Fig. 2. Figure 1 also shows the resulting bolus shape at the 3rd iteration, at which the objective function was almost converged. Growth of the bolus was observed around the area where the PTV reached just under the surface. We plan to create the bolus with the optimized shape by using 3D printer. Then, we will verify improvement of the dose distribution experimentally based on the calculation result.

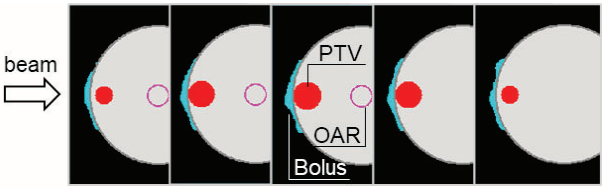

Fig. 1. Phantom geometry with the optimized bolus.

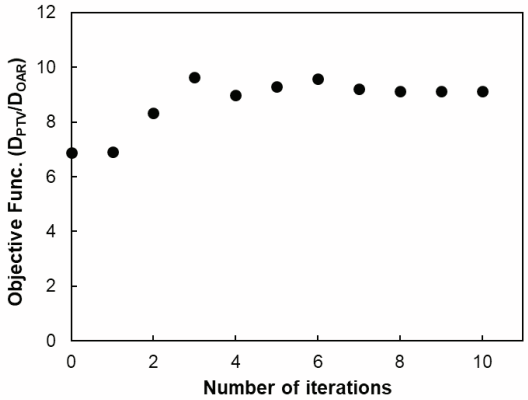

Fig. 2. Change in the objective function according to an iterative calculation.

REFERENCES:

[1] T. Takata *et al.*, KURNS Progress Report 2019 (2020), 56.
[2] D. E. Wessol *et al.*, INEEL/EXT-02-00698 (2002).
[3] Y. Sakurai, T. Kobayashi, Med. Phys. **29** (2002), 2328-2337.

PR9-19 Verification of the annealing capability of boric acid-infused PVA-GTA-I gel dosimeter

H. Yasuda[1], JE. Taño[1,2,3], CAB. Gonzales[1], Y. Sakurai[4]

[1]*Department of Radiation Biophysics, RIRBM, Hiroshima University*
[2] *Graduate School of Biomedical and Health Sciences, Hiroshima University*
[3] *Phoenix Leader Education Program for Renaissance from Radiation Disaster, Hiroshima University*
[4] *Institute for Integrated Radiation and Nuclear Science, Kyoto University (KURNS)*

INTRODUCTION: Previously, the authors investigated the feasibility of infusing boric acid to a radiochromic gel formula made of polyvinyl alcohol (PVA), glutaraldehyde (GTA), and iodide (I); also known as the PVA-GTA-I gel dosimeter. The results of the study demonstrated that boric acid can be infused to the PVA-GTA-I formula gel to increase the sensitivity of the gel to neutron irradiations. The standard PVA-GTA-I formula has been previously reported to be capable of reuse through annealing, where the irradiated gel samples were converted from red to clear after heating with absorbance values similar to fresh and unirradiated samples [1,2]. In the present study, we aim to verify if the same capability can be achieved with boric acid-infused PVA-GTA-I gels after long-term storage of post-irradiation with thermal neutron beams.

EXPERIMENTS: All gel samples were prepared using ultrapure water and analytical grade chemicals. The standard formula of the PVA-GTA-I formula was infused with different boric acid concentrations of 0, 25, and 50 mM. The liquid mixtures were poured into PMMA cuvettes and stored inside a vacuum chamber (-0.08 MPa) for 3-hours. The cuvette samples were then covered with PE lids and stored inside a sterilizing oven at 50°C for 12 hours to convert from liquid to gel.
The neutron irradiations of the samples were performed at the Heavy Water Neutron Irradiation Facility (HWNIF) of Kyoto University Reactor (KUR) with a 1MW nominal power. The samples were fixed on a rail system and irradiated at different periods: 20-, 40-, 80-, and 120-min. After irradiation, the samples were stored at room temperature and measured 55 days after irradiation. The optical absorbances were obtained using a UV-Vis spectrometer (Thermo Fisher Scientific Inc., USA).
After the initial reading, the gel samples were annealed in the oven at 50°C at time intervals of 24, 48, 72, and 96 hours. It should be noted that after each annealing time interval, the samples were stabilized at room temperature for 2 hours before measurement.

RESULTS: Figure 1 shows the dose-response of the gel samples of different boron concentrations. It can be observed that linear dose-response can be achieved with all gel formulations despite the different sensitivities and natural oxidation in the gel after longer storage time. The annealing results for each gel set in Fig. 2 shows that boric acid-infused PVA-GTA-I gels can be annealed even after 55 days post-irradiation, albeit longer annealing time for formulations with higher boric acid concentration.
These findings highlight the possible reuse of the boric acid-infused PVA-GTA-I gels, which is a desirable property for repeated dosimetry using thermal neutron beams.

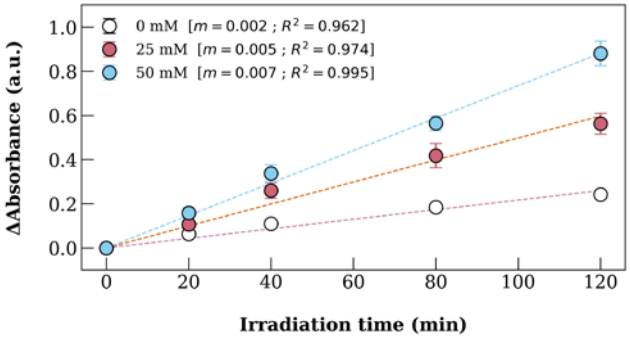

Fig. 1 Dose-response curves of PVA-GTA-I gel samples with various boric acid concentrations. All samples were measured 55 days after irradiation.

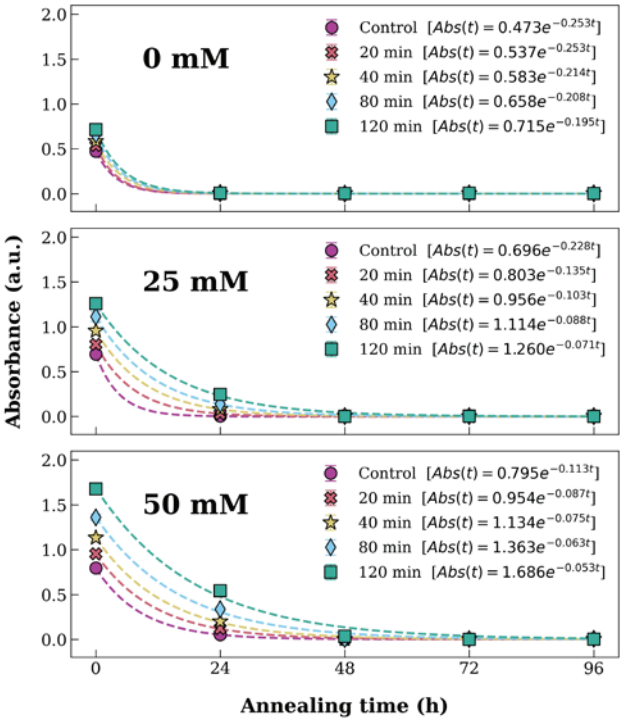

Fig. 2 Absorbance decay plots of the gel samples with different boric acid concentrations annealed at 50°C. All data sets were fitted with an exponential decay function: $A(t) = A_0 * \exp(-kt)$.

REFERENCES:

[1] Taño JE et al. 2019. *J Phys Conf Ser*. **1305** 012034.
[2] Taño JE et al. 2020. *Radiat Meas*. **134** 106311.

PR9-20 Establishment of Quantitative Measurement of Boron Concentration Distribution in vivo by Imaging of Prompt Gamma Rays

S. Komura, T. Mizumoto, T. Mitani, Y. Sakurai[1], N. Kondo[1], M. Suzuki[1], T. Takata[1], H. Kimura[2], T. Tanimori[3] and A. Takada[3]

Fukushima SiC Applied Engineering Inc.
[1]Institute for Integrated Radiation and Nuclear Science, Kyoto University
[2]Department of Analytical and Bioinorganic Chemistry, Kyoto Pharmaceutical University
[3]Graduate School of Science, Kyoto University

INTRODUCTION: Tomographic imaging of 478 keV prompt gamma rays emitted from the $^{10}B(n,\alpha)^{7}Li$ reaction is required to monitor the dose distribution in a patient during boron neutron capture therapy (BNCT). Several gamma-ray imaging systems using SPECT technique have succeeded in imaging large phantoms with a high concentration of ^{10}B [1,2]. However, since their detection efficiency is significantly reduced due to their very thick collimators, they have not been successful in imaging living tumor tissues which is typically small and with a low ^{10}B concentration less than 100 ppm when BPA is administered.
To overcome the current situation, we have been developing a new gamma-ray imaging system using the Electron Tracking Compton Cameras (ETCCs) which determine the arrival direction of gamma rays event by event using the electric collimation. In our previous studies, we demonstrated that our ETCC provides high contrast images of 478 keV prompt gamma rays emitted from a large water phantom with a ^{10}B concentration of 1000 ppm using E-3 Neutron Guide Tube (E-3) at Kyoto University Reactor (KUR) at the 1-MW operation [3].

EXPERIMENTS: We carried out prompt gamma-ray imaging studies using four U87MG tumor-bearing mice treated with BPA. Each mouse was anesthetized and administered 1000 mg/kg of BPA by tail vein injection, then fixed in a plastic case and irradiated with E-3 thermal neutron beam for 90 minutes at the 5-MW operation, one mouse at a time. The case was placed just above the ETCC. The ETCC measured the 478 keV prompt gamma rays emitted from the mouse during the irradiation time and reconstructed a back-projection image.

RESULTS: We were the first to successfully obtain 478 keV prompt gamma-ray images of BPA-treated tumor-bearing mice. For patent reasons, the details are not presented here.

REFERENCES:

[1] D. M. Minsky et al., Appl Radiat Isot., 69 (2011).
[2] T. Katabuchi et al., Appl Radiat Isot., 88 (2014).
[3] T. Mizumoto, KURNS Progress Report 2019 (2020).

I-2. COLLABORATION RESEARCHES

1. *Slow Neutron Physics and Neutron Scattering*
2. *Nuclear Physics and Nuclear Data*
3. *Reactor Physics and Reactor Engineering*
4. *Material Science and Radiation Effects*
5. *Geochemistry and Environmental Science*
6. *Life Science and Medical Science*
7. *Neutron Capture Therapy*
8. *Neutron Radiography and Radiation Application*
9. *TRU and Nuclear Chemistry*
10. *Health Physics and Waste Management*
12. *Others*

CO1-1 Towards larger-m polarizing neutron supermirror

M. Hino[1], T.Oda[1], H.Endo[2], K.Mori[1], F. Funama[3], Y. Kawabata[1]

[1]*Institute for Integrated Radiation and Nuclear Science, Kyoto University (KURNS), Japan*

[2] *IMSS, KEK, Japan*

[3]*Dept., Nucl. Eng., Kyoto University, Japan*

INTRODUCTION: Magnetic multilayer mirror consisting of ferromagnetic layers and nonmagnetic layers is useful to polarize neutron beam. As a polarizing neutron device, larger saturation magnetization of the ferromagnetic layers with lower applied magnetic field is very important. In this sense, pure iron (Fe) is good material. Fe-Co alloy, known as Permendur, is very good material and it had used for many neutron research establishments. Recently brightness of neutron beam has been really increased, and magnetic multilayer contained cobalt is not suitable due to the activation of the element for modern intense neutron facility. The radioactivation of Fe due to neutron irradiation is less serious than the other ferromagnetic materials. Silicon (Si), germanium (Ge) and these compounds are generally used for the nonmagnetic layers because the neutron scattering length density (SLD) of Fe for down spin neutrons. We also have already succeeded in fabricating m~5 Fe/SiGe polarizing neutron supermirrors with high reflectivity using an ion beam sputtering instrument (KUR-IBS) installed to the Institute for Integrated Radiation and Nuclear Science, Kyoto University (KURNS) [1,2]. These polarizing supermirrors have been used as polarizer and analyzer at neutron resonance spin echo spectrometer at BL06 in Materials and Life Science Experimental Facility (MLF), Japan Proton Accelerator Research Complex (J-PARC). The SiGe layer is obtained by simultaneous deposition of Si and Ge target. The composition ratio of Si and Ge is possible to be controlled by changing geometrical configuration of Si and Ge target. Recently detailed investigation of Fe/Si and Fe/Ge multilayer fabricated by ion beam sputtering was reported [3]. The fine-tuning of scattering length density of nonmagnetic material is still very important for high performance polarizing supermirror. With use of the KUR-IBS, SiGe layer tends to be slightly rough comparing with Si and SiC layers by using X-ray reflectometer. Carbon (C) is very good element because they have low incoherent and absorption cross section with less radioactivation. The composition ratio of Si and C is also possible to be controlled by changing geometrical configuration of silicon and carbon target.

EXPERIMENTS:

Figure 1 shows measured hysteresis loops for the Fe/SiC(Si) polarizing supermirror with typical two sample geometry, A and B. After the measurement of A, the sample was rotated by 90 degrees and the measurement of B was conducted. The sample size is about 8 mm in square and the magnetization measurement was conducted with vibrating sample magnetometer of the KURNS. It indicates that there is no in-plane anisotropy and applied magnetic field of 30 mT is possible to saturate magnetically the polarizing supermirror.

RESULTS: Figure 2 shows up and down spin neutron reflectivities by the Fe/SiC(Si) polarizing supermirror under an external field of 60 mT. The reflectivity with high-m area (m>3) was relatively high although the flipping ratio was not so high. The reflectivity of up spin neutrons was rapidly reduced around low-m area (1<m<3). This result supported that the SLD of SiC layer was not so equaled to that of Fe for down spin neutrons. In fact, the SLD of SiC layer was much larger than that of SiGe layer and that layer depended on geometrical configuration of silicon and carbon target. In other words, it indicates that the Fe/SiC(Si) polarizing supermirror is still of great potential for improvement. The accurate SLD of SiC layer with various sputtering condition and the improved performance of larger-m Fe/SiC(Si) polarizing supermirror will be reported in our future.

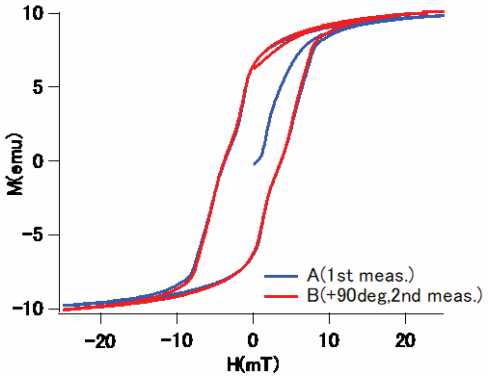

Fig. 1. Measured hysteresis loops of the Fe/SiC(Si) supermirror with two set angle.

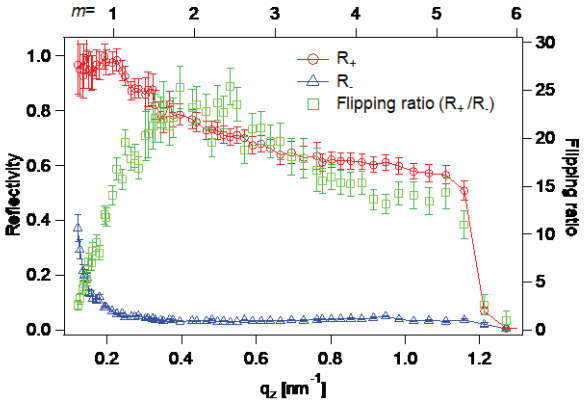

Fig. 2. Polarized neutron reflectivity profiles of the Fe/SiC(Si) polarizing supermirror for spin-up (○) and down (△) neutrons . Here m=qz/Qc, where Qc =0.217 nm^{-1}.

REFERENCES:

[1] M.Hino, *et al.*, Physica B 385&386, 1187(2006).
[2] M.Hino, *et al.*, Nucl. Instr. and Meth., **797**(2015) 265.
[3] R.Maruyama, *et al.*, Nucl. Instr. and Meth., **888,** (2018) 70.

CO1-2 Current Status of Versatile Compact Neutron Diffractometer (VCND) on the B–3 Beam Port of KUR, 2020

K. Mori, R. Okumura, H. Yoshino, H. Nakamura, S. Sato[1], K. Iwase[2], Y. Oba[3], Y. Kaneko[3]

Institute for Integrated Radiation and Nuclear Science, Kyoto University (KURNS)
[1]High Energy Accelerator Research Organization (KEK)
[2]Department of Materials and Engineering, Ibaraki University
[3]Materials Sciences Research Center, Japan Atomic Energy Agency (JAEA)

INTRODUCTION: Neutron diffraction is a powerful tool to precisely determine the positions of light elements (e.g., hydrogen and lithium) in solids. This is the main reason why neutron powder diffractometers are critical for structural investigations of energy storage materials, for example, rechargeable lithium-ion batteries and hydrogen-absorbing materials. The B–3 beam port of Kyoto University Research Reactor (KUR) had long been used as a four-circle single-crystal neutron diffractometer (4CND). For the last decade, however, the 4CND was so old that its research activity on neutron science was quite low. Now, the versatile compact neutron diffractometer (VCND) is installed on the B-3 beam port of KUR [1].

SPECIFICATIONS: Fig. 1 shows the current state of the VCND. The neutron wavelength, λ, which is monochromatized by the (220) plane of a Cu single crystal (i.e., Cu monochromator), is 1.0 Å. To cover the detector area of 6 ° $\leq 2\theta \leq$ 130 °, twenty-five ^{3}He tube detectors (1/2 inch in diameter) are used, where 2θ is the scattering angle. A detector bank including twenty-five ^{3}He tube detectors is placed on the arm of the HUBER-440 goniometer. The distance from the Cu monochromator to the sample is approximately 2 m, and the distance from the sample to the detector is 1.2 m.

CRYSTAL STRUCTURE ANALYSIS: The lanthanum-nickel intermetallic alloy ($LaNi_5$) is well known as a conventional hydrogen-absorbing material. Fig. 2 shows the Rietveld refinement using neutron diffraction data for $LaNi_5$ at room temperature, where $\Delta 2\theta = 0.1°$. In this figure, an excellent fit was obtained between the observed and calculated intensities; the atomic positions, La (0, 0, 0) in the 1*a* site, Ni1 (1/3, 2/3, 0) in the 2*c* site, and Ni2 (1/2, 0, 1/2) in the 3*g* site, were used to refine its crystal structure based on the space group *P*6/*mmm* (hexagonal system). Consequently, the lattice parameters, *a* and *c*, were estimated to be 5.04(7) and 4.01(4) Å, respectively.

REFERENCE

1. K. Mori, R. Okumura, H. Yoshino, M. Kanayama, S. Satoh, Y. Oba, K. Iwase, H. Hiraka, M. Hino, T. Sano, Y. Kawabata, T. Kamiyama, T. Otomo, T. Fukunaga, Commissioning of versatile compact neutron diffractometer (VCND) at the B-3 beam port of Kyoto University Research Reactor (KUR), *JPS Conference Proceedings*, 33 (2021) 011093.

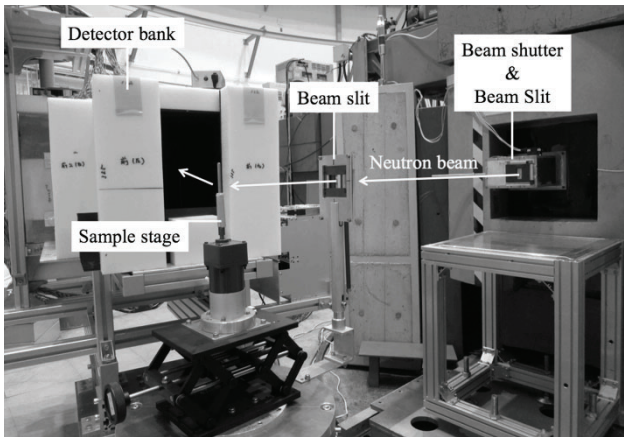

Fig. 1. Versatile compact neutron diffractometer (VCND) installed at the B-3 beam port of Kyoto University Research Reactor (KUR) [1].

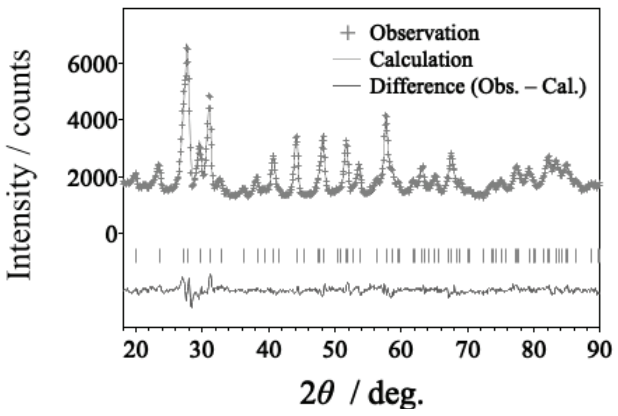

Fig. 2. The crystal structure refinement of $LaNi_5$ using neutron diffraction data collected at the VCND.

CO1-3 Radius of Gyration of Polymer for Viscosity Index Improver at Various Temperatures Evaluated by Small-Angle X-Ray and Neutron Scatterings

T. Hirayama, R. Takahashi[1], Y. Takashima[2], K. Tamura[2], N. Sato[3], M. Sugiyama[3], S.Takada[4]

Dept. of Mechanical Eng. and Science, Graduate School of Kyoto University
[1]Dept. of Mechanical Eng., Graduate School of Doshisha University
[2] Idemitsu Kosan Co., Ltd.
[3]Institute for Integrated Radiation and Nuclear Science, Kyoto University
[4]Japan Atomic Energy Agency

INTRODUCTION: Lubricating oils are necessary for friction reduction and high wear durability of sliding surfaces in machine components, and the development of the best oils is strongly required from industry. Viscosity index improver (VII) is a kind of additives for relieving the reduction of viscosity of lubricating oil due to temperature rise. Classical textbooks say that the VII molecules work with changing their equivalent radius in base oil in accordance with oil temperature. However, there are only few papers investigating the equivalent radius of VII molecules by small-angle X-ray scattering (SAXS) and/or small-angle neutron scattering (SANS)[1], and there is still room for discussion of the behavior and working mechanism of VII molecules in oil. This study tried to investigate the radius of gyration of comb-shaped VII polymers in base oil at various temperatures by SAXS and SANS, and the behavior of polymers was discussed.

EXPERIMENT: To investigate the radius of gyration of VII polymer, we used a SAXS instrument (NANOPIX, Rigaku) with a Cu-target X-ray source emitting X-ray with a wavelength of 1.54 Å, a characteristic line of Cu-Kα. The 1.2 mm-thick aluminum cell having optical windows made of 20-μm thermally-resistant engineering plastic film (Superio-UT, Mitsubishi chemical) was used for the measurement. The cell temperature increased to be 25, 40, 60, 80 and 100ºC in turn, and the last measurement was carried out at 25ºC again after cooling for checking if the VII molecule degenerated or not by heat. Poly(methyl acrylate) (PMA) type VII in comb-shape, as shown in Fig. 1, was prepared as a typical one used in engine oil in the study. Squalane was used as a model base oil, and the concentrations of PMA into squalane were 0.5, 1.0 and 2.0 mass%.

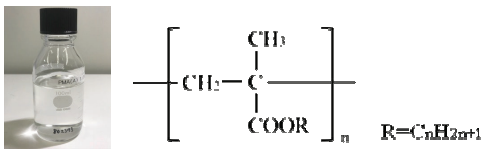

Fig. 1. Chemical structure of Comb-shaped PMA.

RESULTS AND DISCUSSION: The SAXS intensity profiles versus scattering vector q from squalane with 0.5 and 2.0 mass%-PMA type VII at each temperature were shown in Fig. 2, for example. The profiles were obtained by subtracting the intensity profiles from pure squalane at each temperature previously measured with the same liquid cell. We can see that the intensity profiles changed in accordance with the temperature rise. The trend of profile change was similar with the profile obtained by SANS, as shown in the right in Fig. 2. The radius of gyration of this polymer was not possible to be estimated from the profiles because of the profile change. From the whole measurement, we found on the behaviour of comb-shaped PMA in squalane that the shrunk polymers aggregate as 'multimer' in oil at low temperature, but they swell and separate to be 'unimer' in the random coil state at high temperature, resulting in contributing to the viscosity increase of oil, as shown in Fig. 3. Both of X-ray and neutron small-angle scatterings were effective for structural analysis of polymer in oil. Particularly, Kratky plot by SANS was the most powerful for the estimation of molecular structure of VII even in oil.

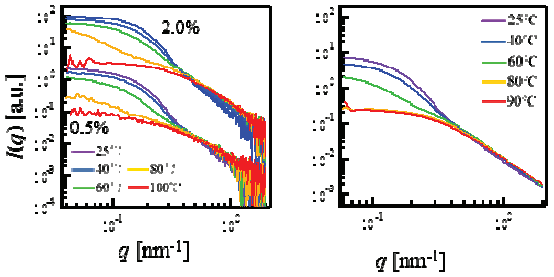

Fig. 2. SAXS profiles from squalane with 0.5 and 2.0 mass% Comb-shaped PMA at various temperatures. (Left: SAXS, right: SANS)

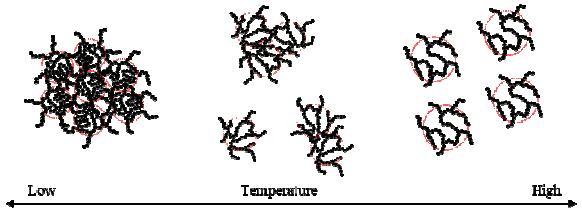

Fig. 3. Structure of comb-shaped PMA with temperature change.

REFERENCES:

[1] M. J. Covitch, K. J. Trickett, How Polymers Behave as Viscosity Index Improvers in Lubricating Oils, Adv. Chem. Eng. Sci., 5 (2015) 134.

CO1-4 Development of High-resolution cold/ultracold neutron detectors using nuclear emulsion

N. Naganawa, M. Hino[1], K. Hirota[2], H. Kawahara[2], M. Kimura[3,4], M. Kitaguchi[2,5], K. Mishima[6,7], A. Muneem[8], N. Muto[2], M. Nakagawa[8], T. R. Saito[8], A. Umemoto[2], and J. Yoshida[8]

Institute of Materials and Systems for Sustainability, Nagoya University,
[1]Institute for Integrated Radiation and Nuclear Science, Kyoto University
[2]Graduate School of Science, Nagoya University
[3]Nagoya Proton Therapy Center, Nagoya City University West Medical Center
[4]Graduate School of Medical Sciences, Nagoya City University
[5]Kobayashi-Maskawa Institute for Origin of Particles and the Universe (KMI), Nagoya University,
[6]High Energy Accelerator Research Organization (KEK)
[7]J-PARC Center
[8]High Energy Nuclear Physics Laboratory, Cluster for Pioneering Research, RIKEN

INTRODUCTION: Nuclear emulsion can be used as slow neutron detectors by combining it with thin layers including nuclide which convert neutrons to ionizing particles or adding such nuclide into emulsion layers. We conducted two experiments, Experiment 1 and 2, using the former and the latter type of detector, respectively. The former type whose spatial resolution was estimated to be finer than 100 nm was developed [1]. It can be a novel device for neutron imaging. In this detector, neutrons are detected by the emission of α particles or ^{7}Li nuclei from the neutron capture reaction, $^{10}B+n\rightarrow\alpha+^{7}Li$, by ^{10}B in the converter layer. One can observe their tracks as series of silver grains under an epi-illumination optical microscope. The lengths of these tracks are approximately 5 and 2 μm, respectively. In the Experiment 1, detectors were produced by sputtering $^{10}B_4C$ (200 nm)-NiC-C layers on Si substrate using ion beam sputtering system [2] at KURRI and applying the fine-grained nuclear emulsion [3] at Nagoya University. We produced several samples that recorded tracks at different densities of them to develop track recognition method that can be applied to various densities of tracks. The latter type of detector can be used for fundamental studies of radiation therapies. We are applying it to the study of the mechanism of proton boron capture therapy (PBCT). The therapy was proposed to improve the dose concentration of proton cancer therapy using $^{11}B(p,\alpha)2\alpha$ reaction. For the study, a fine-grained nuclear emulsion added of natural boron will be developed for the detection of α particles emitted from the reaction point. A uniformity of the distribution of the boron has to be checked. In order to check it, Experiment 2 was conducted. Sodium pentaborate was added to fine-grained nuclear emulsion to introduce boron in it. The emulsion was exposed to neutrons and tracks of α particles and ^{7}Li from reaction $^{10}B+n\rightarrow\alpha+^{7}Li$ were counted.

EXPERIMENT 1: Neutron irradiations were conducted at the CN3 beamline at KURRI. The detectors were individually packed in a light-tight film and placed directly downstream of the neutron guide tube. Irradiations of 1000 s, 10000 s, and 25000 s were conducted under 1 MW thermal power of the reactor. The detectors were developed and observed under the microscope.

RESULTS: 390±16 tracks per 100 μm^2 were observed in the sample for irradiation of 1000 s as shown in Fig.1. Assuming a neutron flux of 7.6×10^{5} /cm^2/sec at the window of the neutron guide tube [4], the neutron conversion efficiency was calculated to be approximately 0.5%. We have scanned these detectors with an optical microscope to obtain a dataset of sample images. Using these images, we are developing image processing for track recognition.

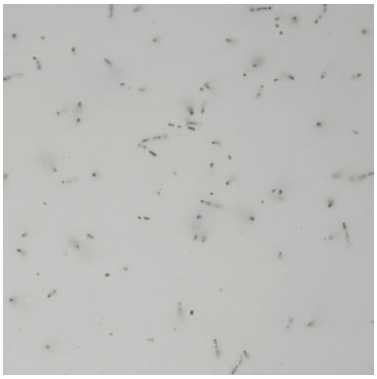

Fig. 1. One of the microscopic images of the detector that recorded tracks of α particle and ^{7}Li from neutron absorption by ^{10}B. The dimension of field of view was 50 ×50 μm^2. About 120 tracks were recorded in this area by 1000 seconds of neutron irradiation.

EXPERIMENT 2: The sample consists of fine-grained emulsion with $Na_2B_{10}O_{16}\cdot10H_2O$ added by a concentration of 1×10^{-1} mol/L. The film was then exposed to 20 meV neutrons at the CN3 beamline. The beam density was 5×10^{8} /cm^2. The exposed film was developed and observed under an epi-illumination optical microscope.

RESULTS: The frequency of the $^{10}B+n\rightarrow\alpha+^{7}Li$ reaction in the exposed emulsion was expected to be 4 per 100×100 μm^2 from the amount of sodium pentaborate and the reaction cross-section. The number of the candidate events was 3.1±0.6 per 100×100 μm^2, which was approximately consistent with the expected one. The reactions were distributed uniformly within statistical error along the depth in the emulsion layer. The results indicated that sodium pentaborate is uniformly distributed.

REFERENCES:

[1] N. Naganawa *et al.*, Eur. Phys. J. C. **78** (2018) 959.
[2] M. Hino *et al.*, Nucl. Instrum. Methods Phys. Res. A 797, 265–270 (2015).
[3] T. Asada *et al.*, Prog. Theor. Exp. Phys. 2017, 2017, 063H01.
[4] M. Hino *et al.*, Annu. Rep. Res. React. Inst. Kyoto Univ. **27** (1994) 196-204.

CO1-5 Optimization of neutron spin flipper with large beam acceptance

M. Kitaguchi, K. Morikawa[1], T. Hasegawa[1], T. Oda[2], and M. Hino[2]

KMI, Nagoya University
[1]*Graduate School of Science, Nagoya University*
[2]*Institute for Integrated Radiation and Nuclear Science, Kyoto University*

INTRODUCTION: The recent values of neutron lifetime deviate far beyond the systematic errors claimed in the past and require the further improvement for the neutron the lifetime puzzle. We are continuing neutron lifetime measurement at the polarized beam branch of the NOP beamline installed at the port BL05 in J-PARC. The system consists of a neutron chopper (SFC) and a gas chamber (TPC) for detecting the electrons from the neutron beta decays. The TPC contains small amount of 3He. The rate of the $^{3}He(n,p)^{3}H$ reaction is measured by counting the protons. The neutron lifetime is measured as the ratio of the electron events to the proton events [1].
The large background via neutron-induced reactions is suppressed by introducing small neutron bunches into the TPC and selectively detecting decay electrons and reaction protons only when neutron bunches are traveling inside the sensitive volume and they were not transmitting through chamber windows and other materials on the beam path. The SFC is a spin-selective optics to switch the neutron beam using the combination of magnetic supermirrors and spin flippers[2]. Polarized neutrons are injected into the SFC. Controlling the timing of spin-flip makes neutron bunches at the exit of the SFC, which can be reflected by the magnetic mirrors successively. By employing the triple series reflection, the present version of the SFC chops the neutron beam with the intensity contrast of about 400. During the lifetime measurement, the bunch length is adjusted as about 50 cm, which is half of the length of TPC sensitive region for maximizing the signal statistics. The cross section of the output bunches is 2 cm ×2 cm. In order to reduce the statistical uncertainties for the lifetime measurement to the order of 1 s, the incident neutron flux into the TPC must be increased. Although the new mirrors have been already assembled to accept large cross section of the neutron beam, large scale of spin flippers are also required. New mirrors and flippers with the beam acceptance of 3 cm ×3 cm can transfer neutrons with the intensity of 4 times larger than that before upgrade.

EXPERIMENTS AND RESULTS: We have tried to install the SFC with large mirrors and flippers into the NOP beamline (fig.1). The magnetic mirrors are kept in the strong magnetic field in order to be saturated. The field is leaking to the flipper position and has the influence on the flipping probability of neutron spin. We measured the distribution of the magnetic field around the flippers. We demonstrated that the probability can be improved by the proper correction of the field with the additional coils. We are now doing optimization of the shape of the flipper coils based on the simulations and experiments performed at CN3 in KUR.

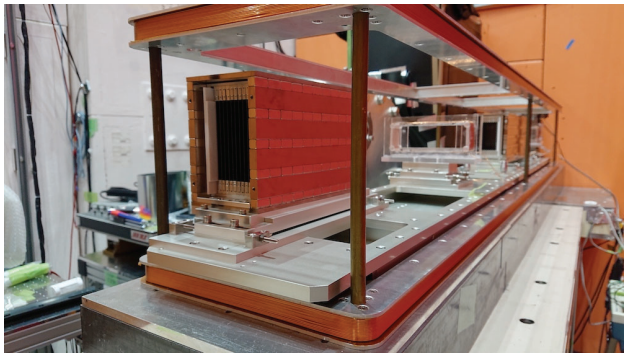

Figure 1: Spin Flip Chopper with large beam acceptance installed into NOP beamline in J-PARC.

REFERENCES:

[1] K Hirota, et al., Prog. Theor. Exp. Phys., 2020, 123C02 (2020).
[2] K. Taketani et al., Nucl. Instr. and Meth. A634 (2011) S134–S137.

CO1-6 Development of multiplayer mirrors for neutron interferometer

M. Kitaguchi, T. Fujiie[1], T. Oda[2], and M. Hino[2]

KMI, Nagoya University
[1]*Graduate School of Science, Nagoya University*
[2]*Institute for Integrated Radiation and Nuclear Science, Kyoto University*

INTRODUCTION: Neutron interferometry is a powerful technique for studying fundamental physics. Numerous interesting experiments [1] have been performed since the first successful test of a single-crystal neutron interferometer [2]. However, the single-crystal interferometer is inherently not able to deal with a neutron that has a wavelength longer than twice its lattice constant. In order to investigate problems of fundamental physics, including tests of quantum measurement theories and searches for non-Newtonian effects of gravitation, the interferometry of cold neutrons is extremely important, since the sensitivity of interferometer for small interaction increases with the neutron wavelength. A large scale of interferometer also has the advantage to increase the sensitivity to small interactions.

One of the solutions is an interferometer using neutron multilayer mirrors [3]. We succeeded in developing a multilayer interferometer for cold neutrons in which two paths are completely separated for the first time using wide-gap etalons [4]. We can easily control parameters such as Bragg angle, reflectivity, and Bragg peak width by selecting the deposited material and tuning the bilayer thickness and the number of layers.

We have started the development of multilayer interferometer at the beamline 05 NOP in MLF. In 2019, we demonstrated the interference fringes with etalons with monochromatic mirrors. Figure 1 shows the interference fringes with etalons according to time-of-flight. The phase of interferogram depends on the wavelength of neutrons. Because the mirrors have narrow bandwidth of the neutron reflectivity, the number of neutrons contributing to the interference is limited. When the neutron supermirrors whose lattice constants vary gradually are utilized in the interferometer, the effective range of neutron wavelength can be broadened to be applicable to a pulsed source. In addition, the wavelength dependence of the interactions can be measured simultaneously by using pulsed neutrons.

EXPERIMENTS AND RESULTS: We are trying to fabricate the neutron mirrors with wide band for the interferometer by using Ion Beam Sputtering facility in KURNS. The mirrors should have the wide and smooth top of the reflectivity with the range of momentum transfer from 0.4 nm^{-1} to 1.0 nm^{-1}. Especially, half mirrors with the wide range of neutron wavelength are needed for the interferometer. We tried to make the half mirrors and to measure the reflectivity at CN3 in KUR.

Figure 2 shows the reflectivity of the half mirror with 538 layers on the fused silica substrate. We are continuing the development of the mirrors for the neutron interferometer.

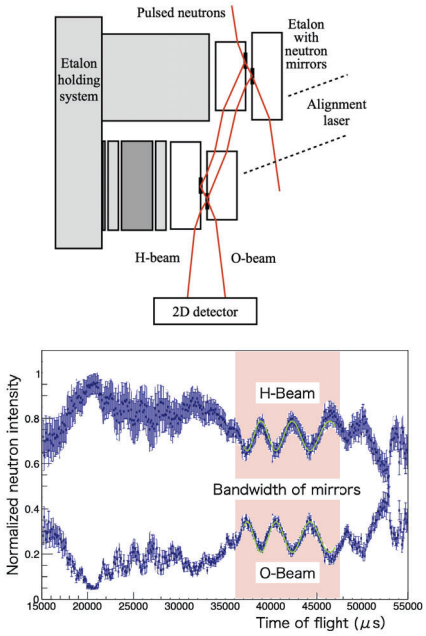

Figure 1: Interference fringes with multiplayer mirrors for pulsed neutrons.

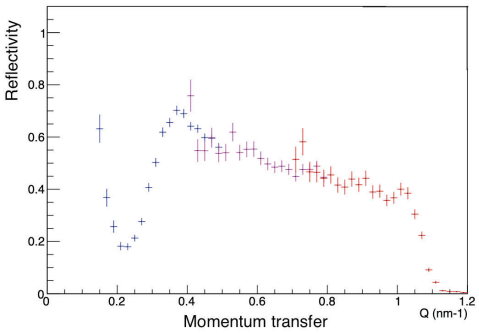

Figure 2: Reflectivity of the half mirror with wide band of neutron wavelength.

REFERENCES:

[1] H. Rauch and S. Werner, Neutron Interferometry Oxford University Press, Oxford, 2000;
J. Byrne, Neutron, Nuclei and Matter Institute of Physics Publishing, London, 1994, Chap. 7;
Mater Wave Interferometry, edited by G. Badurek, H. Rauch, and A. Zeilinger North-Holland, Amsterdam, 1988.
[2] H. Rauch, W. Treimer, and U. Bonse, Phys. Lett. 47A, 369 (1974).
[3] M. Kitaguchi, et.al., Phys. Rev. A 67, 033609 (2003).
[4] Y. Seki, et. al., J. Phys. Soc. Jpn. 79, 124201 (2010).

CO2-1 Quantitation of Gamma Ray Emission from Caputre Reaction of Uranium-238 (2)

Y. Nauchi, J. Hori[1], K. Terada[1], and T. Sano[2]

Nuclear Technology Research Laboratory, Central Research Institute of Electric Power Industry

[1]Kyoto University Institute for Integrated Radiation and Nuclear Science

[2]Atomic Energy Research Institute, Kindai University School of Science

INTRODUCTION: Neutron induced γ ray spectroscopy has been conducted at the LINAC neutron source facility of KURNS to develop a quantification method of fissile enrichment in nuclear material. For that, γ ray emission from ^{238}U(n,γ) reaction has been focused on [1]. In 2019, the first experiment was performed with neutrons induced by pulsed electron of 1 μs width [2]. In 2020, enhancement of the statistical accuracy was examined.

EXPERIMENTS: In the facility, accelerated electron is introduced on a tungsten target and the Bremsstrahlung ray is radiated. Photo-nuclear reaction is induced by the ray and then neutron is radiated. A metal uranium sample was irradiated by the neutron of white spectrum and ^{238}U(n,γ) γ ray was measured with a HP-Ge detector. To determine the incident neutron energy, the time of flight technique was applied with periodically emitted (50 Hz) pulsed electron. The neutron fluence is almost proportional to the pulse width. In this work, neutrons of energy less than 50eV was focused on so that the width does not matter for the accuracy of neutron energy determination. Instead, intense pulse introduces dead time in HP-Ge detector by so-called γ-flash. We adjusted the width up to 3 μs so that we counted γ-rays induced by neutrons of 36.6eV as shown in Fig. 1.

RESULTS: In Fig. 2, the γ ray spectra measured with the electron pulses of 1 and 3 μs are compared. The spectra for the thermal neutron are very similar each other and the counting statistics is enhanced by the pulse of 3 μs width. For the measurement of events induced by the thermal neutron, the electron pulse of 3 μs width is preferable.

On the other hand, for the events induced by the 6.67eV neutrons, the peak pulse height (energy) is shifted lower by ~40keV for the pulse of 3 μs width compared to those for the pulse of 1 μs width. One of the possible reasons of the shift might be undershoot of signal current from the HP-Ge detector short time after the γ flash. Thus, more detailed analyses are now being conducted to quantify the influence of the γ flash on the γ ray spectra induced by neutrons of energy from 5 to 50 eV.

Additionally, we also focused on the γ rays found in the time background region (see Fig, 1) where those emission is out of phase of the electron pulse. By comparison against the JENDL/FPY&FPD-2011[3], we have identified γ rays from fission products (FP) of which half-life is from 0.5 s to 10.4 min. We will quantify the radioactivity of those to validate isotopically FP yields and decay chains used for safety analyses of reactors.

REFERENCES:

[1] Y. Nauchi, et al. Proc. ICNC2019.

[2]Y. Nauchi, J. Hori, T.Sato, KURNS progress report 2019, CO2-2.

[3] J. Katakura, JAEA-Data/Code 2011-025.

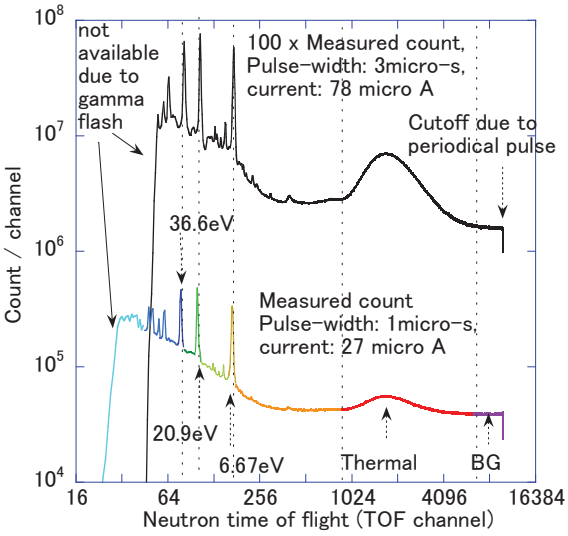

Fig. 1 Time of flight spectra of neutron which induces ^{238}U(n,γ) reaction determined by γ ray detection.

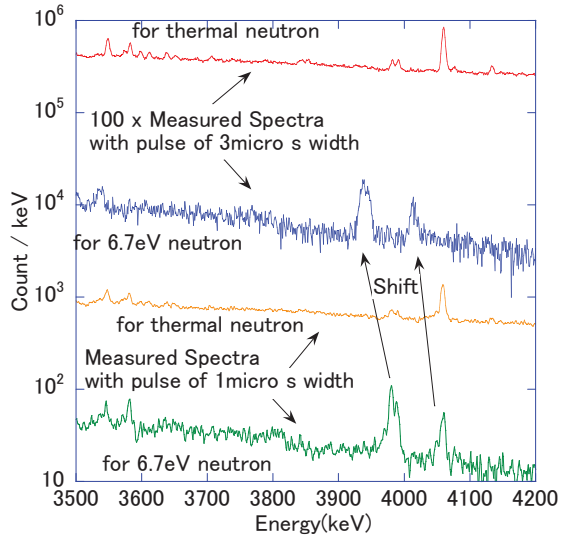

Fig.2 ^{238}U(n,γ) γ ray spectrum measured with pulsed neutrons of 3 μs and 1 μs width.

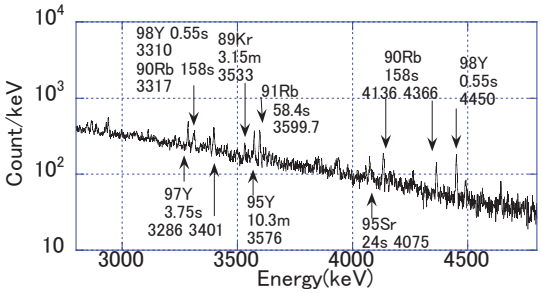

Fig. 3 Short lived fission products measured in time background region.

CO2-2

Thermal-Neutron Capture Cross-Section Measurement of ^{237}Np Using Graphite Thermal Column

S. Nakamura[1], S. Endo[1], A. Kimura[1], Y. Shibahara[2]

[1]*Japan Atomic Energy Agency*
[2]*Institute for Integrated Radiation and Nuclear Science, Kyoto University*

Introduction: Neptunium-237 has a long half-life of 2.14×10^6 years, therefore it causes long-term radiotoxicity in nuclear waste management. A method of converting radionuclides to stable and/or short-lived nuclides has been studied, that is "nuclear transmutation". In nuclear transmutation of ^{237}Np with neutrons, accurate neutron capture cross sections of ^{237}Np are required to obtain transmutation rates. **Figure 1** shows the present status of reported data for the thermal-neutron capture cross section (σ_0) of ^{237}Np. Contradicting data have been reported by many measurements for σ_0 from 1956 to 2020. Thus, the σ_0 of ^{237}Np was measured by a neutron activation method using graphite thermal column of the KUR.

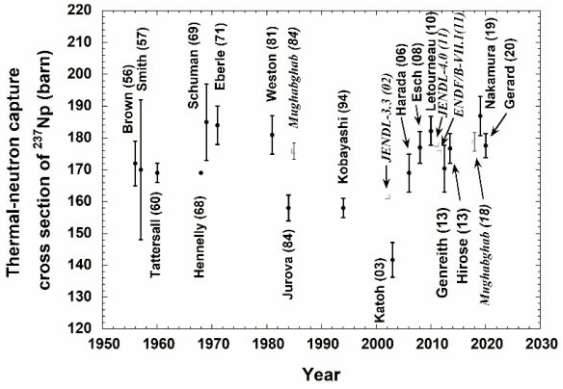

Fig.1 Reported data for σ_0 of ^{237}Np.

Experiments: Nitric acid solutions of ^{237}Np equivalent to 950 Bq were dropped onto a glass micro filter and dried with an infrared lamp. To monitor neutron flux components, a flux monitor set of Au/Al wire, Co, Sc, Mo and Ta foils was attached beside the Np sample. The samples were set on the upper edge of a polyethylene capsule. Neutron irradiation was performed using the graphite thermal column equipment (TC-Pn) outside the core of KUR. The structure of the core plane of the KUR is shown in **Figure 2.** In order to irradiate the capsule at the upper position, two dummy capsules were transferred to the TC-Pn in advance. After that, the capsule containing the samples was transferred and then irradiated for 30 minutes in 1-MW power operation. After irradiations, the samples were enclosed in a vinyl bag one by one, and then measurements were performed by the γ-ray spectroscopy.

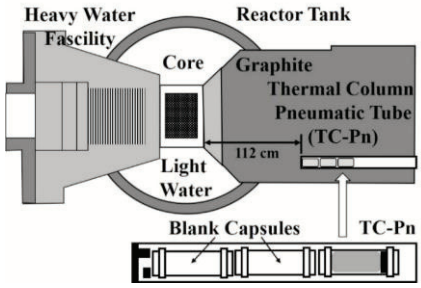

Fig.2 Partial plane structure of the reactor core.

Gamma rays emitted from the sample were measured with a high-purity Ge detector installed in the hot laboratory. A measurement distance was appropriately taken as 100 mm from the front surface of the Ge detector to the sample position. **Figure 3** shows an example of γ-ray spectrum obtained by measurement of the irradiated ^{237}Np sample. Decay γ-rays emitted from ^{238}Np were measured with a good signal-to-noise ratio.

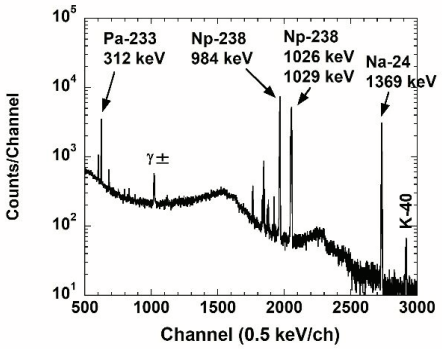

Fig.3 An example of γ-ray spectrum of the irradiated ^{237}Np sample

Analysis: The reaction rates of neutron flux monitors were obtained from their γ-ray yields. The thermal-neutron flux component was analyzed with these reaction rates on the basis of Westcott's convention. The neutron field at the irradiation position was found to be well-thermalized. The ^{237}Np sample was quantified using 312-keV γ rays emitted from ^{233}Pa in in radiative equilibrium with ^{237}Np. The reaction rate of ^{237}Np was obtained with the sample amount and γ-ray yields given by ^{238}Np. The thermal-neutron capture cross section σ_0 is derived straightforward by dividing the reaction rate of ^{237}Np by the thermal-neutron flux component. Currently, data analysis is in progress.

Acknowledgement: The authors would like to appreciate the staff of Kyoto University for their support: Dr. Yuichi Oki, Messrs Daisuke Maki, Ryo Okumura, Yuto Iinuma and Hisao Yoshinaga.

CO2-3 Measurement of Energy Resokution in the KURNS-LINAC Pulsed Neutron Facility

T. Sano, Y. Takahashi[1], K. Terada[1], H. Yashima[1], T. Uemura[2] and J. Hori[1]

Atomic Energy Research Institute, Kindai University
[1]Institute for Integrated Radiation and Nuclear Science, Kyoto University
[2]Department of Nuclear Engineering, Kyoto University

INTRODUCTION: The electron linear accelerator at the Research Reactor Institute, Kyoto University (KURRI-LINAC) had been originally established in 1965 by the High Voltage Engineering Co., USA and started as a 23 MeV machine. In 1971, the machine power had been increased to 46 MeV. The KURRI-linac has two different operation pulse modes. One is a long mode with a maximum repetition rate of 120 Hz, a pulse width of 0.1–4.0 μs and a peak current of about 0.5 A for the measurement at low energies below 10 eV. Another is a short mode with a maximum repetition rate of 300 Hz, a pulse width of 2–100 ns and a peak current of about 5 A for the measurement at high energies above 1 eV. It is worth noting that the peak current of short mode is ten times as large as that of long mode. In measurements of nuclear data, a water-cooled tantalum (Ta) target as a photo-neutron target and a light water moderator are used. There are two kinds of the moderator. One is a water tank type and another is an octagonal shape moderator called "pac-man type". In order to measure accurate nuclear data, it is very important to evaluate the energy resolution (ΔE/E) of a moderator. For example, the energy resolution for pac-man type moderator had been calculated about 0.7 % between energy range of 0.1eV from 10keV [1]. However, measurement and detail evaluation of energy resolutions for the tank type moderator has not carried out in KURRI-LINAC, although the energy resolution has been evaluated by using the simplified evaluation formula [2]. Furthermore, the relationship between energy resolution and beam pulse width is not discussed in Reference [1] and [2].

In this study, the energy resolutions of neutron flux from a tank type moderator were obtained using the TOF technic in two operational mode with different pulse width.

EXPERIMENTS: In this study, the energy resolution of KURNS-LINAC was obtained by transmitted neutron flux via ^{181}Ta sample. In order to measure the transmitted neutron flux, a cylindrical moderator tanks which have 19 cm diameter and 30cm height was installed at the target room. The tanks were filled with light water.

We used the neutron at "12 m room" which is located on 135 deg. axis from the electron beam line. The flight path of neutron flux between the ^{181}Ta sample which has 0.5 mm thickness and the moderator was 12.6 m as shown in Fig.1. In order to obtain the relationship between neutron beam pulse width and energy resolution, the KURNS-LINAC was operated under two different conditions as shown in Table 1. The beam frequency was adjusted to 50 Hz and the pulse width was 1 μsec or 4 μsec (nominally). The beam current was stabilized to about 27 μA and 104 μA. The transmitted neutron flux was measured by TOF technic with Li-glrass scintillation detector.

Table 1 KURNS-LINAC operational condition.

	Frequency (Hz)	Beam pulse width (μsec)	Beam current
Case A	50	1.0	26.68
Case B	50	4.0	103.85

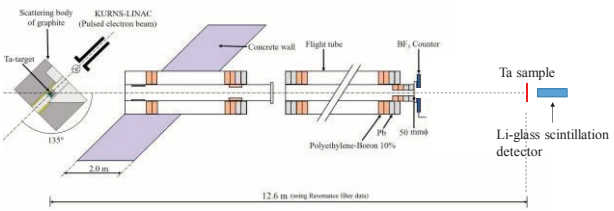

Fig.1 Experimental geometry

RESULTS: Figure 2 shows the TOF spectra of transmitted neutrons with the two pulse widths. From the figure, it was obtained that the dips width of the transmitted neutron flux by the resonance were different between the 4 μ sec and 1 μ sec width. Table 2 shows the FHWMs of the neutron flux dips. The FHWM at the high-energy resonance is larger than that of the low-energy resonance.

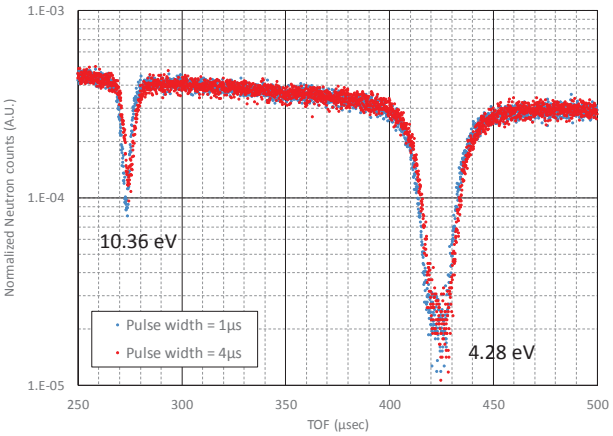

Fig.2 Comparison of TOF spectrum between different beam pulse width.

Table FHWM of neutron flux dip

	1 μ sec	4 μ sec
10.36 eV	5.8 nsec	6.7 nsec
4.28 eV	25.3 nsec	25.5 nsec

REFERENCES:

[1] T. Sano, et al., EPJ web of conference, Vol.146, 03031(2017).
[2] O. Shcherbakov, et al., Nucl. Instrum. Methods Phys. Res. A 517, p269 (2004).

CO2-4 β–Decay Study of Fission Products around A=150 Using the On–Line Mass Separator KUR–ISOL

Y. Irie ,Y. Ishikawa, M. Kanaji , T. Yamaguchi,
T. Miyazawa[1], M. Shibata[2] and A.Taniguchi[3]

Graduate School of Engineering, Nagoya University
[1]School of Engineering, Nagoya University
[2]Radioisotope Research Center, Nagoya University
[3] Institute for Integrated Radiation and Nuclear Science, Kyoto University

INTRODUCTION: Short–lived neutron–rich nuclei of mass numbers around 150 have low fission yields of ^{235}U, so there are few decay information. In order to clarify the decay properties, it is useful to perform highly efficient measurements with large volume Ge detectors. So far, we had measured the γ–rays of the fission products with a clover type Ge detector installed at the on–line mass separator (KUR–ISOL). It has four large Ge crystals with a diameter of 80 mm and a length of 90 mm arranged in the shape of a four–leaf clover around a through hole with a diameter of 15 mm. In the present study, we aimed to measure the ^{153,154}Pr, which locate almost limit region available with the KUR–ISOL. In using the clover detector, the background γ–rays in the reactor room need to be reduced for precise measurements of γ–rays of the nuclei of interest, especially ^{154}Pr. Then, β–ray detectors were developed for β–γ coincidence measurement with the clover detector. The performance of the β–ray detectors were tested by measuring well evaluated some fission products of their decay schemes, and the detectors were adopted for the measurement of ^{154}Pr. In this report, the preliminarily results of ^{153}Pr as well as ^{154}Pr were described.

EXPERIMENTS: The experiment was carried out with the KUR–ISOL. A 72 mg of 93% enriched $^{235}UF_4$ was irradiated with thermal neutrons flux of 3×10^{12} n/cm^2/s under 5 MW operation. The fission products were transported to a surface-ionizing type ion sources by an He-N_2 gas jet. The ionized fission products were transported to the magnetic sector–type mass spectrometer to obtain the nuclei of interests. The radioactive beams were implanted in a thin aluminized Mylar tape, and were periodically transported to the center of the through hole of the clover detector by a computer–controlled tape transport system. For ^{154}Pr, two identical β–ray detectors made of plastic scintillator were installed in the through hole of the clover detector. Those were semi-cylindrical shape of 6 mm thick and 9 cm long. The MPPC (Multi-Pixel Photon Counter) module C13367 of 3×3 mm^2 made by Hamamatsu Photonics were set at the top ends of the scintillators. The β–γ coincidence measurements between β–detectors and the clover detector were carried out. The period of collection–measurement cycle was set at two times of each half–life of the nuclide to be measured, approximately. The whole detectors were shielded with 10 cm thick lead bricks and 10 cm thick polyethylene bricks which contain boron. The data was recorded in the APV8008 and APV8016 DAQ systems made by Techno AP with event by event mode including time information. Measurements of ^{153}Pr ($T_{1/2}$ = 4.3 s) and ^{154}Pr ($T_{1/2}$ = 2.3 s) were performed for 13.5 and 15.5 hours, respectively. The APG-1500 amplifiers (Techno AP) was adopted to match the signals from the MPPC module to the DAQ systems.

RESULTS: The decay schemes were proposed based on the X–γ and γ–γ coincidence relations and the γ–ray singles and add-back spectra. For ^{153}Pr, the proposed decay scheme has excited levels up to 3436 keV and includes observed 72 γ–rays and 25 excited levels. These results are more detailed than the previous result [1]. For ^{154}Pr, the part of the measured β–γ coincidence spectrum is shown in Fig.1. The statistics of the γ–rays are more than one order of magnitude of those of the previous ones [2]. As shown by the arrow in the inset, the γ–ray of 1294 keV by the ^{40}Ar(n,γ)^{41}Ar reaction was clearly reduced in the β–γ coincidence spectrum. The efficiency of the developed β–ray detector was evaluated to be 20% for each for the energy of β–ray at 2 MeV from the calibration measurements of ^{94}Rb, ^{94,95}Sr, ^{94}Y, and ^{146}La. The decay scheme up to 2940 keV including the newly observed 43 γ–rays and 18 excited levels was proposed compared to the previous work [2]. Detailed analysis is in progress.

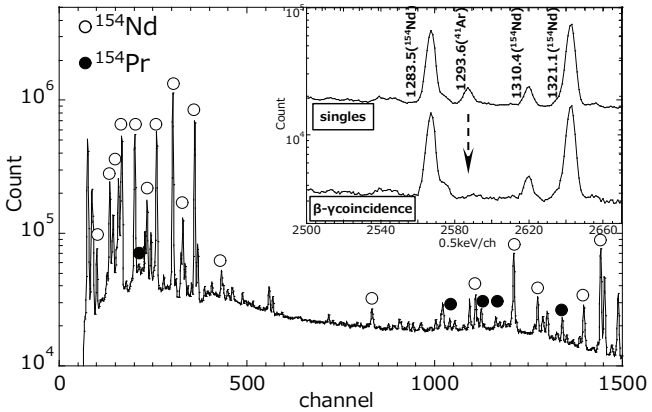

Fig.1 A portion of β–γ coincidence spectrum. The open and closed circle indicate the γ–ray of ^{154}Nd and ^{154}Pr, respectively. The inset shows the comparison of singles spectrum and β–γ coincidence one.

REFERENCES:

[1] A. Taniguchi *et al*., KURRI Prog. Rep. (1995).
[2] Y. Toh *et al*., Z. Phys. A 355,345-346(1996).

CO2-5 Measurements of thermal neutron total and scattering cross section of moderator materials

Jun Nishiyama[1], Kazushi Terada[2], Tadafumi Sano[3] and Jun-ichi Hori[2]

[1]*Laboratory for Advanced Nuclear Energy, Institute of Innovative Research, Tokyo Institute of Technology*
[2]*Institute for Integrated Radiation and Nuclear Science, Kyoto University*
[3]*Atomic Energy Research Institute, Kindai University*

INTRODUCTION: The high temperature gas-cooled reactor is a Generation IV reactor concept that use a graphite moderator. The design takes advantage of the inherent safety characteristics with specific design optimizations. The treatment of thermal scattering caused by crystalline is important for graphite to improve the prediction accuracy of graphite moderated core analysis. There is sufficient thermal scattering law for single crystal graphite, but there is no method has been established to reconstruct thermal scattering cross section for polycrystalline graphite. On the other hand, a new concept of small modular reactor using CaH_2 as solid moderator has been developed [1]. The experimental and evaluated data of the thermal scattering law for CaH_2 are insufficient. In order to provide basic data for thermal neutron scattering law evaluation, the total and scattering cross sections of moderator materials were measured.

EXPERIMENTS: The total and scattering cross sections of moderator materials were measured in the incident neutron energy region from 0.001 to 10 eV by transmission and scattering experiments at the KURNS-LINAC. An experimental arrangement is shown in Fig. 1. Pulsed neutrons were produced from a water-cooled Ta-target by (γ,n) reaction with a pulsed electron beam. The incident neutron spectrum on a sample, the transmitted and scattering neutron spectrum were measured by means of a time-of-flight (TOF) method with a ^{6}Li-glass scintillation detector. A 5.0 mm diameter by 5.0 mm thick ^{6}Li-glass was located 12.0 m from the neutron source. The scattering neutrons were measured by a 50 mm diameter by 5.0 mm thick ^{6}Li-glass scintillation detector. The scattering neutron spectra were observed at angle of 30 degrees and 45 degrees with respect to the neutron beam direction.

The characteristics of the samples are shown in Table 1. The graphite and polyethylene sample are used as a moderator in the KUCA facility.

RESULTS: The total cross sections of moderator materials were derived in the incident neutron energy region from 0.001 to 10 eV. Figure 2 shows the scattering neutron specta for CaH_2 sample. The room scattering neutron background could be properly evaluated by using the measurement without sample. Figure 3 shows the scattering neutron spectrum with the resonance filter (Cd, In, Ag, Mn). It was shown that it is possible to measure quasi-monochromatic neutrons from a white neutron source.

ACKNOWLEDGEMENTS: This research is a collaborative effort of Toshiba Energy Systems & Solutions, Kindai University, Kyoto University and Tokyo Institute of Technology.

REFERENCES:

[1] R. Kimura and S. Wada, Nucl. Sci. Eng., Vol.193, p.1013-1022, (2019).

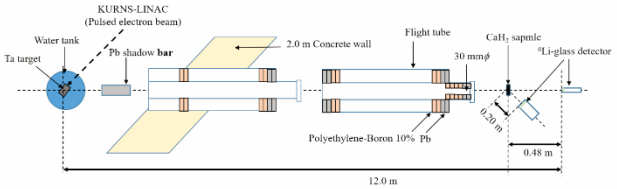

Fig 1. Experimental arrangement

Table 1 characteristics of samples

Sample	Polyethylene	Graphite	CaH_2
Structure	High molecular	Polycrystalline	Powder
Sample shape	Square plate	Square plate	Disk in Al case
Density [g/cm^3]	0.949	1.754	1.200
Size [mm]	50.8×50.8	50.8×50.8	ϕ50
Thickness [mm]	3.18	12.7	5.0
[atoms/b]	1.26×10^{-2}	1.12×10^{-1}	8.63×10^{-3}

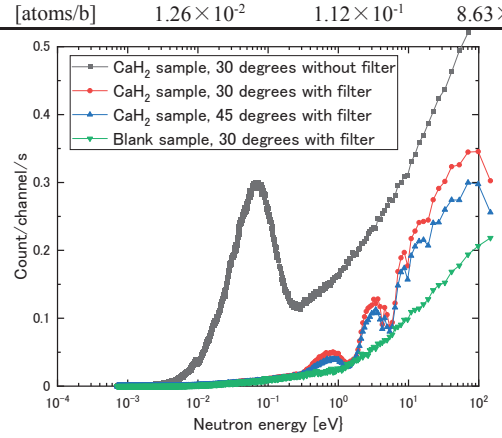

Fig. 2 Scattering neutron energy spectra

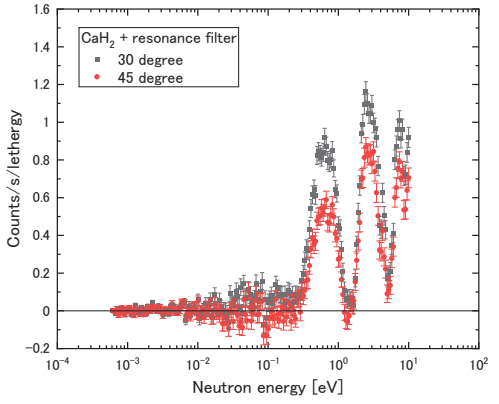

Fig. 3 Scattering neutron energy spectrum with resonance filter (Cd, In, Ag, Mn)

CO2-6 Development of a neutron sintillator for a compact NRTA system

F. Ito[1], J. Lee[1], K. Hironaka[1], T. Takahashi[1], S. Suzuki[1], J. Hori[2], K. Terada[2] and M. Koizumi[1]

[1]Integrated Support Center for Nuclear Nonproliferation and Nuclear Security, Japan Atomic Energy Agency
[2]Institute for Integrated Radiation and Nuclear Science, Kyoto University

INTRODUCTION: The Japan Atomic Energy Agency (JAEA) is developing a compact Neutron Resonance Transmission Analysis (NRTA) [1] system for nuclear material (NM) accountancy applications. NRTA is a neutron TOF technique [2] that utilizes a pulsed neutron source. To realize a compact NRTA system for high accuracy measurements, generation of a short-pulse neutron beam is required [1]. A newly arising laser-driven neutron source (LDNS) is considered potentially to be useful for short-pulse neutron beam generation without using a conventional accelerator. We, therefore, started a feasibility study of a NRTA system with an LDNS [3,4].

Amongst the study, requirements on neutron detector development arose: i.e., neutron detector with high efficiency, applicability to high counting rate, and insensitivity to gamma rays. It should be noted that the 2.2-MeV gamma ray induced by n(^{1}H, γ)^{2}H neutron capture reaction in a moderator is an origin of background in an NRTA measurement. Although the gamma-ray background dies away as time goes by, it will interfere measurement of epithermal neutron transmission with a compact system. Therefore, we started development of a gamma-ray insensitive multi-layer ^{6}Li glass scintillation (MLS) detector [4].

EXPERIMENT AND RESULT: Performance tests of a MLS detector (50×50×5 mm in MLS size) and a 1-cm ^{6}Li-glass scintillation detector (100×100×10 mm) were performed at the 12-m TOF measurement room of the KURNS-LINAC. Pulsed electron beams of about 30 MeV were used for neutron generation with a repetition rate of 50 Hz. The pulse width and the average current were 2 μsec and about 65 μA for the experiments of the MLS detector. Those were reduced to be 0.5 μsec and about 15 μA for the experiments of the 1-cm ^{6}Li-glass detector to prevent detector saturation. The output signals from the detectors were recorded using a 1-GS/s flash waveform digitizer (CAEN V1751). 800-μsec-long waveforms starting with each electron shot were stored in the memory of the digitizer and transferred to a computer. Dynamically moving baseline of measured waveforms were removed off line. Neutron induced signals were counted disregarding noise signals from their pulse shapes.

A reference material filter consisting of In, Ag, Co and Mn (referred to as notch-filters) were placed in the neutron beam path. These materials were thick enough to prevent neutrons with the neutron energy of large resonances (i.e., In-115 (1.46 eV), Ag-109 (5.19 eV), Co-59 (132 eV) and Mn-55 (336 eV)) arriving the detectors. TOF spectra measured by the two detectors are shown in Fig. 1. The ordinate was roughly adjusted making so as the integrations of the 5.19-eV Ag resonance dips are the same. Time dependent backgrounds were evaluated by connecting the bottom of the dips using the following function [5]:

$$B(t) = b_1 e^{-\lambda_1 t} + b_2 e^{-\lambda_2 t}.$$

The first term explains the 2.2-keV gamma-ray background from a moderator, and the second term the background neutron scattering around the detector. The time constant λ_1 is shorter than λ_2. Time dependent total backgrounds, *B(t)*, and gamma-ray backgrounds, $b_1 e^{-\lambda_1 t}$, are also plotted in Fig. 1 (a). Gamma-ray backgrounds are found to be dominant in the early time frame of the TOF spectra. The gamma-ray background of the MLS detector is about half of that of the 1-cm ^{6}Li-glass detector at the Co-59 and Mn-55 resonance region, while the shape of neutron resonance spectra does not change much, as seen in Fig. 1 (b). This describes that an MLS type scintillator can reduce the sensitivity of 2.2-MeV gamma rays without changing much the neutron counting efficiency.

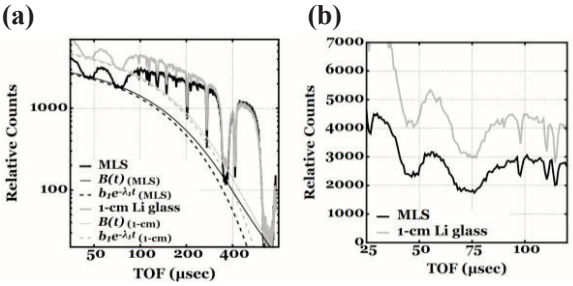

Fig. 1 (a) TOF-spectra taken with the MLS and the 1-cm ^{6}Li-glass neutron detector. (b) Expanded spectra with a linear ordinate scale.

ACKNOWLEDGEMENTS:
The research programs are supported by MEXT (the Ministry of Education, Culture, Sports, Science, and Technology of the Japanese government) under the subsidiary for "promotion of strengthening nuclear security and the like".

REFERENCES:

[1] H. Tsuchiya *et al.*, Plasma Fusion Res., 13, 2406004 (2018).
[2] P. Schillebeeckx *et al.*, Nuclear Data Sheets, 113, p3054-3100 (2012).
[3] J. Lee *et al.*, Proc. on INMMJ, Online, Nov 19-20, p102-104 (2020). Japanese.
[4] F. Ito *et al.*, Proc. on INMMJ, Online, Nov 19-20, p105-107 (2020). Japanese.
[5] P. Schillebeeckx *et al.*, JRC Science and Policy Reports. EUR 26848EN, (2014).

CO2-7 Feasibility study on a current-mode ^{3}He gas neutron detectors for thermal and epi-thermal neutron measurements

T. Matsumoto, A. Masuda, H. Harano, J. Hori[1], K. Terada[1]

National Metrology Institute of Japan, National Institute of Advanced Industrial Science and Technology
[1] KURNS

INTRODUCTION: In the present study, we have developed a current-mode neutron detector [1] that can be used in intense neutron flux fields such as boron neutron capture therapy (BNCT) fields. It is necessary to measure the neutron flux for a large dynamic range because of con-nection between a BNCT field in a hospital and the neutron calibration field in the National Institute of Advanced In-dustrial Science. The difference of neutron fluxes be-tween the BNCT field and the calibration field is more than 5 orders of magnitude. We have tried to extract neutron signals using a current mode ^{3}He gas detector (propor-tional counter and ionization chamber). The current mode gas detector is expected to be high radiation re-sistance in comparison with a photo-multiplier tube in the scintillation detector.

EXPERIMENTS: A collimated neutron beam with 30 mm diameter was obtained by the photo neutron reaction using a tantalum target with a water moderator at the KURRI Linac [2]. Figure 1 shows the experimental setup. In the experiments, we used a ^{3}He proportional counter (Reuter Stokes RS-P4-0806-278). The ^{3}He proportional counter was set at 12 m away from the target. A BF_3 pro-portional counter was used as a neutron monitor. All data were normalized using counts obtained with the BF_3 pro-portional counter. Possibility of a current-mode ^{3}He gas detector was experimentally evaluated by means of the time-of-flight (TOF) method. The measurements were performed for both pulse and current modes. In the pulse mode, signals from the ^{3}He proportional counter were ob-tained using a pre-amplifier (ORTEC 142PC) and main amplifier (ORTEC 570). In the current mode, the signals were obtained using a current integrator (ORTEC 439). Finally, TOF data were extracted using a multi-stop time to digital converter.

RESULTS: Figure 2 shows results of TOF spectra of pulse and current modes for the ^{3}He proportional counter. In the current mode, thermal bump is successfully observed in the TOF spectrum.

The ^{3}He proportional counter has high neutron sensitivity because of high gas pressure. The count rate was 6309 cps in the pulse mode. In this case, the pulse shape after the main amplifier is distorted by the pile-up effect because of 2 μs of shaping time in the amplifier. Moreover, the dis-tortion due to gamma flash is added for the epi-thermal neutron range. On the other hand, TOF spectrum in the current mode is not affected by the distortion of pulse shape in the current mode. However, the present experi-mental setup has large time resolution caused by the integration time in the current integrator that is approximately 1 ms. In the current mode, it is impossible to directly distinguish between signals due to neutrons and gamma rays.

In the next step, the gamma-ray subtraction will be tried to use a ^{4}He proportional counter that is not sensitive to neutrons. Relation among the gas pressure, detection efficiency in the pulse and current modes and linearity in the large flux range in the current mode will be also investigated.

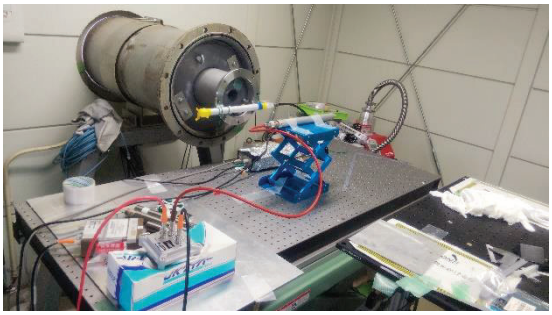

Fig. 1. Experimental setup for the ^{3}He gas detector. The detector was set at 12 m away from the target.

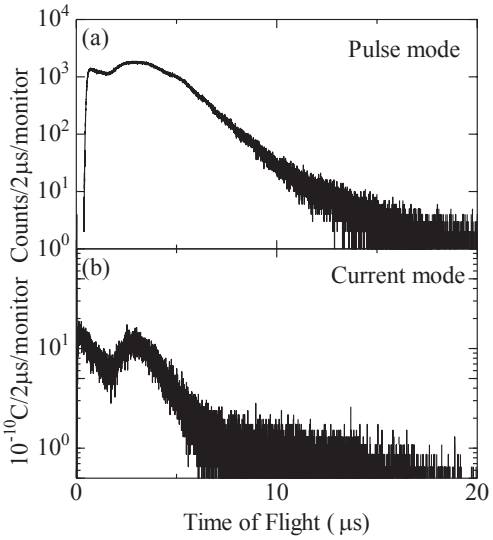

Fig. 2. TOF spectra of (a) pulse and (b) current modes.

REFERENCES:

[1] T. Matsumoto et al., Radiat. Prot. Dosim. 188 (1), 117 (2020).
[2] K. Kobayashi et al., Annu. Rep. Res. Reactorinst. Kyoto Univ. 22, 142 (1989).

This work was supported by JSPS KAKENHI(19K12638).

R2100

CO2-8 Technique of Transferring Radioactive Atomic Nuclei Implanted in Dry Ice Film

A. Taniguchi, P. Strasser[1], M. Tanigaki and Y. Ohkubo

Institute for Integrated Radiation and Nuclear Science, Kyoto University
[1]Muon Science Laboratory, IMSS, KEK

INTRODUCTION: The nuclear charge radius is one of the fundamental parameters that gives information about the effective interactions on nuclear structure. Muonic atoms are ideal tools for the study because the interaction between negative muons and nuclei can be accurately described by electromagnetic interaction. The energies of the X-rays emitted from the muonic atoms are measured for the investigation [1]. The study of muonic atoms for unstable nuclei, however, is little progress mainly because a large amount of radioactivity is needed. We have recently developed a new method using solid hydrogen film to produce muonic atoms with high efficiency. In this method, negative muons (μ^-) are injected to solid deuterium film (D) in which nuclei of interest (A) are implanted beforehand, thereby muonic atoms being formed through the highly-efficient muon transfer reaction: $\mu^-D + A \rightarrow D + \mu^-A$. The feasibility of this method was demonstrated for some stable isotopes and promising results were obtained [2]. In this study, the technical difficulties to be expected in applying this method to unstable nuclei, in particularly concerned with high-efficient recovering of residual radioactivities in deuterium film after experiments, is being approached using a radioactive-isotope beam from KUR-ISOL and dry ice film instead of solid hydrogen film.

EXPERIMENTS: An apparatus capable of implanting radioactivities to dry ice film was installed at the beam line of KUR-ISOL [3]. This apparatus consists of two coolable copper blocks and one CO_2 gas diffuser in the vacuum chamber. Dry ice film is formed on the surface of one cooled block (catcher) by sprayed CO_2 gas through the diffuser and radioactivities are implanted into it. The amounts of radioactivities transferred from the catcher to the other block (trap) are examined under the different conditions of the film formation. In the recent experiments, in order to improve the reproducibility of the transfer efficiency, the film forming parameters were controlled more finely by recording the vacuum degree in the chamber and the temperatures of the copper blocks using a data logger. Moreover, "standing collars" were attached on the four sides of the film formation surface so that more CO_2 gas could retain near the surface during film formation, and during transfer, the collars covered the catcher-trap gap so that more CO_2 gas could agglomerate on the trap block again. About 10^6 ions of $^{146}LaO^+$ were implanted into dry ice film on the catcher in every run. After the implantation, the pre-cooled trap was moved to the frontal vicinity of the catcher, and then the catcher was warmed by stopping LN_2 flow. With this procedure, the atoms of ^{146}Ce and ^{146}Pr, daughter and grandchild nuclides of ^{146}La, were released from the catcher and were re-trapped on the trap together with CO_2 gas. The transfer efficiency was measured by detecting the γ-rays emitted from each of the blocks after the transfer procedure.

RESULTS AND DISCUSSION: The four runs for the two types of films with different thicknesses were performed in two-days of machine time, and their transfer efficiencies were measured. The higher efficiency was obtained although the reproducibility cannot be mentioned due to the small number of runs. (see Fig.1). As in previous reports, the transfer efficiency was derived from the peak counts of 454 keV gamma-ray of ^{146}Pr for the catcher and for the trap by taken into account of the detection efficiency of each Ge detector. The ratio of the counts for the trap to those for the catcher was 12.1:1, while the previous best value was 8.8:1 (=880%) [4].

The experiments to obtain the absolute transfer efficiency are planned while searching for the better conditions for dry ice film formation. In addition to developing a highly efficient recovery method, the experiments focusing on the scattering of radioactivities during the implantation are also planned hereafter.

ACKNOWLEDGMENTS: This research was partially supported by the Ministry of Education, Science, Sports and Culture, Grant-in-Aid for Scientific Research (C) (24540303, Akihiro Taniguchi, and 15K05103, Akihiro Taniguchi).

REFERENCES:

[1] I. Angeli and K.P. Marinova, At. Data Nucl. Data Tables **99** (2013) 69-95.
[2] P. Strasser *et al*., Hyperfine Interact. **193** (2009) 121-127.
[3] A. Taniguchi *et al*., KURRI Prog. Rep. 2013, p.98.
[4] A. Taniguchi *et al*., KURNS Prog. Rep. 2019, p.4

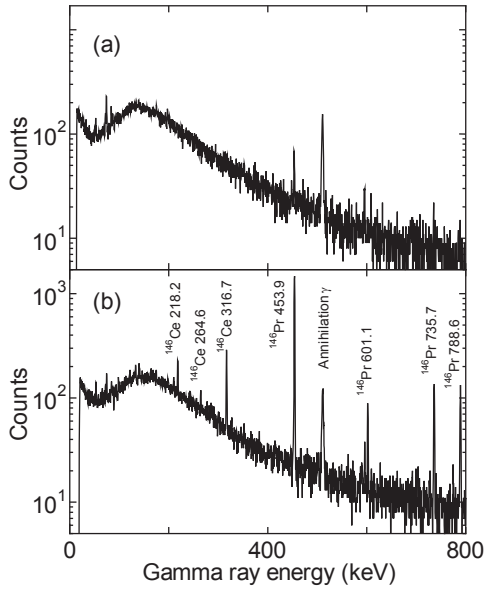

Fig.1 Transfer of radioactivities using a cold trap type recovery apparatus. Gamma-ray spectra of (a) the catcher and (b) the trap after the transfer. Gamma-rays of ^{146}Ce ($T_{1/2}$ = 14 m) and ^{146}Pr ($T_{1/2}$ = 24 m) were observed.

CO3-1 Development of Real-time Subcriticality Monitor Using an Optical Fiber Type Detector

K. Watanabe, T. Endo, A. Uritani, A. Yamazaki, and C. H. Pyeon[1]

Graduate School of Engineering, Nagoya University
[1] Institute for Integrated Radiation and Nuclear Science, Kyoto University

INTRODUCTION: The accelerator-driven system (ADS) has been developed for transmuting minor actinides and long-lived fission products [1-2]. For the ADS system, development of a real-time subcriticality monitor is desired to be developed in order to ensure to keep subcritical condition in any case. Therefore, we are developing a real-time subcriticality monitoring system. For the ADS experiments in Kyoto University Critical Assembly (KUCA), optical fiber neutron detectors were developed. To realize high sensitivity of the detector, neutron scintillator is coated around the wavelength-shifting fiber, which can collect photons from the side surface of the optical fiber. The detector with a long coated region has high sensitivity. In the last year experiments, we used a LiF/Eu:CaF_2 eutectics scintillator, because this scintillator material is transparent and can be thick to improve the sensitivity without attenuation loss of the scintillation photons. However, since this scintillator has relatively low α/β, which is the ratio of light yield for alpha (high LET) and beta (low LET) particles. Therefore, this detector has relatively high beta-ray sensitivity. This detector is influenced from the beta particles, which are emitted from the activated material, such as aluminum sheath of fuel elements, especially under low neutron intensity situation.

In this study, we attempted to fabricate the optical fiber detector with low beta sensitivity but high neutron sensitivity.

EXPERIMENTS: We fabricated the optical fiber neutron detector using LiF/ZnS scintillator. This scintillator material has been used for the optical fiber neutron detector conventionally. In this study, the detector with quite long sensitive region was realized. Figure 1 shows the fabrication processes of the detector. This detector has a sensitive region of 100 mm long. In addition, since the sensitive region was covered by a stainless steel tube with 3 mm outer diameter, this can easily be inserted into a space between fuel elements. We compared the beta sensitivity of the detectors using LiF/Eu:CaF_2 and LiF/ZnS scintillators in the KUCA experiments.

RESULTS: Figure 2 shows the time trends of the measured count rate by the fabricated detectors. We can see that the both detectors have the almost same neutron sensitivity. However, the detector using LiF/ZnS scintillator showed lower count rates when the reactor was shutdown. On the other hand, the detector using LiF/Eu:CaF_2 scintillator showed the decay component after reactor shutdown.

REFERENCES:

[1] Pyeon CH, Lim JY, Takemoto Y et al, *Ann. Nucl. Energy,* **38** (2011) 2298–2302.
[2] Pyeon CH, Yagi T, Sukawa K et al., *Nucl. Sci. Eng.,* **177** (2014) 156-168.

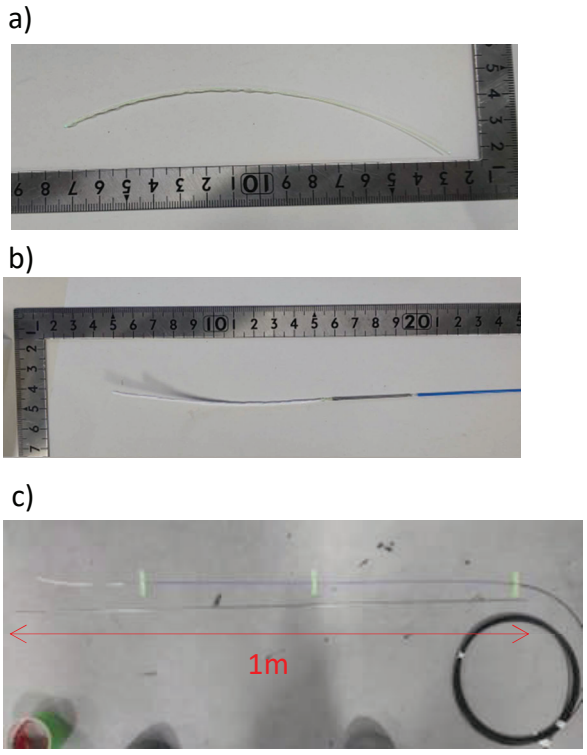

Fig. 1 Photographs of the fabricated optical fiber neutron detector. a) LiF/ZnS scintillator powder coated around a wavelength-shifting fiber. The length of coated region was about 100 mm. b) The scintillator coated region was wrapped by Teflon tape reflector. c) Just before inserting the optical fiber into a stainless tube (for ambient light shielding and support structure) with 1 m long.

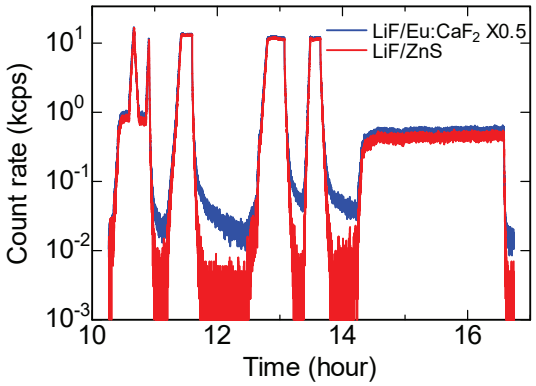

Fig. 2 Time trends of the count rates of the optical fiber detectors using the LiF/ZnS and LiF/Eu:CaF_2 scintillators. The count rates was normalized at the maximum count rate.

CO3-2 Void reactivity measurements of lead and bismuth in the KUCA-A core

R. Katano[1], A. Oizumi[1], M. Fukushima[1] and C. H. Pyeon[2]

[1]*Nuclear Science and Engineering Center, Japan Atomic Energy Agency*
[2]*Institute for integrated Radiation and Nuclear Science, Kyoto University*

INTRODUCTION: The Japan Atomic Energy Agency (JAEA) has investigated neutronics of the accelerator-driven system (ADS) of a lead bismuth eutectic (LBE) cooled-tank-type core to transmute minor actinides discharged from nuclear power plants. For the design study of ADS, integral experimental data of nuclear characteristics of LBE is necessary to validate cross sections of lead (Pb) and bismuth (Bi). Previously, Pb and Bi void reactivity using aluminum (Al) void spacer was measured in a low-enriched uranium (LEU) modeling core [1]. In present study, experiments of Pb and Bi void reactivity using Al void spacer were conducted in a highly-enriched uranium (HEU) core.

EXPERIMENTS: The reference configuration had five test rods as shown in **Figure 1**. **Figure 2** shows each test unit composed of two HEU plates (1/16 inch×2) and two Al plates (1/16 inch×2). The test units were axially and radially surrounded by normal fuel units composed of two HEU plates and a polyethylene plate.

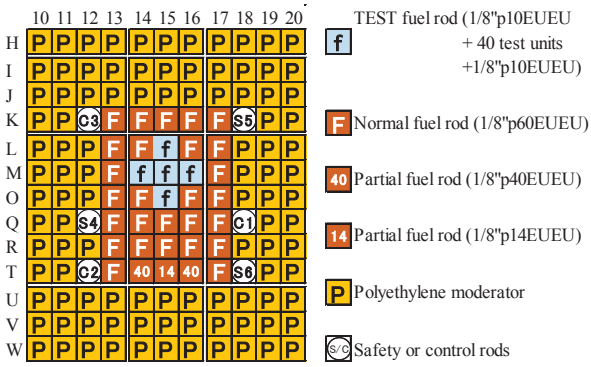

Figure 1. Reference core configuration

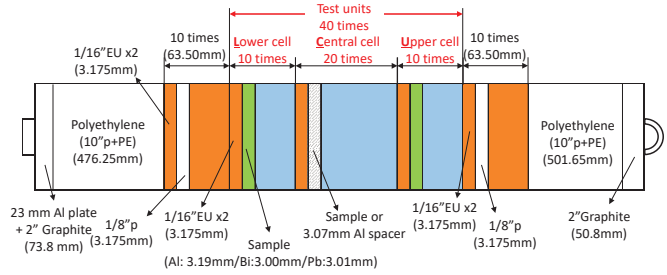

Figure 2. Schematic drawing of test fuel rod

In the previous experiments for sample reactivity worth [2], solid Al plates were substituted for Pb (or Bi) ones, so Al cross sections should be considered as well as Pb one (or Bi) when verifying them. Instead, we used Al void spacers with a low density that was about 1/10 that of solid Al plates to mitigate the Al contribution to reactivity. For the Pb sample reactivity worth, Pb plates instead of Al ones (See Figure 2) were installed in five test rods beforehand, and after then the Pb plates in the central 20 units were substituted for Al void spacers. The Pb sample reactivity worth was estimated as difference between excess reactivities before and after the substitution. Other substitution patterns were summarized together with experimental results in **Table 1**.

Table 1 Experimental results

Case	Pattern (U/**C**/L)[*1]	Excess reactivity (pcm)	Sample Case	Sample worth (pcm)
A	Pb/**Pb**/Pb	241.9 ± 2.4	-	-
B	Pb/**V**[*2]/Pb	37.3 ± 3.3	Pb sample (A - B)	204.7 ± 5.7
C	Pb/**Al**/Pb	158.2 ± 0.6	Al sample (C - B)	121.0 ± 3.9
D	Bi/**Bi**/Bi	163.0 ± 0.2	-	-
E	Bi/**V**[*2]/Bi	0.0 ± 0.0	Bi sample (D - E)	163.0 ± 0.2
F	Bi/**Al**/Bi	120.3 ± 7.8	Al sample (F - E)	120.3 ± 7.8

[*1](Upper 10 units / **Central 20 units** / Lower 10 units) of test regions.
[*2] **V** indicates Al voided spacer. [*3] **Al** indicates solid Al plate.

RESULTS: Numerical analyses were preliminary conducted with MCNP6.2 together with JENDL-4.0 (J40) and ENDF/B-VII.1 (B71). The sample reactivity worth was estimated as the difference between the effective multiplication factors of the sample-loaded and reference configurations, without considering the criticality bias. **Figure 3** shows that MCNP6.2 calculations tend to overestimate sample reactivity worth comparing with experiments. Uncertainty quantification of sample reactivity worth derived from cross sections could be a future task.

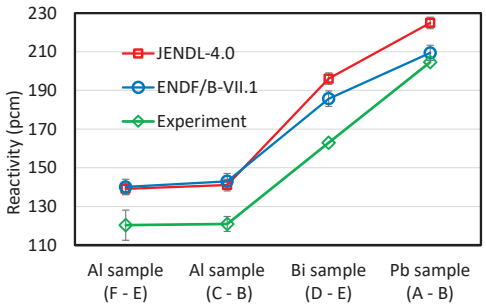

Figure 3. Results of sample reactivity worth

REFERENCES:

[1] M. Fukushima, et al., KURRI Progress Report 2019, 143 (2019).
[2] C. H. Pyeon, et al., J. Nucl. Sci. Technol., **53**, 602-612, (2016), and **55**, 1324-1335, (2018).

CO3-3 Measurement of Reaction Rates of Intermediate Neutrons on Critical Core with Various Neutron Spectra Zone

N. Aizawa, H. Akatsu, T. Abe, K. Kawabata[1] and C. H. Pyeon[2]

Graduate School of Engineering, Tohoku University
[1] School of Engineering, Tohoku University
[2]Institute for Integrated Radiation and Nuclear Science, Kyoto University

INTRODUCTION: The generation of various neutron energy spectra in a reactor core has a potential to apply to the effective transmutation of the radiotoxic nuclides and production of useful radioisotopes. The neutron energy spectrum of reactor core depends on in-core structure and materials. The intermediate neutron energy from several eV to hundreds of keV corresponds to the resonance region of a cross section, and is considered effective for the transmutation and production of nuclides. In the previous study, the measurement of neutron reaction rates has been carried out with using some activation foils sensitive to the intermediate neutron energy ranges for the core composed of polyethylene (PE) moderated highly-enriched uranium fuel and the low-enriched uranium mockup fuel in the critical and the subcritical conditions combined with spallation neutron source, and the knowledge of the measurement of reaction rates of intermediate neutrons has been obtained [1]. The present study performed the measurements of reaction rates for intermediate neutrons in the relatively soft and hard spectrum zone of the critical core to investigate the effect of neutron spectrum on the reaction rate characteristics.

EXPERIMENTS: Figure 1 shows the core configuration in the experiment. The core was constructed in in KUCA A-core with PE-moderated highly-enriched uranium fuel (PE-fuel: brown in Fig. 1) and the Pb-zoned highly-enriched uranium fuel (Pb-fuel: green in Fig.1). The activation foils employed in this study were Ta, W, Cu , In and Au, and set at either (L-M,15) of the Pb-fuel zone or (Q-R,15) of the PE-fuel zone. The Au foils were also set at (Q-R,15) in both irradiation conditions to employ as the normalization factor of reaction rates. The foils were set with and without Cd cover to examine the effect of thermal neutrons.

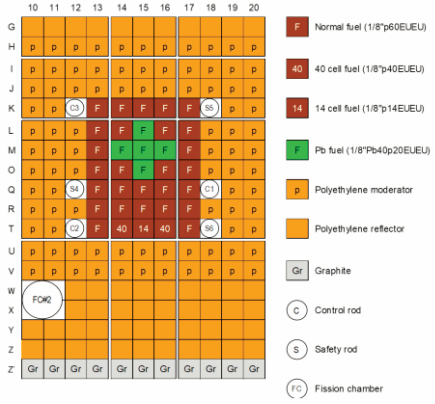

Fig. 1 Core configuration of KUCA A-core

The experimental results of the reaction rates were compared with the numerical calculation results derived by MVP3 [2] for the verification.

RESULTS: The comparison of experimental results with the calculation ones showed that the calculation of the Cd ratios of the reaction rates with/without Cd cover, which is the one of spectrum index, were coincident to the experiment within 1σ range, and the ratios of calculated reaction rate to experiment one (C/E) were almost the same in the case with/without Cd cover in the same zone, and the measured reaction rates was confirmed valid.

Figure 2 shows the experimental results of capture reaction rates of Ta, W, Cu, and In in the PE- and Pb-zone without Cd cover normalized by the Au(n,γ) at (Q-R,15). Some measurement data of In were not included below due to the insufficient accuracy. The Au(n,γ) reaction rate in the Pb-zone was 42.4 % of that in the PE-zone, and Ta, W and Cu capture reaction rates in Pb-zone were 51.6 %, 38.5 % and 34.1 %. These results indicated that the reaction rates of W and Cu were more sensitive to thermal neutrons than Au whereas the influence of harder neutron spectrum became strong in Ta reaction rate.

Table 1 shows the Cd ratios of Ta, W and Cu in PE- and Pb-zones derived from the measurement data. These results meant that the utilization of Cd cover was very effective especially for Cu and W to separate the influence of thermal neutrons and measure the influence of intermediate neutrons.

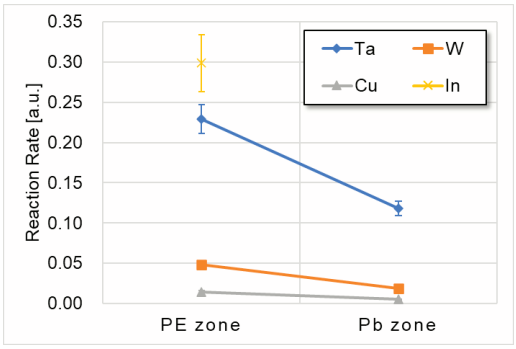

Fig. 2 Reaction rates of activation foils without Cd cover normalized by Au(n,γ) reaction rate

Table 1 Cd ratios of Ta W and Cu in two zones

nuclide	PE-zone	Pb-zone
^{181}Ta	1.17 ± 0.09	1.04 ± 0.08
^{186}W	1.55 ± 0.12	1.08 ± 0.08
^{63}Cu	2.15 ± 0.16	1.28 ± 0.09

REFERENCES:

[1] N. Aizawa *et al.*, KURNS Progress Report 2019, PR2-2, (2019).
[2] Y. Nagaya *et al.*, JAEA-Data/Code 2016-018 (2017).

CO3-4 Measurements of ^{237}Np and ^{243}Am Fission Reaction Rates in Lead Region at A-core of KUCA

A. Oizumi[1], R. Katano[1], R. Kojima[1], M. Fukushima[1], K. Tsujimoto[1], and C. H. Pyeon[2]

[1]*Nuclear Science and Engineering Center, Japan Atomic Energy Agency*
[2]*Institute for integrated Radiation and Nuclear Science, Kyoto University*

INTRODUCTION: To transmute minor actinides (MAs) partitioned from the high-level wastes, the Japan Atomic Energy Agency has investigated neutronics of the accelerator-driven system (ADS) of a lead (Pb) bismuth eutectic cooled-tank-type core. In the nuclear transmutation system such as ADS, the nuclear data validation of MA is required to reduce the uncertainty caused by the nuclear data of MA. To validate the nuclear data, many independent experimental data need to be mutually compared. An expansion of integral experimental data is the important issue since there is a limited number of experimental data of MA. Previously, experiments of measuring fission rate ratio of neptunium-237 (^{237}Np) and americium-241 (^{241}Am) to fission reaction rate of uranium-235 (^{235}U) were carried out in several cores using highly-enriched uranium (HEU) fuel [1, 2]. This study aims to measure the ratios of MA, such as ^{237}Np or the americium-243 (^{243}Am), and ^{235}U fission reaction rates in Pb region at the Kyoto University Critical Assembly (KUCA).

EXPERIMENTS: The irradiation experiments of ^{237}Np, ^{243}Am, and ^{235}U were conducted in the KUCA A-core. Fission reaction rates were measured by using single fission chamber (diameter: 48 mm, height: 120 mm) having a foil such as ^{237}Np (83 μg), ^{243}Am (12 μg), or ^{235}U (10 μg). The simultaneous measurements of MA/^{235}U fission reaction rates were conducted at the void region in the center of the core surrounded by HEU/Pb rods as shown in Fig. 1. The HEU/Pb rod was composed of HEU fuel and Pb plates shown in Fig. 2. The pulsed height distributions from the fission chambers were acquired under the condition at critical state corresponding to reactor powers of 1.5W (^{237}Np/^{235}U) and 3.5W (^{243}Am/^{235}U). The irradiation time was almost 1 hour in both cases.

RESULTS: The distributions of pulsed height of ^{237}Np, ^{243}Am, and ^{235}U fission reactions were observed under the critical condition as shown in Fig. 3. The fission reaction signals need to be separated from noises due to α and γ rays in small pulsed height. For example, the fission reaction events of ^{237}Np and ^{235}U in Fig. 3(a) were determined by integrating the counts at voltages greater than 1.008 and 1.025, respectively. Similarly, the fission reaction counts of ^{243}Am and ^{235}U in Fig. 3(b) were obtained by the integration of signals at voltages greater than 1.078 and 1.038, respectively. Finally, the fission reaction rate ratios of ^{237}Np/^{235}U and ^{243}Am/^{235}U obtained by the total counts, the number of atoms, and a detection efficiency of the fission chamber were 0.048 ± 0.003 and 0.042 ± 0.004, respectively. The measured values will be used for verification of evaluated nuclear data by conducting detailed analyses.

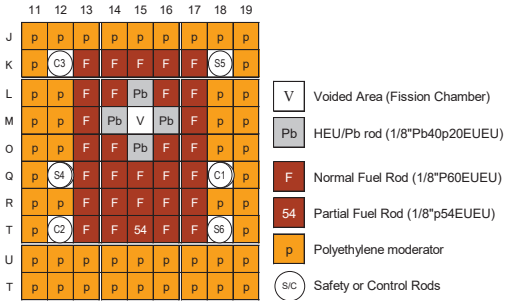

Figure 1. Location of the fission chambers in the A-core of the KUCA.

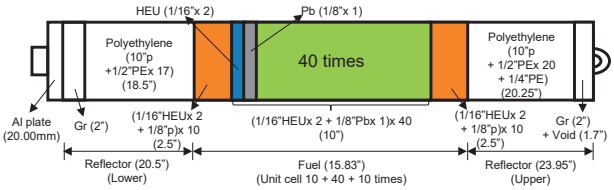

Figure 2. Schematic drawing of HEU/Pb rod in the KUCA-A core showing in Figure 1.

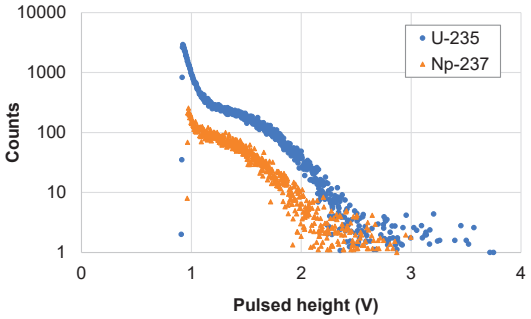

(a) ^{237}Np and ^{235}U

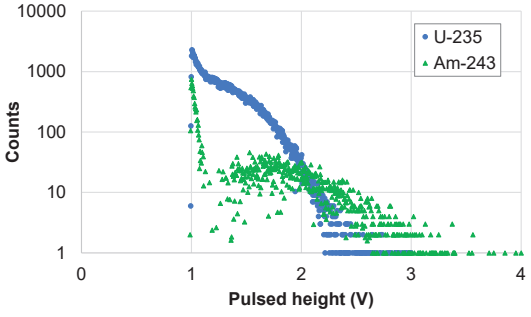

(b) ^{243}Am and ^{235}U

Figure 3. Measured results of fission reaction signals.

REFERENCES:

[1] C. H. Pyeon, et al., Nucl. Sci. Eng., **193**, pp.1023-1032 (2019).
[2] C. H. Pyeon, et al., J. Nucl. Sci. Technol., **56**, 8, pp.684-689, (2019).

CO3-5 Measurement of Very Large Subcriticality by Using Spallation Neutron Source

K. Hashimoto, T. Sano, S. Hohara, A. Sakon, K. Nakajima[1], C. H. Pyeon[2], Y. Takahashi[2]

Atomic Energy Research Institute, Kindai University
[1]Graduate School of Science and Engineering, Kindai University
[2]Institute for Integrated Radiation and Nuclear Science, Kyoto University

INTRODUCTION: Feynman-α analysis and pulsed neutron-source experiment have been conducted to determined prompt-neutron decay constant α in subcriticality range from 0 (critical) to around 10 %Δk/k. However no systematic experiment for much more subcritical core has been reported. The objectives of this study are to measure the decay constant of much more subcritical core than 10 %Δk/k and to investigate the validation of the decay constant.

EXPERIMENTS: Two reactor cores were constructed on the A loading of the Kyoto University Critical Assembly (KUCA). One is referred to as EE05 core consisting of thirty 1/16"P80EUEU(EE05) fuel elements shown in Fig.1. Another is referred to as EE1 core consisting of twenty-one 1/8"P60EUEU(EE1) fuel elements shown in Fig.2. The former core has a much harder neutron energy spectrum than the latter. The subcriticality of the EE05 core ranges from 10 to 25 %Δk/k, while that of the EE1 core ranges from 0.1 to 13 %Δk/k/ A series of Feynman-α analyses and pulsed-neutron-source experiments was carried out for several subcritical states of each core to determine prompt-neutron decay constant. The present Feynman-α analysis was done using a neutron source inherent in the highly enriched uranium fuels of KUCA [1]. In the PNS experiment, the pulsed spallation source of KUCA was used [2].

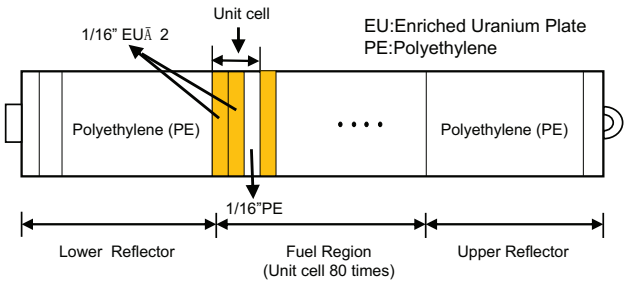

Fig.1. 1/16"P80EUEU (EE05) fuel element.

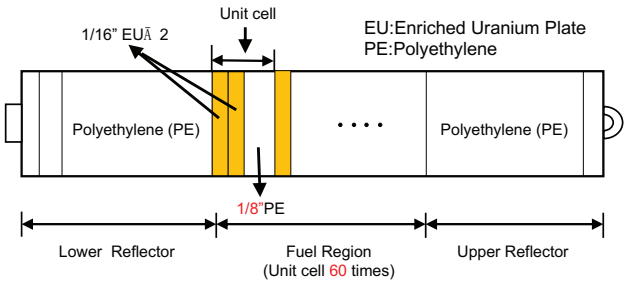

Fig.2. 1/8"P60EUEU (EE1) fuel element.

RESULTS: Figure 3 shows a subcriticality dependence of the prompt-neutron decay constant obtained from Feynman-α analysis, while Fig.4 shows another dependence of the decay constant from pulsed-neutron source (PNS) experiment. Except for a most subcritical state, the decay constants determined from Feynman-α analysis well agree with those from PNS experiment. The difference in the only state is currently under consideration.

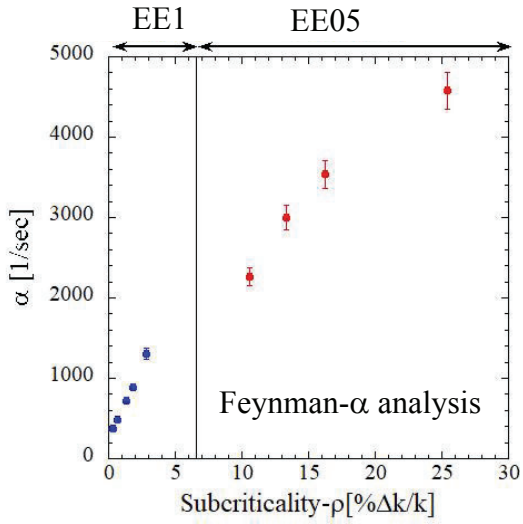

Fig.3. Prompt-neutron decay constant α determined from Feynman-α analysis.

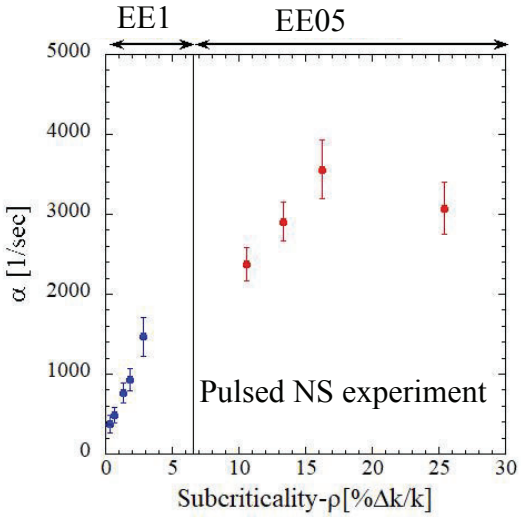

Fig.4. Prompt-neutron decay constant α determined from pulsed neutron source experiment.

REFERENCES:

[1] K. Nakajima *et al.*, J. Nucl. Sci. Technol., **57** (2020) 1152-1166.
[2] C.H. Pyeon *et al.*, J. Nucl. Sci. Technol., **46** (2009) 1091-1093.

CO3-6 Basic Research for Sophistication of High-power Reactor Noise Analysis (III)

S. Hohara[1], T. Sano[1], A. Sakon[1], K. Nakajima[2], K. Hashimoto[1]

[1]*Atomic Energy Research Institute, Kindai University*
[2]*Graduate School of Science and Engineering, Kindai University*

INTRODUCTION:

Reactor noise for high-power reactors were actively measured in the 1960's and 1970's. The major focuses of those researches were for the abnormality diagnosis or the output stabilization diagnosis, and almost researchers were in the field of system control engineering or instrumentation engineering. High-power reactor noise measurements for dynamics' analysis of reactivity change, reactivity feedback or reactor characteristics itself were few in the time (1960's and 1970's), because of the powerless measurement system. In this research, we plan to measure KUR's output with present-day measurement system and plan to analyze with several analysis methods. The results of this work will supply some knowledges and technics in the aspect of sophistication of reactor noise analysis or simulation methods.

In this year, we tried to measure the reactor nuclide noise of the critical state KUR core via a 1-inch ^{3}He counters at CN-1 port. The experimental work was done in 5th November 2020. As the result of the experiment, a result looks like the nuclear reactor noise was observed in 1kW critical state.

EXPERIMENTS:

In this experiment, the output signal of the ^{3}He counters (LND 25291×3) were put into Spectro Scopy AMPs (2022: Canberra and 590A: ORTEC), and the output of the SSAs were measured with a time-series measurement system (HSMCA4106_LC: ANSeeN Inc.). A schematic view of the measurement is shown in Fig.1, and the counter installation overview is shown in Pic.1.

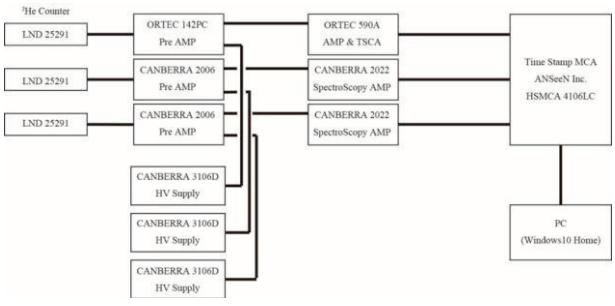

Fig. 1. Schematic view of the measurement.

The experimental condition is shown in Table.1. The reactor Power was set from 20W to 1kW. The measurement time was 800 – 3,600 sec.

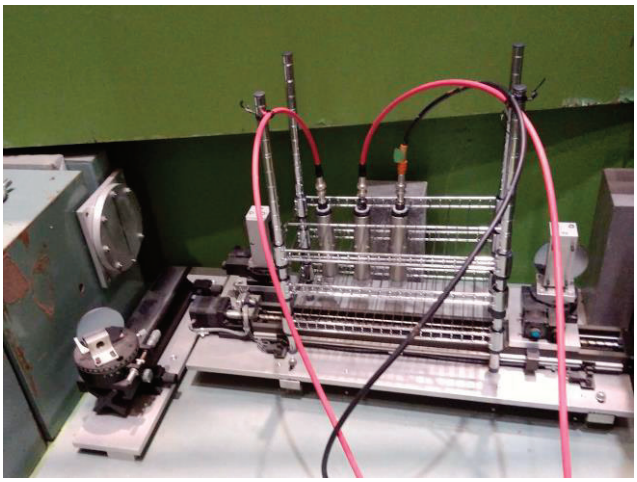

Pic. 1. An overview of the counter installation

Table 1. Experimental condition

No.	Reactor Power [W]	Measurement Time [sec]	Count Rate [cps]
1	1k	3,600	0.7 (#1) 1.1 (#2) 1.4 (#3)
2	10k	5,000	7.2 (#1) 10.3 (#2) 14.1 (#3)

RESULTS:

The measurement results were analyzed by Feynman-α / bunching method, Rossi-α method and Covariance to Mean Ratio method.

As a result of the Feynman-α analysis, plot shapes like Feynman's theoretical formula were obtained for 1kW on #1 & #3 counters and for 10kW on #1 & #2 counters. As a result of the Rossi-α analysis, plot shapes like Orndoff's theoretical formula were obtained for both 1kW and 10kW on the combined value of 3 counters. As a result of the Covariance to mean ratio analysis, plot shapes like Feynman's theoretical formula were obtained for 1kW.

The analysis result is shown in Fig.3. From the results, it is determined that the CN-1 port is likely a place where KUR nuclide noise measurement is possible. However, as can be seen from the measurement results, many of the time correlation information is attenuated, so it takes a long time to measure the KUR nuclide noise on the CN-1 port.

CO4-1 Evaluation of Gamma-ray Induced Current on Triaxial Cables

Y. Gotoh, N. Sato[1], Y. Okuno[2], M. Imaizumi[3], M. Akiyoshi[4], T. Kobayashi[5] and T. Okamoto[6]

Graduate School of Engineering, Kyoto University
[1]Institute for Integrated Radiation and Nuclear Science, Kyoto University
[2]Institute for Materials Research, Tohoku University
[3]Research and Development Directorate, Japan Aerospace Exploration Agency
[4]Radiation Research Center, Osaka Prefecture University
[5]Center for Advanced Photonics, RIKEN
[6]National Institute of Technology, Kisarazu College

INTRODUCTION: In nuclear decommissioning of Fukushima Daiichi Nuclear Power Plant, monitoring of the dose rate of irradiation is necessary. The present study proposes use of solar cell as dosimeter [1]. To monitor the output of the solar cell, it should be confirmed that the signal is not modified by some external circumstances such as electric noise or radiation induced current. In the previous report [2], the current induced on a coaxial cable was investigated, but exact evaluation of the gamma-ray induced current as a function of the dose of irradiation was not possible. The reasons were: lack of the information on dose rate distribution of the space where the cable occupies, and difficulties in fixing the cable to a pre-determined position due to large length of the cable. In this study, these problems were overcome in a following manner. The cable was wound on a wooden frame to identify the position of the cable. The dose rate was measured with the solar cell dosimeter that is currently under development. With these improvements, the current induced on the triaxial cable was investigated.

EXPERIMENTS: Gamma-ray irradiation was performed at the Co-60 gamma-ray irradiation facility, Institute for Integrated Radiation and Nuclear Science. A solar cell dosimeter was prepared in a small can made of stainless steel in which an InGaP solar cell with an area of 1 cm^2 [3] was placed. Prior to the measurements, the sensitivity of the dosimeter was calibrated at the position where the dose of irradiation has been measured. The cable used in the present study was a 1.5D type triaxial cable. A 15 m-long triaxial cable was wound on the wooden frame with the height of 20 cm and the width of 40 cm. The cable was placed at 60 cm away from the gamma-ray source to achieve uniform dose rate for the entire cable. The obtained values of the dose rate of irradiation was 60 Gy h^{-1} at the front face of the wound cable and 40 Gy h^{-1} at the back face. One end of the cable was open and the other end was connected to a pico-ammeter located at the outside of the irradiation room to measure the gamma-ray induced current. Unlike the common usage of the cable, the signal transfer was made with the core wire and the outer shield of the cable; inner shield was either floated or grounded. Since it has already been known that the cable shows a transitional current when the irradiation starts, the induced currents were observed for more than 20 hours. To check the current induced at the cable connecting the sample cable and the pico-ammeter, another triaxial cable was put aside of the sample cable.

RESULTS: Observation started with the inner shield floated. When starting irradiation, the cable showed a large positive transition current as observed so far. Figure 1 shows the variation of the induced current as a function of time of irradiation. The peak current was about 300 pA. It decayed within several minutes, but showed a negative value of -5 pA. The current gradually decreased, but after 21 hours radiation, it showed -3.5 pA, as shown by the dot in Fig. 1. Considering that the induced current once decreased to less than -3 pA, the current would increase again. Connecting the inner shield to ground, the current increased to approximately -10 pA, followed by a relatively rapid decay (time constant of decay, less htan 10 min) to -8.2 pA. Opening the inner shield, the current approached to zero, but rapidly came to -3.8 pA.

It was concluded that the cable showed the cable showed the gamma-ray irradiated charge of 0.14 – 0.21 pC Gy^{-1} cm^{-1} when the inner shield was floated, and 0.33 – 0.49 pC Gy^{-1} cm^{-1} when the inner shield was grounded. These values are lower than the reported values [4].

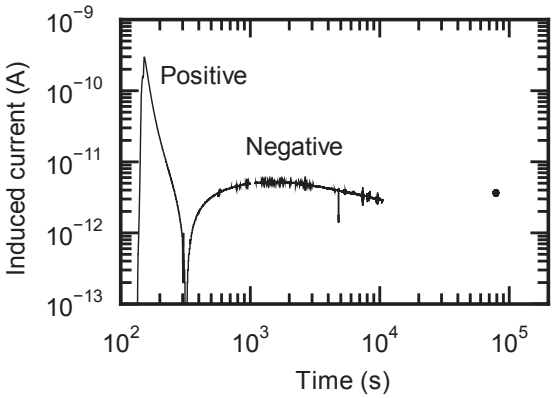

Fig. 1. Observed current under gamma-ray irradiation. The dot shown in the right-hand side is the current observed after 21 hour irradiation.

ACKNOWLEDGMENTS: This work was financially supported by the Nuclear Energy Science & Technology and Human Resource Development Project (through concentrating wisdom) from JAEA/CLADS.

REFERENCES:

[1] T. Okamoto *et al.*, Jpn. J. Appl. Phys. **60**, SBBF02 (2021).
[2] Y Gotoh *et al.*, KURNS Progress Report, CO4-20 (2020).
[3] M. Imaizumi *et al.*, Prog. Photovolt: Res. Appl. **25**, 161 (2017).
[4] K. Yahagi and A. Danno, J. Appl. Phys. **31**, 734 (1960).

CO4-2

Damage Evolution in Neutron-irradiated Metals during Neutron Irradiation at Elevated Temperatures

I. Mukouda and Q. Xu[1]

Hiroshima International University
[1]Institute for Integrated Radiation and Nuclear Science, Kyoto University

INTRODUCTION: It is accumulated an attention that a damage structure in neutron irradiated metals differs if the temperature is varied during irradiation [1]. Especially effect of lower temperature irradiation on the development of damage structure in metals which are irradiated subsequently at higher temperature was reported to be remarkable because the point defects nucleate at lower temperature more frequently during an irradiation. Recently the temperature controlled irradiation devices were developed at KUR [2]. It becomes possible to irradiate continuously at two stage of temperature. In the present work, effects on damage formation in neutron-irradiated copper for the temperature variation were examined for an irradiation at low fluence regime.

EXPERIMENTS: Copper disks of 3mm in diameter were prepared with 99.999% nominal purity specimen. Before an irradiation, they were annealed for 5 hours at 1273 K in vacuum of 10^{-5} Pa. Specimens were irradiated by fission neutrons in a temperature controlled irradiation device in KUR-SSS. In the previous temperature varying irradiation, specimens were irradiated at first at 473K and 573K. After a radiation cooling, they were observed by electron microscopy. A TEM observation was carried out using g = (002) reflection with (g, 5g) condition for the specimens of (110) configuration. Voids were observed in a bright field image by taking a slightly under forcussed image. A triangular image was taken as stacking fault tetrahedra (SFT) and diffused dot image was tentatively taken to be an interstitial cluster.
Present temperature varying irradiation, specimens were irradiated at 473K-6hrs/573K-40hrs, 473K-23hrs/ 573K-23 hrs and 473K-6 hrs/573K-20 hrs at 1MW. TEM observation are carried out recently.

RESULTS: In 473K-10hrs/573K-10hrs irradiation at 5MW, the number density of voids and SFT was smaller than those of constant temperature irradiation at 573K. Especially the decrease of number density of voids was significant [3]. shows dislocations in the specimen. Dislocations were not decorated by interstitial clusters. The number density of SFT was smaller than the value in copper which were irradiated at constant temperature of 573 K. Only one void was observed in specimens as in this picture, which means the formation of voids was suppressed significantly by the present temperature elevation irradiation.
Neutron-irradiated copper at 573K for 10 hours at 5MW, the dislocation structure show no decorated interstitial clusters around dislocation. Interstitial clusters, which were accumulated along dislocation lines, were unified to grow to dislocations. This makes development of complicated structure of dislocations as reported by Mukouda and Shimomura [4].
The suppression of void formation in temperature-varied irradiation suggests that the nucleation of voids during a constant temperature irradiation at 573K in copper occurs during the period of dislocation decoration by interstitial clusters.
In 473K-6hrs/573K-40hrs irradiation at 1MW, the number density of voids and SFT was significant smaller than those of constant temperature irradiation at 573K, some voids were observed. In 473K-6hrs/573K-40hrs irradiation at 1MW as shown in Fig. 1(a). In 473K-23hrs/ 573K-23hrs irradiation at 1MW as shown in Fig. 1(b). Total dose were same as Fig. 1(a) and (b). The suppression of void and small clusters formation in temperature-varied irradiation.

REFERENCES:

[1] N. Yoshida, Q. Xu, H. Watanabe, Y. Miyamoto and T. Muroga, J. Nucl. Mater., 212-215 (1994) 471.
[2] T. Yoshiie, Annual Reports of KUR (1998).
[3] I. Mukouda and Q. Xu, KURNS progress report 2018, Co4-7.
[4] I. Mukouda and Y. Shimomura, Material Science & Engineering A309-310 (2001) 190-197.

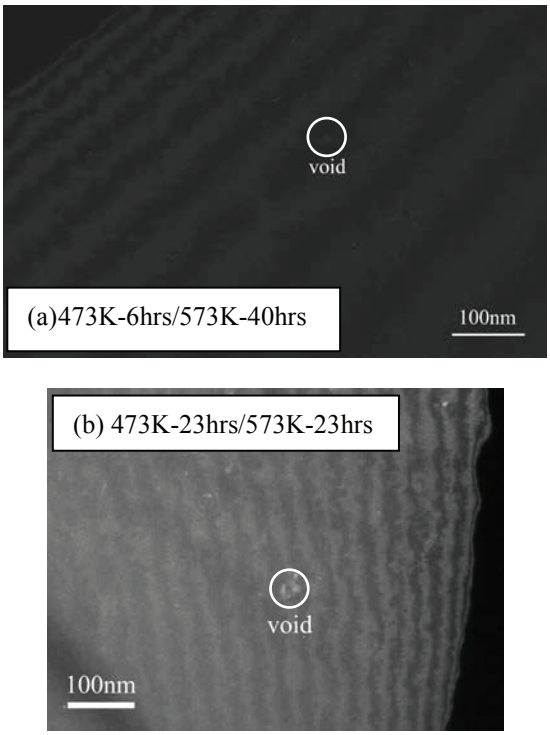

Fig. 1.Damaage structures were observed. The irradiation was carried out at first at 473K and subsequently at 573K at 1MW. Only one void was observed in white circle.

CO4-3 Lattice strain of Al by ECAP process

K. Iwase, K. Mori[1]

Department of Materials Science and Engineering, Ibaraki University

[1]Institute for Integrated Radiation and Nuclear Science, Kyoto University

INTRODUCTION: Equal channel angular pressing (ECAP) has been proved to be an efficient approach to obtain ultrafine-grained materials, and can produce huge plastic strain without changing the section shape of ob-jective materials. Large quantity of investigations about ECAP (Fig. 1) process applied to various materials have been carried out [1–3]. Severe plastic deformation (SPD) has been used to produce ultrafine-grained materials.[4] Equal-channel angular pressing (ECAP) is a processing technique used to achieve SPD. It has been reported that the lattice strain and dislocation density initially increases to a saturation level and then decreases with repetition of ECAP cycles.

In this study, we investigated the lattice strain of Al after ECAP process by neutron diffraction.

EXPERIMENTS: NPD data were collected by using the step-scan mode of a diffractometer (B-3) [5] with 1.0294 Å wavelength. Data analysis was carried out by Rietveld refinement program RIETN-FP [6]. The size of ingot Al is 10×10×5 mm.

RESULTS: Fig. 2 shows the Rietveld refinement pattern of Al before ECAP process. The calculated data fitted well to the observed data. The refined lattice parameter was a = 4.06504(12) Å. Fig. 3 shows the Al block sample after ECAP process, which indicates similar pattern in comparison with before ECAP process. The intensity of Bragg peaks of ECAP sample was smaller than that of Al before ECAP. The refined lattice pa-rameter a was 4.06391(15) Å, which was almost same as before ECAP sample. We determined the full width half of maximum (FWHM) of 111 reflection. The FWHM value is affected on the lattice strain and dis-location density. The FWHM of Al and Al after ECAP was 0.8° and 1.0°, which suggests that dislocation density increases by ECAP process.

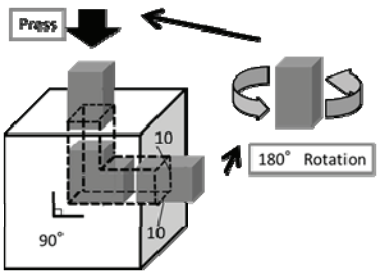

Fig. 1 ECAP process.

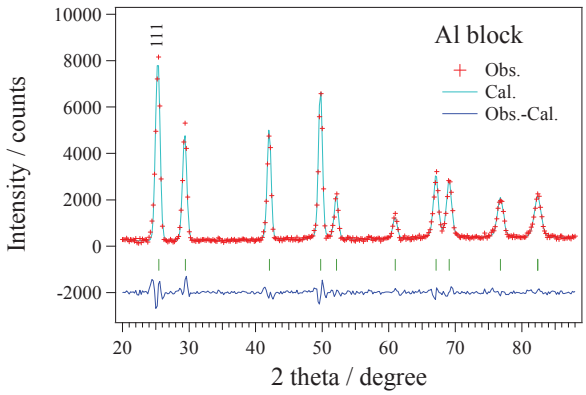

Fig. 2 Rietveld refinement pattern of Al.

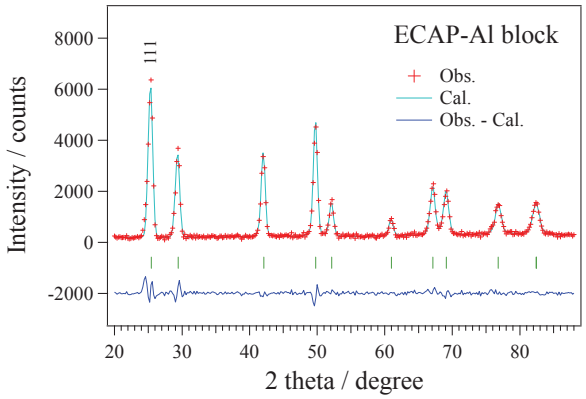

Fig. 3 Rietveld refinement pattern of Al after ECAP process.

REFERENCES:

[1] Z. Zhang *et al.*, Corrosion Science, **49** (2007) 2962-2972.
[2] V.M. Segal, Mater. Sci. Eng. A **271** (1999) 322–333.
[3] J. Wang *et al.*, J. Mater. Res. **8** (1993) 2810–2818.
[4] T. Ishibashi et al., Mater. Trans. 54 (2013) 1562-1569.
[5] K. Mori et al. *Conf. Proc.* 33 (2021) 011093.
[6] F. Izumi and K. Momma, Solid State Phenom., **130**, 15–20 (2007).

CO4-4 Synthesis of complex nanoparticles in water by γ-ray irradiation reduction

F.Hori, K.Zhu, T.Yamada[1], T.Matsui[1], N.Taguchi[2], S.Tanaka[2] and Q.Xu[3]

Dept. of Engineering, Osaka Prefecture University

[1]*Center for Advanced Education of Entrepreneurship and Innovation, Osaka Prefecture University*

[2]*AIST, Kansai Center*

[3]*Institute for Integrated Radiation and Nuclear Science, Kyoto University*

INTRODUCTION: It is known that metal nanoparticles (NPs) have some specific properties, which are not appeared in bulk materials such as catalytic activities, magnetic properties, electric conductivity and light absorption. These properties depend on its size, shape, structure, chemical composition and so on. They have many possibilities to applied for various industrial fields. However, it is not easy to fabricate multi elemental alloy NPs controlling with their structure. Almost fabrication method of NPs with commercially is based on equilibrium chemical reaction in ionic solution with reduction additive. Recently, some reports show that it is possible to fabricate metal NPs under irradiation reduction fields such as ultrasonic, solution plasma, electron beam, ion beam and gamma-ray [1]. By using this radiation reduction method, we have been trying to synthesize various kinds of metal nanoparticles with size and shape. So far, we have successfully synthesized pure Cu and Cu-Au alloy nanoparticles in water by gamma-ray reduction method. In this study, we have studied the reduction rate dependence for the synthesis of various alloy nanoparticles by the reduction under electron and gannma-ray irradiation.

EXPERIMENTS:

Aqueous solutions with various ternary combination of a given concentration of copper complex ($(CH_3COO)_2Cu \cdot H_2O$), $AgNO_3$, NiCl, $Na[AuCl_4]$ and $PdCl_2NaCl_3H_2O$ with an additive of polyvinyl (PVP) and 8.5 vol% ethylene glycol were prepared. The ratio of all ion concentration was adjusted to the same in the solution. The solution was argon gas purged and sealed into polystyrene vessels. They were irradiated at about 300 K with 1.17 and 1.33 MeV gamma-rays from ^{60}Co radio active source at gamma irradiation facility in KURRI, Kyoto University. The total dose was fixed to 10 kGy with the dose rate of 1.0 kGy/h. Also, same solutions were irradiated 8 MeV electron with total dose of 10kGy in about 60 sec by linear accelerator at same facility. After irradiation, the samples were measured for UV–vis absorption spectra. The structures for all colloidal products were measured by X-ray Photoelectron Spectroscopy (XPS) measurement at KEK-PF BL-27 and X-ray diffraction.

RESULTS:

Fig. 1 shows the photograph of before and after electron and gamma-ray irradiated samples. As is seen in this figure, the color of all samples was changed after irradiation, but different it between electron and gamma-ray irradiation. This result reveals that the size and/or state of synthesized particles depend on the reduction rate clearly. Fig. 2 shows the light absorption spectra of AgCuNi and AgAuCu ternary solutions after electron irradiation reduction. No clear characteristic peak of surface plasmon absorption corresponding to pure Au, Cu and Ag nanoparticles was obserbed but broad peaks appears in both samples. The origin of these peaks can not be determined, but the possibility is deduced as mixtured the elemental atoms in formed nanoparticles. XPS results show the formation of some metal bonds, such as Ag-Ni and Ag-Cu. More detailed state of nanoparticles are now examining other methods.

REFERENCE:

[1]. N.Taguchi *et al.*, Rad. Phys. Chem. 78, (2009) 1049-1053.

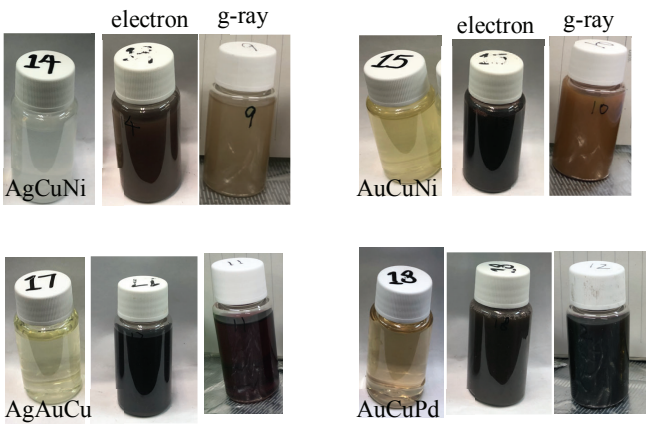

Fig.1 Photographs of electron and gamma-ray irradiation reduction samples.

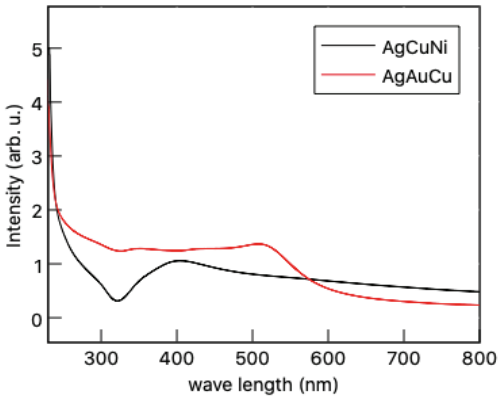

Fig. 2 UV-vis absorption spectra of electron irradiation reduction solutions including Ag, Cu, Ni and Au complexes.

CO4-5 Defect structure and characterization of electron irradiated intermetallic alloys

F.Hori, H.Ohbayashi, H.Ohtomo, Y.Morikuni, K.Ohsawa[1], Q.Xu[2] and N.Abe[2]

Dept. of Quantum & Radiation Eng., Osaka Pref. Univ.
[1]*Res. Inst. of Appl. Mech., Kyushu University*
[2]*Institute for Integrated Radiation and Nuclear Science, Kyoto University*

INTRODUCTION: In general, it is well known that intermetallic compounds have good properties such as specific strength to weight ratio, oxidation resistance and strength in elevated temperature. In addition, some of them can be applied for hydrogen storage material by production of hydride such as Mg and Ni based compound alloys. On the other hand, it found that hydrogen absorption properties in some compound alloys. It is reported that novel Ni- based alloy including defect type free volume can be used as hydrogen permeation membranes to separate H_2 from CO_2 and other gases obtained from water. We also found multi hydrogen atoms trapping at vacancy in B2 ordered FeAl alloy. It is important to clear the interaction between hydrogen and metallic materials for example hydrogen embrittlement, hydride formation and hydrogen induced transformation in hydrogen storage material. However, the nature of defects in various intermetallics is not cleared essentially. We have been studied vacancy type defects in various type of intermetallics. In this study, electron irradiation for Ni-Zr intermetallic alloy have performed in order to examine the defects and their properties.

EXPERIMENTS: $Ni_{30}Zr_{70}$ and $Ni_{63.7}Zr_{36.3}$ alloys were prepared by arc melting method in argon gas atmosphere. Sliced samples with the thickness of 0.5 mm were annealed at 1073 K for 3 h. These specimens were irradiated with 8 MeV electron up to the fluence of 4×10^{18} /cm^2 at KURRI, Kyoto University. Irradiation was carried out at about 330 K with temperature controlling water cool system. Before and after irradiation samples were measured by X-ray diffraction (XRD). Also, micro-Vickers hardness test was performed for before and after irradiation.

RESULTS: Figure 1 shows the XRD spectra of $Ni_{30}Zr_{70}$ alloy before and after electron irradiation. Before irradiation, some peaks correspond to Zr_2Ni, NiZr and pure Zr phases appeared. On the other hand, $Ni_{10}Zr_7$, Ni_7Zr_2 and $Ni_{21}Zr_8$ phases observed in $Ni_{63.7}Zr_{36.3}$ alloy. In figure 1, a peak at 36.5 corresponding to Zr phase disappeared after $4x10^{18}$ /cm^2 electron irradiation, but another peak at 39.5 corresponds to Zr_2Ni phase still remains after $4x10^{18}$ /cm^2 electron irradiation. Originally, Zr phase is not thermally equilibrium phase in this alloy. Therefore, it is considered this Zr phase disappeared by the atomic diffusion using defects introduced by irradiation. Fig.2 shows the micro-Vickers hardness change with electron irradiation fluence. It shows that this difference is originated from their phases included in. Also, it found that the trend of hardness change by the irradiation slightly different for each alloy. This is considered to be due to the difference in the nature of the hardness change of the phase including the defects introduced by irradiation.

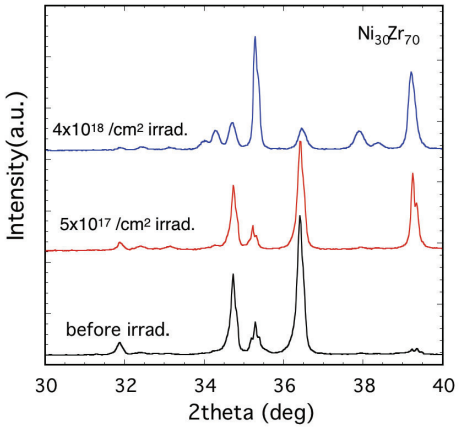

Fig. 1 XRD profiles of $Ni_{30}Zr_{60}$ alloy before and after irradiation.

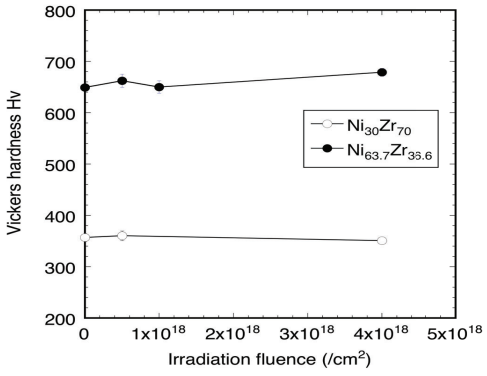

Fig. 2 Hardness chage with wlwctron irradiation fluence for NiZr alloys.

CO4-6 Study on formation mechanisms of nano-structures on Ge surfaces by low-fluence ion irradiations

J. Yanagisawa, T. Furukawa, Q. Xu[1], A. Yabuuchi[1], K. Takamiya[1], and A. Kinomura[1]

School of Engineering, The University of Shiga Prefecture
[1]*Institute for Integrated Radiation and Nuclear Science, Kyoto University*

INTRODUCTION: We have been studying the formation mechanisms of nano-structures on Ge wafer surfaces by ion irradiations using the positron annihilation methods. A peak of the S (line shape) parameter of the positron annihilation was observed by 25 or 50 keV Ar^+ irradiations at ion fluences of $1 \times$ or 5×10^{16} cm^{-2} [1] and 0.5 or 4 keV Ga^+ irradiations at a fluence of 1×10^{15} cm^{-2} [2], indicating the formation of the atomic vacancies and/or voids formed inside regions of the Ge surfaces by the Ar^+ or Ga^+ irradiations. On the other hand, no such peak of the S parameter was observed for the 0.5 keV Ga^+ irradiation at a fluence of 1×10^{14} cm^{-2} [2], indicating that the ion irradiation with such lower energy and/or lower ion fluence induces no damage on Ge surfaces. To study the influences of the lower energy ion irradiations, the effect of the plasma treatment on the surface was investigated as an example of the lower ion irradiation. Ions, as well as radicals, are the main components of plasma, therefore the sample surfaces might be influenced by ions during the plasma treatment. In the present study, we have measured the S parameters for the Si surfaces treated by oxygen plasma.

EXPERIMENTS: Chips of a Si (100) wafer with a size of about 18 mm × 18 mm were exposed to the RF (radio-frequency) plasma at a power of 5 or 100 W with the oxygen gas pressure of 5 or 20 Pa for 30 min. After the treatment, the thickness of the oxide films was measured by an ellipsometer. Table 1 shows the results for the Si samples treated with different plasma conditions, as well as un-treated Si sample as a reference. From this results, thin oxide films were formed for plasma treated samples, indicating that the Si surface was surely influenced by the oxygen ions, as well as oxygen radicals. We have measured the influences of the damages (S parameters) induced by oxygen plasma using the KUR slow positron beam system.

Table 1. O_2 plasma conditions for Si oxidation and measured thickness of SiO_2. The oxidation time was 30 min. The sample #7 is a Si wafer with a natural oxide film as a reference.

sample	RF power	O_2 pressure	SiO_2 thickness
#1	100 W	20 Pa	5.33 nm
#2	100 W	5 Pa	4.92 nm
#3	5 W	20 Pa	2.87 nm
#5	5 W	5 Pa	3.68 nm
#7	–	–	1.57 nm

RESULTS: Figure 1 shows the S parameters for the oxide films as a function of the positron energy. It is found that no peak in the S parameters was observed in these samples, although the oxidation was surely occurred, as shown in Table 1. This indicates that the oxygen plasma might influence on the damage of the oxide films during the oxidation process, but the amount of the damage was small enough for the detection limit of the S parameter. The value of the S parameters of the oxide films formed by larger RF power (100 W) was larger than those by smaller one (5 W), indicating that the acceleration energy of the ion was smaller for smaller RF power. For sample #3, it is observed that the value of S parameter was smaller than that of un-treated Si. The reason of it is not clear at present.

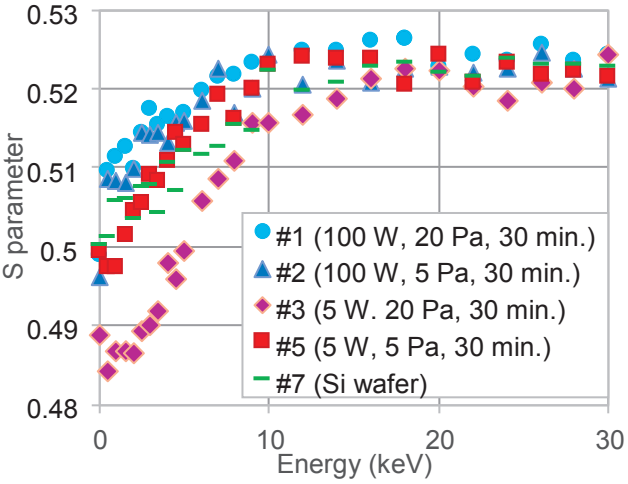

Fig. 1. S parameters for O_2 plasma treated (#1 - #5) and un-treated (#7) Si wafer samples as a function of positron energy.

CONCLUSION: To investigate the effect of damage on surfaces induced by lower energy ion irradiation at lower fluence, oxygen plasma-treated (that is, including low-energy oxygen ion irradiation) Si surface was used in the present study. From the observed S parameters, it is found that almost no damage was induced inside the oxide films by such plasma treatment.

REFERENCES:

[1] J. Yanagisawa, Q. Xu, A. Yabuuchi, K. Takamiya, and A. Kinomura, KURNS Progress Report 2018 (Kyoto University), CO4-15(30037).
[2] J. Yanagisawa, R. Tsukamoto, K. Ishihara, Q. Xu, A. Yabuuchi, K. Takamiya, and A. Kinomura, KURNS Progress Report 2019 (Kyoto University), CO4-16 (31097).

CO4-7 PAC Spectra of the ^{111m}Cd Probe in $Cd_{0.25}Fe_{2.75}O_4$

W. Sato[1,2,3], M. Fujii[2], M. Konaka[3], T. Ito[2], S. Komatsuda[4], and Y. Ohkubo[5]

[1]*Institute of Science and Engineering, Kanazawa University*
[2]*Graduate School of Science and Technology, Kanazawa University*
[3]*College of Science and Engineering, Kanazawa University*
[4]*Institute of Human and Social Sciences, Kanazawa University*
[5]*Institute for Integrated Radiation and Nuclear Science, Kyoto University*

INTRODUCTION: Spinel oxides exhibit various physical properties depending on the constituent metal elements and on their residential positions: the tetrahedral *A* site and octahedral *B* site. Among numerous spinel compounds, iron-based oxides are most promising for application to future spintronic devises; it is therefore very important to obtain microscopic information on their local fields which directly affects their bulk physical properties. In the course of our previous work to measure the local filed in a cadmium ferrite ($CdFe_2O_4$) by means of perturbed angular correlation (PAC) spectroscopy with the ^{111m}Cd probe, we obtained an unexpected spectrum without a defined oscillatory structure as shown in Fig. 1(a) [1]. In general, this kind of spectral pattern is ascribable (1) to spin relaxation of the probe nucleus induced by dynamic perturbation from extranuclear field and/or (2) to damping of the oscillation by a wide distribution of the frequency of the nuclear spin precession. In order to provide insight into the phenomenon, we have further investigated the local fields in cadmium ferrites having intermediate cadmium content between Fe_3O_4 and $CdFe_2O_4$, $Cd_xFe_{3-x}O_4$. Here, part of a preliminary result for $Cd_{0.25}Fe_{2.75}O_4$ is reported.

EXPERIMENTS: Neutron irradiation was performed for cadmium oxide (CdO) enriched with ^{110}Cd in Kyoto University Reactor to produce radioactive ^{111m}Cd by a neutron capture reaction. The radioactive Cd(^{111m}Cd)O powder was mixed well with stoichiometric amounts of CdO and Fe_3O_4 in an agate mortar. The mixture was then pressed into a disk, sealed in a quartz tube in vacuum, and sintered in air at 1373 K for 45 min.

PAC measurements were carried out for the ^{111m}Cd($\rightarrow^{111}$Cd) probe on the 151-245 keV cascade γ rays with the intermediate state of $I = 5/2$ having a half-life of 85.0 ns. In the present work, we obtained the perturbed angular correlation as a function of the time interval of the cascade γ-ray emissions by the following expression:

$$A_{22}G_{22}(t) = \frac{2[N(\pi,t) - N(\pi/2,t)]}{N(\pi,t) + 2N(\pi/2,t)}, \qquad (1)$$

where A_{22} denotes the angular correlation coefficient, $G_{22}(t)$ the time-differential perturbation factor as a function of the time interval t between the cascade γ-ray emissions, and $N(\theta, t)$ the number of the delayed coincidence events observed at an angle θ. The measurements were performed at different temperatures.

RESULTS: The PAC spectra of ^{111m}Cd($\rightarrow^{111}$Cd) in $Cd_{0.25}Fe_{2.75}O_4$ are shown in Fig. 1(b) and 1(c). The spectrum obtained at room temperature (Fig. 1(b)) exhibits oscillatory structure reflecting static interaction with supertransferred magnetic hyperfine field from Fe ions, which is analogous to those observed for Fe_3O_4 [2]. The gradual damping of the oscillation could be attributed to distribution of constituent Cd ions. What should be noted is the spectrum in Fig. 1(c) obtained at 773 K ($> T_C = 753$ K). It was analyzed by assuming a widely distributed electric quadrupole frequency caused by the electric field gradient produced by extranuclear charge distribution. The spectrum is similar to that in Fig. 1(a), leaving a possibility that the damping arises from the distribution of Cd ions. However, a distinct difference is that hard-core like anisotropy still remains in the spectrum in Fig. 1(c), whereas that in Fig. 1(a) hardly does. The cause of the the relaxing trend is still unknown; however, higher-temperature spectra possibly provide a clue to this intriguing phenomenon.

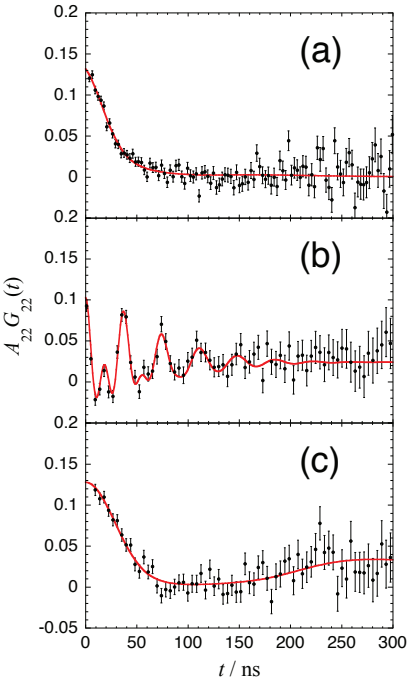

Fig. 1. PAC spectra of ^{111m}Cd($\rightarrow^{111}$Cd) (a) in R.T. $CdFe_2O_4$, (b) in R.T. $Cd_{0.25}Fe_{2.75}O_4$, and (c) in 773-K $Cd_{0.25}Fe_{2.75}O_4$.

REFERENCES:

[1] W. Sato *et al.*, J. Radioanal. Nucl. Chem. **316** (2018) 1289-1293.
[2] W. Sato *et al.*, J. Appl. Phys. **120** (2016) 145104 (1-7).

CO4-8 Characterization of the effect of Au-ion irradiation on $GdBa_2Cu_3O_{7-\delta}$ superconducting tapes using a slow positron beam

T. Ozaki, H. Sakane[1], A. Yabuuchi[2] and A. Kinomura[2]

School of Engineering, Kwansei Gakuin University
[1]SHI-ATEX Co., Ltd.
[2]Institute for Integrated Radiation and Nuclear Science, Kyoto University

INTRODUCTION: Cuprate superconductors, RE-$Ba_2Cu_3O_{7-\delta}$ (REBCO), exhibit high-temperature superconductivity and is expected to be useful for magnetic coils. Critical current properties in magnetic fields are improved by introducing lattice defects using ion-irradiation techniques. Positrons are sensitive to vacancy-type defects, and they are useful for characterizing irradiation-induced defects. In this study, $GdBa_2Cu_3O_{7-\delta}$ (GdBCO) coated conductors (CCs), which were industrially produced with a roll-to-roll process, were irradiated with Au ions at 2 or 10 MeV and probed using a slow-positron beam.

EXPERIMENTS: The GdBCO(500 nm) CCs were irradiated with 2 MeV Au^{2+} (5.0×10^{11}, 4.0×10^{12} cm^{-2}) or 10 MeV Au^{4+} (7.3×10^{11}, 5.5×10^{12} cm^{-2}) ions. The 2 MeV and 10 MeV ions stop in the GdBCO film and penetrate the GdBCO film, respectively. The unirradiated and irradiated samples were probed by the KUR slow positron beam and the Doppler broadening of annihilation radiation (DBAR) spectra were acquired with incident positron energies E_+ varying from 0.03 to 25 keV. The sharpness of the DBAR spectra is evaluated by a value called the *S*-parameter, which becomes generally lower when positrons annihilate in a perfect lattice, and higher when positrons are trapped into vacancies [1].

RESULTS: Figure 1 shows the *S*-parameters of the GdBCO samples before and after irradiation as functions of the incident positron energy. The *S*-parameters for all irradiated samples show a clear reduction, compared with that for the unirradiated sample. This reduction is opposite to the generally expected tendency of the *S*-parameter change caused by ion irradiation. Figure 2 shows the coincidence DBAR spectra for the unirradiated and the high-dose samples normalized to the calculated defect-free GdBCO spectrum. Vacancy clusters were detected in both samples. These results suggest that the size of the newly-formed defects induced by the irradiation is smaller than that of the vacancy clusters initially contained in the samples.

The relation between the *S*-parameter of the GdBCO layer obtained from the VEPFIT analysis and the value of T_c is plotted in Fig. 3. We found that irradiation-induced vacancy-type defects cause a reduction in T_c, demonstrating that a slow positron beam can be a useful tool for characterizing the effects of ion irradiation on commercial superconducting CCs that contain vacancy clusters.

REFERENCES:
[1] R. W. Siegel, Ann. Rev. Mater. Sci., 10 (1980) 393−425.
[2] A. Yabuuchi *et al.*, Appl. Phys. Express, **13** (2020) 123004.

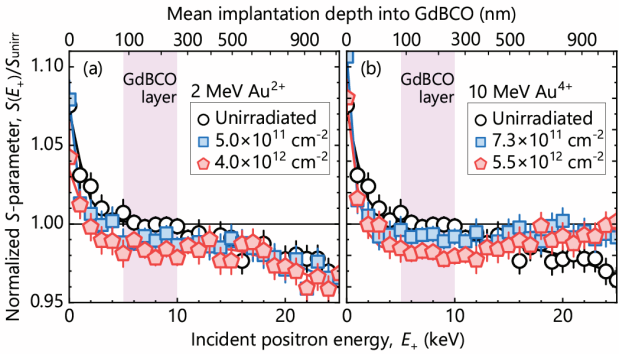

Fig. 1. *S*-parameters as functions of the incident positron energy for (a) 2 MeV Au^{2+} and (b) 10 MeV Au^{4+} irradiated GdBCO samples.[2]

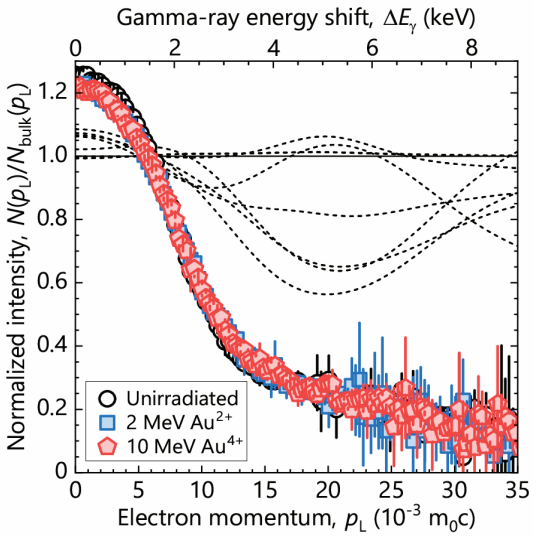

Fig. 2. Coincidence DBAR spectra obtained for unirradiated and high-dose samples. [2]

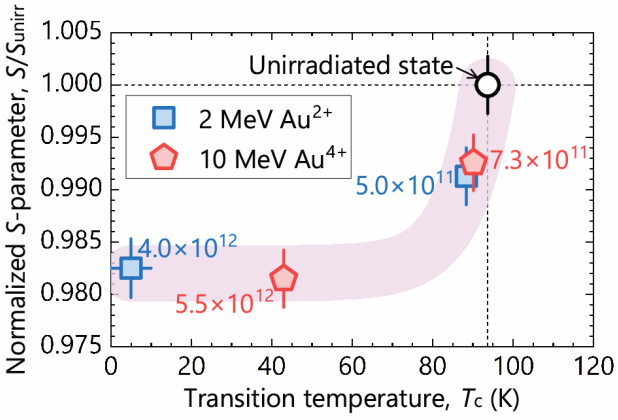

Fig. 3. Normalized *S*-parameters in the GdBCO layer as a function of the T_c. [2]

CO4-9 Local Structure of Cd Impurities doped in $Cd_xSr_{1-x}TiO_3$ Studied by TDPAC Method

S. Komatsuda, W. Sato[1] and Y. Ohkubo[2]

Institute of Human and Social Sciences, Kanazawa University
[1]*Institute of Science and Engineering, Kanazawa University*
[2]*Institute for Integrated Radiation and Nuclear Science, Kyoto University*

INTRODUCTION: Strontium titanate ($SrTiO_3$) is a cubic perovskite compound of ABO_3 type. $SrTiO_3$ doped with metal ions as impurities exhibits a wide variety of electronic properties. Especially, $SrTiO_3$ doped with trivalent metal ions at Ti^{4+} site has attracted much attention because of their excellent photocatalytic activity [1]. For a practical use of $SrTiO_3$, it is necessary to obtain more microscopic information on the impurity site. Therefore, we investigated the local structures at the In^{3+} site in $SrTiO_3$ by means of the time-differential perturbed angular correlation (TDPAC) method using the $^{111}Cd(\leftarrow{}^{111}In)$ probe. In our previous TDPAC study of $^{111}Cd(\leftarrow{}^{111}In)$ probe doped in $SrTiO_3$, three unique quadrupole frequencies were obtained. We proposed three site model of doped $^{111}In^{3+}$ sites; (i) for first components, EFG value was zero suggesting that the $^{111}Cd(\leftarrow{}^{111}In)$ probe reside at defect-free substitutional Sr^{2+} or Ti^{4+} sites in cubic $SrTiO_3$, and (ii) for second and third component, well-defined EFG values were observed, which suggests that second and third component is assignable to ^{111}In at the Sr^{2+} and Ti^{4+} site associating with defect like oxygen vacancy. Because there are a wide variety of the site occupation of $^{111}Cd(\leftarrow{}^{111}In)$ probe, information about structural and electronic properties at the impurity site is uncertain. In order to obtain further information on the local fields at Sr^{2+} or Ti^{4+} site individually, we then adopt the $^{111}Cd(\leftarrow{}^{111m}Cd)$ probe with the same valence to Sr^{2+} expecting replace only A site in $SrTiO_3$. We here report part of the result of TDPAC measurements for the $^{111}Cd(\leftarrow{}^{111m}Cd)$ in $Cd_xSr_{1-x}TiO_3$

EXPERIMENTS: Stoichiometric amount of $SrCO_3$, $CdCO_3$, and TiO_2 powders were mixed in the mortar. The powders were pressed into disks. For TDPAC measurements, about 3 mg of CdO enriched with ^{110}Cd was irradiated with thermal neutrons in a pneumatic tube at Institute for Integrated Radiation and Nuclear Science, and radioactive ^{111m}Cd was generated by $^{110}Cd(n, \gamma)^{111m}Cd$ reaction. The neutron-irradiated CdO powder was dissolved in 6M HCl and added in droplets onto the pre-sintered $Cd_xSr_{1-x}TiO_3$ disk. The disk was sintered in air at 1373 K for 90 min. The TDPAC measurement was carried out for the 151-245 keV cascade γ rays of $^{111}Cd(\leftarrow{}^{111m}Cd)$ probe with the intermediate state of $I = 5/2$ having a half-life of 85.0 ns.

RESULTS: Figure 1 shows the TDPAC spectra of (a) $^{111}Cd(\leftarrow{}^{111}In)$ in $SrTiO_3$ from our previous work, and (b) $^{111}Cd(\leftarrow{}^{111m}Cd)$ in $Cd_{0.15}Sr_{0.85}TiO_3$ at room temperature from this work. The directional anisotropy on the ordinate, $A_{22}G_{22}(t)$, was deduced with the following simple operation for delayed coincidence events of the cascade:

$$A_{22}G_{22}(t) = \frac{2[N(\pi,t) - N(\pi/2,t)]}{N(\pi,t) + 2N(\pi/2,t)}. \quad (1)$$

Here, A_{22} denotes the angular correlation coefficient, $G_{22}(t)$ the time-differential perturbation factor as a function of the time interval, t, between the relevant cascade γ-ray emissions, and $N(\theta,t)$ the number of the coincidence events observed at angle, θ. The spectra in Fig. 1 can be reproduced by a fit with three unique quadrupole frequencies. The parameters of quadrupole frequencies between the two results of Fig.1(a) and (b) were the same within the fitting error range. These observations show that local fields at the $^{111}Cd(\leftarrow{}^{111m}Cd)$ probe in $Cd_{0.15}Sr_{0.85}TiO_3$ composite oxide is identical to that at the $^{111}Cd(\leftarrow{}^{111}In)$ probe in $SrTiO_3$. It is suggested from these result that the $^{111}Cd(\leftarrow{}^{111m}Cd)$ probe also reside at three unique site; (i) for first component of zero EFGs, the $^{111}Cd(\leftarrow{}^{111m}Cd)$ probe substitutes defect-free A or B sites in cubic perovskite structure, and (ii) for second and third components of non-zero EFGs, defects were associated with the $^{111}Cd(\leftarrow{}^{111m}Cd)$ at the site of substitutional A and B site. In addition, the $Cd_{0.15}Sr_{0.85}TiO_3$ has a crystal structure of cubic perovskite of $SrTiO_3$ despite high doping concentration of Cd. For more information on the extranuclear field of the $^{111}Cd(\leftarrow{}^{111m}Cd)$ probe in $Cd_{0.15}Sr_{0.85}TiO_3$, doping rate dependence of TDPAC pattern for $Cd_xSr_{1-x}TiO_3$ is now in progress.

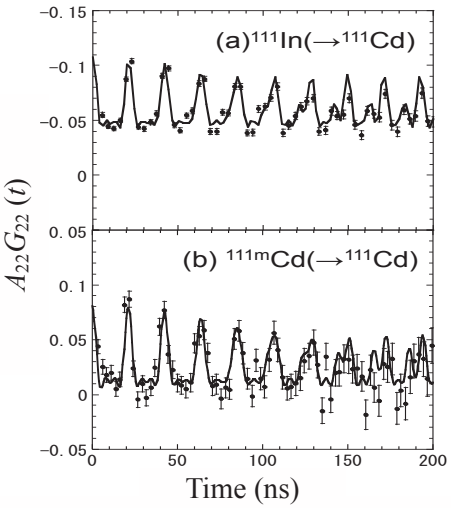

Fig. 1. TDPAC spectra of (a) $^{111}Cd(\leftarrow{}^{111}In)$ in $SrTiO_3$, and (b) $^{111}Cd(\leftarrow{}^{111m}Cd)$ in $Cd_{0.15}Sr_{0.85}TiO_3$. The measurements were perfomed at room temperature.

REFERENCES:

[1] Y. Goto *et al.*, *Joule* **2** (2018) (509-520).

CO4-10 Radiophotoluminescence behavior in Cu-doped silica glass – Dose dependence and effect of heat treatment post irradiation –

Y. Takada, Y. Nishi, A. Kinomura[1], T. Saito[1], A. Okada[2], T. Wakasugi[2], K. Kadono[2]

Graduate School of Science and Technology, Kyoto Institute of Technology
[1]Institute for Integrated Radiation and Nuclear Science, Kyoto University
[2]Faculty of Materials Science and Engineering, Kyoto Institute of Technology.

INTRODUCTION: Radiophotoluminescence (RPL) or radiation-induced photoluminescence phenomena are due to emissions from luminescent centers that are generated in materials by exposure to ionizing radiation. Recently, we have found that Cu-doped aluminoborosilicate glasses exhibit remarkable RPL [1]. The mechanism for the RPL was proposed as follows. First, ionizing radiation generates electron-hole pairs in the Cu-doped glass:

$$\text{Glass} \rightarrow h^+ + e^- \qquad (1)$$

Then, the electrons are captured by Cu^{2+} ions, which are converted to Cu^+ ions:

$$Cu^{2+} + e^- \rightarrow Cu^+ \qquad (2)$$

The Cu^+ ions emit bright luminescence in the visible region by ultraviolet excitation. The reverse reaction, in which holes are captured by Cu^+ ions, can occur:

$$Cu^+ + h^+ \rightarrow Cu^{2+} \qquad (3)$$

However, in the aluminoborosilicate glasses, the copper ions mainly exist as divalent ion, Cu^{2+}, therefore, the reverse reaction hardly occurs. In addition, because of the small amount of copper incorporated in the glasses, the luminescence of Cu^+ before the irradiation is strongly suppressed. In other words, the increase in the photoluminescence is enhanced after irradiation.

In the last year, we reported that a silica glass doped with Cu exhibits RPL. The Cu-doped silica glass was prepared from a porous silica glass derived from a phase separated sodium borosilicate glass. In this research, we investigated the behaviors of the RPL in the Cu-doped silica glass in detail.

EXPERIMENTS: The Cu-doped silica glass was prepared from a porous silica glass by sintering. The method was described in the previous report in detail. The Cu-doped silica glass (abbreviated as Cu-SG, hereafter) was cut and optically polished to 1 mm thickness. The Cu-SG was exposed to γ-ray or X-ray radiations. The γ-ray irradiation experiments were performed with ^{60}Co γ-ray at the Co-60 Gamma-ray Irradiation Facility at Institute for Integrated Radiation and Nuclear Science, Kyoto University. The irradiation dose was represented as absorbed dose for water. The X-ray irradiation was performed using an X-ray source with a Rh target.

RESULTS: Figure 1 shows the photoluminescence spectra for Cu-SG measured before and after the X-ray irradiation. A luminescence band peaked at 2.5 eV was observed for the Cu-SG glass before the irradiation. However, the intensity of the band increased and the peak position shifted to 2.2 eV after the irradiation. The color of the luminescence changed from blue to yellow by the irradiation. The peak decomposition of the luminescence band after the irradiation revealed that the luminescence consists of two bands peaked at 2.5 eV and 2.1 eV and the latter newly appeared after the irradiation. Both bands are attributed to the transition of $3d^9 4s^1$ to $3d^{10}$ in Cu^+ ions. The inset in Fig. 1 shows the dose dependence of the luminescence intensity for the γ-ray irradiation. The intensity proportionally increased with the irradiation dose up to approximately 700 Gy of irradiation dose.

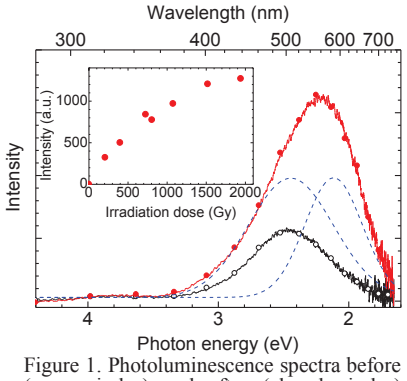

Figure 1. Photoluminescence spectra before (open circles) and after (closed circles) X-ray irradiation. Brocken lines are two components of the band after the irradiation. Inset: γ-ray dose dependence of the luminescence intensity.

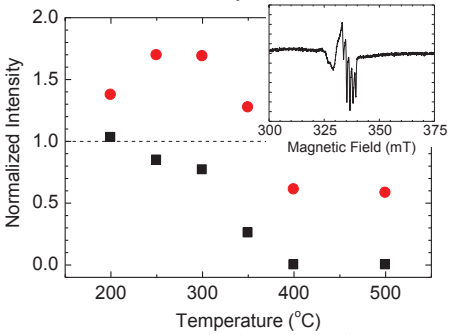

Figure 2. Normalized intensity changes of photoluminescence (circles) and ESR signal assigned to BOHC (squares) with heat treatment temperature after X-ray irradiation. Inset: ESR spectrum of Cu-SG after irradiation.

Figure 2 shows the variation in the photoluminescence intensity with heat treatments for the Cu-SG glass after the X-ray irradiation. The intensity increased with the heat treatments up to 300°C. This may be caused by the capture of electrons which are trapped at relatively stable sites, such as boron E' centers. Then the intensity gradually decreased with the heat treatments and returned to the initial intensity before the irradiation by the heat treatment at 500°C. The decrease in the intensity was consistent with that of the ESR signal intensity of the boron oxygen hole centers (BOHCs). This means that the decrease in the luminescence intensity was caused by the capture of holes which may be supplied from the BOHCs. The thermal stability of the photoluminescence up to 300°C and the prominent RPL in the Cu-SG are owing to the stability of the defects such as BOHC, which are generated in the glass by the exposure to radiation.

REFERENCE:

[1] H. Hashikawa, et al., *J. Am. Cer. Soc.*, **102**(4) (2019) 1642-1651.

CO4-11 Complex Structure of Ions Coordinated with Hydrophilic Polymer 21. Ionic Diffusion in Polymeric Structure Utilized by Polyiodide Ions. (2)

A. Kawaguchi , Y. Morimoto

IIRNS, Kyoto University

INTRODUCTION:

We have been investigating dynamical and interacted structures between iodine and polymers. Here, the term of "iodine" indicates not only simple I_2, but polyiodide ions (I_n^{m-}, *m, n*: integer, $n > 1$) as charged molecules, which suggest concealed potential and diverse availability. [1,2]

Experimentally, while polyiodide ions (and their counter-ions: ex. K^+ ion which exists within I_2-KI(aq)) are prepared as solutes in aqueous solution, both polyiodide ions as anion and counter-ion as cation can be simultaneously diffused into various polymeric matrix without deformation nor melting in macroscopic scale. Especially, diffusion of polyiodides and their counter ions ("iodine doping") into *hydrophilic* polymers advance drastically at room temperature. However, while preparation procedure can be easy operation with aqueous solutions at room temperature, there may be often observed unexpected and paradoxical behavior; for example, in PA6 (polyamide-6) matrices, "modified orientation of PA6 chain" or "diffusion and intercalation of doped elements into PA6 crystallite" can be observed. [3,4]

Additionally, polyiodide ions and counter ions behave as introducers for other following (posteriori diffused) ions and novel structure, including modification of original (non-doped) polymer itself. Or, in some cases, both paradoxical results, such as elimination vs. adsorption (dynamism by and among iodine), or softening vs. hardening (interaction between host polymers and "iodine"), or ordering vs. disordering (mobility of ions or polymer chains at each stage of hierarchic structure), can advance simultaneously.

Furthermore, even though interaction between polyiodide ions and *hydrophilic* polymers is explicit and drastic, there are many suggesting results observed in interaction between polyiodide ions and *hydrophobic* matrices which do not always indicate significant iodine doping quantitatively. [5]

Such interacted mobility of both guest ions and host polymer and complicated results in various polymers with polyiodide ions (or their diverse behavior in structure of host polymeric matrices) should be estimated considering "hierarchic structures" of polymer; it shall suggest potential generality penetrating polymeric structures, which are dominated by essential anisotropy destined through "polymer chains".

DISCUSSION:

Starting fundamentally, ionic diffusion as elemental transportation of solved solutes and diffusion through solvents requires two factors: independency of each ions and free mobilization.

Solving ions in microscopic scale means that molecules or ions are released from bulk solids in micro scale; otherwise, they turn back to aggregation. Such independency depends on affinity (chemical potential) between ions as solutes and solvents.

On the other hand, mobility of ions which are hydrated or solvated in (aqueous) solutions is guaranteed by dynamism of (hydrated or solvated) solvents. Generally, since solvent environments is implicitly regarded as (low) molecules in their liquid phase with activated mobility, solvation is hardly an obstacle against ionic mobility or diffusion. Then, affinity with solvent can be neglected as the obstacle for ionic mobility.

However, affinity with solvents is also viscosity for the solutes which may be the obstacle or a hurdle against mobility of the solutes. If so, affinity of ions as the solutes with the solvents and mobility of them in the solutes are opposed each other.

Then, affinity between "iodine" and polymers should be fixing the ions and should be the obstacles against mobility. Nevertheless, "iodine" or polyiodide ions indicate general affinity with polymeric matrices whereas their coordination also induces enhances mobility of (primary and following) doped ions or chain orientation in some cases (PA6). Here may be hints to explain logics of ionic diffusion through polymer in co-existence with "iodine". We suppose unneglectable suggestion applying generality of polymers behind the "iodine-doped" polymers, which may be regarded as particular cases. [to be continued]

ACKNOWLEDGMENTS: These results are researched with Dr. Gotoh (Shinshu Univ.) and his staff and are partially funded by NEDO.[6]

REFERENCES:

[1] patent. JPN-5444559 (2014).

[2] “Projects for Practical Use from Innovation” sponsored by NEDO (2007-2009).

[3] A. Kawaguchi, Polymer, **35**, 3797-3798. (1994).

[4] KAWAGUCHI Akio, et.al., SPring-8 User Exp. Rep. **5** (2000A), 354-354. (2000).

[5] A.Kawaguchi, Polym.Prep.Jpn., **62**,5116-5117. (2013).

CO4-12 Tritium release behavior from long term heated Li_2TiO_3 pebbles

K. Katayama, A. Ipponsugi, T. Hoshino[1], T. Matsumoto, and Y. Iinuma[2]

Interdisciplinary Graduate School of Engineering Sciences, Kyushu University
[1]Breeding Functional Materials Development Group, Fusion Research and Development Directorate, Quantum and Radiological Science and Technology
[2]Institute for Integrated Radiation and Nuclear Science, Kyoto University

INTRODUCTION: From the viewpoints of the feasibility and safety of the fuel cycle of a fusion reactor, it is important to understand tritium behavior in the blanket. Tritium release behavior from solid tritium breeding materials has been investigated by neutron irradiation in previous studies [1,2]. However, the influence of long-term high-temperature heating expected in a fusion DEMO reactor on tritium release are not sufficiently understood. In our previous study [3], it was observed that a certain amount of Li was evaporated from the Li_2TiO_3 pebbles by heating to a high temperature of 900 ºC and the grain size was increased by the sintering effect. These changes by heating pebbles may affect tritium behavior. In this study, Li_2TiO_3 pebbles were heated at 900 ºC in H_2/Ar flow for 720 hours at most and that was irradiated by neutrons in the Kyoto University Research Reactor. And then, tritium release behaviors from the pebbles by heating were observed in Kyushu University.

EXPERIMENTS: The sample pebbles of Li_2TiO_3 (Li/Ti ratio:2.00) were kindly provided by National Institutes for Quantum and Radiological Science and Technology. 4 samples were prepared by heated at 900 ºC in 1000 Pa H_2/Ar flow for 0, 72, 240, 720 hours, respectively. Each sample was packed in a quartz tube sealed under vacuum and neutron irradiated with the fluence of 1.65×10^{15} cm^{-2}. The irradiated samples were transported to Kyushu University and taken out from the quartz tube in a glove box filled with Ar gas. Each sample was packed in a quartz tube and heated to 1000 ºC in 1000 Pa H_2/Ar flow to enhance tritium release as HT by the isotope exchange reaction. The time variation of tritium concentration in the outlet gas was observed two ionization chambers, IC1 and IC2, which were connected in series. Water bubbler was installed between IC1 and IC2 to collect HTO. Total tritium concentration (HT + HTO) was monitored by IC1 and HT concentration was monitored by IC2.

RESULTS: Fig.1 compares the inner structure of Li_2TiO_3 pebbles as received and that heated at 900 ºC for 720 h. It seems that the particle size increased slightly, and the pores decreased. No considerable changes were seen in the structure after heating for 720 h. Fig.2 and Fig.3 show tritium release curves from Li_2TiO_3 pebbles as received and pre-heated for 720 h. For the sample heated for 720 h, the tritium release rate around 200-300 ºC became slightly slower, and the broad peak at the high temperature was not observed. It can be said that the influence of long-term heating on tritium behavior cannot be ignored.

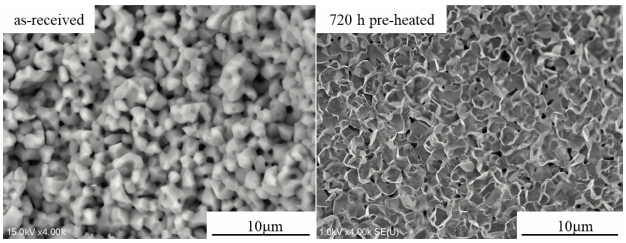

Fig. 1. SEM images inside pebble as received and 720 h pre-heated.

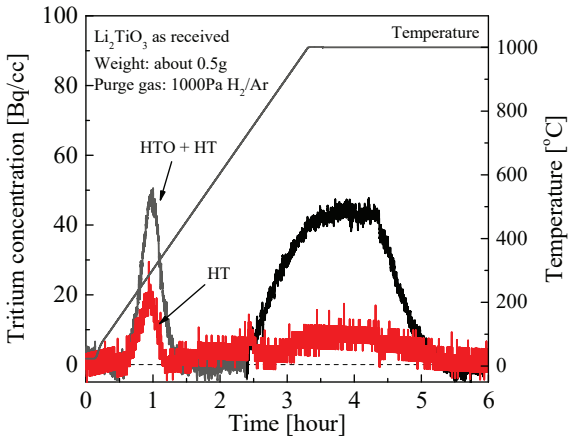

Fig. 2. Tritium release curve from Li_2TiO_3 pebbles as received.

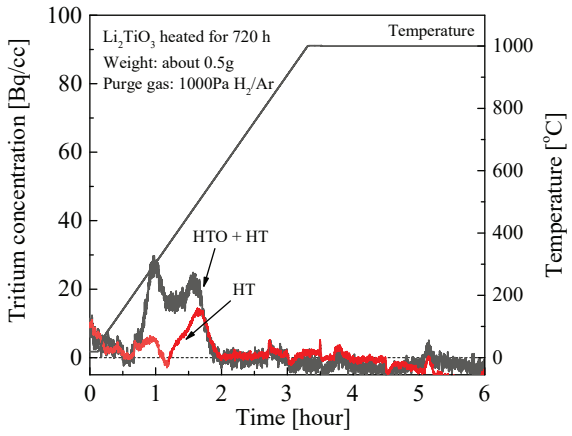

Fig. 3. Tritium release curve from Li_2TiO_3 pebbles pre-heated at 900 ºC for 720 h.

REFERENCES:

[1] T. Kinjyo *et al.*, Fusion Eng. Des. 83 (2008) 580-587.
[2] T. Hoshino *et al.*, Fusion Sci Technol. 67 (2015) 386-389.
[3] A. Ipponsugi *et al.*, Fusion Mater. Energy. 25 (2020) 100777.

CO4-13 Vacancy migration behavior in an $Al_{0.3}CoCrFeNi$ high entropy alloy

K. Sugita, M. Mizuno, H. Araki, A. Yabuuchi[1] and A. Kinomura[1]
Graduate School of Engineering, Osaka University
[1]*Institute for Integrated Radiation and Nuclear Science, Kyoto University*

INTRODUCTION: Alloy design has traditionally been done by selecting the base material and adding the appropriate elements to achieve the desired properties. In the last decade, a new type of multicomponent alloy called "high entropy alloys" containing equiatomic / near-equiatomic ratios of constituent elements was proposed by Yeh et al [1-3]. These alloys often exhibit simple solid solution structures at high temperatures due to the high constituent entropy of random solid solution mixtures. High entropy alloys have been reported to have promising properties for practical use, such as high strength, high fracture toughness, excellent oxidation resistance and corrosion resistance combined with ductility. A major factor in these properties is thought to be the kinetics of "sluggish diffusion". Therefore, the diffusion kinetics of high entropy alloys has been actively studied by diffusion logarithms and tracer diffusion methods, as the atomic diffusion in a multiprincipal element matrix has also been of interest. We have previously investigated the vacancy migration behavior during isochronous annealing after electron irradiation in CoCrFeMnNi high-entropy alloys and their subsystems and reported that the vacancy transfer energy does not change significantly with the number of constituent elements. In this study, we investigated the vacancy migration behavior in $Al_{0.3}CoCrFeNi$ high-entropy alloy and discussed the effect of Al addition on the vacancy migration behavior.

EXPERIMENTS: Arc melted ingots of an $Al_{0.3}CoCrFeNi$ alloy was purchased from Koujundo chemical laboratory (Japan). The ingots were homogenized at 1373K for 24 h in silica tubes under Ar atmosphere and were then machined into 10 × 10 × 0.5 mm plate pieces by electric discharge machining. The specimens were subjected to strain relief annealing at 1373K for 10 h and then rapidly cooled to prevent secondary phase precipitation and to stabilize single-phase FCC structures. The specimens in water flow were exposed to 8 MeV electron beam irradiation for 3 h in KURNS-LINAC. The irradiation damage was evaluated at (1.3 - 1.8) $\times 10^{-4}$ dpa. In order to investigate the thermal stability of vacancies, the electron irradiated specimens were subjected to the subsequent isochronal annealing at 373-673 K for 1 h.
Positron lifetime measurements were carried out by using a digital oscilloscope system with photomultiplier tubes mounted with BaF_2 scintillators, having a time resolution (FWHM) of 185 ps. The positron lifetime measurements require data acquisition for approximately 18 hours with a Na-22 positron source of 0.4 MBq activity in order to acquire 3 million counts in the positron lifetime spectrum. The measured spectra were analyzed using the programs RESOLUTION and POSITRONFIT Extended.

RESULTS: The mean positron lifetime after isochronal annealing of the electron irradiated samples is shown in Fig.1. The positron lifetime spectra of as-irradiated samples show a clear separation into two exponential components of positrons with a long lifetime of 185 ps. This indicates that a part of positrons is trapped by monovacancies or relatively small vacancy clusters introduced by during the electron irradiation. After the subsequent isochronal annealing, the mean positron lifetime is found to decrease sharply around 175°C. This can be attributed to the decrease in vacancy concentrations triggered by the free vacancy-migration. This result indicates that the vacancy migration energy in an $Al_{0.3}CoCrFeMnNi$ high-entropy alloy is lower than that in a CoCrFeNi alloy. This result is in contrast to the fact that the vacancy migration energies in an CoCrFeMnNi high-entropy alloy and its subsystems did not show any significant difference.

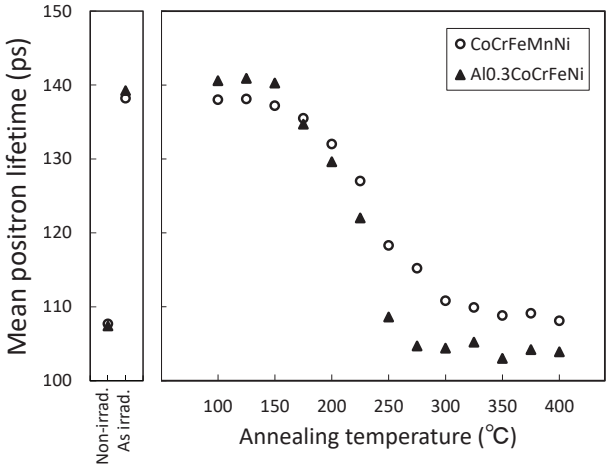

Fig. 1 Mean positron lifetime of electron irradiated CoCrFeMnNi and $Al_{0.3}CoCrFeNi$ high entropy alloys after isochronal annealing.

REFERENCES:
[1] C. Y. Hsu, J. W. Yeh, S. K. Chen, T. T. Shun: Metall. Mater. Trans. 35A, (2004), 1465.
[2] J. W. Yeh, S. K. Chen, S. J. Lin, J. Y. Gan, T. S. Chin, T. T. Shun, C. H. Tsau, S. Y. Chang: Adv. Eng. Mater. 6 (2004). 299.
[3] J. W. Yeh: Ann. Chim. Sci. Mat. 31, (2006), 633.

CO4-14 Construction of EO Sampling Detection System of Coherent Transition Radiation with Optical Cherenkov Radiation

T. Takahashi

Institute for Integrated Radiation and Nuclear Science, Kyoto University

INTRODUCTION: In recent years the THz-TDS has been widely used in the THz spectroscopy. The merit of the system is direct observation of the electric field. The conventional spectroscopic system using a bolometer can detect only the power of THz wave. Therefore the Kramers-Kronig analysis is necessary in order to calculate the optical constant. One of the detection system in the THz-TDS is the Electro-Optical (EO) sampling in which the induced birefringence by the Pockels effect is used. In the coherent THz radiation beamline [1] at the KURNS-LINAC, the bolometer has been used to detect the coherent radiation for a long time. In recent years, the application of the EO sampling to the detection of coherent transition radiation (CTR) in this beamline has been planned. Usually an ultrafast laser is used as a probe light in the THz-TDS. The strong point in this report is the usage of Cherenkov radiation in the visible region as a probe light. There is no jitter between CTR as the excitation light and Cherenkov radiation as the probe light. These are perfectly synchronized each other.

EXPERIMENTAL PROCEDURES: In AY2020, the beamtime of the linac was not enough to perform the experiment due to the covid-19 related confusion and some renovation work in the linac. In this report, only the experimental setup has been reported. The sub-THz radiation is the superposition of the forward CTR from the Ti-window and backward CTR from an aluminum-coated silica grass as shown in the Fig.1. The visible light for a probe of the EO-sampling is the Cherenkov radiation from a silica grass 5 mm thick. A ZnTe plate 1 mm thick is used as the EO device. The visible light is passed through a ZnTe plate, polarizer, a λ/4 retarder, and a Wollaston prism as shown in Fig.2. It is finally detected by a balanced detector which consists of two photo-diode detectors and amplified by a lock-in amplifier.

REFERENCES:

[1] T. Takahashi *et al.*, Rev. Sci. Instrum. **69** (1998) 3770.

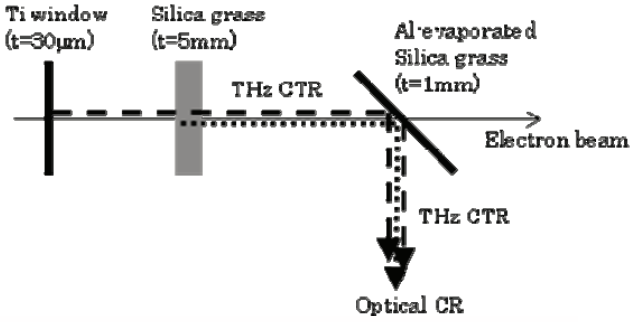

Fig.1. The schematic layout around the radiation source.

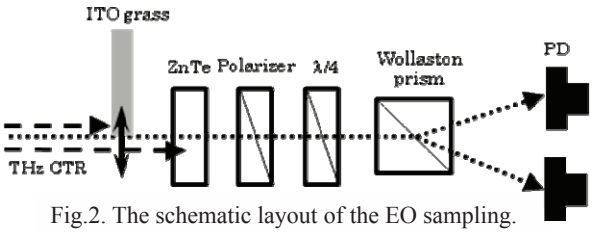

Fig.2. The schematic layout of the EO sampling.

CO4-15 Measurement of the Internal Pressure and Lifetime of Ultrafine Bubbles

D. Hayashi, M. Tanigaki[1]. Y. Ohkubo[1], A. Taniguchi[1], Y. Ueda[2], Y. Tokuda[3]

Graduate School of Science, Kyoto University
[1]KURNS
[2]Research Institute for Sustainable Humanosphere, Kyoto University
[3]Department of Education, Shiga University

INTRODUCTION: Ultrafine bubble (UFB), a bubble smaller than 1 μm, attracts so much attention because of its various applications, e.g., promoting the growth of fishery products. On the other hand, a fundamental study is not well extended because of the difficulty in the optical observation due to its smaller diameter than the wavelength of radiant-ray. Basic physical quantities of UFB are not investigated such as inner pressure, temperature, and lifetime.

Yamakura succeeded in measuring the pressure of UFB directly by the angular correlation measurement [2] based on the dependence of the anisotropy of cascade γ-rays of ^{125}I towards carrier-gas pressure [3].

In this paper, the extended studies of UFB by using the angular correlation measurement on the internal pressure and lifetime of UFB are introduced.

EXPERIMENTS: The pure water containing UFB of natural Xe gas with an average diameter of 100 nm was generated via the pressurized dissolution method. 4.0 ml of UFB water and saturated solution of natural Xe were separately packed to 4.5 ml polypropylene tubes and irradiated by thermal neutrons with the total dose of 6.9×10^{16} n/cm^2 at the slant exposure tube of Kyoto University Research Reactor (KUR) to activate ^{125}Xe through the reaction of ^{124}Xe (n, γ) ^{125}Xe. A different pair of samples was irradiated every few days to evaluate the time dependence of the remaining Xe in the samples. γ-γ cascades of 55 - 188 keV from ^{125}I obtained as the decay product of ^{125}Xe were detected by a CdZnTe detector (CZT) and one of two BaF_2 detectors. These two BaF_2 detectors are placed at the fixed angle of 90°, and a CZT on a turntable moves around the sample tube. With this configuration, the angular correlations of both 90°-θ and 180°+θ are measured at the same time. The correlation function of γ-γ cascade under the existence of hyperfine interaction is given as,

$$W(\theta) = 1 + A_{22}\overline{G_{22}(\infty)}P_2(\cos\theta)$$

where A_{22} is a constant of angular correlation, $\overline{G_{22}(\infty)}$ is a perturbed constant and the attenuation factor caused by hyperfine interactions.

RESULTS AND DISCUSSION: $A_{22}\overline{G_{22}(\infty)}$ for 55-188 keV cascade in ^{125}I was determined to be $+0.088 \pm 0.012$ from the obtained angular correlation (Fig.1). The pressure dependence of $A_{22}\overline{G_{22}(\infty)}$ for the 203 keV state in ^{127}I in Xe gas was well studied by Berek [3]. The result of ^{127}I can be converted to that of ^{125}I by simply applying the A_{22} for these states. From the obtained pressure dependence of $A_{22}\overline{G_{22}(\infty)}$, the internal pressure of UFB is tentatively determined to be $(4.15 \pm 0.67) \times 10^5$ Pa. The present result coincides with the result of Yamakura, $3.4^{+2.3}_{-1.3} \times 10^5$ Pa.

The time dependences of γ-γ cascades for both Xe-UFB samples and saturated Xe solution showed similar trends (Fig.2), and the $A_{22}\overline{G_{22}(\infty)}$ of saturated Xe solution corresponds to that of Xe-UFB. These results strongly imply the existence of Xe-UFB in the samples of saturated Xe solution. Terasaka recently reported the production of Xe-UFB by vibration or pressurization/depressurization of aqueous solutions of the gas [4]. Xe-UFB were possibly produced in the present experiment during the sample preparation or the transportation. Therefore, the lifetime of UFB is tentatively determined to be $(4.5 \pm 3.2) \times 10^2$ h from both time spectra. Additional lifetime measurements in a longer time span are expected.

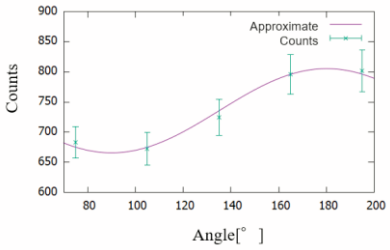

Fig.1. A typical anisotropy of the angle composed of the two 55-188keV cascades from ^{125}I in ^{125}Xe-gas.

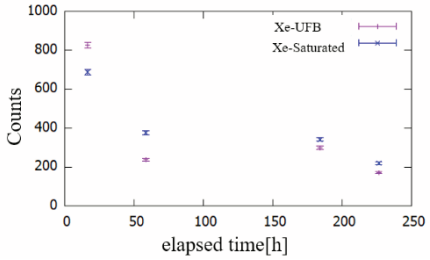

Fig.2. The time dependence of the 55-188keV cascade events of ^{125}I.

REFERENCES:

[1] J.G.HAn et.al, 'Lomg-term stability of hydrogen nanobubble fuel', Fuel 158 (2015) 399–404.
[2] T.Yamakura, Master Thesis 2018.
[3] U.Berek et al., Phys. Lett. 53A (1975) 251.
[4] K.Terasaka et al, Japanese J of Multiphase Flow, 10.3811/jjmf.2020.030.

CO4-16 Porosity Measurements of Sintered-Silver Bonding Plates

K. Wakamoto[1], T. Otsuka[1], K. Nakahara[1], A. Yabuuchi[2] and A. Kinomura[2]
[1]*Power Device R&D Department, ROHM Co., Ltd.*
[2]*Institute for Integrated Radiation and Nuclear Science, Kyoto University*

INTRODUCTION: Sintered silver has attracted much attention as a die-attach material for the power electronics, owing to its high heat dissipation capability [1]. On the other hand, the coefficient of thermal expansion (CTE) inevitably does not match each other of the materials used in a power system. Thus the heat-cycle oriented mechanical stresses deteriorate die-attach materials, and therefore the mechanical properties of sintered silver impinge on the reliability of electricity systems.

However, nobody can predict how long sintered silver sustains, because the material is porous and its mechanical properties heavily depends on how porous it is. Accordingly, the research is highly demanded to measure the porosity.

The porosity rate (p) of sintered silver is reported by some papers [2-3], where p is measured by using cross sectional scanning electron microscopy (SEM). These studies focus only on estimates the μm-order pores of sintered silver materials, not nm-order pores such as crystalline defects. Positron lifetime spectroscopy has advantages for this purpose. In this study, therefore, the authors evaluated nanometer-order pore sizes embedded in sintered silver with various p's by measuring the positron lifetime of the bulk material.

EXPERIMENTS: The fabrication process of sintered silver films is described as follows. Paste including silver nm-particles was stencil printed on a metal plate, and the containing organic solvent was dried at 140ºC for 1 h. These dried films were sintered at 200 - 300 ºC for 10 min with uniaxial press via a carbon buffer sheet with 0.5 – 120 MPa pressure. The film shape was 5 mm square and 50-μm thick. Positron annihilation lifetime spectroscopy was performed to evaluate bulk lifetimes of the samples by using a ^{22}Na source sealed with 12.5 μm Kapton foils. Four sample plates were stacked and measured together to stop all the positrons from the source inside the sample. The measured samples are summarized in Table I.

Table I Summary of the measured specimens.

Set	Sample	Sintering temp. (ºC)	Pressure (MPa)	Sample size
1	B,C,D	300	60,10,5	5mm square and 50-μm thick
2	A,B,C,D	300	120,80, 30,0.5	
3	E,F,G	300,240, 200	30	

The spectrometer consists of two scintillation gamma-ray detectors with BF_2 crystals and a spectrometer based on digital circuits. Total counts for each measurement were approximately 10^6 counts.

RESULTS: The data from the first and second sample sets to investigate pressure dependence was analyzed as follows. Measured lifetime spectra were decomposed into three components as shown in Fig. 1. It should be noted that the second lifetime was fixed to the previously reported value of dislocations in Ag (0.2 ns). The intensity of the second lifetime component changed in the range of 0.5 – 10 MPa, while the intensity of the third lifetime component corresponding to vacancy clusters were almost constant. Average lifetimes calculated from lifetime and intensity values were stable in the range of 0.20 – 0.23 ns (not shown) for all the samples. In previous studies using secondary electron microscopy (SEM), the porosity of the samples significantly changed depending formation pressure in the same range. The result of this study suggests that the information obtained from the positron measurements is clearly different from that obtained by the SEM observation.

In summary, nanometer-order porosity of sintered Ag plates was characterized as a function of formation pressure and temperature by conventional positron annihilation lifetime spectroscopy. The intensity of the second lifetime component corresponding to dislocations changed depending on formation pressure, while the average lifetime was almost constant.

REFERENCES:

[1] KIM S. SIOW, Journal of ELECTRONIC MATERIALS., **43** (2014) 947-961.
[2] T. Yousseff *et al*., Microelectronics Reliability., **55** (2015) 1997-2002.
[3] M. Takesue *et al*., Proc. PCIM., (2018) 148.

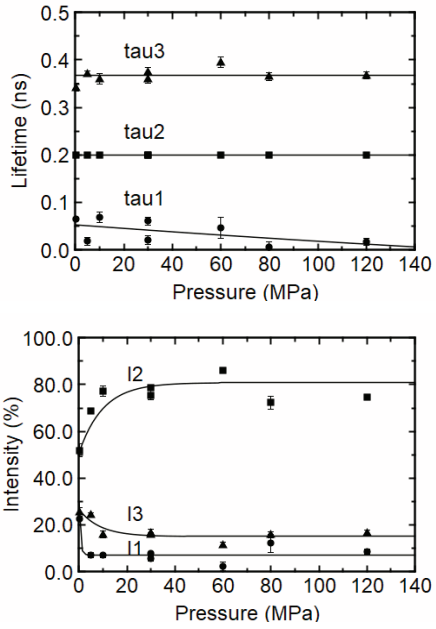

Fig. 1 Lifetimes and their intensities of the samples.

CO4-17 Demagnetization Measurement of Permanent Magnet Materials Against Neutrons Irradiation

Y. Fuwa[1], Y. Iwashita[2], Y. Kuriyama[3] and K. Takamiya[3]

[1]*J-PARC Center, Japan Atomic Energy Agency*
[2]*Insistute for Chemical Research, Kyoto University*
[3]*Institute for Integrated Radiation and Nuclear Science, Kyoto University*

INTRODUCTION: Permanent magnets are essential materials for particle accelerator components such as beam optical devices, insertion devices, and so on. In order to estimate the lifetime of the devices in a high-radiation environment, the demagnetization effects of permanent magnet materials were measured using Kyoto University Research Reactor (KUR). While rare earth magnets, such as NdFeB and SmCo, are known to have radiation demagnetization [1], there is not enough information for ferrite magnets, which are economical but have less remanent field strength. Furthermore, the demagnetization effect of NdFeB magnets is relatively wide fluctuations in the previous research. In order to acquire more precise insight into the demagnetization effect of permanent magnetic materials, we carried out a systematic experiment for measuring the demagnetization rate of the materials.

EXPERIMENTS: Samples for our experiments were anisotropic ferrite magnets, NdFeB magnets, and SmCo magnets. The shape of the samples was cylindrical with 5 mm diameter and 1 mm length that have easy-axis parallel to the cylinder axis.

We compared the magnetic field strength before and after the irradiations. In the measurement, Since the measurement using the Hall probe was sensitive to the positioning error of magnets, another measurement method was developed. In this method, the small magnet samples were rotated in a coil and the amplitude of the induced voltage was taken. This method is less sensitive to positioning errors.

The irradiation times were up to 4 hours at 1 MW operation (for Pn), 46 hours 1 MW operation and 6 hours at 5 MW operation (for HYD), and 4 weeks (for Long term irradiation plug). In these three irradiation conditions, estimated values of thermal neutron fluence on the samples are 7.0 x 10^{16} [n/cm^2], 5.7 x 10^{18} [n/cm^2] and 8.6 x 10^{18} [n/cm^2], respectively. After the residual radioactivity of the magnet and capsule decayed sufficiently, we took out the magnet samples from the capsule and measured the magnetic field.

RESULTS: For the results of NdFeB magnets, which have the highest residual magnetic field among the permanent magnet materials, the demagnetization rate leaches down to 80% with the neutron irradiation dose of 8.8 x 10^{14} [n/cm^2]. In this dose region, no demagnetization effects were detected for SmCo and ferrite magnets. SmCo magnets indicated no demagnetization effect up to 7.0 x 10^{16} [n/cm^2]. For the ferrite magnets, Fig. 1 shows the ratios of the magnetic field strength before and after the irradiation. The error bars show the standard deviations of measured data for each magnet. The broken vertical green line in Fig. 1 denotes the neutron dose at which radiation demagnetization becomes significant for NdFeB magnets as a comparison. According to the data taken so far, the characteristic radiation demagnetization dose is estimated at about 1.4 x 10^{20} [n/cm^2]. Because of the regression function form, the data points at fewer radiations have almost no effect on the fitting result. The magnetization will be degraded to half at a dose of about 1 x 10^{20} [n/cm^2].

PERSPECTICVE: The radiation hardness level of ferrite magnets close to those for SmCo magnets is important information for communities handling radiations. The ferrite magnets would be widely used in such applications. In our experiments, irradiation of ferrite magnets with 8 weeks and 12 weeks was performed. Since residual radioactivity was high for magnetization measurements, the measurement will be performed in 2021 after the radioactivity decays sufficiently. The results will show more information for the demagnetization of ferrite magnets.

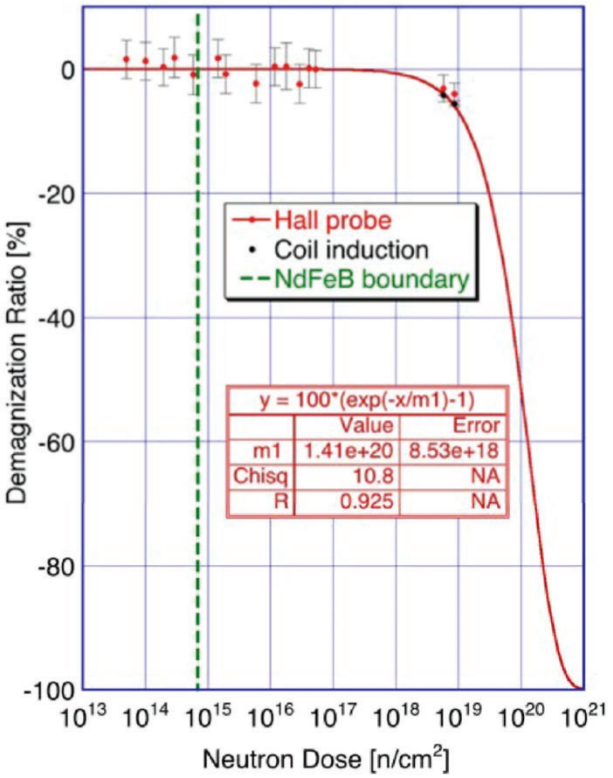

Fig. 1. Ratio of radiation demagnetization of ferrite permanent magnet.

REFERENCES:

[1] X. -M. Marechal, T. Bizen, Y. Asano, H. Kitamura, Proceedings of EPAC, Edinburgh, Scotland, 2006.

CO4-18 Neutron scattering study on microstructure of vitrified radioactive wastes

K. Kaneko, R. Motokawa, Y. Ohba, K. Mori[1], R. Oku-mura[1]

Materials Sciences Research Center, Japan Atomic Energy Agency
[1]Institute for Integrated Radiation and Nuclear Science, Kyoto University

INTRODUCTION:

The vitrification technique is used to immobilize high-level radioactive liquid wastes, which are yielded during reprocessing of nuclear fuels[1]. The high-level wastes are mixed with melted borosilicate glass, that results in forming an oxide. Among the constituents, molybdate tends to precipitate, that cause lowering of durability[2]. The segregation of platinoids is also problematic on fabrication[3]. In order to realize a long-term stability, deep understanding of the vitrification process becomes important.

Neutron diffraction is powerful probe to study structures of glass as it can access to high-Q range. In addition, its high transmission allows to investigate the vitrified waste as it is, namely, without crashing into powder required for x-ray. The latter could be essential to obtain an actual form of the waste. On the other hand, one of difficulties of neutron scattering arises from the fact that one of main constituents, boron, is strong neutron absorber. To avoid this issue, we prepared sample using ^{11}B enriched boron, and succeeded to observe neutron scattering pattern from the borosilicate glass without wastes. We extended the study for the sample with simulated wastes.

EXPERIMENTS:

The borosilicate glass with and without simulated radioactive wastes were prepared with an enriched ^{11}B, and to have cylindrical form with diameters for 5 mm and 10 mm, respectively.

Neutron diffraction experiments were performed on the versatile compact diffractometer installed at the B-3 beam port. Neutrons with a wavelength of 1 Å are provided by a Cu monochromator. An array of the ^{3}He detectors which covers 25˚ in the scattering angle enables efficient measurements.

RESULTS:

Figure 1 shows neutron transmission images of the borosilicate glass with and without simulated radioactive waste measured on the B-3. Whereas the borosilicate glass itself has sufficient transmission over 85 % as in Fig.1(a), almost no neutron can pass through the sample with simulated waste (Fig. 1(b)). By carefully check detailed composition, we identified that the simulated waste contains small fraction of Gd, being known as one of highest neutron absorber. To suppress absorption with keeping chemical characteristics, we replace Gd_2O_3 by La_2O_3. This substitution succeeded to increase transmission over 48 %. Neutron scattering pattern for this simulated waste glass sample is plotted in Fig. 2, together with the same borosilicate glass without wastes. The clear scattering patterns are successfully obtained for both samples. In addition, the data allow to identify that the mixing of waste gives rise to peak shifts and broadening from the raw glass, as clearly seen for peaks around 15˚ and 50˚. This result confirms that a part of wastes is incorporated into a network structure of the glass.

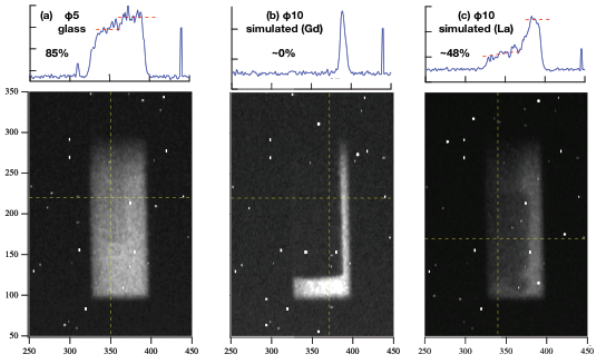

Fig. 1. Neutron transmission image of the borosilicate glass (a) without and (b,c) with simulated radioactive wastes. One of the constituents of simulated waste, Gd_2O_3, in the sample (b) is replaced by La_2O_3 in the sample (c) to avoid strong neutron absorption of Gd.

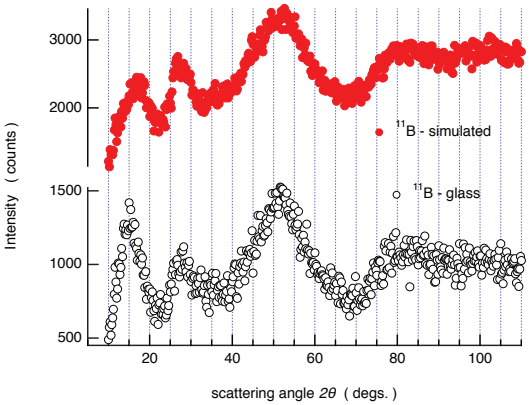

Fig. 2 Neutron scattering pattern of the borosilicate glass with and without simulated radioactive wastes.

The present result proves that neutron scattering can offer further insights into the structure of the borosilicate glass and impact of wastes for it. Further study on the simulated waste with different compositions and fabrication conditions will enable us to optimize the vitrification of the radioactive waste.

REFERENCES:

[1] G. Roth, S. Weisenburger, Nucl. Eng. Des. **202**, 197e207 (2000).
[2] S. Morgan *et al.*, Mater. Res. Soc. Symp. Proc. **807**, 151e156 (2003).
[3] H. Mitamura *et al.*, Nucl. Chem. Waste Maenag. **4**, 245e251 (1983).

CO4-19 Research on Polymer Composite Materials Containing Ion-implanted Metal Nanoparticles Using a Slow Positron Beam

Y. Kobayashi[1], T. Kavetskyy[2], A. Yabuuchi[3] and A. Kinomura[3]

[1]*Waseda Research Institute for Science and Engineering, Waseda University*
[2]*Department of Biology and Chemistry, Drohobych Ivan Franko State Pedagogical University*
[3]*Institute for Integrated Radiation and Nuclear Science (KURNS), Kyoto University*

INTRODUCTION: Controlling the size of nanoparticles (NPs) in a polymer matrix is important for fabrication of nanocomposites with foreseen properties for their applications in nanophotonics, electronics, biomedicine, etc.. In particular, the nanocomposites containing Ag-NPs dispersed in the polymer matrix by low-energy (< 100 keV) ion implantation with high ion fluences (> 10^{16} ions/cm^2) can be used for fabrication of plasmonic waveguides [1] and diffraction gratings as well as for anti-microbial applications.

Positron annihilation spectroscopy (PAS) employing a variable-energy slow positron beam is a versatile technique for characterization of defects in thin films, allowing depth-profiles from tens of nanometers up to several micrometers. This technique has been successfully utilized as a major experimental tool to understand carbon nanostructures kinetics during high fluence B ion implantation into polymethylmethacrylate (B:PMMA) [2].

In our previous studies [2,3], usage of both Doppler broadening and positron lifetime methods in combination with other tools (e.g. UV-Vis absorption and Raman spectroscopy) allowed successful verification of the formation of carbon nanostructures in B:PMMA samples. A key point for such conclusion in the case of ion-implanted B:PMMA was positron annihilation lifetime spectroscopy (PALS) data at the positron energy corresponding to a depth of implanted range of the sample with maximum radiation damage, showing no *ortho*-positronium (*o*-Ps) yield at high ion fluences (> 10^{16} ions/cm^2); the same, there is no *o*-Ps yield in carbon based materials such as, for instance, fullerene C^{60} cage and carbon molecular sieve membranes. Thus, taken this *o*-Ps yield feature in carbon based materials into consideration, it is expected that similar important information should be obtained for investigating the ion-synthesized silver nanoparticles in polymer matrixes containing carbon clusters or carbon nanostructures formed upon ion bombardment.

EXPERIMENTS: The positron pulsing system of the KUR slow positron beam system have been developed for PALS of thin films or near-surface layers. It is confirmed that the pulsing system is effective for samples with relatively short positron lifetimes (τ < 1 ns) such as metals and semiconductors without o-Ps formation. In this study, we examine the validity of the PALS measurement system of the KUR slow positron beamline for samples with o-Ps components. Acceleration energies of 2 - 3 keV was used for PALS measurements.

RESULTS: Figure 1 shows the Kapton spectrum (closed circles) with simulated spectra (solid and broken lines) after background subtraction. The simulated spectra assumed two lifetime components with the Kapton lifetime and longer lifetimes (2, 5 and 10 ns with 10% intensity). One of the problems with PALS measurements in the KUR system is higher background signals. Indeed, unwanted satellite peaks originating from a radiofrequency-driven-buncher exist on the background signals with a period of the buncher signal as shown in Fig. 1. Such signals prevent appropriate o-Ps lifetime/intensity determination in PALS measurements. The simulated spectra in Fig. 1 suggest that relatively shorter o-Ps components (<5ns) are acceptable. But, for the longer o-Ps component, appropriate fitting or background-subtraction procedures are required. Figure 2 shows the lifetime spectrum for a polymer thin film for a trial measurement. In this case, an o-Ps component can be observed but its lifetime is sufficiently shorter to avoid the influence of the satellite peak.

In summary, the PALS measurement system of the KUR slow positron beamline was applied for polymer materials with long lifetime (o-Ps) components. The result suggested that the PALS system was effective for relatively shorter o-Ps components.

REFERENCES:

[1] T. Kavetskyy *et al*., Phys. Status Solidi C, **9** (2012) 2444-2447.
[2] T. Kavetskyy *et al*., J. Phys. Chem. B, **118** (2014) 4194-4200.
[3] T.S. Kavetskyy, A.L. Stepanov, in *Radiation Effects in Materials*, edited by W.A. Monteiro (InTech, Rijeka, 2016), p. 287-308.

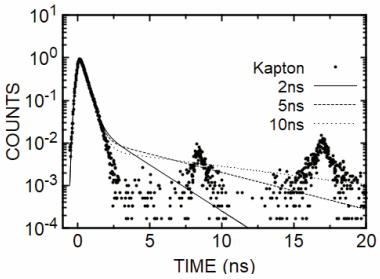

Fig. 1 Kapton spectrum and simulated spectra with long lifetime components.

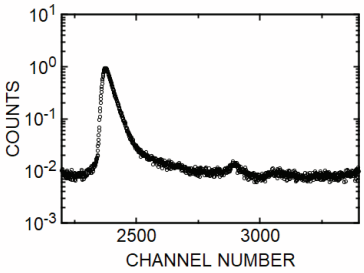

Fig. 2 Spectrum of the measured polymer film.

CO4-20 Study of resonant frequency change with irradiation dose of piezoelectric PZT element

M. Kobayashi, T. Miyachi, S. Takechi[1], Y. Morita[1], Reo Kunimatsu[2] and Ryo Sasaki[2]

Planetary Exploration Research Center, Chiba Institute of Technology
[1]Graduate School of Engineering, Osaka City University
[2]Department of Engineering, Osaka City University

INTRODUCTION: The aim of this research is to establish an inexpensive method for dosimetry in high dose environments. We consider the use of the change in piezoelectricity of piezoelectric elements due to irradiation for dosimetry in high dose environments. For this purpose, we have investigated the mechanism of radiation-induced change in piezoelectricity by experiments. As in the past, this year we conducted another experiment to investigate the change in piezoelectricity caused by electron beams.

In a previous experiment conducted at HIMAC/NIRS, we irradiated a piezoelectric PZT element with 400 MeV/n Xe particles and investigated the decrease in the electromechanical coupling coefficient k [1]. It was shown that the energy imparted was proportional to the decrease in the coupling coefficient of the irradiated PZT element.

In this study, we have conducted an experiment using electron beam to investigate the effect of electron beam on the decrease in the coupling coefficient of the irradiated PZT element at KUR/LINAC. As a result, it was found that the electromechanical coupling coefficients decreased linearly with the absorbed dose in electron irradiation, although the change was smaller than that in Xe irradiation. Even though the absorbed dose is the same, the change in the electromechanical coupling coefficient is more than one order of magnitude smaller for electron irradiation.

Over the past few years, we have been experimenting with improved and modified experimental setups in order to obtain more accurate values. We improved the alignment of the element installation and the air-cooling method to stabilize the element temperature, thereby stabilizing the accumulation of measured values. In addition, we measured the PZT temperature during irradiation and corrected the amount of change in k due to the temperature rise, which was measured separately using a thermostatic bath. With these measures, the variation of the piezoelectricity change was eliminated, and the piezoelectricity change due to electron beam irradiation could be measured accurately.

EXPERIMENTS: Although we found that the piezoelectricity (electromechanical coupling coefficient k) changes linearly with the amount of electron beam irradiation, there was an event where the value of k changed discontinuously before and during the experiment. Until last year, in order to measure k, we soldered a cable to the PZT device and connected it to the impedance analyzer. In other words, when the cable was soldered to the PZT device, the temperature of 200°C or higher was applied locally even for a short period of time, and we could not eliminate the possibility of k changing due to this. To solve this problem, we used a phosphor-bronze plate spring to fabricate an electrode to contact the cylindrical PZT device between them, and used it as an irradiation jig. As a result, the discontinuous change of k before and after the experiment was eliminated, and the change of k in response to the amount of electron irradiation could be investigated more accurately.

FUTURE PERSPECTIVE: Based on the results to date as described above, we are considering the following experiments to be conducted in the future.

(1) *Effect of PZT element shape*: In our previous experiments, we have used a cylindrical PZT element with a diameter of 18mm x t12mm. To calculate the electromechanical coupling coefficient *k, we used an* approximate equation that can be applied to a disk-shaped element (applicable to a diameter > 10 times the thickness), which is probably fine for the purpose of knowing the relative change, but may be problematic when discussing the validity of the approximate equation. Therefore, we would like to investigate the adaptability by using a PZT device with a shape that meets the conditions of the approximation formula (disk shape with diameter > 10 times the thickness).

(2) *Types of PZT elements (soft material, high temperature soft material, high temperature hard material)*: The PZT devices used in our experiments so far are so-called "soft materials" and have a relatively low Curie temperature. By investigating the characteristics of other types of PZT elements, we hope to elucidate the mechanism of piezoelectricity change by radiation irradiation and to apply it to radiation measurement devices.

(3) *Effects of Neutrons*: After electron irradiation, PZT elements radiate and emit characteristic gamma rays. This is the possibility that the PZT element loses its piezoelectricity due to inelastic scattering by neutrons or nuclear reaction by neutron capture. To consider this, we would like to measure the neutron flux during electron irradiation at the LINAC.

REFERENCES:

[1] S. Takechi et al., Japanese Journal of Applied Physics 60 038003 (2021)
[2] M. Kobayashi et al., Japanese Journal of Applied Physics 53, 066602 (2014).
[3] M. Kobayashi et al., Japanese Journal of Applied Physics 52, 126604 (2013).

R2110

CO4-21

Tritium recovery behavior for tritium breeder of Li_4SiO_4 – Li_2TiO_3 mixture material

Y. Oya[1,2], S. Hirata[2] K. Ashizawa[2], Y. Koyama[2], F. Sun[1], Y. Iinuma[3]

[1]*Faculty of Science, Shizuoka University*
[2]*Graduate School of Integrated Science and Technology, Shizuoka University*
[3]*Institute for Integrated Radiation and Nuclear Sci-ence, Kyoto University*

INTRODUCTION: In the fusion reactor blanket, tritium is produced by (n, α) reaction with lithium. Solid lithium ceramic is considered as one of candidates for blanket materials. Especially, Li_2TiO_3 and Li_4SiO_4 are regarded as one of the promising solid breeder candidates due to relatively higher chemical stability and higher lithium atom density. For Li_4SiO_4, lithium atomic density is higher than that for Li_2TiO_3, but its chemical stability is not good. Recently, Li_4SiO_4-Li_2TiO_3 mixture materials are proposed as advanced candidates to compensate for shortcoming, and several mechanical properties have been evaluated. However, the tritium recovery performance was not still understood. In this study, Li_4SiO_4-Li_2TiO_3 mixture materials with various phase ratios were used and their tritium desorption behavior after neutron irradiation was evaluated using tritium thermal desorption spectroscopy (TDS).

EXPERIMENTS: Two kinds of samples with different phase ratios, namely Li_4SiO_4-Li_2TiO_3 (sample 1) and Li_4SiO_4-$2Li_2TiO_3$ (sample 2 and sample 3), were prepared. These materials were pebble samples that dominator 6 mm or less before neutron irradiation. These materials were installed into Kyoto University Research reactor (KUR), and the neutron irradiation was performed with the fluence of ~ 8.0×10^{15} n cm^{-2} or 8.0×10^{16} n cm^{-2}. Only sample 2 was irradiated with higher fluence of 8.0×10^{16} n cm^{-2}. Thereafter, tritium TDS measurement was conducted from R.T. to 1113 K with the heating rates of 5 - 20 K min^{-1}. The amount of desorbed tritium was evaluated by a liquid scintillation counter.

RESULTS AND DISCUSSION: Most of tritium was released as a water-form. Fig. 1 shows TDS spectra for 10 K min^{-1}. Tritium TDS spectra for Li_4SiO_4-$2Li_2TiO_3$ samples with different neutron fluence showed that the release temperature for sample 2 was located at around 520 K and that for sample 3 was around 630 K. Li_4SiO_4-$2Li_2TiO_3$ samples had single tritium desorption stage, and its activation energy was evaluated to be 0.44 - 0.47 eV. This result was almost consistent with that for Li_2TiO_3 sample.[1] The rate-determination step for tritium recovery can be explained by the diffusion-limited process. Li_4SiO_4-Li_2TiO_3 had multi-tritium desorption stages. The activation energy of the most significant tritium desorption peak was estimated to be 0.72 eV. The release temperature for mixture materials was lower than that for Li_2TiO_3 or Li_4SiO_4. The amount of tritium that Li_4SiO_4-$2Li_2TiO_3$ samples released was 1.40 MBq g^{-1} and 1.99 MBq g^{-1}. Lower fluence sample released more tritium than higher fluence sample due to crack-up of samples during neutron irradiation. The amount of tritium for Li_4SiO_4-Li_2TiO_3 sample was 0.79 MBq g^{-1}. Lower activation energy and amount of desorbed tritium, Li_4SiO_4-$2Li_2TiO_3$ has lower activation energy for tritium release, and it will be quite suitable for tritium recovery at lower temperature.

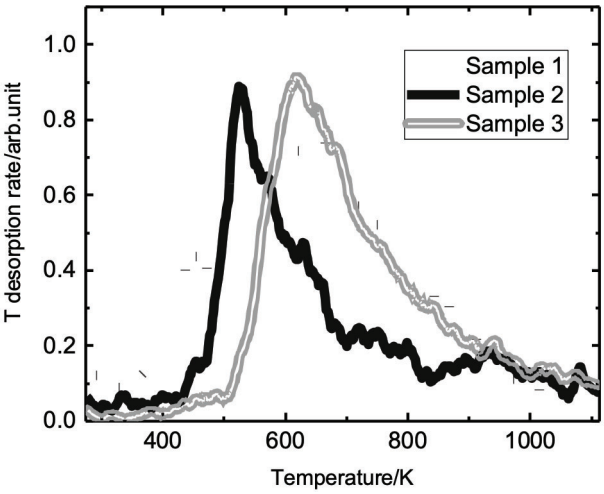

Fig. 1. Tritium TDS spectra for Li_4SiO_4-Li_2TiO_3 (sample 1) and Li_4SiO_4-$2Li_2TiO_3$ (sample 2 and sample 3) with the heating late of 10 K min^{-1}.

REFERENCES:

[1] Qilai Zhou et al., J. Nucl. Mater. 522 (2019) 286-293.

R2115

CO4-22 Formation of radiation defects on tungsten and their influence on effect of hydrogen isotope retention

K. Tokunaga, M. Matsuyama[1], M. Hasegawa,
K. Nakamura and Q. Xu[2]

Research Institute for Applied Mechanics, Khushu University
[1]Hydrogen Isotope Research Center, University of Toyama
[2]Institute for Integrated Radiation and Nuclear Science, Kyoto University

INTRODUCTION: It is of a great importance to clarify phenomena of implantation, retention, diffusion and permeation of tritium (T) on surface of the armor materials of the first wall/blanket and the divertor on fusion device from a viewpoint of precise control of fuel particles, reduction of tritium inventory and safe waste management of materials contaminated with tritium. Refractory metals such as tungsten (W) is potential candidate for the armor of the first wall and the divertor plate of the fusion reactor because of its low erosion yield and good thermal properties. The armor material will be subjected to heavy thermal loads in the steady state or transient mode combined with high energy neutron irradiation that will cause serious material degradation. In addition, high energy runaway electrons would bombard the armor materials along the equatorial plane in fusion device. It is considered that these cause radiation damage and enhance tritium retention. In the present works, T exposure experiments have been carried out on W samples which were irradiated by high energy electrons to investigate effects of high energy electrons irradiation on microstructure and tritium retention of W. In this fiscal year, pure W and recrystallized W were irradiated by high energy electron beam. Before and after that, positron annihilation experiment was carried out to identify the radiation defect. In addition, EBSD（Electron Back Scatter Diffraction Patterns）analyses has been carried out on the specimens before and after the electrons irradiation. Tritium exposure experiments have been carried out using a tritium (T) exposure device.

EXPERIMENTS: W samples used were ITER specification W (ALMT-grade) (SR-W) and its recrystallized W (RC-W). The SR-W was fabricated via a powder metallurgical route including cold isostatic pressing, sintering, hot rolling, and heat treating to relieve the residual stresses. Some of the machined SR specimens were subjected to a full recrystallization treatment at 2000 ºC for 1 hr in vacuum. Sizes of the specimens were 10 mm x 10 mm x 1mm (10 mm x 10 mm : ND-TD). The surface of the both samples were polished to be mirrored. High energy electrons irradiation has been carried out using LINAC in Institute for Integrated Radiation and Nuclear Science, Kyoto University. An peak energy of electron irradiated was 8 MeV and DPA was 5.8 x 10^{-3}. Temperature during the irradiation was measured by thermocouples which was contacted with a backside of the W samples. Before and after that, positron annihilation experiment was carried out to identify the radiation defect. In addi-tion, EBSD（Electron Back Scatter Diffraction Patterns）analyses has been carried out on the specimens before and after the electrons irradiation. T exposure experiments have been carried out using a T exposure device in University of Toyama. Pressure of the T gas was 1.3 kPa and T exposure was kept for 4 h. T concentration in the gas was about 5 %. After the exposure to T gas, T amount retained in surface layers of the sample was evaluated by β-ray-induced X-ray spectrometry (BIXS) and imaging plate (IP) measurements.

RESULTS: Figure 1 shows X-ray spectra observed for the SR-W(a) and RC-W(b) which were not irradiated by the high energy electrons. Temperature of T exposure is 350ºC. In the case of SR-W, WM_α, ArK_α, WL_α and bremsstrahlung X-rays are detected. These results indicate that T exists deeper area than that of RC-W. This is considered that T traps with the internal defects in the SR-W. T exposure on the samples after the electron irradiation is undergoing.

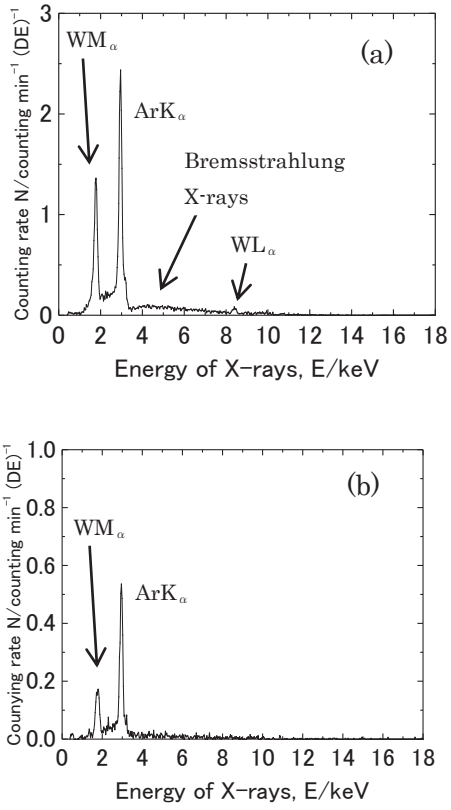

Fig. 1. X-ray spectra for SR-W(a) and RC-W(b) by BIXS.

CO4-23 SAXS Analysis of Heat Denaturation of Soybean Proteins

N. Sato, A. Okuda, K. Morishima, R. Inoue, R. Urade, and M. Sugiyama

Institute for Integrated Radiation and Nuclear Science, Kyoto University

INTRODUCTION: Soybean has long been served as dietary food because of its rich nutritional ingredients, especially proteins. Various kinds of soybean food products such as *miso*, *tofu*, and *tofu* skin (*yuba*) have been produced and eaten as well as unprocessed soybeans themselves. Recently soybean proteins are utilized as soy protein isolate (SPI) in food industries to be added in other food products to improve their physical properties, such as water retention, binding property, and gelling property. Soybeans also play a crucial role in producing mimic meat for vegetarians and vegans. Since soybeans contain an exceptionally high amount of protein for a plant, they are regarded as the most proper alternatives for animal meat. The physical properties of those food products are subject to those of soybean proteins. Therefore it is important to understand the nature of soybean proteins to produce high quality not only soybean food products but also SPI-containing food products, and mimic meat.

Physical properties of protein-containing food products have close relationship with their assembly structure of their component protein molecules in the nanometer scale. In general, raw materials of foods are finely ground, dispersed in water, and then heated. Therefore structural changes of the proteins in hydrates or solutions induced by heat are a significant issue both from scientific and industrial points of view. However, the nanostructural analysis of food products is often difficult owing to their disordered nature, opacity, and aggregation. Small-angle X-ray and neutron scattering (SAXS, SANS) are powerful tools for investigating nanostructure of those kinds of materials. A great number of SAXS and SANS researches has been carried out until now for so-called soft matters, such as rubber, colloids, and polymer gels. By taking advantages of their feature, we have been focusing on the nanostructural analyses of plant food proteins of wheat and soybean by SAXS and SANS. One of our studies is regarding the structure of the assembly of wheat protein gliadins in a wide concentration range of water [1].

In the present study, we investigated thermal denaturation process of two major soybean proteins, β-conglycinin and glycinin, which have been conventionally referred to as 7S and 11S, respectively, according to their sedimentation coefficients determined by analytical ultracentrifugation. Structural changes induced by thermal treatment was investigated by SAXS as the treatment temperature changing was changed, and the difference of heat-resisting property between 7S and 11S was revealed under the various conditions of buffer solutions.

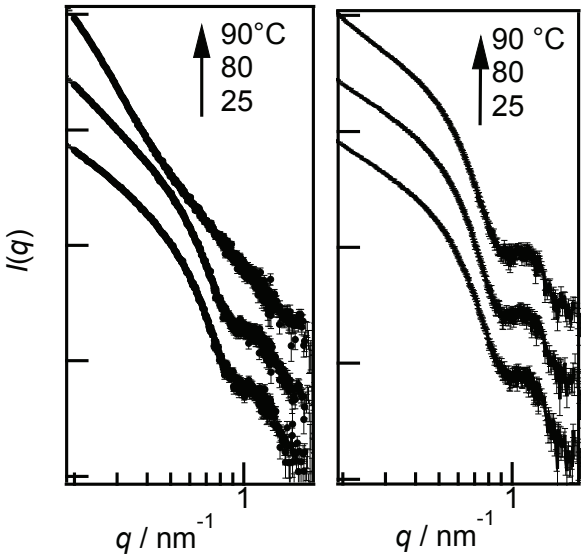

Fig. 1 SAXS profiles for 11S in KPi buffer solutions. NaCl concentration was 0 M(left) and 0.4 M (right).

EXPERIMENTS: Soybean proteins 7S and 11S were extracted from hexane-defatted powder of soybean cultivar "Enrei" under a reducing condition with 2-mercaptoethanol. Isoelectric precipitation was applied to isolation of each protein. By adjusting pH of the extract solutions, 11S and 7S was precipitated at pH 5.8 and pH 4.5, respectively. SAXS measurements were performed with a laboratory SAXS instrument (NANOPIX, Rigaku) installed at Institute for Integrated Radiation and Nuclear Science, Kyoto University. Each protein was dissolved as to be a concentration of 3% in a 35-mM potassium phosphate (KPi) buffer solution at pH 7.5 in presence of 0 or 0.4 M NaCl. The solutions were kept at a given temperature for 5 min and then cooled to 25°C. After that, they were put into aluminum cells and set for SAXS measurements. The wavelength of X-ray was 1.54 Å, the sample-to-detector distance was 1300 mm and the available q-range was 0.1 – 2.0 nm^{-1}.

RESULTS: The SAXS profiles for 7S and 11S showed a peak around 1.2 nm^{-1}, indicating trimer ring structure composed of three subunits of the protein. The peak was obvious for 7S and 11S both with and without NaCl, but became vague for 7S around 75°C. This fact shows that the ring structure of 7S is lost around this temperature due to denaturation of the protein. In contrast, as Figure 1 shows, the peak indicating ring structure remained until 80°C without NaCl, and even until 90°C in the presence of NaCl. This result demonstrates that 11S has higher structural stability than 7S against high temperature, and also that NaCl has strengthening effect for reluctance thermal denaturation.

REFERENCES:

[1] N. Sato *et al.*, *J. Agric. Food Sci.*, **63** (2015) 8715.

CO4-24 Study on HPLC Elution Behavior of Metallofullerenes Encapsulating Heavy Lanthanide Elements

K. Akiyama, K. Amekura, S. Nishimura, K. Ikeda[1], T. Kuroda and S. Kubuki

Graduate School of Science, Tokyo Metropolitan University
Department of Chemistry, Tokyo Metropolitan University

INTRODUCTION: Metallofullerene is well known as one of the clathrate compounds which incorporates metal atom inside fullerene cage [1]. The metallofullerenes encapsulating lanthanide element ($Ln@C_{2n}$, Ln: lanthanide atom, n > 30) have two or three charge transferred electrons on the fullerene surface and their electronic state are strongly affected by the number of the charge transferred electrons [1]. On the other hand, it is known that there is a slight difference in the High-Performance Liquid Chromatography (HPLC) retention time of $Ln@C_{82}$ metallofullerene including different Ln atom despite the same number of the charge transferred electron because the HPLC retention time of the fullerene species is strongly affected by the number of π electrons on the fullerene surface [2]. According to the chromatographic theory, HPLC retention time correlates with equilibrium constant *K* of the adsorption/desorption and also follows the van't Hoff equation [3]. From this correlation, the adsorption/desorption enthalpy can be obtained as the slope of the function $1/T$, which reciprocal of the temperature. Since the adsorption/desorption enthalpy is related to the parameters concerning about the electronic state of metallofullerenes such as the polarizability and the dipole moment, it is possible to obtain information about the electronic states of metallofullerenes by studying the temperature dependence of the retention time.
As mentioned above, it is found difference among HPLC retention time depending on the condition in HPLC development, such as temperature. Accordingly, it is necessary to perform the simultaneous multi-elemental analysis. However, since it is impossible to distinguish each metallofullerene by ordinal detection method for monitoring UV absorption, it is strongly required to employ for the radio chromatography in which γ-rays are monitored.
In this study, we tried to clarify the electronic properties of lanthanide in the fullerene cage affected on the multi-stage adsorption/desorption equilibrium in HPLC separation by the radio chromatography.

EXPERIMENTS: Purified $Tb@C_{82}$ metallofullerenes, which was produced by arc discharge method, was mixed with roughly purified C_{60} as a radical scavenger and then was sealed into polyethylene vials. This sample was irradiated by thermal neutrons at pneumatic irradiation facility of Pn-1 in KUR for 4 hours. After the irradiation, this sample was dissolved into toluene and mixed with each other. This toluene solution was injected into a HPLC column of COSMOSIL Buckyprep with the flow rate of 3.2 mL/min at -50 °C employed ethanol/water mixed solution (volume ratio of 80%/20%) with dry ice as a refrigerant. The eluate from the column were collected by every 1 minute from 30 min to 150 min and γ-rays emitted from each sample were measured by Ge detector.

RESULTS: Figure 1 shows the HPLC chromatogram monitored by UV absorption together with radio chromatogram of ^{160}Tb. The γ ray from ^{160}Tb was only observed in 114 min fraction. At the room temperature, HPLC elution peaks of $Ln@C_{82}$ are found around 60 min. $Tb@C_{82}$ is one of the species which has the largest HPLC retention time among each $Ln@C_{82}$ from our knowledge. It is expected that this tendency will not change even at lower temperature, this result is very important as a guide line for the future works.

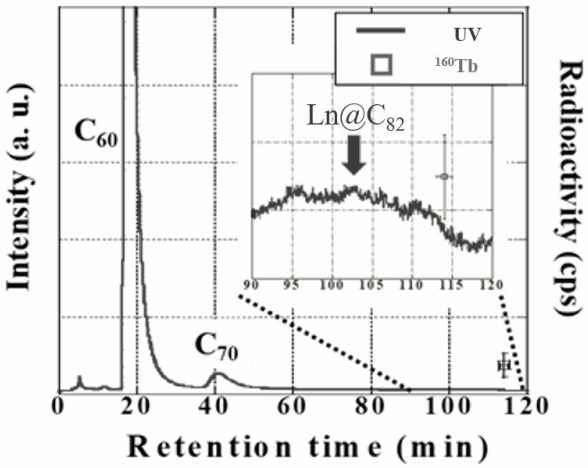

Fig. 1. HPLC chromatogram of fullerenes monitored by UV absorption together with radio-chromatogram monitored by γ-ray emitted from ^{160}Tb.

REFERENCES:
[1] H. Shinohara, Rep. Prog. Phys. **63** (2000) 843-892.
[2] D. Fuchs *et al.*, J. Phys. Chem. **100** (1996) 725-729.
[3] J. Cazes and R. P. W. Scott, in Chromatography Theory (Mercel Dekker, Inc., New York, 2002).

CO4-25 A study on destruction of cesium aluminosilicate compounds by gamma irradiation (2)

H. Ohashi, H. Umetsu, T. Saito[1]

Faculty of Symbiotic Systems Science, Fukushima University
[1]Institute for Integrated Radiation and Nuclear Science, Kyoto University

INTRODUCTION: Pollucite which is one of cesium aluminosilicate compounds have attracted attention as a final storage material of ^{134}Cs and ^{137}Cs. Pollucite is able to synthesized by hydrothermal method in low temperature below 300°C [1]. Pollucite has various properties that favor the immobilization of Cs ions.

However, the damage to the aluminosilicate framework by radiation decay is concerned because it contains ^{137}Cs. It has been reported that the effect of β-ray emission and nuclide conversion by β-decay of ^{137}Cs on aluminosilicate framework is minor [2, 3]. On the other hand, there are few reports of effects by gamma rays on pollucite framework. Therefore, we examined the effect of gamma radiation on the aluminosilicate framework of Pollucite. Pollucite samples were synthesized to investigate the effect of gamma irradiation.

EXPERIMENTS: Sodium aluminate, sodium metasilicate and cesium chloride were dissolved in sodium hydroxide solution. The solution was placed in a Teflon inner cylinder pressure container. Pollucite was synthesized by hydrothermal method, holding the container at 180°C for 48 hours. The resulting precipitate was washed. Thereafter, each solid was collected by filtration and dried at 110 °C for 12 hours or more.

The powder samples were characterized by XRD, and gamma-irradiated at 0 and 100 kGy by ^{60}Co source. The 7 days leaching test by PCT-A method [4] was carried out to evaluate the change of Cs retention performance by framework damage. Concentration of cesium in solution leached was estimated by atomic absorption spectrophotometry.

RESULTS: All the XRD patterns of powders prepared were demonstrated that they were pollucite, and all the patterns showed that they contained only single-phase pollucite.

In our previous study, the irradiated pollucite sample showed little difference from the non-irradiated one in the amount of leached cesium. Then we concluded that frameworks were not destroyed by ^{60}Co-irradiation. However, we found some questions about PCT-A method, then the leaktests were studied again.

It was estimated that amount of leached cesium from samples with and without ^{60}Co-irradiation. Over 45 ppm Cs were measured in most samples regardless of whether irradiated or not, and these values of Cs concentration measured were quite higher than those measured by other researchers[5]. It is considered that the reason why the concentration of cesium ions leaked from pollucite was high to be insufficient washing and cesium adsorbed on the ion exchange site.

REFERENCES:

[1] Y. Yokomori *et al.*, *Sci. Rep.*, **4** (2014), 4195
[2] J. Fortner *et al*., Argonne National Laboratory, Argonne, Illinois 60439 (2001).
[3] N. J. Hess *et al.*, *J. Nucl. Mater.*, **281** (2000), 22-33.
[4] ASTM C 1285-02 (2008).
[5] Z. Jing *et al.*, *J. Hazard. Mater.*, **306** (2016), 220–229.

CO4-26 Defect Structure with Short Positron Lifetime in Tungsten

A. Yabuuchi

Institute for Integrated Radiation and Nuclear Science, Kyoto University

INTRODUCTION: The calculated positron lifetime for a monovacancy in tungsten has been reported to be 193 ps−200 ps [1−3]. The positron lifetime of tungsten irradiated with p^+ or $^3He^+$ in a vacuum has been observed experimentally to be 190 ps−200 ps [4−6]. However, the positron lifetime of tungsten irradiated with electrons in coolant water has been reported to be around 170 ps, which is shorter than the calculated positron lifetime for a monovacancy [3,7,8], and the reason for this is unclear. In this study, positron lifetime measurements of electron-irradiated tungsten and first-principles calculations of positron annihilation properties were conducted.

EXPERIMENTS: Tungsten samples with a purity of 99.999% (5N) were annealed at over 2273 K in a vacuum before irradiation. After the annealing, 8 MeV electrons were irradiated to the samples at around 373 K using the KURNS-LINAC with total doses of 5×10^{19} e^-/cm^2. Positron annihilation lifetime measurements were performed at room temperature.

CALCULATIONS: The calculations were performed using ABINIT 8.10.3 [9], a first-principles electronic structure calculation code based on density functional theory (DFT). The Perdew-Burke-Ernzerhof (PBE) electron-electron exchange-correlation functional [10] and Blöchl's projector augmented wave (PAW) method [11] were used. Positron annihilation calculations were performed with a two-component DFT calculation scheme [12] using the Puska-Seitsonen-Nieminen (PSN) [13] local density approximation as the electron-positron exchange-correlation functional. A computational cell size of 3×3×3 (54 atoms of perfect crystal) was used, and the cutoff energy of the plane wave was set to 408 eV.

RESULTS: In the present study, a positron lifetime of about 170 ps was experimentally observed from electron-irradiated tungsten. On the other hand, the calculation of this work also indicated that the positron lifetime for monovacancy (*V*) is 195 ps, which is comparable to the previous studies. The calculated positron lifetimes of the defect complexes such as *V*-2H, *V*-C, *V*-N, and *V*-O were all around 170 ps. This is comparable to the experimentally observed positron lifetime. In addition, the calculated annihilation gamma-ray Doppler broadening spectra of *V*-2H and *V*-O showed different spectral shapes, indicating that at least *V*-2H and *V*-O can be distinguished from the Doppler broadening measurements.

REFERENCES:

[1] T. Troev *et al.*, Nucl. Instrum. Methods Phys. Res. Sect. B **267** (2009) 535.
[2] P. Staikov, N. Djourelov, Phys. B **413** (2013) 59.
[3] K. Sato *et al.*, J. Nucl. Mater. **496** (2017) 9.
[4] P. E. Lhuillier *et al.*, Phys. Status Solidi C **6** (2009) 2329.
[5] O. V. Ogorodnikova *et al.*, J. Nucl. Mater. **517** (2019) 148.
[6] O. V. Ogorodnikova *et al.*, J. Nucl. Mater. **525** (2019) 22.
[7] T. Toyama *et al.*, J. Nucl. Mater. **499** (2018) 464.
[8] K. Sato *et al.*, Nucl. Mater. Energy **9** (2016) 554.
[9] X. Gonze *et al.*, Comput. Phys. Commun. **205** (2016) 106.
[10] J. P. Perdew *et al.*, Phys. Rev. Lett. **77** (1996) 3865.
[11] P. E. Blöchl, Phys. Rev. B **50** (1994) 17953.
[12] J. Wiktor *et al.*, Phys. Rev. B **87** (2013) 235207.
[13] M. J. Puska *et al.*, Phys. Rev. B **52** (1995) 10947.

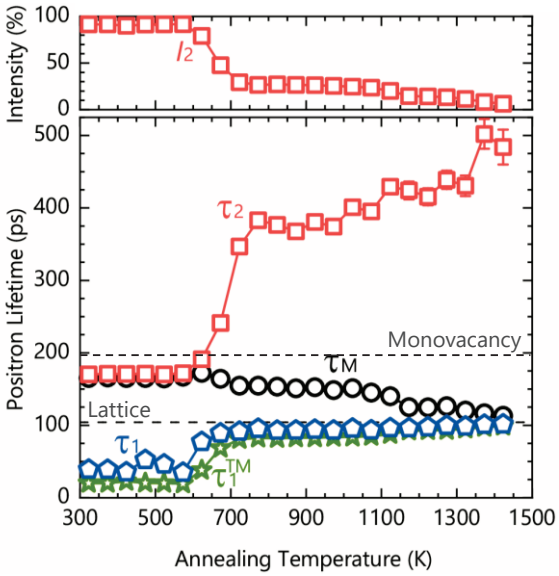

Fig. 1. Annealing behavior of positron lifetime in electron-irradiated tungsten. Lower and upper dashed lines indicate positron lifetimes for perfect lattice and monovacancy, respectively.

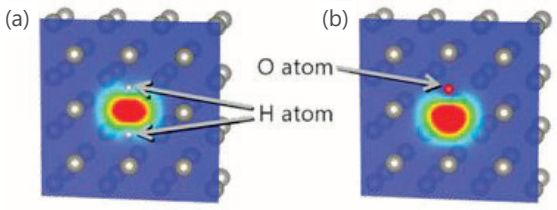

Fig. 2. Calculated atomic configuration and positron density distribution of the defect complexes. (a) *V*-2H, (b) *V*-O.

CO4-27 Elucidation of the Mechanism of the Screw-sense Induction and Helix Inversion of Polymer Main Chain Based on the Small Angle X-ray Scattering, the Dynamic Light Scattering, and the Quasielastic Neutron Scattering Measurements

Y. Nagata[1], M. Suginome[2], M. Sugiyama[3], R. Inoue[3], N. Sato[3], and K. Morishima[3]

[1] *Institute for Chemical Reaction Design and Discovery, Hokkaido University*
[2] *Graduate School of Engendering, Kyoto University*
[3] *Institute for Integrated Radiation and Nuclear Science, Kyoto University*

INTRODUCTION: Much attention has been paid to the structural control of helical polymers owing to their potential applications for asymmetric catalysts, chiral stationary phase, and chiroptical materials. Recently, we have reported that helical poly(quinoxaline-2,3-diyl)s (PQXs) bearing chiral side chains exhibit solvent-dependent helix inversions,[1-3] which can serve as effective scaffold for chirality-switchable materials. [4-7] In order to elucidate the mechanism of the screw-sense induction and the helix inversion of PQXs, we have investigated the detailed structures of a PQX (100mer) with right- or left-handed structures in tetrahydrofran-d_8 (THF-d_8) or a mixed solvent of 1,1,2-trichloroethane-d_3 (1,1,2-TCE-d_3) and THF-d_8 (4/1, v/v) by using small-angle neutron scattering (SANS) experiments, in conjunction with theoretical calculations.[8] The obtained structures of the PQX suggested that the right-handed structure in THF-d_8 is well solvated, while the left-handed structure in 1,1,2-TCE-d_3/ THF-d_8 (4/1, v/v) is less solvated.

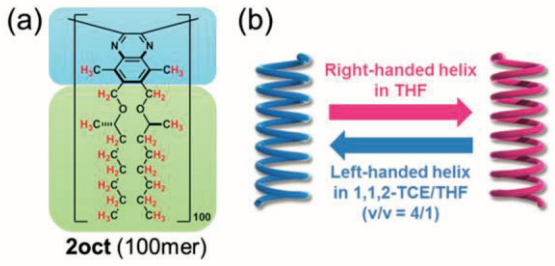

Figure 1. (a) the molecular structure of the PQX bearing (*R*)-2-octyloxymethyl side chains. (b) Solvent-dependent helix inversion of the PQX.

Our recent interest has focused on the effect of the dynamics of the side chains on the screw-sense induction. So far, we have carried out quasielastic neutron scattering (QENS) measurements to elucidate the impact of the molecular dynamics on the solvent-dependent helix inversion of the PQX. In this study, we have carried out QENS measurements and dynamic light scattering (DLS) measurements for the detailed analysis of the results of the QENS measurements.

EXPERIMENTS: A PQX bearing (*R*)-2-octyloxymethyl side chains (100mer) was prepared according to our previous paper.[2] The QENS measurements were carried out at BL-02 DNA in J-PARC. The light scattering measurements were carried out with a 22-mW He-Ne laser, an Avalanche Photo Diode (APD, ALV, Germany) mounted on static/dynamic compact goniometer, ALV/LSE-5003 electronics, and ALV-5000 Correlator (ALV-Laser Vertriebsgesellschaft GmbH, Langen, Germany). The measurements were performed at 313 K and CONTIN analysis was used to obtain the probability of decay rate at each Q.

RESULTS: The PQX was dissolved in THF-d_8 or a mixed solvent of 1,1,2-trichloroethane-d_3 (1,1,2-TCE-d_3) and THF-d_8 (4/1, v/v), respectively, to carry out DLS measurements. In both cases, the decay constant Γ and the square of the wave vector q^2 showed linear relationship, affording the diffusion constants in these solvents. We are now working on the analysis of the QENS measurements by using the results of the DLS measurements. In addition, we are now trying to reveal the detailed behavior of the screw-sense induction and the helix inversion using molecular-dynamics simulations using the BIOVIA Materials Studio with the COMPASS II force field.

REFERENCES:

(1) Yamada, T.; Nagata, Y.; Suginome, M. *Chem. Commun.* **2010**, *46*, 4914-4916.
(2) Nagata, Y.; Yamada, T.; Adachi, T.; Akai, Y.; Yamamoto, T.; Suginome, M. *J. Am. Chem. Soc.* **2013**, *135*, 10104-10113.
(3) Nagata, Y.; Nishikawa, T.; Suginome, M. *J. Am. Chem. Soc.* **2015**, *137*, 4070-4073.
(4) Nagata, Y.; Nishikawa, T.; Suginome, M. *Chem. Commun.* **2012**, *48*, 11193-11195.
(5) Nagata, Y.; Takagi, K.; Suginome, M. *J. Am. Chem. Soc.* **2014**, *136*, 9858-9861.
(6)Nagata, Y.; Uno, M.; Suginome, M. *Angew. Chem. Int. Ed.* **2016**, *55,* , 7126-7130.
(7) Nishikawa, T.; Nagata, Y.; Suginome, M. *ACS Macro Lett.* **2017**, *6*, 431-435.
(8) Nagata, Y.; Nishikawa, T.; Suginome, M.; Sato, S.; Sugiyama, M.; Porcar, L.; Martel, A.; Inoue, R.; Sato, N. *J. Am. Chem. Soc.* **2018**, *140*, 2722-2726.

CO4-28 Neutron irradiation tests for ITER plasma diagnostics

M. Ishikawa, E. Yatsuka, R. Imazawa, T. Ushiki, H. Murakami and T. Hatae

National Institutes for Quantum and Radiological Science and Technology

INTRODUCTION: International Thermonuclear Experimental Reactor (ITER) [1] is being built in France by international cooperation. This study focuses on neutron irradiation effects on optical elements and piezo-actuators used in ITER. Expected 1 MeV Silicon equivalent fluence is 10^{12}-10^{15} n/c m^2 depending on locations of components. In order to investigate the effect of such high fluence on the actual components in a short time, neutron irradiation was performed using the slant exposure tube and the pneumatic tubes of the KUR. This report mainly presents effect of neutron irradiation on piezo actuators for Poloidal Polarimeter (PoPola) system and briefly describes the tests for other systems such as Edge Thomson Scattering system (ETS), Infrared Thermography (IRTh) system and the Microfission Chamber system (MFC).

The authors carried out the irradiation test of a piezo actuator. Piezo actuators will be used in various systems of ITER and will be used for adjustment of mirror angle in the case of PoPola. The previous study [2] assessed radiation hardness of a piezo actuator for other system of ITER and shows that the piezo actuator is operational in the ITER radiological environment. However, since the piezo actuator selected for PoPola is different from that used in the previous study, the authors need to conduct an irradiation test of the piezo actuator of PoPola to confirm whether it can be used in the ITER environment.

EXPERIMENTS: At the place where the piezo actuator was placed in the slant exposure tube of KUR, the neutron flux is 9.6x10^{11} (n/cm^2/s), the cadmium ratio is 34.0, and the gamma flux is 50 (kGy/h). The duration of irradiation was one hour in total, so the total neutron flux was 3.5x10^{15} (n/cm2), which is equivalent to the expected fluence at the position of the PoPola piezo actuator in ITER.

The tested piezo actuator was PZA 12 released by Newport Company. The motion of the piezo actuator is as discrete as that of a stepping motor. The driver of the piezo actuator sends polyphase voltage signals to the piezo actuator, and then the shaft of the piezo actuator moves in discrete steps. The aims of this test are as follows;

- To confirm whether the stroke force of the piezo actuator is over 25 N.
- To confirm whether the maximum stroke length of the piezo actuator is over 7.4 mm.

The values of 25 N and 7.4 mm come from mechanical and optical design of the PoPola system. It should be noted that the stroke length per step is not important because the mirror angle is controlled in a closed loop using both the mirror angle sensor and the piezo actuator. Thus, what is important for PoPola is that the piezo actuator can travel the distance of 7.4 mm or more with the stroke force of 25 N or more after irradiation.

Figure 1 shows the schematics and the photograph of the device that the authors developed for this test. The test device always applies axial load of 45 N to the piezo actuator during the test by using constant force springs (Sunko, model: NWS 1.5-1). The axial load can be changed by exchanging the constant force springs. The motion of the piezo actuator is monitored by a micrometer (Mitsutoyo Corporation, model: 2050S, minimum scale division: 10 μm).

RESULTS: The functional test was conducted after the neutron irradiation. By using the device shown in Fig. 1, the authors confirmed that the piezo travel the distance of 10 mm or more with the stroke force of 45 N. Thus, it can be concluded that the selected piezo actuator has radiation hardness enough for PoPola in the ITER environment.

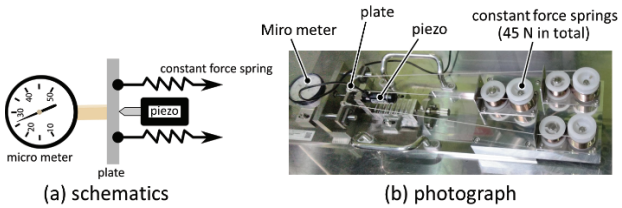

Fig. 1: Functional test device of piezo actuator.

ON GOING INVESTIGATIONS AND PROSPECTS:

RETS will use a silica core optical fiber to transmit scattered light from plasma to the spectrometer. If the silica core contains a large amount of OH groups, it becomes resistant to deterioration of light transmittance due to neutron irradiation in the visible light, but absorption occurs regardless of irradiation in the near infrared. Experiments are on-going to investigate the relationship between OH group content and spectral transmittance.

IRTh will use Au coating mirrors, AR coated sapphire vacuum windows and several lens materials in the ITER environment. In order to investigate threshold value of the total dose for keeping their optical performances, irradiation tests of several candidate materials for mirror, windows and lens have been conducted since 2019. Then, the they will be completed by 2021. In 2020, irradiation tests for several kinds of materials for mirrors and windows were conducted and threshold values of those materials are being investigated.

The feedthrough of MFC plays an important role for vacuum and tritium confinement of the ITER vacuum vessel. However, ceramic material used in the feedthrough may suffer damage due to high neutron irradiation and it could cause leakage of vacuum and tritium. In order to demonstrate radiational hardness of the feedthrough, equivalent neutron fluence to that at the location of the feedthrough in ITER was irradiated. The leak test of the ceramic part will be carried out to confirm its confinement function in 2021.

REFERENCES:

[1] B. Bigot, Fusion Eng. Des., **146**, 124 (2019).
[2] M. Pillon *et al*., Fusion Eng. Des., **96-97**, 329 (2015).

CO4-29 Irradiation Experiment of Accident Tolerant Control Rod Materials (2)

H. Ohta[1], K. Nakamura[1], Y. Takahashi[2], H. Unesaki[2], T. Sano[2*]
[1]*Nuclear Research Technology Laboratory, Central Research Institute of Electric Power Industry*
[2]*Institute for Integrated Radiation and Nuclear Science, Kyoto University*
[*]*Present affiliation: Atomic Energy Research Institute, Kindai University*

INTRODUCTION: Various concepts of "enhanced-accident tolerant fuels and core components" have been developed in many countries to improve core safety under any operation conditions including severe accidents (SAs), while maintaining or improving the economic efficiency of light water reactors (LWRs). The Central Research Institute of Electric Power Industry (CRIEPI) has been developing the accident tolerant control rods (ATCRs) where the novel neutron absorbing materials including rare-earth oxides (RE_2O_3) are applied[1] to prevent control rods (CRs) from damaging prior to fuel rods in the early stages of SAs. Preliminary analyses[1] revealed the ATCR concept improves the reactor shutdown margin and neutronic lifetime. RE_2O_3 (RE = Sm or Eu) has excellent high temperature compatibility with the stainless steel CR cladding and will not be damaged less than 1200 °C. On the other hand, it is known to have extremely high hygroscopicity and is unstable, but it was experimentally confirmed that physicochemical stability is improved even under high temperature steam atmosphere by mixing and sintering with MO_2 (M = Zr or Hf)[2]. In addition, thermal neutron irradiation characteristics of the mixtures of RE_2O_3-MO_2 are needed to be confirmed to evaluate the applicability as a control rod for LWRs. In this study, dimensional stability of a candidate material by neutron irradiation will be confirmed.

EXPERIMENTS and RESULTS

Sample Preparation: The powders of Sm_2O_3 and ZrO_2 were mechanically mixed at a molar ratio of 1 : 1 and sintered to form a pellet with a density of 6.55 g/cm^3 corresponding to 93.7 %TD. Since the sintered mixtures of any combinations of RE_2O_3-MO_2 (RE = Sm or Eu, M = Zr or Hf) with a molar ratio of 1 : 1 is known to form a fluorite crystal structure, it is considered that the irradiation experimental results of Sm_2O_3-ZrO_2 are applicable to the other combination materials. For minimizing the radioactivation induced by the neutron irradiation, the sintered pellet was cut into small pieces. The appearance and surface microstructure of the cut sample pieces before irradiation was observed with an optical microscope and scanning electron microscope (SEM), and their weights were measured.

Irradiation Conditions: Irradiation experiment has been carried out using long-term irradiation plug in Kyoto University Research Reactor (KUR). Three Sm_2O_3-ZrO_2 sample pieces were enclosed in an Al capsule dedicated for long-term irradiation experiment and irradiated for 254.7 hours at a rated power of 1 MW and 55.2 hours at a high power of 5 MW at 85 - 90 °C. The fast and total neutron fluences at the end of irradiation experiment are estimated to be 5.35×10^{18} n/cm^2 and 2.38×10^{19} n/cm^2, respectively, which is almost equivalent to irradiation fluence for ~1 day in typical PWRs.

Postirradiation observations: After ~2 years cooling, the appearances and surface microstructure of the irradiated samples were observed, and their weights were also measured. The weight change before and after irradiation was within ± 1.0% and not remarkable, as shown in Table I. Figure 1 shows the appearance of each sample before and after irradiation. No changes in the appearance and the dimensions due to neutron irradiation were confirmed. Furthermore, the microstructure on the surface of the irradiated samples observed with SEM showed no sign of change as compared with the unirradiated sample as shown in Figure 2.

Table I Weight changes of Sm_2O_3-ZrO_2 samples before and after irradiation[3].

Sample No.	(1)	(2)	(3)
Before irrad.	1.95 mg	6.21 mg	5.15 mg
After irrad.	1.97 mg	6.15 mg	5.11 mg

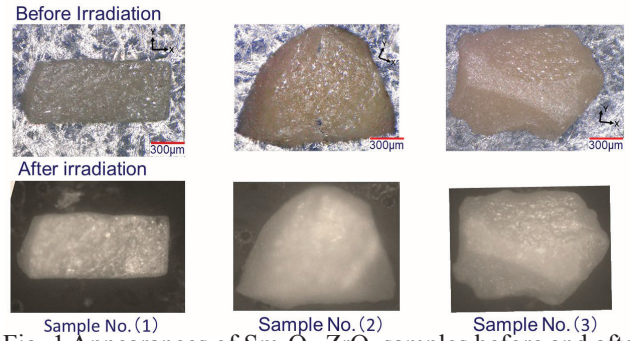

Fig. 1 Appearances of Sm_2O_3-ZrO_2 samples before and after irradiation [3].

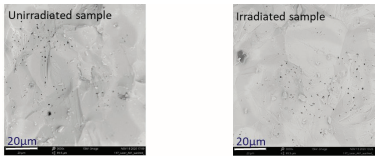

Fig. 2 SEM images of Sm_2O_3-ZrO_2 samples before and after irradiation[3].

CONCLUSION: Irradiation experiment of sintered Sm_2O_3-ZrO_2 samples in long-term irradiation plug of KUR showed that the irradiation stability of the ATCR neutron absorbers was maintained under a fast neutron fluence of 5.35×10^{18} n/cm^2.

REFERENCES:

[1] H. Ohta, et al., TopFuel 2016, 17556 (2016).
[2] K. Nakamura, et al., *AESJ 2017 spring meeting*, 1I06.
[3] H. Ohta et al., *AESJ 2021 spring meeting*, 2K02.

CO4-30 Radiochemical Research for the Advancement of $^{99}Mo/^{99m}Tc$ Generator by (n, γ) Method (3)

Y. Fujita, M. Seki, Y. Namekawa, K. Nishikata, F. Daigo, H. Ide, K. Tsuchiya, T. Sano[1], Y. Fujihara[2], J. Hori[2], H. Yoshinaga[2]. J. Zhang[2], T. Suzuki[3] and H. Suematsu[3]

Department of JMTR, Japan Atomic Energy Agency
[1] Atomic Energy Research Institute, Kindai University
[2]Institute for Integrated Radiation and Nuclear Science, Kyoto University
[3]Graduate School of Engineering, Nagaoka University of Technology

INTRODUCTION: The research and development (R&D) has been carried out for the production of Molybdenum-99 (^{99}Mo) by the neutron activation method ((n, γ) method) from viewpoints of limited availability of high-enriched uranium, no-proliferation and nuclear security and disposal of nuclear fissile materials. The amount of ^{99}Mo to be produced by (n, γ) reaction is very low. Thus, the solvent extraction was applied as a Master-Milker in order to increase the concentration of ^{99m}Tc in the final product [1]. This method employs MEK to extract ^{99m}Tc from ^{99}Mo. In this study, the extraction property of ^{99m}Tc was evaluated using the Mo solution with irradiated MoO_3 by MEK and characterization of ^{99m}Tc solution was performed by the column chromatography after the extraction of ^{99m}Tc. Additionally, high-density MoO_3 pellets irradiated with KUR were transported to JMTR-HL, and the similar experiments were conducted as a scale-up test.

EXPERIMENTS: The MoO_3 pellet pieces (about 1.5 g) were irradiated in the condition of 20min×5MW in the Pn-2 of the KUR. After the irradiation, the irradiated MoO_3 pellet pieces were dissolved with 6M-NaOH solution (3.75 mL) and mixed with other Mo solution dissolved un-irradiated MoO_3 powder (33 g) and 6M-NaOH (85 mL). Two kinds of Mo solution samples were prepared. One is the Mo solution (hereinafter referred to as "MoSol-A") containing water (8mL). The other is the Mo solution (hereinafter referred to as "MoSol-B") containing water (6 mL) and saline (2 mL). MEK was added to each Mo solution, only MEK was extracted after stirring. The extracted MEK was purified using the basic alumina columns, and ^{99m}Tc in MEK was adsorbed using the acidic alumina column. The ^{99m}Tc was eluted from the acidic alumina column with saline of 10 mL. Radioactivity in Mo solution and Tc solution in each step was measured by the γ-ray spectrometer.

RESULTS: Fig.1 shows the ^{99m}Tc content in medium of each step. The ^{99m}Tc content is the ratio of the amount of ^{99m}Tc contained in medium to the amount of ^{99m}Tc in the Mo solution at the start of extraction. The ^{99m}Tc radioactivity was corrected at the start of extraction. In the experiment using Mo solution of MoSol-A, the ^{99m}Tc content was stable until the adsorption step of acidic alumina column. In the experiment using Mo solution of MoSol-B, the ^{99m}Tc content was reduced at the extraction step from Mo solution of MoSol-B at the first day. On the other hand, the ^{99m}Tc content was stable until the adsorption step of acidic alumina column at the 2nd and 3rd days. It seems that the extraction of ^{99m}Tc by MEK is affected by Cl^- ion contents in the Mo solution. At the elution step from the acidic alumina column, ^{99m}Tc elution amount reduced in all cases. The cause may be the preparation method and filling amount of the acidic alumina, the elution rate, etc. The effects from them need to be investigated and improved.

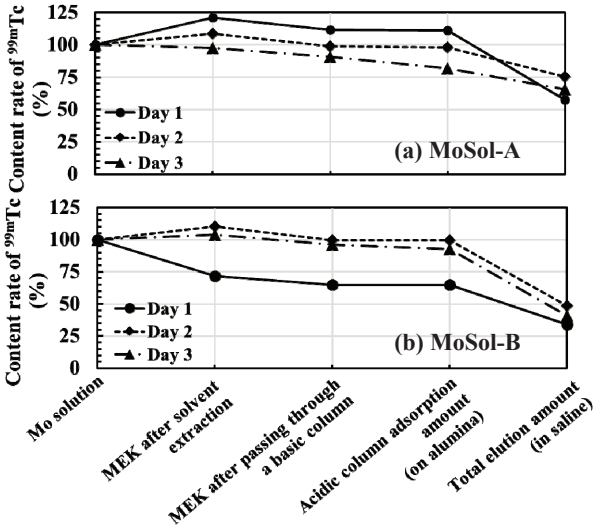

Fig.1 ^{99m}Tc content in medium of each step.

Fig.2 shows ^{99m}Tc elution fraction from the acidic alumina column. As a result, it was found that the elution property was the same tendency in all cases and that almost 100% of ^{99m}Tc could be eluted with about 4 mL of saline.

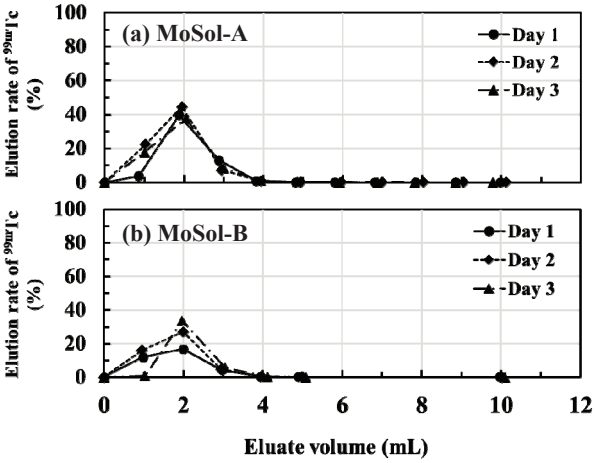

Fig.2 ^{99m}Tc elution fraction from the acidic alumina column.

REFERENCES:

[1] S. Chattopadhyay *et al.*, Appl. Radiat. Isot., **68** (2010) 1–4

CO4-31 The Absorbance Measurement for Color Dosimeter of Gamma-ray Using a Photochromic Diarylethene Containing Additives

S. Komatsuda, M. Takeshita[1], R. Maeda[1], A. Taniguchi[2], and Y. Ohkubo[2]

Institute of Human and Social Sciences, Kanazawa University
[1]*College of Human and Social Sciences, Kanazawa University*
[2]*Institute for Integrated Radiation and Nuclear Science, Kyoto University*

INTRODUCTION:

Diarylethene (DAE) is one of the most intriguing photochromic materials which has a reversibly structure-changed part by irradiating ultraviolet (UV) ray or gamma ray. The DAE is colored by this structural change and returned to original structure by irradiating visible rays. Because of their excellent thermostability and reversibility, the DAE has attracted much attention as radiation-induced color dosimeter. In addition, for practical use of DAE, a sensitizer such as aromatic compound is contained with DAE to enhance sensitivity.

It was found from previous studies that a DAE containing aromatic compound was colored visually by irradiating gamma-ray of 100 Gy[1]. However, for practical use of DAE as color dosimeter, it is necessary to obtain highly sensitive DAE colored by irradiating gamma-ray of 0.1~1 Gy. Therefore, it is required to obtain more information on suitable sensitizer of aromatic compound for DAE color dosimeter. For that purpose, we then study the sensitizing effect of various aromatic compounds contained in DAE solution, observing the absorption spectra of DAE irradiated by gamma-ray.

EXPERIMENTS: A measuring sample is constituted of a toluene solution containing diarylethene(concentration of 2.6×10^{-3} mol/L) and an additive(concentration of 2.6×10^{-3} mol/L). Commercially available 1,2-bis(2,4-dimethyl-5-phenyl-3-thienyl)-3,3,4,4,5,5-hexafluoro-1-cyclopentene (DAE) and additives such as naphthalene, anthracene, biphenyl, and *p*-terphenyl were dissolved in toluene solution, respectively. The solutions were dispensed into vials and irradiated at room temperature with Co-60 Gamma-ray Irradiation Facility at Institute for Integrated Radiation and Nuclear Science. The irradiation dose of gamma-ray was 361 Gy. The absorbance measurements were carried out with JASCO V-570.

RESULTS: Figure 1 shows the absorption spectra of irradiated DAE samples. Table 1 summarizes the maximum absorption wavelength λ_{max} of the DAE at 575 nm. The absorption peaks of the samples are increased by containing additives compared with sample without additives, which exhibits that the additives of aromatic compounds have the sensitizing effect. Especially, biphenyl and *p*-terphenyl have a high sensitizing effect. Focusing on λ_{max} and quantum yield of additives, there are two common features for effective additives of aromatic compound; (i) for one thing, λ_{max} of additives is about 265 nm, and (ii) for other thing, the additives show high quantum yield. In order to corroborate this proposal, we performed additional preliminary experiment measuring UV irradiated DAE samples for examining the sensitizing effect of another additives (such as *p*-xylene, phenylacetylene, and anisole) which shows high quantum yield and λ_{max} at about 265 nm. For the result of this additional experiment, it is suggested that the sensitizing effect of anisole is nearly equals to biphenyl which shows the best sensitizing effect in this work. This observation is consistent with our proposal on the sensitizing effect of additives. For more information on the condition of effective additives, additional experiments using gamma-ray is now in progress.

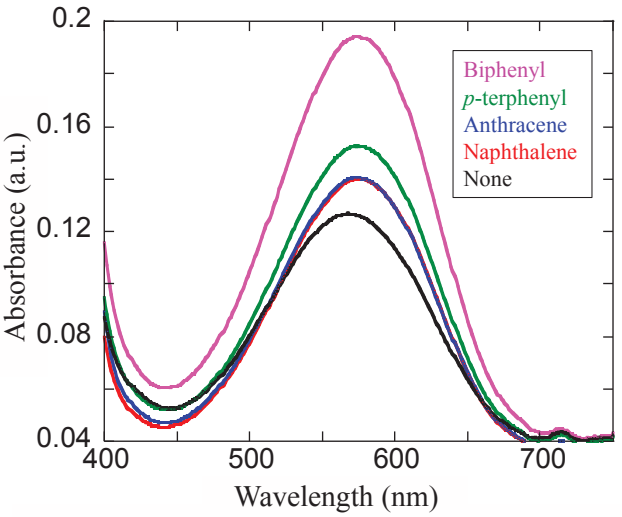

Fig. 1. Absorption spectra of DAE samples in toluene solution.

Table 1 Measured absorbance at 575 nm of samples irradiated by Co-60 gamma-ray

Additives	Absorbance at 575 nm	λ_{max} of additives (nm)	Fluorescence quantum yield of additives
None	0.12	—	—
Naphthalene	0.14	286	0.23
Anthracene	0.14	358	0.36
Biphenyl	0.19	247	0.18
p-terphenyl	0.15	276	0.80

REFERENCES:

[1] S. Irie *et al.*, *The Chem. Soc. Jpn.* **75** (2002) (2071-2074).

Synthesis and superconducting properties of $EuSn_2As_2$

***R. Takahashi*[1], *Y. Tani*[1], *N. Nagasawa*[1], *S. Ikeda*[1], *N. Kawamura*[2], *K. Mimura*[3], *A. Yamaguchi*[1], *A. Sumiyama*[1], *H. Kobayashi*[1], *H. Wadati*[1]**

[1]*Graduate School of Material Science, University of Hyogo, Ako, Hyogo 678-1297, Japan*
[2]*Japan Synchrotron Radiation Research Institute (JASRI), Sayo, Hyogo 679-5198, Japan*
[3]*Graduate School of Engineering, Osaka Prefecture University, Sakai 599-8531, Japan*

INTRODUCTION: $EuSn_2As_2$ is one of the two-dimensional stacked van der Waals materials which providing attractive platform to realize various properties by changing the element, temperature and pressure [1, 2]. Recently, it has been reported that this material exhibits abnormal superconductivity, and its origin is urgently elucidated. The point of particular attention is that while the superconducting state in the ab direction is realized, the resistance does not become zero in the c direction, which is thought to be due to the Josephson junction with the Eu layer as the insulating layer, however, it is unclear [2]. This time, we focused on the electronic state of the Eu layer and tried to identify its valence state.

EXPERIMENTS: The sample was prepared by the Sn-flux method [1]. Samples were evaluated using laboratory X-Ray Diffractometer (Cu-Kα) and Energy Dispersive X-ray Spectroscopy. Since the crystallinity and composition were highly dependent on the sample, the one with the lattice constant closest to the previous study[1] and the composition closest to Eu: Sn: As = 1: 2: 2 was selected from the measured samples, and the single crystal $EuSn_2As_2$ sample was selected. Then, magnetization measurement, resistivity measurement, and specific heat measurement were performed using PPMS and MPMS-5SH (Quantum design). We also performed high energy resolution fluorescence detected X-ray absorption fine structure spectroscopy measurements on SPring-8 BL39XU at T = 2.7, 300 K to identify the valence state of Eu.

RESULTS: From the measurement of magnetization, the effective magnetic moment was found to be 7.337 μ_B/Eu [Fig. 1 (b)] slightly lower than that of theoretical value 7.94 μ_B/Eu^{2+} (J = 7/2) and Meissner effect was observed at 3.7 K (B = 0.5 mT). We also measured Eu-L_3 edge High Energy Resolution Fluorescence Detected X-ray Absorption Fine Structure (HERFD-XAFS) spectroscopy for the $EuSn_2As_2$ single crystal [Fig. 1 (c)]. Only Eu^{2+} peak was observed at both 300 K and 3 K and there was no Eu^{3+}. We would like to discuss the difference between magnetic properties and valence of Eu, and superconducting properties of $EuSn_2As_2$.

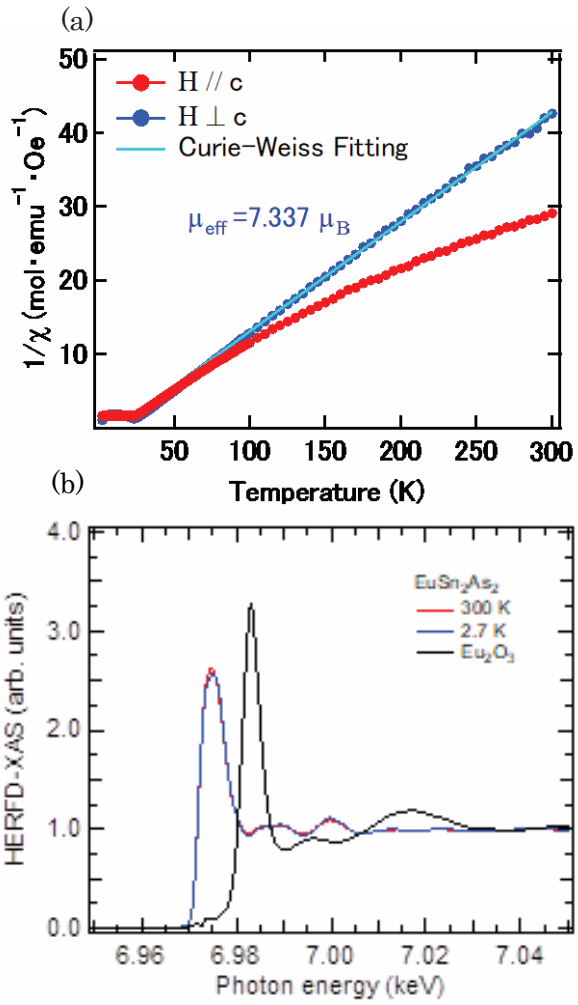

Fig. 1. (a) Magnetic susceptivity of $EuSn_2As_2$. (b) HERFD-XAFS spectra.

REFERENCES:

[1] H. Li *et al.*, Phys. Rev. X **9**, 041039 (2019).
[2] S. Sakuragi *et al.*, arXiv:2001.07991.

CO5-1 Production of technetium-99 by neutron irradiation of molybdenum trioxide

T. Kubota, T. Chida[1] and Y. Niibori[1]
Institute for Integrated Radiation and Nuclear Science, Kyoto University

[1]Department of Quantum Science and Energy Engineering, Tohoku University

INTRODUCTION: Technetium-99 is a pure beta emitter with a half-life of 2.11×10^5 (y) and is a fission product with its yield of 6.0%. Technetium forms anionic TcO_4^- to be mobile species under oxidic condition. Hence, its migration behavior in the environment is an important research field for the safety assessment on the disposal of high-level radioactive waste [1]. Investigations on the interaction of ^{99}Tc with various materials in the environment require methods other than radiation measurement, such as spectrophotometry, due to its weak radioactivity. In this report the production of adequate amount of ^{99}Tc tracer was investigated.

EXPERIMENTS: Technetium-99 was produced by the neutron irradiation of natural isotopic molybdenum. A 2 g of MoO_3 powder was encapsulated in a quartz test tube under vacuum and the test tube was placed in an aluminum capsule filled with water. The capsule was irradiated for 47 hours at the reactor power of 1 MW and then for 6 hours at 5 MW in the Hydraulic Conveyer Facility (Hyd.) of the Kyoto University Reactor (KUR). Technetium-99 was recovered by solvent extraction at 75 days after irradiation. The MoO_3 powder irradiated was dissolved with NaOH and then contacted with methyl ethyl ketone (MEK) [2]. The radioactivity of NaOH and MEK phase was measured by γ-spectrometry. The amount of ^{99}Tc produced was evaluated from the radioactivity of ^{99m}Tc by assuming that ^{99m}Tc was in radioactive equilibrium with ^{99}Mo at the end of irradiation.

RESULTS: The gamma ray spectrum of initial NaOH solution in the Fig. 1 shows no 145 keV gamma ray line of ^{99m}Tc on the contrary strong lines of ^{134}Cs and ^{124}Sb. The line of ^{99m}Tc is found in MEK solution after the solvent extraction, which yielded the distribution ratio of ^{134}Cs and ^{124}Sb was lower than 1/1000. Theses impurities would be completely removed by repeated solvent extraction. Besides ^{99m}Tc, in Fig. 1 shows the 155 keV line of ^{188}Re, which was determined by its half-life of 0.71 d in Fig. 2. It is reasonable that ^{188}Re was produced from tungsten as an impurity in MoO_3. Tungsten is a homologous element of molybdenum; thus, its amount is likely to be larger than other elements. The radioactivity of ^{99m}Tc finally decreased to lower than the detection limit, which shows no ^{99}Mo extracted in MEK phase and high separation efficiency of ^{99m}Tc and ^{99}Tc. The amount of ^{99}Tc was evaluated from that of ^{99}Mo at the end of irradiation to be 4.6 nmol, if ^{99}Mo and ^{99m}Tc is totally decayed. In conclusion, ^{99}Tc can be separated from Mo as a target material and antimony, cesium, and tungsten as an impurity by using solvent extraction with MEK and the irradiation of as much as 30 g MoO_3 would yield an enough amount for an optical analysis.

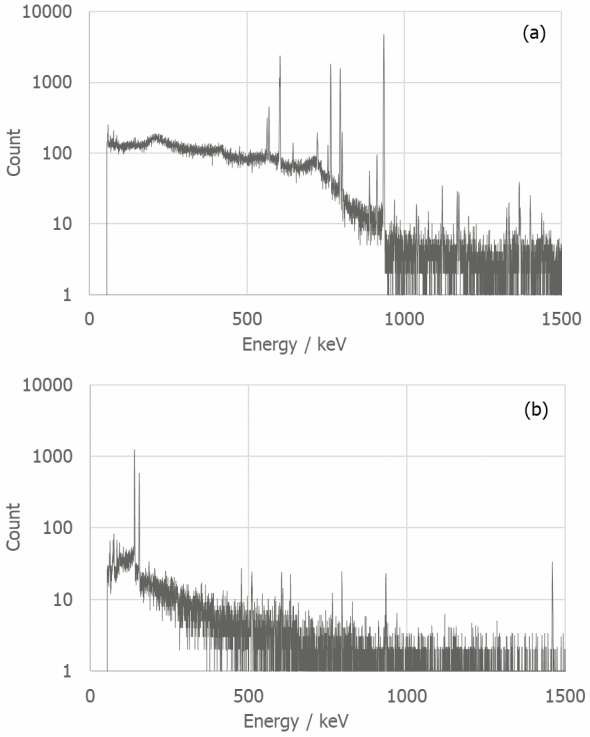

Fig. 1. Gamma ray spectra from high purity germanium detector. (a) NaOH solution. (b) MEK solution

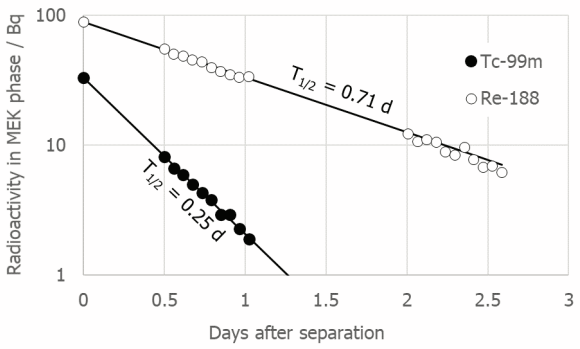

Fig. 2. Radioactive decay curve of ^{99m}Tc and ^{188}Re

REFERENCES:

[1] S. Luksic *et al.*, J. Nucl. Mat., **466** (2015) 526-538.
[2] P. Martini *et al.*, App. Rad. Iso., **139** (2018) 325-331

CO5-2 Volcanic and Tectonic History of Philippine Sea Plate (South of Japan) Revealed by $^{40}Ar/^{39}Ar$ Dating Technique

O. Ishizuka, S. Sekimoto[1], R. Okumura[1], H. Yoshinaga[1], Y. Iinuma[1], T. Fujii[2]
Geological Survey of Japan, AIST
[1]Institute for Integrated Radiation and Nuclear Science, Kyoto University
[2]Graduate School of Engineering, Osaka University

INTRODUCTION: Submarine volcanic rocks are known to give ages different from their true eruption ages in some cases. This is due to the existence of excess ^{40}Ar in the rapidly quenched glass or Ar loss and K remobilization caused by reaction with seawater or hydrothermal fluids. Stepwise-heating analysis in $^{40}Ar/^{39}Ar$ dating is particularly useful for dating submarine volcanics.

Tectonic reconstruction of the Philippine Sea Plate for the period immediately before and after subduction initiation at ~52 Ma to form the Izu-Bonin-Mariana (IBM) arc is prerequisite to understand cause of subduction initiation (SI) and test competing hypotheses for SI such as spontaneous or induced nucleation. There is increasing evidence that multiple geological events related to changing stress fields took place in and around Philippine Sea plate about the time of SI ~52 Ma (e.g., Ishizuka et al., 2020). It is important to understand the pattern and tempo of these geological events, particularly the duration and extent of seafloor spreading in the proto arc associated with SI, and its temporal relationship with spreading in the West Philippine Basin (WPB).

EXPERIMENTS: Samples were wrapped in an aluminum foil packet and the packets were piled up in a pure aluminum (99.5% Al) irradiation capsule (9 mm diameter and 30 mm long). The irradiation capsule was partitioned into 3 compartments to minimize the horizontal flux variation across the capsule, and was wrapped with Cd foil to suppress contribution of thermal neutron.

For the experiments described here, around 5 mg of sample was analysed. Only minimum acid leaching was applied to the glass samples, i.e., ultrasonic cleaning with 3M HCl for 10 minutes at room temperature. In case of altered samples, they were leached with HCl, and then HNO_3 at 95°C using hot stirrer. After this acid treatment, the samples were examined under binocular microscope before packed for irradiation.

RESULTS: Recent cruises (KS-17-15 and YK19-07S cruises) in the Philippine Sea basins investigated origin and age of formation of ocean basins in and around the Daito Ridge group. The data are still preliminary, but some fresh basalt samples returned well-defined $^{40}Ar/^{39}Ar$ ages older than the age of onset of subduction along the IBM arc at c. 52 Ma. Combined with interpretation of seafloor magnetic anomaly data, this strongly implies that some part of the Philippine Sea basins such as the West Philippine Basin existed prior to the IBM arc, and this basin could be a part of overriding plate at subduction initiation.

Temporal variation of geochemical characteristics of basalts in the Philippine Sea basins appears to indicate that major compositional variation occurred in sub-Philippine Sea mantle subsequent to subduction initiation. This might imply that sinking of large volume of Pacific Plate along the entire IBM arc margin triggered counterflow of asthenospheric mantle and reorganization of sub-Philippine Sea mantle.

The Kita-Daito Basin separates the Amami Plateau and the Daito Ridge, both of which belong to the Daito Ridge Group. No rock sampling has been reported from this basin to constrain its age and origin of this basin. The Vp model of the Kita-Daito Basin suggests the presence of a 4 – 6 km thick crust, similar to the backarc basin oceanic crust in the Shikoku and Parece Vela Basins, as revealed by Nishizawa et al. (2011, 2013). These features seem to imply that rifting and seafloor spreading occurred between the Amami Plateau and Daito Ridge to form the Kita-Daito Basin. Dredge sampling and Shinkai 6500 submersible survey observed and recovered samples from the crustal sections exposed in the deepest part of the basin. Collected samples are mostly composed of volcanic rocks, porphyries and trace amount of sedimentary rock and conglomerate. The volcanic rocks are basalt to andesite clasts. These samples show geochemical characteristics implying influence of material released from subducting slab. This implies that these rocks are not part of ocean crust composed of MORB. These volcanic rocks gave ages of middle Eocene, which indicates that these volcanic rocks formed after the period of subduction initiation of Izu-Bonin-Mariana arc. These observations seem to imply that the Kita-Daito Basin did not exist at the subduction initiation, and formed by rifting in middle Eocene accompanied by basaltic to andesitic volcanism (Fig. 1).

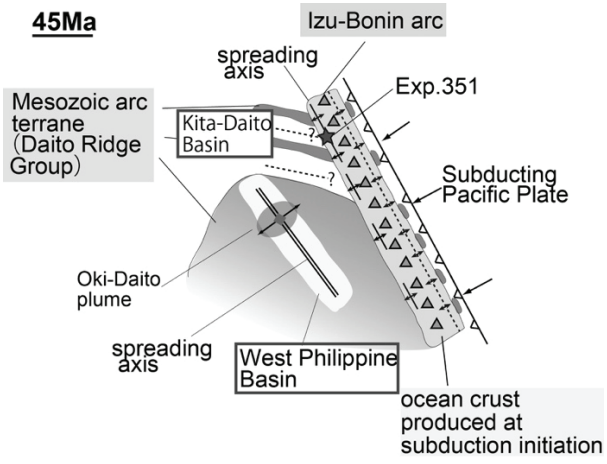

Fig. 1 Reconstruction of Philippine Sea Plate based on ArAr dating results.

CO5-3 Ar-Ar dating of basaltic rocks within accretionary complex to reconstruct the tectonic settings of paleo-Japanese archipelago

N. Hirano, H. Sumino[1], S. Sekimoto[2]

Center for Northeast Asian Studies, Tohoku University
[1] Graduate School of Arts and Sciences, the University of Tokyo
[2] Institute for Integrated Radiation and Nuclear Science, Kyoto University

INTRODUCTION:

Petit-spot submarine volcanoes erupted on an outer rise at the subducting NW Pacific Plate, recognized as new kind of volcano on the Earth [1]. Such volcanoes are likely ubiquitous in zones of plate flexure as several examples have been reported from oceanward slopes of trench in the world [2][3][4]. The widespread occurrence of petit-spot prior to plate subduction is supported by the reinterpretation of the origin of alkaline basalts found within accretionary complexes. The entrained xenolith from the depleted mantle is geochemically disturbed by the wall–rock interaction [5]. Tonegawa et al. [6] observed some structural changes in the NW Pacific crust and moho caused by the plate flexures and petit-spot volcanic activities. The accreted petit-spot would be a successful candidate to know the subsurface structure of subducting plates.

EXPERIMENTS:

We examined the "potential petit-spot" in Cretaceous accretionary complexes and forearc basins of the Pacific Rim (Chichibu Belts of SW Japan, Hidaka Belt of central Hokkaido, Tokoro and Nemuro Belts of E Hokkaido) (Fig. 1), and additionally with the Cretaceous seamounts on present western Pacific before their accretion.

Fig. 1. The sampling sites of basaltic rocks to analyze Ar-Ar datings in this study, shown by stars.

Radiometric Ar-Ar dating is commonly used to determine the ages of submarine lava samples, because the traditional K-Ar dating is impossible to remove the alteration part of fraction. The rock-samples, crushed to 100-500 μm grains, were irradiated by neutrons in the reactor, KUR, to produce ^{39}Ar from ^{39}K during three hours. During the irradiation, samples were packed with EB-1 biotite flux monitors, K_2SO_4 and CaF_2 as correcting factors in an aluminum capsule. The radiogenic ^{40}Ar, daughter nuclide of radioactive ^{40}K and parent, ^{39}Ar instead of ^{40}K, were simultaneously analyzed using a mass-spectrometer with an extraction technique of multi-step heating of approximately every 50 to 100 °C between 500 to 1500 °C at the University of Tokyo.

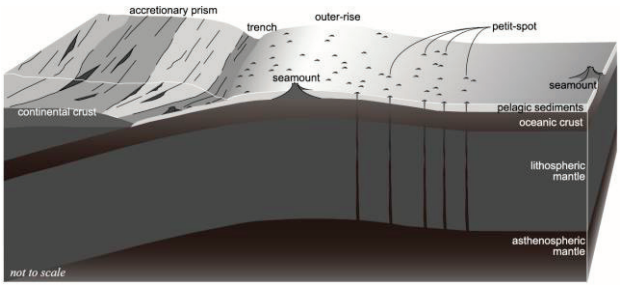

Fig. 2. Schematic model to accrete volcanic edifices on subducting plate.

RESULTS:

Although alkali basalts in the accretionary complex had traditionally been discriminated as ocean island basalts implying a seamount accretion, we newly report some of lavas, sills, and lamprophyres recognized as "accreted" petit-spots prior to plate subduction as well. They are all characterized by occurrences without reefal limestones [7]. Their Ar-Ar ages are generally younger than those of ocean island basalt because the petit-spot volcanisms occur at the outer-rise just prior to the plate-subduction (Fig. 2). In other way, we determined some seamounts and petit-spots on the present Pacific plate (around Minamitorishima Island) prior to its subduction as an analogue for the accreted basalts into accretionary complex. Their young and Paleogene Ar-Ar ages are first reported, implying the presence of petit-spot and post-Cretaceous volcanoes on present Western Pacific plate [8][9].

REFERENCES:

[1] N. Hirano et al., *Science*, **313** (2006), 1426-1428.
[2] N. Hirano et al., *Basin Res.*, **20** (2008), 543-553.
[3] N. Hirano et al., *Geochem. J.*, **47** (2013), 249-257.
[4] R. Taneja et al., *Gondwana Res.*, **28** (2014), 391-406.
[5] S. Pilet et al., *Nature Geosci.*, **9** (2016), 898-903.
[6] T. Tonegawa et al., *Earth Planets Space*, **70** (2018), 106.
[7] S. Sakai et al., *Geol. Mag.*, **158** (2021), 72-83.
[8] N. Hirano et al., *Deep-Sea Res. I*, **154** (2019), 103142.
[9] N. Hirano et al., *Island Arc*, **30** (2021), e12386.

CO5-4 INAA, Halogen Analysis, and Ar-Ar/I-Xe Dating for the Hayabusa2-return sample

R. Okazaki[1], S. Sekimoto[2], N. Iwata[3], N. Shirai[4], and Y. Miura[5]

[1]*Department of Earth and Planetary Sciences, Kyushu University*
[2]*KURNS*
[3]*Faculty of Science, Yamagata University*
[4]*Department of Chemistry, Tokyo Metropolitan University*
[5]*Earthquake Research Institute, University of Tokyo*

INTRODUCTION: In 2020 Dec, the spacecraft Hayabusa2 returned and brought back the samples collected from the asteroid Ryugu to the Earth [1, 2]. The Ryugu samples will be allocated to and studied by the initial analysis teams consisting of the 6 sub-teams, 1) chemistry (elements and isotopes), 2) petrology and mineralogy of coarse grains, 3) petrology and mineralogy of fine grains, 4) volatiles, 5) insoluble organic matter, and 6) soluble organic matter [3]. We belong to the volatile sub-team, and will conduct a combination analysis of INAA, halogen measurement, and Ar-Ar/I-Xe dating.

We have carried out rehearsal measurements since 2013 (project #: 25066, PI: S.S.), and established the analytical method.

The main object in this proposal is to evaluate the neutron flux variation among the samples irradiated, by using two orthoclase mineral standards that were located at the top and the bottom in one irradiation capsule. Gamma-ray measurements and noble gas analyses were also performed for various standard and meteorite samples as a realistic rehearsal for the Ryugu sample analysis.

EXPERIMENTS: Prepared samples for the November irradiation were three meteorite samples (Allende CV chondrite, Murchison CM chondrite, Bjurböle L/LL4 chondrite) and our standard samples (JB-1, BHVO-2, orthoclase, sanidine, and wollastonite). For the December irradiation, orthoclase, sanidine, and Allende samples were prepared. Each of the samples was placed in a conical dimple (φ1, depth ~ 0.5 mm) of a sapphire disk (φ5.5, 1.5 mm thick), and covered with a sapphire disk (φ5.5, 0.3 mm thick). Each of the sapphire container was wrapped with pure aluminum foil. These Al-wrapped containers were stacked and sealed in the capsules for the Long-term irradiation. Condition of the Long-term irradiations were 94 hours under 1MW-operation + 12 h under 5MW-operation and 141 hours under 1MW-operation + 18 h under 5MW-operation for the Nov and Dec irradiations, respectively.

In order to reduce the radioactivity from the sapphire containers and Al foil, the samples were moved to non-irradiated sapphire containers after the irradiation. Gamma-ray measurements of radioactive nuclides were performed at KURNS, preceding noble gas analysis at Kyushu Univ.

REUSLTS and DISCUSSION: The gamma-ray measurements for four Allende samples (the sample weights are 1.312 mg, 0.176 mg, 0.260 mg, and 0.162 mg) confirmed the homogeneity of the sample. Also, the homogeneity of JB-1 (1.090 mg, 0.681 mg, 0.966 mg) and BHVO-2 (1.037 mg, 1.094 mg, 0.827 mg) standard samples were confirmed.

Most of the ^{40}Ar concentrations in the orthoclase standard samples converges on the right value of 3.0E-4 cm^{3}STP/g, whereas a few data are away from the value (Fig. 1). This problem is due to the small sample size (~100 μg), and can be solved by multiple measurements. Comparing the average values, the December irradiation samples contain about 1.5 times more ^{39}Ar produced via the ^{39}K(n, p)^{39}Ar reaction than the November samples. The difference in the ^{39}Ar concentrations is in good agreement with that in the irradiation duration.

The concentrations of ^{39}Ar also depend on the location within the irradiation capsule. There is an about 20% difference between the two orthoclase samples irradiated in the Nov irradiation. These two samples were ca. 5cm apart each other, and other samples were between the two orthoclase samples. Therefore, the neutron flux should be corrected with respect to the sample location within the irradiation capsule.

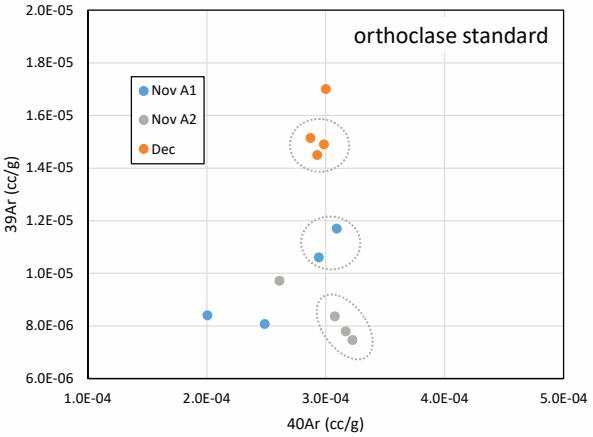

Fig. 1. Concentrations of ^{39}Ar and ^{40}Ar in the irradiated orthoclase standard samples

REFERENCES:

[1] Tachibana *et al.* 52nd Lunar and Planetary Science Conference, abstract #1289 (2021).
[2] Yada *et al.* 52nd Lunar and Planetary Science Conference, abstract #2008 (2021).
[3] Tachibana *et al.* American Geophysical Union, Fall Meeting 2018, abstract #P33C-3846 (2018).

CO5-5 Determination of Abundance of Rare Metal Elements in Seafloor Hydrothermal Ore Deposits by INAA Techniques-7: Cross check with ICP-QMS analysis

J. Ishibashi, Y. Sekiya[1], K. Yonezu[1], T. Nozaki[2], Y. Takaya[3], R. Okumura[4], Y. Iinuma[4] and K. Takamiya[4]

Department of Earth and Planetary Sciences, Faculty of Science, Kyushu University
[1]Department of Earth Resources Engineering, Faculty of Engineering, Kyushu University
[2]Submarine Resources Research Center, Research Institute for Marine Resources Utilization, Japan Agency for Marine-Earth Science and Technology (JAMSTEC)
[3]Department of Systems Innovation, School of Engineering, the University of Tokyo
[4]Institute for Integrated Radiation and Nuclear Science, Kyoto University

INTRODUCTION: Instrumental neutron activation analysis (INAA) has several advantages for geochemical tools to provide useful information for mineral exploration. For example, INAA enables highly sensitive multi-element analysis without geochemical pretreatment. We have conducted preliminary studies using mineralized samples collected from active seafloor hydrothermal fields, with a view to confirm and extend the range of application of this technique. Here, we report a result of cross check with inductively coupled plasma quadrupole mass spectrometry (ICP-QMS analysis).

EXPERIMENTS: Sulfide deposits collected from an active seafloor hydrothermal field in the Okinawa Trough were provided for a cross check analysis. For INAA analysis, 10-20 mg of powdered samples were irradiated at Pn-2 (thermal neutron flux = 5.5×10^{12} n/cm^2/sec at 1 MW operation) for 25 minutes, and the gamma ray activity was measured for 15 minutes after adequate cooling time (~30 hours). ICP-QMS analysis followed procedure reported in other studies (Nozaki et al., 2021). Powdered samples weighing ca. 50 mg were dissolved by HNO_3-$HClO_4$-HF digestion in Teflon PFA screw-cap beakers, then heated overnight on a hot plate at 110 °C. The digested samples were progressively evaporated at 110 °C for more than 12 h, 130 °C for 3 h and 160 °C until dryness. The residue was dissolved in 5 mL Milli-Q de-ionized water combined with 4 mL HNO_3 and 1 mL HCl, then further diluted to 1:100 by mass (total dilution factor ca. 20,000) before introduction into the ICP-QMS (Agilent 7500ce).

RESULTS: A result of cross check is illustrated in Fig. 1, where content of eight elements (Au, Sb, Ag, As, Zn, Cu, Mn and Na) determined by INAA is plotted against that by ICP-QMS analysis, and plots are represented by element symbols. Basically, contents determined two analytical techniques well agreed, which supports analytical accuracy for trace element analysis employing INAA. A few plots are in the region beneath the diagonal line, which means notable discrepancies that content determined by INAA is lower than that by ICP-QMS. Such discrepancies are likely to be attributed to high background in the gamma ray spectrum due to excess activations of some specific nuclides.

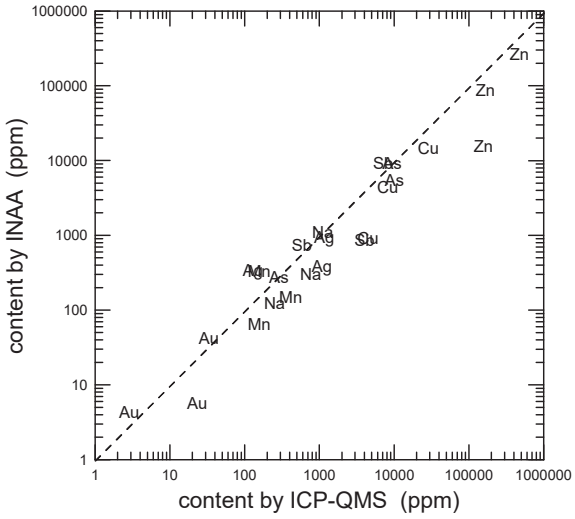

Fig. 1. A result of cross check analyses between ICP-QMS and INAA for three sulfide deposit samples. Contents of element (Au, Sb, Ag, As, Zn, Cu, Mn and Na) in each sample are plotted using element symbols.

[1] Nozaki *et al.*, Sci. Rep., **11**, 8809 (2021).

CO5-6 Size distribution of main constituents(Al,Ca,Fe) in soil particles of the atmospheric aerosols.

Norio Ito, Akira Mizohata, Yuto Iimura[1], Hisao Yoshinaga[1] Radiation Research Center, Osaka Prefecture University,[1] Institute for Integrated Radiation and Nuclear Science, Kyoto University

The soil particles in the atmosphere are main part of the coarse atmospheric aerosols in some land areas. At our observation site,Sakai,Osaka where a city and industry area can be found and about 2000 west from the China land , soil particles are locally produced from the near land surfaces such as raw earth surface, road surface and farmland and have the sources at the long distance areas, mainly coming from the China land, called Kosa mainly coming on spring. There might be the difference of element constituents in the locally produced soil particles and soil particles coming from China land. The difference could be the indicator of the contribution of the effect of the China land soil on the local soil effect. From the result of elemental constituent in coarse aerosol by the size distribution(small soil particle can come into Sakai on the long distance) and seasonal change(on spring Kosa frequently comes) , we can investigate the effect of China land soil effect .

In this report,we analyze the size distribution of main constituents of soil particle, Al,Ca,Fe, of which concentrations are 1～10% using the Ca,Fe ratio to Al. The data is the analysis results of the elemental concentrations in the atmospheric aerosols observed at Sakai from 1995,about 50 sampling periods. In the sampling period(1 week) , the aerosols were collected by Andersen sampler that can separate the particles by 9 particle diameter range. The concentrations of element were obtained by the neutron activation analysis using Kyoto university neutron reactor.

From some results(period:2000-2003) of size distribution of Al,Ca,Fe(Fig.1), the soil particles can be found mainly coarse particle range (d>1.0μm) and on spring have higher concentrations than that of the other seasons. The ratios Ca/Al(Fig2a) show a flat behaviour on the particle size larger than 3μm, on smaller than 3μm the ratio decreasing. On the seasonally change of the ratio(Ca/Al), spring ratio, strongly effected from China land,has the smallest values suggesting the ratio(Ca/Al) is smaller than that of locally produced soil particles. On the other hand, the ratio (Fe/Al) has increase behaviour as the diameter decrease. This behaviour shows an different effect of the concentration difference of the China land soil particles. But the spring ratio(Fe/Ca) has the smallest values, indicating the source of Fe in the small particle(<2μm) might be particles from industry rather than soil particles.

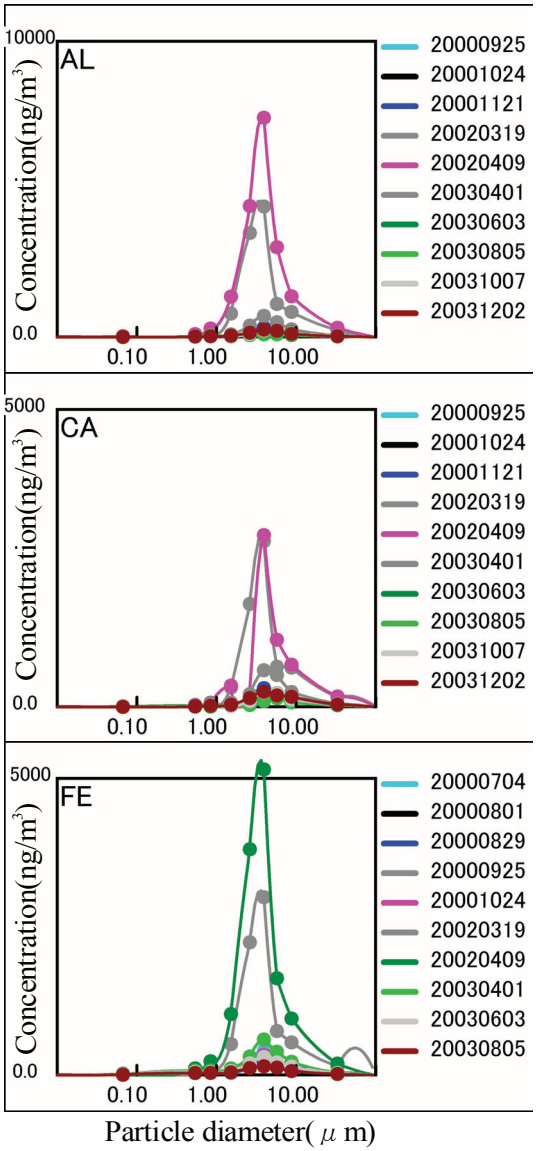

Fig.1 Size distribution of Al,Ca,Fe in the atmospheric aerosols observed at Sakai, 2000-2003.

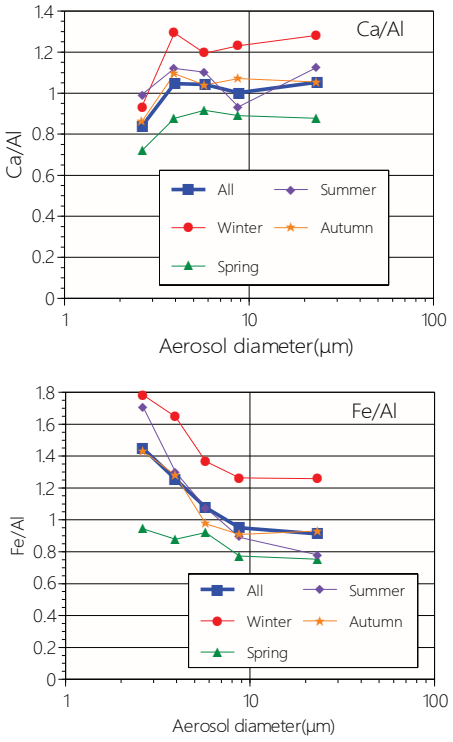

Fig.2 Change in ratio to Al of Ca and Fe by the particle size for all period and each seasons.

R2044

CO5-7 Mineral Luminescence and Application to Seismic Fault Geochronology

N. Hasebe, K. Miura[1], U. Uyangaa[1], Y. Igarashi[1], K. Oohashi[2], S.Akutsu[2], and Y. Iinuma[3]

Institute of Nature and Environmental Technology, Kanazawa University

[1]Graduate School of Natural Science and Technology, Kanazawa University

[2]Graduate School of Science and Technology for Innovation, Yamaguchi University

[3] Institute for Integrated Radiation and Nuclear Science, Kyoto University

INTRODUCTION: Luminescence dating observes the natural accumulated radiation damage caused by radioisotopes such as U and Th as the form of glow after stimulation by heating or lightening. Because of age range applicable, luminescence dating has been applied to Quaternary active fault (e.g., Ganzawa et al., 2013). However, little comprehensive studies on the effect of rock deformation or destruction through the faulting on luminescence signal have been reported so far. Oohashi et al. (2020) report the effect of faulting on the luminescence signal using quarts extracted from a granite sample. They gave a known radiation dose first, and artificially ground them to observe the behavior of luminescence sites during the faulting. They found frictional heating, that is controlled by the sample depth (normal stress), slip rate, and displacement length, is a major factor to reduce the luminescence intensity by the faulting. However, luminescence signal from the granitic quartz varies among quartz grains, causing a significant statistical uncertainty in the result. In this study, a sample with more stable luminescence signal was sought and an artificial grounding experiment was carried out to see the effect of starting material difference related to the difference in Geology.

EXPERIMENTS: Quartz were extracted from the sediment deposited on the beach, Kasado Island, Yamaguchi Prefecture. Conventional mineral separation processes were applied and luminescence characteristics were examined for quartz grains with the size of 150 -250 μm. Samples were wrapped with aluminum foil and irradiated at gamma-ray irradiation facility at KUR to give a known dose of 200 Gy. To check the initial status, some part of samples were brought to Kanazawa University and optically stimulated luminescence (OSL) was measured. Afterwards, samples were brought to Yamaguchi University and friction experiment to simulate fault activity was performed.

RESULTS: The quartz from Kasado inland mainly composed of fast and medium luminescence components (Fig. 1). Suitability of Kasado quarts in luminescence measurement was examined through preheat plateau test, dose recovery test and recycling ratio check (Fig. 2). When we estimated the amount of accumulated dose by luminescence measurement after the gamma irradiation, the accumulated dose was smaller than expected, and they are in the range of 0.4-17 Gy. This discrepancy may be caused by the different ionization efficiency between quartz and water, which is used to determine the dose distribution in the gamma irradiation facility. The frictional experiment resulted in the consistent behavior in luminescence signal decrease with the previous result (Oohashi et al., 2020), demonstrating that the luminescence signal decrease by faulting is a general phenomenon regardless of quartz source or luminescence component.

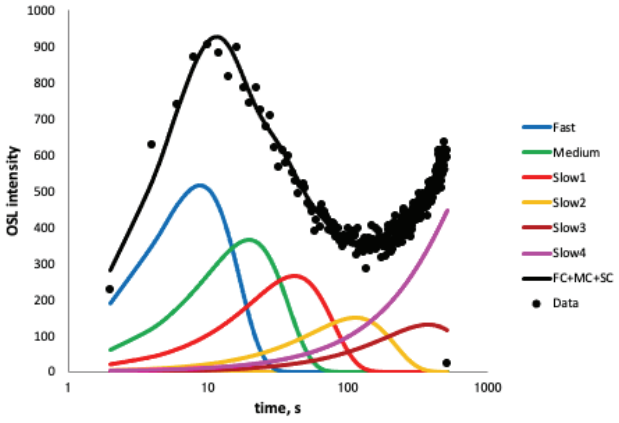

Fig. 1. Example of LM-OSL signal and the results of deconvolution.

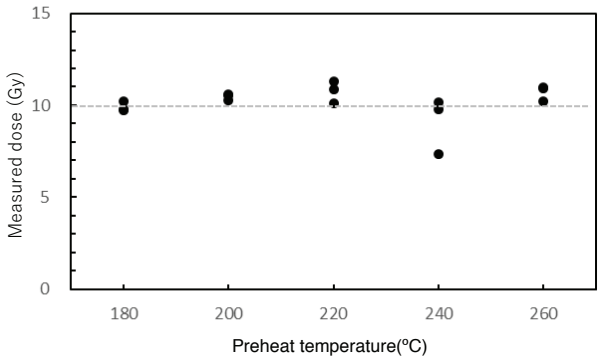

Fig. 2. Results of preheat plateau test

REFERENCES:

[1] Y. Ganzawa *et al.*, Jour. Geol. Soc. Japan, **119** (2013 714-726.

[2] K. Oohashi et al., JGR Solid Earth (2020) https://doi.org/10.1029/2020JB019900

CO5-8 Absorption of alkali metal ions by white radish sprouts (II)

M. Yanaga, S. Konagai[1], M. Hasegawa[1], H. Yoshinaga[2], R. Okumura[2] and Y. Iinuma[2]

Center for Radioscience Education and Research, Faculty of Science, Shizuoka University
[1]*Department of Chemistry, Faculty of Science, Shizuoka University*
[2]*Institute for Integrated Radiation and Nuclear Science, Kyoto University*

INTRODUCTION: According to a rumor damage survey on agriculture, forestry and fishery products in the disaster area conducted by the Consumer Affairs Agency in January 2021, 8.1% people still answered that they "hesitate" to purchase food from Fukushima Prefecture even though it has been about 10 years since the Fukushima Daiichi Power Plant accident occurred[1]. It seems that the damage caused by rumors will not disappear as long as radioactive substances remain in the field soil. Radioactive cesium is especially a problem because of its long half-life. However, simply removing the contaminated soil will result in a large amount of radioactive waste. Therefore, separating radioactive cesium from the soil is necessary to prevent damage by rumors and to minimize the quantity of radioactive waste.

Our previous reports have shown that the absorption of radioactive cesium from artificially contaminated soil into rice plants increased by adding a stable isotope to irrigation water and that the possibility that the cesium atoms added were replaced with radioactive cesium atoms in soil [2, 3]. However, addition of excess amount of stable cesium caused an obstacle to growth of rice plant [4]. Therefore, we recently conduct hydroponic culture of white radish sprouts and analyze trace elements contained in leaves and stems to investigate the behavior of cesium added to the culture solution and the competitive relationship between alkali metals.

EXPERIMENTS: *Materials and Method* Cultivation of white radish sprouts was carried out by adding alkali metal ions, such as potassium ions, rubidium ions and/or cesium ions, to a diluted solution of a commercially obtained culture solution, HYPONeX® (HYPONeX JAPAN CORP.,LTD.).

Seeds of white radish sprouts were soaked in ultrapure water and germinated in a dark place (1st day). The germinated white radish sprouts were transferred to a bright place, and 20 mL of culture solution diluted to 1/2000 concentration was added on 4th day. On 8th day, (Exp. 1) 20 mL of CsCl or RbCl aqueous solution ($1.0 - 30.0 \times 10^{-6}$ mol/L) or 20 mL of ultrapure water, or (Exp. 2) 20 mL of CsCl (20.0×10^{-6} mol/L), and 20 mL of KCl aqueous solution ($1.0 - 30.0 \times 10^{-6}$ mol/L) or 20 mL of ultrapure water, was added. Then, they were harvested on the 12th day.

INAA The samples in polyethylene capsules were irra-diated in Pn-3 for 90 seconds and in Pn-2 for 4 hours, for short and long irradiation, respectively. As comparative standards, the certified NIST Standard Reference Mate-rial 1577b Bovine Liver as well as elemental standard for Cs was used. The γ-ray spectroscopic measurements with an HPGe detector were performed repeatedly for the short-irradiated samples: the first measurements for 120 – 900 seconds after decay time of 5 - 15 minutes and the second one for 250 - 1200 seconds after 60 - 150 minutes. The long-irradiated samples were measured for 1 - 24 hours after an adequate cooling time (15 - 60 days).

RESULTS: Previously, we reported that increasing the concentration of cesium ions in the culture medium caused leaf discoloration and growth disorders[5]. No such disorder was observed in the range of cesium ion concentration in Exp.1 of the present work. However, average manganese concentration in the leaves and stems of white radish sprouts grown with the addition of cesium ions was 19.1 ± 0.9 μg/g, whereas that with the addition of rubidium ions was 22.3 ± 0.5 μg/g. This suggests that the decrease in manganese concentration due to the addition of cesium ions may cause plant growth troubles.

Increasing the concentration of cesium or rubidium ions in culture medium increased the cesium or rubidium concentration in the leaves and stems. On the other hand, when the cesium ion concentration in the culture solution was kept constant and the potassium ion concentration was increased, the cesium ion concentration in the leaves and stems decreased (Exp. 2). This means that potassium ions suppress the absorption of cesium ions, or that potassium ions are more easily absorbed. However, no correlation was found between those effects and potassium ion concentration, and it depended only on the presence of potassium ions. In order to realize phytoremediation by adding stable isotope cesium, it is necessary to investigate furthermore the behavior of various essential elements such as potassium and manganese necessary for plant growth.

REFERENCES:

[1] Consumer Affairs Agency, Survey of consumer awareness regarding reputational damage (14th), https://www.caa.go.jp/notice/entry/023300/ [in Japanese].
[2] M. Yanaga *et al.*, NMCC ANNUAL REPORT, 22 (2015)185-190.
[3] M. Yanaga *et al.*, NMCC ANNUAL REPORT, 23 (2016)172-179.
[4] M. Yanaga *et al.*, KURNS Progress Report 2018 (2019)CO5-10.
[5] M. Yanaga et al., KURNS Progress Report 2019 (2020)CO5-9.

CO5-9 Study on the variation of the concentration of elements diffusing in the atmosphere by INAA

N. Hagura[1, 2], H. Matsuura[1, 2], T. Uchiyama[2], Y. Okada[2]

[1] Nuclear Safety Engineering, Tokyo City University
[2] Atomic Energy Research Laboratory, Tokyo City University

INTRODUCTION: Since 2002, sampling of airborne particulate matter have been performed on our facility, the Atomic Energy Research Laboratory of Tokyo City University (TCU-AERL). Even before that, studies on the measurement of radioactivity in the environment has been conducted, and the concentration distribution of Be-7 and Pb-210 and chemical forms in deposition have been analyzed [1]. These studies mainly focused on the biological characteristics of yellow sand that came to the Japanese archipelago. Samples are collected approximately every week. As partial example, Figure 1 shows the annual variation of atmospheric particulate matter (APM) concentration between 2011 and 2014 at TCU-AERL.

After the accident in Fukushima in March 2011, studies on the dynamics of radioactive cesium have been conducted [2, 3]. And we are also working on "Modeling of time series data of radioactive cesium concentration in lake water of Lake Onuma on Mt. Akagi [4]" and "Development of mathematical model for long-term prediction of radioactive cesium concentration in airborne particulate matter [5]" as a joint research program with Tsukuba University. These research themes have in common the elucidation of the dynamic behavior of cesium at low concentrations, and the neutron activation analysis method, which is a trace element analysis method, can serve as an important tool.

The sampled filters have been accumulated in the laboratory and are ready to be analyzed again. In this year we aimed to detect the trace elements by neutron activation analysis, targeting the samples from 2012 to 2014.

In the future, we plan to proceed with the analysis of a large number of samples in combination with the PIXE analysis method using the tandem accelerator at our facility (TCU-Tandem) [6], because it is impractical to analyze all samples by the Instrumental Neutron Activation Analysis (INAA) method.

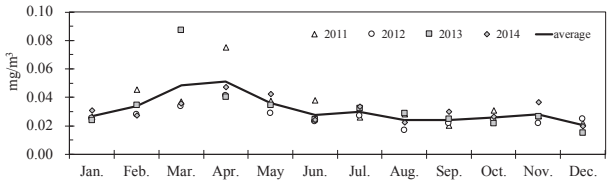

Fig. 1. Annual variation of APM concentration between 2011 and 2014 at TCU-AERL

EXPERIMENTS: We use a high volume air sampler (Shibata Scientific Technology LTD., HV-1000F, filter: ADVANTEC, QR-100 (collection efficiency: 99.99% for 0.3 μm particles)) with an inhalation flow rate of 700 L min^{-1}. The radioactivity of the filter that has collected dust is measured by a high-purity germanium semiconductor detector, and a part of the filter was stored for neutron activation analysis.

Irradiation was performed at the research reactor KUR at the Institute for Integrated Radiation and Nuclear Science, Kyoto University, between the November and December with four machine times in FY2020. The irradiation conditions are shown in Table 1. The measurement of radioactivity of short half-life nuclides was carried out using the HP-Ge semiconductor detector of the hot laboratory of KUR. And long and medium-lived nuclides, after cooling for one or two weeks, transported to the TCU-AERL, and was measured by a HP-Ge semiconductor detector. JLk-1 was used as a comparative standard substance.

Table 1. Irradiation conditions

Irradiation			Operating power	Thermal neutron flux
date	time	position		
2020/11/17	30 sec	Pn-3	1 MW	4.7 x 10^{12} n/cm^2/sec
2020/12/1	60 min	Pn-2		5.5 x 10^{12} n/cm^2/sec
2020/12/8	30 sec	Pn-3		4.7 x 10^{12} n/cm^2/sec
2020/12/15	60 min	Pn-2		5.5 x 10^{12} n/cm^2/sec

RESULTS: Focusing on the gamma-ray energy of 604 keV from Cs-134, the yearly cesium concentrations are discussed in Fig. 2. In this figure, the values for 2013 and 2014 are shown with respect to 2012. The error bars are the standard deviation of the variability of the seven samples for each year. This result shows that there is no significant difference in the amount of stable cesium sampled from year to year. We will continue to compare the trace elements contained in the filters.

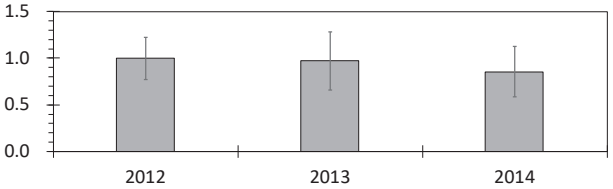

Fig. 2. Comparison of cesium concentration in 2013 and 2014 with respect to 2012.

REFERENCES:

[1] K. Hirose, et al., Atmospheric Environment, 38 (38), pp. 6601-6608 (2004).
[2] K. Nakamachi, et al., Bunseki Kagaku, 64 (8) pp. 589-594 (2015).
[3] N. Hagura, et al., Bunseki Kagaku, 66 (3), pp. 201-204 (2017).
[4] Y. Okada, et al., 6th Fukushima University IER Annual Symposium, P-129 (2020).
[5] E. Suetomi, et al., 6th Fukushima University IER Annual Symposium, P-130 (2020).
[6] N. Hagura, et al., Transactions of the Atomic Energy Society of Japan, 17 (3-4), pp. 111-117 (2018).

CO5-10 Neutron activation analysis of carbonate reference materials: coral (JCp-1) and giant clam (JCt-1)

S. Sekimoto, Y. Homura[a], V.D. Ho[1], M. Inagaki, N. Shirai[2], T. Ohtsuki

Institute for Integrated Radiation and Nuclear Science, Kyoto University
[1]Nuclear Research Institute, Vietnam Atomic Energy Institute
[2]Department of Chemistry, Tokyo Metropolitan University
[a]Present address: Novaltis Farma

INTRODUCTION: Geochemists are often interested in the abundance of halogen elements in geochemical materials such as crustal rocks, mantle materials, and meteorite samples, because halogens play an important role in investigating the petrogenesis of such materials and assist in tracing their origins and/or precursor materials [1-3]. In our previous work, radiochemical neutron activation analysis (RNAA) was refined to accurately determine even trace amounts of halogens (chlorine, bromine, and iodine) in sedimentary rock reference samples [4]. Subsequently, U.S. Geological Survey (USGS) geochemical reference materials were subjected to RNAA, and the data obtained were compared with literature data [5]. The two kinds of carbonate reference materials investigated here, JCp-1 (Coral) and JCt-1(Giant Clam), are prepared by the Geological Survey of Japan/National Institute of Advanced Industrial Science and Technology (GSJ/AIST), and the concentrations of many major and a few trace elements in these materials have been determined [6-8]. Data about the halogen contents in these materials is expected to significantly contribute to a better understanding of the chemistry of seawater and the marine environment, since halogens (especially iodine) are known to be extremely useful in investigating the geochemical circulation of terrestrial materials [9]. However, to our knowledge, there is not much data on the halogen contents of these carbonate materials.
The present study aims to use RNAA and instrumental NAA (INAA) to determine trace amounts of three halogens in JCp-1 and JCt-1, together with other elements. Based on the halogen data, the differences between the two carbonate reference materials is investigated. The INAA values obtained in the present study are compared with literature values, and the consistency between our data and the data from known literature is evaluated.

RESULTS: To probe the utility of the halogen data in interpreting geochemical formations, we have compared the halogen contents in these two carbonate materials with those in nine sedimentary rock materials (RNAA was used to determine the halogen content in all cases [4]). Since the carbonate materials contain CaO as the major component, the I/CaO and Br/CaO ratios in the two carbonates, as well as in the nine sedimentary rocks were determined and are shown in Fig 1. In spite of the fact that the CaO contents in the sedimentary rocks vary over a wide range (0.56% for JSd-3 (stream sediment) to 55.1% for JLs-1 (limestone)), the sedimentary rocks seem to exhibit a good correlation between these two ratios, except for JCh-1 (chert). As for the two carbonate reference materials, JCp-1 (Coral) also shows a reasonable correlation between the two ratios, implying that fractionation between Br and I may not have occurred in the formation of a coral like JCp-1 and the sedimentary rocks, except for JCh-1. On the other hand, JCt-1 (Giant Clam) clearly does not exhibit such a correlation, suggesting the possibility of fractionation of I from Br during its formation.

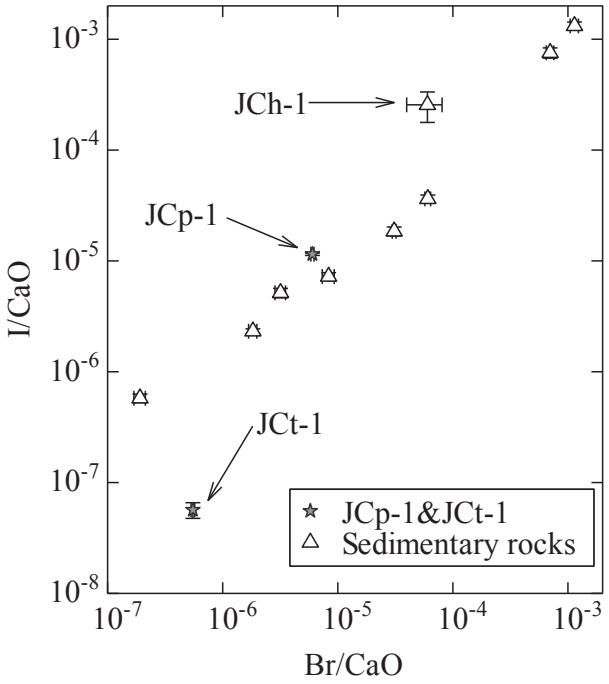

Fig. 1 I/CaO vs. Br/CaO ratios for JCp-1, JCt-1 and sedimentary rocks.

REFERENCES:

[1] MA Kndrick *et al.*, Geochim. Cosmochim. Acta **235** (2018) 285-304.
[2] L. Hughes *et al.*, Geochim. Cosmochim. Acta **243** (2018) 1-23.
[3] DE Harlov *et al.*, The Role of Halogens in Terrestrial and Extraterrestrial Geochemical Processes Springer Geochemistry, Gewerbestrasse, Switzerland (2018)
[4] S. Sekimoto *et al.*, Anal. Chem. **85** (2013) 6336-6341.
[5] S. Sekimoto *et al*., Geostand. Geoanal. Res. **41** (2017) 213-219.
[6] S. Aizawa, J. Radioanal. Nucl. Chem. **278** (2008) 349-352.
[7] M. Inoue *et al*., Geostand. Geoanal. Res. **28** (2004) 411-416.
[8] T. Okai *et al*., Chikyuukagaku **38** (2004) 281-286.
[9] B. Deruelle et al., Earth Planet. Sci. Lett. **108** (1992) 217−227.

CO5-11 ^{40}Ar-^{39}Ar Dating of Extraterrestrial Materials in KURNS

N. Iwata, S. Sekimoto[1], R. Okazaki[2] and Y. N. Miura[3]

Faculty of Science, Yamagata University
[1]Institute for Integrated Radiation and Nuclear Science, Kyoto University
[2]Department of Earth and Planetary Sciences, Kyushu University
[3]Earthquake Research Institute, University of Tokyo

INTRODUCTION: Radiometric dating is useful tool for unveiling formation and evolution process of planetary material. ^{40}Ar-^{39}Ar method is invaluable to date the timing of heating events on planetesimal and asteroid (e.g. Swindle et al. (2014) [1]). Especially, ^{40}Ar-^{39}Ar dating method with laser heating technique is suitable for small amount sample (e.g. Kelley, 1995 [2] and Hyodo, 2008 [3]).
For example, tiny material returned from asteroid 25143 Itokawa is dated using laser heating ^{40}Ar-^{39}Ar dating method by Park et al. (2015) [4] and Jourdan et al. (2017) [5]. Park et al. (2015) reported an age of 1.3 ± 0.3 Ga. Jourdan et al. (2017) reported an age of 2.3 ± 0.1 Ga. These ages indicate the timing of catastrophic events which were occurred on Itokawa's precursor body. Combining the ^{40}Ar-^{39}Ar ages and other chronological data, Terada et al. (2018) [6] overviewed the time evolution of the Itokawa asteroid. Similar investigation, the integration of multichronological data is proposed to the material that recovered from asteroid 162173 Ryugu and other extraterrestrial materials. ^{40}Ar-^{39}Ar dating will play an important role within the investigations.
To implement of dating of extraterrestrial material by ^{40}Ar-^{39}Ar method, we will develop a system which includes gas extraction and gas purification line in KURNS (Fig. 1).

EXPERIMENTS: Dr. R. Okazaki of Kyushu University designed the system. Fig.1 shows schematic diagram of the system. A continuous Nd-YAG laser (~60 W) extract gas from neutron irradiated sample. The extracted gas is purified using a Sorb-AC getter pump in purification part. Gas trap tree consists of several metal gas traps. The purified gas is encapsulated into metal gas trap (CH) in gas trap tree part. The purified gas in the metal gas trap is transported to laboratories of noble gas analysis (e.g. Kyushu University), and then, argon isotope of the gas is analyzed using noble gas mass spectrometer. Whole of the extraction and purification parts are evacuated by two oil rotary pumps, two turbo molecular pumps and an ion pump to ultra-high vacuum condition.
We have a plan to connect a quadrupole mass spectrometer (QMS) to this system, to perform on-lined laser heating ^{40}Ar-^{39}Ar dating in future.

RESULTS: We started assembling of the laser-heating gas extraction and purification system in KURNS in 2019. The design work and configuration of the system is almost completed in 2020. We are going to continue setting the system up during 2021.

REFERENCES:
[1] T. D. Swindle *et al.*, in *Advances in ^{40}Ar/^{39}Ar Dating: from Archaeology to Planetary Sciences*, edited by Jourdan, Mark, Verati (Geol. Soc., London, Spec. Pub. **378**, 2014) 333-347.
[2] S. P. Kelley, in *Microprobe techniques in the earth sciences*, edited by Potts, Bowles, Reed, Cave (Chapman & Hall, London, 1995) 327-358.
[3] H. Hyodo., Gondwana Res. **14** (2008) 609-616.
[4] J. Park *et al.*, Meteorit. and Planet. Sci., **50** (2015) 2087-2098.
[5] F. Jourdan *et al.*, Geology, **45** (2017) 819-822.
[6] K. Terada *et al.*, Sci. Rep., **8** (2018) #11806.

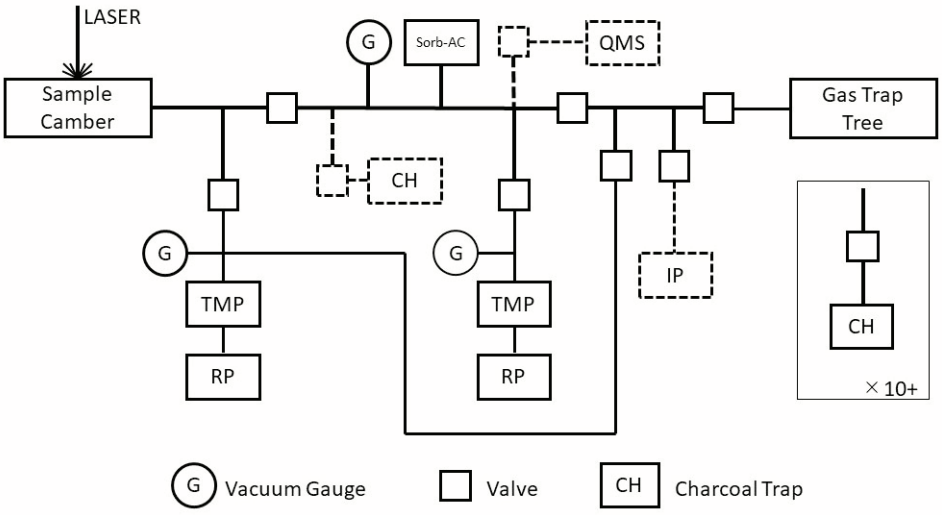

Fig. 1. Schematic diagram of gas extraction and purification line in KURNS. RP, TMP, IP and QMS respectively denotes rotary pump, turbo molecular pump, ion pump and quadrupole mass spectrometer. Components with dashed line are connected during 2021.

Neutron Activation Analysis of Iron Meteorites

N. Shirai[1], S. Sekimoto[2]

[1]*Department of Chemistry, Tokyo Metropolitan University*
[2] ***Institute for Integrated Radiation and Nuclear Science, Kyoto University***

INTRODUCTION: Iron meteorites are made of FeNi metal phases with such minor minerals as schreibersite, troilite, and cohenite. Most iron meteorites are considered to be samples of metallic cores and pools that formed in small planetary bodies, petrological, mineralogical and chemical studies of iron meteorites are fundamental for unraveling the processes of planetary differentiation. Iron meteorites are classified into 13 groups based on their structure and chemical compositions [1]. Iron meteorites which do not fit into an established group are described as ungrouped. The structural classification is based on the presence or absence of the Widmanstätten pattern, which develops as a two-phase intergrowth of kamacite and taenite. Chemical classification is based on the abundances of trace elements (Ga, Ge and Ir). Traditionally, Ni was used as the independent variable in classifying iron meteorites. Recently, Au has been used due to a much better estimate of a meteorite's position within the fractional crystallization [2]. In this study, our analytical procedure of INAA for iron meteorites [3] was modified so that it can be applied to the new chemical classification. Based on the analytical results, accuracy of our data obtained by using the modified procedure and how promisingly our analytical method can be applied to classification of iron meteorites.

EXPERIMENTS: Odessa (IAB-MG), Canyon Diablo (IAB-MG), Cape York (IIIAB), Muonionalusta (IVA) and Dronino (ungrouped) iron meteorites were analyzed in this study. These iron meteorites were sawn into plate roughly 1 x 4 x 4 mm in size by using a ISOMET low speed saw. After cutting, each iron meteorite was cleaned by sandpaper. Then, iron meteorites were washed in ultrasonic bath by using acetone. The analytical procedure used in this study is basically similar to that described by Shirai et al. [3]. Sample was irradiated for 10 sec. at the pn-3 of Institute for Integrated Radiation and Nuclear Science, Kyoto University, Kyoto with thermal and fast neutron fluxes of 4.6 x 10^{12} and 9.6 x 10^{11} $cm^{-2}s^{-1}$, respectively. After irradiation, sample was immediately measured for gamma-ray emissions for the determination of Co, Ni, Cu, Ge and Rh. After one day cooling, sample was measured for gamma-ray emissions for the determination of Fe, Co, Ni, Ga, As, W, Ir and Au. Chemical standards were prepared from high-purity chemical reagents for the elements of interest. For Fe, Co and Ni, metal was used. For the other elements, single-element standard solution for atomic absorption analysis was used. These single-element standard solutions were separately prepared by dropping known concentration of these ele-ments on the filter papers.

RESULTS: For all iron meteorites analyzed in this study, five elements (Fe, Co, Ni, Cu, Rh and Au) could be detected. Our values for these elements are in good agreement with the corresponding literature values [4-6]. In contrast, Ge and Ge in Muonionalsuta and Dronino, As in Dronino, W in Cape York, Muonionalusta and Dronino and Ir in Muonionalusta could not be detected due to their low concentrations.

Gallium abundances for iron meteorites are plotted against Au abundance in Fig. 1. Our data for Odessa and Canyon Diablo, and Cape York are plotted in the field of IAB and IIIAB, respectively, indicating that these iron meteorites are classified into IAB and IIIAB. Our observations are consistent with the previous studies [4-6]. The detection limit of the modified analytical procedure is about 10 ppm of Ga. Except for some IAB, IIF, IIIF, IVA and IVB, Ga abundances for the most iron meteorites can be determined by using the modified analytical procedure. The detection limit obtained in this study is 17 times higher than those in the previous study [3]. In the analysis of iron meteorites with having less than 10 ppm of Ga, iron meteorite is reirradiated for 4 hrs at the pn-2 [3] or other elements such as Ir can be used for the classification of iron meteorites. It is concluded that our modified analytical procedure of INAA is more simple than the previous procedure [3].

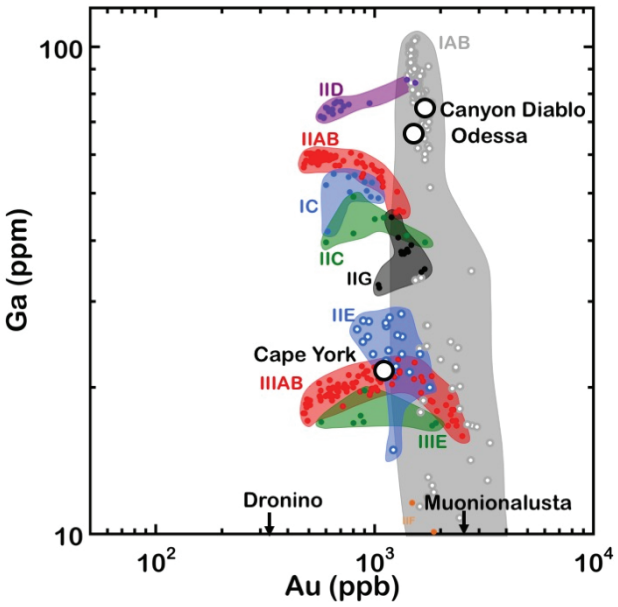

Fig. 1. Au abundances versus Ga abundances for iron meteorites.

REFERENCES:

[1] J. I. Goldstein *et al.*, Chem. Erde., **69** (2009) 293-325.
[2] J. T. Wasson *et al.*, Geochim. Cosmochim. Acta **62** (1998) 715-724.
[3] N. Shirai *et al.*, J. Radioanal. Nucl. Chem., **303** (2015) 1375-1380.
[4] J. T. Wasson, Geochim. Cosmochim. Acta **63** (1999) 2875-2889.
[5] J. T. Wasson and J. W. Richardson, Geochim. Cosmochim. Acta **65** (2001) 951-970.
[6] J. T. Wasson and G. W. Kallemeyn, Geochim. Cosmochim. Acta **66** (2002) 2445-2473.

CO5-13 Neutron activation analysis of stable cesium and trace elements in the lake water of Lake Onuma on Mt. Akagi

Y. Okada [1], N. Kumagai [2],T. Uchiyama [1], N. Hagura [3], H. Matsuura [3] and Y Iinuma [4]

[1]*Atomic Energy Research Laboratory, Tokyo City University*
[2]*Cooperative major in Nuclear Energy, Tokyo City University*
[3]*Department of Nuclear Safety Engineering, Tokyo City University*
[4] *Institute for Integrated Radiation and Nuclear Science, Kyoto University*

INTRODUCTION: Lake Onuma on Mt. Akagi in Gunma Prefecture has been confirmed to be contaminated by radioactive Cs due to the accident at the Fukushima Daiichi Nuclear Power Plant in 2011. We have been investigating the lake for the past eight years, but the decrease in the concentration of radioactive Cs in the lake water and in the inhabiting pond smelt has been very slow[1,2)]. In order to investigate the cause of this, we analyzed trace elements in sediments and phytoplankton last year. In this study, trace elements in the lake water were analyzed by neutron activation analysis. From these results, we aim to derive the relationship between trace elements and the movement of radioactive Cs in Lake Onuma.

EXPERIMENTS: Samples were collected at depths of 0 m, 8 m and 15 m in 2018 and 2019. Two types of lake water samples were collected untreated samples (bulk samples) and filtered through a 0.45 μm filter (soluble form). Approximately 500 mL of each sample was freeze-dried. 27 samples (approximately 1 mg to 2mg of drying weights) and reference standard materials (JLk1,NIES8) were irradiated with KUR Pn3 (thermal neutron flux: 4.68 x 10^{12} /ncm $^{-2}$/ s $^{-1}$) for 30s, followed by cooling for 3 to 5 min, and ɤ-ray measurements were performed. In addition, was irradiated with KUR Pn2 (thermal neutron flux: 5.5 x 10^{12}/ ncm^{-2} /s $^{-1}$) for 1 hour, followed by cooling for 7to 14 days, and ɤ-ray measurements were performed. The analysis was carried out using software (Gamma Studio : SEIKO EG &G Co.). The analytical values for the particle form were obtained by subtracting the value for the soluble form from the analytical value for the bulk sample.

RESULTS: Seventeen elements (Al, Mg, Mn, Na, Fe, V, Ca, K, Sc, Cr, Co, Zn, Rb, Sb, Cs, Ba and Ce) in the lake water were measured by neutron activation analysis. The results showed that Cs and Rb were detected in all samples. The elements detected in the bulk samples were Al, V, Mg, and Ca. In addition, Fe, Mn, and Cr were detected in bulk samples and soluble forms collected in August 2018.

Figure 1 shows the concentrations of stable Cs at 0, 8, and 15 m depth in the lake. The concentration of stable Cs in the bulk samples varied from 0.1 μg/L to 0.4 μg/L at water depths of 0, 8, and 15 m. It was found that the surface layer at 0 m contained more cesium in the particle form than in the soluble form, regardless of the season.

Research on radioactive cesium in lake water has been conducted since 2012. As a result, we found that the concentration of soluble forms radioactive cesium increases in summer in the deep layer of 15m depth. This time, the same result was obtained for stable cesium in the lake water.

In Lake Onuma, a water temperature dynamic layer is formed within the lake bottom during the summer, which is divided into a surface layer and a deep layer. In the deep layer, oxygen depletion phenomenon occurs. In this study, 1.2 mg/L of Fe and 0.77 mg/L of soluble forms Fe were detected in the 15 m bulk in Aug. 2018. These results suggest that the deep water is in a reducing state during the summer. It was suggested that the reducing state was related to the increase in soluble forms Cs. The concentration of Rb, the same alkali metal, varied in the range of 0.7 μg/L to 2.5 μg/L. Similar to Cs, Rb was found to be more abundant in soluble form in August. Looking at the concentration of K, the same alkali metal, 0.04 μg/L to 0.06 μg/L was contained in the soluble form, and no seasonal variation was observed.

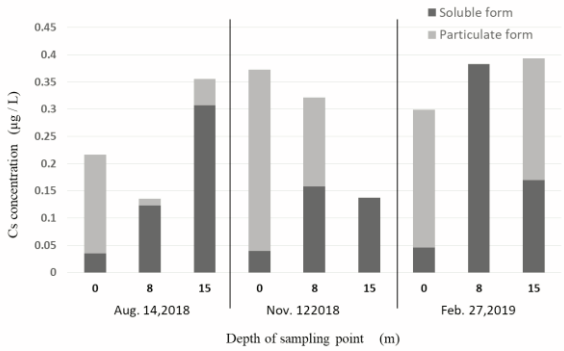

Fig. 1 Stable cesium concentration of lake water in Lake Onuma

In the future, it will be necessary to consider the material balance.

REFERENCES:

1) M.Mori,K.Tsunoda, *et al*., Sci. Total Envron., **575**,1247-1254 (2017).
2) K.Suzuki, S.Watanabe*et, al.*, Sci. Total Envron., **622**,1153-1164 (2018).

CO5-14 Transfer of silver, cesium, and rubidium from nutrient solution to radish (*Raphanus sativus* var. sativus)

T. Kubota, S. Fukutani, and Y. Shibahara

Institute for Integrated Radiation and Nuclear Science, Kyoto University

INTRODUCTION: Silver-110m is one of the radionuclides that is significantly detected in the environmental samples after the accident of the Fukushima Dai-ich nuclear power plants [1]. Its effect on internal exposure was insufficiently reported compared to other major radionuclides, such as cesium-137. Evaluations of internal exposure require various environmental parameters. Among them, the transfer behavior of radionuclides to and inside editable plants, radish (*Raphanus sativus* var. sativus), was investigated under hydroponic condition. Besides of radioactive silver and cesium, radioactive rubidium was added to compare their transfer behavior.

EXPERIMENTS: Silver-105, cesium-136, and rubisium-83 used as tracers were produced through photo nuclear reaction at KURNS-LINAC and purified by precipitation and ion chromatography [2]. Radish samples were cultivated from seed in non-radioactive nutrient solution [3] for four weeks and then were replaced to fresh nutrient solution containing above radionuclides followed by cultivation for one, three, and five days. After each cultivation time, the root was washed by reverse-osmosis water and the washing solution was returned to its original nutrient solution. The cultivated sample was divided into three parts, root, radish, and leaf to be dried at 75 ºC for more than 12 hours. The radioactivity of dried samples and nutrient solution was measured by γ-spectrometry to determine the transfer and distribution ratio of three elements.

RESULTS: The transfer ratio of silver from nutrient to plant saturated at only one day, which was different from cesium and rubidium in Table 1. However, the ratio reached at most 60%. The transfer tendency of cesium was similar to rubidium while the ratio was smaller than rubidium. The distribution ratio of radionuclides between root and whole plant body was constant over cultivation time in Table 2. Silver almost completely remained in root and hardly moved to other parts. Even though the total amount of cesium and rubidium in the whole plant body increased as seen in Table 1, it is interesting that the distribution ration of those was constant. The distribution ratio of cesium and rubidium between radish and whole plant body decreased with cultivation time in Table 3. On the contrary, the distribution ratio of those between leaf and whole plant body increased in Table 4. This opposite tendency would be ascribed to the difference of the translocation rate of root to radish and radish to leaf. The same transfer tendency of silver between radish and lettuce (*Lacutuca sativa* var. crispa) [4] suggests that silver uptaken through root surface is one of elements that are unlike to translocate from root to other plant parts.

Table 1 Transfer ratio of radionuclides from initial nutrient solution to plant

Day	^{105}Ag	^{136}Cs	^{83}Rb
1	0.56	0.05	0.11
3	0.62	0.15	0.32
5	0.56	0.33	0.61

Table 2 Distribution ratio of radionuclides between root and whole plant body

Day	^{105}Ag	^{136}Cs	^{83}Rb
1	0.96	0.24	0.15
3	0.96	0.24	0.15
5	0.95	0.26	0.15

Table 3 Distribution ratio of radionuclides between radish and whole plant body

Day	^{105}Ag	^{136}Cs	^{83}Rb
1	0.01	0.22	0.31
3	0.01	0.19	0.24
5	0.02	0.10	0.16

Table 4 Distribution ratio of radionuclides between leaf and whole plant body

Day	^{105}Ag	^{136}Cs	^{83}Rb
1	0.01	0.47	0.49
3	0.03	0.58	0.61
5	0.03	0.64	0.70

REFERENCES:

[1] K. Saito *et al.*, J. Env. Rad., **139** (2015) 308 - 309.
[2] T. Kubota *et al*., KURNS Progress Report (2018) 209.
[3] K. Fujiwara *et al.*, Jpn. J. Health Phys., **50** (2015) 189 - 193.
[4] K. Iwata *et al*., Proc. 18th Workshop on Environmen-tal Radioactivity, (2017) 163-166.

CO5-15 Neutron Activation Analysis of Environmental Samples

Y. Oura and Md. S. Reza

Graduate School of Science, Tokyo Metropolitan University

INTRODUCTION: Environmental pollution is an important issue for our healthy life. Determination of elemental composition is one of the ways for an environmental examination. For example, shellfish are commonly used for an assessment of ocean environment. In this case soft tissues in shellfish (e.g., mussels) are mainly analyzed for elemental concentration, whereas shells seem not to be analyzed. Thus, we tried to determine elemental concentrations in shell if they are effective in assessing the coastal/lake environment. In this work, Japanese basket clam (scientific name: corbicula japonica) living in brackish-water lake was selected because it is easily available, and it has an easily handled size. For atmospheric environment, attention has been focused on the effects of very small particles called PM2.5 on human health in recent year. Elemental composition of particulates plays an important role for estimation of their origins. We have collected PM2.5 particulates at Hachioji, Tokyo and determination of elemental concentration in PM2.5 particulate has been continued since 2018.

EXPERIMENTS:

Shells

Japanese basket clam (Yamato Shijimi) yielded at different four lakes were got from a supermarket. After discarding soft tissues, clamshells were cleaned properly by ultrapure water using an ultrasonic water bath. Then they were made powder after drying. Shells of two individuals were made powder together to prepare a sample. Five samples (total 10 individuals) were subjected to analysis for each lake. About 180 mg of each sample was irradiated together with reference materials (GSJ JCp-1, JCt-1, and JB-1a) for 30 seconds and 4 hours at KUR (1 MW operation). After irradiation gamma-rays were measured by HPGe detector.

PM2.5

PM2.5 particulates have been collected on a Nucleopore polycarbonate filter with 0.2 μm of pore size for three weekdays every week at a rooftop of a building in Minami-Osawa campus of Tokyo Metropolitan University. Polycarbonate filters on which PM2.5 was collected were cut in half, then one half was subjected to analysis. Filter sample in clean polyethylene bag was irradiated together with reference materials (NIST 1648, NIST 1632c, NIES No.8, and GSJ JB-1a) for 5 minutes at KUR (1 MW operation) and 1 hour at KUR (5 MW operation). After irradiation, gamma-rays were measured by Ge detector.

RESULTS:

Shells

Shijimi shells in four different lakes (in Hokkaido, Aomori, Ibaraki, and Shimane) were analyzed and eight elements (Na, Ca, Mn, Fe, Zn, Br, Sr, and Ba) were determined. Mean elemental concentrations of 5 determination values for each location (H, A, I, and S) are shown in Fig.1 together with standard deviations expressed by error bars. Calcium is the most abundant element among determined elements because shell is calcium carbonate, thus no deviations of concentrations are observed in 20 samples. And Na, Zn, and Sr concentrations are also less deviation. For Fe, large deviation was observed in 5 samples of each 4 location, but the average values are almost consistent. On the other hand, the mean values of Mn and Ba for 4 locations are varied. Although Ba is a homologous element of Ca and Sr, a behavior of Ba is possibly different from that of Ca when shell production. And it is interesting to see if Mn is a kind of environmental indicator.

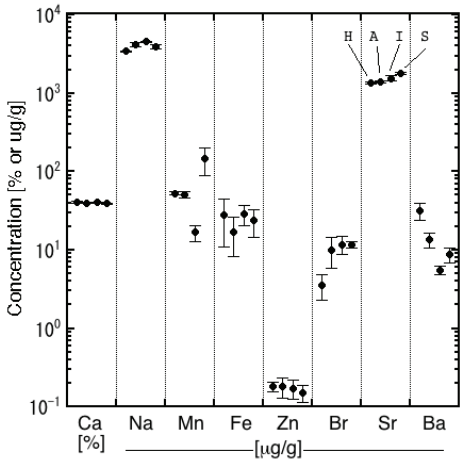

Fig. 1. Means of elemental concentrations in shells yielded in different lakes. Error bars express standard deviations of 5 samples for each lake.

PM2.5

Mass concentrations of PM2.5 particulates collected in FY2020 (Jan. to Sep.) ranged from 3 to 22 μg m^{-3}, and their median of 12 μg m^{-3} was almost same as the median in 2018 and 2019. Determined elemental concentrations in PM2.5 particulates collected in 2020 are compared to those in 2018 and 2019. The median values of elemental concentrations in 2018 and 2019 are similar in general like the mass concentrations. Atmospheric environment around our university seems not to be different yearly among in 2018, 2019, and 2020 on the average.

CO5-16 I-Xe ages of solar noble gas-rich meteorites

H. Sumino, K. Arai[1], S. Tachibana[1], J. Ren,
A. Takenouchi[2], M. Koike[3], R. Okumura[4], Y. IInuma[4],
H. Yoshinaga[4] and S. Sekimoto[4]

Graduate School of Arts and Sciences, University of Tokyo
[1]Graduate School of Science, University of Tokyo
[2]National Institute of Polar Research
[3]Graduate School of Advanced Science and Engineering, Hiroshima University
[4]Institute for Integrated Radiation and Nuclear Science, Kyoto University

INTRODUCTION: During the formation of planets from nebula gas and dust composing protoplanetary disk in the early solar system, the activity of the primordial sun increased at a certain period, and a large amount of nebula gas was blown away from the planet formation region by the strong solar wind. The lifetime of protoplanetary disk gas ranges 1-10 million years, which depends on viscous dissipation and photo-evaporation of the disk gas. It is not clear how long the Sun's protoplanetary disk held its gas component, during which gas giants formed. Ca-, Al-rich inclusions and chondrules are considered to have formed in the presence of disk gas, but the timing of clearing of disk gas has not yet been tightly constrained [1]. Bajo [2] found a correlation between Solar-wind derived noble gas concentrations and I-Xe ages of brecciated chondrites. Bajo [2] hypothesized that the I-Xe ages, which could represent impact ages [3], of solar-wind-rich meteorites indicated the timing of disk-gas clearing because the solar wind reaches to the surface of small bodies only after the complete dissipation of disk gas. In this study, to test this hypothesis, I-Xe ages and solar-wind noble gas concentrations of Zag (H36) and Northwest Africa 801 (CR2) (NWA 801) meteorites were determined.

EXPERIMENTS: About 30 mg fragments of these meteorites, irradiated with neutrons at the Kyoto University research reactor, were heated in vacuum stepwisely in the temperatures range of 400-1800°C to extract xenon isotopes, including naturally-occurring radiogenic ^{129}Xe derived from ^{129}I and ^{128}Xe produced from ^{127}I by (n, β) reaction in the reactor. After purifying the noble gases extracted at each heating step, xenon isotope ratios were measured using a magnetic-sector-type mass spectrometer VG3600 [4]. The obtained ^{129}Xe/^{128}Xe ratios of the samples after corrections for low-temperature alteration and trapped component were converted to relative I-Xe ages by comparing with ^{129}Xe/^{128}Xe ratio of the Shallowater meteorite standard and was irradiated with neutrons together with the samples. About 5 mg fragments of the same meteorite specimen were heated in vacuum at 800 and 1700℃ for naturally-occurring noble gas analysis to determine concentrations of solar-wind-derived noble gases.

RESULTS: The obtained ^{129}Xe/^{128}Xe ratios of the samples after corrections for low temperature alteration and trapped component were converted to relative I-Xe ages by comparing with ^{129}Xe/^{128}Xe ratio of the Shallowater meteorite with the absolute age of 4.5633±0.0004 billion years [5]. Although our new I-Xe ages are associated with relatively lager errors compared to those reported in [2] due to less neutron fluence to produce ^{128}Xe, two samples from the solar-wind-poor portion of Zag was systematically older (4.551 ± 0.008 and 4.558 ± 0.013 billion years) than those from the solar-wind-rich portion (4.554 ± 0.009 and 4.551 ± 0.006 billion years), which are consistent with the previous research [2]. The weighted mean of I-Xe ages of the solar-wind-poor and solar-wind-rich portions are 4.557 ± 0.004 and 4.550 ± 0.002 billion years (errors are 95% confidence levels), respectively, suggesting that solar nebular gas dissipation would have occurred between these ages. NWA 801, which is also a solar-wind-rich meteorite, yielded I-Xe age of 4.529 ± 0.016 billion years. The present dataset is broadly consistent with the hypothesis [2] and suggests that the timing of gas dispersal in the Sun's protoplanetary disk would be ~10 million years after the first solid formation (CAI condensation, 4.56730 ± 0.00016 billion years [6]), but further data with lesser analytical uncertainties is surely required.

REFERENCES:

[1] I. Pascucci and S. Tachibana, in *Protoplanetary Dust*, edited by D. Apai and D. S. Lauretta (Cambridge University Press, 2010).
[2] K. Bajo, Ph.D. Thesis, Univ. Tokyo (2010).
[3] J. D. Gilmour and M. J. Filtness, Nature Astronomy, **3** (2019), 326-331.
[4] Ebisawa *et al.*, J. Mass Spectrom. Soc. Jpn., **52** (2004) 219-229.
[5] J. D. Gilmour *et al.*, Meteorit. Planet. Sci., **41** (2006), 19-31.
[6] Connelly J.N. *et al.*, Science, **338** (2012) 651-655.

CO5-17 Bulk Chemical Compositions of two LL7 Chondrites

M. Ebihara, Y. Hidaka, J. Sakuma, A. Ueda, S., N. Shirai[1] and S. Sekimoto[2]

Department of Earth Science, Waseda University
[1]Department of Chemistry, Tokyo Metropolitan Univ.
[2]KURNS

INTRODUCTION: Chondrites are acknowledged to be the most primitive materials accessible to us for studying the early history of our solar system. Chondrites are grouped into three major chemical groups, carbonaceous, ordinary and enstatite chondrites, and into six petrological groups, types 1 to 6. Ordinary chondrites account for more than 80 % of meteorites. Most ordinary chondrites are petrographically classified into type 3 (more primitive and unequilibrated) to type 6 (differentiated and equilibrated). With further thermal alteration during the early differentiation process, chondrites were transformed to primitive achondrites with partly melting and, then, to achondrites, which had experienced melting and, eventually, lost the primitiveness. In this study, we studied chemical compositions of ordinary chondrite samples classified as LL7. Here, "LL" means that these samples contain low metals and low iron and "7" means that they were highly thermally altered but not totally melted. Type 7 chondrites were first proposed by Dodd et al. [1] for such meteorites which experienced higher degree of thermal alteration than that for type 6 (or less metamorphosed) chondrites. So far, 68 meteorites are classified into LL7 ordinary chondrites (Meteoritical Bulletin). Type 7 meteorites are believed to be "bridges" between chondrites and achondrites. In this study, two LL7 chondrites were analyzed for their elemental compositions by means of instrumental neutron activation analysis (INAA). Our goal is to understand the material differentiation process at the early solar system, especially a transient process from type 6 chondrites to primitive achondrite and further to achondrites.

EXPERIMENTS: Bulk chemical compositions of two LL7 chondrites (Y-790144 and Y-791067) have been determined by INAA. Several chips of each meteorite weighing 400-600 mg were powdered in a clean agate mortar. A portion (30-40 mg) of each powdered meteorite was used for INAA. Each meteorite sample doubly sealed in plastic bags was irradiated with neutron firstly for 10 s for determining elements using short-lived neutron-induced radionuclides. The same sample was irradiated secondly for 4 h for determining elements using long-lived nuclides. Quantification was done by comparison method using JB-1 (basaltic powder sample) and the Smithsonian Allende meteorite powder as reference samples. Gamma-ray spectrometry was done at KURNS for short-lived nuclides and Tokyo Metropolitan University for long-lived nuclides.

RESULTS: The INAA results are summarized in Table 1. Note that these data are preliminary at this stage. Numerical values of element contents were determined for 15 elements and upper limits were obtained for 12 elements. Compared with LL chondrite means, the two LL7 chondrites were depleted in Ca, Al and V. These elements were determined by using short-lived nuclides, which could be related to systematically low contents. Although our results are mostly consistent with literature values [2, 3], some inconsistency was observed. Besides INAA, ICP-MS was performed for rare earth elements. Based on INAA and ICP-MS data, cosmochemical discussion is to be held.

Table 1 Preliminary results obtained by INAA*

	. -790144	. -791067
Na(%)	0.686±0.016	0.639±0.017
Mg(%)	11.7±0.6	11.0±0.7
Al(%)	0.793±0.056	0.728±0.057
Ca(%)	0.565±0.222	0.906±0.252
S. (.. .)	7.84±0.8	8.15±0.08
V(.. .)	41.8±8.0	27.3±8.3
Cr(ppm)	3741±15	4006±16
Mn(%)	0.209±0.007	0.223±0.008
Fe(%)	20.6±0.1	19.5±0.1
Co(ppm)	501±3	302±2
Ni(%)	0.902±0.019	0.650±0.016
Zn(ppm)	<112	<111
Br(ppm)	<0.876	<0.866
Sb(ppb)	<231	<216
Ba(ppm)	<155	<147
La(ppb)	354±97	370±100
Sm(ppb)	259±25	208±25
Eu(ppb)	<264	<266
Gd(ppb)	<622	<598
Yb(ppb)	<500	<471
Lu(ppb)	<77.5	<73.3
Hf(ppb)	<978	<895
Ta(ppb)	<841	<722
Ir(ppb)	387±15	239±13
Au(ppb)	138±7	88.8±6.3
Th(ppb)	<886	<841
U(ppb)	<1679	<1501

*Uncertainties are due to counting statistics (1s). Upper limits are defined as 10s.

REFERENCES:

[1] R. T. Dodd et al. Geochim. Cosmochim. Acta **39** (1975) 1585-1594.
[2] J. M. Friedrich et al. Geochim. Cosmochim. Acta **139** (2014) 83-97.
[3] T. Yoshioka. 修士論文 (首都大学東京) (2016) .

CO5-18 Metamorphic age of Acasta gneiss and regional cooling history

H. Hyodo[1], K. Sato[1,2,3], H. Kumagai[3]and K. Takamiya[4]
[1] *Institute of Frontier Science and Technology, Okayama University of Science*
[2]*Department of Applied Chemistry and Biochemistry, National Institute of Technology, Fukushima College*
[3] *Submarine Resources Research Center Japan Agency for Marine-Earth Science and Technology*
[4] *Institute for Integrated Radiation and Nuclear Science, Kyoto University*

INTRODUCTION: Biotite age of Acasta gneiss is reported as 1.935 Ga [1], which gives large difference from U-Pb zircon SHRIMP age of 4.0 Ga [2]. The results from other samples suggest the biotite age is regional, and it seem to be consistent with U-Pb apatite age (1.9 Ga) [3].

Typical minerals in K-Ar system such as hornblende and biotite have its own diffusion characteristics which provide regional temperature at specific timing of cooling orogen.

EXPERIMENTS: Experimental procedure is the same as described as previous studies on single grain datings. Rock samples were crushed and sieved in #25-100 mesh. After ultrasonic cleaning in distilled water, single mineral grains were handpicked. The mineral grains were irradiated using the hydraulic facility of KUR for 47 hours at 1 MW, and subsequently 6 hours at 5MW. The total neutron flux was monitored by 3gr hornblende age standard [4], irradiated in the same sample holder. In the same batch, $CaSi_2$ and $KAlSi_3O_8$ salts were used for interfering isotope correction. A typical J-value was $(1.729 \pm 0.022) \times 10^{-2}$. In stepwise heating experiment, the minerals were heated under defocused laser beam, and temperature of sub-millimeter grains was measured using infrared thermometer of which spatial resolution is 0.3 mm in diameter with a precision of 5 degrees. A feedback circuit for relatively long time-lag heating control is used not to overshoot the programmed temperature [5]. Argon isotopes were measured using a mass spectrometer with mass resolution of approximately 400, allowing to separate hydrocarbon from ^{39}Ar and other argon isotopes.

RESULTS: An example of $^{40}Ar/^{39}Ar$ age spectra of hornblende grains is illustrated in Fig. 1. The plateau age 1.965 Ga is consistent with 1.935 Ga of the biotite and the U-Pb age of apatite of the Acasta gneiss, These ages of ca. 1.9 Ga were obtained from samples approx. 20 km apart. Thus, it represents the cooling age of the regional metamorphism by Wopmay orogen. . SHRIMP U-Pb age study on zircon gave 4.0 Ga. The closure temperature (T_c) of zircon, 800 - 900 ^oC suggests that the Wopmay orogen heated the area above hornblende T_c, 500 ^oC, but not above zircon's T_c. The relatively small difference in the cooling ages between biotite and hornblende also suggests that the regional event has characteristics of a slow cooling process. A trial run on impurities in Acasta zircons was attempted. Because of its small amount and heat resistivity of zircon, we have not obtained conclusive results yet. A fraction with a small error gave an age ca. 2.0 Ga, suggesting age resetting of impurities in the zircons while U-Pb system is not.

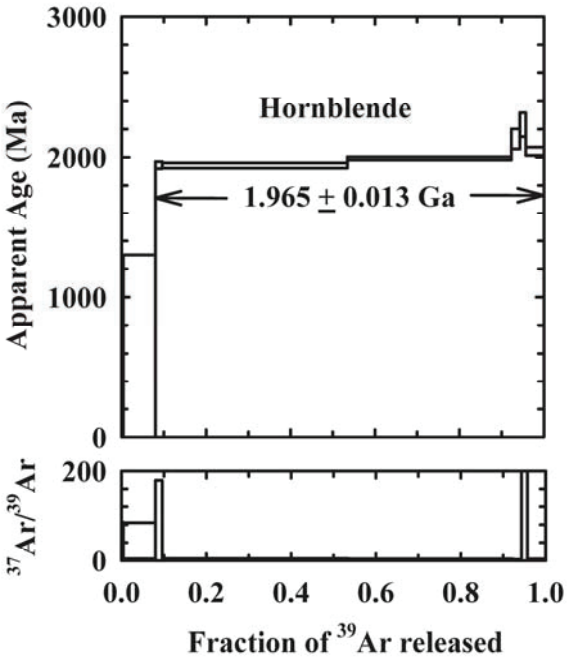

Fig. 1. $^{40}Ar/^{39}Ar$ age spectra of a hornblende grain from Acasta gneiss. More than 90% of total fraction defines plateau age of 1.965 Ga. The $^{37}Ar/^{39}Ar$ error (lower figure) seems to have little effect on the age in the plateau region.

REFERENCES:

[1] H. Hyodo, K.Sato, H.Kumagai and K. Takamiya, *KURNS Progress Report* 2019 CO5-7.
[2] S.A.Bowring and I.S. Williams, *Contributions to Mineralogy and Petrology*, **134** (1999) 3–16.
[3] Y. Sano, et al. *Geochimica Cosmochimica Acta* **63** (1999) 899–905.
[4] J.C. Roddick, *Geochim. Cosmochim. Acta* **47** (1983) 887-898.
[5] H. Hyodo, *Gondwana Research* **14** (2008) 609-616.

CO6-1 Structural study of the overlapping tri-nucleosome in solution

M. Nishimura[1], K. Nozawa[1], K. Morishima[2], R. Inoue[2], M. Sugiyama[2], and H. Kurumizaka[1]

[1]*Laboratory of Chromatin Structure and Function, Institute for Quantitative Biosciences, The University of Tokyo*

[2]*Institute for Integrated Radiation and Nuclear Science , Kyoto University(KURNS)*

INTRODUCTION:

In eukaryote, the genomic DNA is organized hierarchically into chromatin structures, and is stored in the nucleus. The basic unit of chromatin is the nucleosome, in which approximately 145 base-pairs of DNA are wrapped around the histone octamer containing two molecules of each core histone, H2A, H2B, H3, and H4. Emerging evidence suggests that the chromatin includes diverse repertoire of basic structural units [1]. Our group previously reported the three-dimensional structure of an overlapping dinucleosome: OLDN, which is an intermediate structure formed when two nucleosomes collide and release one H2A-H2B dimer in chromatin [2]. In the OLDN structure, the octameric histone core and the hexameric histone core are intimately associated each other, and 250 base-pairs of DNA are continuously wrapped around it. Assuming that the OLDN forms a further higher-order complex, we prepared an overlapping tri-nucleosome; OLTN, in which one octameric histone core and two hexameric histone cores are intimately associated, and approximately 350 bp DNAs are wrapped around the core. In this study, we analyzed the solution structure of the canonical nucleosome, OLDN, and OLTN by small-angle X-ray scattering (SAXS) and analytical ultracentrifuge (AUC).

EXPERIMENTS:

To generate OLTN, we prepared a DNA fragment with tandemly arranged three nucleosome positioning sequences derived from the Widom 601 sequence in a 353 bp fragment. The canonical nucleosome, OLDN, and OLTN were reconstituted by the salt dialysis method with recombinant human histones and DNAs, as previously described [2]. The reconstituted nucleosomes were purified by non-denaturing gel electrophoresis. SAXS analyses were performed with a NANOPIX instrument (RIGAKU) at the Institute of Radiation and Nuclear Science, Kyoto University. In order to cover the wide *q*-range, we employed two sample-to-detector distance: 1,330 mm and 350 mm, and then combined these data. We also performed the standard procedures of transmission correction, buffer solution scattering subtraction, and conversion to an absolute scale with water scattering. Nucleosome samples for SAXS included slight aggregates. To correct for the scattering data from those aggregates, we then performed AUC and corrected the SAXS data as previously described [3].

RESULTS:

We obtained the SAXS curves of the canonical nucleosome, OLDN, and OLTN, and the values of the radius of gyration (*Rg*) were calculated. As results, the *Rg* values of the nucleosome, OLDN, and OLTN were calculated as 43.6, 57.0, and 70.1, respectively [Fig.1]. However, the estimated molecular weight from the scattering intensity at the origin, was significantly lower than that from DNA sequence and histone amino acid sequence, implying that the OLTN solution include aggregates. The subsequent AUC experiment revealed that the nucleosome and OLDN samples resulted almost a monodispersed peak. On the other hand, the OLTN sample was separated by several peaks, suggesting that the OLTN solution contained aggregates. We then recalculated the SAXS profile by removing the portion corresponding to aggregates. We finally examined the OLTN structure by generating ab initio 3D-modeling from the corrected SAXS profile, followed by NMA refinements. The result revealed that the solution structure of OLTN is likely to be the octasome-hexasome-hexasome arrangement, but not the hexasome-octasome-hexasome structure [Fig. 2].

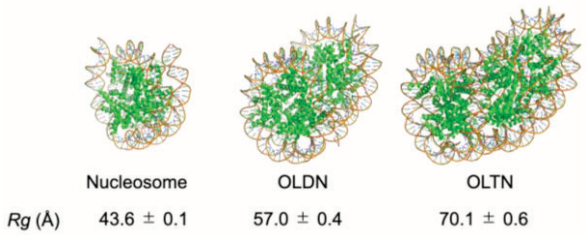

Fig.1 The *Rg* values of the nucleosome, OLDN, and OLTN in derived from SAXS-AUC analysis

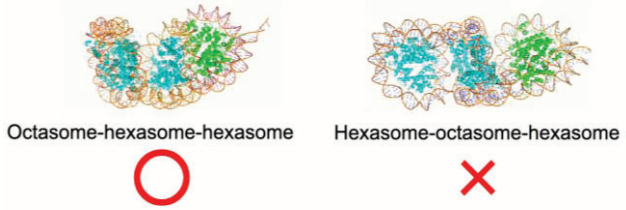

Fig.2 The schematic representations of the putative solution structures of OLTN.

REFERENCES:

[1] M. Koyama and H. Kurumizaka, J. Biochem. **163** (2018) 85-95.
[2] D. Kato *et al*., Science. **356** (2017) 205-208.
[3] K. Morishima *et al*., Commun. Biol. **3** (2020) 294.

CO6-2 Character of DNA damage induced by nuclear palnt neutron beams

H. Terato, T. Hanafusa, M. Isobe, M. Takigawa[1], S. Ihara[2], K. Mori[3], Y. Tokuyama[3], Y. Sakurai[4], and T. Saito[4]

Advanced Science Research Center, Okayama University

[1]Graduate School of Medicine, Dentistry, and Pharmceutical Sciences, Okayama University

[2]Graduate School of Engineering, Saga University

[3]Analytical Research Center for Experimental Sciences, Saga University

[4]KURNS

INTRODUCTION: Ionizing radiation takes severe biological consequences such as respective acute and chronic effects. These effects are usually arrived via the DNA damaging, because DNA brings the genetic information. Radiation DNA damage are produced by direct and indirect effects of ionizing radiation. Ionizing radiation attack DNA directly and via the generated reactive oxygen species (ROS) in direct and indirect effect pathways. We have had a lot of studies for radiation DNA damage after the discovery of X-rays by WC Roentgen in 1895. But the most of these studies have been derived from X-rays and gamma-rays, because we had not certain procedures to deliver the various ionizing radiation. Therefore, we have studied for the DNA damage with heavy ion beams, previously [1, 2]. These studies indicated that the DNA damage with heavy ion beams were unique, indicating that a lot of clustered DNA damage were generated including DNA double strand break (DSB), clustered base lesions, and these mixtures. Clustered DNA damage is a complex damage containing multiple lesions in the local region of DNA. This damage is mainly produced by the direct effect and highly concentrated ROS with heavy ion beam. This damage can inhibit DNA polymerization with high efficiently stopping of DNA polymerase moving on DNA. Also, this damage shows less repairable.

Neutron beam also shows severe biological damage like heavy ion beams, but the mechanism showing the consequence have not been unveiled yet. Thus, we analyze the DNA damage with neutrons from nuclear power plant to unveil the molecular mechanism of neutron biological effect in this study. The neutron beam is also high LET radiation as same as heavy ion beam. Therefore, we will find some interesting character of DNA damage with neutron like heavy ion beam. In the previous study periods, we found the relatively higher yields of DNA damage with the neutron beams than gamma-rays. In this year, we repeated DNA damage estimation for the result accuracy assurance, and investigated the cell effect for the neutron beams for the biological effect of this radiation.

EXPERIMENTS: Cultured cells of Chinese hamster ovary (CHO) AA8 strain were irradiated with neutron beams in the Kyoto University Reactor. The cells were cultivated with the conventional method. The logarithmic growing cells were recovered by trypsinization, and set into a polypropylene tube for irradiation. The estimated dose rate of neutron was 1Gy h^{-1}. The irradiated cells extracted in every 30 minutes up to 3 hours. After irradiation, the cells were immediately dissolved again with the cultured medium and reseeded into fresh medium. The cells were cultivated for 10 days for growing the colony. The colony was fixed with ethanol and stained with methylene blue. The colony number was counted for estimation of the irradiated cell viability. Simultaneously a half of the sampled cells were analyzed by agarose gel electrophoresis for DNA damage estimation. In DNA damage analysis, the irradiated cells were immediately frozen and stored at -80°C until the analysis. The frozen cells were embedded in low melting agarose plug and treated by protease. Then the plugs were subjected by electrophoresis.

RESULTS AND DISCUSSION: The sensitivity of the cells to neutron radiation increased in a dose-dependent manner. The increase in sensitivity was linear with dose, similar to radiosensitivity with other ionizing radiation species. On the other hand, the degree of sensitivity with D_{37} being 0.35 Gy was larger for gamma-rays and X-rays. The D_{37} is 1/10 of that of gamma-rays, and is consistent with the high biological effects of neutron radiation as well as other high-LET radiation. The dosimetry of the neutrons indicates that a half of dose of the reactor neutrons is derived from the contaminated gamma-rays. Gamma-rays usually show that the D_{37} is around 4 Gy. This result suggests that the neutron has greater efficiency for the biological effect. We already have the result indicating that the neutron showed relatively higher efficiency to generate the DNA damage than gamma-rays. Thus, the severe biological effect with neutron beam seems to be derived from the higher yield of DNA damage. The result of the cell viability is also consistent with the high DNA damage yield of neutron radiation obtained in the previous and this years' results. The results showed low yields of DSBs, which are considered to be directly related to cell survival, unlike other high-LET radiation. Therefore, it is necessary to clarify the DNA damage species involved in the high sensitivity to neutron radiation.

REFERENCES:

[1] H. Terato et al., J. Radiat. Res., 49 (2008) 133-146.
[2] Y. Tokuyama et al., J. Radiat. Res., 56 (2015) 446-455.

CO6-3

Evaluation of radiation resistance of lens constituent proteins involved in age-related cataract

T. Takata[1] and K. Lampi[2]

[1] *Institute for Integrated Radiation and Nuclear Science, Kyoto University*
[2] *Oregon Health & Science University*

INTRODUCTION:

The transparency and high refraction of the lens are maintained by the stable long-lived protein interactions, comprising α-, β-, and γ-crystallin families. As exposed outside body tissues, various damages of lens protein, such as oxidative damage, is increased during life. The lens contains various protection systems to prevent oxidative stress; however, damaged proteins can still accumulate because these protection systems are lost with aging, and there is no protein turnover or exclusion system in the lens. The damaged proteins include human lens crystallins that have been further subjected to the oxidation of amino acid residues [1].

These modifications, which are generated by UV light, ionizing irradiation and oxidative stress, decrease lens transparency and ultimately lead to the development of age-related cataracts [2, 3]. There are many data on the oxidation "sites" of aged human lens crystallins, but there are few studies of the oxidation "effects" of modification of amino acid in each crystallin species that have been subjected to γ-irradiation. γ-Irradiation generates free radicals and reactive oxygen species (ROS) such as hydroxyl radicals, superoxide, and singlet oxygen, which have been predicted to induce the oxidation of amino acids, as well as the truncation and cross-linking of proteins.

The aim of this study was to identify the effect of oxidation that occur in recombinantly expressed lens βB2-crystallin irradiated with low-dose γ-rays. The irradiated human lens βB2-crystallin (recombinantly expressed in *E. coli*) were loaded into reducing SDS-PAGE or digested by trypsin. The resulting peptides were analyzed by LC–MS/MS to identify the specific sites of oxidation in βB2-crystallin.

EXPERIMENTS:

Material Recombinantly lens βB2-crystallin were prepared and purified as described previously [4].

Gamma-irradiation βB2-crystallin, dissolved in 50 mM sodium phosphate buffer (pH 7.4), 150 mM NaCl were irradiated with γ-rays at a dose of 5, 50 or 500 Gy. γ-Irradiation was carried out at the Co-60 Gamma-ray Irradiation Facility of the Kyoto University Research Reactor Institute.

SDS-PAGE of Irradiated lens βB2-crystallin Each sample after irradiation was suspended in 50 μl of Laemmli SDS sample buffer (50 mM Tris-HCl, pH 6.8, 100 mM dithiothreitol, 2% SDS, 10% glycerol and 0.1% bromphenol blue). Each sample were loaded into 10% poly-acrylamide gel, then stained with coomassie brilliant blue to visualize the abnormal size oligomer.

LC-MS analysis Peptides from irradiated βB2-crystallins were obtained by in-gel digestion. The extracted tryptic peptides were filtered and injected into LC-MS/MS for modification analysis as previously reported [5]. Each sample was eluted over 60 min with a linear gradient (5%–45%) formed by mixing solvent A (0.1% formic acid aqueous solution) and solvent B (100% acetonitrile containing 0.1% formic acid). The oxidation was screened using by Proteome Discoverer™ 1.0 software (ThermoFisher, USA).

RESULTS:

Dose-dependent increasing size of βB2-crystallin after irradiation was observed (Fig. 1). The dimeric band was increased with decreased monomeric band of βB2-crystallin. The reason for the dimer formation was obscured, under the reducing situation during electrophoresis. Abnormal cross-linking molecules, such as tyrosine cross-linking, would be involved. There was also presenting truncated βB2-crystallin after irradiation. The band pattern was not ladder state, but suggested distinct state, thus this truncation would be site-specific in βB2-crystallin. LC-MS/MS analysis detected the oxidation of some tryptophan residues (W58, W150) on the βB2-crystallin after irradiation. Both sites have been previously reported, but still unknown the effect of modification. Further experiments to investigate the modification effect to induce abnormal aggregate using with mimic βB2-crystallin protein.

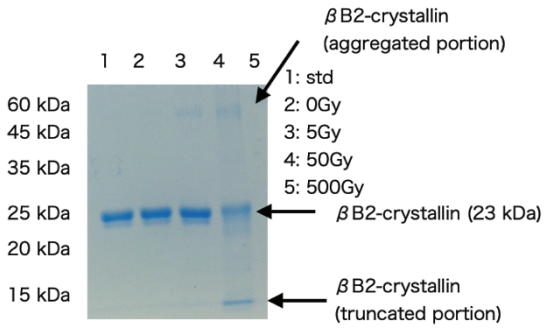

Fig. 1. Reducing SDS-polyacrylamide gel electrophoresis for irradiated βB2-crystallin.

REFERENCES:

[1] B. Searle *et al.*, *J Proteome Res*, **4** (2005) 546-554.
[2] S. Cai *et al.*, *Free Radic Biol Med.* **65** (2013) 1037-1046.
[3] E. C. Finley *et al.*, *Photochem Photobiol.* **68** (1998) 9-15.
[4] K. Lampi *et al.*, Biochemistry. **45** (2006) 3146-3153.
[5] T. Takata *et al.*, *FEBS Lett.* **285** (2018) 2263-2277.

CO6-4 A feasibility study of inverse contrast-matching small-angle neutron scattering method combined with size exclusion chromatography using antibody interactions as model systems

M. Yagi-Utsumi, K. Kato, S. Yanaka, R. Yogo, N. Sato[1], K. Morishima[1], R. Inoue[1], and M. Sugiyama[1]
Exploratory Research Center for Life and Living Systems (ExCELLS) and Institute for Molecular Science (IMS), National Institutes of Natural Sciences
[1]*Institute for Integrated Radiation and Nuclear Science, Kyoto University*

INTRODUCTION: Small-angle neutron scattering (SANS) and small-angle X-ray scattering (SAXS) are powerful techniques for the structural characterization of biomolecular complexes. In particular, SANS enables a selective observation of specific components in complexes by selective deuteration with contrast-matching techniques. In most cases, however, biomolecular interaction systems with heterogeneous oligomers often contain unfavorable aggregates and unbound species, hampering data interpretation. To overcome these problems, SAXS has been recently combined with size exclusion chromatography (SEC), which enables the isolation of the target complex in a multi-component system. By contrast, SEC–SANS is only at a preliminary stage. Hence, we herein perform a feasibility study of this method based on inverse contrast-matching (iCM) SANS technique using antibody interactions as model systems.

EXPERIMENTS: We perform a feasibility study of SEC–iCM–SANS using antibody interactions as models. Namely, immunoglobulin G (IgG) or its Fc fragment was mixed with 75% deuterated Fc-binding proteins, i.e. IgG-degrading enzyme of *Streptococcus pyogenes* (IdeS) and a soluble form of Fcγ receptor IIIb (sFcγRIIIb, hereafter referred to simply as FcγR). SEC–SAXS measurements were performed at 25°C with the La-SSS system installed into the laboratory-based SAXS instruments (NANOPIX, Rigaku). SEC–SANS measurements were conducted with a SEC–SANS system equipped with instrument D22 of ILL (Fig.1).

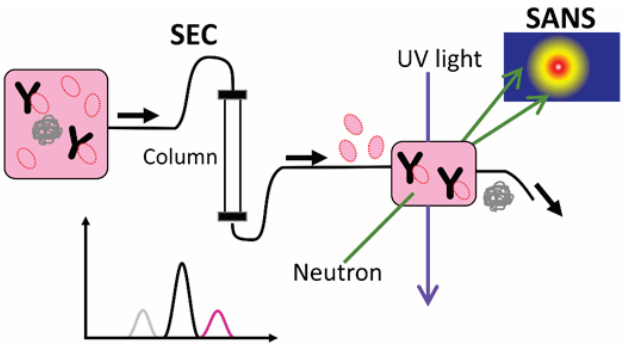

Fig. 1. Schematic illustration of SEC–iCM–SANS. The target complex can be selectively observed excluding the higher molecular weight aggregates and unbound species.

RESULTS: We attempted to apply the SEC–iCM–SANS method to the larger IgG–FcγR interaction system. A 1:1 mixture of IgG and FcγR was subjected to the SEC–SANS system and SEC–SAXS as a reference. In both systems, SEC enabled the selective acquisition of scattering data of free Fc and IgG–FcγR complex (Fig. 2). The FcγR-bound IgG had smaller R_g values (50.4 ± 1.4 Å in SAXS and 47.9 ± 1.9 Å in SANS) than those obtained for free IgG (54.9 ± 1.5 Å in SAXS and 52.0 ± 1.9 Å in SANS). We also measured the SEC–SANS profile of the complex formed with dFcγR and non-deuterated IgG, thereby providing the R_g value of IgG in the complex as 53.4 ± 1.7 Å, which was equivalent with the R_g value of free IgG due to the reasonably unobservable FcγR. In general, R_g becomes larger when the molecules form a complex. It should be noted, however, that R_g rather reduces upon complex formation when the inner space of the molecule is filled with another molecule, further resulting in an increased mass density around the original gravity center. The apparent recovery of the R_g value in the iCM–SANS observed with 75% deuterated FcγR as "transparent" binding partner is consistent with the above explanation. Indeed, the crystal structures of Fc in complex with FcγR (or its homologous sFcγRIIIa) have revealed that the receptor binding is carried primarily by the hinge-proximal part in Fc, which corresponds to the nearly central part in the intact IgG molecule.

The SEC–iCM–SANS approach demonstrated in this study will provide a technical basis for an undertaking, leading to elucidation of the dynamic structures of functional IgG molecules that interact with antigens together with FcγR.

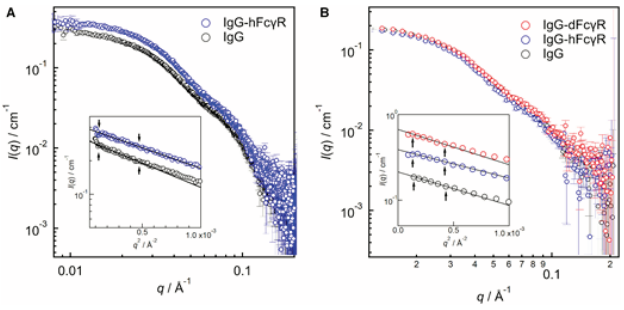

Fig. 2. (A) SEC–SAXS of IgG and IgG–hFcγR complex and (B) SEC–SANS profiles of IgG and IgG–hFcγR and IgG–dFcγR complexes. Guinier plots are shown in the insets in which the small arrows indicate fitting ranges.

REFERENCES:

[1] N. Sato *et al.*, *J. Biochem*, in press (2021). DOI: 10.1093/jb/mvab012

CO6-5 Structural characterization of circadian clock potein complexes

H. Yagi[1], Y. Yunoki[1,2], K. Morishima[3], A. Matsumoto[4], N. Sato[3], L. Porcar[5], A. Martel[5], R. Inoue[3], H. Kono[4], M. Sugiyama[3] and K. Kato[1,2]

[1]*Graduate School of Pharmaceutical Sciences, Nagoya City University*
[2]*Exploratory Research Center on Life and Living Systems, National Institutes of Natural Sciences*
[3]*Institute for Integrated Radiation and Nuclear Science, Kyoto University*
[4]*National Institutes for Quantum and Radiological Science and Technology*
[5]*Institut Laue-Langevin*

INTRODUCTION: The molecular machinery of the cyanobacterial circadian clock comprises three proteins: KaiA, KaiB, and KaiC. Through interactions among the three Kai proteins, the phosphorylation states of KaiC generate circadian oscillations *in vitro* in the presence of adenosine triphosphate (ATP). We especially focused on the KaiA-KaiB-KaiC ternary complex (ABC complex), which is considered to play the key role of the negative feedback loop of circadian rhythm. Recently, the cryo-electron microscopy (EM) structure of the ABC complex has been reported. However, the N-domains of KaiA subunits were poorly resolved due to their missing electron density maps. This observation probably reflected a high flexibility of linker between N- and C-domains. The whole structure of ABC complex has remained to be elucidated. Herein, for characterization of the overall structure of ABC complex, we conducted integrative techniques using small-angle X-ray scattering (SAXS), inverse contrast-matching small-angle neutron scattering (iCM-SANS), and native analytical ultracentrifugation (AUC) in conjunction with computer simulations.

EXPERIMENTS: The expression and purification of clock proteins, KaiA, KaiB and KaiC were performed according to methods previously described [1]. X-rays from a high-brilliance point-focused X-ray generator (MicroMAX-007HF, Rigaku, Tokyo, Japan) were focused with a confocal mirror (OptiSAXS) and collimated with a confocal multilayer mirror and two pinholes collimation system with the lower parasitic scattering, "ClearPinhole". The scattered X-rays were detected with a two-dimensional semiconductor detector (HyPix-6000, Rigaku, Tokyo, Japan). The sample-to-detector distance and wavelength of X-ray used for present work was 1320 mm and 1.542 Å, respectively. For removal of unfavorable aggregates from the sample solution, the laboratory-based SEC-SAXS System (LA-SSS) was employed to measure the SAXS profile in the Q range (0.01 $Å^{-1}$–0.2$Å^{-1}$). The SANS experiments were performed using the D22 instrument installed at the Institut Laue-Langevin (ILL), Grenoble, France. The sample-to-detector distance and wavelength of neutron used for present work was 5600 mm and 6.0 Å, respectively. SEC-SANS system was also utilized for present work.

RESULTS: To date, we have been conducting structural analysis of the ABC complex, which plays a key role in generating negative feedback in the regulation of circadian rhythms. Specifically, by combining solution scattering methods such as SAXS and SANS with gel filtration chromatography, we have extracted the overall structure of the ABC complex. The structural information of KaiA in the complex have succeeded in constructing structural models. In this year, the stability of the structural models was evaluated by molecular dynamics (MD) simulations. One hundred nsec MD simulations revealed that the N-domains of the 12 molecules of KaiA were highly mobile and there was little correlation of motion between the 12 molecules. The electron microscopic analysis of the ABC complex reported in the previous study assumed six-fold axial symmetry, and thus could not capture the structural information of the highly motile KaiA N-domain. Interestingly, the N-domains of KaiA cover the C-domains in one of stable ABC complex models (Fig. 1), which prevents KaiA from interacting with other KaiC molecules via its C-tail regions. In other words, KaiA changes its own conformation through the interaction with the KaiB-KaiC complex and negatively regulates the binding of other KaiC molecules in solution. Thus, the present study shows that the combination of solution scattering, computational modeling, and MD simulations enable us to construct a 3D structural model of the Kai protein complex, even in regions of high mobility.

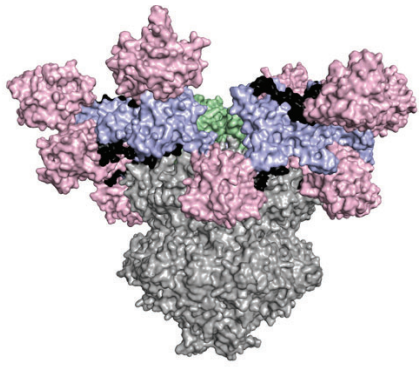

Fig. 1
A stable structural model of ABC complex evaluated by MD simulation.
N- and C-domains and linkers of KaiA, KaiB and KaiC are shown in pink, cyan, black, green and gray, respectively.

REFERENCES:
[1] M. Sugiyama *et al.*, Si. Rep., **6:35567 |** (2016).

CO6-6 Radioresistance Mechanisms Acquired by Adaptive Evolution and their Evolutionary Mechanisms

T. Saito

Institute for Integrated Radiation and Nuclear Science, Kyoto University

INTRODUCTION: In nature, organisms have evolved diversely by adapting themselves to various environmental conditions. Some organisms have been found to survive in extremely severe environments. Elucidating the mechanisms by which organisms adapt to severe environmental conditions can provide meaningful information regarding evolution and diversity. Some bacteria, known as radioresistant bacteria, demonstrate extreme resistance to ionizing radiation [1]. The mechanisms by which these bacteria resistant damage from to ionizing radiation is an interesting area of research on the adaptations employed by organisms in nature. In order to elucidate the mechanisms of radioresistance in these organisms, it is important to investigate their biological defense mechanisms against external stresses at the molecular level. However, studies conducted on radioresistant organisms in nature are particularly difficult due to limited knowledge of their genetic and biochemical properties. Therefore, in this study, radioresistant *Escherichia coli*, the wild-type genetic and biochemical characteristics of which have been elucidated in detail, were generated by an adaptive evolution experiment using gamma rays as the selective pressure, and the characteristics of the evolved radioresistant *E. coli* were compared to those of the wild-type. The generation of radioresistant *E. coli* with 7.9-fold resistance to gamma radiation compared to wild-type *E. coli* has been described in a previous report of this study [2]. In this report, the differences in gene expression status between wild-type and radioresistant *E. coli* are described.

EXPERIMENTS: Extraction of total RNA and RNA sequencing : Total RNA was extracted from *E. coli* cells using RNAiso Plus (Takara) and further purified using NucleoSpin RNA Clean-up XS (Macherey-Nagel). The quality of the resulting total RNA was evaluated and confirmed using the Agilent 2200 TapeStation (Agilent). rRNA was removed from total RNA using Ribo-Zero Magnetic Kit (Gram-Negative Bacteria) (Illumina). The sequence library was prepared from the resulting RNA using TruSeq Stranded mRNA Sample Prep Kit (Illumina). The quality of the sequence library was evaluated and confirmed using the Agilent 2100 Bioanalyzer (Agilent). Sequence analysis was performed using the NovaSeq 6000 (Illumina), NovaSeq 6000 S4 Reagent Kit (Illumina), and NovaSeq Xp 4-Lane Kit (Illumina). Gene expression levels were analyzed using the Genedata Profiler Genome (Genedata) and STAR [3]. All procedures were performed according to the manufacturer's instructions.

Analysis of gene expression status: In the analysis, gene expression data with “fragments per kilobase of exon per million reads mapped” values less than 1 for all samples from the two groups were filtered out to eliminate noise data. Genes differentially expressed in radioresistant *E. coli* compared to those in wild-type *E. coli* were identified by Welch's t-test and correction for multiple testing using the Benjamini and Hochberg method (BH method) [4]. In addition, Gene Ontology (GO) analysis for the differentially expressed genes (DEGs) in radioresistant *E. coli* was performed using the Database for Annotation, Visualization and Integrated Discovery bioinformatics resources ver.6.8.

Statistical analysis: Welch's t-test and BH method were used to identify DEGs among many genes, and a q-value of less than 0.05 was considered statistically significant. The Expression Analysis Systematic Explorer score was used to test for significance in the GO analysis, and a P-value of less than 0.05 was considered statistically significant [5].

RESULTS: The expression levels of 171 genes were significantly different in radioresistant *E. coli* than in wild-type *E. coli*. Among these genes, the expression levels of 115 genes were increased and 56 genes were decreased. GO analysis of genes highly expressed in radioresistant *E. coli* compared to wild-type *E. coli* showed that genes involved in SOS response, response to stimulus, DNA repair, and DNA metabolism were included in Annotation Cluster 1 with an Enrichment Score of 2.43. These results strongly suggest that the increased expression of genes involved in cell recovery, DNA repair, cell survival, and response to stress is involved in the high radioresistance mechanism in evolved radioresistant *E. coli*. In the future, more detailed studies are needed to understand how the increased expression of these genes is involved in the radioresistance mechanism of radioresistant *E. coli*.

REFERENCES:

[1] T. Saito, Viva Origino, **30** (2007) 85–92.
[2] T. Saito, KURNS ProgressReport 2019 (2020) 211.
[3] A. Dobin *et al.*, Bioinfomatics, **29** (2013) 15–21.
[4] Y. Benjamini and Y. Hochberg, J. R. Statist. Soc. B, **57** (1995) 289–300.
[5] D. W. Huang *et al.*, Nat. Protoc. **4** (2009) 44–57.

CO6-7 SAXS analysis of the formation process of the nucleation intermediate of insulin B chain: The measurement at different pH conditions

Y. Yoshikawa, N. Yamamoto[1], R. Inoue[2], M. Sugiyama[2], and E. Chatani

Graduate School of Science, Kobe University
[1]School of Medicine, Jichi Medical University
[2]Institute for Integrated Radiation and Nuclear Science, Kyoto University

INTRODUCTION: Amyloid fibrils are protein aggregates that are often associated with diseases. They are commonly characterized by β-sheet-rich structure and formed through nucleation and elongation steps. However, detailed mechanisms of protein association especially in the nucleation remain unclear.

In our previous work, we found that nucleation intermediates were formed in the early phases of amyloid formation of human insulin B chain [1]. This result suggested that early protein aggregation is sometimes involved in the nucleation process. In addition, our subsequent study showed that similar intermediate-mediated fibrillation occurs over a wide pH range of 5.2 to 9.1 [2]. Since the final amyloid fibril structure appears to vary with pH, it is worth investigating whether different types of intermediates are observed depending on pH.

In this study, we analyzed structural properties of the nucleation intermediates formed at pH5.2 by using small-angle X-ray scattering (SAXS). We previously measured time-resolved SAXS of the fibrillation reaction of insulin B chain at pH8.7, and it was found that the nucleation intermediate shows a rod-like shape and its size gradually increased during the formation (Yamamoto et al., submitted). By measuring the time course of the intermediate formation at pH 5.2 in comparison with that at pH 8.7, we discuss the structural property of the nucleation intermediate and furthermore, the effect of pH on the formation process.

EXPERIMENTS: B chain was prepared from human insulin as described previously [1]. The stock insulin B chain was diluted with 50 mM acetate buffer (pH5.2) at a concentration of 1.4 mg/ml. Immediately after the preparation, the sample solution was then put in a 1-mm path-length quartz cell. The SAXS pattern was collected at 25 °C with NANOPIX equipped with HyPix-6000 (Rigaku Corporation, Japan). A Cu K-α line (MicroMAX-007HF) was used as a beam source, which was further focused and collimated with a confocal multilayer mirror (OptiSAXS). Scattering data were collected continuously with an exposure time of 15 min. The camera length was set to 1.33 m and the range of the scattering vector q was from 0.0085 to 0.2 Å^{-1}.

RESULTS: Fig. 1 shows SAXS profiles of insulin B chain monitored at several time points in the process of the formation of the nucleation intermediate at pH5.2. Because the reaction speed was higher than that at pH8.7, only slight time-dependent change in the scattering profiles was observed. The slope of the log-log plot of was close to -1 within the time range of the measurement, from which we performed the analysis of a cross-section plot assuming that the shape of the peptide aggregates can be approximated as a rod.

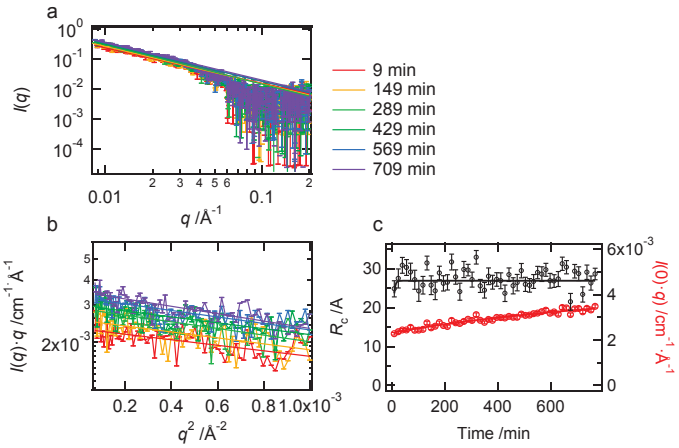

Fig. 1. (a) SAXS profiles of insulin B chain monitored at different time points. The lines indicate slopes obtained by line fit. (b) Cross-section plots of the profiles in panel (a). (c) Time dependence of the R_c (black) and the $I(0)\cdot q$ (red) values obtained from the cross-section plots.

We next performed the analysis of cross-section plot to obtain the radius (R_c) of the rod. Fig. 1b represents the plot and Fig. 1c shows the time dependence of R_c and the intercept ($I(0)\cdot q$) to represent the time dependency of the size development. The result suggested that the rod-shaped intermediates maintain the same radius. The radius of the rod (R_p), which is equal to $\sqrt{2}R_c$, was calculated to be 3.8±0.4 nm, and it was almost similar to that estimated at pH8.7 (3.6±0.1 nm). We further tried to estimate the length (L) of the rod based on Broersma's relationship using the R_p value and a diffusion coefficient obtained from a DLS measurement [2]. As a result, it is tentatively concluded that the basic size and shape of the nucleation intermediate at pH5.2 and pH8.7 are similar, although more detailed data analysis is necessary to lead the final conclusion. We are also planning to verify the similarity or difference of the nucleation intermediates formed at different pHs in terms of internal microscopic structure by using circular dichroism and other analytical techniques.

REFERENCES:

[1] N. Yamamoto *et al*., Sci. Rep., **8** (2018) 62.
[2] Y. Yoshikawa, Master Thesis, Kobe Univ. (2020).

CO6-8

Evaluation of boron neutron capture therapy (BNCT) using brain tumor bearing rats or mice models

Hideki Kashiwagi[1], Shinji Kawabata[1], Yusuke Fukuo[1], Takuya Kanemitsu[1], Koji Takeuchi[1], Gen Futamura[1], Ryo Hiramatsu[1], Hiroyuki Nakamura[2], Tsubasa Watanabe[3], Takushi Takata[3], Hiroki Tanaka[3], Minoru Suzuki[3], Shin-Ichi Miyatake[4], Koji Ono[4], Masahiko Wanibuchi[1]

[1] *Department of Neurosurgery, Osaka Medical and Pharmaceutical University*
[2] *Laboratory for Chemistry and Life Science, Institute of Innovative Research, Tokyo Institute of Technology*
[3] *Institute for Integrated Radiation and Nuclear Science, Kyoto University*
[4] *Kansai BNCT Medical Center, Osaka Medical and Pharmaceutical University*

INTRODUCTION:
Some BNCT clinical trials for glioblastoma have been conducted and have been showed the efficacy of BNCT for glioblastoma in our facility[1]. The development of new boron compounds for BNCT previously have been conducted all over the world in order to improve the effect of BNCT, however, there were no compounds to used clinical medicine except for BPA (boronophenylalanine) and BSH (borocaptate sodium). In this study, we focused on serum albumin, which is used for drug delivery. The serum albumin conjugate of a boron compound, maleimide-functionalized *closo*-dodecaborate albumin conjugate (MID-AC), has been developed by our group. We have previously found to be significantly inhibited the growth of tumor in a mouse colon 26 subcutaneous tumor model that received thermal neutron irradiation after MID-AC administration[2]. The therapeutic effect of MID-AC in BNCT for malignant gliomas was evaluated in this study.

Materials and Methods:
To evaluate the therapeutic effect of thermal neutron irradiation after MID-AC administration to F98 rat glioma models, an in vivo neutron irradiation experiment was performed at KUR. F98 rat glioma cells and Fischer rats were used and created F98 rat glioma models. The result was analyzed using Kaplan-Meier survival curves. The reactor power of KUR was 5 MW and the irradiation time was 20 minutes. The F98 rat glioma models were divided to 5 groups bellow: untreated control group (Untreated), neutron irradiated control group (Neutron only), neutron irradiation at 3 hours after BPA intravenous administration (i.v.) group (BNCT BPA), neutron irradiation at 3 hours after MID-AC i.v. group (BNCT MID-AC 3h), neutron irradiation at 24 hours after MID-AC i.v. group (BNCT MID-AC 24h).

RESULTS:
The result of neutron irradiation experiment was showed Table 1. below. The median survival times (MST) for each group were as follows: Untreated, 24.5 days〔95% confidence interval (CI); 23-27 days〕; Neutron only, 24.5 days〔95% CI; 23-27 days〕; BNCT BPA, 31.5 days〔95% CI; 28-40 days〕; BNCT MID-AC 3h, 33.5 days〔95% CI; 23-40 days〕; BNCT MID-AC 24h, 33.0 days〔95% CI; 27-36 days〕. MTS were prolonged significantly in the neutron irradiation group following boron compounds administration compared with Untreated (vs. BNCT BPA, $p < 0.0001$; vs. BNCT MID-AC 3h, $p = 0.0019$; vs. BNCT MID-AC 24h, $p = 0.0005$, respectively, log-rank test). MST were no significant differences in BNCT MID-AC 3h or 24h compared to BNCT BPA (vs. BNCT MID-AC 3h, $p = 0.94$; vs. BNCT MID-AC 24h, $p = 0.67$, respectively, log-rank test).

Table 1. The result of neutron irradiation experiment for the F98 rat glioma models

Group	n	MST (days)	95% CI (days)
Untreated	6	24.5	23-27
Neutron only	6	24.5	23-27
BNCT BPA	8	31.5	28-40
BNCT MID-AC 3h	8	33.5	23-40
BNCT MID-AC 24h	7	33.0	27-36

Ongoing research:
We have focused on folate acid (FA) and the folate receptor (FR) in addition to serum albumin. FA has a high affinity for FR, which are expressed to a limited extent in normal human tissues, but overexpressed in many cancer cells, including glioblastoma[3]. We have developed and evaluated PBC-IP, whose pteroyl group interacts with FR and has the ability to bind serum albumin. In vitro, PBCIP has been found higher cellular uptakes of boron in F98 rat glioma cells than BPA. The aim of the next study is to evaluate the therapeutic effect of PBC-IP on BNCT in the F98 rat glioma models.

REFERENCES:
[1] Kawabata, S., et al., Journal of Radiation Research, 2009. **50**(1): p. 51-60.
[2] Kikuchi, S., et al., J Control Release, 2016. **237**: p. 160-7.
[3] Nagai, T., et al., Cancer Immunol Immunother, 2009. **58**(10): p. 1577-86.

CO6-9

The study of boron neutron capture therapy (BNCT) for primary central nervous system lymphoma (PCNSL)

Hideki Kashiwagi[1], Shinji Kawabata[1], Yusuke Fukuo[1], Takuya Kanemitsu[1], Koji Takeuchi[1], Gen Futamura[1], Ryo Hiramatsu[1], Tsubasa Watanabe[2], Takushi Takata[2], Hiroki Tanaka[2], Minoru Suzuki[2], Shin-Ichi Miyatake[3], Koji Ono[3], Masahiko Wanibuchi[1]

[1] Department of Neurosurgery, Osaka Medical and Pharmaceutical University
[2] Institute for Integrated Radiation and Nuclear Science, Kyoto University
[3] Kansai BNCT Medical Center, Osaka Medical and Pharmaceutical University

INTRODUCTION:
Primary central nervous system lymphoma (PCNSL) is classified as a WHO Grade IV and accounts for 5% of all brain tumors[1]. The treatment for PCNSL is based on whole brain irradiation following high dose methotrexate (HD-MTX) chemotherapy. PCNSL is highly radiosensitive and the initial response rate is relatively high however the recurrence rate is high[2]. In the case of the recurrence additional irradiation is often difficult due to radiation damage. BNCT is considered to be an effective treatment for PCNSL recurrence because it is a highly cell-selective particle therapy. To expand the indications for PCNSL recurrence treatment, we conducted basic experiments of BNCT for PCNSL.

Materials and Methods:
A mouse PCNSL model was created using the Raji human lymphoma cell line, which has been shown to accumulate boron in tumor cells in vitro. In this model, the biodistribution was evaluated beforehand, and it was confirmed that the tumor-normal brain ratio was approximately 2 times. The boron compound used was boronophenylalanine (BPA), which was administered intraperitoneally and the dose was 500mg/kg body weight. The reactor power of the KUR was 5 MW and the irradiation times were 10 or 20 minutes. The models were randomly divided into the following 5 groups for neutron irradiation experiments: untreated control group (Untreated), neutron irradiation control group (Irrad.5MW 10min), neutron irradiation control group (Irrad.5MW 20min), BPA administration followed by neutron irradiation group (BPA 5MW 10min), and BPA administration followed by neutron irradiation group (BPA 5MW 20min). The results were analyzed using Kaplan-Meier survival curves.

RESULTS:
The PCNSL models were divided to 5 groups described above and the results were showed Table 1. below. The median survival times (MST) for each group were as follows: Untreated, 32.0 days〔95% confidence interval (CI); 27-45 days〕; Irrad.10min, 37.0 days〔95% CI; 25-60 days〕; Irrad.20min, 53.0 days〔95% CI; 25-78 days〕; BPA 10min, 30.0 days〔95% CI; 30-34 days〕; BPA 20min, 27.0 days〔95% CI; 27-29 days〕. The median survival times was significantly shorter in BPA 20min than in the Untreated ($p = 0.043 < 0.05$, log-rank test). The median survival time of Irrad.20min tends to be longer than Untreated ($p = 0.051$, log-rank test).

Table 1. The results of neutron irradiation experiments for the PCNSL models

Group	n	MST (days)	95% CI (days)
Untreated	6	32	27-45
Irrad.5MW 10min	6	37	25-60
Irrad.5MW 20min	6	53	25-78
BPA 5MW 10min	5	30	30-34
BPA 5MW 20min	6	27	27-29

Ongoing study:
In the PCNSL models using Raji lymphoma cells, the results of Kaplan-Meier survival curves of the neutron irradiation experiments predicted that the photon equivalent dose at 5MW 20min irradiation was the optimal dose. Early mortality in this study was considered to be due to acute oral mucosal damage caused by irradiation. Therefore, the predicted mucosal tissue doses were calculated assuming the compound biological effectiveness of BPA for oral mucosal tissues to be 4.9[3] and the boron concentration in mucosal tissue to be about 10 μg/g as measured in our laboratory; the photon equivalent dose of mucosa for BPA 5MW 10min was estimated to be about 10.9 Gy-Eq, and that for BPA 5MW 20min was about 17.8 Gy-Eq. When only the dose due to beam irradiation was calculated, the dose at Irrad.5MW 20min was about 3.9 Gy-Eq. We would like to use these dose results for dose adjustment in our next study and apply them to the treatment of the PCNSL models with BNCT using BPA.

REFERENCES:
[1] Neurol Med Chir (Tokyo), 2017. **57**(Suppl 1): p. 9-102.
[2] Nelson, D.F., et al., Int J Radiat Oncol Biol Phys, 1992. **23**(1): p. 9-17.
[3] Suzuki, M., et al., Journal of Radiation Research, 2014. **55**(1): p. 146-153.

CO6-10 Identification of amino acid residues responsible for the temperature dependency of sHsps from methanogens

M. Yohda, R. Midorikawa, K. Morishima[1], R. Inoue[1], M. Sugiyama[1]

Department of Biotechnology and Life Science, Tokyo University of Agriculture and Technology
[1]Institute for Integrated Radiation and Nuclear Science, Kyoto University

INTRODUCTION: Small heat-shock proteins (sHsps) are molecular chaperones ubiquitously present in all biological domains. It has a relatively conserved α-crystallin domain surrounded by variable N-terminal and C-terminal domains[1]. Each sHsp exists as a stable oligomer at around the optimum growth temperature of the organism. Oligomers dissociate into small oligomers under stress conditions such as high temperature to expose hydrophobic regions and capture denatured proteins to prevent aggregation. However, the temperature-dependent oligomer dissociation mechanism of sHsp has not been elucidated. Methanogenic archaea grow in a variety of environments. The optimum temperature of a hyperthemophilic one, *Methanocaldococcus jannaschii,* is 85°C. The sHsp of *M. jannaschii* (MJsHsp) exhibits high amino acid homology with that of the mesophilic *Methanococcus maripaludis,* which optimally grows at 38°C (MMsHsp). In this study, we tried to identify amino acid residues which determine the temperature dependency of sHsps from methanogens.

EXPERIMENTS: MJsHsp, MMsHsp, and their variants were expressed in *E. coli* using a pET23b vector. They were purified by anion exchange chromatography using TOYOPEARL DEAE-650, TOYOPEARL SuperQ-650 , and gel filtration chromatography using Superdex 200. The size of the oligomer structure under various temperature conditions was examined by size exclusion chromatography on HPLC (SEC), electron microscopy, and analytical ultracentrifugation (AUC). The chaperone activity was analyzed as the activity for protecting porcine heart citrate synthase from thermal aggregation.

RESULTS: In analytical ultracentrifuge, MJsHsp mainly existed as 24mer, which should correspond to the crystal structure[2]. Besides, larger oligomers were observed. MMsHsp also formed 24mer with partial dissociation into dimers (Fig. 1). This dissociation was concentration-dependent. The relative abundance of dimers increased at the lower the concentration. MJsHsp and MMsHsp) share significantly high amino acid sequence homology except for the N-terminus but differ greatly in temperature dependence. To verify whether the N-terminal domain determines temperature sensitivity, we created N-terminal exchange mutants and analyzed their temperature-dependent dissociation. However, it was revealed that the N-terminal domain is not related to temperature sensitivity. Then, we compared amino acid sequences of various methanogenic sHsps, and found a couple of amino acid replacements between hyperthermophilic sHsps and mesophilic ones. Two Gln residues at the N-terminus of the α-crystallin domain of MJsHsp (Q36, Q52) are changed to Glu in MMsHsp (E43, E59). The conserved C-terminal IXI motif of MJsHsp is INI (N145), and that of MMsHsp is IDI (D152). E118 of MJsHsp is changed to Gly in the mesophilic sHsps.

We constructed mutated sHsps and analyzed their temperature dependencies by gel filtration chromatography. Among various mutants of MMsHsp, MME43Q and MMD152N oligomers exhibited relatively high thermal stability (Fig. 2). Partial improvement in thermal stability was observed in the double mutant. However, the mutants were less stable than MJsHsp at the high temperature. MJsHsp did not show any change in temperature sensitivity for any of the mutants, leading to the conclusion that we cannot explain the temperature dependence by these mutants. The combination of various amino acid residues might be responsible for the temperature dependency.

Fig.1 AUC analyses of MJsHsp and MMsHsp

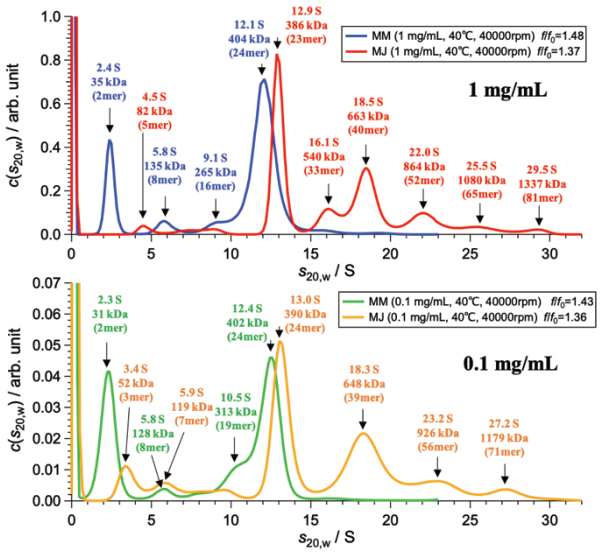

Fig. 2 Temperature dependency of MM variants

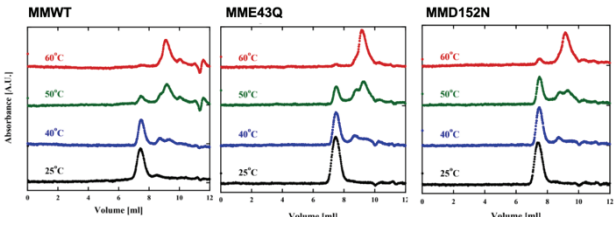

REFERENCES:

[1] C. Garrido *et al*., Int. J. Biochem. Cell Biol. **44** (2012) 1588–1592.
[2] K. K. Kim *et al*., Nature **394** (1998) 595–599.

CO6-11 Quantitative analysis of contribution of tumor vascular damage to antitumor effect of X-ray using BNCR

K. Ono[1], T. Watanabe[2], H. Tanaka[2], T. Takata[2], S. Suzuki[2]

[1]BNCT Joint Clinical Institute, Osaka Medical Pharmaceutical University
[2]Institute for Integrated Radiation and Nuclear Science, Kyoto University

NTRODUCTION: Tumor tissue consists of tumor cells and stroma, especially the vasculature that supplies the cells with oxygen and nutrients. The antitumor effect in BNCT is almost specific to cells accumulating boron compounds. In this study, we compare the effect of this tumor cell-specific BNCT with the effect of X-rays that has no tumor cell specificity, and quantitatively elucidate the effect of damage caused in the vascular system on the overall antitumor effect. This is the purpose of this research.

In fiscal 2020, we conducted an experiment to confirm the effect of BNCR on B-16 melanoma transplanted in C57-Black mice. This article reports the experimental results.

EXPERIMENTS: ***Mice, BPA administration and neutron irradiation.***

Mice: Eight-week-old C57-Black mice were prepared. The B-16 melanoma cells were transplanted to the right thigh, 10 days after then tumor grew to the size of average of 5mm.

BPA administration and measurement of ^{10}B concentration: ^{10}B-BPA in the form of a fructose complex (500 mg/kg body weight in terms of BPA) was administered subcutaneously in the posterior neck of mice. 30, 60 and 90 minutes after BPA injection, the tumors were removed and ^{10}B concentration was measured by using prompt γ-ray analysis.

Neutron irradiation: Based upon these concentration data (presented later), around 60 minutes after BPA injection, the neutrons were irradiated to the tumors in the thigh. The rest of the body was shielded with LiF plates. The highest neutron flux was 2.78×10^9/cm^{2}s. The flux was determined by the amount of activity induced in the gold foil.

Evaluation of radiation response.

In vivo evaluation by tumor growth delay: The tumor diameter of three directions was measured almost every 2 days by caliper. And tumor volume was calculated according to the following formula of π/6xabc.

In vitro colony formation assay: The tumor removed after neutron irradiation was minced by scissors, and digested with trypsin solution for about 15 minutes. After cell counting, an appropriate number of cells were plated onto the plastic petri dishes filled with fresh medium containing FCS. Twelve days later, the colonies were fixed with ethanol and stained with crystal violet. The numbers of colonies were counted by naked eye.

RESULTS and DISCUSSION:

^{10}B concentration with time after BPA injection.

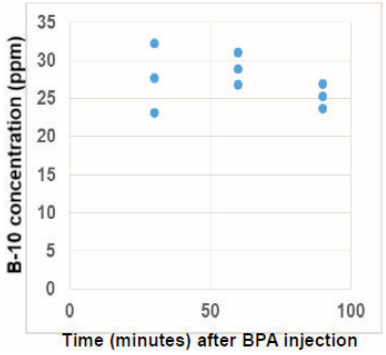

As presented in the figure, the ^{10}B concentration was around 28 ppm at 60 minutes. SUV (standerlized uptake value) was 1.1.

In vivo evaluation by tumor growth delay:

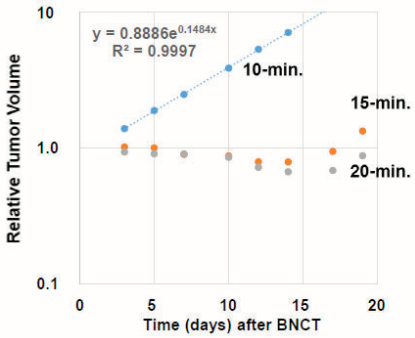

The effect of 10-minutes BNCT was quite small compared with 15, 20-minutes BNCT.

In vitro colony formation assay:

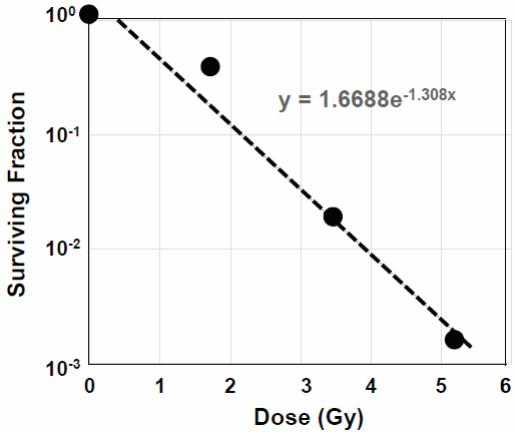

The result is a D_0 value of 0.765Gy to 0.846Gy. The value is in good agreement with the one estimated according to the formula established by K. Ono (2019 JRR).

CO6-12 ^{11}C medical-isotope production via the ^{12}C(γ,n)^{11}C reaction with carbon nano-tube (CNT)

N. Takahashi[1,2], M. Kurosawa[1], M. Tamura[1], M. Fujiwara[1],N. Abe[3], T. Kubota[3] and T. Takahashi[3]

[1]*Research Center for Nuclear Physics, Osaka University*
[2]*Kyoto Medical Technology Co., Ltd*
[3]*Institute for Integrated Radiation and Nuclear Science, Kyoto University*

INTRODUCTION: Nowadays, L-[^{11}C]-Methionine is widely recognized as a useful positron emission tomography (PET) reagents for the medical diagnosis of brain tumors [1]. The medical ^{11}C radioisotopes are most frequently produced in a cyclotron via the ^{14}N(p,α)^{11}C reaction by bombarding enriched nitrogen gas with a proton beam [2,3,4]. The produced ^{11}C radioactivities are mixed together with O_2 and target nitrogen gas. After some chemical processes under various controlled temperatures, the $^{11}CO_2$ is isolated from the target nitrogen gas [5]. Then, we can synthesize L-[^{11}C]-Methionine using the automated apparatuses. At present, Hokkaido University and Osaka University are actively working in collaboration, in order to obtain the formal government permission of the PET examination with L-[^{11}C]-Methionine for checking the metastasis and recurrence test of the brain tumor patient [6,7].

Apart from the cyclotron ^{11}C production, we studied a new method of the ^{11}C production using the bremsstrahlung γ-rays. There are important reasons for pursuing these kinds of investigations in series, since we have studied the medical isotope productions such as ^{99m}Tc, ^{18}F, ^{15}O isotopes via the photoreactions on natural Mo, Ne and O targets [8,9,10].

In the case of the ^{11}C production, we cannot use a ordinary ^{12}C target. Although the cross sections of the ^{12}C(γ,n)^{11}C reaction is very large, the specific activity of ^{11}C becomes very poor because of the number of ^{12}C in the target is extremely large. We cannot isolate the ^{11}C radioactivities from an enormous number of ^{12}C. Our idea to get the reasonable number of the ^{11}C specific activity, using the carbon nano-tube (CNT) as a target, instead of the ordinary carbon block or powder.

EXPERIMENTS: Figure 1 shows a carbon nano-tube (CNT) made of carbons strongly bonded together in a network with a diameter typically in a nanometer size. When the ^{12}C(γ,n)^{11}C reaction happens with incident high energy γ-rays, ^{11}C and neutron are released from the target nanotube. We introduce oxygen flow gas in the CNT powder target. The recoiled ^{11}C is captured by O_2 gas, making a $^{11}CO_2$ molecule. We prepare the O_2 gas circulation system, consisting mainly of 1) a CNT target with a nanotube powder isolated by two CNT sheets, 2) O_2 gas tubes, and 3) molecular sieves. We seal the CNT powders in the Al target vessel with the two CNT sheets for gas inlet and outlet. The O_2 gas flows through the CNT sheet and the CNT powders. We can trap the $^{11}CO_2$ using the molecular sieves. The ^{12}C(γ,n)^{11}C reaction experiment has been done using the bremsstrahlung γ-rays at the Linac facilty.

RESULTS: We confirmed that the $^{11}CO_2$ flowed out from the CNT target vessel through the CNT sheet by observing the 511 keV γ-rays at the molecular sieves. The measured decay curve of 511 keV γ-rays was well in agreement with the ^{11}C half-life of 20 minutes. The subjects remained are to determin the ^{11}C extraction efficiency from the CNT target and the specific activity with a ratio of ^{11}C/^{12}C. These work remained as future problems to be solved.

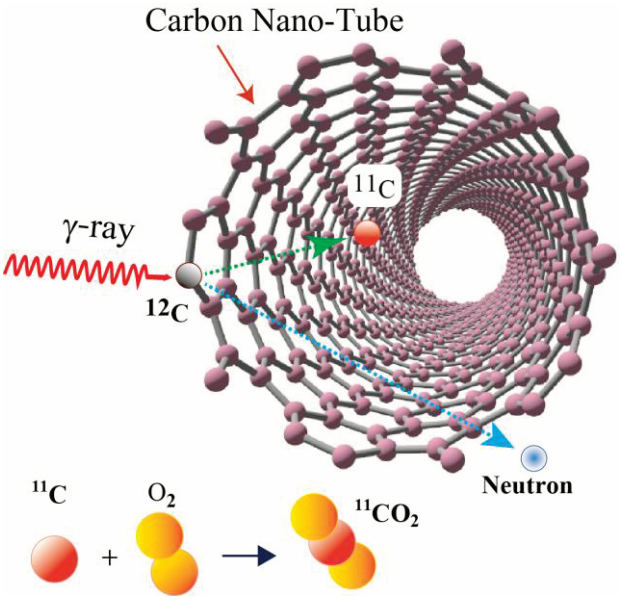

Fig. 1. Scheme of the ^{11}C medical-isotope production via the ^{12}C(γ,n)^{11}C reaction with the carbon nanotube (CNT). Neutron and ^{11}C are released from the strong bonding network of CNT after the ^{12}C(γ,n)^{11}C reaction following the nuclear two-body kinematics. Since the recoiled ^{11}C is chemically active, a $^{11}CO_2$ molecule is produced via the $^{11}C+O_2 \rightarrow {}^{11}CO_2$ chemical process.

REFERENCES:

[1] Y. Komatsu *et al.*, Radioisotopes, **67** (2018) 75-83.
[2] T.J. Ruth. A.P. Wolf, IEEE Trans., NS-**26** (1979) 1710.
[3] G.T. Bida et al., Radiochim. Acta., **27** (1979) 181.
[4] T.J. Ruth and M.J. Adam, Jornal of Radioanalytical and Nuclear Chemistry, **203** (1996) 457-469.
[5] M. Maziere *et al.*, Journal of Radioanalytical Chemistry, **56** (1980) 229-235.
[6] T. Nariai *et al.*, J. Neurosurg **103** (2005) 498-507.
[7] K. Isohashi *et al.*, EINMMI Resaerch **3** (2013) 27.
[8] T. Takeda *et al.*, Journal of Radioanalytical Chemistry, **318** (2018) 811-821.
[9] M. Kurosawa *et al.*, in preparation
[10] M. Fujiwara *et al.*, submitted to Journal of Radioanalytical Chemistry.

CO6-13

Demostrated Measuring by Laser Device of the Thickness of A Human Thigh Calcified Artery Vascular Tissue

N. Miyoshi and T. Takahashi[1]

Department of Gastroenterology/ Optical Clinic, Faculty of Medicine, Tsukuba University
[1] LINAC Beam-Line, Research Reactor Institute for Nuclear Science and Safety Nuclear Systems Research Center Accelerator Applied Engineering Research Field, Kyoto University

INTRODUCTION: The LINAC beam source in Kyoto University is unique one of higher purity and higher energy in the far infrared field. It is very sensitive spectroscopic measurements for the medical samples although the sample thickness is changes variously. It will be need to correct of the thickness effects. We tried the measurement them by the demonstrated measuring machine (Type CL-P.030) in this year (2020/30-31). As the thickness is proportional to the absorbance of a sample, the value of the absorbance is affected by dividing with the thickness to be corrected.

EXPERIMENTS: (1) Sample: A human thigh calcified artery vascular tissue was shown in Figure 1. **(2)** The mapping area of 4 lines (Z= 0, 1, 2, 3) are 14.7mm x 5mm x3 (220.5 mm^2) in Figure 1. **(3)** The laser device (Type CL-P030, Keyence Co., Osaka, Japan) was used to measure of the thickness of the sample in Figure 2.

RESULTS: [I] The area of 4 lines (Z=0, 1, 2, 3) was mapping of 14.7mm x 5mm x 3 (220.5 mm^2) through a human thigh calcified artery vascular tissue for 30 x 4 = 120 points as shown in Fig. 1.

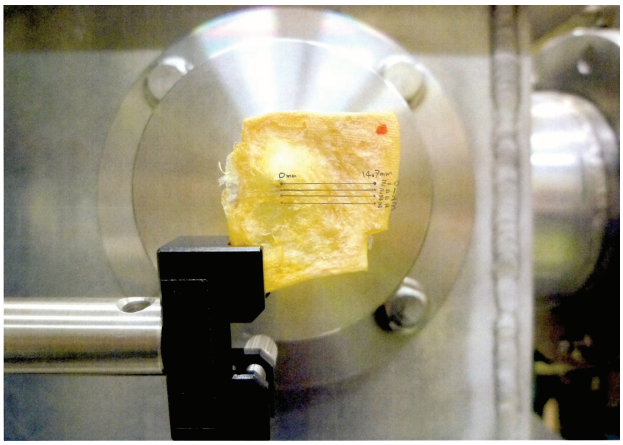

Fig.1: The mapping area of 4 lines (Z=0, 1, 2, 3) was 14.7mm x 5mm x3 (220.5 mm^2) of a human thigh calcified artery vascular tissue, respectively.

[II] The laser device was used for the demonstrated measuring of the sample thickness of the type of spot (minimum size: 38μm of diameter) as shown the performances in Fig.2.

Fig.2: The performance for the laser device of Type CLP030 (Spot-type: Right hand side) for the measurement of a sample thickness.

[III] The mapping measurement was automated drive on the sample stage by T. Takahashi.

[IV] The measured data were not so satisfied unstable as the thickness too sensitive, especially, transmitted lights at the demonstrated measurement. Detailed ingenuity will be required for the use it to develop of the thickness correction because the transmission will depend on the points of calcified or the normal vascular tissue.

The laser device instrument (Type CL-P030) was demonstrated from Keyence Co. and thanked for the demonstration to apply for the Basic Research A in the Grants-in-Aid for the Scientific Research on the last year (2020).

CO6-14 Design, Synthesis, and Evaluation of Glucose and Macrocyclic Polyamine-type Boron Carriers for NCT

S. Aoki[1,2], H. Ueda[1], M. Suzuki[3], Tanaka, T.[1] S. Masunaga[3], N. Kondo[3], and Y. Sakurai[3]

[1]*Faculty of Pharmaceutical Sciences, Tokyo University of Science*

[2]*Research Institute for Science and Technology, Tokyo University of Science*

[3]*KURNS*

INTRODUCTION: Boron neutron capture therapy (BNCT) is one of powerful therapies for local tumor control in the treatment of brain tumor, melanoma, and so on [1]. To date, only two boron-containing drugs, BSH (sodium mercaptoundecahydrododecaborate, $Na_2B_{12}H_{11}SH$) and L-4-boronophenylalanine (BPA) have been approved as clinically test compounds, and development of better BNCT agents is highly required.

We previously reported on the design and synthesis, of 2-boryl-1,2-dideoxy-D-glucose derivatives and other boryl-sugar analogs, although their intracellular uptake was not satisfying [2]. In this paper, we report on new phenylboronic acid-pendant macrocyclic polyamines **1~3** and their corresponding Zn^{2+} complexes **4~6** (Fig. 1).

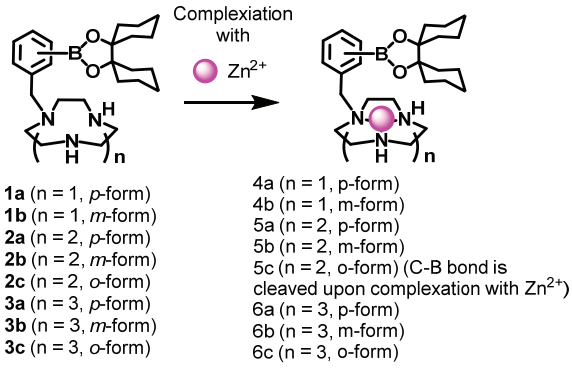

Fig. 1. Structures of boron-containing macrocyclic polyamines and the corresponding Zn^{2+} complexes

EXPERIMENTS and RESULTS: The synthesis of **1~3** and their Zn^{2+} complexes was carried out from s achieved according to our previous paper [3] and their cytotoxicity and cellular uptake activity against cancer cell lines (HeLa and A549 cells) and normal cell line (IMR-90) on ICP-MS (inductivity coupled plasma-mass spectrometer). As shown in Fig. 2., it was found that the intracellular uptake of **1~3 i**s higher than that of BSH and BPA, possibly due to the cationic charges of these molecules. The detailed study at low temperature and in the presence of specific inhibitors of the polyamine transporter system (PTS) suggest that the intracellular uptake of **1~3** is mediated by the clathrin-endocytosis pathway, possibly including PTS.

By comparison of the intracellular uptake, T/N (tumor/normal cell) ratios, and cytotoxicity of **1~3**, **1b**, **2b**, and **3a** were chosen as potent candidates for BNCT experiments. Because these molecules contained ^{10}B and ^{11}B in a natural abundance ratio ($^{10}B/^{11}B$ = 19.9/89.1), we synthesized the corresponding ^{10}B-enriched analogs, **^{10}B-1b**, **^{10}B-2b**, **^{10}B-3a** and their Zn^{2+} complexes **^{10}B-4b**, **^{10}B-5b**, **^{10}B-6a** *in situ* for BNCT experiments [4].

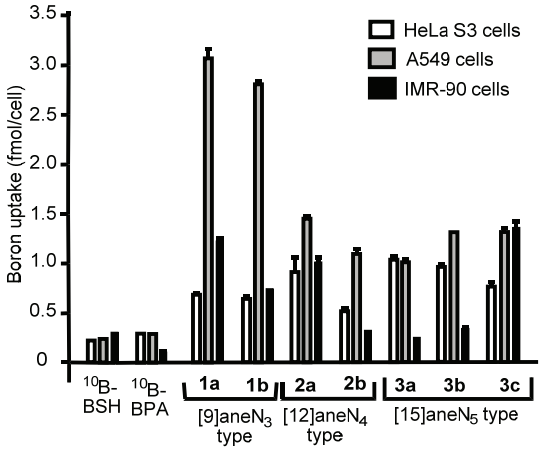

Fig. 2. The intracellular uptake **1~3** (30 μM) in HeLa S3 cells as determined on ICP-MS after the incubation with these drugs at 37 ºC for 24 hr. Data represent the mean ±SD of at least three replicates.

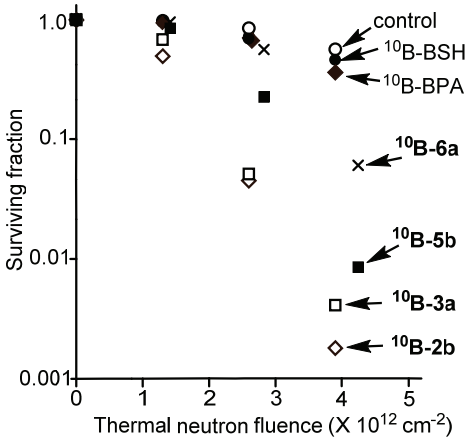

Fig. 3. Antitumor effect of ^{10}B-enriched BSH, BPA, **2b, 3a, 5b,** and **6a** (30 μM) against A549 cells upon irradiation with thermal neutron (averaged thermal neutron flux was 1.4 X 10^9 n/cm^2·s), as evaluated by a colony assay.

The results of BNCT of the these ^{10}B-enriched agents are summarized in Fig. 3, which indicates more potent BNCT effect of **^{10}B-2b**, **^{10}B-3a** **^{10}B-5b**, and **^{10}B-6a** than that of BSH and BPA [4]. The design and synthesis of boron carriers that have higher intracellular uptake and more potent BNCT effect are now in progress.

REFERENCES:

[1] a) R. F. Barth *et al.*, *Clin. Cancer Res.*, **11** (2005) 3987-4002. b) R. F. Barth et al. *Rad. Oncol*. **7** (2012) 146-166.

[2] T. Itoh, et al., *Bioorg. Med. Chem.* **26** (2018) 5922-5933.

[3] M. Kitamura, et al. *Inorg. Chem.* **50** (2011) 11568-11580.

[4] H. Ueda, et al. submitted for publication.

CO6-15 Preparation and Characterization of BPA-uridine conjugate for BNCT

K. Tanabe[1], M. Suzuki[2], and T. Nishihara[1]

[1]*Department of Chemistry and Biological Science, College of Science and Engineering, Aoyama Gakuin University*

[2]*Institute for Integrated Radiation and Nuclear Science, Kyoto University*

INTRODUCTION:

Modified nucleobases have been widely used as functional materials, and a variety of them have significant functions in biological systems. For example, 5-fluorouridine (5FU), 5-fluorodeoxyuridines (FdUrd) or cytarabine are well-known antitumor drugs and their derivatives act as stimuli-responsive prodrugs.[1] Thus, modified nucleobases are important as newly developed functional drugs.

In this study, we employed nucleobases as solubilizer of drugs for Boron Neutron Capture Therapy (BNCT) into aqueous solution as well as transport agent of drugs into the cells. We combined uridine and BPA and found that the resulting complex (BPA-uridine conjugate) smoothly dissolved in water. The cellular experiments revealed that BPA showed efficient cytotoxic effects in the presence of uridine and thermal neutron irradiation. Thus, uridine seems to be good agents for drug delivery system.

EXPERIMENTS:

Preparation of BPA-uridine conjugate. BPA was added to the aqueous solution of uridine and then the resulting mixture was heated to 80 °C for 6 h. After the BPA was dissolved in the solution, the mixture was cooled to room temperature to obtain BPA-uridine conjugate.

Cellular experiments using BPA and uridine in aqueous solution. The conjugate consisted of BPA (6 mM) and uridine was administered to the A549 cells and then the cells were incubated for 2 h. After incubation, the cells were irradiated (neutron, 1 MW) for 45 min at KUR. After incubation, WST 8 was added to the cells, and the cell viability assay was performed using Microplate Reader.

RESULTS:

Conventionally, fluctose has been used to solubilize BPA in water for the formation of their complex that showed hydrophilic properties. We expected that the uridine bearing ribose unit formed similar complex with BPA, and thus we combined BPA with uridine and prepared their conjugate. Eventually, we found that BPA-uridine conjugate was smoothly dissolved in water, and then applied them to cellular experiments.

For understanding of the biological activity of BPA in the presence of uridine, we measured the cytotoxicity of BPA-uridine conjugate against A549 cells, which were exposed to neutron (1 MW) in the presence of aqueous solution consisted of BPA and uridine and then incubated at 37 ˚C. Cell survival was determined by WST assay. Figure 1B and 1C compares cell survivals in the presence and absence of BPA-uridine after irradiation. The cytotoxic effect of radiation was significantly enhanced when the cells were irradiated in the presence of BPA-uridine. It is likely that BPA is effectively activated in the cells and thereby exhibits high cytotoxicity against tumor cells upon irradiation. In a separate experiment, we evaluated the cytotoxic effect of BPA in the presence of fluctose that complexed with BPA to dissolve into water. The cytotoxic assay revealed that BPA-fluctose conjugate showed similar cyototoxic effect upon irradiation. Thus, it is reasonable to conclude that BPA-uridine conjugate is a potent candidate agents for BNCT. In vivo experiments to evaluate the function of BPA-uridine is in progress.

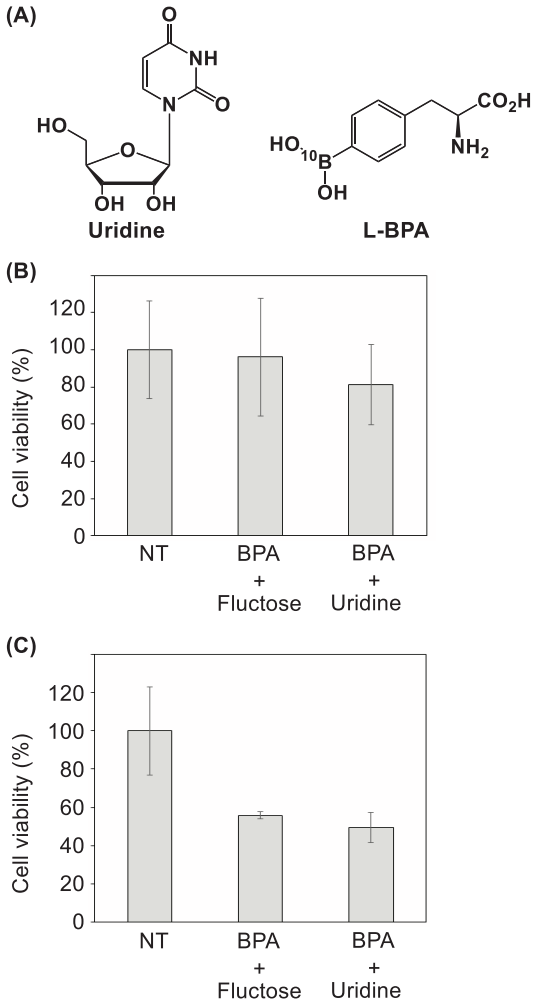

Figure 1. (A) Chemical structures of uridine and BPA. (B, C) Cytotoxic effect of BPA-uridine conjugate or BPA-fluctose conjugate upon ODN 1 upon thermal neutron irradiation (1 MW, 45 min).

REFERENCES:

[1] K. Tanabe *et al.*, *Org. Biomol. Chem.* **7** (2009), 651–654.

CO6-16 Asp racemization/isomerization in shedding products of cell adhesion molecule 1 is potentially involved in the neurodegeneration induced by elevated pressure

A. Yoneshige[1], A. Ito[1] and T. Takata[2]

[1]*Department of Pathology, Kindai University*
[2]*KURNS*

INTRODUCTION: The elevation of internal pressure is often involved in neurodegeneration; intraocular and intraventricular pressure elevations over 20–30 cmH_2O cause glaucoma and hydrocephalus, respectively.
Previously, to investigate the mechanisms by which elevation of intraluminal pressure causes cell or tissue degeneration, we devised a novel two-chamber culture system that enabled us to subject cultured cells to low levels of water pressure (2-50 cmH_2O pressure load) [1,2]. We found that mouse primary neurons degenerated when the water pressure was above 30 cmH_2O, and that ectodomain shedding of synaptic cell adhesion molecule 1 (CADM1) increased in a water pressure-dependent manner [1]. We also discovered that the increase of intracellular product of CADM1 shedding (C-terminal fragment, CADM1-CTF) resulted in decreased neurite density with punctate localization of CADM1 suggesting its aggregation in neurites [1].
CADM1-CTF is rich in Asp residues neighbored by Ala residues, and the conversion of these amino acids to poly-Gly diminished its aggregation state. Since the racemization and isomerization of Asp residues contributes to aggregation of various proteins and it likely occurred when the neighboring residues are small [3,4], these insights led us to hypothesize an involvement of Asp racemization/isomerization in the neurodegeneration induced by internal pressure elevation.

EXPERIMENTS:
(1) Synthetic peptide of internal sequence of CADM1-CTF (GADDAADADTAIINAEGGQNNSEEK) was incubated at 50°C for 0-15 days and applied to LC-MS to identify Asp isomer-containing peptides.
(2) Mouse neuroblastoma cell line Neuro-2a cells with exogenously expressed CADM1-CTF were cultured under 50 cmH_2O and were prepared for LC-MS analysis.
(3) To mimic the human ocular hypertension, immortal mouse neuroretinal cell line RGC-5 cells, primary neuroretinal cells, and mouse retinal explant cultures were prepared to exsert water pressure on to cells or tissues.
(4) The retinae or optic nerves of DBA/2J mice, a glaucoma model with ocular hypertension, were collected and subjected to CADM1 immunoblot analysis.

RESULTS:
(1) In LC-MS analysis of CADM1-CTF synthetic peptide, multiple peaks were detected after 1 day at pH 6.0 or pH 7.0 indicating that Asp racemization/isomerization could be occurred at neutral pH.
(2) CADM1-CTF proteins in Neuro-2a cells were solubilized with water, Triton X-100 containing buffer, or SDS containing buffer after 3 days culture under 50 cmH_2O, and CADM1 immunoblot was carried out. CADM1-CTF protein yields (CADM1-CTF / total proteins) were in the order Triton X-100 > SDS > water, however, the peptide peak was not identified using with LC-MS. The optimal conditions for LC-MS analysis should be determined in future study.
(3) Under 50 cmH_2O in the two-chamber culture device, the number of primary neuroretinal cells remained unchanged for 3 days with intact neurites, while the number of differentiated RGC-5 cells decreased after 2 days with loss of neurites. Primary neuroretinal cells would be more suitable for studying the effects of pressure elevation than RGC-5 cells. In retinal explant cultures, since PI-positive necrotic cells have begun to appear after 3 days at atmospheric pressure, the cultured retinae were collected at 2 days in vitro. The number of TUNEL-positive apoptotic retinal ganglion cells and the degree of GFAP-positive gliosis were analyzed histologically. Those neurodegenerative features were reproduced experimentally in cultured retinae at 50 cmH_2O (Fig. 1). Future experiments exploring Asp isomer-containing fragments in these crude cell/tissue lysates are planned.
(4) The CADM1 shedding rates were not changed in DBA/2J retinae, regardless of intraocular pressure. Further studies are necessary to elucidate whether Asp racemization/isomerization take place in full length CADM1 and its effects on CADM1 solubility and distribution.

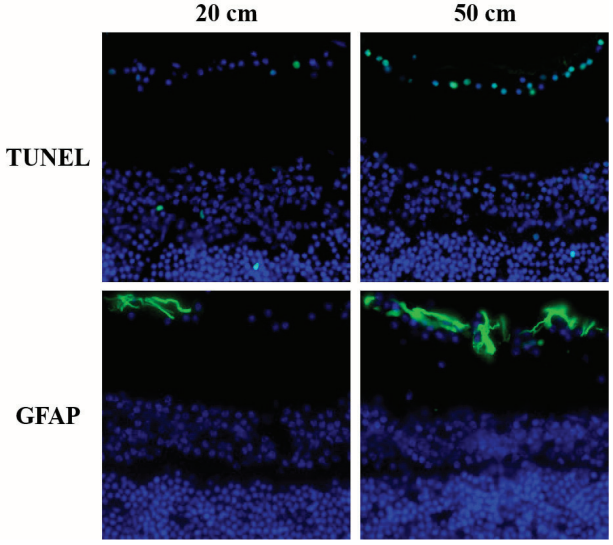

Fig. 1. Histological examinations of cultured retina with 2-50 cmH_2O pressure loading

REFERENCES:
[1] A. Yoneshige *et al.*, Mol. Neurobiol., **54** (2017) 6378-6390.
[2] M. Hagiyama *et al.*, Front. Physiol., **8** (2017) 997.
[3] N. Fujii *et al.*, J. Biochem., **116** (1994) 663-669.
[4] T. Takata *et al.*, Protein Sci., **29** (2020) 955-965.

CO7-1 Establichment of a novel mutation breeding using Boron Neutron Capture Reaction (BNCR)

M.Kirihata, S. Segami[1], Y. Hattori, T. Kinouchi, Y. Kinashi[2]

Research Center of BNCT, Osaka Prefecture University

[1]Research Institute of Environment, Agriculture and Fisheries, Osaka Prefecture

[2]KURNS

INTRODUCTION: Boron Neutron Capture Reaction (BNCR) is based on the nuclear reaction of ^{10}B atom with thermal/epithermal neutron already applied to cancer treatment (BNCT) [1, 2]. As a new utilization method of BNCR, the purpose of this study is to establish a novel mutation breeding using BNCR.

This method uses the principle of inducing mutation by an alpha particle and ^{7}Li recoil nuclei high linear energy transfer and short range when irradiated with neutrons (low energy thermal neutrons (< 0.5 eV) can be absorbed the ^{10}B atoms, leading to generating high linier energy transfer alpha particles (~ 150 keV/μm) and ^{7}Li nuclei (~ 175 keV/μm)) that are produced by BNCR of ^{10}B selectively taken into the meristematic cell with thermal neutron. This principle is different from both chemical mutagens, such as EMS and MNU, and physical mutagens, such as gamma rays and ion beams, used for mutation breeding so far. In other words, the mutagenic effect depends on chemical and physical factors, such as ^{10}B concentration, thermal neutron intensity, and irradiation time.

The germination rate is used as one of the traits to verify the effect of mutagenesis[3]. In previous report, the seeds were immersed into different concentrations (0, 10, 100, 200 ppm) of ^{10}B-enriched *p*-boronophenylalanine (BPA) [4] for 16 h, re-dried seeds were irradiated with thermal neutron for 90 minutes. The germination rate of these irradiated seeds was investigated, and no BPA concentration-dependent effect on germination rate was observed. In other words, in order to study the optimal treatment conditions for mutagenesis, need to try a stronger process. This time, new treatment conditions were investigated by increasing the ^{10}B concentration of the treatment solution by using BPA as a fructose complex and by extending the immersion time.

EXPERIMENTS: The experimental material used *Oryza sativa* L. cv. Nipponbare. The dry seeds were immersed into different concentrations (0, 10, 100 mM) of ^{10}B-enriched *p*-boronophenylalanine-fructose complex (BPA-Fc) for 24 h or 48 h. The samples were washed with water and re-dried. The seeds in 2-mL tubes were irradiated with thermal neutron for 90 minutes in the Kyoto University Research Reactor (KUR). The irradiated seeds were sown in cell trays on May 31, 2020, germinated in a germination machine, grown outdoors, and the germination rate was examined 20 days after sowing.

RESULTS: The germination rate not decreased with BPA-Fc concentrations. But the germination rate decreased with immersion time (Table 1). Although there was a significant decrease in germination rate in the strongest treatment, the 100 mM BPA-Fc for 48h condition, the germination rate was similar to the control 48 h condition. Therefore, the decrease in germination rate in 48h immersing was not due to BNCR, but simply due to the effect of longer immersion time. In this experiment, we used BPA-Fc to increase the ^{10}B concentration, but again, we could not confirm any decrease in germination rate due to the BNCR under the examined conditions. It is unclear at this time whether the accumulation of ^{10}B in the meristematic cell of the seeds is not going well or whether this method is less likely to cause a decrease in germination rate. However, considering the solubility of BPA, the concentration of ^{10}B in BPA is considered to be at the upper limit of the current conditions, and there may be differences in the uptake by plant seeds depending on the compound. Therefore, we are planning to study the treatment with boron compounds other than BPA.

Table 1. The relationship each treatment conditions and germination rate.

Concentrations of BPA-Fc (mM)	Immersion time (hour)	No. of seeds	No of seeds germinated	germination rate (%)
0	24	40	28	70.0
10 (100 ppm)		80	72	90.0
100 (1000 ppm)		80	66	82.5
0	48	40	23	57.5
10 (100 ppm)		80	55	68.8
100 (1000 ppm)		80	45	56.3

* Numbers in ( ) indicate ^{10}B concentrations.

REFERENCES:

[1] H. A. Soloway *et al.*, Chem. Rev., **98** (1998), 1515-1562.

[2] B. Farhood, *et al*., *Rep. Pract. Oncol. Radiother.* **23** (2018), 462-473.

[3] Tanaka A. *et al*., *Int. J. Radiat. Biol*., **72**, (1997), 121-127.

[4] H. R. Snyder, *et al*., *J. Am. Chem. Soc.* **80** (1958), 835-838.

CO7-2 Development of antibody-tagged boron compounds using Fc-binding peptide for on-demand receptor target in boron neutron capture therapy

I. Nakase[1,2], A. Aoki[1,2], Y. Sakai[3], S. Hirase[1,2], M. Ishimura[3], T. Takatani-Nakase[4,5], Y. Hattori[3], and M. Kirihata[3]

[1]*Graduate School of Science, Osaka Prefecture University, Japan*
[2]*NanoSquare Research Institute, Osaka Prefecture University, Japan*
[3]*Research Center of BNCT, Osaka Prefecture University, Japan*
[4]*School of Pharmacy and Pharmaceutical Sciences, Mukogawa Women's University, Japan*
[5]*Institute for Bioscience, Mukogawa Women's University, Japan*

INTRODUCTION: Boron Neutron Capture Therapy (BNCT) is a radiation therapeutic method for cancer therapy. Cancer cellular uptake of boron-10 (^{10}B) atoms induces the cell death by the generation of alpha particles and recoiling lithium-7 (^{7}Li) nuclei when irradiated with low-energy thermal neutrons. Current BNCT technology shows effective therapeutic benefits in refractory cancers such as brain tumor and head and neck cancer. However, improvement of insufficient cancer targeting and cellular uptake efficacy of boron compounds, and expansion of disease coverage in BNCT are strongly desired. In this research, we aimed to develop antibody-based drug delivery technology for BNCT using Z33 peptide [1], which shows specific interaction recognition with the Fc of human IgG antibody, for on-demand receptor target. In addition, we found that macropinocytosis induction during the antibody-based drug delivery is important for the biological activity in BNCT *in vitro* assay.

EXPERIMENTS: Z33 peptides were synthesized via Fmoc solid-phase synthesis methods. For preparation of dodecaborate-Z33 peptide conjugate, Z33 peptides was subjected to react with bismaleimide ethane and then to react with mercaptoundecahydrododecaborate (BSH).

RESULTS: We designed Z33 peptide-conjugated boron compounds (Z33-BSH), and we examined the cell membrane accumulation and cellular uptake of Z33-BSH with or without complex of cetuximab antibody, which specifically target epidermal growth factor receptor (EGFR). As a result, in A431 cells (highly expressing EGFR), complex of cetuximab antibody (100 nM) with Z33-BSH (200 nM) highly enhanced their accumulation on the cancer cell plasma membranes. However, only their attachment on plasma membranes with very low cellular uptake were observed. Macropinocytosis (accompanied by actin reorganization, ruffling of plasma membrane, and engulfment of large volumes of extracellular fluid) [2] is considered to be important cellular uptake pathway, and activation of EGFR leads to macropinocytosis induction. Therefore, we next checked effects of treatment of EGF on their cellular uptake. As our results, co-treatment of EGF with cetuximab antibody/Z33-BSH complex significantly increased their cellular uptake, and in the thermal neutron irradiation experiment under the same conditions, the cell killing effect of cetuximab antibody/Z33-BSH complex was enhanced through macropinocytosis induction by EGFR activation [3].

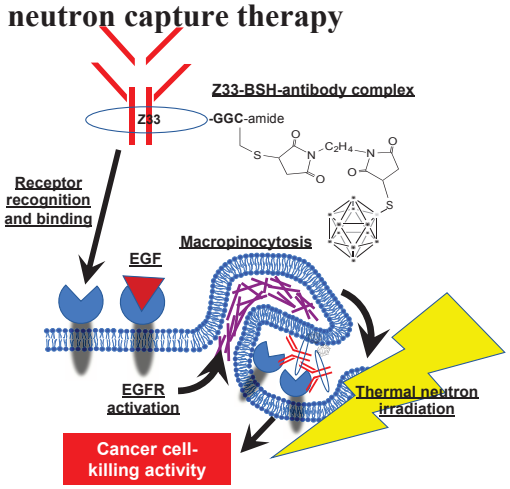

Figure 1. Schematic representation of the receptor targeted delivery of boron compounds. Z33-BSH-antibody recognizes the targeted receptors on cancer cells. EGFR activation induces macropinocytotic cellular uptake of the BSH, leading to increased efficacy of the cancer cell-killing activity after thermal neutron irradiation.

CONCLUSION: In this research, we developed antibody-based receptor target system and found importance of macropinocytosis induction in BNCT. These results provide fundamental knowledge for the further development of receptor target system in BNCT.

REFERENCES:

[1] A.C. Braisted, J.A. Wells, *Proc. Natl. Acad. Sci. USA*, **93** (1996) 5688-5692.
[2] J.A. Swanson, *Nat. Rev. Mol. Cell Biol.*, **9** (2008) 639-649.
[3] I. Nakase, *et al. ACS Omega*, **5** (2020) 22731-22738.

CO7-3 Development of cyclic RGD-functionalized *closo*-dodecaborate albumin conjugates for boron neutron capture therapy

Hiroyuki Nakamura[1,2], Kai Nishimura[2], Kazuki Kawai[2], Satoshi Okada[1,2], Takushi Tanaka[3], Minoru Suzuki[3]⇑

[1]*Laboratory for Chemistry and Life Science, Institute of Innovative Research, Tokyo Institute of Technology, Yokohama, Japan*
[2]*School of Life Science and Technology, Tokyo Institute of Technology, Yokohama, Japan*
[3]*Institute for Integrated Radiation and Nuclear Science, Kyoto University, Osaka 590-0494, Japan*

INTRODUCTION: Boron Neutron Capture Therapy (BNCT) is an expecting cancer therapy for the treatment of harsh and un-operatable malignant tumors. The efficiency of boron agent depends highly on tumor selectivity, sufficient amount of boron agent in tumor site, non-toxicity, tumour/normal tissues ratio (>3) and absorption of thermal neutrons by boron. In 2020, accelerator-based BNCT for head and neck cancer using L-BPA was approved by the Pharmaceuticals and Medical Devices Agency in Japan, making BNCT more accessible treatment. L-BPA is known to actively accumulate into tumor cells thorough L-type amino acid transporter 1 (LAT-1). However, there are many cancers with low L-BPA accumulation, therefore there is a need for new boron drugs that exhibit a cancer-selective uptake mechanism different from that of L-BPA. In this study, we focused on serum albumin as a boron carrier. The serum albumin is an abundant protein that has an extraordinary ligand-binding capacity to carry various endogenous and exogenous compounds in plasma. It accumulates in tumor due to the combination of leaky and abnormal blood vessels with the absence of the lymphatic drainage system known as the enhanced permeability and retention (EPR) effect.
We have developed maleimide-conjugated *closo*-dodecaborate (MID). MID-conjugated albumins accumulated in tumor and exhibited significant tumor suppression in tumor-bearing mice after neutron irradiation [1]. In order to improve further accumulation in tumor, we designed cyclic RGD (cRGD) peptide-conjugated boronated albumin. It is known that cRGD peptide strongly binds to αvβ3 integrin, which overexpress in many cancer cells. BNCT studies were performed at Kyoto University Research Reactor Institute (KURRI).

EXPERIMENTS: U87MG tumor bearing mice (Balb/cCrSlc nu/nu female, 5−6 weeks old, 16−20 g) were injected via the tail vein with 200 μ L of MID-BSA (7.5 mg [^{10}B]/kg) or cRGD-MID-BSA (7.5 mg [^{10}B]/kg). The whole bodies of mice were placed in an acrylic mouse holder and fixed on a 5-mm-thick thermo-plastic plate. At 12 h after administration, the right thighs of mice were irradiated with neutrons in the KUR nuclear reactor. BNCT effects were evaluated on the basis of the changes in tumor volume of the mice.

RESULTS: Anti-tumor effects of cRGD-MID-BSA and MID-BSA were compared in the U87MG xenograft tumor model at the same dose. cRGD-MID-BSA and MID-BSA were injected into U87MG xenograft tumor model mice via the tail vein, and thermal neutron irradiation was performed 12h after injection. Tumor growth curves are shown in Fig. 1 [2].

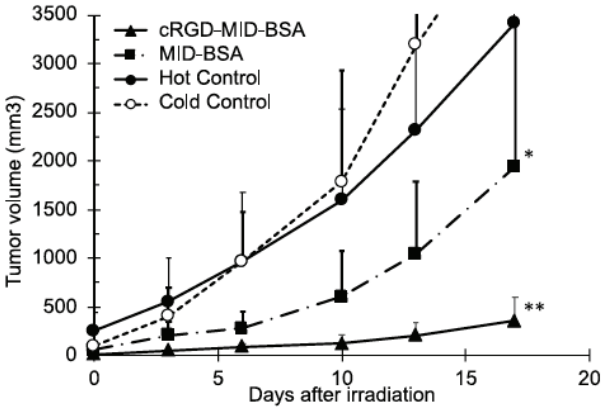

Fig. 1. Tumor volume in U87MG xenograft tumor model mice irradiated with thermal neutron (hot) for 50 min (1.8 x 10^{12} neutrons/cm^2) or without irradiation (cold). The irradiation was performed at 12 h after i.v. injection of cRGD-MID-BSA and MID-BSA (7.5 mg [^{10}B]/kg). Data are expressed as means ± SD (n = 5). Statistical significance: *P< 0.05 and **P < 0.001 compared with hot controls. Reproduced from ref 2. Copyright 2020 American Chemical Society.

CONCLUSION: We succeeded in the preparation of cRGD-MID-BSA. The conjugation of the cRGD peptide ligand at Cys 34 in BSA was confirmed by MALDI-TOF-MS analysis after trypsin digestion. In vivo fluorescence live imaging of near infrared dye (NID)-conjugated cRGD-MID-BSA and MID-BSA revealed that both cRGD-MID-BSA and MID-BSA similarly reached the maximum accumulation during 8−12 h after injection. However, NID-cRGD-MID-BSA was more selectively accumulated and retained in tumor than NID-MID-BSA after 24 h. An *in vivo* BNCT study emerged with the cRGD peptide ligand enhanced accumulation of MID-BSA in tumor cells through αvβ3 integrin, attributed to significant tumor growth suppression after neutron irradiation. Therefore, the MID-albumin conjugate is a potential platform not only for tumor targeted by introducing tumor-affinity ligands but also for *in vivo* live imaging by introducing visualization functional groups, providing a possible theranostic module for BNCT.

REFERENCES:
[1] H. Nakamura *et al.*, Pure Appl. Chem., **90** (2018) 745-753.
[2] K. Kawai *et al.*, Mol. Pharm., **17** (2020) 3740–3747.

CO7-4 Development of *closo*-dodecaborate-containing pteroyl derivatives targeting folate receptor-positive tumors for boron neutron capture therapy

Hiroyuki Nakamura[1,2], Kai Nishimura[2], Fumiko Nakagawa[2], Satoshi Okada[1,2], Taiki Morita[1,2], Shinji Kawabata[3], Takushi Tanaka[4], Minoru Suzuki[4]

[1]*Laboratory for Chemistry and Life Science, Institute of Innovative Research, Tokyo Institute of Technology, Yokohama, Japan*
[2]*School of Life Science and Technology, Tokyo Institute of Technology, Yokohama, Japan*
[3]*Department of Neurosurgery, Osaka Medical College, Osaka 569-8686, Japan*
[4]*Institute for Integrated Radiation and Nuclear Science, Kyoto University, Osaka 590-0494, Japan*

INTRODUCTION: Boron Neutron Capture Therapy (BNCT) has been attracting attention as a noninvasive radiotherapy in cancer treatment. In 2020, accelerator-based BNCT for head and neck cancer using L-BPA was approved by the Pharmaceuticals and Medical Devices Agency in Japan. L-BPA is known to accumulate into tumor cells thorough L-type amino acid transporter 1 (LAT-1). However, there are many cancers with low L-BPA accumulation, therefore there is a need for new boron drugs that exhibit a cancer-selective uptake mechanism different from that of L-BPA. We focused on folate receptor α (FRα). Folate is one of the B vitamins and known to be taken into cells via FRs, which are overexpressed on the surface of many cancer cells including HeLa and U-87 MG. Therefore, FRs have attracted attention as targets for cancer treatment. In this study, we synthesized pteroyl-*closo*-dodecaborate conjugate (PBC) and examined their cell uptake using folate receptor (FRα) positive and negative cells. It is known that the pteroyl group of folate is essential for the interaction with folate receptors, which overexpress in many cancer cells.

EXPERIMENTS: (1) WTT Assay: Cells were seeded in 96-well plates in medium at the density of 5×10^3 cells/well. After 24 h of cell attachment, the cells were exposed to PBC and L-BPA-Fructose complex at final concentration ranging from 0 to 3 mM (L-BPA : 0 to 10 mM), for 72 h at 37°C. At the end of the incubation period, the mitochondrial function was verified with 0.5 mg/ml MTT (3-(4,5-dimethylthiazol-2-yl)-2,5-diphenyltetrazolium bromide) for 2 h at 37°C and quantified spectrophotometrically at 595 nm by Biorad microplate reader.
(2) *In vitro* BNCT Effects toward U87MG Cells: Cells were plated on 96-well plates (500 cells per well) 12 h before irradiation. They were incubated with PBCs or L-BPA-fructose (25 or 50 ppm [^{10}B]) for 3 h at 37 °C and irradiated with thermal neutron for 100 min (2.03×10^{12} – 1.05×10^{13} neutrons/cm^2) in the KUR nuclear reactor. After replaced by a flesh medium, the cells were further incubated for 72 h. A PBS solution of MTT (2.5 mg/mL) was added to each well (10 μ L per well), and the plate was incubated for 2 h at 37 °C. After the medium was removed, dimethyl sulfoxide (DMSO) was added to each well (100 μ L per well). Absorbance at 570 nm was measured with a plate reader (TECAN, infinite F200). The irradiated cell viability was calculated by comparison of the absorbance of a nonirradiated cell (cold control).

RESULTS: A high dose is necessary to achieve the required boron concentration in the tumor for BNCT. Thus, low cytotoxicity is essential for BNCT boron agents. We first examined the cytotoxicity of synthesized PBCs toward three human cancer cell lines using MTT assay: HeLa (human cervical carcinoma) and U87MG (human glioblastoma) cells are FRα positive and A549 (human alveolar adenocarcinoma) cells are FRα negative. L-BPA was used as a positive control. PBC exhibited IC_{50} values (the concentrations required for 50% inhibition) in a range of 1–3 mM toward these human cancer cells, indicating that PBC has adequately low cytotoxity, enough to use as BNCT boron agents. We next compared BNCT anti-tumor effect between PBC and L-BPA toward U87MG human glioblastoma cells (FRα positive cells). Irradiation dose-dependent BNCT effects toward U87MG cells as shown in Fig. 1 indicated that PBC exhibited more potent than L-BPA at 25 ppm B concentration and that the cell-killing effect of PBC at 25 ppm B concentration was higher than that at 50 ppm B concentration.

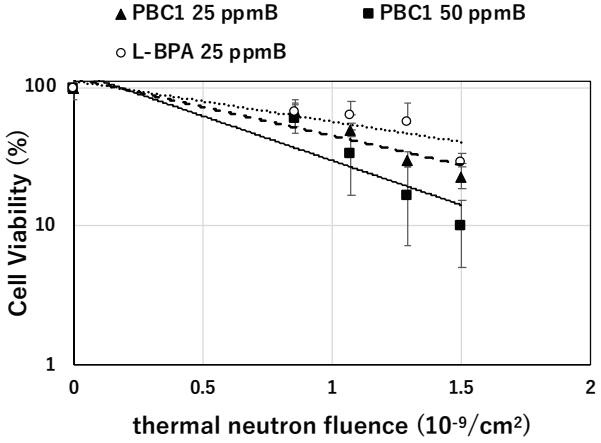

Fig. 1. BNCT effect of PBC toward U87MG after thermal neutron irradiation for 100 min (2.03×10^{12} – 1.05×10^{13} neutrons/cm^2) in the KUR nuclear reactor. L-BPA was used as a positive control.

CONCLUSION: We succeeded in the development of PBC targeting folate receptor positive tumor cells. PBC showed higher cell-killing effects than L-BPA against U87MG FRα positive cells after thermal neutron irradiation. Therefore, PBC is considered to be a promising boron agent for the treatment of L-BPA negative patients in BNCT.

REFERENCES:
[1] F. Nakagawa *et al.*, Cells, **9** (2020) 1615.

CO7-5

Influence of the abscopal effect to the survival rate following head neutron-irradiation between the different inbred mice

Y. Kinashi[1], T. Takata[1], Y. Sakurai[1], H. Tanaka[1]

[1]*Institute for Integrated Radiation and Nuclear Science Kyoto University*

INTRODUCTION: It is reported that immune response is activated by partial radiation [1]. The influence on immune organization of the mouse at the time of the head irradiation is not well known. The purpose of this study is to evaluate the relative biological effectiveness in the severe combined immunodeficiency (SCID), so-called SCID mice, those are having well-known high radiation sensitivity following thermal neutron irradiation for mice cranial.

EXPERIMENTS: CB17/Icr-*Prkdc*^{scid}/CrICrIj (SCID mice) were obtained from Charles River Inc. As a comparison experiment for the SCID mice, Balb/c and C3H/He mice were obtained from Japan Animal Inc.
Neutron irradiation and Gamma-ray irradiation was performed as follows. The Heavy Water Facility of the Kyoto University Research Reactor (KUR) was used. Mice were restrained in a plastic box on a radiation board. Neutron fluence was measured by radio-activation of gold foil and gamma-ray doses by TLD. Gamma rays were delivered with a ^{60}Co gamma ray machine. Mice were restrained in a plastic box on a radiation shelf. For the apoptotic assay of the splenic cells, the cell suspension was adjusted and incubated for 1weeks. At 2 days after irradiation, apoptotic induction of the cells was examined by Cell Death Detection ELISA (Roche).

RESULTS: As shown in Table 1, the RBE values estimated by the apoptotic changes of the SCID, Balb/c and C3H mice splenic cells following the partial neutron irradiation.

Table1. RBE (Relative Biological Effectiveness) calculated from apoptosis of splenic cells following neutron radiation

	SCID	Balb/c	C3H
RBE*	1.57	2.09	2.28

*RBE was calculated the Enrichment factor at 3Gy neutron radiation dose / the Enrichment factor at 3Gy gamma-ray radiation dose.

The apoptotic induction of the splenocytes of SCID mice was larger than that of Balb/c and C3H mice at 2 days after irradiation.

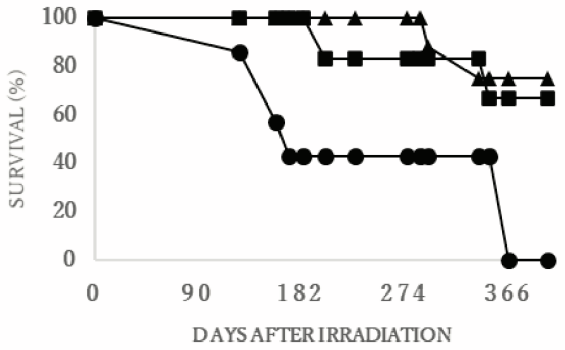

Fig.1 The survival rate after the partial head-irradiation of the neutron by KUR. Each marker shows the survival rate of the three kinds of mice. (●: SCID, ■: Balb/c, ▲: C3H)

Figure 1 shows that the survival rate after the partial head-irradiation of the neutron by KUR. The partial head-radiation dose was about 1Gy that does not cause the bone-marrow death to a mouse. By the experiment of the acute radiation damage of the SCID mouse, the dose of $LD_{50/30}$ (the dose that 50% die within 30 days after radiation exposure) is reported around 4Gy.

DISSCUSSION
In the radiation sensitive mice study, the RBE values of SCID mice was 1.57, comparing the neutron and the gamma studies. The RBE values of Balb/c and C3H/He mice was 2.09 and 2.28, respectively. SCID mice show extreme sensitivity to ionizing radiation, because cells lack functional DNA-dependent protein kinase. Our results suggest that the difference of RBEs for radiation sensitive mice were smaller than the wild type mice, that is to say, the hyper radiation sensitivity does not have a disadvantage in BNCT. On the other hand, 60% of the SCID mice died by partial neutron head-irradiation after 100 days and died all on the 356th day. Because neutron sensitivity becomes higher, as for the SCID mouse inferior to a wildtype mouse in immunoreaction, BNCT works in the survival rate disadvantageously.

REFERENCES:
[1] K Reynders *et al.*, Cancer Treatment Reviews, **41**(2015)503-5.

CO7-6 Optimization of chemical structures of polymer-BPA complexes for a nonclinical study

T. Nomoto[1], K. Konarita[1], K. Uehara[2], M. Ishimura[2], Y. Ishino[2], A. Sudani[2], Y. Sakurai[3], M. Suzuki[3], N. Nishiyama[1]

[1]*Institute of Innovative Research, Tokyo Institute of Technology*
[2]*Stella Pharma Corporation*
[3] *Institute for Integrated Radiation and Nuclear Science, Kyoto University*

INTRODUCTION: *p*-Boronophenylalanine (BPA) has been most widely investigated in clinical studies of boron neutron capture therapy (BNCT) because of its selective accumulation within tumor cells through LAT1 amino acid transporter overexpressed on many tumor cells [1]. However, the antiport mechanism of LAT1 sometimes causes unfavorable efflux of intracellular BPA by exchanging it with extracellular amino acids including tyrosine [2], resulting in short retention time within a target tumor and compromised therapeutic efficiency.

In this regard, we recently reported that poly(vinyl alcohol) (PVA) can form a complex with multiple BPA molecules through boronate ester formation and that PVA-BPA complex can be internalized into the cells through LAT1-mediated endocytosis and entrapped in endo-/lysosomes, thereby preventing the unfavorable efflux by LAT1 antiport mechanism [3]. Even in *in vivo* studies, PVA-BPA exhibited prolonged retention within the target tumor and significantly augmented antitumor efficiency with thermal neutron irradiation.

For the clinical application of PVA-BPA, it is important to optimize the composition of PVA-BPA especially from the viewpoint of molecular weight because it usually affects biodistribution. Herein, to optimize the chemical structure of PVA-BPA, we prepared a series of PVA-BPA complexes with various physicochemical properties and examined their antitumor efficacy in BNCT.

EXPERIMENTS: BALB/c mice bearing subcutaneous CT26 tumors were prepared by subcutaneous injection of the cell suspension. PVA-BPA was intravenously injected to the mouse at a dose of 10 mg BPA/mouse, and the thermal neutrons were irradiated to the tumor using KUR 3 h after injection. The tumor volume (V) was calculated using the following equation:

$$V = 1/2 \times a \times b^2$$

where a and b denote major and minor axes of a tumor, respectively.

RESULTS: As shown in Fig. 1, PVA-BPA with different physicochemical properties exhibited the strong antitumor effect with thermal neutron irradiation, indicating that the physicochemical properties of PVA did not critically affect the potency of PVA-BPA. This tendency may be advantageous in manufacturing PVA for PVA-BPA complexes in practical applications.

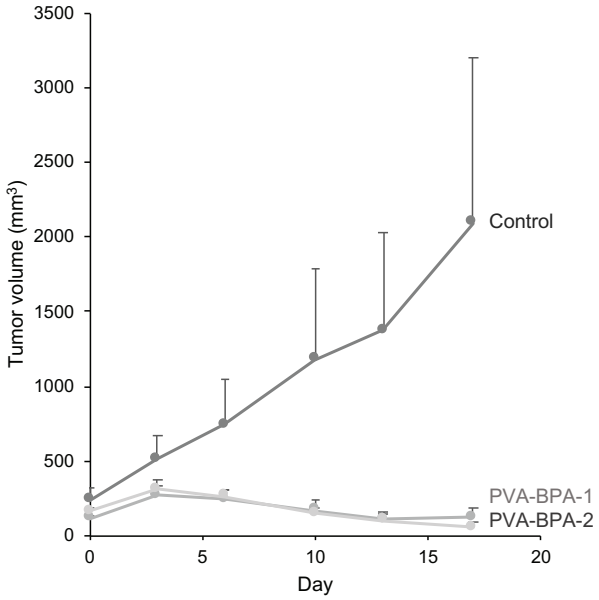

Fig. 1. Antitumor efficacy of representative PVA-BPA complexes (PVA-BPA-1 and PVA-BPA-2) to subcutaneous CT26 tumor models.

REFERENCES:

[1] P. Wongthai *et al.*, Cancer Science, **106** (2015) 279-286.
[2] A. Wittig, *et al.*, Radiat. Res., **153** (2000) 173-180.
[3] T. Nomoto *et al.*, Sci. Adv., 6 (2020) eaaz1722.

CO7-7 OKD-001-based BNCT successfully prolongs the overall survival of orthotopic xenograft mouse model of a patient-derived glioblastoma stem-like cell line

A. Fujimura[1,2], .K.Igawa[2], H. Michiue[2], A. Ueda[2], N. Kondo[3], Y. Sakurai[3] and M. Suzuki[3]

[1]*Graduate School of Medicine, Dentistry and Pharmaceutical Sciences, Department of Physiology, Okayama University*

[2]*Neutron Therapy Research Center, Okayama University*

[3]*Institute for Integrated Radiation and Nuclear Science, Kyoto University*

INTRODUCTION:

Boron neutron capture therapy (BNCT) is a fine-tuned intracellular atomic reaction of ^{10}B boron. Because BNCT utilizes a combination of ^{10}B pre-treatment and neutron irradiation, and thus induces a consequent ^{10}B nuclear reaction inside cancer cells, a highly cancer-specific ^{10}B delivery system is required for safety and efficacy. In 2020, a promising BNCT system with BPA (4-borono-L-phenylalanine) has been approved as a treatment against head and neck (H&N) cancer in Japan. BPA is a ^{10}B-added derivative of tyrosine/phenylalanine and therefore is mainly transported into cells via amino acid transporters, such as LAT1[(1)]. In H&N cancers, the expression levels of LAT1 are upregulated in almost all cases. However, in glioblastoma patients, there are many cases with low expression levels of LAT1. To expand the possibility of BNCT against these patients, the other types of boron agents are necessary. In this study, we showed an efficacy of BNCT with a novel boron agent, OKD-001[(2)], against orthotopic xenograft mouse models of a patient-derived glioblastoma stem-like cell line.

EXPERIMENTS:

NOD-SCID mice were orthotopically transplanted with 100,000 cells of a patient-derived glioblastoma stem-like cell line, MGG8[(3)] 15 days before BNCT with OKD-001. On the day before neutron irradiation, the mice were injected with 40 mg/kg of mercaptoundecahydrododecaborate (BSH) or OKD-001 (a mixture of BSH and A6K self-assembling peptide). On the next day, these mice were irradiated with neutron for 1 hour at KUR under anesthesia. Note that the neutron irradiation was done only on head part, not on whole body of mice. After BNCT, these mice were checked twice a week to obtain the overall survival time.

RESULTS:

As shown in Table 1, the medians of overall survival time of non-irradiated group (Group A: cold control, n=6), BSH-pretreated group (Group B), and OKD-001-pretreated group (Group C) are 36±5.8, 41±5.7, 51.5±3.9 days, respectively. OKD-001-BNCT, but not BSH-BNCT, significantly improved the prognosis of the orthotopic xenograft models.

	Group A	Group B	Group C
	cold control	BSH (40 mg/kg)	OKD-001 (40 mg/kg)
Median	36	41	51.5
stdev	5.8	5.7	3.9

Table 1. OKD-001, but not BSH, successfully prolonged the overall survival time (days) in the orthotopic xenograft mouse model of patient-derived glioblastoma stem-like cell line. MGG8.

REFERENCES:

1. P. Wongthai et al., "Boronophenylalanine, a boron delivery agent for boron neutron capture therapy, is transported by $ATB^{0,+}$, LAT1, and LAT2." ***Cancer Sci.***, 106 (2015) 279-286.

2. H. Michiue, et al., "Self-assembling A6K peptide nanotubes as a mercaptoundecahydrododecaborate (BSH) delivery system for boron neutron capture therapy (BNCT)." ***Journal of Controlled Release*** 330 (2021) 788-796.

3. M.L. Suva, et al., "Reconstructing and reprogramming the tumor-propagating potential of glioblastoma stem-like cells." ***Cell*** 157 (2014) 580-594.

CO7-8 Enhancement of the cancer cell-killing effects of boron neutron capture therapy by overexpression of *LAT1* in human cancer cells

K. Ohnishi[1], M. Misawa[2], N. Sikano[3] and M. Suzuki[4]
Departments of [1]Biology, [3]Radiological Science, Ibaraki Prefectural University of Health Sciences
[2]National Institute of Advanced Industrial Science and Technology
[4]Institute for Integrated Radiation and Nuclear Science, Kyoto University

INTRODUCTION: Outcome from BNCT largely depends on amount of intracellular accumulation of boron compound. L-type amino-acid transporter 1 (LAT1) [1], through which boronophenylalanine (BPA) is transported into cells, is frequently expressed in various types of tumor cells including glioblastoma but not in normal cells [2]. We transfected *pCMV/LAT1-GFP* plasmids into a glioblastoma cell line, T98G, and selected several clones and confirmed that those clones stably overexpress LAT1 in cell membrane with confocal laser microscopic observation and western blot analysis. In this study, we measured the sensitivity to the neutron and gamma-ray fluences generated by KUR in T98G/K1 and T98G/K4 clones that uptake ^{14}C-BPA 2.5 and 5.0 times, respectively, larger than T98G/KC2 control clone.

EXPERIMENTS: We repeated the previous experiments performed in 2019. The experiments are as follows. T98G/K1, T98G/K4, T98G/KC2 and transiently *pCMV/LAT1-GFP*-lipofected T98G/KC2 cells (treated with Lipofectamine 2000 overnight) were treated with medium containing ^{10}BPA (0, 5 or 20 ppm) for 3 hours. The cells were trypsinized and the cell suspensions in 1.5-ml cryo-tubes were irradiated with the fluences (0.4 or 0.8 Gy in total doses of neutrons and γ-rays) from KUR. The irradiated cells were plated on three replicate dishes for colony formation assay. The cells were fixed with ethanol and stained with crystal violet after cell culture for 10-14 days.

RESULTS: We confirmed the previous results obtained from 2019 experiments. The results are as follows. T98G/K4 cells showed slightly enhanced sensitivity to the fluences compared with T98G/K1, T98G/KC2 and the lipofected T98G/KC2 cells in the case of 5 ppm ^{10}BSA treatment. There is no significant difference in the sensitivity between T98G/K1 and T98G/KC2 cells as well as transiently lipofected T98G/KC2 cells. In the case of 20 ppm ^{10}BSA treatment, T98G/K4 and the lipofected T98G/KC2 cells showed largely enhanced sensitivity to the fluences compared with T98G/KC2 cells (ER=1.5). T98G/K1 cells showed slightly enhanced sensitivity (ER=1.2). The sensitivity of the cells to the fluences was correlated with the expression level of LAT1 of the cells. Figures of results are now in press for publication in Radiation Research [3].

CONCLUSION: This study confirmed the conclusion of 2019 report that overexpression of LAT1 in cancer cells causes enhanced anticancer effects of BNCT and BNCT combined with gene therapy is beneficial for tumors bearing low LAT1 expression.

REFERENCES:

[1] Y. Kanai *et al.*, J. Biol. Chem., **273** (1998) 23629-23632.
[2] K. Kaira *et al*., Br. J. Cancer, **107** (2012) 632-638.
[3] K. Ohnishi *et al*., Radiat. Res., in press.

CO7-9 Mechanism of Glioma Stem Cells' Survival Conferred by Glioma Niche after BNCT

N. Kondo[1], E. Hirata[2], M. Natsumeda[3], M. Nakada[4], Y. Sakurai[1], T. Takata[1], T. Kinouchi[1] and M. Suzuki[1]

[1] Institute for Integrated Radiation and Nuclear Science, Kyoto University (KURNS)
[2]Division of Tumor Cell Biology and Bioimaging Cancer Research Institute of Kanazawa University
[3]Department of Neurosurgery, Brain Research Institute, Niigata University
[4]Department of Neurosurgery, Kanazawa University Graduate School of Medical Science

INTRODUCTION: Boron Neutron Capture Therapy (BNCT) have been applied to recurrent malignant glioma and even after standard therapy (surgery, chemo-radiation therapy) because of the selective damage to the tumor. Especially, glioblastoma (GBM) is the most miserable cancer, whose patient survival is 14.6 months and remarkably resistant to chemo-radiation and immunotherapy. With BNCT, we achieved better local control and survival benefit in malignant glioma using thermal neutrons produced by the reactor in Kyoto University. However, the recurrence is inevitable after BNCT. Reasons for recurrence after BNCT have not been fully elucidated.

Glioma stem cells is known to be resistant to chemo-radiation therapy. This study is aimed to investigate whether glioma stem like cells (GSLCs), which is resistant to chemo-radiation therapy, take up a boron compound, p-boronophenylalanine (BPA) or not.

EXPERIMENTS:

Cell culture: We used human GBM cell lines that were established from tumor samples from two patients and named the cell lines no. 1 and no. 2. Cells were cultured as non-adherent spheroids in serum-free DMEM/F12 containing GlutaMax (Thermo Fisher Scientific), B27 without vitamin A (Thermo Fisher Scientific), penicillin and streptomycin (Nacalai Tesque, Kyoto, Japan), hEGF (20 ng/mL) and hFGF (20 ng/mL, Peprotech, TX, USA). To induce cell differentiation, we exposed the cells to media containing 10% FBS for 24 h. We dissociated cells to single cells using accutase (Nacalai Tesque) and rinsed them with PBS before mass cytometry analysis at 37 °C in CO_2 incubator.

Boronophenylalanine (BPA) Treatment and Thermal Neutron Irradiation: We treated cells with medium containing BPA at the concentration of 25 ppm for 24 h. The BPA was formulated and its concentration was measured as previously described [1].

Multiparameter Mass Cytometry: Cells were dissociated into single cells, labelled with heavy metal conjugated antibodies and analyzed by mass cytometer [2].

RESULTS: The percentage of the total BPA-positive cells decreased in differentiated cells compared with GSLCs in both no. one and no. two cells (stem vs. differentiated cells: no. one, 56.0% vs. 25.7% and no. two, 35.8% vs. 21.5%) (Table 1). In differentiated no. one cells, only 9.3% were BPA+/Oct3/4+ cells compared with 29.4% of no. one GSLCs. Similarly, lower percentages of no. one differentiated cells expressed both BPA and a stem cell marker than detected in no. one GSLCs. In contrast, 18.4% and 24.9% of differentiated cells positive for BPA were positive for GFAP and Tuj1, respectively, compared with 20.5% and 21.2% in GSLCs positive for BPA (Table 1). In differentiated no. two cells, only 2.9% were BPA+/SOX2+ cells compared with 15.5% of no. two GSLCs. Similarly, lower percentages of no. two differentiated cells expressed both BPA and a stem cell marker than were seen among the no. two GSLCs. In no. two cells, 8.6% and 9.4% of differentiated cells positive for BPA were positive for GFAP and Tuj1, respectively, compared with 10.5% and 11.1% GSLCs positive for BPA (Table 1).

BPA$^+$	No. 1 Stem	No. 1 DC	No. 2 Stem	No. 2 DC
Total	56.0	25.7	35.8	21.5
Differentiation$^+$				
GFAP	20.5	18.4	10.5	8.6
Tuj1	21.2	24.9	11.1	9.4
Stem $^+$				
Oct3/4	29.4	9.3	11.4	4.9
CD15	19.2	10.6	11.0	6.1
CD171	21.3	13.9	8.0	4.2
IL6Ra	15.1	6.4	8.1	4.1
SOX2	51.9	15.2	15.5	2.9
Nestin	35.0	8.3	12.8	3.6
CD144	11.6	5.3	6.8	3.9
Musashi-1	28.1	14.5	19.0	8.2
CD133	18.8	9.0	11.6	5.8
PDGFRα	44.9	15.6	12.0	4.6
Notch2	18.9	12.1	11.8	4.6
CD44	19.1	9.9	11.6	5.9
Nanog	20.6	6.9	11.5	5.0
STAT3	44.9	17.2	16.2	1.1
CXCR4	18.7	12.2	13.5	5.7
c-Myc	27.1	11.6	13.2	5.7
CD49f	29.8	18.7	15.0	2.0

Table 1. Percentages of total *p*-boronophenylalanine (BPA$^+$) cells, BPA$^+$/differentiation marker$^+$ cells and BPA$^+$/stem marker$^+$ cells among glioma stem-like cells (Stem) and differentiated cells (DC) from no. 1 and no. 2.

****

REFERENCES:

[1] N. Kondo *et al.* Radiat. Environ. Biophys. 55 (2016) 89–94.

[2] N. Kondo *et al.* , Cancers, 2020, 12, 3040; doi:10.3390/cancers12103040

CO7-10 Establishment of protocol for neutron capture therapy for head and neck cancer

I. Ota[1], H. Uemura[1], A. Nishimura[1], T. Kimura[2], S. Mikami[1], T. Yamanaka[1], M. Suzuki[3], Y. Sakurai[3], H. Tanaka[3], N. Kondo[3], T. Tamamoto[2], M. Hasegawa[2] and T. Kitahara[1]

[1]Department of Otolaryngology-Head & Neck Surgery,
[2]Department of Radiation Oncology, Nara Medical University
[3]Institute for Integrated Radiation and Nuclear Science, Kyoto University

INTRODUCTION: Neutron capture therapy (BNCT) for head and neck tumors has been clinically studied since 2001, with the BNCT research group at Kyoto University Reactor Laboratory, which is a co-investigator, highly effective, with high safety. It is being established. Since November 2012, we implemented the therapy as a joint research with Kyoto University Reactor Laboratory, with the consent of the patients in 4 cases of refractory recurrent head and neck cancer. As a result, the response rate was a very high 100%. The tumor reduction effect in recurrent cases after radical irradiation, which could not be achieved by conventional treatment methods, strongly suggests the possibility of expanding the indications for BNCT for refractory carcinomas as well as for head and neck cancer cases. Here, we will perform BNCT for refractory and recurrent head and neck tumors and examine their efficacy and optimal protocol.

EXPERIMENTS: We will treat BNCT for refractory and recurrent head and neck tumors that meet the following criteria and examine their efficacy and optimal protocol.

Inclusion Criteria

(1) The patient with local recurrence of head and neck cancer who cannot perform the standard therapy any more after radiotherapy.
(2) The patient with local recurrence of head and neck cancer by the imaging diagnosis, such as CT, MRI and PET.
(3) The patient with previous radiotherapy (total 40-75 Gy, 2Gy/fq) for the recurrent region.
(4) The patient with the period of more than one month since the previous treatment.
(5) The patient with recurrence lesion in the less than 6cm of depth from skin as GTV for BNCT.
(6) The Patients who have PS less than 2 and are expected to survive more than 6 months after BNCT.
(7) The patient with good condition of renal function: creatinine <1.2 mg/dl for male and
<1.0 mg/dl for female.
(8) The patient with the age between 20 and 80.
(9) Written informed consent with one own will.

Exclusion Criteria

(1) The patient with active multiple primary cancers; synchronous or metachronous (within 5 years) double cancers .
(2) The patient with metastatic lesion.
(3) The patients with severe complications.
(4)The patients with infection requiring systemic treatment.
(5) The patient with severe adverse event
(>Grade3, CTCAE v4.0) in the BNCT region.
(6) The patient with cardiac pacemaker.
(7) The patient judged to have difficulty in maintain posture during the protocol treatment.
(8) The patient with WBC; < 3000/mm3, PLT; < 100000/mm3
(9) The patient with recurrence lesion invasive to carotid artery and toskin.
(10) Patients with phenylketonuria.

RESULTS: We enrolled no patient and did not undertake BNCT during this period. However, the patient enrolled last year was followed up safely.

Patient #1: 46 y.o. female
Recurrence of cancer of the external ear
Histology: squamous cell carcinoma
Effect: SD
SAE: none; dermatitis, Grade 2

CONCLUSION:
We have accumulated the cases carefully to establish a safe and stable treatment of BNCT. Finally we will evaluate to the efficacy of BNCT for refractory and recurrent head and neck tumors.

CO7-11 Identification of host immunostimulatory effects induced by boron neutron capture therapy

Tsubasa Watanabe[1], Hiroki Tanaka[1], Takushi Takata[1], Yoshinori Sakurai[1], Minoru Suzuki [1]

[1]Institute of Institute for Integrated Radiation and Nuclear Science, Kyoto University

INTRODUCTION: Boron neutron capture therapy is a type of radiation therapy that utilizes the physical phenomenon of boron atoms (^{10}B) fissioning into alpha particles and lithium nuclei when they capture neutrons. The particles generated are heavy particle beams with a high cell-killing effect, and each particle has a short range of less than 10 μm (less than the diameter of a cell). Therefore, by selectively delivering boron atoms to tumor cells and then irradiating them with neutrons from outside the body, it is theoretically possible to selectively treat only tumor cells. Radiation has classically been thought to weaken the immunity of the irradiated organism, but this is only the case for the whole body or large areas of bone marrow irradiation. However, this is only the case for irradiation of the whole body or a large area of bone marrow. As technology has advanced, it has recently become clear that radiotherapy can have an anti-tumor immunostimulatory effect on the host, especially when the irradiation is focused on the tumor. In this research project, we investigated the effects of boron neutron capture therapy on host immune cells and evaluate whether boron neutron capture therapy has the same immune-stimulating effects that are known to occur with reference radiation such as X-rays/gamma-rays. In addition, we explored the possibility of combining boron neutron capture therapy and immunotherapy using a mouse model to provide a basis for combination therapy in actual clinical practice.

EXPERIMENTS: Mouse-derived malignant melanoma cell B16 and mouse-derived squamous cell carcinoma SCCVII were implanted subcutaneously in the lower leg of C57BL/6 and C3H mice, respectively. Tumors of a specific size were irradiated with BNCT or the same dose of reference radiation (γ-ray), and the effect of host immune response was evaluated.

RESULTS: When CD8 positive T cells in the mouse body are removed simultaneously with reference radiation using removal antibodies, a similar tumor volume reduction effect is usually observed up to about 7 days after irradiation, but after that, the anti-tumor effect of radiation is weakened and the tumor volume becomes significantly larger. Using model mice, the BNCT group and the CD8-positive T cell removal antibody simultaneously with BNCT showed a different course from the standard reference radiation. In the case of the reference radiation, the initial effect of the radiation was not only a direct anti-tumor effect but also an immune contribution, whereas the direct anti-tumor effect of BNCT was intense, suggesting that the initial effect was not significantly affected by the immune status of the host. On the other hand, the use of antibodies to remove CD8-positive T cells resulted in statistically significant tumor regrowth compared to the BNCT group after about 2-3 weeks, reflecting the importance of host immune function in regrowth after BNCT. Since the results obtained were unexpected, we next examined whether BNCT and immunotherapy (anti-PD-1 antibody) could be used to prevent tumor repopulation and recurrence, reflecting the results. When anti-PD-1 antibody was administered at the same time as BNCT, tumor regrowth was usually observed 3 weeks after treatment in this mouse model, but when anti-PD-1 antibody was used in combination with BNCT, regrowth was suppressed and the survival rate was improved. In addition, the immune function of the host is involved in repopulation and recurrence after BNCT, suggesting that combined immunotherapy may be effective in reducing the risk of recurrence after BNCT. The detailed mechanism remains to be elucidated, and as a future prospect, we would like to analyze the mechanism that inhibits recurrence using RNA-seq and flow cytometry.

REFERENCES:

[1] Tsubasa Watanabe, Elke Firat, Jutta Scholber, Simone Gaedicke, Corinne Heinrich, Ren Luo, Nicolas Ehrat, Gabriele Multhoff, Annette Schmitt-Graeff, Anca-Ligia Grosu, Amir Abdollahi, Jessica C Hassel, Dagmar von Bubnoff, Frank Meiss, Gabriele Niedermann. Deep abscopal response to radiotherapy and anti-PD-1 in an oligometastatic melanoma patient with unfavorable pretreatment immune signature. Cancer Immunology Immunotherapy 2020;69:1823-32.

[2] Hiroki Tanaka, Takushi Takata, Tsubasa Watanabe, Minoru Suzuki, Toshinori Mitsumoto, Shinji Kawabata, Shin-ichiro Masunaga, Yuko Kinashi, Yoshinori Sakurai, Akira Maruhashi, Koji Ono. Characteristic evaluation of the thermal neutron irradiation field using a 30MeV cyclotron accelerator for basic research on neutron capture therapy. Nuclear Inst. and Methods in Physics Research, A. 2020;983:164533.

[3] Satoshi Takeno, Hiroki Tanaka, Tsubasa Watanabe, Takashi Mizowaki, Minoru Suzuki. Quantitative autoradiography in boron neutron capture therapy considering the particle ranges in the samples. Phys Med. 2021;82:306-320.

CO7-12 Preliminary study of antitumor effectivity by Gd-neutron capture therapy using RGD binding Gd-DTPA-incorporated calcium phosphate nanoparticles to canine hemangiosarcoma model

M. Yanagawa [1], H Xuan [2,3], H. Yanagie[4,5,6], Y. Sakurai[5,6], K. Mouri[6], N. Dewi[6], H. Cabral[3], T. Nagasaki[7], Y. Sakurai[8], H. Tanaka[8], M. Suzuki[8], S. Masunaga[8], and H. Takahashi[2,3,4,5]

[1]Obihiro Univ of Agriculture and Veterinary Medicine, [2]Dept of Nuclear Engineering & Management, School of Engineering, Univ of Tokyo, [3]Dept of Bioengineering, School of Engineering, Univ of Tokyo, [4]Institute of Engineering Innovation, School of Engineering, Univ of Tokyo, [5]Cooperative Unit of Medicine & Engineering, Univ of Tokyo Hospital, [6]Niigata Univ of Pharmacy & Applied Life Sciences, [7]Osaka City University Graduate School of Engineering, [8]Kyoto Univ Institute for Integrated Radiation & Nuclear Science, JAPAN

INTRODUCTION: Hemangiosarcoma is a malignant tumor arising from vascular endothelial cells, and common tumor of the canine spleen [1]. Hemangiosarcoma of the spleen has early distant metastases and peritoneal dissemination and has a poor prognosis despite surgery and chemotherapy [2].

Gadolinium neutron capture therapy (Gd-NCT) is the unique radiation therapy that uses ^{157}Gd and has a large thermal neutron cross section (255,000 barns). The range of induced high LET Auger electrons is few micron, so increase of ^{157}Gd concentration in the cancer cells is important for increasing the therapeutic effect. We had reported that the gadolinium neutron capture reaction (GdNCR) showed the tumour growth suppression, and could be applied to the intensive cancer treatmens in near future [3,4,5].

Recently, Arg-Gly-Asp(RGD) sequence is very impressive in the targeting fields of pharmaceutical sciences, because, RGD sequence can bind to the Integrin receptor of cancer cell surface. So, it can be used for cancer targeting by endocytosis mechanism of RGD sequence [6].

In this work, we prepared the RGD motief binded Gd-DTPA/CaP nanoparticles for selective cancer targeting, and applied the GdNCR to the canine hemangiosarcoma model by intraveneous injection.

EXPERIMENTS: Canine hemangiosarcoma cell line (Ju-A1) was cultured in RPMI1640 supplemented with 10% FBS, L-glutamate, penicillin and streptomycin. 8×10^5 cells subcutaneously injected into the right hindlimb of nude mice.

RGD sequense binding nanomicelle and Gd-DTPA / CaP nanomicelle were injected tumor-bearing mice via the tail vein 24 hours prior to neutron irradiation.

In vivo evaluation was performed on Ju-A1 tumor-bearing mice irradiated for 60 minutes at nuclear reactor facility of Kyoto University Institute for Integrated Radiation & Nuclear Science with average neutron fluence of 3.0×10^{12} n/cm^2. Antitumor effect was evaluated on the basis of the change in tumor growth.

RESULTS:
Tumor growth was suppressed in the groups of RGD sequence binding Gd-DTPA/CaP nanomicelle and bare Gd-DTPA/CaP nanomicelle compared with the non-irradiated groups with the injection of same DDS.

The tumour volume was decreased after GdNCT. In this preliminary experiment, the tumour decresence by RGD sequence binding Gd-DTPA/CaP nanomicelle was superior than the group of bare Gd-DTPA/CaP nanomicelle.

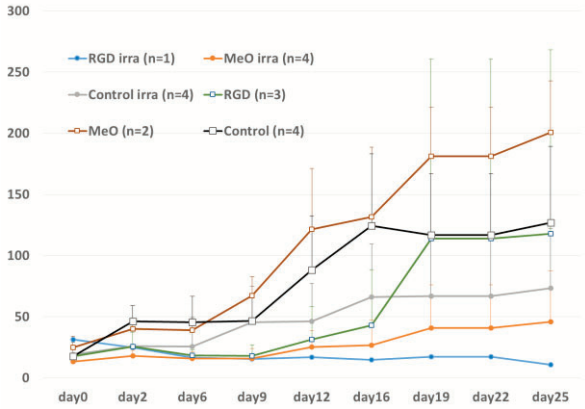

Figure 1. Tumor growth suppression in the group of RGD sequence binding Gd-DTPA/CaP nanomicelle and bare Gd-DTPA/CaP nanomicelle on canine hemangiosarcoma model

In the next experiments, we will check the expression of integrin receptors on the surface of canine hemangiosarcoma cells on liver metastasis, and also hope to check the uptake of ^{157}Gd atoms in the cancer cells by endocytosis. We hope to apply RGD Gd-DTPA/CaP nanomicelle to liver metastatic tumors by intra-arterial injection for GdNCT, and evaluate the mechanism of cytotoxicity on GdNCT, for examples, apoptosis, autophagy, etc.

We hope to apply this delivery systems to the clinical studies of GdNCT for canine patients in the future.

Thease preliminary results indicate that RGD sequence binding Gd-DTPA /CaP nanomicelle has the possibility as novel active targeting ^{157}Gd carrier to canine hemangiosarcoma for GdNCT.

REFERENCES:

[1] JH Kim *et al,*.Vet Sci. (2015) **2**(4):388-405.
[2] DM Vail *et al,*.Withrow & MacEwen's small animal Clinical Oncology 6th (Elsevier, 2020).
[3] Dewi N et al., Biomed & Pharmacother (2013) **67**:451-7.
[4] Dewi N et al., J Can.Res.Clin.Oncol. (2016) **142**(4):767-75.
[5] Mi P, et al.: J Cont. Release (2014) **174**:63-71.
[6] Miyako et al., J Cont. Release (2017) **261**:275-2

CO7-13 **Screening of boron compounds for BNCT on 2020 International collaboration studies**

M. Takagaki[1], Kazuko Uno[2], and M. Suzuki[3]

[1]*RCNP, Osaka University*
[2]*Louis Pasteur Center for Medical Research*
[3]*IIRNS, Kyoto University*

We have been investigating boron/gadolinium compounds for screening them as a candidate for B/Gd-NCT and also to promote boron chemistry for educational purpose in worldwide.
BNCT effect for malignant brain tumors has been still controversial, and investigation for further effective boron/gadolinium compounds (B-com) has been expected national wide for accelerator based BNCT of Cancer. To promote this investigation, we will academically provide quick bioassay of new boron compounds for BNCT with easy free access. The project is supported by motivation and enthusiasm for BNCT of Kyoto University researchers for neutron irradiation experiments as well as Pasteur researchers. We hope our project might improve BNCT research for cancer patients. Our areas of research concerns are not only for BNCT, but also boron science. This project is supported by a joint use research program of Institute for Integrated Radiation and Nuclear Science, Kyoto University.

In the joint use experiment in 2020, screening experiments of 6 samples of boron and gadolinium compounds in 3 countries were investigated for B/Gd-NCT. The compound concept for brain tumors and experimental methods are described at the following URL:

Screening Protocol:
Samples are first look screening of experiments 1, 2 and 3, and they are investigated more along 4 and 5.
1. Solubility in a physiological condition
2. Cell toxicity
3. Cellular BNCT (in-vitro BNCT)
4. Bio-distribution study (neutron induced boron autoradiography)
5. Animal BNCT (in-vivo BNCT)
6. Pre-clinical study

Concept:
https://1458ab30-7501-42df-8c2e-ff59d20cecb7.filesusr.com/ugd/ddd07a_6d26937e29ee4177bfa37ea6d33de022.pdf

Method:
https://1458ab30-7501-42df-8c2e-ff59d20cecb7.filesusr.com/ugd/ddd07a_cbe194d92fd14397a5db1690d68a185c.pdf

Samples and Results:
The samples were a carborane-containing small protein docking to epidermal growth factor receptor (EGFR), gadolinium Nano inclusion bodies, and a carborane-containing glioma cells infiltration inhibitor. In each case, a higher BNCT effect than the existing BPA was confirmed, and it is planned to continue to be investigated for this fiscal year's experimental plan. The experimental results are being prepared for quick submissions and publications.

CO7-14 The evaluation of boron neutron capture therapy (BNCT) to the novel mouse model of pelvic recurrence of colorectal cancer

J. Arima[1], M. Yamamoto[1], K. Taniguchi[1,2], H. Hamamoto[1], Y. Inomata[1], A. Miyamoto[1], H. Kashiwagi[3], S. Kawabata[3], S. Miyatake[4], M. Suzuki[5], K. Tanaka[1], J. Okuda[1] and K. Uchiyama[1]

[1] *Department of General and Gastroenterological Surgery, Osaka Medical College, Osaka, Japan*
[2] *Translational Research Program, Osaka Medical College, Osaka, Japan*
[3] *Department of Neurosurgery, Osaka Medical College, Osaka, Japan*
[4] *Section for Advanced Medical Development, Cancer Center, Osaka Medical College, Osaka, Japan*
[5] *Department of Particle Radiation Oncology, Research Reactor Institute, Kyoto University, Kumatori, Osaka, Japan.*

INTRODUCTION: Colorectal cancer is the most common cancer worldwide. Surgical resection is the mainstay treatment of colorectal cancer. However, local recurrence still occurs in 5% to 13% of patients after curative resection. When the tumor is unresectable, it needs alternative therapeutic strategy.
In this study, we investigated the effectiveness of boron neutron capture therapy to pelvic colorectal cancer using the mouse model of pelvic recurrence of colorectal cancer.
****
****

EXPERIMENTS: We used Boronophenylalanine (BPA) as a boron compound. Colon26-Luc cells were concentrated to 1.0×10^6/150μL in 0.15ml of PBS and injected into the pelvic cavity of each mouse. Animals were divided into three groups (8 animals per group); BNCT with BPA (i.p.) without tumor, only neutron irradiation, BNCT with BPA (i.p.).
****
****

RESULTS: We performed the histopathological assessments of tumor, rectum and vagina of three groups. In the both groups of only neutron irradiation and BNCT with BPA, tumors infiltrated to rectum and vagina. In the control group of BNCT with BPA (i.p.) without tumor, all mice did not have symptoms such as diarrhea and survived until the endpoint. It suggested that BNCT induced no side effect. (Fig.1)
****
****

Figure.1

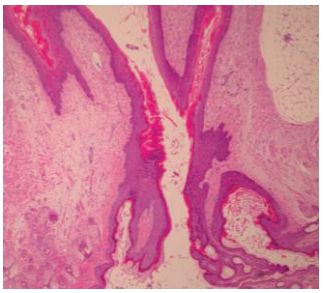

vagina

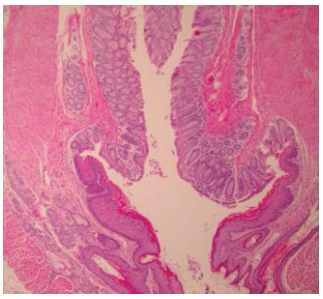

rectum

In the histopathological assessments of the control group, there was not structural change.

Ongoing study: We changed BALB/c mice to nude mice at the present because we would like to use a human colorectal cancer. We implanted DLD-1 clone#1-LUC to the pelvis of nude mice and observed the growth of tumors. The average overall survival was about a month. We are planning to investigate the usefulness of BNCT comparing with control. Moreover, we developed BSH-transferrin-PEG-liposome as a novel boron drug. We are planning to use this boron drug in our mouse model.
We will continue this study and the results will be published in the future.

REFERENCES:

[1] K. Takahara *et al.*, PLoS One., **10**. (2015) e0136981. doi: 10.1371/journal.pone.0136981.
[2] M. Yamamoto *et al.*, Sci Rep., **9** (2019) 19630. doi: 10.1038/s41598-019-56152-0.

CO7-15 Self-assembling A6K peptide nanotubes for BSH delivery

Hiroyuki Michiue [1]*, Mizuki Kitamatsu[2], Asami Fukunaga[3], Nobushige Tsuboi[4], Atsushi Fujimura[3], Hiroaki Matsushita[3], Kazuyo Igawa [1], Tomonari Kasai [1], Natsuko Kondo[5], Hideki Matsui [1, 3], Shuichi Furuya [1]

[1]*Neutron Therapy Research Center, Okayama University,*
[2]*Department of Applied Chemistry, Kindai University,*
[3]*Department of Physiology, Okayama University,*
[4]*Department of Neurological Surgery, Okayama University*
[5]*Institute for Integrated Radiation and Nuclear Science, Kyoto University,*

INTRODUCTION:
Drug delivery systems (DDS) for boron agents, including polymeric macromolecule DDS such as liposomes and emulsions, which combine BSH and several boron compounds, are interesting and adaptable tools in preclinical BNCT experiments. In this work, we focused on a peptide DDS using A6K peptide. A6K comprises six alanine residues and one lysine (AAAAAAK) and has been reported as an siRNA (small interfering RNA) delivery tool. In this work we aimed to demonstrate a new boron delivery system based on A6K peptide and BSH, and open up a novel direction for boron agents in the next generation of BNCT.

EXPERIMENTS: 24 h before neutron irradiation, the U87 delta EGFR cell line was treated with 200 µM A6K/2 mM BSH or 100 µM A6K/1 mM BSH. Just before neutron irradiation, the cell samples were transferred to collecting tubes and subjected to 1 MW neutron irradiation (thermal neutron flux 1.4×109 neutron/cm2/s) for 5 min, 15 min or 30 min (Fig 1-A, C, D). In addition, U87 delta EGFR were treated with 2 mM BSH; 200 µM A6K/2 mM BSH; or 100 µM A6K/1 mM BSH (final concentrations) and subjected to 1 MW neutron irradiation at the KURNS facility for 15 min and 30 min. After irradiation, all glioma cells were re-cultured in 96 well plates (9×103 cells/well) for 24 h and 48 h, and cell proliferation was measured with Cell Proliferation Reagent WST-1 using a microplate reader (Fig.1-B). A colony formation assay was carried out after 2 weeks of culture with U87 delta EGFR in 60 mm culture dishes (n=4) and all culture cells were stained with 0.5% Crystal Violet (CV) in 20% methanol. The colonies of CV stained samples were counted automatically with an aCOLyte 3 automatic colony counter machine, and all data were statistically analyzed.

RESULTS: The U87 delta EGFR cell line was treated with 100 µM A6K/1 mM BSH or 200 µM A6K/2 mM BSH 24 h before neutron irradiation. Following 1 MW neutron irradiation, we carried out a cell proliferation assay (WST-1 assay) over 48 h and colony formation assay over 14 days (Fig. 1-A, C, D). Figure 1-B shows the WST-1 assay results for U87 delta EGFR after 24 h and 48 h, following 1 MW neutron irradiation at KURNS

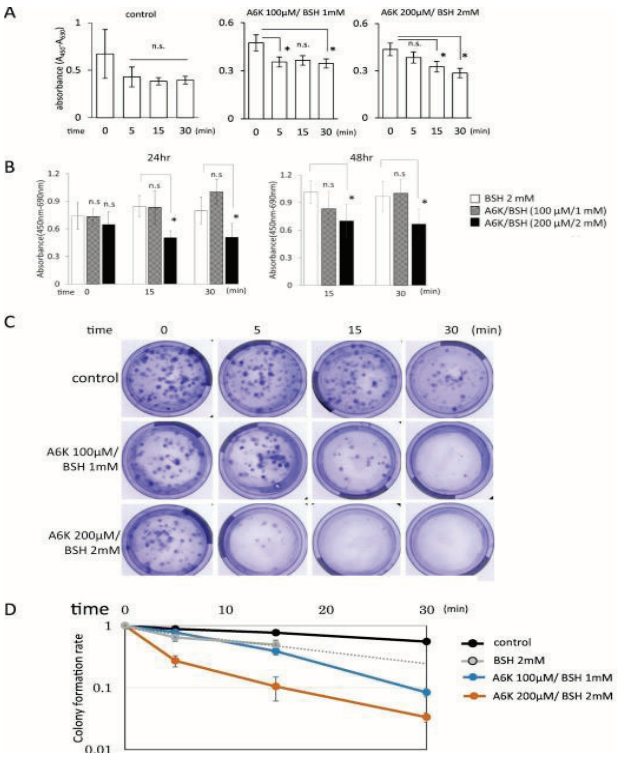

Fig. 1. **The boron neutron reaction *in vitro* with low or high dose A6K/BSH complex in U87 delta EGFR cells analyzed at KURNS: (A)(B) Cell proliferation by WST-1 assay after 24 and 48 h incubation for different neutron irradiation times (C)(D) U87 delta EGFR cell colony formation assay with CV staining after 14 days for different neutron irradiation times (black line: control group, gray line: 2 mM BSH, blue line: low dose 100 µM A6K/1 mM BSH, and orange line high dose 200 µM A6K/ 2 mM BSH, in each case n=4).**

for 15 min, or 30 min. No significant differences were observed for the control group for any radiation time (Fig. 1-A). In contrast, the 100 µM A6K/1 mM BSH and 200 µM A6K/2 mM BSH groups showed inhibition of cell proliferation dependent on neutron radiation dose and irradiation time (Fig.1-A). In addition, the colony formation assay carried out 14 days after the boron neutron reaction showed late and slow cell reaction (Fig. 1-C, D). The colony formation assay for the A6K/BSH complex groups showed survival ratios of 1, 0.78, 0.39, and 0.08 and 1, 0.27, 0.10, and 0.03, for 0, 5, 15, and 30 min neutron irradiation periods, respectively (Figure 1-C, D). The group treated with BSH only showed ratios of 1, 0.65, and 0.5 for 0, 5, and 15 min neutron irradiation periods. In the colony formation assay, the suppressive effect was clear for both A6K/BSH complex groups with thermal neutron irradiation dose escalation (Figure 1-D). Compared with the 2 mM BSH treated group, the A6K/BSH complex groups showed inhibition of cell proliferation following 15 min and 30 min neutron irradiation in both 24 h and 48 h WST-1 assays (Figure 1-B).

REFERENCES:

[1] H. Michiue *et al.*, J Control Release.., **330** (2021) 788-796.

CO7-16 Experiment on BNCR Effect of a Novel BPA Formulation using Ionic Liquid by Thermal Neutron Irradiation

M. Shirakawa[1,2], Y. Sato[1], N. Kamegawa[3], R. Takeuchi[3], K. Nakai[2], A. Zaboronok[2], F. Yoshida[2], T. Tsurubuchi[2], T. Takata[4], M. Suzuki[4], A. Matsumura[2] and H. Hori[3,5]

[1]Department of Pharmaceutical Sciences, University of Fukuyama
[2]Department of Neurosurgery, Faculty of Medicine, University of Tsukuba
[3] Morita Pharmaceutical Ind., Ltd.
[4] Institute for Integrated Radiation and Nuclear Science, Kyoto University
[5] Niigata University of Pharmacy and Applied Life Sciences

INTRODUCTION: Owing to its outstanding anti-tumor effect by thermal neutron irradiation, *p*-boronophenylalanine (BPA) have been used in clinical on BNCT. However, BPA formulation dissolved in a fructose complex is known that a large dose is required for clinical use due to its poor solubility. In other words, a fructose-based BPA formulation imposes a large physical burden on the patient as well as management and transportation costs.

Therefore, we have studied the use of Ionic Liquids (ILs) as a novel solvent for BPA. ILs are composed of organic cations and anions, and have been attracting more attention in pharmaceutical fields because of their high solubility and stability [1].

We have already studied various combinations of compounds for cations and anions, some of which have resulted in high solubility exceeding that of fructose complex [2]. This paper presents the experimental results obtained on anti-tumor effect *in vivo* using BPA dissolved in ILs (BPA-ILs).

EXPERIMENTS:

1. Synthesis of ILs and Preparation of BPA-ILs

ILs using experiment of this paper were synthesized in meglumine as the cations and L-serine as the anion. Equimolar meglumine and L-serine solutions were stirred at room temperature for 24 hours, after that the water content contained within ILs was removed to 50 wt% by rotary evaporator at 100℃.

BPA-ILs was prepared by dissolving BPA in its ILs and mixing it with buffer solution (PBS), Tween 80, ethanol and citric acid.

2. Anti-tumor effect using BPA-ILs by BNCT

The tumor-bearing mice were prepared by grafting 2 x 10^6 of mouse colon carcinoma cells (CT26) to the right thigh of female BALB/cA mice (4 weeks old, weighing 16-20 g) to have a tumor diameter of 6-8 mm. These mice were purchased at the age of 3 weeks from CLEA Japan Inc. (Tokyo, Japan) and tamed in Institute for Integrated Radiation and Nuclear Science, Kyoto University.

About 10 days after, 200μL of BPA-ILs were administrated by intraperitoneal injection before irradiation. The dosage was 24mg^{10}B/kg and similarly, BPA fructose complex (BPA-Fru) was administered. At the interval was 2hours, the irradiation was performed with thermal neutrons with a flux of 2.0-5.6 x 10^9 neutrons/cm^2/s over 12 min. The tumor size was measured over time after the irradiation until Day 29 and calculated using the general formula [3].

Also, a significant difference in tumor size on the last measurement day of each group was calculated by independent t-test. The value of the significant difference and the number of asterisks are as follows.
(* : p<0.05, ** : p<0.01, *** : p<0.005, **** : p<0.001, ns: No significant difference)

RESULTS: As shown in Fig. 1 and Fig. 2, BPA-ILs significantly suppressed the tumor growth as compared to other control groups without remarkable side effect (e.g. weight loss) similarly to BPA-Fru.

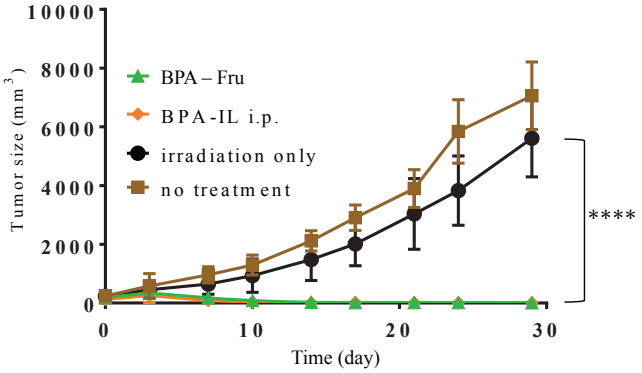

Fig.1) Anti-tumor effect of BNCT by BPA-ILs.
(BPA-ILs vs. BPA-Fru : ns, vs. irradiation only : ****, vs. no treatment : ****)

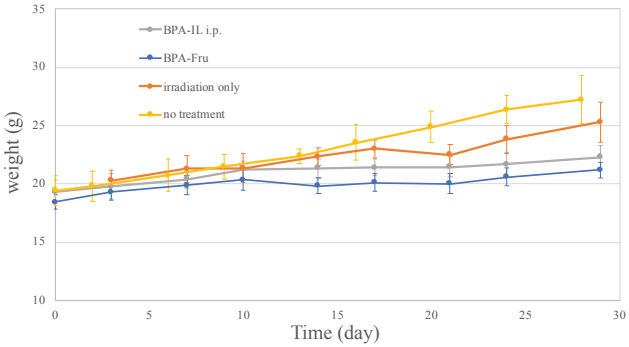

Fig.2) Body weight of mice after irradiation with the injection of BPA-ILs

REFERENCES:

[1] Ksenia S., et al., Chem. Rev., 117, 7132-7189, (2017).
[2] M. Shirakawa, et al., Patent applications 2020-067196 (2020).
[3] M. Shirakawa, et. al., KURNS PROGRESS REPORT 2018, 55, (2019).

CO7-17 Application of Intra-Tumoral Injection of Gadolinium-Polyplex for Gadolinium-Neutron Capture Therapy to Pancreatic Cancer Model *in vivo*

Hironobu Yanagie[1,2,3], Yoshiteru Yanagie[4], Xuan Hou[5], Masashi Yanagawa[6], Tatsuya Ishikawa[3], Yuriko Sakurai[1,2,3], Kikue Mouri[3], Novriana Dewi[3], Yasuyuki Morishita[7], Changyuan Qin[5], Takehisa Matsukawa[8], Ayano Kubota[8], Minoru Suzuki[9], Shin-ichiro Masunaga[9], Yoshinori Sakurai[9], Hiroki Tanaka[9], Takeshi Nagasaki[10], Kazuhito Yokoyama[8], Takefumi Hirata[11], Masayuki Nashimoto[3], Jun Nakajima[2,12], Minoru Ono[2,13], Horacio Cabral[5], Takumichi Sugihara[3], and Hiroyuki Takahashi[1,2,5]

[1]Institute of Engineering Innovation, School of Engineering, Univ of Tokyo, [2]Cooperative Unit of Medicine & Engineering, Univ of Tokyo Hospital, [3]Niigata Univ of Pharmacy & Applied Life Sciences, [4]Faculty of Medicine, Teikyo University, [5]Dept of Bioengineering, School of Engineering, Univ of Tokyo, [6]Obihiro Univ of Agriculture and Veterinary Medicine, [7]Dept of Human & Molecular Pathology, Graduate School of Medicine, The University of Tokyo, [8]Department of Hygiene, Faculty of Medicine, Juntendo University, [9]Kyoto Univ Institute for Integrated Radiation & Nuclear Science, [10]Osaka City University Graduate School of Engineering, [11]Geochemical Research Center, School of Science, The University of Tokyo, [12]Dept. of Pulmonary Surgery, The University of Tokyo Hospital, [13]Dept. of Cardiac Surgery, The University of Tokyo Hospital, JAPAN

INTRODUCTION:

Gadolinium-neutron capture therapy(GdNCT) is a particle beam therapy using gadolinium and thermal neutron [1, 2, 3]. Gadolinium reacts thermal neutron and offers cytotoxic effect by 1μm-range high LET Auger electron, and long-range gamma rays. Therefore, for effective GdNCT, it is necessary to accumulate Gadolinium atoms into the tumor tissues selectively. Compared with the conventional boron NCT, because Gd compound can be used as MRI contrast agent, it allowed for MRI-guided GdNCT. In this study, we evaluated gadolinium / hyaluronic acid / protamine-mixed with cationic liposome (^{157}Gd-plex) as neutron capture therapy agent by in vivo experiment on AsPC-1 human pancreatic tumor-bearing mice.

EXPERIMENTS:

We prepared nanoparticles mixed with 1.5mL of Gadolinium compound "Gadovist" (MW: 604.71), 0.2mL of a solution of 10mg/mL-hyaluronic acid sodium, and 0.1mL of 20mg/mL of protamine incubating at room temperature for 30min. Then, these mixing solutions were poured into Coatsome EL-C. Human pancreatic cancer AsPC-1 cell was used for the *in vivo* anti-tumor effect evaluation. We prepared AsPC-1($5x10^5$) model by transplanting to right lower leg. Twelve hours after intra-tumoral injection of 0.2mL of ^{157}Gd -plex, we performed thermal neutron irradiation at Institute for Integrated Radiation and Nuclear Science, Kyoto University (average neutron fluence of 2.0×10^{12} n/cm^2). The change in tumor growth and survival rate of the mice reflected the anti-tumor effect of ^{157}Gd-plex. While measuring the size of tumor, the weight change was also recorded for evaluation of the toxicity of these samples.

RESULTS:

The ^{157}Gd concentration in the ^{157}Gd -plex was 13700ppm by measured ICP-AES, and the diameter was 200nm. Thirty percent of tumor growth suppression was achieved in the ^{157}Gd -plex injected NCT group compared with non-irradiated group. The tumor growth suppression of the ^{157}Gd -plex injected group was superior than the only Gdovist injected group by NCT.

We attempted enhancement of retention of gadolinium atoms by mixing Gd-polyplex. The experimental results showed that the tumor growth suppression of ^{157}Gd -plex-injected irradiated group was revealed superiority compared to the group with Gd solution injection, or non-treated control group after NCT, and no significant weight loss were observed after treatment suggesting low systemic toxicity of this system. We would like to consider the best irradiation time and dose of administration. The ^{157}Gd -plex will become one of the candidates for Gd delivery system on NCT. Moreover, the body weight of the mice did not decrease after the treatments, which indicate the safety of ^{157}Gd-plex and the GdNCT.

Table1. Tumor growth suppression of subcutaneous AsPC-1 model by intra-tumoral injection of ^{157}Gd-plex with thermal neutron irradiation *in vivo*

	Tumor growth rate		
	Day6	Day10	Day13
GdNCT			
^{157}Gd sol.	**1.55±0.38**	**2.29±0.67**	**2.50±0.42**
^{157}Gd-plex	**1.58±0.71**	**1.82±0.81**	**2.14±0.93**
Non-treat.	**1.62±0.06**	**2.30±0.27**	**2.64±0.07**
Non NCT			
^{157}Gd sol.	**1.79±0.34**	**3.92±1.33**	**4.64±1.64**
^{157}Gd-plex	**1.41±0.17**	**2.26±0.18**	**2.62±0.03**
Non-treat.	**1.62**	**2.02**	**3.21**

Tumor growth suppression in ^{157}Gd-plex group by NCT was 30 % superior compared with non-irradiated group. Tumor growth suppression in ^{157}Gd-plex injected group was 25 % superior compared with ^{157}Gd solution injected group in NCT groups.

REFERENCES:

[1] Dewi N et al., Biomed & Pharmacother (2013) **67**:451-7.

[2] Dewi N et al., J Can.Res.Clin.Oncol. (2016) **142**(4):767-75.

[3] Mi P, et al.: J Cont. Release (2014) **174**:63-71.

CO7-18 Functionalization of Boron-Containing Nanoparticle and its Application to Boron Neutron Capture Therapy

Yuquan Wang[1], Heon Gyu Kang[1], Masahiro Nishikawa[1], Minoru Suzuki[2] and Komatsu Naoki[1]

[1] *Graduate School of Human and Environmental Studies, Kyoto University*
[2] *Institute for Integrated Radiation and Nuclear Science, Kyoto University*

INTRODUCTION: Boron neutron capture therapy (BNCT) is one of the promising cancer therapy with minimized side effect, because ^{10}B atoms located in the cancer tissue generate alpha particles locally upon neutron irradiation. Herein, we will report that boron-containing nanoparticle (B-NP) is functionalized with polyglycerol (B-NP-PG) and the resulting B-NP-PG was employed for the pharmacokinetic experiments to make clear the biodistribution of B-NP-PG.

EXPERIMENTS: B-NP was functionalized with PG according to the method previously reported by us [1-3]. The resulting B-NP-PG was fully characterized by nuclear magnetic resonance (NMR) spectroscopy, Fourier transfer infrared (FTIR) spectroscopy and thermogravimetric analysis (TGA).

PBS dispersion (200 μL) of B-NP-PG was intravenously injected to the BALB/c tumor-bearing mice from the tail vein. After the mice were euthanized, the ^{10}B contents were assessed in blood, tumor and organs (liver, spleen and kidney) by the prompt γ-ray microanalysis system.

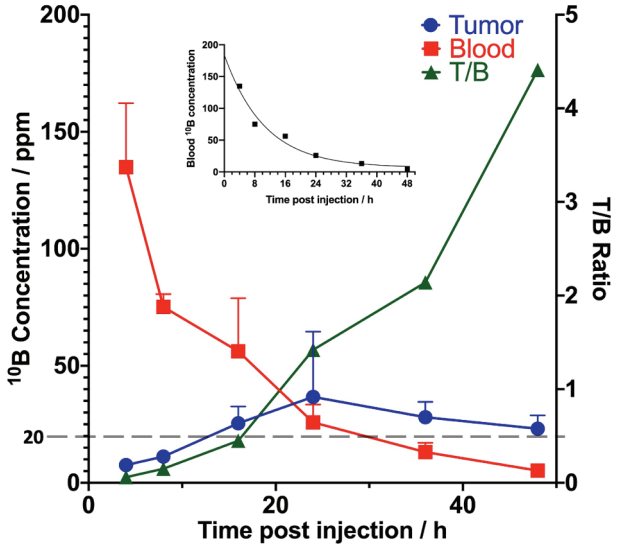

Figure 1. ^{10}B concentrations in tumor (T) and blood (B), and the T/B ratio. Data are presented as mean ± SD. Half-life (7.3 h) is calculated by one phase decay fitting of blood ^{10}B concentration shown in the inset.

RESULTS: B-NP-PG is dispersed in a phosphate buffer saline (PBS) at very high concentration and the resulting dispersion is very stable for more than one month.

While the enough ^{10}B concentration level for BNCT is kept in tumor for 30 h from 18 h to 48 h, the ^{10}B concentration in blood decreases gradually with the half-life of 7.3 h as shown in Figure 1. Accordingly, the T/B ratio increases with time and reaches 4.4 at 48 h which fulfills the requirement 3) (T/B ratio ≥ 3). After evaluation of these pharmacokinetic data based on the requirements, we decided the timing of neutron irradiation to be at 24 and 48 h after B-NP-PG administration exhibiting the highest ^{10}B tumor concentration (36.7 ppm) and T/B ratio (4.4), respectively [3].

REFERENCES:

[1] L. Zhao, T. Takimoto, M. Ito, N. Kitagawa, T. Kimura, and N. Komatsu,* *Angew. Chem. Int. Ed.*, *50*, 1388 (2011).

[2] T. Kobayashi, and K. Kanda, *Nucl. Instrum. Methods*, *204*, 525 (1983).

[3] Y. Wang, H. G. Kang, Y. Zou, Y. Ishikawa, M. Suzuki, and N. Komatsu, submitted.

CO7-19 Basic research to expand the application of BNCT to companion animals.

Y. Wada[1,2] and M. Suzuki[2].

[1] Veterinary Medical Center, Osaka Prefecture University
[2]*Particle Radiation Oncology Research Center, Institute for Integrated Radiation and Nuclear Science, Kyoto University*

Introduction

In veterinary medicine, radiation therapy is often used to treat head and neck tumors in recent years. However, in most cases, re-growth is observed. Therefore, it is desirable to expand the indications for BNCT in the veterinary field. Squamous cell carcinoma of the canine oral cavity is one of the diseases that can be treated with radiation therapy. Squamous cell carcinoma in the oral cavity has a different behavior between tonsillar and non-tonsillar origin.

Tonsillar squamous cell carcinoma (TSCC) has been demonstrated as not only locally invasive, with extension into surrounding tissues commonly seen at the time of diagnosis。Although surgery, chemotherapy and radiotherapy seem to increase the median survival time of dogs diagnosed with tonsillar squamous cell carcinoma, there is no highly effective treatment for canine TSCC. Non-tonsillar oral squamous cell carcinoma (NTSCC) shows good results when combined with surgery and radiotherapy, but there are many cases where surgery cannot be performed and only radiotherapy can be performed. However, in many cases with radiotherapy alone results in recurrent tumor. The purpose of this study is to investigate whether canine TSCC and NTSCC are eligible for BNCT.

Experiments

TSCC (TSCCLN-5) cell line and NTSCC (oSCC-4) was used for this experiment. First, a chlorogenic assay was performed to confirm the radiation response to X-rays in vitro. In addition, the cells were incubated under 50 ppm BPA for 2 hours and then irradiated with neutrons for clonogenic assay to check the response of the cells to BNCT.

Result

As shown in Fig. 1, the survival rate was significantly lower in oSCC at 2, 4, 8, and 12 Gy of X-ray irradiation**.** As shown in Fig. 2, BNCT-induced cell death was higher in oSCC than in TSCCLN.

In the future, we plan to investigate the uptake of BPA into cells and the expression of LAT-1, and to study the response in vivo.

Fig.1

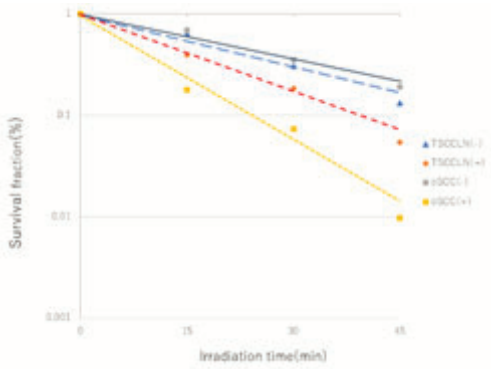

Fig. 2

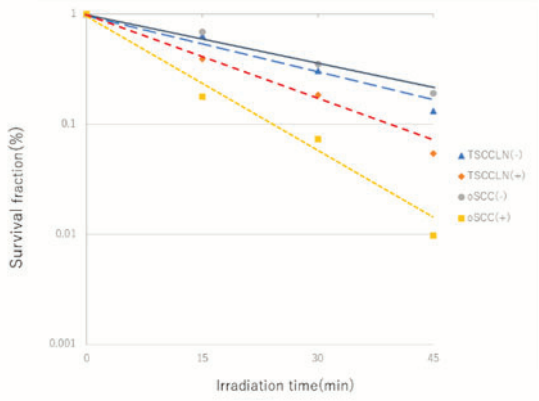

CO7-20 Development of real-time boron-concentration estimation system for whole-organ-irradiation BNCT

Y. Sakurai, H. Matsunaga[1], T. Takata, H. Tanaka and M. Suzuki

Institute for Integrated Radiation and Nuclear Science, Kyoto University
[1]Graduate School of Engineering, Kyoto University

INTRODUCTION: Whole organ irradiation in radiotherapy is effective on multiple tumors and minimal residual tumors, such as whole brain irradiation for brain metastasis, whole conserved-breast irradiation in conservative therapy for breast tumor, etc.. However, it cannot be realized for liver and lung tumors. It is because the tolerant dose of these organs is 20 to 40 Gy, which is smaller than the tumor control dose of 50 to 80 Gy. In BNCT, the ranges of the heavy charged particles due to the $^{10}B(n,\alpha\gamma)^{7}Li$ reaction in the boron compound, which selectively accumulates in tumor cells, are too short to reach the adjacent normal cells. Therefore, BNCTs with the whole organ irradiation for liver and lung tumors can be realized as radiotherapy.

In BNCT clinical studies for liver and lung tumors at KUR, the equivalent doses for normal liver and/or lung have been estimated on the basis of boron concentration in blood, which is measurable by prompt gamma-ray analysis. But actually, the variation for the boron concentration in normal liver and/or lung is assumed to be larger among the patients with basal disease, such as cirrhosis, pulmonary fibrosis, pulmonary emphysema, etc..

The purpose of this research is the development of the real-time boron-concentration estimation system in liver and/or lung during BNCT, in order to improve the dose estimation accuracy for BNCTs with the whole-liver and/or whole-lung irradiation. In this system, the technique of prompt gamma-ray telescope is applied. A gamma-ray telescope system has been in use for liver tumor BNCT at Heavy Water Neutron Irradiation Facility of KUR (KUR-HWNIF) from 2005 [1]. The collimation system of this telescope was improved in 2017 [2].

In 2020, verification experiment for the discrimination-ability between tumor and normal parts using this telescope system were performed.

MATERIALS AND METHODS: A liquid rectangular phantom of 20 cm in width, 20 cm in length and 40 cm in depth was used in the experiment. An acrylic hollow sphere of 5 cm in outer diameter, which was filled with boric acid of 193 ppm for B-10 concentration, was placed as a tumor part in the phantom. The phantom liquid was pure water or boric-acid water of 23 ppm for B-10 concentration. The epi-thermal neutron irradiation was performed in the irradiation field of 12 cm in diameter. The initial position of the tumor-sphere center was settled to be the center for the telescope-view-field on the beam axis, and it was moved from 0 to 6 cm in the right direction for the view from the beam-aperture side.

The positions of two telescope collimators were fixed to be the lowest. At these positions, the effective telescope-view-field on the beam axis was within 3 cm in width in the right direction for the view from the beam-aperture side. The prompt gamma rays due to the neutron reactions with B-10 and hydrogen (H-1) from the tumor part and its surroundings during the epi-thermal neutron irradiation were counted.

RESULTS AND DISCUSSION: Figure 1 shows the relationship between the position of the tumor-sphere center and the count ratio for B-10 gamma rays to H-1 gamma rays (B/H count ratio). It was confirmed that the B/H count ratio was larger as the position of the tumor-sphere center was closer to the beam axis, namely as it was closer to the center of the effective telescope-view-field. It was also confirmed that the B/H count ratio was larger for the boron-acid water phantom than for the pure water phantom. It is because that the B-10 gamma rays from the boric-acid water of 23 ppm for B-10 concentration in the telescope view-field additionally contribute to the B-10 gamma-ray count.

CONCLUSION: The B-10 concentration ratio for the tumor sphere to the boron-acid water phantom was 8.4 in this experiment. For such a level of the concentration ratio, the discrimination between tumor and normal parts can be expected by comparing the count ratio between the cases with and without the tumor part in the telescope view-field. In the actual BNCT clinical study, the B-10 concentration of the normal part is 10 to 25 ppm, and that of the tumor part is more than three times larger. In future, the more precise estimation will be performed for the B-10 concentration, size and position of the tumor sphere, and for the position of two telescope collimators. Moreover, the effective range for the discrimination between tumor and normal parts will be clarified.

ACKNOWLEDGEMENTS: This study was supported by The Kyoto University Research Fund (Core Stage Back-up, in 2017).

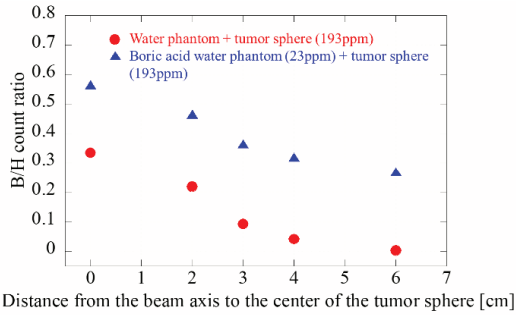

Fig. 1. Relationship between the center position of the tumor sphere and the B/H count ratio.

REFERENCES:

[1] Y. Sakurai *et al.*, Appl. Radiat. Isot. **61** (2004) 829-833.

[2] Y. Sakurai *et al.*, Appl. Radiat. Isot. **165** (2020) 109256.

CO7-21 Development of ^{10}Boron-loaded silica nanoparticles for BNCT application

F. Tamanoi[1], K. Matsumoto[1] and M. Suzuki[2]

[1] *Institute for Advanced Study*
Institute for Integrated Cell-Materials Sciences, Kyoto University
[2]*Institute for Integrated Radiation and Nuclear Science, Kyoto University*

INTRODUCTION: Boron neutron capture therapy (BNCT) was proposed as novel type of radiation therapy in 1936 and has been investigated in a variety clinical studies against brain cancer, head and neck tumor or other type of cancer. Boron phenylalanine (BPA) is a useful boron compound which advanced BNCT therapy yielding promising results. However, new types of boron reagents with increased tumor accumulation and less toxicity are being sought by a number of groups. We have developed biodegradable periodic mesoporous organosilica (BPMO) based reagents which have a large surface area where BPA can be attached for BNCT application.

To investigate the potential of BPA-loaded BPMO (BPA-BPMO) for BNCT, we used chicken chorioallantoic membrane model (CAM model) which is generated by transplanting human cancers onto the CAM membrane. This assay is versatile and convenient. After intravenous injection of BPA-BPMO to the blood stream, chicken eggs were irradiated with neutron beams to evaluate the tumor growth inhibition effect. Dramatic inhibition of tumor growth was observed.

EXPERIMENTS: BPMO was synthesized by sol-gel synthesis of two precursors, bis[3-(triethoxysilyl) propyl] tetrasulfide and 1, 2-bis(triethoxysilyl) ethane. This resulted in the incorporation of tetrasulfide bonds into the framework of the nanoparticles. BPMO was then processed to modify with GOPTS (3-glycidyloxypropyl trimethoxysilane) that contain epoxy groups. After converting epoxy groups to diols, BPA was mixed with diol-BPMO to graft BPA using a method to chelate boron with diol groups.

To investigate how BPA-BPMO behaves in biological systems, we evaluated cellular uptake of BPA-BPMO to cancer cells. Various types of cancer cells such as FaDu human head and neck cancer, OVCAR8 human ovarian cancer and A549 human lung cancer, were used. They were incubated with BPA-BPMO for 24 h at 37℃ humidified CO_2. Cellular uptake of BPA-BPMO was observed by confocal microscopy. We then used the CAM model to gain insight into tumor accumulation of BPA-BPMO. 2.0×10^6 of OVCAR8 cells were transplanted onto CAM of fertilized chicken egg to form tumor. 0.2 mg of BPA-BPMO was intravenously injected into the chicken egg, and tumor accumulation of BPA-BPMO was examined by red fluorescence of Rhodamine B-labeled BPMO by stereomicroscopy and confocal microscopy.

We finally tested whether the growth of the CAM tumor can be inhibited the neutron exposure. After injection of BPA-BPMO to chicken eggs that have OVCAR8 tumor on CAM, the eggs were placed at the center of the emerging neutron beam. Eggs were irradiated with thermal neutron for 1 h at an operating power of 1MW. After the irradiation, eggs were incubated for 3 days at 37℃ with 65% humidity. Tumors were then cut out to evaluate the tumor size and weight.

RESULTS: BPMO synthesized had approximately 200 nm of diameter and homogenous shapes examined by SEM and TEM microscopy. BPMO had 985.96 m^2/g of surface area, 0.557 cm^3/g of pore volume and 2.34 nm of pore diameter as determined by nitrogen adsorption-desorption analysis. FT-IR analysis showed diagnostic peaks of typical Si-O-Si, -C-S-, -$(CH_2)_2$- and -CH_2- vibrations. After loading of BPA to BPMO, we analyzed surface charge of BPA-BPMO which was negative due to modification with phosphonate. The zeta potential of BPA-BPMO was -42.48 mV.

Cellular uptake of BPA-BPMO to various types of cancer cells was observed. From confocal microscopy and flow cytometry analysis, the red fluorescence of BPA-BPMO could be observed inside these cells and was localized at the perinuclear region. These results are consistent with our previous observation that mesoporous silica-based nanoparticles are efficiently taken up by endocytosis system [1]. We also observed tumor accumulation of BPA-BPMO on CAM model. Significant red fluorescence of BPA-BPMO was detected in the tumor that was formed using GFP-expressed OVCAR8; overlapping of red and green fluorescence was detected. The red fluorescence of BPA-BPMO was also detected in liver and kidney, but the level of fluorescence was less than that seen in the tumor.

We finally investigated tumor growth inhibition effect on BPA-BPMO. After injecting BPA-BPMO, the eggs were subjected to neutron irradiation. As seen in Figure 1, the weight of tumor after neutron irradiation exposure with the BPA-BPMO-administered samples were around 12 mg, while the tumor weight of control (no injection or empty BPMO injection) was around 60 mg. 80% inhibition was observed by BPA-BPMO injection. Thus BPA-BPMO exhibits efficacy in BNCT. These results are published. Mouse experiments to follow up this study are ongoing.

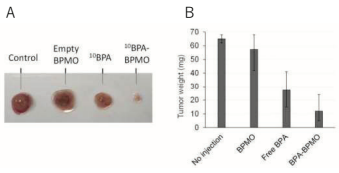

Figure 1. Tumor growth inhibition by neutron irradiation. (A) Pictures of CAM tumors after neutron irradiation; (B) Tumor weight mesurment

EFERENCES:

[1] Lu, J *et al.*, Nanobiotechnology., **3** (2008) 89-95.
[2] Tamanoi, F. *et al*., Int. J. Mol. Sci. **22**, 2251 (2021).

R2155

CO7-22 Three dimentional model for pre-clinical investigations in BNCT

K.Igawa, [1]A.Sasaki, [2]K.Izumi, [2] E.Naito, [3]M.Suzuki, [3]N.Kondo, [3] Y.Sakurai

Neutron Therapy Research Center, Okayama University
[1]Department of Oral Maxillofacial Surgery, Okayama University
[2]Graduate School of Medical and Dental Sciences Oral Life, Niigata University
[3]Research Reactor Institute for Integrated Radiation and Nuclear Science, Kyoto University

INTRODUCTION: In Boron Neutron Capture Therapy (BNCT), the Boron dose and neutron dose in tumor cells are the key factors. The development of boron agents for BNCT requires the evaluation system bridging the gap between *in vivo* and *in vitro* research. Also, from the viewpoint of the animal welfare and the 3Rs: Replacement, Reduction and Refinement, the humane alternative research methods that do not use animals, are required for BNCT. On the other hand, three-dimensional (3D) models have been widely used in cancer research due to their ability to mimic multiple features of the tumor microenvironment [1]. Therefore, the validity of the 3D cancer model for pre-clinical investigations in BNCT is examined in this study.

EXPERIMENTS: First, we measured the distribution of neutron irradiation dose in an acellular collagen gel on a 6 wells plate, identical to the culture vessel to fabricate the oral cancer 3D model. The neutron fluence on six different locations of a 6 well plate was measured using the gold foils. Based on this mock irradiation, the optimal irradiation time for 3D model is calculated. For the development of oral cancer 3D model, the oral mucosal fibroblast cells （Niigata University）and oral squamous cell lines（SAS, JCRB） were embedded and cultured on type I -A collagen (Niita-gelatin, Japan) in αMEM medium (Wako, Japan) supplemented with 10 % fetal bovine serum (Sigma -Aldrich, USA) and 100 unit/ml penicillin and 100 μg/ml streptomycin (1% p/s) (Thermo Fisher Scientific, USA) [2,3]. Before neutron irradiation, Boron (Steboronine®, Stella pharma, Japan) or Phosphate Buffered Saline（PBS, Sigma -Aldrich, USA）was added to the oral cancer 3D model and incubated for 2 hour. After washing by PBS, the 3 D models were irradiated by neutron and cultured for another 7 days (Fig. 1). The 3D models were fixed with 10 % formalin, embedded in paraffin, cut in 5 μm sections and stained with hematoxylin and eosin.

RESULTS: The neutron fluence at six various points of a 6 wells plate was measured using the gold foil as shown Fig.2. The mean value of neutron fluence on the top and bottom of a 6 wells plate (1.42×10^{12} cm^{-2}) is almost same value in the collagen gel (①, ②). Therefore, the neutron dose in 3D model is decided to measure on the top and bottom of a 6 wells plate to keep sterilization.

The histological examinations of the oral cancer 3D model after boron neutron capture reaction revealed that the epithelial thickness of cancer cell layers on the top of the fibroblasts-embedded collagen gel was thinner, compared with control as shown in Fig.3. However, the thickness of fibroblast-embedded collagen gel did not differ between the two. These results indicate the 3D model would be an alternative tool to animal test for boron neutron capture reaction.

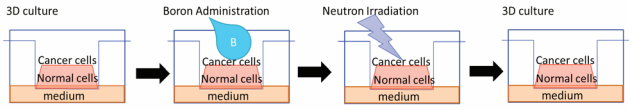

Fig. 1. The 3D model evaluation system for BNCT.

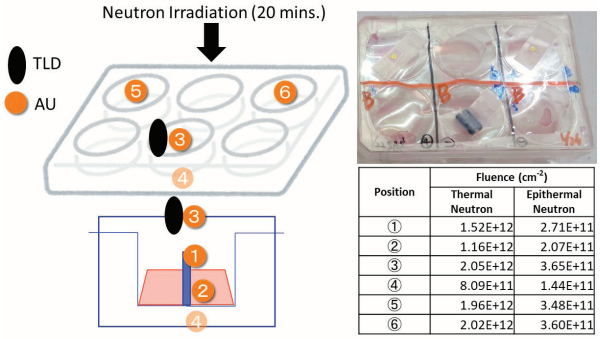

Position	Fluence (cm^{-2})	
	Thermal Neutron	Epithermal Neutron
①	1.52E+12	2.71E+11
②	1.16E+12	2.07E+11
③	2.05E+12	3.65E+11
④	8.09E+11	1.44E+11
⑤	1.96E+12	3.48E+11
⑥	2.02E+12	3.60E+11

Fig. 2. The measurement of dosimetry in 3D model.

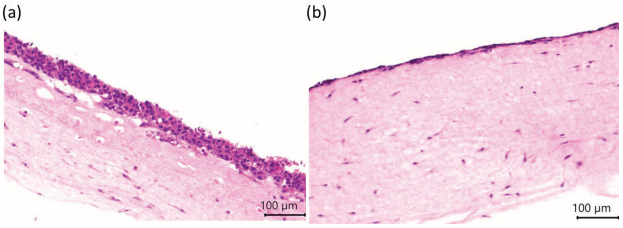

Fig. 3. Histology of the oral cancer 3D model at 7 days after neutron irradiation. Before neutron irradiation, (a) PBS or (b) Boron was injected into the 3D model.

REFERENCES:

[1] F D Modugno *et al.*, Journal of Experimental & Clinical Cancer Research 38:117 (2019).
[2] A Uneyama *et al.,* Bioscience, Biotechnology, and Biochemistry 80 (79 1344-1355 (2016).
[3] K Izumi *et al.* cells Tissues Organs 176:134-152 (2004).

CO7-23

A novel carbon nanohorns for BNCT *in vitro* study

T. Tsurubuchi[1], F. Yoshida[1], A. Zaboronok[1], K. Nakai[1,2], M. Shirakawa[3], M. Suzuki[4]

Graduate School of Science, Kyoto University
[1] Department of Neurosurgery, Faculty of Medicine, University of Tsukuba
[2] Department of Radiation Oncology, Faculty of Medicine, University of Tsukuba
[3] Department of Pharmaceutical Sciences, University of Fukuyama
[4] Institute for Integrated Radiation and Nuclear science, Kyoto University

INTRODUCTION:

Only p-boronophenylalanine (BPA), sodium borocaptate (BSH) already have been used in Boron Neutron Capture Therapy (BNCT) trials as boron compounds. However, to keep enough tumor to normal concentration ratio of boron for effective BNCT, BPA and BSH usually need to be continuously administrated to the patient just before neutron irradiation. Less toxicity, more accumulation and retention in tumor cells but not in the normal cells, and clear washout from the normal tissue are the important points for newly boron comounds for BNCT.

We developed the BN-CNH was coated with phospholipid polyethylene glycol having folate, BN-CNH/PLPEG-FA (Iizumi 2015) called carbon nanohorns.

The previous experiment data (Tsurubuchi 2019) showed carbon nanohorns effectively suppressed the colony forming units of GL261 mice glioma cells. We considered whether carbon nanohorns accumulated in other types of tumor cells. To assess the therapeutic effects of carbon nanohorns in BNCT, we tried another irradiation study in vitro in the Kyoto University Research Reactor (KUR).

EXPERIMENTS: This time, CT26, mice colon tumor cells were used for colony formation test. The $1*10^6$ cells were plated on wells of 6 well plate 24 hours before experiment. The drug, carbon nanohorns were added to each well 24 hours before irradiation. The BPA were added 2 hours before irradiation. The control group was radiation only group without drug. For counting plating efficiencies (PE), each group had only CT26 tumor cells without treatment. The cells were trypsinized and counted. The irradiation was performed with thermal neutrons with a flux of 1.6×10^{12} neutrons/cm^2 over 15min at the KUR. The 200 cells per dish were plated respectively. PE were checked after counting colonies on day 14. The colony forming units were calculated as mean colony counts devided by PE. This time carbon nanohorns only contains natural boron.

RESULTS: The carbon nanohorns group showed better tumor suppression compared to irradiation only group (Figure 1). Wash treatment did not reduce colony form-ing units. The BPA group showed better tumor suppres-sion effect compared to the carbon nanohorns group. Considering our carbon nanohorn consisting of natural boron, the carbon nanohorns group showed the same tu-mor suppression effect compared to the BPA group. The irradiation experiment using carbon nanohorns showed enough tumor suppression effect independent on the dif-ferent kinds of tumor cells.

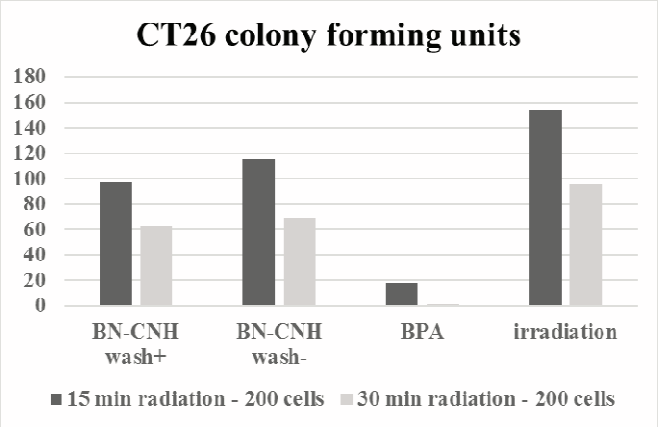

Figure 1 The results of CT26 colony forming units

REFERENCES:

[1] Y. Iizumi et al., CARBON **93** (2015) 595-603.
[2] T. Tsurubuchi et al., KUR report 2019 (2020).

CO7-24 Development of ^{10}BPA-loaded mesoporous silica-based nanoparticles and preliminary evaluation in BNCT mouse experiments

F. Tamanoi[1], K. Matsumoto[1] A. Komatsu[1], S. Chinnathambi[1], M. Laird[1], Y. Higashi[1] and M. Suzuki[2]

[1]*Institute for Advanced Study*
Institute for Integrated Cell-Materials Sciences, Kyoto University
[2]*Institute for Integrated Radiation and Nuclear Science, Kyoto University*

INTRODUCTION: Boron phenylalanine (BPA) has been developed as useful boron compound which is available for Boron neutron capture therapy (BNCT) therapy. We have recently developed two types of mesoporous silica-based nanoparticles that are loaded with BPA. One is mesoporous silica nanoparticles loaded with BPA. Another is biodegradable periodic mesoporous organosilica (BPMO) loaded with BPA. These nanoparticles have a large surface area where BPA can be attached for BNCT application. We have found and reported that BPA-BPMO exhibits efficacy in BNCT experiments which used chicken. chorioallantoic membrane model (CAM model) [1]. In this study, we carried out experiments to prepare for mouse experiments to evaluate their BNCT efficacy.

EXPERIMENTS: MSN was synthesized by sol-gel synthesis employing TEOS as a precursor. BPMO was synthesized by sol-gel synthesis of two precursors, bis[3-(triethoxysilyl) propyl] tetrasulfide and 1, 2-bis(triethoxysilyl) ethane. This resulted in the incorporation of tetrasulfide bonds into the framework of the nanoparticles. MSN and BPMO were then processed to modify with GOPTS (3-glycidyloxypropyl trimethoxysilane) that contain epoxy groups. After converting epoxy groups to diols, BPA was mixed with diol-BPMO to graft BPA using a method to chelate boron with diol groups. The synthesized nanoparticles were characterized by using SEM, TEM, FT-IR, nitrogen adsorption-desorption analysis and zeta potential. The amount of boron attached on the nanoparticles was examined by ICP, and boron content was determined.

Mouse model was established by transplanting mouse colon cancer cells CT26 to BALB/c mouse. After injection of BPA-loaded nanoparticles, amount of boron in the tumor was examined by ICP.

Irradiation of mice with neutron beams was carried out by placing mice in specially prepared holders. Irradiation was carried out with thermal neutron for 12 min at an operating power of 5MW. After the irradiation, mice were returned to cage, and tumor size was longitudinally and transversely measured every 2 days for up to 25 days.

RESULTS: Nanoparticles synthesized had approximately 80-100 nm of diameter and homogenous shapes examined by SEM and TEM microscopy. FT-IR analysis of BPMO showed diagnostic peaks of typical Si-O-Si, $-(CH_2)_2-$ and $-CH_2-$ vibrations. After loading of BPA to BPMO, we analyzed surface charge of BPA-BPMO which was negative due to modification with phosphonate. The zeta potential of BPA-BPMO was -41.38 mV.

Boron accumulation in the CT26 tumor was investigated with ICP. We were able to achieve delivery of boron in the tumor but the route of delivery needs to be further investigated. We also observed accumulation of BPA-BPMO in the tumor by confocal microscopy. When BPA-BPMO was injected to tumor, the red fluorescence of BPA-BPMO could be observed in the tumor. However, the distribution was not even. We are further investigating the optimum condition for BPA-BPMO accumulation in the tumor.

Investigation of tumor growth inhibition effect of BPA-loaded nanoparticles is currently ongoing. After injecting the nanoparticles, all mice are subjected to neutron irradiation and tumor growth is followed for 25days. BNCT efficacy of BPA-loaded nanoparticles is compared with that of free BPA.

REFERENCES:
[1] Tamanoi, F. *et al*., Int. J. Mol. Sci. **22**, 2251 (2021).

CO7-25 Effects of overexpression of *LAT1* on suppression of tumor growth by boron neutron capture therapy

K. Ohnishi[1], M. Misawa[2], N. Sikano[3] and M. Suzuki[4]
Departments of [1]Biology, [3]Radiological Science, Ibaraki Prefectural University of Health Sciences
[2]National Institute of Advanced Industrial Science and Technology
[4]Institute for Integrated Radiation and Nuclear Science, Kyoto University

INTRODUCTION: Outcome from BNCT largely depends on amount of intracellular accumulation of boron compound. L-type amino-acid transporter 1 (LAT1) [1], through which boronophenylalanine (BPA) is transported into cells, is frequently expressed in various types of tumor cells including glioblastoma but not in normal cells [2]. We transfected *pCMV/LAT1-GFP* plasmids into a glioblastoma cell line, T98G, and selected several clones and confirmed that those clones stably overexpress LAT1 in cell membrane with confocal laser microscopic observation and western blot analysis. Our *in vitro* neutron irradiation experiments using LAT1 overexpressing clone showed that overexpression of LAT1 in cancer cells causes enhanced anticancer effects of BNCT and BNCT combined with gene therapy is beneficial for tumors bearing low LAT1 expression [3]. In this study, we transplanted LAT1 overexpressing clone (T98G/K4) into nude mice and effects of neutron irradiation on tumor growth were preliminary examined after ^{10}BPA treatment.

EXPERIMENTS: We transplanted minced tumors formed with LAT1 overexpressing clone (T98G/K4) into femoral area of nude mice. Accumulated amounts of ^{10}BPA in blood and tumor were measured using prompt gamma-ray assay (PGA) on 1 h after ^{10}BPA s.c. injection (100 mg/kg, 1 h before irradiation). The transplanted tumors in 4 mice were irradiated with thermal neutron beam at the fluences of 3.3x 10^{12} n/cm^{-2} on 1h after the ^{10}BPA injection.

RESULTS: Accumulated amounts of ^{10}BPA in blood and tumor were 7.2 ppm and 19.4 ppm, respectively. The relative tumor volumes in ^{10}BPA-treated 3 mice and ^{10}BPA-nontreated 1 mouse were 0.049, 0.127, 0.586 and 1.830, respectively on 24th day after the irradiation.

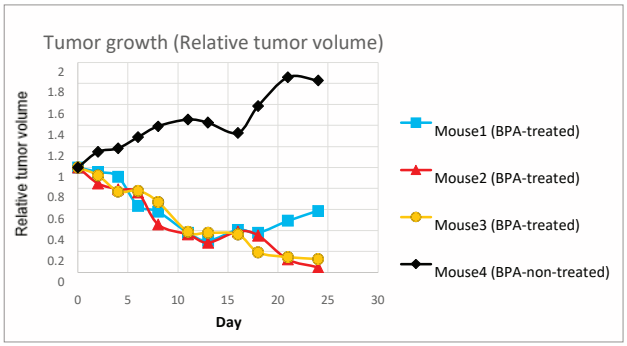

Fig. 1. Tumor growth curves of LAT1 overexpressing tumors (T98G/K4) in ^{10}BPA-treated 3 mice and ^{10}BPA-non-treated 1 mouse.

CONCLUSION: We obtained preliminary data from this study. On the basis of the data, we plan to perform further detailed studies.

REFERENCES:

[1] Y. Kanai *et al.*, J. Biol. Chem., **273** (1998) 23629-23632.
[2] K. Kaira *et al.*, Br. J. Cancer, **107** (2012) 632-638.
[3] K. Ohnishi *et al.*, Radiat. Res., in press.

CO7-26 Synthesis of a Novel Boron Compound with Potential Peptide-Related Nuclear Import

M. Shirakawa[1,2], A. Okuda[3], A. Zaboronok[4], Y. Sato[1], A. Shigenaga[1], N. Kamegawa[5], R. Takeuchi[5], H. Hori[5,6] and M. Sugiyama[3]

[1]*Department of Pharmaceutical Sciences, Fukuyama University*
[2]*Department of Radiation Oncology, Faculty of Medicine, University of Tsukuba*
[3] *Institute for Integrated Radiation and Nuclear Science, Kyoto University*
[4] *Department of Neurosurgery, Faculty of Medicine, University of Tsukuba*
[5] *Morita Pharmaceutical Ind., Ltd.*
[6] *Niigata University of Pharmacy and Applied Life Sciences*

INTRODUCTION:

The therapeutic effect of BNCT is provided by the alpha -rays generated in the ^{10}B neutron capture reaction, which leads to double-strand DNA breaks in tumor cells. Based on its principle, the anti-tumor effect of BNCT is presumed to be maximized when ^{10}B is present in or near the nucleus of the tumor cell [1].

Therefore, we developed a peptide-based carrier that can efficiently and selectively transport boron in the nucleus of the tumor cell. This article presents the obtained experimental results of the synthesis of a novel boron peptide combined with the Cell Penetrating Peptide (CPP), Nuclear Localization Signal (NLS), and the membrane fusion peptide.

EXPERIMENTS:

Boron peptides were combined with mercaptododecaborate (BSH) and two functional peptides, and the synthesis was performed on Fmoc-Lys(ivDde)-wang resin by the Fmoc solid-phase method [2]. As a peptide sequence, we selected two of TAT (GRKKRRQRRRPQ), H5 (HHHHH), H16 (HHHHHHHHHHHHHHHH), R8 (RRRRRRRR), c-Myc (PAAKRVKLD), GALA (WEAALAEALAEALAEHLAEALAEALEALAA) and synthesized them by inserting a linker between the two peptides. After that, BSH was conjugated with the peptide C-terminal region.

Each amino acid coupling reaction was carried out for 3 min at 90℃ using a microwave. De-protection and cleavage of resin were accomplished with a cleavage cocktail at room temperature, then precipitated by adding a large amount of diethyl ether. After the drying procedure, we obtained the desired compound.

RESULTS: As shown in Fig. 1 and Fig. 2, we succeeded in synthesizing the novel boron peptide (e.g., TAT-GALA-BSH). In the identification of this boron peptide, the Ultra Performance Liquid Chromatography (UPLC) analysis showed almost one peak (retention time at 4.72min), and the substance was confirmed to be of high purity (96%). Also, MALDI-TOFMS (Matrix Assisted Laser Desorption/Ionization-Time-of-Flight Mass Spectrometry) showed *m/z* 4978 of the peak as an exact mass of *m/z* 4978.

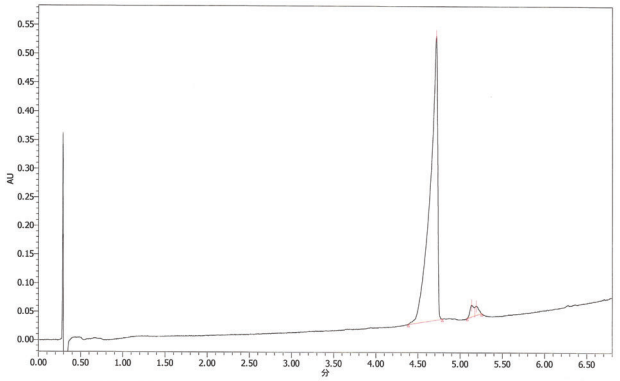

Fig.1) Purity of TAT-GALA-BSH by UPLC

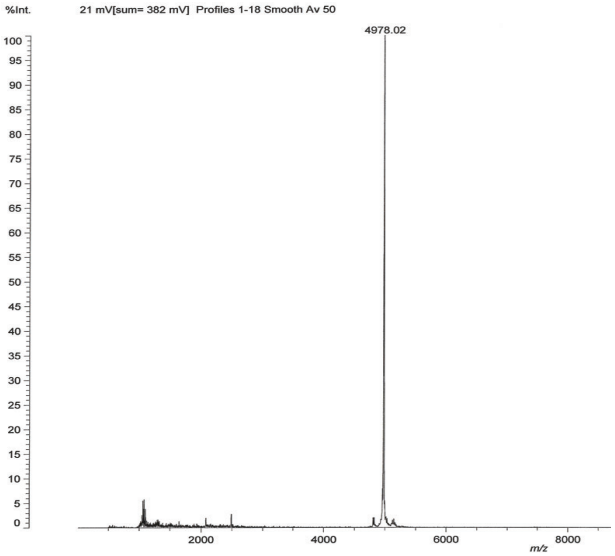

Fig.2) Identification of TAT-GALA-BSH by MALDI-TOFMS.

REFERENCES:

[1] Sato T., et al., *Sci. Rep*., **8**, 988, (2018).
[2] Gongora-Benitez, M.; Tulla-Puche, J.; Albericio, F. *ACS Comb. Sci*., **15**, 5, 217-228, (2013).

CO8-1 Developments for an innovative method to detect nuclear materials

M. Komeda[1], Y. Toh[1], Y. Kitamura[2], T. Misawa[2] and K.Tanabe[3]

[1]*Nuclear Science and Engineering Center, Japan Atomic Energy Agency*
[2]*Institute for Integrated Radiation and Nuclear Science, Kyoto University*
[3]*National Research Institute of Police Science*

INTRODUCTION: Devices for detecting nuclear materials have become increasingly important with the increase of today's global terrorism. In particular, a compact and low-cost non-destructive assay system to detect hidden nuclear material is required in the fields of nuclear security. We have therefore developed an innovative nuclear material detection method by using a neutron source of Californium-252, which is capable to assemble such system. In this method, a neutron source is rotated at a speed of thousands of rpm nearby the target. Meanwhile, it is possible to detect nuclear materials by confirming the deformation of the time-distribution spectrum obtained by a neutron detector near the target. The machine to rotate the neutron source is quite compact that its width, depth, and height is 60 cm each. We have installed the machine at an experimental laboratory in the KUCA. In the previous study, we presented experimental verifications for this new method [1]. However, we used expensive detectors based on He-3, so that we have studied to develop a low-cost detector for this new method. A water Cherenkov detector has a potential ability as a low-cost neutron detector. Unfortunately, our experiments in this year are severely limited due to the influence of the COVID-19.

EXPERIMENTS: The left side of the Fig.1 shows a water Cherenkov detector. Four PMTs (Photomultiplier tube) are mounted on the aquarium. The diameter of the PMT is 2 inches. The aquarium (25x25x30cm) is a commercial item and reasonable price. It is covered with a black sheet and boron sheet in order to prevent light and thermal neutrons. The aquarium is filled with the gadolinium aqueous solution with approximately 0.5wt%. The gadolinium was added in order to increase the amount of the Cherenkov light. This detector can be constructed at a much lower cost than He-3 detectors. Since high energy gamma ray, for example from hydrogen in water, also causes the Cherenkov light, we discriminate neutron signal by using pulse height difference. Measurements of the neutron time distribution were performed by a multi-channel scaler (MCS) that is synchronized with the disc rotation. The right side of the Fig.1 shows a rotation machine to rotate a neutron source. The neutron source was installed at the outer periphery of a disc of 32 cm diameter. The maximum rotation speed is 4000 rpm.

RESULTS: Figure 2 shows an example of experimental results of a blank sample (only polyethylene blocks) under the condition that the rotation speed is 3000 rpm. The neutron source was closest to the polyethylene blocks approximately at 8500 micro-seconds in Fig. 2. Since the neutron source, the polyethylene blocks and the neutron detector system have a complicated geometry, the dips in the times spectrum appear before and after the peak. We have confirmed that this Cherenkov detector is able to measure as same as He-3 detectors. It means that we can construct a new detection system for nuclear materials that is low cost and transportable. Further improvement of the Cherenkov detector is possible and desirable. Therefore, more detailed experimental study with nuclear materials would be required.

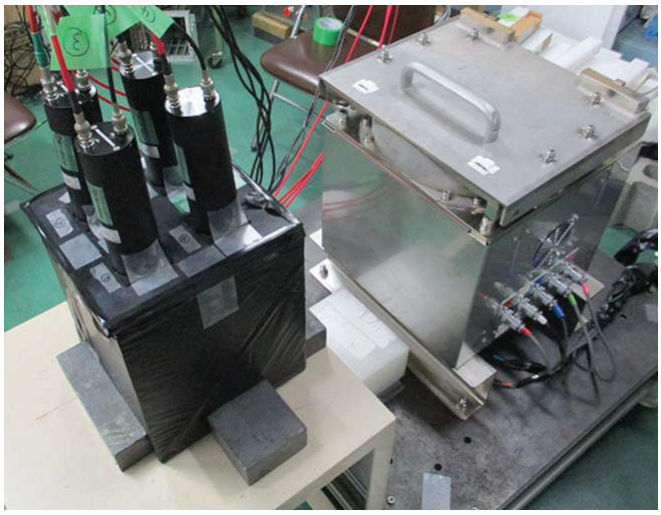

Fig. 1. Water Cherenkov detector (left) and rotation machine (right). A black sheet and boron sheet are covered over the detector in the neutron measurements.

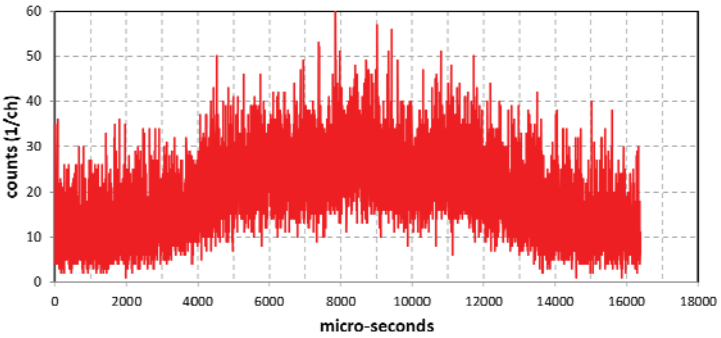

Fig. 2 Experimental examples of a blank sample. The measurement time was 30 minutes with the rotation speed of 3000 rpm.

REFERENCES:

[1] M. Komeda, Y. Toh, K. Tanabe, Y. Kitamura, T. Misawa, "First demonstration experiment of the neutron rotation method for detecting nuclear material", Annals of Nuclear Energy (in press).

CO8-2 Neutron Phase Imaging with Talbot-Lau Interferometer at CN-3

T. Shinohara, M. Hino[1], T. Oda[1], Y. Seki[2]

J-PARC Center, Japan Atomic Energy Agency
[1]Institute for Integrated Radiation and Nuclear Science, Kyoto University
[2] Institute for Liberal Arts and Sciences, Osaka Electro-Communication University

INTRODUCTION:
Neutron phase imaging is a method which can directly access the phase information of the neutron wave function, and provide a higher sensitively to thinner objects than the conventional neutron imaging technique and a sensitivity of small structures in the sample, which can be analyzed by means of small-angle scattering technique. We have been developing neutron phase imaging technique with the Talbot-Lau interferometer consisting of three gratings [1, 2], that is, the most upstream absorption grating (G0), the middle phase grating (G1), and the most downstream absorption grating (G2). G0 works as a multi-slit and forms an array of spatially coherent line sources. Each source produces an interference pattern or a "moiré fringe" constructively through G1 grating and G2 grating. Based on the important characteristics of the Tal-bot-Lau interferometer such as availability for a relatively broad wavelength-range neutron beam and an adaptability to a low-coherent and low-intensity neutron beam, we have constructed a Talbot-Lau interferometry apparatus optimized to the KUR CN-3 port and conducted neutron phase imaging experiments.

EXPERIMENTS: For the neutron phase imaging experiments, three gratings optimized to the spectra of CN-3 beam port, the central wavelength was 2.4 Å, were fabricated. In addition, we have employed a new image detector system consisting of a CMOS camera and a LiF/ZnS scintillator screen. Using this new apparatus, we at first aligned all the gratings so as to maximize the visibility of moire pattern and then decided the fringe step condition. The fringe scan was conducted by moving G2 along horizontal axis, and one period of the grating was divided into 10 steps. The exposure time of one image was 10 sec and repeated by 5 times for each step. The samples used for the demonstration study were Fe-Si-Al magnetic alloy powder (average radius = 30 μm) and a mixture of powder and grains (average radius = 2 mm) filled in rectangular quartz cells. The samples were placed between G1 and G2 gratings.

RESULTS: Visibility image obtained without sample is shown in Fig. 1(a). There appeared a very strong visibility distribution ranging from 0.2 to 0.4 along horizontal axis. This is thought to come from the beam divergence due to the neutron guide tube installed in front of the G0 grating.
Fig.2 shows the results of sample measurements. The absorption image shown Fig.2 (a) indicated that the neutron transmission is high and there was very small difference between the powder and the mixture of powder and grains. On the other hand, the visibility image clearly displayed a contrast between them. This is the clear indication that visibility image obtained by the neutron phase imaging can distinguish micro-meter scale structure inside the object.

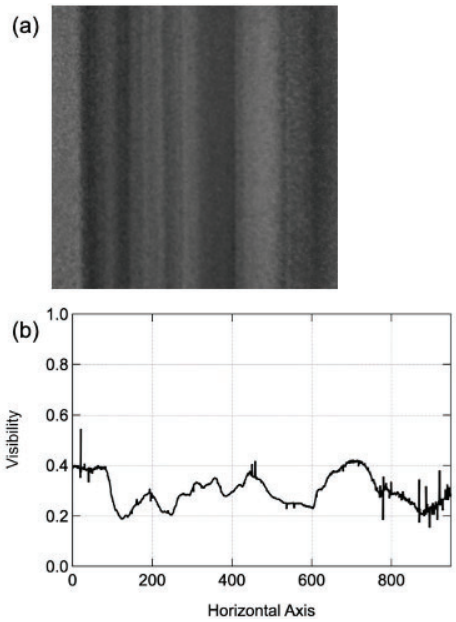

Fig. 1 Visibility of the direct beam. (a) Visibility image, (b) cross section profile along horizontal axis.

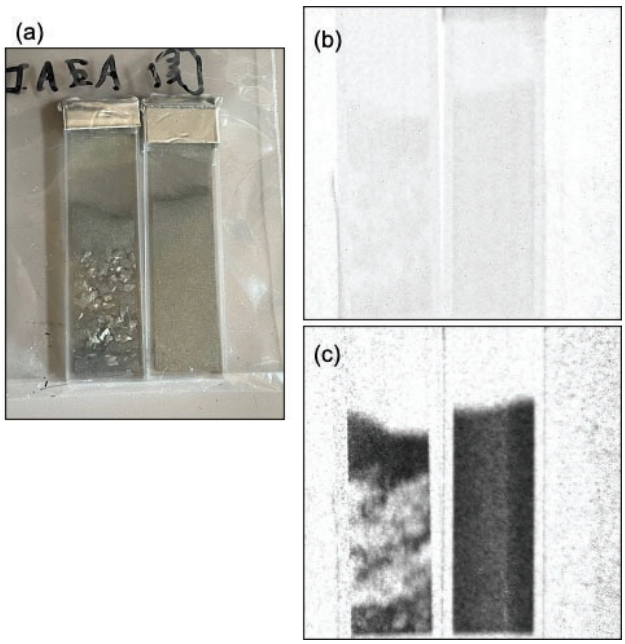

Fig. 2 Result of demonstration study using magnetic samples. (a) the photograph of the sample. (b) Absorption contrast image, (c) visibility image.

REFERENCES:
[1] Y. Seki *et al.*, J. Phys. Soc. Jpn., **86** (2017) 044001.
[2] Y. Seki *et al.*, EPL, **123** (2018) 12002.

CO8-3 Neutron Resonance Spectrometry for Nuclear Security and Safeguards Education

J. Kawarabayashi, R. Sasaki, T. Yokota, H. Tagawa, Y. Ikeda, K. Mitsui and J. Hori[1]

Department of nuclear safety engineering, Tokyo City University

[1]Institute for Integrated Radiation and Nuclear Science, Kyoto University

INTRODUCTION: In order to support nuclear facility regulations in Japan for safe use, it is necessary to develop educational training course with broad knowledge associated with nuclear engineering. Nuclear facilities include reprocessing, nuclear fuel factories, research facilities, etc. in addition to nuclear power plants, it is important to teach not only the knowledge of radiation, reactor physics, but also the physics of nuclear material itself at each stage of the nuclear fuel cycle. The knowledge of physical and chemical properties of nuclear material is also needed for effective regulation. As a part of this human resource development, we have proposed an isotope ratio measurement training program with uranium using pulsed neutron spectrometry as a candidate for the nuclear regulatory educational course to deepen the understanding of the nuclides in nuclear fuel cycle. Observation of the neutron resonance absorption phenomena of natural, enriched and depleted uranium will develop the understanding of the isotope itself and the properties of the nucleus of uranium. In this fiscal year, as the pandemic of Covid-19 limited our student to travel to Kyoto University, we attempted to establish an online experiment to acquire neutron resonance absorption spectra of various samples.

EXPERIMENTS: Metal plates of four different elements (Ag, Ta, Zr, Co) were irradiated at KURRI-LINAC to record neutron transmission spectrum. A ^{3}He proportional counter followed by a multiple-stop time spectrometer (ORTEC EASY-MCS) was located just behind the sample at 13m experimental room and generated timing signal of neutron detection. A signal from the accelerator was used as the start signal of the time spectrometer. The timing calibration between start signal and output signal of the ^{3}He proportional counter was performed with an oscilloscope by gamma-flash signal generated at the Ta target of the accelerator. Without and with Ta, Zr, Ag, Co plates was arranged at in front of the neutron irradiation port and time spectra of neutron transmission were recorded. Five students participated in the experiment over computer network by Zoom meeting software.

RESULTS: As shown in Fig. 1, a resonance dip of ^{109}Ag was clearly observed in the time spectrum with the sample of silver plate (thickness: 0.05 mm) successfully, with measurement of 80,000 sweeps and 20 msec. range. The accelerometer was running at 50Hz with mode of 4 micro sec. per pulse. The time spectrum was recorded within about 27 minutes. The energy of this dip was estimated to be 5.3 eV derived from the source-detector distance of 12 m and dip position of 0.377 msec. The first energy level of ^{109}Ag is 5.19 eV [1]. There is a good agreement between the experimental result and literature value. In Fig.2, time spectrum with Ta plate (thickness: 1 mm) were obtained. There were some resonance dips corresponding to ^{181}Ta. We confirmed the dips corresponded to resonant absorption energies of 4.28 eV, 10.36 eV, 13.95eV, 20.29 eV and 22.72 eV [1]. Only two dips were observed for the resonance energies of 34.19 eV, 35.14 eV, 35.90 eV, because time resolution of our system was not enough to separate them. The screen of the PC acquiring these spectra was shared with online students through Zoom. The online students were able to observe the acquisition of neutron transmission spectra in real time. The experimental system and conditions were explained online with a video taken in the morning of the day when the experiment was carried out. Interviews with students after training showed that the content of the experiment could be understood online.

CONCLUSION: We proposed pulsed neutron spectrometry as a candidate for the nuclear regulatory educational course to deepen the understanding of the nuclides in nuclear fuel cycle and performed online training program. The results showed that online program was sufficient to understand the experiment. The next work is to establish the online program when the uranium is actually used as the measurement target and a larger number of students joint online at once.

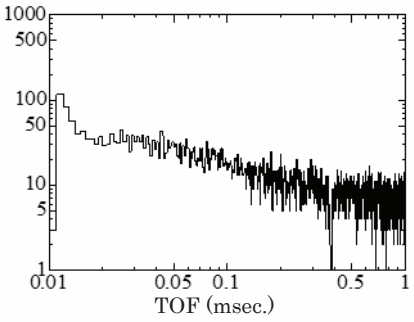

Fig. 1. ToF spectrum of Ag.

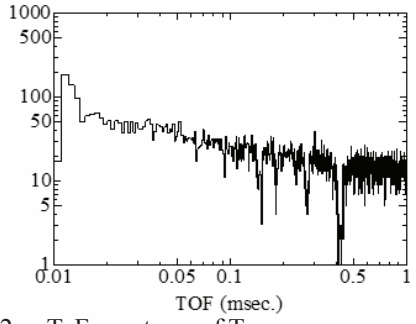

Fig. 2. ToF spectrum of Ta.

REFERENCES:

[1] S. F. Mughabghab, Atlas of Neutron Resonances.

CO8-4 Coolant Visualization in the Accumulated Square Rod Arrays

M. Kaneda, K. Suga, M. Sugimoto, K. Wada, Z. Li

Department of Mechanical Engineering, Osaka Prefecture University

INTRODUCTION: Electric motors used in vehicles has been required to have high performance, more power, and compactness [1]. This results in the higher emission heat density from the motor package and the effective cooling scheme of the stator coil has been important. The actual vehicle stator coils are cooled by the coolant poured from a nozzle above. For the evaluation, the temperature measurement was carried out [2, 3]. However, the coolant profile inside the coil has not been clarified yet and the pouring conditions are decided empirically. In this study, therefore, the coolant profile inside the simplified stator system is studied by using the neutron radiography.

EXPERIMENTS: The schematic model of the experiment is shown in Fig.1(a). The stator coil is presumed by the accumulated square rod arrays shown in Fig.1(b) where the coolant is directly poured from above. Each square rod is made of aluminum and horizontally aligned with a gap of 1mm. This single layer is accumulated to four and bundled in the coolant circulation system consisted of a pump, flowmeter, temperature measurement devices, etc. The flow rate of the coolant is 0.5L/min. The neutron beam is in horizontal direction so does the coolant visualization. The experiment is carried out in the room temperature.

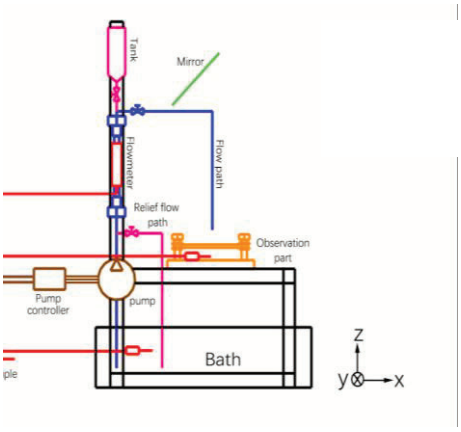

(a) overall setup

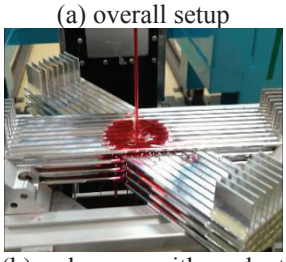

(b) rod arrays with coolant

Fig. 1. Experimental setup.

RESULTS: First, for the evaluation, the visualization of the coolant between the two rods is carried out. The result is shown in Fig.2(a). As in the figure, the coolant can be visualized due to the large attenuation rate difference between the aluminum and coolant.

Next, the coolant in the accumulated rod arrays is visualized as shown in Fig.2(b). The coolant spreads in each array layer. It is found that the coolant in the below layer has larger area of coolant. This can be explained by the structure. At the top layer, the coolant can spread not only in the rod direction but also the spanwise direction due to the viscosity and the wettability of the coolant. The coolant escapes down and hit the lower layer. The coolant can spread in the same manner. Each array is accumulated with an angle. This suggests that the coolant is partially sandwiched by the above and below rods. This may induce the capillary effect and the horizontal spreading is enhanced. This is repeated as the coolant goes lower layer, resulting in the wider spread as it goes down.

(a) Between two horizontal aluminum rods.

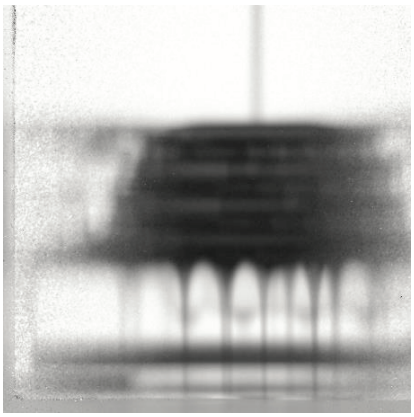

(b) Inside the accumulated rod arrays

Fig. 2. Visualized coolant.

REFERENCES:

[1] N. Kobayashi and T. Ikegami, Thermal Sci. Eng., **15**, 2 (2007) 49-54.

[2] T. Davin *et al.*, Applied Thermal Eng., **75** (2015) 1-13.

[3] S. Onimaru e*t al.*, Denso Technical Review, **13** (2008) 19-25.

CO9-1 Solid phase transformation of tetravalent metal hydroxide at elevated temperatures

T. Kobayashi, Y. Sato, T. Suzuki, T. Sasaki, K. Mori[1], K. Takamiya[1]

Graduate School of Engineering, Kyoto University
[1] Institute for Integrated Radiation and Nuclear Science, Kyoto University

INTRODUCTION: For the reliable prediction of radionuclide migration behavior under relevant radioactive waste disposal conditions, it is necessary to establish a thermodynamic model on the solubility limits of radionuclides in groundwater. Several actinides and long half-life fission products such as ^{93}Zr are known to exhibit a tetravalent oxidation state in repository systems and easily precipitate as an amorphous hydroxide ($M(OH)_4$(am)) due to strong hydrolysis reactions. Although the solubility is primarily controlled by the amorphous hydroxide, $M(OH)_4$(am) is thermodynamically meta-stable, and can be converted to stable crystalline oxide of MO_2(cr) by heating or calcinations [1]. Since the decay heat emissions are transferred to the groundwater surrounding the waste packages, the repository systems are expected to be under elevated temperature conditions [2]. Therefore, it is important to reveal an impact of elevated temperature on the solid phase transformation of $M(OH)_4$(am) for the prediction of the solubility limits of radionuclides in tetravalent oxidation state. On the other hand, a number of literatures have investigated the solubility of MO_2(cr) and several studies suggested that the surface of MO_2(cr) are possibly hydrolyzed to form hydroxide layer, which is controlling the apparent solubility [3]. Since the solubility product (K_s) of MO_2(cr) and $M(OH)_4$(am) differs more than several orders of magnitude, it is of importance to clarify the solid phase transformation between MO_2(cr) and $M(OH)_4$(am) for establishing the robust thermodynamic model on the solubility of radionuclides in tetravalent oxidation state.
In the present study, we focused Zr as one of the fission products in tetravalent oxidation state under the repository conditions. ZrO_2(cr) powder were first measured by a versatile compact neutron diffractometer (VCND) at the B-3 beam port of KUR as references. Then the neutron diffraction patterns of amorphous zirconium deuterium hydroxide ($Zr(OD)_4$(am)) aged at 25 to 90 ºC were collected to investigate a temperature effect on the transformation of ZrO_2(cr) and $Zr(OD)_4$(am).

EXPERIMENTS: The powder samples of ZrO_2(cr) was purchased from WAKO Pure Chem. and put in sample holders without further treatment. The samples of $Zr(OD)_4$(am) was prepared by an oversaturation method. A few grams of $ZrCl_4$ (WAKO Pure Chem.) was dissolved in D_2O to prepare the Zr stock solution ([Zr] = 0.2 M). Portions of deuterium hydroxide (NaOD) were then added in the stock solution to adjust the pHc at pHc = 2.7. The sample suspensions were placed in ovens kept at 25, 40, 60, and 90 ºC for 3 weeks. After the aging periods at each temperature, the pHc of the sample solutions was measured. The solid phases were separated by centrifugation and dried in vacuum desiccator. After the dryness, the powder samples were put in sample holders and measured by a VCND installed at the B-3 beam port of KUR. A Cu monochromator with 40 mm diameter was used to monochromatize the neutron wavelength of 1.0Å. The beam size was approximately 10 mm in width and 30 mm in height. The beam flux was 1.3×10^5 n/s·cm^2 during the operation at the power of 5 MW on KUR.

RESULTS: Figure 1 shows the neutron diffraction (ND) pattern of ZrO_2(cr) in comparison with the X-ray diffraction (XRD) patterns [1]. The ND patterns exhibited intense peaks at low d ($d = \lambda/2 \sin\theta$), while the peaks in the XRD patterns showed less intensities. The peak positions of both methods agreed and indicated the monoclinic structure of ZrO_2(cr).

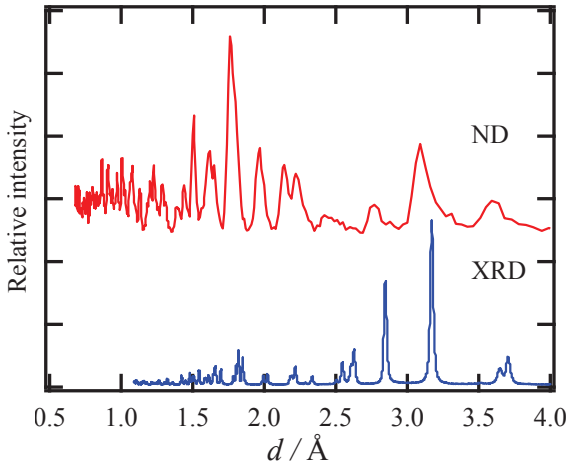

Fig. 1 Neutron diffraction (ND) and X-ray diffraction (XRD) patterns of ZrO_2(cr).

The neutron diffraction pattern of $Zr(OD)_4$(am) after aging at 25 ºC showed a halo pattern typical for amorphous phase. With increasing the aging temperatures, the peaks corresponding to ZrO_2(cr) appeared and those after aging at 90 ºC became clear with large intensities, indicating the progress of crystallization by heating. Further investigation is planned by an undersaturation approach from ZrO_2(cr), and also for other elements in tetravalent oxidation state.

REFERENCES:
[1] T. Kobayashi *et al.* Langmuir **35**, (2019) 7995.
[2] JNC Report TN1410 2000-001; JNC: Tokai, Japan, (2000).
[3] D. Rai *et al.*, Radiochim. Acta **79**, (1997) 239.

CO9-2 Deterioration of simulated fuel debris in aqueous environment

T. Sasaki, R. Tonna, N. Sato[1], A. Kirishima[1], D. Akiyama[1], T. Kobayashi, K. Takamiya[2], S. Sekimoto[2]

Graduate School of Engineering, Kyoto University
[1] Institute of Multidisciplinary Research for Advanced Materials, Tohoku University
[2] Institute for Integrated Radiation and Nuclear Science, Kyoto University

INTRODUCTION:

The fuel debris generated by the accident at the Tokyo Electric Power Company (TEPCO) Fukushima Daiichi Nuclear Power Station (FDNPS) is still in contact with water, and it deteriorates over time with the dissolution of nuclides due to a solid-liquid reaction on the debris surface. Since it takes a long time to plan an extraction method of the debris from the plant, it is essential to accumulate basic knowledge for predicting changes of the chemical property of debris, but there are few knowledges about debris containing UO_2, zircaloy, and structural materials such as SUS304 stainless steel (SUS).

In order to simulate the dissolution behavior of nuclides from 1F debris, we have some prepared alloy-based debris samples and focused the elution behavior of uranium and fission products (FPs). Two evaluation methods are adopted in this study. One is an addition method in which non-radioactive elements (as cold FPs) were added to a sample in advance. The other is an irradiation method. The debris sample was irradiated with short-time thermal neutrons to produce FPs.

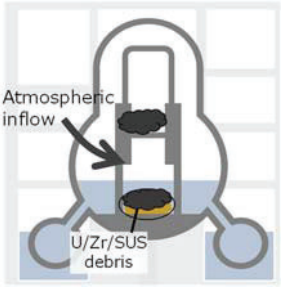

Fig.1 Schematic overview of 1F core melting

EXPERIMENTS:

A powder mixture of UO_2 obtained by hydrogen reduction of U_3O_8 and SUS was heated in an oxidizing atmosphere (2% O_2 + 98% Ar, 1200 °C) to prepare simulated debris, and a powder XRD was adopted. The representative solid phases are follows; #XO (U_3O_8 (A)), #ZO (A+$U_{1-y}Zr_yO_{2+x}$), #SO (A+U(Fe)CrO_4), #FO (A), #CO (A+$UCrO_4$), which were prepared from UO_2 (B), B+ZrO_2, B+SUS, B+Fe, B+Cr, respectively.

The solid-phase sample sealed in a quartz ampoule was inserted into a polyethylene capsule and irradiated using Pn-2 of Kyoto University Reactor. FPs are ^{137}Cs, ^{131}I, ^{140}Ba, ^{103}Ru, ^{95}Zr (irradiation method), Cs, Sr, Eu (addition method). After contacting the sample with 0.1 M $NaClO_4$, pure water, and artificial seawater at 25 °C, the nuclide concentration before and after the immersion was determined by γ-ray spectroscopy and ICP-MS for in the irradiation method and the addition method, respectively. The cumulative γ radioactivity of nuclide M dissolved during a given period was determined by considering a decay correction, in accordance with the method used. The leaching ratio (r_M) is defined as

$$r_M = A_{f,M} \exp\left(\frac{t\ln 2}{t_{1/2}}\right) / A_{i,M} \qquad (1)$$

where $A_{i,M}$ expresses the initial inventory (Bq) of M initially present in the solid solution sample, $A_{f,M}$ expresses the radioactivity (Bq) in the filtrate measured after the leaching period (t), and $t_{1/2}$ expresses the half-life of the nuclide. In the addition method, since a cold FP partly volatilized during heat treatment, the sample was dissolved by acid to correct the inventory. For uranium and cold-FPs, the unit of Bq is replaced by mole. R_M corresponds to r_M/r_U and is the dissolution ratio of M normalized by that of uranium.

RESULTS:

In the samples #XO, #ZO and #SO, Cs was preferentially leached over U, immediately after immersion in both the irradiation method and the addition method (R_{Cs}≈10^3), and then the R_{Cs} value decreased with time. It was suggested that easily soluble nuclides on the surface of the solid phase could leach immediately just after immersion of sample, but after that, matrix uranium dissolution might become a rate-determining reaction. It was found that divalent Ba (irradiation method) and Sr (addition method) same as in Cs leached preferentially over U, while a trivalent Eu showed a strong tendency for a harmonized dissolution with U. Thus, the addition method could provide the knowledge of trivalent ions. The r_U was in the order of pure water << Na perchlorate solution < seawater, and the influence of anion-U complex formation contained in the liquid phase was observed. At this time, R_{Cs} and R_{Sr} tended to be pure water >> Na perchlorate solution > seawater, while R_{Eu} was in the order of pure water < Na perchlorate, seawater, depending on the valence of the ions.

REFERENCES:

[1] V. Almjashev et al., Radiochem. **53** (2011) 13.
[2] X. Guo et al., Dalton Transactions **45** (2016) 4622.
[3] H. Ikeuchi et al., J. Nucl. Sci. Technol. **51** (2014) 996.
[4] B. Sailaja et al., Physical Sciences **74** (2004) 399.

CO9-3 The solvent extraction behavior of Antimony in nitric acid solution using TDdDGA

Y. Nakamura[1], S. Ogawa, S. Takahashi, C. Kato, S. Fukutani[1], T. Matsumura[2], H. Suzuki[2], and T. Fujii

Graduate School of Engineering, Osaka University
[1]Institute for Integrated Radiation and Nuclear Science, Kyoto University
[2]Nuclear Science and Engineering Center, Japan Atomic Energy Agency

INTRODUCTION: ^{125}Sb, an isotope of antimony (Sb), is a fission product (FP) nuclide in the high-level liquid waste and understanding its extraction behavior is crucial for the reprocessing be highly active liquid waste. Although the amount contained in the nuclear waste is relatively small compared to other elements (0.026 mM for a synthetic solution [1]), its short half-life of 2.76 years [2] is problematic and therefore the influence of Sb should be considered. *N,N,N',N'*-tetradodecyldiglycolamide (TDdDGA) is an extractant synthesized at Japan Atomic Energy Agency (JAEA) for the recovery of minor actinides (MA) and rare earth elements (REE) from the high-level liquid waste, but the extraction behavior of Sb has not been studied using this extractant. In this study, the solvent extraction behavior of Sb by TDdDGA and its dependency on nitric acid solution and also the separation factor from neodymium (Nd), a REE, were studied and determined.

EXPERIMENTS: For the HNO_3 concentration dependency, TDdDGA was used as the extractant and a mixed solution of n-dodecane and 1-octanol was used as solvents to adjust the TDdDGA concentration to 0.1 M. A Sb shot was placed in 7 M HNO_3 for 18 hours at room temperature to dissolve and then diluted to form the HNO_3 concentration of 0.1, 0.2, 0.5, 1, 1.5, 2, 3, 4, 5 M. Both phases were stirred for 30 mins to reach equilibrium. The solution was separated by centrifugation and the aqueous phase was exchanged with a 0.1 M HNO_3 and back extraction was performed. For the Nd separation experiment, the concentration of Nd and Sb were adjusted to be the same in a 1 M and 3 M HNO_3 solution for the aqueous phase. The organic phase was 0.1 M TDdDGA diluted by n-dodecane and 1-octanol. All experiments were carried out at room temperature. The Sb and Nd concentration of the aqueous phase before and after both extractions were measured by Inductively Coupled Plasma-Atomic Emission Spectrometry (ICP-AES) and Inductively Coupled Plasma-Mass Spectrometry (ICP-MS) at the Institute for Integrated Radiation and Nuclear Science, Kyoto University, and the distribution ratios and separation factors were determined.

RESULTS AND DISCUSSIONS: The results for the HNO_3 dependency are shown in Fig. 1. For the concentrations above 0.5 M HNO_3, from slope analysis, there is a slope 1 positive correlation between the distribution ratio and HNO_3 concentration. On the other hand, below 0.5 M HNO_3, there was no correlation. This suggests that

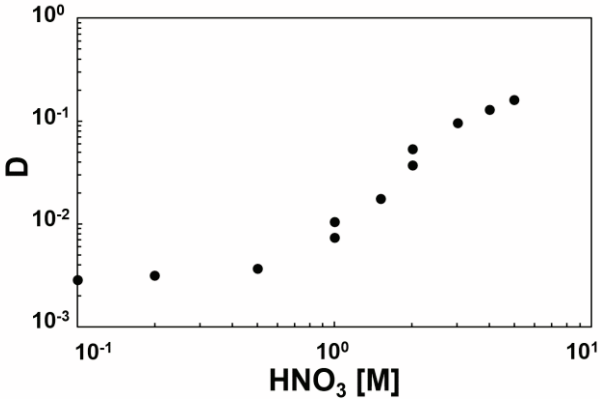

Fig. 1. Dependence of D on nitric acid concentration for Sb.

1) Sb and TDdDGA form a compound in a 1:1 ratio from HNO3 concentrations greater than 0.5 M and 2) the oxidation state of Sb changes around 0.5 M, due to the HNO_3 concentration. The possible ligands that can form at the HNO_3 concentrations used in this study is SbO_2^+, SbO^+, $HSbO_2$ and $Sb(OH)_6$- [3] which are either Sb(III) or Sb(V). This supports the observation of the correlation change at 0.5 M HNO_3.
The separation factor for Sb/Nd was 6.8×10^3 and 9.1×10^3 for 1M and 3M HNO_3 respectively. Furthermore, the distribution ratios of Sb (1M: 0.0054, 3M: 0.086) of and Nd (1M: 36.7, 3M: 786) show that the Sb and Nd can be clearly separated into different phases. Compared with TODGA [4], separation of Sb from a trivalent lanthanide or actinide element is efficient using TDdDGA.

CONCLUSIONS: The extraction behavior of Sb in varying nitric acid concentrations using TDdDGA was studied by using the solvent extraction method. The separation factor of Sb and Nd was also determined. Sb and TDdDGA had a 1:1 bond for HNO_3 concentrations of 0.5 M and above. TDdDGA is an efficient extractant to separate Sb from trivalent F block elements.

REFERENCES:
[1] Savantesson I. *et al.*, J. Inorg. Nucl. Chem., **41** 383-389 (1979).
[2] Meija J. *et al.*, Pure Appl. Chem., **88** 3 293-306 (2016).
[3] Pitman A. L. *et al.*, J. Electrochem. Soc., **104** 10 594-600 (1957).
[4] Zhu Z.-X *et al.*, Anal. Chim. Acta., **527** 2 163-168 (2004).

CO9-4 Electrochemical behavior of U^{3+} on Ru electrode in LiCl-KCl melts

T. Murakami[1], Y. Sakamura[1], K. Uozumi[1], M. Iizuka[1], and K. Takamiya[2]

[1]*Central Research Institute of Electric Power Industry*
[2]*Institute for Integrated Radiation and Nuclear Science, Kyoto University*

INTRODUCTION: Actinides form alloys with noble metal fission products during the irradiation of metallic fuel [1]. To understand the detailed behavior of actinides during electrorefining process of the irradiated metallic fuel, it is necessary to accumulate the basic knowledge on the electrochemical properties of the actinides-noble metal alloys. This study focused on U-Ru alloy and investigated the electrochemical behavior of U-Ru alloy in LiCl-KCl-UCl_3 melts at 773 K.

EXPERIMENTS: Electrochemical measurements were performed in an Ar atmosphere glove box. LiCl-KCl eutectic salt containing 0.16 mol% UCl_3 was melted at 773 K and used as the electrolyte. The working electrode was a Ru metal plate electrode (1mm×2mm×7mm (immersion depth into the melt), 99.5 % purity, Nilaco) or a W wire electrode (1 mmφ, 3 mm immersion depth into the melt). The counter electrode was a glassy carbon rod. Another W wire was used as the quasi reference electrode, of which potential was calibrated to Ag/AgCl reference electrode potential periodically.

RESULTS: Cyclic voltammogram of the W electrode in the LiCl-KCl-UCl_3 melts showed a cathodic (c1) and anodic (a1) current couple ascribing to U metal deposition and dissolution, respectively, at around -1.4 V (vs. Ag/AgCl) as seen in Fig. 1(a),

$$U^{3+} + 3e^- \rightleftarrows U \qquad (1)$$

In the cyclic voltammogram of the Ru electrode (Fig. 1(b)), cathodic current peaks (c2 and c3) were observed at more positive potential than that of U metal deposition (c1). Taking into account that five alloy phases, U_2Ru, URu, U_3Ru_4, U_3Ru_5 and URu_3, exist in U-Ru binary system [2], the cathodic current peaks, c2 and c3, were considered to be due to U-Ru alloy formation,

$$U^{3+} + xRu + 3e^- \rightarrow URu_x \qquad (2)$$

During the anodic scan in Fig. 1(b), an anodic current peak a4, a broad anodic current peak a3 and an anodic current peak with a shoulder a2 were found, which might have corresponded to U dissolution from the U-Ru alloy. For the purpose of determining the U-Ru alloy formation and deformation potentials in detail, a galvanostatic electrolysis at 0.1 mA was conducted using the Ru electrode on which U metal had been deposited by a potentiostatic electrolysis at -1.44 V for 10 s. As seen in Fig. 2, the potential of the Ru electrode was initially that of the deposited U metal. Then, the potential shifted to a positive direction along with time, showing several potential plateaus. A different pair of two U-Ru alloy phases should exist on the surface of the electrode at each potential plateau. Similar electrochemical measurements will be carried out at different temperature to obtain thermodynamic properties of U-Ru system.

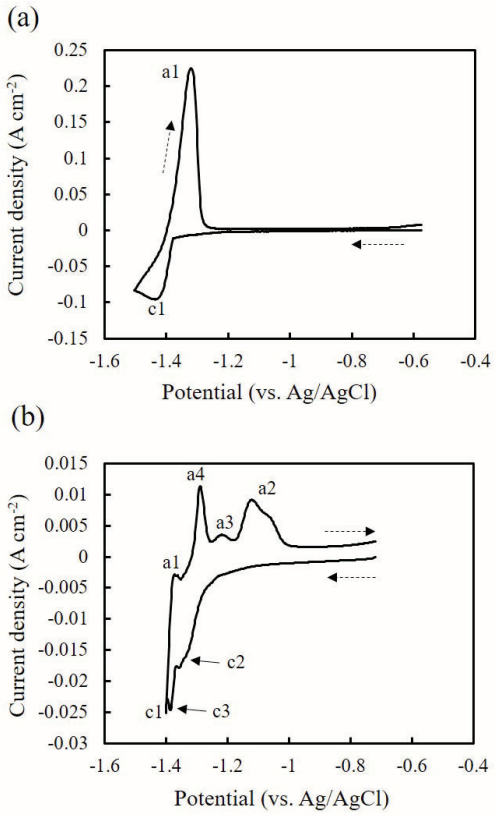

Fig. 1 Cyclic voltammograms of (a) W and (b) Ru electrodes in LiCl-KCl-0.16mol%UCl_3 melts at 773 K. Scan rate was 50 mVs^{-1}.

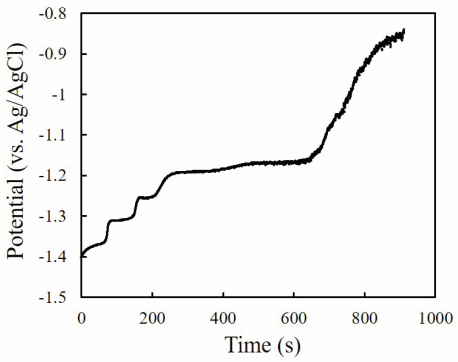

Fig. 2 Potential change of Ru electrode during galvanostatic electrolysis at 0.1 mA after U had been deposited on the Ru electrode by a potentiostatic electrolysis at -1.44 V for 10 s at 773 K.

REFERENCES:

[1] K. Inagaki *et al.*, Trans. Am. Nucl. Soc., **110** (2014) 786-787.
[2] T. B. Massalski ed., BINARY ALLOY PHASE DIAGRAMS SECOND EDITION, ASM International (1990).

CO9-5 Coprecipitation of Ca, Sr, Ba, and Ra with barium sulfate toward the chemical study of Nobelium

S. Hayami, Y. Kasamatsu, E. Watanabe, R. Nakanishi, K. Sawamura, K. Takamiya[1], and A. Shinohara

Graduate School of Science, Osaka University
[1]Institute for Integrated Radiation and Nuclear Science, Kyoto University

INTRODUCTION: Nobelium (No) with atomic number 102 is one of actinide elements. It is reported that stable oxidation state of No is +2 although those of the other heavy actinide elements are all +3. The chemical behavior of No is reported to be similar to that of group 2 elements in HCl [1]. However, it is difficult to investigate the chemical properties of No because of low production rates and short half-lives of the No nuclides. Fundamental experiments of group 2 elements for various chemical reactions are needed to establish new chemical experiments for No.

Previously, we reported new experimental method in which the hydroxide complexation of the target elements can be studied from the coprecipitation behavior with samarium hydroxide [2]. So far, we have qualitatively investigated the coprecipitation behaviors of various elements, and we successfully applied the method to element 104, rutherfordium (Rf) [3]. In this study, in order to elucidate the new chemical properties of No, we focused on the reaction with sulfate ions, and experimentally investigated the coprecipitation behavior of group 2 elements: Ca, Sr, Ba, and Ra, with $BaSO_4$ using ammonium sulfate in addition to sulfate precipitation behavior. Suitable experimental conditions for coprecipitation experiment of No were determined.

EXPERIMENTS: ^{85}Sr and ^{133}Ba samples were prepared by irradiating protons on pellet samples of RbCl for 1 h and of CsCl for 10 h using the AVF cyclotron at RCNP. ^{47}Ca sample was prepared by irradiating thermal neutrons (3×10^{13} cm^{-2} s^{-1}) on a powder sample of CaO for 1 h using the reactor at KURNS. They were separated from other majority of radioisotopes by cation-exchange and anion-exchange methods. ^{226}Ra tracer was used to investigate the behavior of Ra.

In the coprecipitation experiment, 20 μL (20 μg) of $BaCl_2$ solution was added into the RI tracer solution. In case of the precipitation experiment, 20-1000 μg of Sr or Ba chloride or ~10 mg of ^{47}CaO in aqueous solution was added. After mixing it, 2 mL of ammonium sulfate solution was added to generate sulfate precipitate. Then, these solutions (0.0010–2.0 M) were stirred for 5 min at room temperature. The precipitate was collected on a membrane filter by suction filtration. The precipitate and filtrate samples were subsequently dried on heater at 100 degree C, and were assayed by γ-ray measurements. The (co)precipitation yields were determined from the radioactivities of the γ rays counted.

RESULTS: The precipitation and coprecipitation yields were determined from the equation: A_{ppt} / (A_{ppt} + A_{fil}), where A represents the radioactivity, and ppt and fil indicate the precipitate and filtrate, respectively.

The coprecipitation behavior of Sr and Ba was basically consistent with that in precipitation, suggesting that sulfate precipitation (complexation) properties of the group 2 elements can be investigated based on their sulfate coprecipitation behavior. The coprecipitation yields of Ca, Sr, Ba, and Ra are shown in Fig.1. The yield increases with an increase of the atomic number; namely, ionic radius, and this trend is qualitatively consistent with that in their solubility products. The ionic radius of No is between Ca and Sr and thus, the yields of No might be between those of Ca and Sr. Maybe, due to the influence of strong relativistic effects on the orbital electrons in No, No will show different behavior from a simple prediction based on the tendency among group 2 elements. It is very intriguing to experimentally investigate the sulfate coprecipitation behavior of No with barium sulfate.

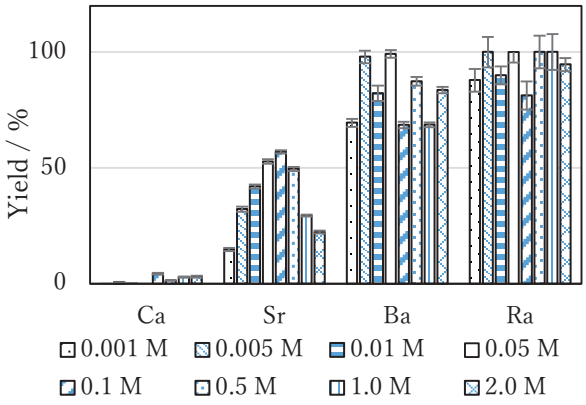

Fig. 1. The yields in sulfate coprecipitation experiment.

REFERENCES:

[1] R. J. Silva *et al*., J. Inorg. Chem., **13**, 9, 2233-2237 (1974).
[2] Y. Kasamatsu, *et al*., Appl. Radiat. Isot. **118**, 105-116 (2016).
[3] Y. Kasamatsu, *et al*., Nature Chem. **13**, 226–230, (2021).

CO9-6

Electrostatic Interaction between Fission Products and Solution Aerosol Particles in Radioaerosol Generation Process

K. Takamiya, T. Takeuchi, M. Inagaki, S. Sekimoto, Y. Oki and T. Ohtsuki

Institute for Integrated Radiation and Nuclear Science, Kyoto University

INTRODUCTION: One of the major forms which had spread radioactive materials in the environment at the severe accident of Fukushima Daiichi Nuclear Power Plant (FDNPP) is radioactive aerosol. Radioactive cesium and other radio isotopes released from the plant were transported by aerosol particles [1]. Part of the radioaerosol particles containing fission products were generated in the reactor building. Fission products released from nuclear fuels by high temperature might attach to surface of aerosol particles to generate radioaerosol particles. The generation processes of the radioaerosol particles are important to understand surrounding condition of nuclear fuels. Experimental approach to elucidate the generation process of the radioactive aerosols has been performed in our previous work [2-5]. In the present work, the attachment behavior of fission products to solution aerosol particles has been observed using neutron irradiated UO_2 powder as a source of fission products. Fission products released from the irradiated UO_2 by heating move with thermal velocity and might attach to surface of aerosol particle by electrostatic interaction.

EXPERIMENTS: The experimental method to generate and collect radioactive aerosol particles containing fission products is shown in the previous report [5]. Powder of UO_2 was encapsulated in a quartz tube under reduced pressure, and the quartz tube covered by a polyethylene tube was inserted into polyethylene capsule to irradiate neutrons using pneumatic transport system, Pn-2, at the power of 1MW on KUR. The amount of UO_2 was 10 mg, and the neutron irradiation time was 5 min. A few mg of irradiated UO_2 powder was extracted to another quartz tube placed in an electric furnace within 60 min after the irradiation. Fission products produced in the irradiated UO_2 powder was released by heating the furnace up to 1000°C. On the other hand, atomizer filled with 0.01 M solution generate solution aerosol particles. Four kinds of solution; sodium chloride, sodium bromide, sodium iodide and ammonium sulfate, were used in the present work. Both released fission products and solution aerosol particles were aspirated by a suction pomp to inject into a cylindrical chamber. Radioactive aerosol particles were generated by attaching fission products to aerosol particles in the chamber, and the difference of interaction time causes the difference of effective surface area of aerosol particles to attach fission products. The produced radioactive aerosol particles were collected on a polycarbonate filter at downstream of the chamber. The amount of fission products which was attached to aerosol particles were estimated by gamma-ray spectrometry for the filter using a Ge-detector (Canberra, GC2020). On the other hand, the total amount of fission products released from the irradiated UO_2 powder by heating was estimated by subtraction of gamma-ray spectra measured before and after release of fission products by heating.

RESULTS: The attachment ratio of short half-lived fission products; ^{91,92}Sr, ^{138}Cs, ^{134,135}I, ^{134}Te and ^{128}Sn, to NaCl , NaBr, NaI and $(NH_4)_2SO_4$ solution aerosol particles is estimated in the present work and shown in Figure 1. The attachment ratio of Sr isotopes is not shown in the figure because the ratio was below the detection limit. The varieties of attachment ratio of each nuclide to different solution aerosol are around one order. On the other hand, the differences of the ratio among nuclides to the same solution aerosol is up to three order. The result indicates that the attachment ratio depends on the chemical properties of fission products released from UO_2 more than those of solution aerosol particles. The fission products of ^{91,92}Sr, ^{138}Cs and ^{134,135}I are isotopes of important radionuclides; ^{90}Sr, ^{134,137}Cs and ^{131,133}I, which had been released from FDNPP and affected high dose rate in the environment. The result will contribute to the severe accident simulation in the aspect of estimating the radioactivity released from the power plant.

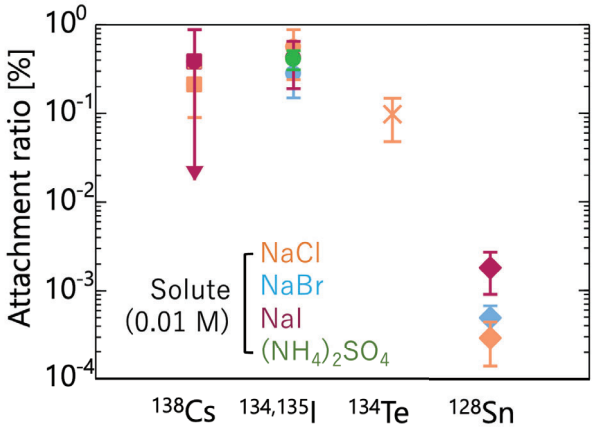

Fig. 1 Attachment ratio of five fission products to four different solution aerosol particles.

This work was supported by JSPS KAKENHI Grant Numbers JP24110005 and JP26286076.

REFERENCES:

[1] N. Kaneyasu et al. Env. Sci. Technol. **46**(11), 5720–5726 (2012).
[2] K. Takamiya et al., J. Radioanal. Nucl. Chem. **307** (2016) 2227-2230.
[3] K. Takamiya et al., J Radiat. Prot. Res. **41** (2016) 350–353.
[4] K. Takamiya et al., KURRI Progress Report 2017 (2018) 13-13.
[5] K. Takamiya et al., KURNS Progress Report 2018 (2019) 95-95.

CO10-1 Assessment of non-homogenous exposure of radiation workers in an accelerator facility – situation in the small linac facility -

M. KOWATARI, and T. KUBOTA[2]

[1]Center for Advanced Radiation Emergency Medicine, National Institutes for Quantum and Radiological Science and Technology
[2] Institute for Integrated Radiation and Nuclear Science, Kyoto University

INTRODUCTION: The annual dose limit of the lens of the eye for occupationally exposed personnel has been declined down to o 20 mSv averaged over five consecutive years and 50 mSv in any single year followed by the International Atomic Energy Agency [1], the European Union [2] and the United States [3].

The purpose of the study is to clarify the situations where inhomogeneous exposure is taken place for radiation workers engaged in the accelerator facility and to assess whether the additional monitoring of the eye lens dose should be performed for the workers. The authors introduce a quantitative index, homogenous index (HI), which is defined as the ratio of the personal dose equivalent for the eye lens and the extremity monitoring to that for the whole-body monitoring. The HIs were then experimentally estimated using the physical and mathematical phantoms for specific works accompanying inhomogeneous exposure to radiation from activated materials.

EXPERIMENTS: The authors focused on the exposure situation of radiation workers who are engaged in the handling of the activated target in the linac facility. As shown in the Figure 1, the physical phantom was placed in the workplace to mimic the respective work. The Optically Stimulated Luminescence (OSL) dosimeters (nanoDot^{TM}, Nagase Landauer Ltd.) were put on the water-filled phantom. The OSL dosimeters were put on the fingers and palms of the physical phantom as well as positions of eye lens, neck and chest. The ambient dose equivalent rate at the distance of 1 m from the target was measured to be 600 μSv h^{-1}. The physical phantom with the OSL dosimeters was set for 2 hours and the OSL dosimeters were read after the irradiation. The Monte Carlo calculations were carried out to estimate the HIs in the actual situations, introducing the PHITS 3.06 and the mathematical phantom.

Figure 1 Experimental setup for mimicing the actual radiation work engaged in the linac facility

RESULTS: Comparison of the ratio of the eye lens dose or the extremity dose to the trunk dose measured on the physical phantom and calculated by Monte Carlo calculation is listed in the Table 1. To simulate the Ta target handling, the physical phantom was set close to the target and put the palm onto Ta target directly, As shown in the table 1, the theoretically estimated HIs can predict the measured HIs accurately. As for extremity, the discrepancy between analytically estimated and measured HIs were found to be more than factor 2. On the other hand, calculated HIs reproduce the measured HIs within uncertainties. This would be explained by the main source of exposure is gamma rays from ^{182}Ta and well simulated geometry.

REFERENCES:

[1] International Atomic Energy Agency (IAEA). Radiation protection and safety of radiation sources: International Basic Safety Standards. General Safety Requirements Part 3.
[2] European Union (EU). Basic safety standards for protection against the dangers arising from exposure to ionizing radiation. Council Directive 2013/59/EURATOM.
[3] NCRP Commentary No. 26 - Guidance on Radiation Dose Limits for the Lens of the Eye (2016). ISBN 978-0-913392-17-1.

Table 1 Evaluated HIs from measurement using the physical phantom and the OSLs in the exposure situation which the adjustment of the target is simulated

	Experimentally obtained HI^{eye} or HI^{ext}	Ratio analytically estimated from the inverse square law	HI^{eye} or HI^{ext} estimated by Monte Carlo calculations
Right eye lens dose vs Trunk dose $H_p(3)_{eye}$ / $H_p(10)_{trunk}$	0.42 ± 0.02	0.39	0.38 ± 0.06
Left eye lens dose vs Trunk dose $H_p(3)_{eye}$ / $H_p(10)_{trunk}$	0.37 ± 0.02	0.39	0.38 ± 0.06
Right finger dose vs Trunk dose $H_p(0.07)_{ext}$ / $H_p(10)_{trunk}$	33.5 ± 0.7	63.1	35.9 ± 2.3
Left finger dose vs Trunk dose $H_p(0.07)_{ext}$ / $H_p(10)_{trunk}$	1.84 ± 0.04	5.15	1.40 ± 0.11

CO10-2 Effective Measures on Safety, Security, Hygiene and Disaster Prevention in Laboratories

T. Iimoto[1], Y. Igarashi[1], J. Nakayama[1], R. Miura[1], K. Yamamoto[1], E.W.Katengeza[1], M.M. Hasan[1], H. Koike[1], Q. Jin[1], K. Fukuda[1], T. Takahashi[2]

[1] The University of Tokyo

[2] Integrated Radiation and Nuclear Science, Kyoto University

INTRODUCTION: Important aspects of the study can be found in the following keywords, such as safety, security, hygiene and disaster prevention. Nuclear research reactor is one of representative facilities together with these keywords under their operation. It is effective to investigate the latest status on practical measures on these keywords in various facilities including nuclear research reactors, to compare each other among facilities, and to discuss more optimized ones for our positive safety management. Through this process, it is also essential to investigate the latest international and/or national regulations and the movement of revision of them. In addition, development of human resource and public literacy on nuclear science and technology is also within the scope of the research. The total discussion contents and their fruits are directly useful for all relating laboratories.

RESEARCH APPROACH:

General research approach is as follows.

- Measures of safety management during operation or standstill status of the real facilities would be investigated. This information would be used for our research discussion on the positive and more optimized safety management.
- It would not be a single year research, but maybe two to three years research for one theme.
- Information source of facilities would not be only KUR, KUCA or the other facilities in Kyoto University, but also the Kinki university research nuclear reactor or the facility of National Institute of Fusion Science, etc. This research is an active joint-research with these relating facilities and positive researchers on safety management.
- One of the distinctive features of this research is to involve office staffs as cooperators as well as researchers and technical staffs. In The University of Tokyo, most of the members in Division for Environment, Health and Safety are office staffs who knows real situation of safety management in laboratories very well.

Concrete discussion target in FY of 2020 was determined as following two; “developing a set of educational videos for safety managers and workers in universities on application of small amount of U and Th” and “opinion survey on radiation safety culture activity” through our member discussion.

DEVELOPING EDUCATIONAL VIDEOS IN UNIV. FOR SMALL AMOUNT U & Th APPLICATION:

Safety education system for managers and users of small amounts of U and Th had been discussed to standardize it in universities by the FY 2019. The discussion fruits were published in the early 2020 as the reference [1]. Based on the results, we developed a set of new safety educational videos, which is 5-10 min for each; (1) Domestic and international situation regarding nuclear material management (2) Basics of radiation (3) Radiation exposure and its human body effects (4) Properties of nuclear material and precautions for handling (5) State System of Accounting for and Control: SSAC (6) Trouble cases related to K-facility (7) Points to keep in mind for workers in research reactors, etc. These videos will be opened and used from FY 2021 in The University of Tokyo.

OPINION SURVEY ON RADIATION SAFETY CULTURE ACTIVITY:

We conducted questionnaires on safety culture mainly to radiation safety managers at radiation facilities. This has two objectives: (a) Extracting keywords for fostering a safety culture at radiation facilities mainly for radiation safety managers; (b) Organize and analyze trends in opinions of radiation safety managers and radiation workers. A deeper level of information is needed for Objective (a). Therefore, an open-ended questionnaire was adopted. Objective (b) requires a lot of data to analyze it. For this reason, a selective questionnaire was adopted. The questionnaire showed trends based mainly on differences in the size and purpose of radiation facilities. There was a big difference in the tendency to recognize "accidents, incidents, troubles and failure cases" between small- and large-scale facilities. Many respondents from large-scale facilities answered that they could easily share the latest related information in their facilities. This is probably because large-scale facilities usually have existing systems and chances to share information relating accidents in contrast to small-scale facilities. A part of the discussion fruits is presented in International Conference on Radiation Safety: Improving Radiation Protection in Practice hosted by IAEA Headquarters, held in Dec. 2020. We continue the analysis of the questionnaire responds.

REFERENCES:

[1] K. Yasuda, M. Takahashi, T.Iimoto *et.al*., RADIOISOTOPES, **69**, 55–65 (2020).

CO10-3 Mass balance trend of organochlorine and organobromine in a sediment core from Beppu Bay

K. Ito[1], T. Fujimori[2], K. Oshita[1], S. Fukutani[3], S. Takahashi[4], H. Q. Anh.[4]

[1]*Department of Environmental Engineering, Graduate School of Engineering, Kyoto University*

[2]*Faculty of Advanced Science and Technology, Ryukoku University*

[3] *KURNS*

[4] *Graduate School of Agriculture, Ehime University*

INTRODUCTION: Among organochlorine and bromine compounds, persistent organic pollutants (POPs) are subject to international regulation of production and use and reduction of unintentional generation under the Stockholm Convention because they are persistent, highly accumulative, and long-lasting. The number of compounds registered as POPs is increasing, and some of the alternatives have been reported to have the same properties as POPs. Therefore, a comprehensive evaluation is needed. POPs released into the environment are known to be distributed in sediment [1].

Therefore, the purpose of this study was to evaluate the potential pollution in the environment using sediment samples from Beppu Bay. The concentration change of the fraction of extractable organohalogens (EOX : X = Cl, Br) with a molecular weight of 1000 g/mol or less (EOX-L) in the sediment was compared with the concentration changes of individual substances (Polychlorinated Biphenyls (PCBs), Polybrominated diphenyl ethers (PBDEs) and Decabromo diphenyl ethane (DBDPE)).

EXPERIMENTS: The samples were collected from Beppu Bay, where well-preserved sediment cores are available. 2 g of freeze-dried sample was Soxhlet extracted with toluene and the extract was replaced with hexane. Inorganic chlorine and bromine were washed out, and then fractionation was carried out using gel permeation column chromatography based on a molecular weight of 1000 g/mol. Each extract was concentrated to 1-2 mL, and it was diluted to 5mL with hexane. 2 mL of diluted extract was nitrogen-concentrated to 1 mL and placed in a polyethylene (PE) bag along with filter paper. The mixture was dried under normal temperature and pressure until the liquid components were completely volatilized, and then sealed with a sealer. The samples were folded into 1.5 cm squares, placed in PE bags, double sealed with PE bags, and finally sealed in thin PE bags. Samples were irradiated for 15 min with a thermal neutron flux of $2.0–2.4\times10^{13}$ $cm^{-2}\cdot S^{-1}$ at KURNS. ^{38}Cl ($t_{1/2}$ = 37.18 min, E_γ = 1642, 2168 keV) and ^{80}Br ($t_{1/2}$ = 17.6 min, Eγ = 616 keV) were measured by using a Ge semiconductor detector for 60 sec. In the same way, samples of PE bag only, filter paper and PE bag only were also prepared and measured. The concentration of halogens in the sediment samples was determined by excluding the amount of halogens from the PE bags and filter papers.

RESULTS: The experimental results for chlorine and bromine are shown in Figure1, and the concentration of PCBs, PBDEs and DBDPE were reported in the previous reports [2,3]. The amount of chlorine in the samples was found to exist in the ratio of sediment-derived: PE bag-derived: filter paper-derived = 1.0: 1.6: 5.4. Due to the high amount of non sediment-derived chlorine, the calculation of some samples resulted in negative values. In Fig.1(A), The concentrations of EOCl-L and PCBs both increased around 1970, but since 1980, PCBs concentrations have been decreasing while EOCl-L concentrations have been increasing, indicating different trends. In Figure1(B), EOBr, PBDEs, and DBDPE increased from 1980 to 1995, but PBDEs have been decreasing since 1995, while EOBr-L and DBDPE have been increasing.

Although there is a large difference in the concentrations of EOX and individual substances, the timing of the increase in EOCl-L and PCBs around 1970 and the increase in EOBr-L, PBDEs, and DBDPE around 1980 coincides with each other, suggesting that changes in the concentrations of POPs and other substances have some effect on EOX-L. Therefore, EOX-L can be used as an indicator for monitoring the contamination status of POPs and other POPs-like substances. In the future, it is necessary to improve the sample preparation method of chlorine in neutron activation analysis and to investigate the sediment in other areas.

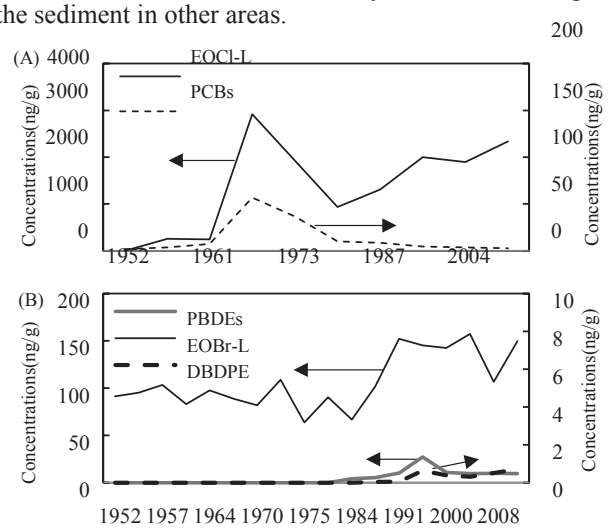

Fig. 1. (A) Concentrations of EOCl-L and PCBs. (B) Concentrations of EOBr-L, PBDEs and DBDPE.

ACKNOWLEDGEMENT:
We would like to thank Mr. Kota Mukai for his analytical support.

REFERENCES:

[1] P. Bigus *et al*., *Marine Pollution. Bulletin*., **78** (2014) 26-42. 1-2.

[2] S. Takahashi *et al*., *Science of Total Environment*., **743** (2020) 140763.

[3] Q. H. Anh *et al*., *Chemosphere*., 266(2021) 12918.

R2040

CO10-4 Application of KURAMA-II to Radiation Monitoring of Public Facilities in Fukushima Prefecture

A. Maekawa, K. Kusakabe, H. Inoue and M. Tanigaki[1]

Fukushima Prefectural Centre for Environmental Creation
[1]Institute for Integrated Radiation and Nuclear Science, Kyoto University

INTRODUCTION: KURAMA (Kyoto University RAdiation MApping system)-II is a radiation measurement system characterized by its compactness, autonomous operation, and acquisition of pulse-height spectrum data [1]. KURAMA-II measures ambient dose equivalent rate $H^*(10)$ (hereafter referred to as air dose rate) and GPS position and automatically transmits them to a dedicated cloud server. Air dose rate maps and pulse-height spectra are easily checked by accessing the server via the Internet (Figs. 1 and 2). We used the system in a backpack style (Fig. 3) and evaluated its effectiveness for radiation monitoring of public facilities in Fukushima prefecture.
EXPERIMENTS: The air dose rates of five public facilities were measured by walking with a KURAMA-II in a backpack. The situation of the sites are as follows.

Fig. 1. A typical example of air dose rate maps obtained by KURAMA-II measurement.

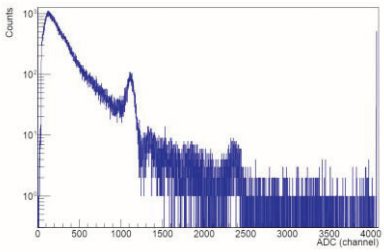

Fig. 2. A typical example of pulse-height spectra obtained by KURAMA-II measurement.

Fig. 3. KURAMA-II in a backpack.

Site A: School grounds and surrounding road
Site B: Gymnasium grounds and surrounding road
Site C: Community center grounds and surrounding road
Site D: School grounds and surrounding road
Site E: Park in forest

A CsI(Tl) scintillation detector (C12137-01, Hamamatsu Photonics) was used for measurement. The air dose rate and GPS position were measured every 3 seconds. The same route was also measured by walking with a GAMMA-plotter H (Japan Radiation Engineering) to examine the dependences of the result towards the walk survey systems. Air dose rates at 10-14 points in each site were measured by a NaI(Tl) scintillation survey meter (TCS-172B, Hitachi) for validity confirmation.
RESULTS: Air dose rates measured by KURAMA-II and GAMMA-plotter H were basically the same at all measurement sites (Fig. 4), and they were well consistent with the results from the survey meter.
Additionally, the air dose rate owing to artificial radionuclide were separately evaluated using pulse-height spectrum data by KURAMA-II, referring to previous report [2]. As shown in Table 1, the mean air dose rates owing to artificial radionuclides were 0.035-0.102 μSv/h and the ratio towards the total air dose rate was 0.43-0.67.
In conclusion, KURAMA-II showed the sufficient performance for monitoring of public facilities.

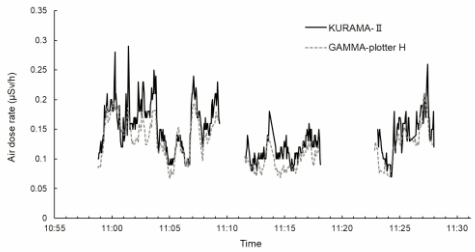

Fig. 4. A typical result of air dose rates measured by KURAMA-II and GAMMA-plotter H.

Table 1. The air dose rate owing to artificial radionuclide evaluated by KURAMA-II. The values are averaged for each measurement site.

Site	Mean air dose rate (μSv/h)		Ratio (Artificial/Total)
	Total	Artificial	
A	0.099	0.062	0.62
B	0.114	0.063	0.55
C	0.083	0.035	0.43
D	0.140	0.090	0.64
E	0.153	0.102	0.67

REFERENCES:
[1] M. Tanigaki *et al.*, Nucl. Instrum. Meth. Phys. Res. **781** (2015) 57–64.
[2] M. Andoh *et al.*, T. J. At. Energy Soc. Jpn., **16**[2] (2017) 63-80 [in Japanese].

CO10-5 Theoretical Study on Soil Adsorption/Desorption Characteristics of Cs and Sr Using PHREEQC

K. Yoshida[1], M. Yoneda[1], Y. Shimada[1], S. Fukutani[2], M. Ikegami[2]

[1]*Graduate School of Engineering, Kyoto University*
[2]*Institute for Integrated Radiation and Nuclear Science, Kyoto University*

INTRODUCTION: To remediate the contamination by radioactive Cs and Sr caused by an atomic power plant accident, it is necessary to elucidate their elution mechanism in soil. This study tries to estimate elution quantity of Cs and Sr considering competitive sorption by other cations using PHREEQC which is a free and versatile geochemical code.

THEORY AND EXPERIMENTS: Ca^{2+}, K^+, Mg^{2+}, and NH_4^+ are considered as cations which can adsorb to RES (Regular ion Exchange Site) and can be competitive with Sr^{2+} adsorption. K^+ and NH_4^+ are considered as cations which can adsorb to FES (Frayed Edge Site which has high adsorption-selectivity of Cs) and can be competitive with Cs^+ adsorption. These cations adsorption to each site was analyzed by PHREEQC with the surface complex model.

For modelling the adsorption site in PHREEQC, adsorption reaction formula and equilibrium constants are necessary to be defined. The equilibrium constants regarding RES were defined as follows:

$$K_{r-Sr} = [SrXr^+]/([Sr^{2+}][Xr^-]) \quad (1)$$
$$K_{r-Ca} = [CaXr^+]/([Ca^{2+}][Xr^-]) \quad (2)$$
$$K_{r-K} = [KXr]/([K^+][Xr^-]) \quad (3)$$
$$K_{r-Mg} = [MgXr^+]/([Mg^{2+}][Xr^-]) \quad (4)$$
$$K_{r-NH4} = [NH_4Xr]/([NH_4^+][Xr^-]) \quad (5)$$

Where,
K_{r-M} : equilibrium constant of cation M to RES (L/meq),
$[MXr]$: adsorption quantity of cation M(meq/100g-soil),
$[M^+]$: concentration of cation M in the solution(meq/L),
$[Xr^-]$: quantity of free site of RES(meq/100g-soil).
All cations are considered exchangeable and quantity of RES is considered to be same as that of CEC (Cation Exchange Capacity), and so, sum of cations existed in the solution and cations adsorbed on RES is considered as the quantity of exchangeable cations. Based on these assumptions, each equilibrium constant regarding RES can be estimated by measurement of CEC of the soil, quantity of each exchangeable ion, and concentration of each cation in the solution, and then, adsorption site of RES can be numerically defined in PHREEQC.

Adsorption reactions to FES are defined as follows:

$$K_{f-Cs} = [CsXf]/([Cs^+][Xf^-]) \quad (6)$$
$$K_{f-K} = [KXf]/([K^+][Xf^-]) \quad (7)$$
$$K_{f-NH4} = [NH_4Xf]/([NH_4^+][Xf^-]) \quad (8)$$

Where,
K_{f-M} : equilibrium constant of cation M to FES (L/meq),
$[MXf]$: quantity of adsorbed cation M (meq/100g-soil),
$[Xf^-]$: quantity of free site of FES (meq/100g-soil).
Assuming that only Cs is adsorbed to FES at the beginning, that quantity of Cs adsorbed to FES is small enough compared to the quantity of FES, and that all Cs adsorbed to FES is considered exchangeable, equilibrium constant of each cation to FES can be estimated by considering selectivity constant of Cs^+ to K^+ and NH_4^+ for adsorption to FES and by measurement of quantity of exchangeable Cs and the concentration of Cs in the solution, and then, adsorption characteristics of FES can be numerically defined in PHREEQC for calculation of adsorption reaction. Therefore, measurement of concentration of Sr^{2+}, Ca^{2+}, K^+, Mg^{2+}, NH_4^+, and Cs^+ in the solution, their exchangeable quantities, and CEC of the soil can make it possible to estimate equilibrium constants of each cation to RES and FES.

So, some experiments to measure quantity of each exchangeable cation and CEC were carried out, and elution tests by pure water were carried out to measure concentration of each cation in the eluting solution.

In this study, soils got from cedar forest (soil A) and red pine forest (soil B) in the experiment forest of Iwate University were used. The soils were sieved with 2mm sieve, and then, dried one day in 45 °C for the untreated soil or heated one hour in 500 °C for the heat treatment soil. The change of the concentration of each cation was measured for the test of each cation addition to the solution. Experiments using each soil were carried out triplicate and their averages were considered as the measurement values.

RESULTS: Using the equilibrium constants obtained by the experiments, the results of the experiments for the untreated soil and the heat treatment soil were tried to be simulated by the calculation with PHREEQC. Comparing the results simulated by FHREEQC to the results of the experiments, the two results matched each other in the precision of one effective digit regarding Sr, Ca, and K in the case of heat treatment soil. However, the calculated values of the concentration of Cs in the solution were two or three times higher than that obtained by the experiment in the all cases. Regarding untreated soil, simulated concentration of Sr matched in the precision of one efficient digit to that obtained by the experiment in the case of K and NH_4 addition, however, the simulated results was much more different from that obtained by the experiments in the cases of Ca and Mg addition. The simulated concentration of Cs in the solution was 10 to 15 times higher than that obtained by the experiments in the most cases. Especially, the difference was bigger in the case of K addition. To improve the precision of the simulation by FREEQC, it seems necessary to consider adsorption of hydrogen ion, quantity of originally adsorbed Cs at FES and RES, and so on.

CO10-6 An Attempt to Measure Size Distribution of Radioactive Aerosol Particles Produced in an Electron LINAC Facility Using a Diffusion Battery and Imaging Plates

Y. Oki and R. Taniguchi[1]

Institute for Integrated Radiation and Nuclear Science, Kyoto University
[1]Faculty of Engineering, Kyoto University

INTRODUCTION: High intensity accelerators have been developed for various purposes such as isotope production and cancer therapy. Understanding of the nature of radioactive species in air of the accelerator rooms is very important to maintain the safety of accelerator and radiation in the high intensity accelerators.

Radiation-induced aerosol particles in the size range of several nm to ca. 100 nm are produced in addition to radioactive gases in the air of the accelerator rooms during machine operation. The size for the radioactive aerosol particles was often measured using wire screen techniques in accelerator facilities. A combination technique with imaging plate (IP) was employed in a proton accelerator facility [1].

In this work, an attempt was made to measure the size of ^{13}N-bearing aerosol particles using the combination technique of screen-type diffusion battery (SDB) and IPs in an electron linear accelerator facility.

EXPERIMENTS:

Principle of SDB: When very fine aerosol particles pass through a stack of wire screens, a part of the particles is deposited on the wire surface of the screens by their diffusion according to their particle size. The loss by the screens is expressed as a function of particle size, coarseness and number of screens, and flow rate of particles. The radioactivity-based size distribution of the aerosol particles can be calculated by measuring the penetration ratio (A/A_0), where A_0 and A are activity of the nuclide of the aerosol particles before and after penetrating screens, respectively.

Measurement method: The SDB employed in this work consists of 40 pieces of 500-mesh stainless steel wire screen and a backup filter (PTFE membrane filter). After collection of the aerosol particles with the SDB, selected screens and the backup filter were measured with an IP.

Formation and collection of radiation-induced aerosols: The air-irradiation experiment was carried out in the 46-MeV electron LINAC of the Institute for Integrated Radiation and Nuclear Science, Kyoto University (KURNS). An irradiation chamber was placed at a rear position of a platinum target in the target room. During the irradiation, aerosol-free air was introduced to the chamber from the experiment room next to the target room. The target was bombarded with a 30-MeV electron beam to produce bremsstrahlung. The bremsstrahlung ionizes air and produces the radiation-induced aerosol. The beam current was ca. 100 μA. The irradiated air was sampled with the SDB at the measurement station in the experiment room.

Estimation of size distribution of radioactive aerosol particles: The IP image of the selected screens and the backup filter was simultaneously taken using a single large IP (Size: 43 x 35 cm). The penetration ratio for the i-th screen was calculated by the dividing total activity of the screens downstream of the i-th screen and the backup filter by the total activity of all screens and the backup filter. In this calculation, the activity of each 500-mesh screen was estimated by fitting of the intensity of photostimulated luminescence (PSL) of the measured 500-mesh screens.

RESULTS: A part of the irradiated air was introduced to an SMPS (Scanning Mobility Particle Sizer) to monitor the number-based aerosol size simultaneously with the SDB collection. A stable lognormal size distribution was observed during the collection of the aerosol by the SMPS measurement.

The penetration ratio for each screen was calculated as described above. The curve of the penetration ratios was fitted to a theoretical function [2] for lognormal distributions to obtain the geometric mean and geometric standard deviation of particle diameter. When the air was introduced to the chamber and the SDB at the same flow rate of 12 L/min, the preliminary result of the size was ca. 60 nm.in diameter, which coincided with the particle size previously reported by another method [3].

Most of ^{13}N atoms formed in the air exist as gas forms in accelerator rooms. Even a small amount of condensation of acidic radioactive gases like $H^{13}NO_3$ gas on the screen surface may influence greatly the estimation of aerosol size. An effective compensation technique was discussed to eliminate the influence.

REFERENCES:

[1] Y. Oki *et al.*, J. Radiat. Prot. Res., **41** (2016) 216-221.
[2] Y.S. Cheng and H.C. Yeh, J. Aerosol Sci., **11** (1980) 313-320.
[3] Y. Oki, KURNS Prog. Rep., (2019) CO10-7.

CO12-1 Study on Superposition of Coherent Transition Radiation Using a Ring Resonator

N. Sei, T. Takahashi[1]

Research Institute for Measurement and Analytical Instrumentation, National Institute of Advanced Industrial Science and Technology
[1]Institute for Integrated Radiation and Nuclear Science, Kyoto University

INTRODUCTION: As peak power of light sources in the terahertz (THz) region increase notably, novel applications using THz lights are pioneered to solve various issues. THz lights are no longer just probe lights for inspections. It has been reported that a THz light beam causes dissolution of a fibrous peptide [1], and it is expected that the THz light beam is applied to a new treatment technology. Developments of intense THz light sources will become increasingly important.

A key technique for increasing power of light pulses is to superimpose the electromagnetic field of the light pulses. We have confirmed that coherent diffraction radiation nonlinearly amplifies at resonant frequencies by using periodical diffractors [2]. In order to further develop this technique, we have experimented with confining and superimposing coherent radiation generated by a pulse train of electron bunches in a ring-type resonator. Although a resonant light extracted from the ring-type resonator though a coupling hole of a mirror was observed, a background level of coherent diffraction radiation was high. Therefor, in order to decrease the background, we performed experiments with a thin substrate inserted in the resonator as a coupling device.

EXPERIMENTS: The experiments were performed using an electron beam with the energy of 42 MeV and the macropulse duration of 47 ns in an L-band linac at Kyoto University Institute for Integrated Radiation and Nuclear Science. The repetition frequency of the macropulse of the electron beam was 30 Hz. Schematic layout of the ring-type resonator used in the experiments is shown in Fig. 1. The electron beam generated coherent transition radiation (CTR) at two thin polyethylene films vapor-deposited with aluminum when it passed through them. The thickness of the polyethylene film was 6 μm. The current of the electron beam passed through the polyethylene film was approximately 60 μA. These polyethylene films were also used as mirrors constituting the ring resonator. The two CTR beams were confined in the ring resonator composed of four mirrors, which included two parabolic mirrors with the focal length of 508 mm. The length of the resonator was 922 mm, which was four times the interval of the electron bunches. In order to extract the resonate CTR beam from the optical cavity, a ZEONEX substrate with a thickness of 3 mm was inserted into the resonator at an angle of 45 degrees with respect to the optical axis. The ZEONEX was almost transparent in a frequency range below 1 THz, and its refractive index was 1.53. Although the CER was reflected on both sides of the substrate, the two reflected beams did not interfere due to the thickness of the substrate.

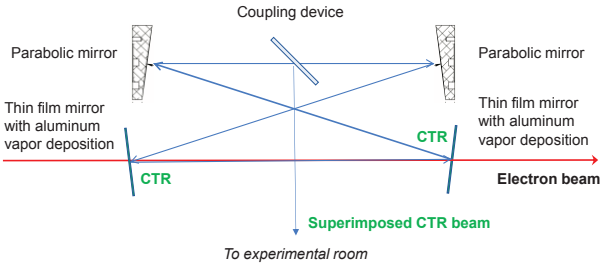

Fig. 1 Schematic layout of the ring-type resonator.

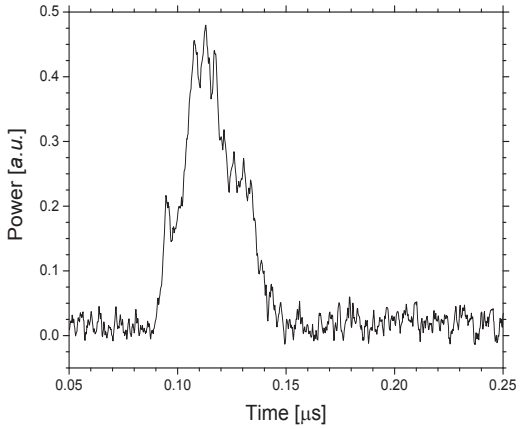

Fig. 2 Measured CTR power extracted from the ring-type resonator in the D-band.

RESULTS: The CTR beam transported to the experimental room was measured by a D-band diode detector (Militech Inc., DXP-06). As shown in Fig. 2, several peaks were observed in the macropulse of the measured CTR power but did not have periodicity. Because micropulse structure of the CTR beam disappeared in the macropulse, it was considered that the ring-type resonator deviated from the resonance condition. By adjusting position of a stage on which the parabolic mirror was installed, the resonance conditions could have been improved. Moreover, it was difficult to detect detailed structure in the macropulse due to the low CTR power. To increase efficiency of CTR extraction from the resonator, we consider using a material with a high refractive index as the coupling device. We also plan to use thin coupling device so that the reflected CTR beams on the both sides of the coupling device can be coherent.

REFERENCES:

[1] T. Kawasaki *et al.*, Sci. Rep. **9** (2019) 10636.
[2] N. Sei and T. Takahashi, Sci. Rep. **10** (2020) 7526.

CO12-2 Empirical Research on the Effective Introduction and Unification of Ambient Dose Rate Mapping Methods Using Car-borne Survey System for Monitoring of Nuclear Facilities by Local Governments

H. Tanaka[1], M. Tanigaki[2]

[1]*Japan Chemical Analysis Center*
[2]*Institute for Integrated Radiation and Nuclear Science, Kyoto University*

INTRODUCTION: The car-borne survey of ambient dose rate is categorized by NRA (Nuclear Regulation Authority) as one of the monitoring methods in emergency situations at nuclear facilities. Therefore, it is important to effectively introduce and standardize the method for mapping the ambient dose rate measured by the car-borne survey conducted by local governments.
This time, we researched the nationwide unification of mapping procedure of carborne surveys. In this study, ambient dose rate maps obtained by KURAMA-II (Kyoto University Radiation Mapping system) [1] (Fig.1) were used.

EXPERIMENTS: The data for the mapping were measured using KURAMA-II in the several areas in Japan where the ambient dose rate levels are different:
(1) Data measured at around the TEPCO Fukushima Daiichi Nuclear Power Plant (Fukushima prefecture) [2]
(2) Data measured at low level areas of ambient dose rate level (Iwate prefecture and Shizuoka prefecture).
The acquired data were stored in the cloud server for KURAMA-II of Kyoto university, and each ambient dose rate map was created.
A questionnaire survey about effectiveness of each map was conducted to the staff of local governments who should be involved to car-borne surveys for monitoring nuclear facilities.

RESULTS: As shown in Fig. 2, ambient dose rate maps were created for each data.

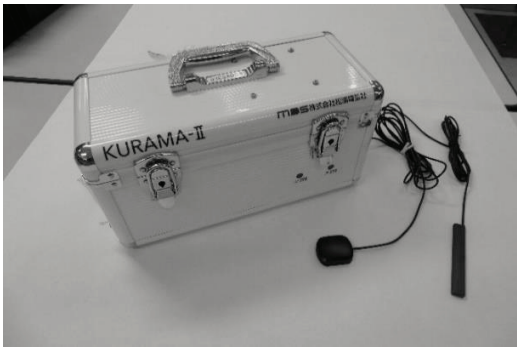

Fig.1 KURAMA-II.

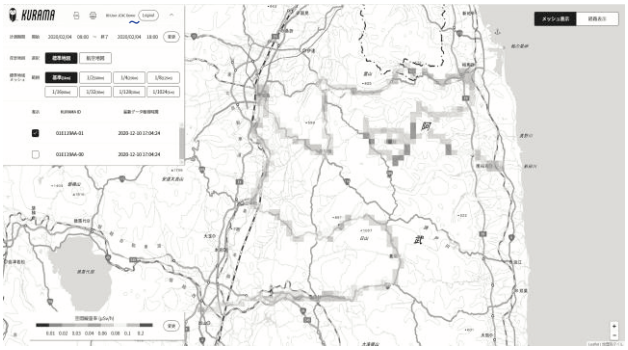

Fig.2 Ambient dose rate map by data measured in Fukushima prefecture.

Nine responses were obtained from local government organizations and individuals belonging to them.
From the results of the questionnaire, the current ambient dose rate maps basically have essential information and functions required by the local government for emergency monitoring.
Followings are comments to the current ambient dose rate map. We continue to work for the improvements to the map based on these comments.

Information that should be implemented to the map
- Landmarks (public facilities such as schools and government offices, shelters, etc.)
- Distance display on concentric circles from nuclear facilities, distance scale, 16 directions. (It would be effective to be able to select display / non-display by selection.)
- Area display of nuclear disaster countermeasure priority areas (PAZ, UPZ, etc.)
- Boundary display of evacuation units

Functions that should be implemented to the map
- Cooperation with the national emergency radiation monitoring information sharing system
- Easy-to-read color of ambient dose rate display
- Spectrum display
- Easy-to-input of measurement period

REFERENCES:
[1] M. Tanigaki et al., Nucl. Instrum. Meth. **A781**(2015)57-64.
[2] Japan Chemical Analysis Center, Report of the survey of technical specifications with various carborne survey systems granted by NRA (2020).

CO12-3 Development of neutron imager based on hole-type MPGD with glass capillary plate

F. Tokanai[1], T. Moriya[1], T. Sumiyoshi[2], H. Kondo[3], H. Sugiyama[3], T. Okada[3], M. Hino[4], T. Oda[4]

[1]*Faculty of Science, Yamagata University*
[2]*Graduate School of Science, Tokyo Metropolitan University*
[3]*Electron Tube Division, Hamamatsu Photonics K. K.*
[3]*Institute for Integrated Radiation and Nuclear Science, Kyoto University*

INTRODUCTION: High position resolution with a moderate effective area is required in practical applications of neutron imaging. We have been developing a high-spatial-resolution neutron gas scintillation imager (n-GSI) with a capillary plate gas detector (CPGD) [1,2]. Fig. 1 shows a schematic view of the n-GSI. It consists of a $^{10}B_4C$ converter layer, a CPGD filled with a Ne (90%) + CF_4 (10%) gas mixture, a mirror, a lens optics, an imaging intensifier (I.I.) unit, and a CMOS camera. Neutrons passing through a sample enter the n-GSI. The $^{10}B_4C$ converter is directly mounted on the inlet surface of the CP. Charged particles (α-rays and ^{7}Li nuclei) are generated by a nuclear reaction between incident neutrons and ^{10}B. The charged particles ionize the gas molecules, resulting in the generation of electrons in the gas. Scintillation light is emitted from capillary holes upon gas excitation, simultaneously with electron multiplication. The scintillation light from each capillary is read out as the imaging signal through the optical mirror and lens system using an I.I. CMOS camera.

Since the ^{10}B converter is directly mounted on the inlet surface of the CP, the track length of the charged particles is restricted to within the capillary. Thus, the spatial resolution of incident neutrons is expected to be close to the capillary diameter. In this measurement, the imaging capability was investigated through comparison with a conventional neutron scintillation detector.

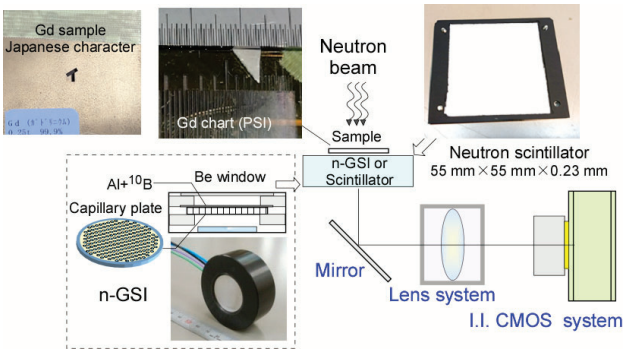

Fig. 1. Experimental setup of the n-GSI. A conventional neutron scintillation detector (NSD) is installed in place of the n-GSI.

EXPERIMENTS: The imaging capability of the n-GSI were investigated using the cold neutron beamline CN-3 installed at the Kyoto University Reactor (KUR) [3]. The neutron wavelength giving the maximum intensity and the total flux of the CN-3 guide tube were 2 Å and 3.8 × 10^6 neutrons cm^{-2} s^{-1}, respectively. The n-GSI system was placed 300 mm from the downstream exit of the neutron guide. The neutrons were irradiated into a sample. In this measurement, a conventional neutron scintillation detector (NSD) was installed in place of the n-GSI. and the performance test was conducted for comparison.

RESULTS: The neutron transmission images of a Japanese character and a Gd chart obtained with the n-GSI and the NSD are shown in Fig. 2 and Fig. 3, respectively. The exposure times for the images were 100 s. The image of the NSD is brighter than that of n-GSI. The light yield of the NSD, defined as the mean counts in the ROI, is about 2 times higher than that obtained by n-GSI. The contrast is expected to improve on applying a higher gap voltage across the CP since the light yield of the n-GSI increases exponentially with the gap voltage. Moderate imaging capabilities were evident from the two neutron images of the Gd chart. More detailed analysis is in progress.

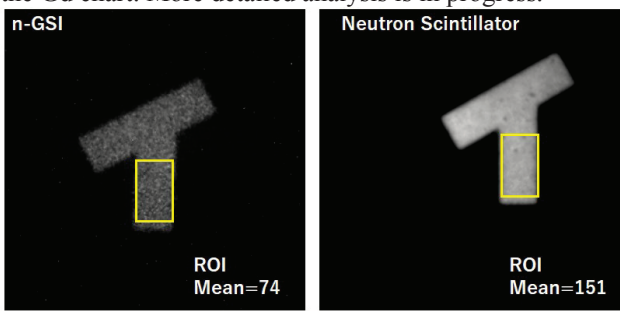

Fig. 2. Neutron transmission image of a Japanese character obtained using the n-GSI (left) and the NSD (right). The region of interest ROI (yellow) is defined to investigate the light yield of the neutron transmission image.

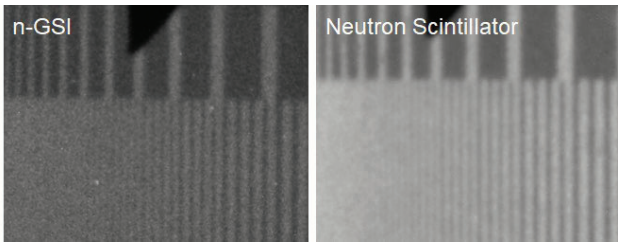

Fig. 3. Neutron transmission image of a Gd test chart obtained using the n-GSI (left) and the NSD (right).

ACKNOWLEDGEMENT:
We would like to thank Dr. T. Shinohara for generously providing us the neutron scintillator.

REFERENCES:

[1] H. Kondo et al., Plasma Fusion Res. 13 (2018) 2406018.
[2] H. Kondo et al., Nucl. Instrum. and Methods. A 958 (2020) 162804.
[3] H. Sugiyama et al., IEEE Trans Nucl Sci. 67 (2020) 1035.
[4] M. Hino et al., Nucl. Instrum. and Methods. A 797 (2015) 265.

CO12-4 Stability Monitoring of Hf Oxide Films by Neutron Activation Analysis

T. Takatsuka, K. Hirata, Y. Iinuma[1], R. Okumura[1], H. Yoshinaga, and K. Takamiya[1]

National Metrology Institute of Japan, National Institute of Advanced Industrial Science and Technology
[1]Institute for Integrated Radiation and Nuclear Science, Kyoto University

INTRODUCTION: Hafnium (Hf) oxide is utilized as high-*k* dielectric films for semiconductor devices especially with fast and low-power operation. Additionally, the films are being introduced as ferroelectric material on ferroelectric transistors and memories. The device fabrication process should be precisely controlled for such dielectric films. Certified reference material NMIJ-CRM 5605-a was developed in 2012 [1, 2], which is applicable to quantify the film thickness with small uncertainties. This study aims to confirm the stability of hafnium quantity in thin hafnium oxide films by neutron activation analysis (NAA), to keep the reliability of the certified reference material.

EXPERIMENTS: Hf oxide films were deposited on 4-inch Si wafers by magnetron sputtering. The target thickness was set to 4 nm. The prepared wafers with the films were cut into 10 mm × 10 mm pieces for the measurements. The surface areas of specimens were precisely calculated from the optically scanned images, with the length calibration using JCSS calibrated standard scales.

Hafnium amounts were evaluated by NAA with internal standards. For the production of standards to calibrate hafnium amounts, standard solutions were prepared by diluting NIST SRM 3122: Hf and 3102: Sb gravimetrically. Four concentration levels of working standard solutions were prepared: an internal standard solution of Sb, three Hf and Sb mixed standard solutions with different Hf concentrations for the calibration. Weighed portion of the Sb working standard solution was dropped onto a cleaned filter paper on every specimen. As for standards, aliquots of the working standard solutions of Hf and Sb mixture were weighed and dropped onto filter papers.

All the samples were sealed up separately in clean polyethylene bags, followed by being stacked in a polyethylene container for the neutron irradiation. The irradiation was performed for 4 hours with a 5.5×10^{12} $cm^{-2} \cdot s^{-1}$ thermal neutron fluence rate at Pn-2 in the Kyoto university research reactor (KUR). The gamma-ray activity of each sample was measured by a high-purity germanium detector (CANBERRA).

RESULTS: From the gamma-ray spectrum, the gamma-ray relative intensities (^{181}Hf cps) / (^{124}Sb cps/ ng) were calculated for the specimens and the standards. Figure 1 shows typical calibration curve plotting the relative intensities to the Hf amounts. The hafnium content in each specimen was estimated from the calibration curve.

Dividing each Hf amount by the measured surface area, the area density was calculated for each measured specimen. The evaluated area densities of CRM 5605-a specimens are plotted with the uncertainty (error bars), in Fig. 2, the horizontal axis shows when the measurements were conducted in year and month. The area densities consistent with each other when considering the uncertainties. This result shows the stability of hafnium quantity in thin hafnium oxide films on the CRM.

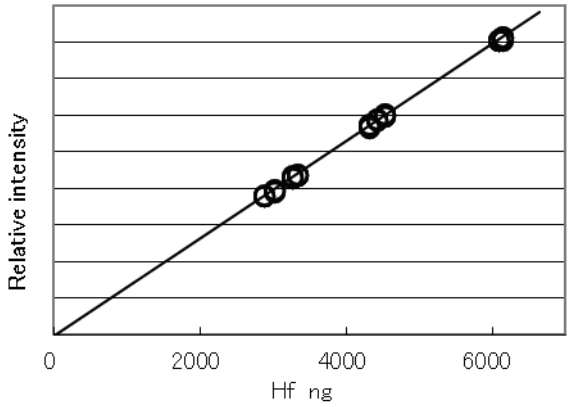

Fig. 1. Calibration curve for determining the Hf contents by the internal standard method.

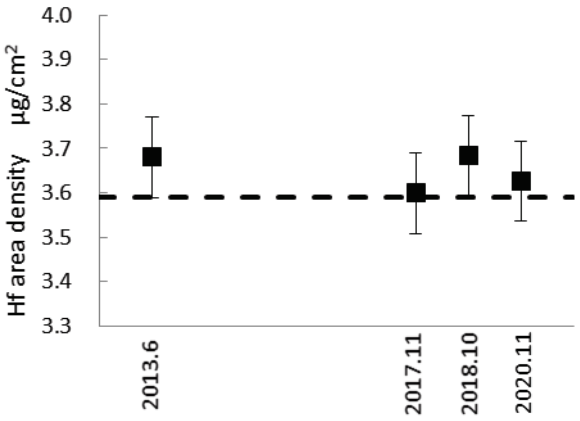

Fig. 2. Stability monitoring of the Hf area density by the internal standard method. The broken line indicates the certified value of CRM 5605-a.

REFERENCES:

[1] Certificate of NMIJ CRM 5605-a: Hafnium Oxide Film for Quantitative Analysis of Hafnium.
[2] KURRI Progress Report 2012.

Neutron irradiation test at KUR CN-3

H. Ohshita, H. Endo, T. Seya, Y. Yasu, M. Hino[1], T. Oda[1]

Institute of Materials Structure Science, KEK
[1]Institute of Integrated Radiation and Nuclear Science, Kyoto University

INTRODUCTION: Kyoto University Research Reactor (KUR) is a light-water moderated tank-type reactor with a thermal power of 5 MW. The cold neutron beam line (CN-3) [1] is built facing the direction of the cold neutron moderator of the KUR. Neutrons between 1 Å and 6 Å are led by neutron supermirror guides to the experimental area. The total length of the CN-3 is 10.5 m. The neutron supermirror guide consists of 15 elements with a length of 70 cm each. In addition, the guide has a curvature radius of 441 m. Furthermore, the CN-3 is curved at the carry-in entrance. Therefore, fast neutrons are not able to reach the experimental area. The beam corresponds to the size of the neutron supermirror guide and has a height of 90 mm and a width of 20 mm. Because neutrons with garland reflection have a shorter wavelength than those with zigzag reflection, the outside (SANS side) component that has many neutrons with garland reflection shifts to a shorter wavelength than that of the inside (the carry-in entrance side) component. Currently, the cold neutron moderator is nonfunctional. The expected neutron intensity is 7.6×10^5 neutrons/s·cm^2·MW. We carried out the neutron irradiation test at the KUR CN-3 in addition to developing some neutron detectors. In this study, we will discuss the neutron yield of CN-3.

EXPERIMENTS AND RESULTS: An experimental setup for the measurement of neutron intensity is shown in Figure 1. An L-shaped neutron shield is placed around the beam duct. A movable slit, neutron beam monitor, and disk chopper with a ϕ500 mm disk are set on the inside. A ^{3}He filled proportional counter is also set on the outside. The fixed movable slit has a height of 20 mm and a width of 10 mm. The neutron beam monitor (MNH10/4.2), which is filled with little amounts of ^{3}He and P-10 gases, attains a neutron efficiency of order 10^{-4}. The total pressure of the monitor is 130 kPa. The typical counting rate is approximately 218.4 events/s·MW and is used as the normalization factor. Heavy neutron irradiation with a continuous beam is carried out upstream of the chopper. A composite board with a ^{6}LiF tile (5 mm*t*) and a Cd plate (1 mm*t*) is set as the fixed collimator for the chopper. The chopper has adjustable slit sizes of 0.5 mm, 1 mm, 5 mm, and 40 mm. The chopper has four openings and a rotation rate of 30 Hz. The neutron shield of the chopper consists of a B_4C rubber (6 mm*t*) and a Cd plate (2 mm*t*). Time-of-flight (TOF) measurement is carried out downstream. In simple Monte Carlo simulation, the expected neutron intensity with a slit size of 1 mm width is 937.4 neutrons/s·cm^2·MW. In the simulation, only the geometrical condition and movement of the chopper are considered. The ^{3}He filled proportional counter (RS-P4-0806-264) covered with a B_4C resin shield is used to measure the TOF. The counter has a gas mixture of ^{3}He and CO_2 (99:1), and the total pressure is 1003.19 kPa. The counter is cylindrical in shape with a 1 inch diameter. The opening area of the B_4C resin shield is 10 mm × 10 mm. As the measurement results, the neutron beam scan by moving the counter laterally from the carry-in entrance side is shown in Figure 2. The effect between garland and zigzag reflections is illustrated. The neutron intensity is estimated as 694.5±0.5 neutrons/s·cm^2·MW, as shown in Figure 3. To understand the difference between the measurement and the simulation, we plan to realign neutron optics. This study was carried out in part under the support of JSPS KAKENHI; Grant Numbers JP20K12503 and JP20H04462.

REFERENCES:

[1] M. Hino, *et al.*, Annu. Rep. Res. Reactor Inst. Kyoto Univ. **27** (1994) 196-204.

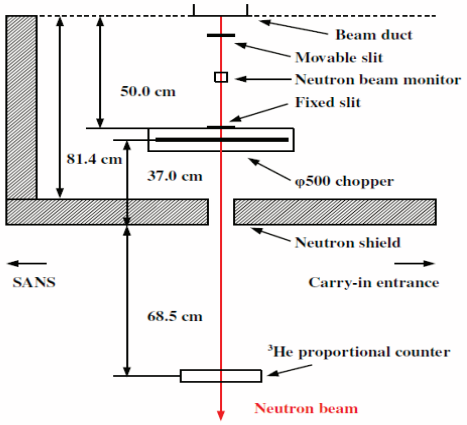

Figure 1 Experimental setup.

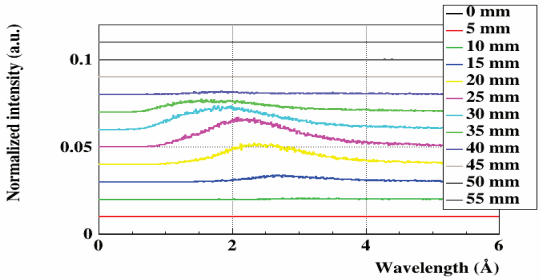

Figure 2 Neutron beam scan.

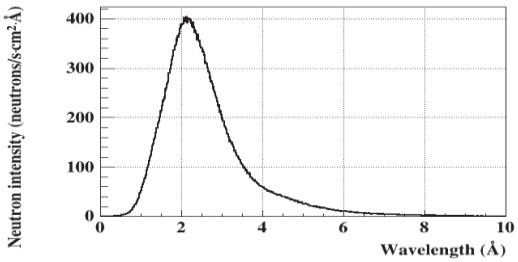

Figure 3 Neutron intensity.

CO12-6 A Study of Polyvinylalcohol-borate hydrogels using small angle X-ray scattering

T. Tominaga[1], Y. Sasaki[2], H. Seto[2], R. Inoue[3], N. Sato[3], and M. Sugiyama[3]

[1]Neutron Science and Technology Center, Comprehensive Research Organization for Science and Society (CROSS)
[2]Institute of Materials Structure Science / J-PARC Center, High Energy Accelerator Research Organization, Tokai, Japan
[3]Institute for Integrated Radiation and Nuclear Science, Kyoto University

INTRODUCTION: One of the features of soft matter is that it undergoes great deformation. Polyvinylalcohol-borate hydrogels (so called 'slime') composed of polyvinylalcohol (PVA), borax and water has long been known as a toy are a soft matter that is known to undergo great deformation. As the amount of borax increases, the hydrogels become less deformed. On the other hand, when the amount of borax is reduced, the PVA hydrogels can be deformed, it becomes soft but does not stretch.

When various additives are added to the hydrogels, the hydrogels become stretchable. One is glycerin, and the other is vinyl acetate granular resin (size: approximately 5 μm) with PVA chains on surface. These are substances with hydroxyl groups like PVA. It is considered that they reduce friction between PVA chains when stretching, but the details are unclear.

In this experiment, the structural change of PVA hydrogels by the addition of borax and vinyl acetate resin was confirmed by small angle X-ray scattering (SAXS).

EXPERIMENTS: PVA hydrogels were prepared in the following weight ratios: PVA: 6.5%, glycerin: 3.6%, borax: 0.4%, vinyl acetate granular resin and: 1.8% water: 88%. The amount of borax was kept constant for all hydrogels, and samples without glycerin, without borax, and without glycerin and borax were prepared. The hydrogels thickness was 0.8 mm and sandwiched between a polyetherimide resin (Sperio, Mitsubishi, Japan). The Cu-SAXS (RIGAKU Nanopix) available at Institute for Integrated Radiation and Nuclear Science, Kyoto University of high-resolution mode was utilized. The empty container was subtracted to account for the transmission, and the SAXS profile was obtained by circular averaging.

RESULTS: SAXS profiles of PVA hydorgels are shown in Fig. 1. The PVA hydrogels without both glycerin and vinyl acetate granular resin had a homogeneous structure at $Q < 10^{-2}$ Å^{-1}, while the hydrogels containing the additives was inhomogeneous in this Q region.

PVA is known to be a crystalline polymer and the structure observed at about 3–8 × 10^{-2} Å^{-1} is considered to be an ordered structure due to the crystalline nature of PVA [1]. This structure appeared to shift toward a larger Q with the addition of additives, i.e., the crystal size becamed smaller.

The additives contributed significantly to the local homogeneity of PVA hydrogels. On the other hand, the inhomogeneity increased in the macroscale structure. This indicates that the crystal structure has a negative effect on the sliding property between the polymer chains, therefore reducing the crystal size improves the sliding property locally, and reducing the friction site number is consistent with mechanical properties of stretchable hydrogels, which in turn correlates with the inhomogeneous structure observed at large scale.
Although more detailed analysis is required, this is an important insight as a key point for the deformation of soft matters.

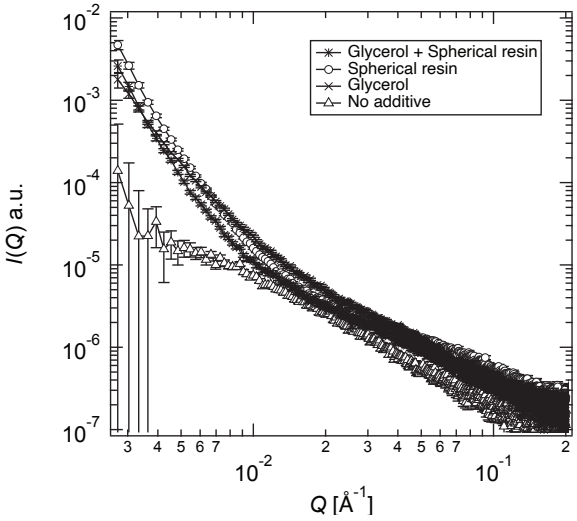

Fig. 1. SAXS profile of PVA hydrogels with PVA, water, and borax as common components. Both glycerin and spherical resin (*), only spherical resin (○), only glycerin (×), and none of the above (△)

REFERENCES:
[1] Toshiji Kanaya et al., Polymer Journal (2012) 44, 83–94 (2012).

CO12-7 Evaluation of LAN cable sheath degradation by gamma irradiation

Taiki Tominaga[1], Toshiyuki Chatake[2], Takeshi Saito[2], Nobuhiro Sato[2], Rintaro Inoue[2], Masaaki Sugiyama[2]

[1]Neutron Science and Technology Center, Comprehensive Research Organization for Science and Society (CROSS)
[2]Institute for Integrated Radiation and Nuclear Science, Kyoto University

INTRODUCTION: A light yellow liquid was found in the vacuum scattering chamber where the neutron detector is installed at the J-PARC MLF BL02 spectrometer [1]. The substance was evaluated and found to be plasticizers for polyvinylchloride cable sheaths such as dioctylphthalate, dinonylphthalate and didecylphthalate. Content ratio of these plasticizers vary from application to application, but generally account for 35–40% of the polyvinylchloride (PVC) cable sheathing [2]. Because these compounds contaminate the vacuum vessel and may be a factor to increase the background in the data of neutron experiments, a prompt investigation of the mechanism is necessary.

PVC sheathed cables are often used for LAN (Local Area Network) cables. Therefore, the possibility of plasticizer elution under vacuum and the possibility of plasticizer elution due to cable sheath degradation by gamma irradiation were evaluated by examining the change in weight before and after vacuum treatment and the change in Young's modulus before and after gamma irradiation.

EXPERIMENTS: Three types of commercial PVC LAN cables and two types of polyolefin (PO) LAN cables were prepared. The LAN cable has a double sheath structure, in which eight conductors are strung together two by two, and then they are loosely combined into one outer cable sheath. In this experiment, only the outer cable sheath was taken as a sample. The weight change was calculated as the average of three values under each condition, and the weight change was evaluated before and after vacuum treatment at 60℃, 5 Pa, for 5 h, and before and after gamma irradiation. The gamma irradiation experiments were conducted at the Co-60 Gamma-ray Irradiation Facility in the Institute for Integrated Radiation and Nuclear Science, Kyoto University. The samples were irradiated with 1 kGy gamma rays at a dose rate of 5 Gy/min in air. Cable sheaths were cut into 4 mm wide strips and tensile tested; the slope of the strain from 1 to 3% was analyzed, and the average value of the three test results was used as Young's modulus.

RESULTS: The weight loss of all cable sheaths unirradiated with gamma radiation was less than 0.1%. This suggests the additives such as plasticizers, flame retardants, etc. in the cable sheaths do not flow out simply by vacuum treatment. Next, the gamma-irradiated samples were further vacuum-treated, and the outflow of additives was evaluated from the weight change. Similarly, the weight change was less than 0.1%. The weight of the gamma-irradiated samples increased slightly, suggesting that the gamma-irradiation had a slight effect on oxidation.

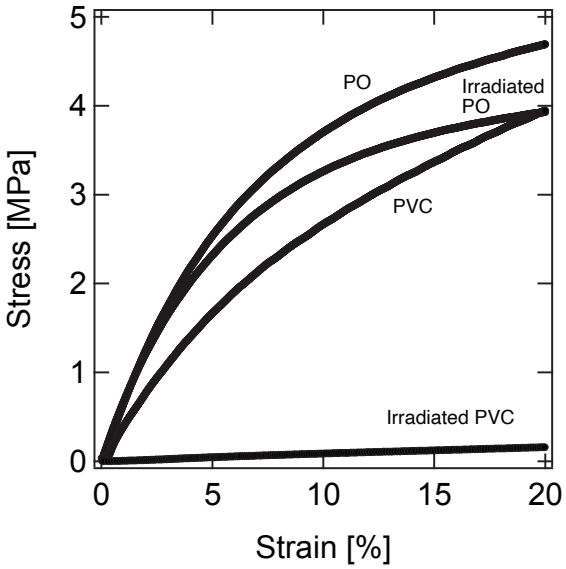

Fig. 1. Stress-strain curves of cable sheaths before and after gamma irradiation of a PVC sheath and a PO sheath.

Although there was no obvious trend in Young's modulus changes due to gamma irradiation between PO and PVC sheaths, both cable sheaths were damaged by gamma irradiation at a total dose of 1 kGy (Young's modulus decrease: 44–99% for PO sheaths and 2–72% for PVC sheaths). The s-s curves of the PO sheath with the smallest damage and the PVC sheath with the greatest damage are shown in Figure 1. The PO sheath cable with the minimum degradation due to gamma radiation is a non-halogenated cable available as eco-material (EM) cable, which may be affected by additives such as plasticizers and flame retardants in the cables, however the details are unclear.

The experimental results show that The 1 kGy dose of gamma radiation was insufficient to cause damage equivalent to that of the cable sheaths in the BL02 spectrometer. We are investigating the possibility of cable sheath degradation due to ultra-short-range irradiation caused by neutron absorption-induced activation.

REFERENCES:

[1] K. Shibata et al., JPS Conf. Proc. 8, 036022 (2015).
[2] R. Navarro et al., Macromolecules 43, 5, 2377–2381 (2010).

CO12-8 Competitive Adsorption Behaviour of Additives in Lubricating Oil Analyzed by Neutron Reflectometry

T. Hirayama, N. Yamashita[1], M. Hino[2], N. L. Yamada[3]

Dept. of Mechanical Eng. and Science, Graduate School of Kyoto University
[1]Dept. of Mechanical Eng. and Science, Graduate School of Kyoto University
[2]Institute for Integrated Radiation and Nuclear Science, Kyoto University
[3]Institute of Materials Structure Science, KEK

INTRODUCTION: General lubricating oil is a blend of base oil such as mineral oil and synthetic oil with additives, and it contributes to saving energy by reducing the friction loss of the machines. Therefore, among various additives, those having a friction reducing effect under boundary lubricated conditions are blended in the lubricating oil. However, the effect of additives when two or more kinds of additives are mixed in lubricating oil is still unknown. Classical textbook says that competitive adsorption of additives limits the improvement of friction reduction effect when several kinds of additives are mixed in lubricating oil together. Therefore, in this study, we investigated the structure of the adsorption layer and its coefficient of friction when fatty acids and alcohol, which are typical oiliness additives, were mixed in the base oil together, by using neutron reflectometry and atomic force microscope.

EXPERIMENTS:

For the structural analysis of adsorbed layer formed by additives, we used the time-of-flight (TOF) type neutron reflectometer SOFIA installed at the J-PARC in Tokai, Ibaraki. In order to grasp the film thickness and density of the boundary lubrication layer formed on the Cu surface in lubricant, we conducted fitting procedure for the obtained neutron reflectivity profiles in each case.

The base oil we used was hexadecane, and stearic acid and stearyl alcohol were used as a model of oiliness additives. We compared the neutron reflectivity profiles for two lubricants for checking the possibility of competitive adsorption by the combination use of additives; the first was with 0.1 mass% deuterated acid, while the second was with 0.05 mass% deuterated acid and 0.05 mass% deuterated alcohol.

RESULTS:

In the experiment, three neutron reflectivity profiles were obtained: (1) with base oil only, (2) immediately after the lubricant containing the additive was added, and (3) two hours after the lubricant containing the additive was added.

The obtained profiles are shown in Fig. 1. Since the width of the fringe in the reflectivity profile becomes wider as time goes by, it can be said that the total film thickness tended to become thinner. Since the extracted lubricant turned 'blue' after the experiment, it is probable that the additive was adsorbed, causing corrosion of the Cu surface.

It can be seen that the change in fringe width was larger when the acid and alcohol were mixed than when the acid alone was used. This suggests that when stearic acid and alcohol were mixed, the corrosive action became greater, that is, the adsorption performance became higher than that of stearic acid alone. It was expected before the experiment that alcohol would suppress the adsorption of fatty acids and suppress corrosion, but the results showed the opposite.

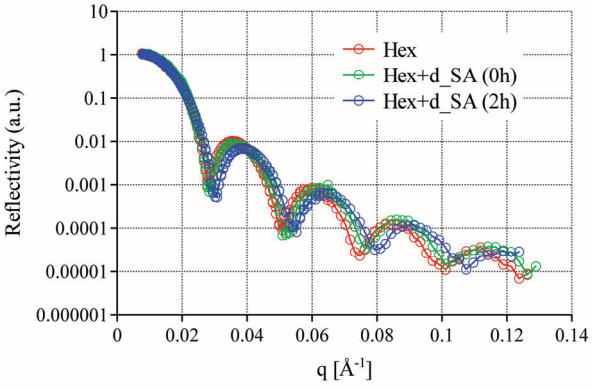

(a) With stearic acid

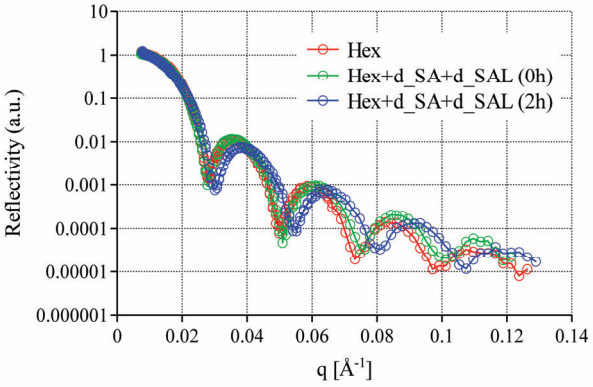

(b) With stearic acid and stearyl alcohol

Fig. 1 Neutron reflectivity profiles for the interface between Cu substrate and lubricant.

In addition, the friction tests were conducted under the lubricants only with stearic acid and with both of stearic acid and stearyl alcohol. For the friction test, an atomic force microscope was used owing to its higher sensitivity for the coefficient of friction of adsorption layer. As a result, a lower coefficient of friction was obtained when two were mixed than when only stearic acid was mixed in the base oil. These results suggested that the mixing of multiple kinds of additives may further promote the adsorption, bringing lower friction characteristics.

CO12-9 Multi-element neutron activation analysis of selected Japanese food samples by meutron activation analysis

M. Fukushima[1], T. Maeda[1], Y. Iinuma[2]

[1]*Faculty of Sciences and Engineering, Ishinomaki Senshu University*

[2]*Institute for Integrated Radiation and Nuclear Science, Kyoto University*

INTRODUCTION: It is important to obtain multi element levels in food samples for nutritional purposes. For the analysis of multi elements in food samples, atomic absorption spectrometry (AAS) and induced coupled plasma spectrometry (ICP-AES) are widely used after pre-treatment of acid extraction or acid digestion. Though complete acid digestion is needed for obtaining total levels of elements in food samples, it is not easy by the presence of high concentrations of lipids, polysaccharides, *etc*. preventing acid digestion. For eliminating this problem, neutron activation analysis (INAA) was used for multi elements analysis of Japanese food samples. Wild plants have played an important role as ingredients especially in mountain areas in Japan from long time ago. Unlike vegetables grown in the field, it is known wild plants grown in mountains accumulate specific elements in them. Several species of wild plants were collected from small areas and analyzed elements by INAA.

EXPERIMENTAL: Samples are shown in Table 1.

Table 1. Wild plant samples

Wild plants (Japanese name)	Collected areas
Kogomi	Akita Pref., Marumori*, Tome*
Sidoke	Yamagata Pref.
Hosta (Urui)	Fukushima Pref.
Bracken (Warabi)	Ibaraki Pref.
Udo	Akita Pref., Ichihazama*
Aralia elata (Taranome)	Yamagata Pref.
Mizu	Ichihazama*
Wasabi	Ichihazama*
Japanese knotweed (Itadori)	Ichihazama*
Japanese butter bur (Fuki)	Ichihazama*
Water drop wort	Kahoku*

*Miyagi Pref.

Wild plants were collected in April-May, 2020. Samples were washed with tap water, separated edible parts, freeze dried, and pulverized for dried powder samples. NAA was done by two different conditions according to nuclides for the interest. 1) One portion of samples was irradiated for 1-1.5 min in TcPn site. After 3 minutes decay, gamma spectrum was measured for 10 minutes by Ge detector with CSS. Levels of Br, Ca, Cl, I, K, Mg, Mn, Na, and V were analyzed using ^{80}Br, ^{49}Ca, ^{38}Cl, ^{128}I, ^{42}K, ^{27}Mg, ^{56}Mn, ^{24}Na, and ^{52}V. 2) Another portion of samples was irradiated for 1 hour, and gamma spectrum was measured for 20 minutes after 1 month decay for analyzing Ag, Co, Cr, Cs, Fe, Rb, Sc, Se, and Zn using ^{110m}Ag, ^{60}Co, ^{51}Cr, ^{134}Cs, ^{59}Fe, ^{86}Rb, ^{46}Sc, ^{75}Se, and ^{65}Zn, respectively. NAA method used was validated using NIST SRM 1570a Spinach Leaves, NIST SRM 1566b Oyster Tissue, NIST SRM 1575 Pine Needles, and NIST SRM 1573a Tomato Leaves.

RESULTS: Six different species of wild plants were collected from small area of Ichihazama, Miyagi on same day. Mizu accumulated Mg, Ca, and Fe comparing other species, Wasabi did Rb and Fe, Japanese butter bur did Ca and Rb in them. Those tendencies are thought to be their characteristics, since those six species were growing in small areas.

Elemental levels of Udos collected from five different areas (results of Ishinomaki, Iwadeyama, and Unnan were obtained in 2019) were compared each other. are shown in Fig. 1, and Mn, Rb, and Zn levels differed much each other. Also, elemental levels of Bracken from Tsukuba were compared with those from Ishinomaki and Kahoku in 2019, and shown in Fig. 2. Levels of Mn differed each other in three areas.

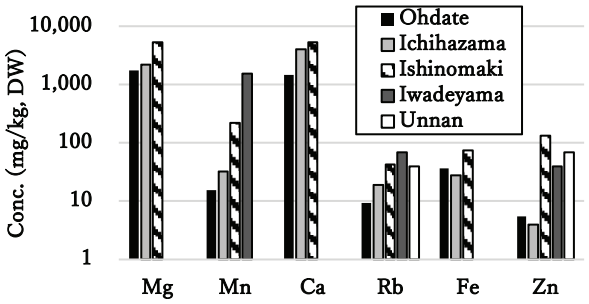

Fig.1 Elemental levels of Udos collected from five different areas.

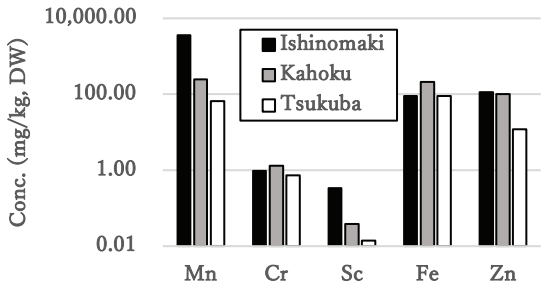

Fig. 2 Elemental levels of Brackens collected from two different areas.

Acknowledgement: We would like to thank Dr. Toshiroh Sato for collecting wild plants in his mountains in Ichihazama, Miyagi Pref..

CO12-10 Analyzing the Texture of Roof-tile toward Detailed Provenancial Studies of Excavated Ceramics by NAA

M. Tomii, K. Takamiya[1], H. Yoshii, M. Kidachi[2], A. Ito, J. Sterba[3], M. Shinoto[4], Y. Chiba

Graduate School of Letters, Kyoto University
[1]Institute for Integrated Radiation and Nuclear Science, Kyoto University
[2] College of Letters, Ritsumeikan University
[3]Atominstitut, TU Wien
[4]Institut für Ur- und Frühgeschichte und Vorderasiatische Archäologie, Universität Heidelberg

INTRODUCTION: Aiming to establish the procedures to archaeologically identify local groups for production of ceramics (pottery and roof-tiles) in historical times in Japan, a collection of excavated roof-tiles is analyzed. Considerable amount of fragmented roof-tiles were excavated at the archaeological site in the campus of Kyoto University (KU) which had been roofed, prior to the occupation of KU, on the temporal house for the garrison from *Tosa* domain (today's Kochi prefecture) in the middle of 18th century. This collection includes many pieces that have stamp impressions indicating that they had been made by the tile-makers within *Tosa* region [1]. Despite difference in potter's names written in the impressions, the technological difference among tiles in the collection has been improbable to recognize.

In order to archaeologically understand the local ceramics production system in historical times with high resolution, this study tries to check whether the difference in stamp impressions, suggesting different production groups, corresponds with the texture of tiles in detail. In the present work, the elemental compositions of the tile samples have been determined by neutron activation method.

EXPERIMENTS: Conventional INAA was applied to determine the elemental composition of tile samples. The tile sample was drilled into a fine powder (Fig.1) and enclosed in a polyethylene bag [2]. The bag was covered with another polyethylene bag to suppress contamination in handling. Each sample was neutron irradiated at Pn-3 of KUR (1 MW) for 90 seconds to detect short-lived nuclides. And all samples were irradiated at Pn-2 (1 MW) for 1 hour to determine long-lived ones. The comparative standards (JR-3, JB-1b) were irradiated with the same condition. The gamma-ray spectrometry of the irradiated samples for short-lived nuclides had been performed just after the irradiation several times, repeatedly. The samples for long-lived ones were measured three weeks after the irradiation. The photo-peak analysis was performed by using FitzPeaks [3]. Concentrations of elements included in the samples were estimated by comparison of the intensity of gamma-rays between the comparative standard and tile samples.

Fig. 1 Sampling with drilling on the broken side of the excavated roof-tile in the site in KU campus, the other side of which has a stamp impression indicating the symbol of the maker in the mid-18th century.

RESULTS: Concentrations of eight elements (Na, Mg, Al, K, Mn, La, Sm and Th) in the roof-tile sample "KS92-277B" were determined by analyzing photo peaks of short half-lived nuclides. The results are listed in Table 1. Concentrations of Na and La were weighted average values since multiple photo peaks of 24Na and 140La were detected. Concentration values estimated for the multiple photo peaks correspond with each other, and the validity of the analysis was confirmed. Estimation of the elemental concentrations for long-lived nuclides and other samples will be performed in the near future, and elemental composition will be compared each other to find out the index elements which shows the specific characteristics of the tiles.

Table 1 Concentrations of eight elements determined for the roof-tile "KS92-277B".

Element	Concentration (μ g/g)		
Na	9.41E+00	±	4.8E-02
Mg	6.88E+02	±	1.3E+02
Al	3.67E+04	±	4.5E+02
K	6.17E+05	±	3.0E+04
Mn	1.49E+02	±	3.1E+00
La	7.26E+02	±	3.8E+01
Sm	1.37E+02	±	1.3E+01
Th	2.07E+01	±	3.8E+00

REFERENCES:

[1] Y. Chiba *et al.*, *Annual Report of Archaeological Researches in KU sites for 1992*. (1995) 65-125.
[2] J. Sterba, *J. Radio. Nucl. Chem.*, **316** (2018) 753-759
[3] J. Fitzgerald, FitzPeaks Gamma Analysis and Calibration Software, https://www.jimfitz.co.uk/fitzpeak.htm

CO12-11 Development of high-count rate two-dimensional neutron detector system

S. Sato, K. Mori[1], Y. Yoshino[1], T. Seya, T. Otomo, H. Oshita

High Energy Accelerator Laboratory, KEK
[1] Institute for Integrated Radiation and Nuclear Science, Kyoto University

INTRODUCTION: Most of the neutron detectors currently in use are ^{3}He gas detectors, and some neutron scintillator detectors are used to obtain high counting rate and high position resolution. In this study, the LiTA system [1] has been developed as a high counting rate two-dimensional detector system. However, it is expensive and difficult to use, and it has been not widely used. Therefore, we have developed an ADCnet64 system as a low-cost, simple using, and high-counting-rate two-dimensional neutron detector system instead of the LiTA system. The performance of the ADC net64 system was evaluated using the B3 port of KUR.

EXPERIMENTS: The ADCnet64 system is a readout circuit for high-speed scintillators. It has 64 channel high-speed analog to digital converters (ADCs) with 10 bits 80 MHz sampling rate to read a 5 cm square 8 × 8 multi-anode type photomultiplier tube. Although the ADCnet64 system is inferior to the LiTA system in performance, the similar data are obtained by fewer circuits and easy way. Figure 1 shows a two-dimensional graph using the ADCnet64 with the Cd "KENS" characters affixed. As a neutron scintillator, 1 mm thick ^{6}Li glass was used. Figure 2 shows the pulse waveform of several scintillators. These light emission times are compared with a ^{6}Li scintillator. In this case, full width at half maximums were about 20 ns for APLF, 20 ns for Ce-APLF2019, 30 ns for Ce-APLF2020, and 40 ns for 6Li. In addition, the tail of after-blow of 60 ns for Ce-APLF2019, 120 ns for Ce-APLF2020, and 1000 ns or more for 6Li were confirmed.

RESULTS: We have developed the ADCnet64 system with a low-cost, simple, high-counting-rate, and two-dimensional neutron detector. We have evaluated its performance using the B3 port at KUR.

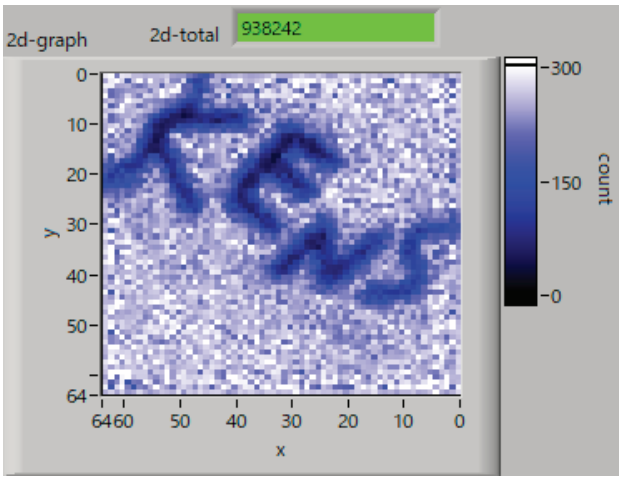

Fig. 1. Two-dimensional graph using the ADCnet64 with the Cd "KENS" characters attached.

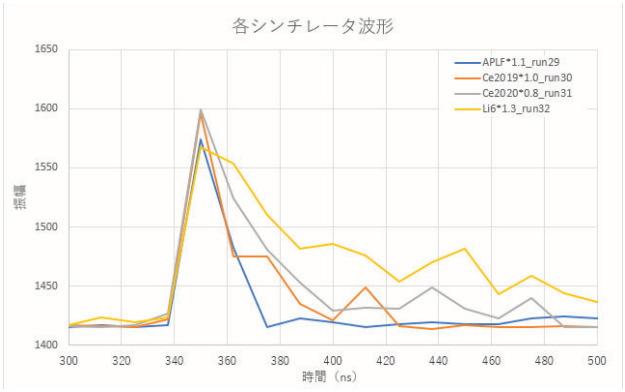

Fig. 2. Pulse waveform of several scintillators.

REFERENCES:

[1] S. Satoh, UCANS-V 2015, DOI 10.1393/ncc/i2015-15197-7.

CO12-12 A response of inner-through type ionization chamber to ^{133}Xe

A. Yunoki, H. Yashima[1], R. Okumura[1], T. Yamada[2]

National Metrology Institute of Japan, National Institute of Industrial Science and Technology
[1]KURNS
[2]Kindai University Atomic Energy Research Institute

INTRODUCTION: The national metrology institute of Japan (NMIJ) calibrates a response of equipment for monitoring a radioactivity in gaseous effluents. The response is obtained by dividing the indication of the equipment by the activity per unit volume. It can be determined by using an inner-through type ionization chamber (Ohkura ionization chamber: type I-4096 01/06) which is calibrated by a set of proportional counters. ^{85}Kr is used for calibrating the monitoring equipment [1-3]. For monitoring purpose, an energy dependence of the equipment should be assessed. ^{133}Xe and ^{41}Ar are useful, however, it is difficult to purchase them commercially. Therefore, we planned to produce them and perform the assessment. We tested the response of the inner-through type ionization chamber using ^{41}Ar produced in KUR-SLY last year [4]. This year, we tested the response using radioactive xenon gas.

SOURCE PREPARATION: The source of radioactive xenon was produced by activating stable xenon (^{128}Xe, ^{130}Xe, ^{132}Xe, ^{134}Xe, ^{136}Xe) with irradiating thermal neutron. A xenon gas diluted by P-10 was poured to a small vessel of acrylic resin whose volume was 62 cm^3. A pressure of the gas was 100 kPa. Then, the vessel was placed at the bottom of the KUR-SLY operating at 1 MW for 60 s. The nominal flux of the thermal neutron was 7.84×10^{11} [n^{-1} s^{-1} cm^{-2}]. The ^{133}Xe of 17.4 kBq was produced through ^{132}Xe (n, γ) ^{133}Xe reaction, while impurities of ^{129m}Xe, ^{131m}Xe, ^{133m}Xe, ^{135m}Xe, ^{135}Xe and ^{137}Xe were also produced. The radioactive xenon gas was then transported to Kindai University Atomic Energy Research Institute where a measurement system was temporally installed. The ^{41}Ar was also produced in KUR and used in the test.

MEASUREMENTS: A particle emission rate of radioactive xenon gas was assessed by using a set of proportional counters connected in series. Conventional pulse counting electronics were connected to the counters. The designs of the counters are the same except for their length. To eliminate distortion of counts near both ends of the counter, the net count rate was used which was obtained by subtracting a count rate obtained by a shorter counter from that obtained by a longer counter. The particle emission rate can be easily converted to activity for ^{85}Kr and ^{41}Ar. The pure ^{85}Kr is commercially available and pure ^{41}Ar can be produced in KUR. However, pure ^{133}Xe is difficult to obtain because pure stable ^{132}Xe is difficult to prepare and there exist impurities (^{129m}Xe, ^{131m}Xe) of longer life. Therefore, results of this test are not for an activity per unit volume but for a particle emission rate per unit volume including from impurities.

RESULTS: Fig. 1 shows pulse height spectra of signals obtained from the proportional counters whose volumes are 100 cm^3 (LL), 60 cm^3 (M), 44 cm^3 (S), 30 cm^3 (SS). A continuous spectrum of beta particles from ^{133}Xe are observed with several peaks of internal conversion electrons and Auger electrons due to impurities. Fig. 2 shows a pulse count rate as a function of a volume of proportional counter. A count rate per unit volume is derived from an inclination of approximate straight line obtained by the least square method. It was 35 s^{-1} cm^{-3}. The output of inner through ionization chamber flown by the radioactive xenon gas was 13.7 pA. Then, the response of 0.39 pA (s^{-1} cm^{-3})$^{-1}$ was obtained.

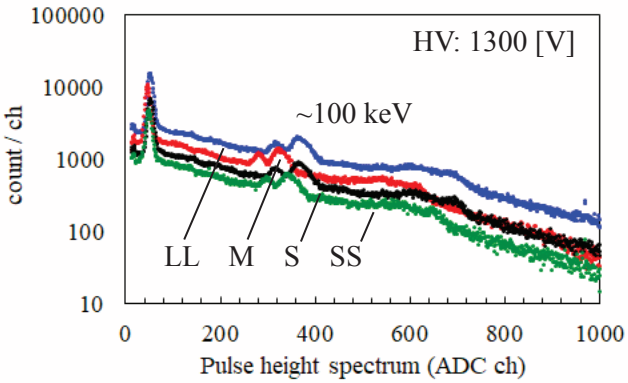

Fig. 1. Pulse height spectra of signals.

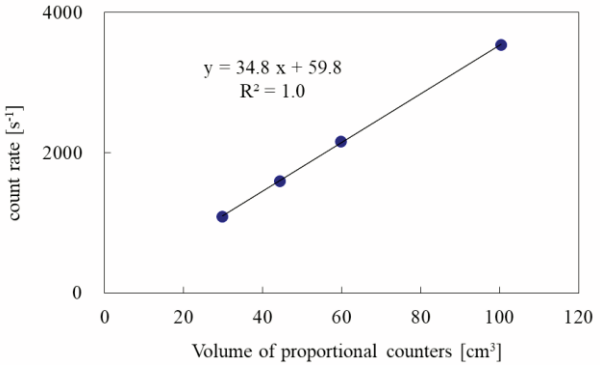

Fig. 2. Count rates as a function of a volume of proportional counter.

As for the response test using ^{41}Ar, we inserted lead shield of 10 cm in thickness between each proportional counter and the chamber. The production of ^{41}Ar and measurements were performed similarly.

REFERENCES:

[1] A. Yunoki, et. al., Applied Radiation and Isotopes, Vol. 68 (2010) pp.1340-1343.
[2] M Unterweger, L Johansson, L Karam, M Rodrigues and A Yunoki, Metrologia 52 (2015) S156-S164.
[3] A. Yunoki, et. al., Applied Radiation and Isotopes, Vol. 134 (2018) pp.325-328.
[4] A. Yunoki, et. al., KURNS Progress Report 2019, ISSN 2434-9488, CO12-5 (31059).

CO12-13 Study of Isotope Separation via Chemical Exchange Reaction

R. Hazama, T. Yoshimoto, A. Rittirong, Y. Sakuma[1], T. Fujii[2], T. Fukutani[3], Y. Shibahara[3], A. Sunaga[3]

Graduate School of Human Environment, Osaka Sangyo University
[1]Laboratory for Advanced Nuclear Energy, Tokyo Institute of Technology,
[2]Graduate School of Engineering, Osaka University
[3]Institute for Integrated Radiation and Nuclear Science, Kyoto University

INTRODUCTION: Chemical isotope separation for calcium and lithium has been studied by liquid-liquid extraction (LLE) with DC18C6 crown-ether [1, 2]. This report describes how two important factors of distribution coefficient (D) and separation factor (α) behave in terms of the aqueous phase concentration and different solvent of water and 12M HCl.

EXPERIMENTS: Chemical Isotopic exchange occurs according to the following chemical exchange reaction:

$$^{40}Ca^{2+}_{(aq)} + {}^{48}CaL^{2+}_{(org)} \rightarrow {}^{48}Ca^{2+}_{(aq)} + {}^{40}CaL^{2+}_{(org)} \quad (1)$$

, where L represents macrocyclic polyether(18-crown-6). Various concentrations ranging from 10% to 30% (w/w) $CaCl_2$ and LiCl was used, with/without the addition of 0.3%, 3%, and 30% 12M HCl, and organic solution (0.07M DC18C6 in chloroform) were mixed by a magnetic stirrer for 1 minute and separated with a constant standing time of 10 minutes. Ca and Li concentration measured by AAS (Shimadzu AA-6800). The isotopic analysis performed by ICP-MS (Agilent 7900) (Fig 1, 2). It is noted that the calcium isotope analysis by ICP-MS is in progress.

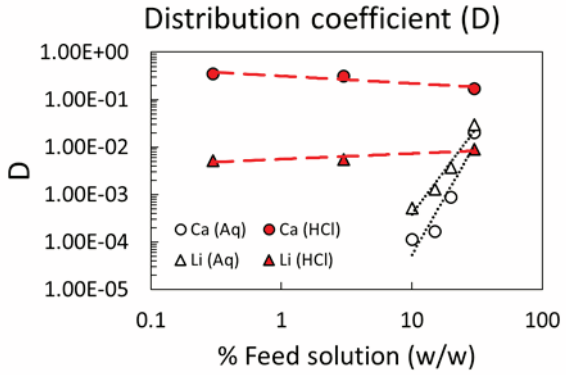

Fig 1. Distribution coefficient (D= $[ion]_{Org}$ / $[ion]_{Aq}$) of LLE: Preliminary.

The distribution coefficient (D) in aqueous solvent significantly decreases when the feed concentration is reduced. On the other hand, 12M HCl solvent improved and maintained the affinity of ion-crown complex, especially on the calcium extraction by LLE to the higher extractable salt. At 30% (w/w) of $CaCl_2$, it is found to be about nine times higher by using 12M HCl as a solvent. The result on acidity solvent corresponded to the study on crown-ether resin for calcium isotope separation using the chromatographic method to absorb calcium ion to crown-ether resin [3]. However, the distribution coefficient (D) on lithium was found to be slightly lower by using HCl solvent. The lithium single stage separation factor (α) analyzed by ICP-MS provided 1.008 ± 0.004 and 1.009 ± 0.003 for 12M HCl and an aqueous solvent, respectively.

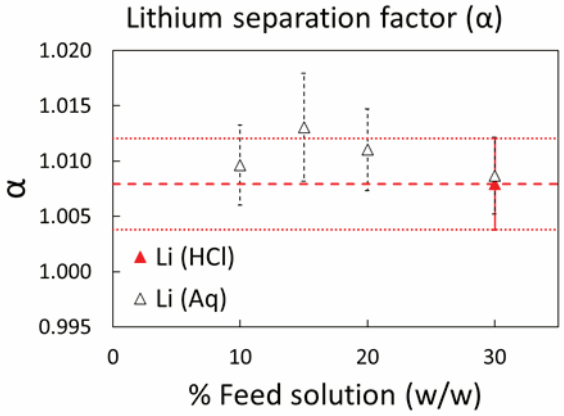

Fig 2. Lithium single stage separation factor (α= $[^6Li/^7Li]_{Org}/[^6Li/^7Li]_{Aq}$): Preliminary.

RESULTS: It is noted that the recovery of cation content significantly influences a scale-up on mass production progress of isotope enrichment. With the current setup, we found that the formation of ion-crown complex is reduced, where the feed concentration is decreased for aqueous solvent. However, the formation of ion-crown complex is significantly increased with the addition of 12M HCl solvent, especially in the case of calcium. The requirement for the multi-stage iteration to obtain about ten times enrichment of ^{48}Ca is relaxed with the current improvement utilized by acidity solvent. It requires several thousand times for aqueous solvent, but it is only 1400 times if we utilize 12M HCl as a solvent. For comparison, the same crown-ether was used for both Ca and Li in this study, but the optimization of crown-ether, solvent, molar ratio between these two, temperature, etc is required to improve mass production cost-effectively.

REFERENCES:

[1] R. Hazama *et al*., KURRI Progress Report 2017, 104.
[2] R. Hazama *et al*., KURNS Progress Report 2019, 282.
[3] S. Nemoto et al., Journal of Nuclear Science and Technology 2012, 49.4: 425-4

CO12-14 Beam test of radiation detectors for a muon-electron conversion search experiment, DeeMe

M. Aoki, N. Abe[1], Y. Higashino, H. Ikeuchi[2], K. Komukai[2], D. Nagao, H. Natori[4], Y. Seiya[2,3], K. Sugita, T. Takahashi[1], N. Teshima[2,3], T. Uematsu[2] and K. Yamamoto[2,3]

School of Science, Osaka University

[1]*Kyoto University Institute for Integrated Radiation and Nuclear Science, Kyoto University (KURNS)*

[2]*Faculty of Science, Osaka City University*

[3]*Nambu Yoichiro Institute of Theoretical and Experimental Physics (NITEP), Osaka City University*

[4]*Institute of Materials Structure Science, KEK*

INTRODUCTION: Charged-lepton flavor violation (CLFV) process such as $\mu \to e\gamma$, μ-e conversion, τ-CLFV decays are heavily suppressed in the standard model of particle physics (SM). However, in the most of the models beyond SM, it is considered to occur with a strength that can be reached in the coming experiments. DeeMe is one of experiments that aims to search for μ-e conversion in nuclear field [1] at a level of 10^{-13} of the branching ratio in the single event sensitivity. It uses high-power high-purity pulsed proton beam from J-PARC RCS. The detector of DeeMe should be operational after $\mathcal{O}(\mu s)$ from a burst of particles (100 GHz/mm^2) produced by the proton pulse.

In order to solve this prompt-burst issue, a multi wire proportional chamber (MWPC) with high-voltage switching technique was successfully developed [2]. Since then, the improvements of the MWPC such as reducing the delayed false signals have been performed. Because that it is critically important to improve the overall performance of the momentum-measuring system, we decided to extend our development beyond the MWPC including a fiber tracker that can provide extra information to reduce the bad impact from the delayed false pulses.

We also made use of the burst-beam test technique we had developed with a LINAC at KURNS for the development of a beam-profile monitor that can be used in the pulsed-beam facilities.

EXPERIMENTS: Three independent measurements/tests by using the burst-beam test technique were performed at the LINAC at KURNS. One is the further test of the MWPC, second is the test of the plastic-scintillation fiber tracker, and the third is a test of beam profile monitor.

In the test for the MWPC, the two different geometrical configurations of the MWPC were tested: 3 mm of half-gap and 4 mm of half-gap.

In the plastic-scintillation fiber tracker test, we had tried to understand the nature of unexpectedly delayed signals observed in the SiPM output from the fiber after a prompt burst irradiated. By comparing three different fiber configurations, it was concluded that the cause of delayed pulses is likely to be in the SiPM. Then, we had used a newly developed bias-voltage switching SiPM to see the response of the SiPM against a burst input hoping that the burst-tolerance of the SiPM could be improved by turning-off the SiPM during the burst input.

The beam profile monitor we are developing is optimized to the pulsed beam line, where the individual beam particles cannot be separated. In order to obtain 2-dimensional beam profile, a small-sized detector head is moved in a grid by an industrial robot. The head should produce a pulse whose amplitude is proportional to the number of beam electrons without contamination from beam muons at 105 MeV/c. Figure 1(a) shows the newly developed prototype of the detector head that uses Cherenkov radiation to separate electrons from muons.

RESULTS: The time spectra of the fiber signals read by the switching SiPM for two different switching timings showed that turning-off the SiPM during the burst did not suppress the delayed pulses. The further study aiming to understand the cause of the delayed pulses and to reduce them are ongoing.

Figure 1(b) shows the result of the burst-electron detection performance for the beam profile monitor head tested at the LINAC [3]. The head showed good performance and can be used in the coming beamline commissioning at J-PARC.

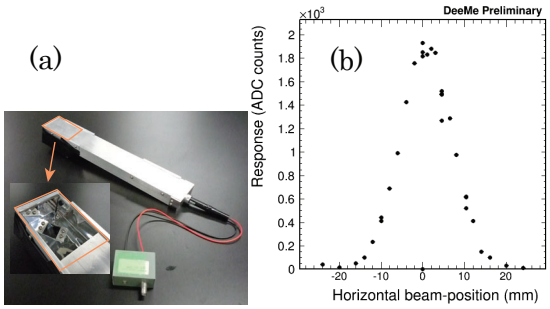

Fig. 1 (a): a detector head of a pulsed-beam profile monitor. (b): profile of a pulsed-beam measured by the Cherenkov detector head at the LINAC.

REFERENCES:

[1] N. Teshima on behalf of the DeeMe Collaboration, "DeeMe experiment to search for muon to electron conversion at J-PARC MLF", in proceedings of NUFACT conference PoS (NuFact2017) 109 (2018).

[2] H. Natori, *et al*., "A fast high-voltage switching multi-wire proportional chamber", Prog. Theor. Exp. Phys. 2017(2) 023C01 (2017).

[3] K. Komukai, "Development of beam-profile scanning devides for a pulsed beamline", Master Thesis, Osaka City University, March 2021.

CO12-15 Neutron activation analysis of Ar, Cl, Br and I in Pd metal

T. Miura, N. Yoshinaga[1], Y. Iinuma[1] and S. Sekimoto[1]

National Metrology Institute of Japan, AIST
[1]Institute for Integrated Radiation and Nuclear Sciences, Kyoto University

INTRODUCTION: National Metrology Institute of Japan (NMIJ) is responsible for developing certified reference materials and for establishing the traceability of SI (The International System of Units) on chemical metrology in Japan. To establish SI traceability, the primary method of measurements should be applied to the characterization of the certified reference materials. Recently, neutron activation analysis using comparator standard is recognized as a potential primary ratio method [1]. Despite the potential of neutron activation analysis as primary ratio method, the evaluation of the measurement uncertainty is required in any analysis. In general, there are three main components of uncertainty in neutron activation analysis, that is, sample preparation uncertainty, neutron flux homogeneity, and gamma ray measurement uncertainty. Usually, flux monitor is used to correct the neutron flux in-homogeneity. However, although the flux monitor can correct the neutron flux variation using the count rate of the known amount of the monitor nuclide, it does not reflect the neutron flux of the actual sample. The most practical method to eliminate neutron flux in-homogeneity and to improve gamma ray measurement uncertainty is an internal standard method [2, 3]. For the development of primary inorganic standard solution as national standard, the purity of starting material has to be determined. The high purity Pd metal was candidate starting material for preparation of Pd standard solution as national standard of Japan. The several trace analytical methods including neutron activation analysis, were used for purity determination of the high purity Pd metal. In this work, we presented that capability of instrumental neutron activation analysis for determination of Ar and halogens in high purity Pd metal.

EXPERIMENTS: The high purity Pd metal was purchased from Tanaka precious metals. The informative purity value of the Pd metal was 99.9 %. The ambient air in pre-cleaned 2 mL volume of Polyethylene vials were used as Ar calibration standard. The volumes of polyethylene vials were calibrated by weighing mass of pure water prepared from Mill-Q Advance pure water system filled in each vial. The calibration of volume Mettler Toredo XP205 semi-micro balance was used for volume calibration. NMIJ CRM 3802a Cl standard solution, NMIJ CRM 3808a Br standard solution and NMIJ CRM 3810a I standard solution were used for used as Cl, Br and I calibration standard, respectively. The standard solutions were added on filter papers to prepare the calibration standard for Cl, Br, and I analysis. The calibrated polyethylene vials, Cl, Br, and I calibration standard were heat sealed into polyethylene bags. Thirty mg of the Pd metal samples were used for Ar, Cl, Br and I analysis. The neutron irradiations were performed by KUR (Kyoto University Research Reactor) Pn3 (thermal neutron flux: 4.7 x 10^{12} $cm^{-2}s^{-1}$) for 1 min. The γ ray measurement system consisted of an ORTEC GEM 30-76-LB-C-HJ Ge detector and a multichannel analyzer SEIKO EG & G MCA 7.

RESULTS: In this experiment, Ar, Cl, Br and I in the high purity Pd metal sample could not be detected by instrumental neutron activation analysis. Therefore, the detection limits of Ar, Cl, Br and I in the high purity Pd metal sample were estimated from the count rate of energy region of γ rays emitted by induced radioactive nuclides. The estimated detection limits were shown on Table.

Table Analytical results of Ar, Cl, Br and I in high purity Pd metal

	Detection limits, g/g
Ar	$< 4\times10^{-6}$
Cl	$< 3\times10^{-6}$
Br	$< 2\times10^{-6}$
I	$< 0.5\times10^{-6}$

REFERENCES:

[1] R.Greenberg, P. Bode, E. De Nardi Fernandes, Spectrochim. Acta B, 66 (2011) 193-241.
[2] T. Miura, K.Chiba, T. Kuroiwa, T. Narukawa, A.Hioki, H. Matsue, Talanta, 82 (2010) 1143-1148.
[3] T. Miura, R. Okumura, Y. Iinuma, S. Sekimoto, K. Takamiya, M. Ohata, A.Hioki, J. Radioanal. Nucl. Chem., 303(2105), 1417-1420.
[4] NuDat 2, National Nuclear Data Center in Brookhaven National Laboratory, https://www.nndc.bnl.gov/nudat2/index.jsp

CO12-16 Evaluation of Structural Vacancies in Icosahedral Cluster Solids using Positron Annihilation

M. Yamamoto[2], R. Nakajima[3], K. Kitahara[1], A. Yabuuchi[3], N. Oshima[4], I. Kanazawa[2], A. Kinomura[3], K. Kimura[1]

[1]Department of Advanced Materials Science, The University of Tokyo
[2]Department of Physics, Tokyo Gakugei University
[3]Institute for Integrated Radiation and Nuclear Science, Kyoto University
[4]National Institute of Advanced Industrial Science and Technology (AIST)

INTRODUCTION: Stable Al-based icosahedral quasicrystals of multinary aluminium-transition metal alloys are known to exhibit semiconductor-like and even insulator-like electronic transport properties [1]. It has been suggested that the semiconductor-like properties might be interpreted by the combnination of a pseudogap around the Fermi energy and localization tendency. One of origins of the pseudogap at E_F in quasicrystals might be ascribed to a Hume-Rothery like mechanism, namely the scattering of electrons around E_F by planes of pseudo-Brillouin zone constructed from the most intense diffraction peaks. So far, the origin of the pseudogap is not confirmed. Janet and de Boissien [2] proposed a cluster model to explain the properties and the stability of quasicrystals. The icosahedral structure is based upon clusters that contain a number of electrons which stabilizes the structure of atomic aggregates. Mayon *et.al.* [3] proposed a possible explanation for the unusual transport properties of Al-based quasicrystals in terms of hopping processed between wave functions mainly localized inside icosahedral clusters. Kimura *et.al.* [4] have discussed the importance of vacant centers of the Al icosahedral clusters in the anomalous transport properties and stabilities of Al-based quasicrystals. They have shown that 12-atoms Al icosahedra with a vacant center have a covalent bonding nature, while 13-atoms with a center atom have a metallic bonding nature. Positron annihilation method is powerful one for detecting structural vacancies of icosahedral quasicrystals [5]. Recently Kimura and coworkers [6] have done positron annihilation measurements of the positron lifetime, coincidence Doppler broadening (CDB), and depth profiling by slow positron beams for 1/1 AlReSi approximant crystals. They showed that 1/1 AlReSi approximant crystal has structural vacancies in the order of 10^{-3}, which are identified to be center sites of the first shell of icosahedral clusters, and then found that the structural vacancy density of metallic 1/1 AlReSi with less Re is lower than that of non-metallic AlReSi with more Re. These results are consistent with a hypothesis by Kimura *et.al.* [4] and accelerate further investigation of the relationship between structure, bonding nature, and electrical properties for Al-based quasicrystals and approximant crystals, leading to better understanding of physics behind quasicrystals and approximant crystals in terms of the proposed metallic-covalent binding conversion which occurs according to the occupation and vacancy of the center sites of the Al icosahedral clusters.

EXPERIMENTS and RESULTS:
Figure shows X-ray diffraction patterns of quasicrystals $Al_{71}Pd_{18}Ru_{11}$ (upper) and $Al_{71.5}Pd_{18}Ru_{10.5}$(middle), and one calculated by the structural model(lower). By using the slow positron beam, we have estimated the change in S-parameter with positron-incident energies in 2/1 approximant crystal AlPdRu, and 1/0 approximant crystal AlPdRu.

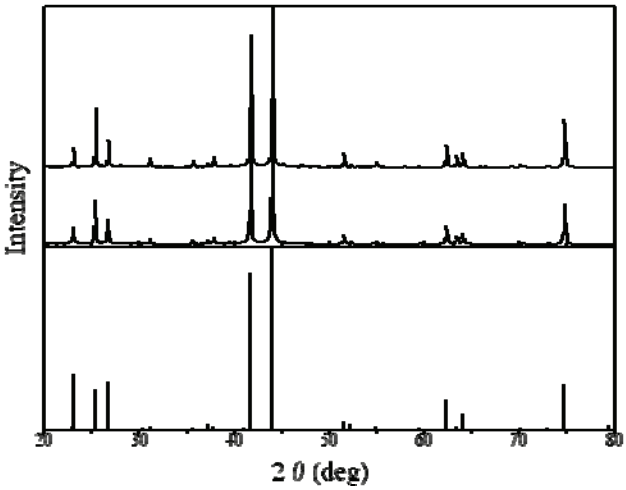

Figure X-ray diffraction patterns of the samples.

We have measured the change of S-parameter of quasicrystal AlPdRu, 2/1 approximant crystal AlPdRu, and 1/0 approximate crystal AlPdRu, due to the positron incident energy. These results show that the density of structural vacancies is the highest in quasicrystal AlPdRu, the second highest in 2/1 approximant crystal, and the lowest in 1/0 approximant crystal. These results are consistent with ones of positron lifetimes of these three samples by slow positron beams (unpublished data). Furthermore, the present results seem to be reasonable from the standpoint of the metallic-covalent bonding conversion which occurs according to the occupation and vacancy of the center sites of the Al icosahedral clusters. We have also done the coincidence Doppler broadening spectra of these three samples. To identify the positron trapping sites in these samples, the core electron momentum distribution of the samples was measured. Experimental results suggest strongly that the trapping sites of quasicrystal AlPdRu, 2/1 approximant crystal AlPdRu, and 1/0 approximant crystal AlPdRu seem to be similar, and are surrounded by Al or Ru.

REFERENCES:
[1] K. Kimura and S. Takeuchi,in Quasicrystals:The State of Art, 2nd ed.,D.P. Divincenzo and P.J. Steinhart,eds.,(World Scientific, Singapore, 1999) pp.325-309.
[2] C. Janot and M.de Boission, Phys. Rev. Lett. **72** (1994) 1674.
[3] D. Mayou et al. Phys. Rev. Lett. **70** (1993) 3915.
[4] K. Kimura et al., J. Solid State Chem. **133** (1981) 302.
[5] I. Kanazawa et al., Phys. Rev. Lett. **79** (1997) 2269.
[6] K. Yamada et al., Philog. Mag. **98** (2018) 107.

CO12-17 Basic experiment for nuclear reactor power monitoring with heat-resistant self-powered gamma ray detector

K. Okada, A. Fushimi, Y. Sato, Y. Murakami, S. Sekimoto[1], T. Ohtsuki[1], Ryo Okumura[1]

Center for Technology Innovation – Decarbonized Energy, Research and Development Group, Hitachi, Ltd.
[1] Institute for Integrated Radiation and Nuclear Science, Kyoto University

INTRODUCTION: Conventionally, thermal neutron measurements have been used for nuclear power monitoring in current commercial nuclear reactors. Recently, ion chambers, which are gamma ray detectors, have been adopted overseas as part of the monitoring systems. Gamma ray measurements have an advantage that the installation position dependence is small because of the large neutron flux gradients and the small gamma flux gradients in the water gap between fuel elements [1]. However, the applied gamma ray measurement devices and systems have a long time constant.

We have been developing a self-powered gamma ray detector (SPGD) which measures a current value generated by electrons ejected from an emitter by gamma ray irradiation. As the name suggests, this SPGD does not require a power supply. We assumed that SPGDs were placed in a mixed field of neutrons and gamma rays in a commercial reactor core and at high temperature. We manufactured a prototype of the SPGD characterized by the Pb-Bi emitter which has sensitivity for gamma rays and a low melting point [2]. The prototype SPGD could be used at high temperatures such as in the inner reactor core because it remained functional even if the emitter melted. In this study, we used the Kyoto University Research Reactor (KUR) facility to measure the current value at high dose rate and high neutron flux in order to investigate the correlation between the reactor power and the SPGD current value under the conditions of an operating reactor core.

EXPERIMENTS: The experiments were carried out by using the Slant Exposure Tube (SLY) of the KUR facility. The experimental geometry is shown in Fig.1. The SPGD was inserted into the reactor core from the subpool. The SPGD was connected to a picoammeter by a MI (mineral insulated) cable of 30 m and a coaxial cable of 30 m. Measurement data were transmitted from the picoammeter to control a PC with the GPIB interface. The data were collected for three points per second.

The measurement was performed twice at the time of reactor start-up of 0 MW to 1 MW and the time of reactor powering up of 1 MW to 5 MW. The assumed neutron flux around the SPGD was about 10^{12} n/cm^2/s, which is equivalent to 1 % of the neutron environment of the rated power of commercial nuclear reactors. There was a concern that the SPGD could not be extracted from the reactor core because of radioactivation by irradiation at high neutron flux. Thus, the time to set SPGD in the reactor core was limited to within 30 minutes.

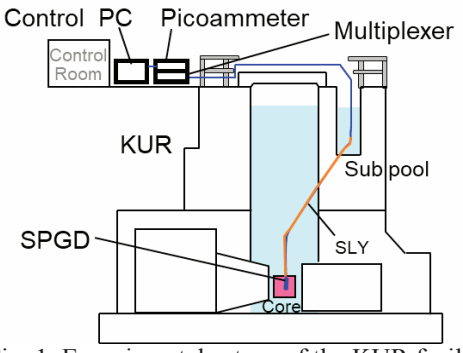

Fig. 1. Experimental set-up of the KUR facility.

RESULTS: Typical measurement results as a time trend of SPGD current value at the time of the reactor start-up are shown in Fig.2. The SPGD current value was increased in response to the rise in the reactor power. The SPGD current value rose after reaching reactor power of 1 MW. The correlation between the reactor power and the SPGD current value was investigated using this result (Fig.3). The SPGD current value at 1 MW was spread over a wide range. The reason was that the SPGD current value continued to rise even after the reactor power had reached 1 MW. This suggested that there might be a time lag before the reactor power was reflected in the SPGD current value.

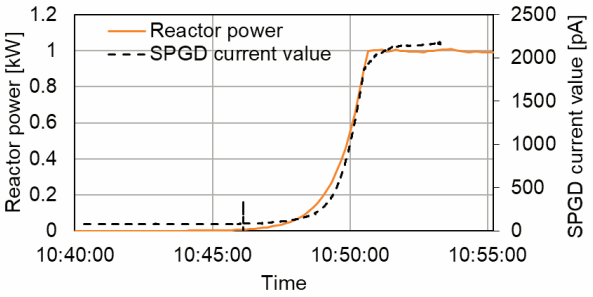

Fig. 2. Time trend of the reactor power and the current.

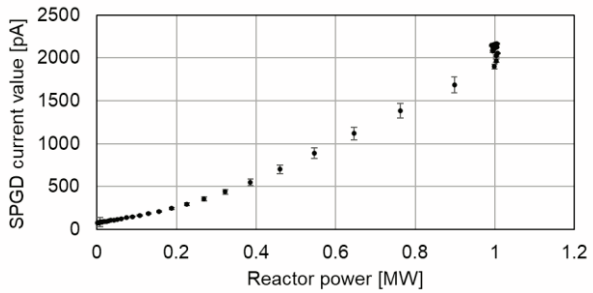

Fig. 3. Correlation between reactor power and SPGD current value.

REFERENCES:

[1] W. Harfst, IWG-NPPCI--84/1(1985).
[2] K. Okada, et al., Abstract of 2020 Annual Conference of Fundamentals and Materials Society, IEE Japan (2020).

II. PUBLICATION LIST
(APRIL 2020 – MARCH 2021)

1. Slow Neutron Physics and Neutron Scattering

Papers

MONOPOL - A traveling-wave magnetic neutron spin resonator for tailoring polarized neutron beams
Jericha Erwin, Gösselsberger Christoph, Abele Hartmut, Baumgartner Stefan, Berger Bernhard Maximilian, Geltenbort Peter, Hino Masahiro, Oda Tatsuro, Raab Robert, Badurek Gerald
Scientific Reports 10(1) (2020) 5815

Neutron gas scintillation imager with glass capillary plate
Kondo Haruyasu, Sugiyama Hiroyuki, Okada Teruyuki, Hayashi Masahiro, Moriya Toru, Ishizawa Satoshi, Itoh Ryutaro, Tokanai Fuyuki, Hanayama Ryohei, Hino Masahiro, Tasaki Seiji, Hirose Masanori, Sumiyoshi Takayuki
Nuclear Instruments and Methods in Physics Research Section A: Accelerators, Spectrometers, Detectors and Associated Equipment 958 (2020) 162804

Application of Anomalous X-ray Scattering Method to Liquid Electrolytes Used in a Battery: Local Structural Analysis around a Dilute Metallic Ion
Kimura Koji, Kiuchi Hisao, Hayashi Kouichi, Nakata Akiyoshi, Fujisaki Fumika, Nishio Koji, Fukunaga Toshiharu, Matsubara Eiichiro
Analytical Chemistry 92(14) (2020) 9956-9962

Hydrogen/deuterium exchange behavior in tetragonal hen egg-white lysozyme crystals affected by solution state
Kita Akiko, Morimoto Yukio
Journal of Applied Crystallography 53(3) (2020) 837- 840

Development and application of a ^{3}He Neutron Spin Filter at J-PARC
Okudaira T., Oku T., Ino T., Hayashida H., Kira H., Sakai K., Hiroi K., Takahashi S., Aizawa K., Endo H.,Endo S., Hino M., Hirota K., Honda T., Ikeda K., Kakurai K., Kambara W., Kitaguchi M.,Oda T., Ohshita H., Otomo T., Shimizu H.M., Shinohara T., Suzuki J., Yamamoto T.
Nuclear Instruments and Methods in Physics Research Section A: Accelerators, Spectrometers, Detectors and Associated Equipment 977 (2020) 164301

Observation of TOF−MIEZE Signals with Focusing Mirrors at BL06, MLF, J-PARC
Funama F., Hino M., Oda T., Endo H., Hosobata T., Yamagata Y., Tasaki S.
Journal of Surface Investigation: X-ray, Synchrotron and Neutron Techniques S1 (2020) S50-S55

Tuning Neutron Resonance Spin-Echo Spectrometers with Pulsed Beams
Oda Tatsuro, Hino Masahiro, Endo Hitoshi, Seto Hideki, Kawabata Yuji
Physical Review Applied 5 (2020) 54032

Application of precise neutron focusing mirrors for neutron reflectometry: latest results and future prospects
Yamada Norifumi L., Hosobata Takuya, Nemoto Fumiya, Hori Koichiro, Hino Masahiro, Izumi Jun, Suzuki Kota, Hirayama Masaaki, Kanno Ryoji,Yamagata Yutaka
Journal of Applied Crystallography 53(6) (2020) 1462-1470

Crystallization of magnetic skyrmions in MnSi investigated by neutron spin echo spectroscopy
Nakajima Taro, Oda Tatsuro, Hino Masahiro, Endo Hitoshi, Ohishi Kazuki, Kakurai Kazuhisa, Kikkawa Akiko, Taguchi Yasujiro, Tokura Yoshinori, Arima Taka-hisa
Physical Review Research 4(2) (2020) 043393

Neutron lifetime measurement with pulsed cold neutrons
Hirota K,Ichikawa G,Ieki S,Ino T,Iwashita Y,Kitaguchi M,Kitahara R,Koga J,Mishima K,Mogi T,Morikawa K,Morishita A,Nagakura N,Oide H,Okabe H,Otono H,Seki Y,Sekiba D,Shima T,Shimizu H M,Sumi N,Sumino H,Tomita T,Uehara H,Yamada T,Yamashita S,Yano K,Yokohashi M,Yoshioka T
Progress of Theoretical and Experimental Physics 2020(12) (2020) 123C2

Deuteration Aiming for Neutron Scattering
Okuda Aya, Inoue Rintaro, Morishima Ken, Saio Tomohide, Yunoki Yasuhiro, Yagi-Utsumi Maho, Yagi Hirokazu, Shimizu Masahiro, Sato Nobuhiro, Urade Reiko, Kato Koichi, Sugiyama Masaaki
Biophysics and Physicobiology 18 (2021) 16-27

Neutron Imaging Using a Fine-Grained Nuclear Emulsion
Hirota Katsuya, Ariga Tomoko, Hino Masahiro, Ichikawa Go, Kawasaki Shinsuke, Kitaguchi Masaaki, Mishima Kenji, Muto Naoto, Naganawa Naotaka, Shimizu Hirohiko M.
Journal of Imaging 7(1) (2021) 4

Proceedings

Probing the Open Spaces Channels in CPL-1 with Positron Lifetime Spectroscopy
M. Kanaji, Y. Irie, Y. Ishikawa, M. Shibata and A. Taniguchi
Proceedings of the Specialists'Meeting on "Nuclear Spectroscopy and Condensed Matter Physics Using Short-Lived Nuclei Ⅵ" and Meeting on "11th Nuclear Spectroscopy Research Using Stop and Slow Unstable Nuclei (SSRI)" Kumatori, Japan (Jan. 16-17, 2020) 77-82 (in Japanese)

Search for isomers and β-decay spectroscopic studies of fission products using a through-hole type clover detector Daiki Ueda, Kiminori Sato, and Takafumi Kitazawa
Proceedings of the Specialists' Meeting on "Nuclear Spectroscopy and Condensed Matter Physics Using Short-Lived Nuclei Ⅵ" and Meeting on "11th Nuclear Spectroscopy Research Using Stop and Slow Unstable Nuclei (SSRI)" Kumatori, Japan (Jan. 16-17, 2020) 60-63 (in Japanese)

Development of neutron focusing mirror and feasibility study of directional neutron source
Tatsuro Oda, Masahiro Hino,Yuji Kawabata, Hitoshi Endo, Hidetoshi Ohshita, Tomohiro Seya, Yoshiji Yasu, Hideki Seto
Proceedings of the 55th KURNS Scientific Meeting Web Meeting 2020 (Jan. 28-29, 2021) 22 (in Japanese)

Present status of the neutron resonance spin echo spectrometers VIN ROSE at BL06 at J-PARC MLF
Yuya Nagata, Michinori Suginome, Masaaki Sugiyama, Rintaro Inoue, Nobuhito Sato, Ken Morishima
Proceedings of the 55th KURNS Scientific Meeting Web Meeting 2020 (Jan. 28-29, 2021) 30 (in Japanese)

Elucidation of the mechanism of the solvent-dependent helix inversion of polymer backbones by using quasielastic neutron scattering and light measurements
Masahiro Hino,Tatsuro Oda, Fumiaki Funama, Hisao Yoshinaga,Abe Yutaka,Yuji Kawabata,Takuya Hosobata, Yutaka Yamagata, Hitoshi Endo, Norifumi L Yamagata
Proceedings of the 55th KURNS Scientific Meeting Web Meeting 2020 (Jan. 28-29, 2021) 21 (in Japanese)

A Study of Focusing TOF-MIEZE Spectrometer with Small-angle Neutron Scattering
Funama Fumiaki, Hino Masahiro, Oda Tatsuro, Endo Hitoshi, Hosobata Takuya, Yamagata Yutaka, Tasaki Seiji, Kawabata Yuji
JPS Conference Proceedings 33 (2021) 11088

Commissioning of Versatile Compact Neutron Diffractometer (VCND) at the B-3 Beam Port of Kyoto University Research Reactor (KUR)
Mori Kazuhiro, Okumura Ryo, Yoshino Hirofumi, Kanayama Masaya, Satoh Setsuo, Oba Yojiro, Iwase Kenji, Hiraka Haruhiro, Hino Masahiro, Sano Tadafumi, Kawabata Yuji, Kamiyama Takashi, Otomo Toshiya, Fukunaga Toshiharu
JPS Conference Proceedings (J-PARC2019) 33 (2021) 11093

Reviews

C3-1-2(MINE)ポートの現状と展望
日野正裕,小田達郎
日本中性子科学会誌 31 (2021) 36-37 (in Japanese)

2. Nuclear Physics and Nuclear Data

Papers

Per atom muon capture ratios and effects of molecular structure on muon capture by γ-Fe_2O_3 and Fe_3O_4
Ninomiya Kazuhiko, Kajino Meito, Inagaki Makoto,Terada Kentaro, Sato Akira, Tomono Dai, Kawashima Yoshitaka, Shinohara Atsushi
Journal of Radioanalytical and Nuclear Chemistry 324 (2020) 403-408

Measurement of cesium isotopic ratio by thermal ionization mass spectrometry for neutron capture reaction studies on ^{135}Cs
Shibahara Yuji,Nakamura Shoji,Uehara Akihiro,Fujii Toshiyuki,Fukutani Satoshi,Kimura Atsushi, Iwamoto Osamu
Journal of Radioanalytical and Nuclear Chemistry 325 (2020) 155-165

Neutron capture cross-section measurement and resolved resonance analysis of ^{237}Np
Rovira Gerard, Katabuchi Tatsuya,Tosaka Kenichi,Matsuura Shota,Terada Kazushi,Iwamoto Osamu,Kimura Atsushi,Nakamura Shoji,Iwamoto Nobuyuki,Segawa Mariko,Maeda Makoto
Journal of Nuclear Science and Technology 57(1) (2020) 24-39

In-gas-cell laser ionization spectroscopy of Os194,196 isotopes by using a multireflection time-of-flight mass spectrograph
Choi H., Hirayama Y., Choi S., Hashimoto T., Jeong S. C., Miyatake H., Moon J. Y., Mukai M., Niwase T., Oyaizu M., Rosenbusch M., Schury P., Taniguchi A., Watanabe Y. X., Wada M.
Physical Review C 102(3) (2020) 034309

Measurements of thermal-neutron capture cross-section of Cesium-135 by applying mass spectrometry
Nakamura Shoji, Shibahara Yuji, Kimura Atsushi, Iwamoto Osamu, Uehara Akihiro, Fujii Toshiyuki
Journal of Nuclear Science and Technology 4 (2020) 388-400

Absolute X-ray energy measurement using a high-accuracy angle encoder
Masuda Takahiko, Watanabe Tsukasa ,Beeks Kjeld, Fujimoto Hiroyuki, Hiraki Takahiro, Kaino Hiroyuki, Kitao Shinji, Miyamoto Yuki, Okai Koichi, Sasao Noboru, Seto Makoto, Schumm Thorsten, Shigekawa Yudai, Tamasaku Kenji, Uetake Satoshi,Yamaguchi Atsushi,Yoda Yoshitaka,Yoshimi Akihiro,Yoshimura Koji
Journal of Synchrotron Radiation 28(1) (2021) 111-119

Mixed-valence state and structure changes of EuH_x ($x=2$ and $2<x\leq3$) under high-pressure H_2 atmosphere
Kuno Keiji,Matsuoka Takahiro,Masuda Ryo,Mitsui Takaya, Seto Makoto, Machida Akihiko, Fujihisa Hiroshi, Hirao Naohisa, Ohishi Yasuo, Shimizu Katsuya, Sasaki Shigeo
Journal of Alloys and Compounds (2021) 158637

Monte Carlo perturbation calculation for geometry change in fixed source problems with the perturbation source method
Yamamoto Toshihiro, Sakamoto Hiroki
Progress in Nuclear Energy 132 (2021) 103611

Appearance of pentavalent Fe ion as a result of a charge disproportionation in Fe-substituted Li_2MnO_3
Tabuchi Mitsuharu, Kobayashi Yasuhiro
Journal of Physics and Chemistry of Solids 150 (2021) 109862

Proceedings

Investigation of Valence Fluctuation Behaviors Using Synchrotron-Radiation-Based Mössbauer Spectroscopy and X-ray Absorption Spectroscopy H. Miyatake
Proceedings of the Specialists' Meeting on "Nuclear Spectroscopy and Condensed Matter Physics Using Short-Lived Nuclei VI" and Meeting on "11th Nuclear Spectroscopy Research Using Stop and Slow Unstable Nuclei (SSRI)" Kumatori, Japan (Jan. 16-17, 2020) 1-7 (in Japanese)

Development of Oxygen NMR Probe Nucleus ^{19}O
W. Sato, S. Komatsuda, H. Shimizu, R. Moriichi, S. Abe, S. Watanabe, S. Komatsu, T. Terai, S. Kawata, and Y. Ohkubo

Proceedings of the Specialists'Meeting on "Nuclear Spectroscopy and Condensed Matter Physics Using Short-Lived Nuclei VI" and Meeting on "11th Nuclear Spectroscopy Research Using Stop and Slow Unstable Nuclei (SSRI)" Kumatori, Japan (Jan. 16-17, 2020) 21-24 (in Japanese)

^{57}Mn/^{57}Fe Emission Mössbauer Study on Local Increase of Currie Temperature of $Y_3Fe_5O_{12}$
M. Mihara, K. Matsuta, M. Fukuda, R. Wakabayashi, N. Okimoto, M. Fukutome, T. Izumikawa, N. Noguchi, M. Ogose, T. Ohtsubo, D. Nishimura, A. Gladkov, A. Kitagawa, and S. Sato
Proceedings of the Specialists'Meeting on "Nuclear Spectroscopy and Condensed Matter Physics Using Short-Lived Nuclei VI" and Meeting on "11th Nuclear Spectroscopy Research Using Stop and Slow Unstable Nuclei (SSRI)" Kumatori, Japan (Jan. 16-17, 2020) 25-30 (in Japanese)

Researches of nuclear spectroscopy at KISS facility
S. Komatsuda, W. Sato, and Y. Ohkubo
Proceedings of the Specialists'Meeting on "Nuclear Spectroscopy and Condensed Matter Physics Using Short-Lived Nuclei VI" and Meeting on "11th Nuclear Spectroscopy Research Using Stop and Slow Unstable Nuclei (SSRI)" Kumatori, Japan (Jan. 16-17, 2020) 35-37 (in Japanese)

Present Status and Future Prospects of Mössbauer Spectroscopy using Synchrotron Radia-tion
Y. Kobayashi, T. Kubota, S. Kitao, M. Saito, R. Masuda, M. Kurokuzu, S. Hosokawa, H. Tajima, N. Umetani and M. Seto
Proceedings of the Specialists'Meeting on "Nuclear Spectroscopy and Condensed Matter Physics Using Short-Lived Nuclei VI" and Meeting on "11th Nuclear Spectroscopy Research Using Stop and Slow Unstable Nuclei (SSRI)" Kumatori, Japan (Jan. 16-17, 2020) 38-40 (in Japanese)

^{61}Ni Mössbauer Spectroscopy
K.Matsuta, Y. Masuda, M. Mihara, and T. Yoshida
Proceedings of the Specialists'Meeting on "Nuclear Spectroscopy and Condensed Matter Physics Using Short-Lived Nuclei VI" and Meeting on "11th Nuclear Spectroscopy Research Using Stop and Slow Unstable Nuclei (SSRI)" Kumatori, Japan (Jan. 16-17, 2020) 41-45 (in Japanese)

^{61}Ni Mössbauer Spectroscopy for Hofmann-like Spin Crossover Coordination Polymer
S. Tsutsui
Proceedings of the Specialists'Meeting on "Nuclear Spectroscopy and Condensed Matter Physics Using Short-Lived Nuclei VI" and Meeting on "11th Nuclear Spectroscopy Research Using Stop and Slow Unstable Nuclei (SSRI)" Kumatori, Japan (Jan. 16-17, 2020) 45-50 (in Japanese)

Mössbauer spectroscopy of Spin Crossover Complex Fe (3-cyano-4-methylpyridine)$_2$ [Ag(CN)$_2$]$_2$
K. Kitase, M.Takhahasi, and T. Kitazawa
Proceedings of the Specialists'Meeting on "Nuclear Spectroscopy and Condensed Matter Physics Using Short-Lived Nuclei VI" and Meeting on "11th Nuclear Spectroscopy Research Using Stop and Slow Unstable Nuclei (SSRI)" Kumatori, Japan (Jan. 16-17, 2020) 51-54 (in Japanese)

Mössbauer spectroscopy of Fe–Ag type spin-crossover Hofmann-type complex
S. Kitao
Proceedings of the Specialists'Meeting on "Nuclear Spectroscopy and Condensed Matter Physics Using Short-Lived Nuclei VI" and Meeting on "11th Nuclear Spectroscopy Research Using Stop and Slow Unstable Nuclei (SSRI)" Kumatori, Japan (Jan. 16-17, 2020) 55-59 (in Japanese)

Observation of Local Fields at the ^{111}Cd(←^{111}In) probe in $SrTiO_3$
T. Kitazawa, K. Kitase, T. Kawasaki, Y. Kobayashi, S. Kitao and M. Seto
Proceedings of the Specialists'Meeting on "Nuclear Spectroscopy and Condensed Matter Physics Using Short-Lived Nuclei VI" and Meeting on "11th Nuclear Spectroscopy Research Using Stop and Slow Unstable Nuclei (SSRI)" Kumatori, Japan (Jan. 16-17, 2020) 64-67 (in Japanese)

Polaronic Local Structures in $La_{0.7}Ca_{0.3}MnO_3$ Observed through Spin Relaxation of Unstable Nuclei
Y. Makido, T. Kosone, M. Takahashi, and T. Kitazawa
Proceedings of the Specialists'Meeting on "Nuclear Spectroscopy and Condensed Matter Physics Using Short-Lived Nuclei VI" and Meeting on "11th Nuclear Spectroscopy Research Using Stop and Slow Unstable Nuclei (SSRI)" Kumatori, Japan (Jan. 16-17, 2020) 68-71 (in Japanese)

Compensator of Environmental Magnetic Fields for Neutron EDM Search
K. Nomura, P. B. Krastev ,H. P. Gunnlaugsson, K. Bharuth Ram, B. Qi, H. Masenda, T. E. Mølholt, D. Naidoo, S. Ólafsson, A. T. Martín-Luengo, I. Unzueta, K. Johnston, J. Schell and H. P. Gislason
Proceedings of the Specialists' Meeting on "Nuclear Spectroscopy and Condensed Matter Physics Using Short-Lived Nuclei VI" and Meeting on "11th Nuclear Spectroscopy Research Using Stop and Slow Unstable Nuclei (SSRI)" Kumatori, Japan (Jan. 16-17, 2020) 87-89 (in Japanese)

Detection of gamma ray from short-lived fission product at KUCA and KURNS-LINAC
Y.NAUCHI, J. HORI, T. SANO, Y. TAKAHASHI, K. KUSUMI and Hi. UNESAKI
2020 Symposium on Nuclear Data OnLine (Nov. 26-27, 2020)

Leaching behavior gamma-emitting fission products, iron and uranium from $UFeO_4$
Yasutoshi Kuriyama, Hiroki Tanaka, Yoahishisa Iwashita, Yoshihiro Ishi, Tomonori Uesugi, Masahiro Hino
Proceedings of the 55th KURNS Scientific Meeting Web Meeting 2020 (Jan. 28-29, 2021) 36 (in Japanese)

Design of an accelerator driven neutron source using source using a 30MeV Cyclotron
Ryutaro Tonnna, Takayuki Sasaki, Taishi Kobayashi, Shun Sekimoto
Proceedings of the 55th KURNS Scientific Meeting Web Meeting 2020 (Jan. 28-29, 2021) 29 (in Japanese)

Reviews

Artificial Production of the Lowest Energy Nuclear Excited State, ^{229m}Th
HIRAKI Takahiro, KAINO Hiroyuki, MASUDA Takahiko, OKAI Kouichi, SASAO Noboru, YOSHIMI Akihiro, YOSHIMURA Koji, KITAO Shinji, SETO Makoto, TAMASAKU Kenji, YODA Yoshitaka
SPring-8/SACLA Information 25(2) (2020) 88-95 (in Japanese)

Others

燃料集合体での FP γ線スペクトル測定
名内泰志, 佐野忠史, 高橋佳之,宇根崎博信,楠見紘司,堀順一
第 41 回日本核物質管理学会年次大会 On Line 2020 (in Japanese)

3. Reactor Physics and Reactor Engineering

Papers

Basic consideration of a nuclear power monitoring system using neutron-induced prompt gamma rays
Okada Koichi, Fushimi Atsushi, Sekimoto Shun, Ohtsuki Tsutomu
Journal of Nuclear Science and Technology 57(5) (2020) 514-522

Detection of subcriticality changes by Simmons-King and Sjöstrand methods
Kitamura Yasunori, Misawa Tsuyoshi
Annals of Nuclear Energy 138 (2020) 107209

Reaction Rate Analyses of High-Energy Neutrons by Injection of 100 MeV Protons onto Lead-Bismuth Target
C. H. Pyeon, M. Yamanaka and B. Lee
Annals of Nuclear Energy 144 (2020) 107498

First demonstration of coherent resonant backward diffraction radiation for a quasi-monochromatic terahertz-light source
Sei Norihiro, Takahashi Toshiharu
Scientific Reports 10(1) (2020) 7526

Local measurements of upward air-water two-phase flows in a vertical 6 × 6 rod bundle
Shen Xiuzhong, Miwa Shuichiro, Xiao Yigeng, Han Xu, Hibiki Takashi
Experimental and Computational Multiphase Flow 1(3) (2020) 186-200

Monte Carlo sensitivity analysis method for the effective delayed neutron fraction with the differential operator sampling method
Yamamoto Toshihiro, Sakamoto Hiroki

Annals of Nuclear Energy 140 (2020) 107108

Feasibility Study on the Development of A Fiber-Optic Humidity Sensor System for the Monitoring and Detection of Coolant Leakage in a Nuclear Power Plant
H. J. Kim, H. Y. Shin, C. H. Pyeon, S. Kim and B. Lee
Nuclear Engineering and Technology 52 (2020) 1689-1696

Meltwater Behavior During the Defrosting Process By Using X-ray Radiography
Ryosuke MATSUMOTO, Takahiro SHIOKAWA, Yuto NISHIURA, Yutaka ODA, Daisuke ITO, Yasushi SAITO
Transactions of the Japan Society of Refrigerating and Air Conditioning Engineers (2020) 1-8 (in Japanese)

Interaction of Liquid $CsIO_3$ with a Polycrystalline UO_2 Solid Surface
ISHII Hiroto, OHISHI Yuji, MUTA Hiroaki, UNO Masayoshi, KUROSAKI Ken
Transactions of the Atomic Energy Society of Japan 19(3) (2020) 147-151 (in Japanese)

Single-crystal growth, structure and luminescence properties of $Cs_2HfCl_3Br_3$
Kodama Shohei, Kurosawa Shunsuke, Fujii Kotaro, Murakami Taito, Yashima Masatomo, Pejchal Jan, Král Robert, Nikl Martin, Yamaji Akihiro, Yoshino Masao, Toyoda Satoshi, Sato Hiroki, Ohashi Yuji, Kamada Kei, Yokota Yuui, Yoshikawa Akira
Optical Materials 106 (2020) 109942

Analysis of Hydrogen Content in Pure Palladium via Neutron Radiography and Tomography
Shimizu Kazuyuki, Toda Hiroyuki, Hirayama Kyosuke, Fujihara Hiro, Matsumoto Yoshihisa, Ito Daisuke, Saito Yasushi, Kamada Yasuhiro
Journal of the Japan Institute of Metals and Materials 84(8) (2020) 270-275 (in Japanese)

Frequency domain Monte Carlo simulations of void velocity measurements in an actual experimental setup using a neutron noise technique
Yamamoto Toshihiro, Sakamoto Hiroki
Journal of Nuclear Science and Technology 58(2) (2020) 190-200

Convergence characteristics and Wielandt acceleration of the time source method for Monte Carlo alpha eigenvalue calculations Yamamoto Toshihiro, Sakamoto Hiroki
Annals of Nuclear Energy 146 (2020) 107627

Source Multiplication Measurements and Neutron Correlation Analyses for a Highly-Enriched Uranium Subcritical Core Driven by an Inherent Source in Kyoto University Critical Assembly
K. Nakajima, T. Sano, K. Takahashi, A. Sakon, M. Yamanaka, S. Hohara, C. H. Pyeon and K. Hashimoto
Journal of Nuclear Science and Technology 57 (2020) 1152-1166

Drift-flux correlation for upward gas-liquid two-phase flow in vertical rod bundle flow channel
Han Xu, Shen Xiuzhong, Yamamoto Toshihiro, Nakajima Ken, Hibiki Takashi
International Journal of Heat and Mass Transfer 162 (2020) 120341

Neutron Generation Time in Highly-Enriched Uranium Core at Kyoto University Critical Assembly
C. H. Pyeon, M. Yamanaka, T. Endo, G. Chiba, W. F. G. van Rooijen and K. Watanabe
Nuclear Science and Engineering 194 (2020) 1116-1127

New variants of Bennett variance method with correlation indices for reducing delayed-neutron contribution
Kitamura Yasunori, Misawa Tsuyoshi
Annals of Nuclear Energy 148 (2020) 107696

Development of a Wide Dynamic Range Neutron Flux Measurement Instrument Having Fast Time Response for Fusion Experiments
ITO Daijiro, YAZAWA Hiroyuki, TOMITAKA Makoto, KUMAGAI Tsuyoshi, KONO Shigehiro, YAMAUCHI Michinori, MISAWA Tsuyoshi, KOBUCHI Takashi, HAYASHI Hiroshi, MIYAKE Hitoshi, OGAWA Kunihiro, NISHITANI Takeo, ISOBE Mitsutaka
Plasma and Fusion Research 16 (2021) 1405018

Distribution parameter and drift velocity for upward gas-liquid metal two-phase flow
Shen Xiuzhong, Hibiki Takashi

Applied Thermal Engineering 184 (2021) 116242

Feynman-alpha and Rossi-alpha Analyses for a Subcritical Reactor System Driven by a Pulsed Spallation Neutron Source in Kyoto University Critical Assembly
K. Nakajima, T. Sano, S. Hohara, A. Sakon, K. Takahashi, M. Yamanaka, C. H. Pyeon and K. Hashimoto
Journal of Nuclear Science and Technology 58 (2021) 117-135

Power Spectral Analysis for a Subcritical Reactor System Driven by a Pulsed Spallation Neutron Source in Kyoto University Critical Assembly
K. Nakajima, A. Sakon, T. Sano, S. Hohara, K. Takahashi, M. Yamanaka, C. H. Pyeon and K. Hashimoto
Journal of Nuclear Science and Technology 58 (2021) 372-382

X-Ray Radiography and Numerical Simulation of Bubble Behavior in Centrifugal Pump
ITO Kei, XIONG Rendong, ITO Daisuke, SAITO Yasushi, USHIFUSA Hiroyuki, SHINOZAKI Masaru, ASAI Yugo
Japanese Journal of Multiphase Flow 35(1) (2021) 101-108 (in Japanese)

Proceedings

Measurement of the Internal Pressure of Ultrafine Bubble Using the Perturbed Angular Correlation Technique
ARAKI Kyoya, MURAKAWA Hideki, SUGIMOTO Katsumi, ASANO Hitoshi, ITO Daisuke
The Proceedings of the National Symposium on Power and Energy Systems, online (Jun. 20-21, 2020) E144 (in Japanese)

Effect of Pitch-to-Diameter Ratio on Heat Transfer and Flow Characteristics of Air-Water TwoPhase Flow in Horizontal Tube Bundle"
M.Tanigaki, T. Yamakura, Y. Ueda, A. Taniguchi, Y. Tokuda, and Y. Ohkubo
Proceedings of the Specialists' Meeting on "Nuclear Spectroscopy and Condensed Matter Physics Using Short-Lived Nuclei VI" and Meeting on "11th Nuclear Spectroscopy Research Using Stop and Slow Unstable Nuclei (SSRI)", Kumatori, Japan (Jan. 16-17, 2020) 72 76 (in Japanese)

Flow characteristics of upward two-phase flows in a rod bundle geometry
Han, Xu, Shen Xiuzhong, Yamamoto Toshihiro, Nakajima, Ken, Hibiki, Takashi
Proceedings of ASME's Power 2020 and Nuclear Engineering Conference powered by ICONE, On-Line (Aug. 4-5, 2020) 14568

Subcriticality Estimation using Unscented Kalman Filter for Reactivity- and Source-Transients T. Endo, A. Yamamoto, M. Yamanaka and C. H. Pyeon
Proceeding of theVirtual Winter Meeting of the American Nuclear Society U.S.A. (Nov. 16-19, 2020) 1-4

燃料集合体からの FP γ線スペクトル測定
名内 泰志, 佐野 忠史, 高橋 佳之,宇根崎 博信, 楠見 紘司, 堀 順一
第 41回核物質管理学会 On Line (Nov. 19-20, 2020) (in Japanese)

Stydy on neutron capture cross sections of ^{241}Am
Xu Han, Xiuzhong Shen, Toshihiro Yamamoto, Ken Nakajima, Takashi Hibiki
Proceedings of the 55th KURNS Scientific Meeting Web Meeting 2020 (Jan. 28-29, 2021) 14 (in Japanese)

Distribution parameter and drift velocity for low and high pressure two-phase flows in rod bundle geometry
Yasuhito Goto, Nobuhiro Sato, Yasuki Okuno, Masafumi Akiyoshi, Mitsuru Imaizumi, Tomohiro Kobayashi, Tamotsu Okamoto
Proceedings of the 55th KURNS Scientific Meeting Web Meeting 2020 (Jan. 28-29, 2021) 27 (in Japanese)

Leaching behavior of fission products from simulated fuel debis in the UO_2 system
Takayuki Sasaki, Yuji Kodama, Ryutaro Tonna, Taishi Kobayashi, Yuta Kumagai, Ryoji Kusaka, Masayuki Watanabe, Daisuke Akiyama, AkiraKirishima, Nobuaki Sato, Kouichi Takamiya, Shun Sekimoto
Proceedings of the 55th KURNS Scientific Meeting Web Meeting 2020 (Jan. 28-29, 2021) 15 (in Japanese)

Dataild stractire of gas-liquid two-phase flow in a packed bed of spheres
Kazushi Terada

Proceedings of the 55th KURNS Scientific Meeting Web Meeting 2020 (Jan. 28-29, 2021) 12-13 (in Japanese)

Measurement of current induced on coaxial cables under gamma-ray irradiation
Naoya Odaira, Yuji Arita
Proceedings of the 55th KURNS Scientific Meeting Web Meeting 2020 (Jan. 28-29, 2021) 44-46 (in Japanese)

Measurements of turbulence in a gas-liquid two-phase flow by using PIV methods and an electro-magnetic probe Yukihide Doda, Naoya Odaira, Daisuke Ito, Kei Ito, Yasushi Saito
Proceedings of the 55th KURNS Scientific Meeting Web Meeting 2020 (Jan. 28-29, 2021) 39 (in Japanese)

Internal pressure induced by lead bishmuth eutectic (LBE and its behavior
Akito Fujitsu, Naoya Odaira, Daisuke Ito Kei Ito, Yasushi Saito
Proceedings of the 55th KURNS Scientific Meeting Web Meeting 2020 (Jan. 28-29, 2021) 26 (in Japanese)

Reviews

Subcriticality - from basics to applications (6)
Katano Ryota, Yamanaka Masao
Journal of the Atomic Energy Society of Japan 62(3) (2020) 158-162

Subcriticality - from basics to applications (8)
Toshihiro Yamamoto
Journal of the Atomic Energy Society of Japan 62(5) (2020) 285-289

Books

Fundamentals of Nuclear Physics
C. H. Pyeon and D. Ito
Fundamental of Thermal and Nuclear Power Engineering
Elsevier (2020)

Accelerator-Driven System at Kyoto University Critical Assembly
C. H. Pyeon
Springer (2021)

4. Material Science and Radiation Effects

Papers

Accurate Synchrotron Hard X-ray Diffraction Mesurements on High-Temperature Liquid Oxides
K. Ohara, Y. Onodera, S. Kohara, C. Koyama, A. Masuno, A. Mizuno, J. T. Okada, S. Tahara, Y. Watanabe, H. Oda, Y. Nakata, H. Tamaru, T. Ishikawa, O. Sakata
International Journal of Microgravity Science and Application 37(2) (2020) 370202

Controlling oxygen coordination and valence of network forming cations
T. Aoyagi, S. Kohara, T. Naito, Y. Onodera, M. Kodama, T. Onodera, D. Takamatsu, S. Tahara, O. Sakata, T. Miyake, K. Suzuya, K. Ohara, T. Usuki, Y. Hayashi, H. Takizawa
Scientific Reports 10 (2020) 7178

Development of a Field Emission Image Sensor Tolerant to Gamma-Ray Irradiation
Gotoh Yasuhito, Tsuji Hiroshi, Nagao Masayoshi, Masuzawa Tomoaki, Neo Yoichiro, Mimura Hidenori, Okamoto Tamotsu, Igari Tomoya, Akiyoshi Masafumi, Sato Nobuhiro, Takagi Ikuji
IEEE Transactions on Electron Devices 67(4) (2020) 1660-1665

Sensitivity of Positrons at Hydrogen Storage Sites in FeCr Alloy Containing Vacancy and Helium Atom
T. Zhu, B.Y. Wang, L.G. Song, X.S. Liu, Y.M. Song, Y.L. Liu, P. Zhang, X.Z. Cao, Q. Xu,
International Journal of Hydrogen Energy 45 (2020) 15571-15577

Simultaneous Measurement of γ-ray and Conversion Electron Mössbauer Spectra of Fe Films under Total Reflection Conditions Using Synchrotron Mössbauer Source
Mitsui Takaya, Mibu Ko, Tanaka Masaaki, Kitao Shinji, Kobayashi Yasuhiro ,Masuda Ryo, Seto Makoto
Journal of the Physical Society of Japan 89(5) (2020) 054707

Change in the Positron Annihilation Lifetime of Vacancies Containing Hydrogen Atoms in Electron-Irradiated Tungsten K. Sato, Y. Kondo, M. Ohta, A. Hirosako, M. Onoue, M. Hatakeyama, S. Sunada, Q. Xu
JPS Conference Proceedings 28 (2020) 061001

Fluorescence anisotropy study of radiation-induced DNA damage clustering based on FRET
Akamatsu Ken, Shikazono Naoya, Saito Takeshi
Analytical and Bioanalytical Chemistry 256 (2020) 127021

Migration Behaviour of Vacancies and Damage Structure Recovery in A Fe-Based Fe-Cr-Mn-Cu-Mo Multi-Component Alloy
Q. Xu, Z.H. Zhong, T. Zhu, X.Z. Cao, H. Tsuchida
Philosophical Magazine 100 (2020) 1733-1748

Positron Annihilation Spectroscopy Characterization of Formation of Helium / Hydrogen-Vacancy Nano-Clusters in FeCr Alloy
T. Zhu, B.Y. Wang, X.N. Lian, S.X. Jin, R.S. Yu, X.Z. Cao, Q. Xu
ACTA PHYSICA POLONICA A 137 (2020) 235-237

Principal Vibration Modes of the La_2O_3-Ga_2O_3 Binary Glass by Diverse Coordination Environments of Oxygen Atoms
K. Yoshimoto, A. Masuno, I. Sato, Y. Ezura, H. Inoue, M. Ueda, M. Mizuguchi, Y. Yanada, T. Kawashima, T. Oya, Y. Onodera, S. Kohara, K. Ohara
The Journal of Physical Chemistry B 124(24) (2020) 5056-5066

Quantitative Structure Analysis of a Near-Ideal Polymer Network with Deuterium Label by Small-Angle Neutron Scattering
Ohira Masashi, Tsuji Yui, Watanabe Nobuyuki, Morishima Ken, Gilbert Elliot P., Li Xiang, Shibayama Mitsuhiro
Macromolecules 53(10) (2020) 4047-4054

Vanadium coordination environment in phospho-vanadate glass for improving water durability
T. Aoyagi, D. Takamatsu, Y. Onodera, T. Naito, T. Onodera, T. Miyake, S. Kohara, T. Ina, Y. Hayashi, H. Takizawa
Journal of the Ceramic Society of Japan 128 (2020) 273-278

^{57}Fe Mössbauer study of high-valent Fe ions in Fe-substituted Li_2MnO_3
Kobayashi Yasuhiro, Tabuchi Mitsuharu, Seto Makoto
Hyperfine Interactions 57(1) (2020) 241

Very sharp diffraction peak in nonglass-forming liquid with the formation of distorted tetraclusters
C. Koyama, S. Tahara, S. Kohara, Y. Onodera, D. R. Smabraten, S. M. Selbach, J. Akola, T. Ishikawa, A. Masuno, A. Mizuno, J. T. Okada, Y. Watanabe, Y. Nakata, K. Ohara, H. Tamaru, H. Oda, I. Obayashi, Y. Hiraoka, O. Sakata
NPG Asia Materials 12 (2020) 43

Correction to: Development of ^{166}Er Mössbauer spectroscopy in KURNS
Nakamura Shin, Yokota Hiroko, Kitao Shinji, Kobayashi Yasuhiro, Saito Makina, Masuda Ryo, Seto Makoto
Hyperfine Interactions 240 (2020) 75

Correlation between structure and physical properties of binary ZnO-P_2O_5 glasses
H. Masai, Y. Onodera, S. Kohara, T. Ohkubo, A. Koreeda, Y. Fujii, M. Koshimizu, M. Yamawaki
Physica Status Solidi B 257 (2020) 2000186

D_2 Retention Behavior and Microstructural Evolution of "W-2wt.%Y_2O_3 Alloy during He-Ion Irradiation at High Temperatures
Q. Xu, L.M. Luo, Z. Chen, M. Hirakawa, M. Miyamoto, H.C. Chen, K. Sato, H. Tsuchida
Journal of Nuclear Materials 539 (2020) 152273

Dynamics Study of Superionic Conducting Glass Na_3PS_4 Using Quasi-Elastic Gamma-ray Scattering: Analysis Based on Diffraction and RMC-DFT Modeling
Makina Saito, Yohei Onodera, Koji Ohara, Masayuki Kurokuzu, Yoshitaka Yoda, Makoto Seto
Physica Status Solidi B 257(11) (2020) 2000113

Nanostructural Characterization of Oleyl Acid Phosphate in Poly-α-olefin Using Small-angle X-ray Scattering
Oba Yojiro, Motokawa Ryuhei, Hino Masahiro, Adachi Nozomu, Todaka Yoshikazu, Inoue Rintaro, Sugiyama Masaaki
Chemistry Letters 49(7) (2020) 823-825

Preparation Technology of Ultra-Fine Tungsten Carbide Powders: An Overview
Y.C. Wu, Y. Yang, X.Y. Tan, L.M. Luo, X. Zan, X.Y. Zhu, Q. Xu, J.G. Cheng
Frontiers in Materials 7 (2020) 94

The Influence of Different Isochronal Annealing Temperature on Helium Ion Irradiation Damage of W-Nb Composites H.Y. Chen, Y.F. Zhou, M.Y. Xu, L.M. Luo, Q. Xu, X.Y. Zhu, Y.C. Wu
Fusion Engineering and Design 159 (2020) 111857

Behavior of Lead-Bismuth eutectic (LBE) expansion caused by phase transition in response to heat treatment
Odaira Naoya, Fujiwara Takuma, Arita Yuji
Nuclear Engineering and Design 365 (2020) 110714

Enhanced extraction via surface asperities of light generated around the boundary plane in poly (ethylene naphthalate
Nakamura Hidehito, Mori Kazuhiro,Sato Nobuhiro,Kamata Takashi,Kanayama Masaya
Physica Scripta 95(9) (2020) 095303

Metamagnetic transitions and magnetoelectric responses in the chiral polar helimagnet Ni_2InSbO_6
Araki Y., Sato T., Fujima Y., Abe N., Tokunaga M., Kimura S., Morikawa D., Ukleev V., Yamasaki Y., Tabata C., Nakao H., Murakami Y., Sagayama H., Ohishi K., Tokunaga Y., Arima T.
Physical Review B 102(5) (2020) 054409

Short positron lifetime at vacancies observed in electron-irradiated tungsten: Experiments and first-principles calculations
A. Yabuuchi, M. Tanaka, A. Kinomura
Journal of Nuclear Materials 542 (2020) 152473

Effect of pulse irradiation on the evolution of damage structure
Yoshiie T., Kinomura A.
Nuclear Instruments and Methods in Physics Research Section B: Beam Interactions with Materials and Atoms 479 (2020) 51- 54

Valence Transition of $EuRh_2Si_2$ Studied by Synchrotron Mössbauer Spectroscopy
Mitsuda Akihiro, Wada Hirofumi, Masuda Ryo, Kitao Shinji, Seto Makoto, Yoda Yoshitaka, Kobayashi Hisao
Journal of the Physical Society of Japan 89(10) (2020) 104703

Comparison of tritium release behavior in Li_2TiO_3 and promising core-shell Li_2TiO_3−Li_4SiO_4 biphasic ceramic pebbles
Qi Qiang, Wang Jing, Zhou Qilai, Zhang Yingchun, Zhao Mingzhong, Gu Shouxi, Nakata Moeko, Zhou Haishan, Oya Yasuhisa, Luo Guang-Nan
Journal of Nuclear Materials 539 (2020) 152330

Defects and Microstructural Evolution of Cold-Rolled Pure Zirconium under Isochronal Annealing Conditions
M.P. Wan, T. Zhu, Q. Xu
Rare Metal Materials and Engineering 49 (2020) 3377-3381

Effect of gamma-irradiation on complexation of humic substances with divalent calcium ion
Zhao Qi, Goto Ryohei, Saito Takeshi, Kobayashi Taishi, Sasaki Takayuki
Chemosphere 256 (2020) 127021

Chemical state of Fe^{3+} in a Fe^{3+} -type cation exchange resin for the removal and recovery of phosphate ions and the adsorption mechanism of phosphate ion to the resin

Juntarasakul Onchanok, Yonezu Kotaro, Kawamoto Daisuke, Ohashi Hironori, Kobayashi Yasuhiro, Sugiyama Takeharu, Watanabe Koichiro, Yokoyama Takushi
Colloids and Surfaces A: Physicochemical and Engineering Aspects 605 (2020) 125314

Design and properties of $FeAl/Al_2O_3/TiO_2$ composite tritium-resistant coating prepared through pack cementation and sol−gel method
Zhu Liu, Zheng Liang, Xie Hao, Liu Dong-Guang, Xu Qiu, Luo Lai-Ma, Wu Yu-Cheng
Materials Today Communications (2020) 101848

Effect of grain boundary on the friction coefficient of pure Fe under the oil lubrication
Adachi Nozomu, Matsuo Yasutaka, Todaka Yoshikazu, Fujimoto Mikiya, Hino Masahiro, Mitsuhara Masatoshi, Oba Yojiro, Shiihara Yoshinori, Umeno Yoshitaka, Nishida Minoru
Tribology International 155 (2020) 106781

Effect of Irradiation on Randomness of Element Distribution in CoCrFeMnNi Equiatomic High-Entropy Alloy
X.L. Ren, B.D. Yao, T. Zhu, Z.H. Zhong, Y.X. Wang, X.Z. Cao, S. Jinno, Q. Xu
Intermetallics 126 (2020) 106942

Synchrotron Mössbauer Diffraction of Natural Iron Fe_3BO_6
Nakamura Shin, Mitsui Takaya, Kobayashi Yasuhiro, Kurokuzu Masayuki, Shimomura Susumu
Journal of the Physical Society of Japan 89(12) (2020) 125001

Characterization of the effect of ion irradiation on industrially produced $GdBa_2Cu_3O_{7-\delta}$ superconducting tapes using a slow positron beam
Yabuuchi Atsushi, Ozaki Toshinori, Sakane Hitoshi, Okazaki Hiroyuki, Koshikawa Hiroshi, Yamamoto Shunya, Yamaki Tetsuya
Applied Physics Express 13 (2020) 123004

Magnetic Friedel Oscillation at the Fe(001) Surface: Direct Observation by Atomic-Layer-Resolved Synchrotron Radiation ^{57}Fe Mössbauer Spectroscopy
Mitsui T., Sakai S., Li S., Ueno T., Watanuki T., Kobayashi Y., Masuda R., Seto M., Akai H.
Physical Review Letters 125(23) (2020) 236806

Microstructure Evolution and Effect on Deuterium Retention in Oxide Dispersion Strengthened Tungsten during He^+ Irradiation
X.Y. Ding, Q. Xu, X.Y. Zhu, L.M. Luo, J.J. Huang, B. Yu, X. Gao, J.G. Li, Y.C. Wu
Nuclear Engineering and Technology 52 (2020) 2860-866

Relationship between the First Sharp Diffraction Peak and Physical Properties of Silicon Dioxide (SiO_2 Glasses Possessing Different Fictive Temperatures
H. Masai, S. Kohara, Y. Onodera, A. Koreeda, K. Saito, E. H. Sekiya, N. Kitamura
Journal of the Ceramic Society of Japan 128 (2020) 1038-1044

Research Status and Development Trend of Preparation Technology of Ceramic Particle Dispersion Strengthened Copper-Matrix Composites
Y.Q. Qin, Y. Tian, Y.Q. Peng, L.M. Luo, X. Zan, Q. Xu, Y.C. Wu
Journal of Alloys and Compounds 848 (2020) 156475

Structure and properties of densified silica glass: characterizing the order within disorder
Onodera Yohei, Kohara Shinji, Salmon Philip S., Hirata Akihiko, Nishiyama Norimasa, Kitani Suguru, Zeidler Anita, Shiga Motoki, Masuno Atsunobu, Inoue Hiroyuki, Tahara Shuta, Polidori Annalisa, Fischer Henry E., Mori Tatsuya, Kojima Seiji, Kawaji Hitoshi, Kolesnikov Alexander I., Stone Matthew B., Tucker Matthew G., McDonnell Marshall T., Hannon Alex C., Hiraoka Yasuaki, Obayashi Ippei, Nakamura Takenobu, Akola Jaakko, Fujii Yasuhiro, Ohara Koji, Taniguchi Takashi, Sakata Osami
NPG Asia Materials 12 (2020) 85

Change in the Positron Annihilation Lifetime of Vacancy Clusters Containing Hydrogen Atoms in Electron-Irradiated F82H
Sato Koichi, Kondo Yohei, Ohta Masakiyo, Xu Qiu, Yabuuchi Atsushi, Kinomura Atsushi, Onoue Masahira, Onitsuka Takashi, Hatakeyama Masahiko, Iwakiri Hirotomo, Kato Daiji, Watanabe Yoshiyuki, Tanigawa Hiroyasu
Materials Science Forum 1024 (2021) 71-78

Gamma-irradiation-induced molecular-weight distribution and complexation affinity of humic acid with Cs^{+}, Sr^{2+}, and Eu^{3+}
Zhao Qi, Kobayashi Taishi, Saito Takeshi, Sasaki Takayuki
Journal of Hazardous Materials 411 (2021) 125071

Gamma-ray induced photo emission from GaN single crystal wafer
Nakamura Toshihiro, Nishimura Tomoaki, Kuriyama Kazuo, Nakamura Tohru, Kinomura Atsushi
Applied Physics Letters 3 (2021) 032106

Irradiation resistance mechanism of the CoCrFeMnNi equiatomic high-entropy alloy
Xu Q., Guan H. Q., Zhong Z. H., Huang S. S., Zhao J.
Scientific Reports 11(1) (2021) 608

Uncertainty derived from elemental analysis and its effect on the separation of radioactive waste into low-level radioactive waste and waste for clearance
Kinoshita Norikazu, Noto Takuma, Kosako Kazuaki, Asada Motoyuki, Torii Kazuyuki, Tada Akane, Urabe Kohei, Ohtsuki Tsutomu, Sekimoto Shun
Progress in Nuclear Energy 331 (2021) 103597

A feasibility study of inverse contrast-matching small-angle neutron scattering method combined with size exclusion chromatography using antibody interactions as model systems
Sato Nobuhiro, Yogo Rina, Yanaka Saeko, Martel Anne, Porcar Lionel, Morishima Ken, Inoue Rintaro, Tominaga Taiki, Arimori Takao, Takagi Junichi, Sugiyama Masaaki, Kato Koichi
The Journal of Biochemistry mvab012 (2021)

Effect on ^{99}Mo-adsorption/^{99m}Tc-elution properties of alumina with different surface structures
Fujita Yoshitaka, Seki Misaki, Sano Tadafumi, Fujihara Yasuyuki, Kitagawa Tomoya, Matsukura Minoru, Hori Junichi, Suzuki Tatsuya, Tsuchiya Kunihiko
Journal of Radioanalytical and Nuclear Chemistry 3 (2021) 1355-1363

Comparison of Hydrogen Thermal Desorption Analysis Curves of Electron-Irradiated F82H and Creep-Ruptured Pure Fe Obtained by Experiments and Simulations
Kamimura Takuya,Yamashita Hayato, Sato Koichi, Ohyama Tsunakazu, Kimoto Yoshinori, Xu Qiu, Komazaki Shin Ichi
Materials Science Forum 1024 (2021) 135-144

Effects of Alloying Elements Mn, Mo, Ti, Si, P and C on the Incubation Period of Void Swelling in Austenitic Stainless Steels
T. Yoshiie, Q. Xu
Tungsten 3 (2021) 3-19

Perpendicular magnetic anisotropy at the Fe/Au(111 interface studied by Mössbauer, x-ray absorption, and photoemission spectroscopies
Okabayashi Jun, Li Songtian, Sakai Seiji, Kobayashi Yasuhiro, Mitsui Takaya, Tanaka Kiyohisa, Miura Yoshio, Mitani Seiji
Physical Review B 103(10) (2021) 504435

Plasma-surface interaction experimental device: PSIEC and its first plasma exposure experiments on bulk tungsten and coatings
Xu Yue, Xu Yunfeng, Wu Zuosheng, Luo Laima, Zan Xiang, Yao Gang, Xi Ya, Wang Yafeng, Ding Xiaoyu, Bi Hailin, Zhu Xiaoyong, Xu Qiu, Wu Jiefeng, Wu Yucheng
Fusion Engineering and Design 164 (2021) 112198

Radiophotoluminescence of Cu-doped silica glass derived from phase-separated sodium borosilicate glass
Takada Yuya, Yamamoto Keigo, Kinomura Atsushi, Saito Takeshi, Ichinose Nobuyuki, Okada Arifumi, Wakasugi Takashi, Kadono Kohei
AIP Advances 11(3) (2021) 035208

Small-angle neutron scattering geometry with ring-shaped collimation for compact neutron sources
Funama F., Adachi Y., Tasaki S., Abe Y.
Nuclear Instruments and Methods in Physics Research Section A: Accelerators, Spectrometers, Detectors and Associated Equipment 992 (2021) 165013

The influence of the long-term heating under H2 atmosphere on the tritium release behavior from the neutron-irradiated Li_2TiO_3
Ipponsugi Akito, Katayama Kazunari, Hoshino Tsuyoshi
Fusion Engineering and Design 170 (2021) 112495

Reduction of background radiation effects for positron lifetime measurements in the slow positron beamline at the Kyoto University Research Reactor
M. Nakajima, R.T aguchi, A. Yabuuchi, A. Kinomura
Review of Scientific Instruments 91(12) (2020) 125109

Proceedings

Chemical states of Fe atoms in Iron hydride
M. Sato, Y. Kobayashi, Y. Yamada, M. K. Kubo, M. Mihara, W. Sato, T. Nagatomo, A. Okazawa, Y. Sato, M. Kiji, K. Hamano, S. Sato, and A. Kitagawa
Proceedings of the Specialists'Meeting on"Nuclear Spectroscopy and Condensed Matter Physics Using Short-Lived Nuclei VI" and Meeting on"11th Nuclear Spectroscopy Research Using Stop and Slow Unstable Nuclei (SSRI)" Kumatori, Japan (Jan. 16-17, 2020) 17-20 (in Japanese)

Can we trace lithium diffusion on interference in between solid electrode and solid electrolytes in lithium battery?
T. Funabashi, Y. Kobayashi, and Y. Yamada
Proceedings of the Specialists'Meeting on "Nuclear Spectroscopy and Condensed Matter Physics Using Short-Lived Nuclei VI" and Meeting on "11th Nuclear Spectroscopy Research Using Stop and Slow Unstable Nuclei (SSRI)" Kumatori, Japan (Jan. 16-17, 2020) 7-12 (in Japanese)

Effects of heat treatments on metastable iron carbide thin films produced by pulsed laser deposition of iron in methane atmosphere
H. Ishiyama, S.C. Jeong, Y.X. Watanabe, Y. Hirayama, M. Oyaizu, M. Wada, H. Miyatake, K. Nishio, H. Makii, A. Osa, Y. Otokawa, M. Matsuda, T.K. Sato, N. Kuwata, I. Katayama, A. Takamine, S. Iimura, H. Ueno, S. Kimura and M. Mukai
Proceedings of the Specialists'Meeting on "Nuclear Spectroscopy and Condensed Matter Physics Using Short-Lived Nuclei VI" and Meeting on "11th Nuclear Spectroscopy Research Using Stop and Slow Unstable Nuclei (SSRI)" Kumatori, Japan (Jan. 16-17, 2020) 31-34 (in Japanese)

Development of RF Carpet Type Gas Cell in SLOWRI for BigRIPS Beam
S. Iimura, A. Takamine, M. Rosenbusch, M. Wada, S. Chen, J. Liu, P. Schury, T. Sonoda, T. M. Kojima, Y. X. Watanabe, A. Odahara, and H. Ishiyama
Proceedings of the Specialists'Meeting on "Nuclear Spectroscopy and Condensed Matter Physics Using Short-Lived Nuclei VI" and Meeting on "11th Nuclear Spectroscopy Research Using Stop and Slow Unstable Nuclei (SSRI)" Kumatori, Japan (Jan. 16-17, 2020) 83-86 (in Japanese)

Development of multi-element Mössbauer spectroscopy probed by specific isotope
Kenji Murotan, Hidetsugu Tsuchida, Qiu XU
Proceedings of the 55th KURNS Scientific Meeting Web Meeting 2020 (Jan. 28-29, 2021) 37 (in Japanese)

Aggregation removal analysis with concerted use of small angle scattering and analytical ultracentrifugation (AUC-SAS)
Ken Morishima, Yousuke Miyamoto, Aya Okuda, Masahiro Shimizu, Nobuhiro Sato, Rintaro Inoue, Reiko Urade, Msaaki Sugiyama
Proceedings of the 55th KURNS Scientific Meeting Web Meeting 2020 (Jan. 28-29, 2021) 25 25 (in Japanese)

Effect of Mo addition on deuterium accumulation in $W\text{-}Y_2O_3$
Tomoko Hirayama, Naoki Yamashita, Masahiro Hino, Norifumi Yamada
Proceedings of the 55th KURNS Scientific Meeting Web Meeting 2020 (Jan. 28-29, 2021) 43 (in Japanese)

Structural analysis of boundary layer formed by multiple addutuves by neutron reflectometry
Shinji Kitao, Yasuhiro Kobayashi, Makina Saito, Takumi Kubota, Masayuki Kurokuzu, Shuichi Hosokawa, Hiroyuki Tajima, Shinichiro Yazaki, Naoki Umetani, Hiroki Taniguchi, Keiji Shinoda, Hiroshi Fujii, Yimi

Yakiyama, Yoko Akiyama, Yasuko Yamamoto, Norimichi Kojima, Hironori, Ohashi, Shigeomi Takai, Yoshiteru Meno, Yoichi Kamihara, Haruno Murayama, Goro Miyamoto, Ryo Masuda, Makoto Seto
Proceedings of the 55th KURNS Scientific Meeting Web Meeting 2020 (Jan. 28-29, 2021) 7-9 (in Japanese

Change in the Annihilation Lifetime of Vacancy Clusters Containing Hydrogen Atoms in Electron-Irradiated F82H K. Sato, Y. Kondo, M. Ohta, Q. Xu, A. Yabuuchi, A. Kinomura, M. Onoue, T. Onitsuka, M. Hatakeyama, H. Iwakiri, D. Kato, Y. Watanabe, H. Tanigawa
Materials Science Forum 1024 (2020) 71-78

Comparison oh Hydrogen Thermal Desorption Analysis Curves of Electron-Irradiated F82H and Creep-Ruptured Pure Fe Obtained by Experiments and Simulations
T. Kamimura, H. Yamashita, K. Sato, T. Ohyama, Y. Kimoto, Q. Xu, S. Komazaki,
Materials Science Forum 1024 (2020) 135-144

Local- and Intermediate-Range Atomic Order in $Ga_2Ge_3Se_9$ Glass: Complementary Use of X-Rays and Neutrons
Hosokawa Shinya, Stellhorn Jens Rüdiger, Onodera Yohei, Kohara Shinji, Tajiri Hiroo, Magome Eisuke, Pusztai László, Ikeda Kazutaka, Otomo Toshiya, Krbal Milos, Wagner Tomas
JPS Conference Proceedings 33 (2021) 011069

Reviews

Structure and Dynamics of Highly Crosslinked Rubber as Studied by Neutron Scattering
MASHITA RYO, INOUE RINTARO, KISHIMOTO HIROYUKI, KANAYA TOSHIJI
Sen'i Gakkaishi 76(6) (2020) 219-224 (in Japanese)

陽電子の消滅と欠陥への捕獲
薮内敦, 藤浪真紀
陽電子科学会誌 15(3) (2020) 3-9 (in Japanese)

ガラスにならない Er_2O_3 液体が持つ特異構造
小山千尋，小原真司，田原周太，小野寺陽平，石川毅彦
放射光 34 (2021) 30-36 (in Japanese)

Origin of the Mixed Alkali Effect in Silicate Glass
Y. Onodera, Y. Takimoto, H. Hijiya, T. Taniguchi, S. Urata, S. Inaba, S. Fujita, I. Obayashi, Y. Hiraoka, and S. Kohara
MLF Annual Report 2019 (2021) 54-56

Books

Synchrotron-Radiation-Based Energy-Domain Mössbauer Spectroscopy, Nuclear Resonant Inelastic Scattering, and Quasielastic Scattering Using Mössbauer Gamma Rays
Seto Makoto, Masuda Ryo, Saito Makina
Modern Mössbauer Spectroscopy
Yutaka Yoshida Guido Langouche
Springer (2021)

15 章-光学的性質, 10-メスバウアースペクトル
瀬戸 誠
化学便覧 基礎編 改訂6版
日本化学会 編
丸善出版 (2021) (in Japanese)

Others

事故耐性の高い軽水炉用制御棒の開発 (4) 京大炉による新型中性子吸収材の照射試験
太田宏一, 中村勤也, 高橋佳之, 佐野忠史

5. Geochemistry and Environmental Science
Papers

The pale grass blue butterfly in ex-evacuation zones 5.5 years after the Fukushima nuclear accident: Contributions of initial high-dose exposure to transgenerational effects
Sakauchi Ko, Taira Wataru,Hiyama Atsuki,Imanaka Tetsuji,Otaki Joji M.
Journal of Asia-Pacific Entomology 23(1) (2020) 242-252

The effects of possible contamination by sample holders on samples to be returned by Hayabusa2
Shirai Naoki, Karouji Yuzuru, Kumagai Kazuya, Uesugi Masayuki, Hirahara Kaori, Ito Motoo, Tomioka Naotaka, Uesugi Kentaro, Yamaguchi Akira, Imae Naoya, Ohigashi Takuji, Yada Toru, Abe Masanao
Meteoritics & Planetary Science 55(7) (2020) 1665-1680

Modeling Transition Metals in East Asia and Japan and Its Emission Sources
Kajino Mizuo, Hagino Hiroyuki, Fujitani Yuji, Morikawa Tazuko, Fukui Tetsuo, Onishi Kazunari, Okuda Tomoaki, Kajikawa Tomoki, Igarashi Yasuhito
GeoHealth 9 (2020) e2020GH000259

Project IPAD, a database to catalogue the analysis of Fukushima Daiichi accident fragmental release material
Martin Peter, Alhaddad Omran, Verbelen Yannick, Satou Yukihiko, Igarashi Yasuhito, Scott Thomas B.
Scientific Data 7(1) (2020) 282

Observation of morphological abnormalities in silkworm pupae after feeding ^{137}CsCl-supplemented diet to evaluate the effects of low dose-rate exposure
Tanaka Sota, Kinouchi Tadatoshi, Fujii Tsuguru, Imanaka Tetsuji, Takahashi Tomoyuki, Fukutani Satoshi, Maki Daisuke, Nohtomi Akihiro,Takahashi Sentaro
Scientific Reports 10(1) (2020) 16055

Paleomagnetism, paleointensity and geochronology of a Proterozoic dolerite dyke from southern West Greenland
Miki Masako, Seki Hanae, Yamamoto Yuhji, Gouzu Chitaro, Hyodo Hironobu, Uno Koji, Otofuji Yo-ichiro
Journal of Geodynamics 139 (2020) 101752

Rain-induced bioecological resuspension of radiocaesium in a polluted forest in Japan
Kita Kazuyuki, Igarashi Yasuhito, Kinase Takeshi, Hayashi Naho, Ishizuka Masahide, Adachi Kouji, Koitabashi Motoo, Sekiyama Tsuyoshi Thomas, Onda Yuichi
Scientific Reports 10(1) (2020) 15330

Numerical Analyses of Transport Processes of Bioaerosol Released from a Temperate Deciduous Broad-Leaved Forest
Kotaro MINAMI, Genki KATATA, Kazuyuki KITA, Atsuyuki SORIMACHI, Kentaro HOSAKA, Yasuhito IGARASHI
Earozoru Kenkyu 35(3) (2020) 208-218 (in Japanese)

Comparison of three aerosol representations of NHM-Chem (v1.0 for the simulations of air quality and climate-relevant variables
Kajino Mizuo, Deushi Makoto, Sekiyama Tsuyoshi Thomas, Oshima Naga, Yumimoto Keiya, Tanaka Taichu Yasumichi, Ching Joseph, Hashimoto Akihiro, Yamamoto Tetsuya, Ikegami Masaaki, Kamada Akane, Miyashita Makoto, Inomata Yayoi, Shima Shin-ichiro, Khatri Pradeep, Shimizu Atsushi, Irie Hitoshi, Adachi Kouji, Zaizen Yuji, Igarashi Yasuhito, Ueda Hiromasa, Maki Takashi, Mikami Masao
Geoscientific Model Development Discussions 14(4) (2020) 2235-2264

Extractable organochlorine (EOCl and extractable organobromine (EOBr in GPC-fractionated extracts from high-trophic-level mammals: Species-specific profiles and contributions of legacy organohalogen contaminants
Mukai Kota, Fujimori Takashi, Anh Hoang Quoc, Fukutani Satoshi, Kunisue Tatsuya, Nomiyama Kei, Takahashi Shin
Science of The Total Environment (2020) 143843

Isolation, characterization and source analysis of radiocaesium micro-particles in soil sample collected from vicinity of Fukushima Dai-ichi nuclear power plant
Futagami Fumiya, Soliman Mohamed, Takamiya Koichi, Sekimoto Shun, Oki Yuichi, Kubota Takumi, Konno Mitsuyuki, Mizuno Satoshi, Ohtsuki Tsutomu
Journal of Environmental Radioactivity 223-224 (2020) 106388

Deposition and Dispersion of Radio-Cesium Released due to the Fukushima Nuclear Accident: 2. Sensitivity to Aerosol Microphysical Properties of Cs-Bearing Microparticles (CsMPs)
Kajino Mizuo, Adachi Kouji, Igarashi Yasuhito, Satou Yukihiko, Sawada Morihiro, Thomas Sekiyama Tsuyoshi, Zaizen Yuji, Saya Akane, Tsuruta Haruo, Moriguchi Yuichi
Journal of Geophysical Research: Atmospheres 1 (2020)

Role of advection in atmospheric ammonia: A case study at a Japanese lake basin influenced by agricultural ammonia sources
Kubota T., Kuroda H., Watanabe M., Takahashi A., Nakazato R., Tarui M., Matsumoto S., Nakagawa K., Numata Y., Ouchi T., Hosoi H., Nakagawa M., Shinohara R., Kajino M., Fukushima K., Igarashi Y., Imamura N., Katata G.
Atmospheric Environment 243 (2020) 117856

Temporal variations of ^{90}Sr and ^{137}Cs in atmospheric depositions after the Fukushima Daiichi Nuclear Power Plant accident with long-term observations
Kinase Takeshi,Adachi Kouji,Sekiyama Tsuyoshi Thomas,Kajino Mizuo, Zaizen Yuji, Igarashi Yasuhito
Scientific Reports 10(1) (2020) 21627

Teshima pyroclastics: Onset of characteristic Setouchi magmatism induced by slab melting at 14.8 Ma Nakaoka Reina, Kado Soko, Hasegawa Shuichi, Suzuki-Kamata Keiko, Ishizuka Osamu, Sekimoto Shun, Kawabata Hiroshi, Tatsumi Yoshiyuki
Island Arc 30(1) (2020) 12378

Synergy effect of organic acids from plants on mineral dissolution by siderophore - producing bacteria Tatsuki KIMURA, Naofumi KOZAI, Fuminori SAKAMOTO, Satoshi FUKUTANI, Maiko IKEGAMI
Journal of Japan Society of Civil Engineers, Ser. G (Environmental Research) 76(7) (2020) 375-382 (in Japanese)

The change in structure of clay minerals and elution of cs and sr by heat Treatment
Maiko IKEGAMI, Kenshin KUROKI, Satoshi FUKUTANI, Minoru YONEDA
Journal of Japan Society of Civil Engineers, Ser. G (Environmental Research) 76(7) (2020) 403-410 (in Japanese)

A Paleogene magmatic overprint on Cretaceous seamounts of the western Pacific
Hirano Naoto, Sumino Hirochika, Morishita Taisei, Machida Shiki, Kawano Takaomi, Yasukawa Kazutaka, Hirata Takafumi,Kato Yasuhiro,Ishii Teruaki
Island Arc 30(1) (2021) e12386

Poirierite, a dense metastable polymorph of magnesium iron silicate in shocked meteorites
Tomioka, N., Bindi, L., Okuchi, T., Miyahara, M., Iitaka, T., Li, Z., Kawatsu, T., Xie, X., Purevjav, N., Tani, R., Kodama, Y.
Communications Earth & Environment 2(1) (2021) 16

Survey of elemental composition in dewatered sludge in Japan
Chen Minhsuan, Oshita Kazuyuki, Mahzoun Yahya, Takaoka Masaki, Fukutani Satoshi, Shiota Kenji
Science of The Total Environment 752 (2021) 141857

Widespread distribution of radiocesium-bearing microparticles over the greater Kanto Region resulting from the Fukushima nuclear accident
Abe Yoshinari, Onozaki Seika, Nakai Izumi, Adachi Kouji, Igarashi Yasuhito, Oura Yasuji, Ebihara Mitsuru, Miyasaka Takafumi, Nakamura Hisashi, Sueki Keisuke, Tsuruta Haruo, Moriguchi Yuichi
Progress in Earth and Planetary Science 8(1) (2021) 13

Co-precipitation behaviour of single atoms of rutherfordium in basic solutions

Kasamatsu Yoshitaka, Toyomura Keigo, Haba Hiromitsu, Yokokita Takuya, Shigekawa Yudai, Kino Aiko, Yasuda Yuki, Komori Yukiko, Kanaya Jumpei, Huang Minghui, Murakami Masashi, Kikunaga Hidetoshi, Watanabe Eisuke, Yoshimura Takashi, Morita Kosuke, Mitsugashira Toshiaki, Takamiya Koichi, Ohtsuki Tsutomu, Shinohara
Atsushi Nature Chemistry 13(3) (2021) 226-230

Simple Pretreatment Method for Tritium Measurement in Environmental Water Samples using a Liquid Scintillation Counter
NAKASONE Shunya, YOKOYAMA Sumi, TAKAHASHI Tomoyuki, OTA Masakazu, KAKIUCHI Hideki, SUGIHARA Shinji, HIRAO Shigekazu, MOMOSHIMA Noriyuki, TAMARI Toshiya, SHIMA Nagayoshi, ATARASHI-ANDOH Mariko, FUKUTANI Satoshi, NAKAMURA Kaori, ISHIMINE Akinobu, FURUKAWA Masahide, TANAKA Masahiro, AKATA Naofumi
Plasma and Fusion Research 16 (2021) 2405035

Effect of bacterial siderophore on cesium dissolution from biotite
Kimura Tatsuki,Fukutani Satoshi, Ikegami Maiko, Sakamoto Fuminori, Kozai Naofumi, Grambow Bernd, Yoneda Minoru
Chemosphere 276 (2021) 130121

Simulation of the transition metal-based cumulative oxidative potential in East Asia and its emission sources in Japan Kajino Mizuo, Hagino Hiroyuki, Fujitani Yuji, Morikawa Tazuko, Fukui Tetsuo, Onishi Kazunari, Okuda Tomoaki, Igarashi Yasuhito
Scientific Reports 11 (2021) 6550

Proceedings

Mössbauer Spectra of Paddy Field Soils in Fukushima and One Consideration Concerning Transfer of Radioactive Cesium from Soil to Rice Plants
S. Nakashima, H. T. Nguyen, and M. Tsujimoto
Proceedings of the Specialists' Meeting on"Nuclear Spectroscopy and Condensed Matter Physics Using Short-Lived Nuclei VI" and Meeting on"11th Nuclear Spectroscopy Research Using Stop and Slow Unstable Nuclei (SSRI)"13-16 (in Japanese)

Crystallography of hydrogen in the deep Earth by scattering
Norio Ito, Akira Mizohata, Hisao Yoshinaga, Yuto iimura
Proceedings of the 55th KURNS Scientific Meeting Web Meeting 2020 (Jan. 28-29, 2021) 19 (in Japanese)

Size distribution of Chlorine(Cl) and Bromine(Br) in the atmosphric aerosols
Takuo Okuchi
Proceedings of the 55th KURNS Scientific Meeting Web Meeting 2020 (Jan. 28-29, 2021) 10-11 (in Japanese)

Reviews

Origin of 1 mSv per Year Regulation and Discussion on Low Level Radiation Risk
Tetsuji Imanaka
TRENDS IN THE SCIENCES 25(3) (2020) 52-59 (in Japanese)

Development of a Radiation Mapping System for the Long-Term Contamination after a Nuclear Disaster
Minoru Tanigaki
Butsuri 75(12) (2020) 766-769 (in Japanese)

Basics of Fission-track Geo- and Thermo-chronometry: Revisiting Its History to Explore Future Potential
Noriko Hasebe, Shigeru Sueoka, Takahiro Tagami
RADIOISOTOPES 70(3) (2021) 117 -130 (in Japanese)

Recent Evolution of Fission-track Chronometry ―Advanced Analytical Methods, Understanding of Annealing Kinetics, and Developments of New Dating Systems―
Shigeru Sueoka, Koji Shimada, Noriko Hasebe, Takahiro Tagami

RADIOISOTOPES 70(3) (2021) 189 207 (in Japanese)

Bioaerosols Emission from Forest Ecosystem ─Close Look at Fungal Spore─"
Yasuhito IGARASHI
Earozoru Kenkyu 36(1) (2021) 5-18 (in Japanese)

Accurate determination of three halogen elements (Cl, Br, and I)in U.S. Geological Survey geochemical reference materials by radiochemicalneutron activation analysis and an exhaustive comparison with literaturedata: a review
Shun Sekimoto, Mitsuru Ebihara
Journal of Nuclear and Radiochemical Science 20 (2020) 12-19

Books

Radioactive Cesium Contamination of Arthropods and Earthworms After the Fukushima Daiichi Nuclear Power Plant Accident
Tanaka Sota, Adati Tarô,Takahashi Tomoyuki,Takahashi Sentaro
Low-Dose Radiation Effects on Animals and Ecosystems
Manabu Fukumoto
Springer Singapore (2021)

6. Life Science and Medical Science
Papers

Site-specific rapid deamidation and isomerization in human lens αA-crystallin in vitro
Takata Takumi, Ha Seongmin, Koide TamakiFujii Noriko
Protein Science 29(4) (2020) 941-951

Space Radiation Biology for "Living in Space"
Furukawa Satoshi, Nagamatsu Aiko, Nenoi Mitsuru, Fujimori Akira, Kakinuma Shizuko, Katsube Takanori, Wang Bing, Tsuruoka Chizuru, Shirai Toshiyuki, Nakamura Asako J., Sakaue-Sawano Asako, Miyawaki Atsushi, Harada Hiroshi, Kobayashi Minoru, Kobayashi Junya, Kunieda Takekazu, Funayama Tomoo, Suzuki Michiyo, Miyamoto Tatsuo ,Hidema Jun, Yoshida Yukari, Takahashi Akihisa
BioMed Research International (2020) 4703286

The combined effect of neutron irradiation and temozolomide on glioblastoma cell lines with different MGMT and P53 status
Kinashi Yuko, Ikawa Tomoyuki, Takahashi Sentaro
Applied Radiation and Isotopes 163 (2020) 109204

Versatile whole-organ/body staining and imaging based on electrolyte-gel properties of biological tissues
Susaki Etsuo A., Shimizu Chika, Kuno Akihiro, Tainaka Kazuki, Li Xiang, Nishi Kengo, Morishima Ken, Ono Hiroaki, Ode Koji L., Saeki Yuki, Miyamichi Kazunari, Isa Kaoru, Yokoyama Chihiro, Kitaura Hiroki, Ikemura Masako, Ushiku Tetsuo, Shimizu Yoshihiro, Saito Takashi, Saido Takaomi C., Fukayama Masashi, Onoe Hirotaka, Touhara Kazushige, Isa Tadashi, Kakita Akiyoshi, Shibayama Mitsuhiro, Ueda Hiroki R.
Nature Communications 11(1) (2020) 1982

A Simplified Cluster Analysis of Electron Track Structure for Estimating Complex DNA Damage Yields
Matsuya Yusuke,Nakano Toshiaki,Kai Takeshi,Shikazono Naoya,Akamatsu Ken,Yoshii Yuji,Sato Tatsuhiko
International Journal of Molecular Sciences 21(5) (2020) 1701

Amphiphilic Cationic Triscyclometalated Iridium(III) Complex−Peptide Hybrids Induce Paraptosis-like Cell Death of Cancer Cells via an Intracellular Ca^{+}-Dependent Pathway
Yokoi Kenta, Balachandran Chandrasekar, Umezawa Masakazu, Tsuchiya Koji, Mitrić Aleksandra, Aoki Shin
ACS Omega 5(12) (2020) 6983-7001

Design and Synthesis of Cyclometalated Iridium(III) Complexes─Chromophore Hybrids that Exhibit Long-Emission Lifetimes Based on a Reversible Electronic Energy Transfer Mechanism
Kazama Ayami, Imai Yuki, Okayasu Yoshinori, Yamada Yasuyuki, Yuasa Junpei, Aoki Shin
Inorganic Chemistry 59(10) (2020) 6905-6922

ROS-Responsive Chitosan Coated Magnetic Iron Oxide Nanoparticles as Potential Vehicles for Targeted Drug Delivery in Cancer Therapy
Ayyanaar Srinivasan, Balachandran Chandrasekar,Bhaskar Rangaswamy Chinnabba ,Kesavan Mookkandi Palsamy, Aoki Shin, Raja Ramachandran Palpandi, Rajesh Jegathalaprathaban, Webster Thomas J, Rajagopal Gurusamy
International Journal of Nanomedicine 15 (2020) 3333-3346

Development of Antibody−Oligonucleotide Complexes for Targeting Exosomal MicroRNA
Yamayoshi Asako, Oyama Shota, Kishimoto Yusuke, Konishi Ryo, Yamamoto Tsuyoshi, Kobori Akio, Harada Hiroshi, Ashihara Eishi, Sugiyama Hiroshi, Murakami Akira
Pharmaceutics 12(6) (2020) 545

Integral approach to biomacromolecular structure by analytical-ultracentrifugation and small-angle scattering
Morishima Ken, Okuda Aya, Inoue Rintaro, Sato Nobuhiro, Miyamoto Yosuke, Urade Reiko, Yagi-Utsumi Maho, Kato Koichi, Hirano Rina, Kujirai Tomoya, Kurumizaka Hitoshi, Sugiyama Masaaki
Communications Biology 3(1) (2020) 294

Participation of TDP1 in the repair of formaldehyde-induced DNA-protein cross-links in chicken DT40 cells
Nakano Toshiaki, Shoulkamy Mahmoud I., Tsuda Masataka, Sasanuma Hiroyuki, Hirota Kouji, Takata Minoru, Masunaga Shin-ichiro, Takeda Shunichi, Ide Hiroshi, Bessho Tadayoshi, Tano Keizo
PLOS ONE 15(6) (2020) e0234859

Synthesis, characterization, theoretical, molecular docking and in vitro biological activity studies of Ru(II) (η 6-p-cymene) complexes with novel aniline substituted aroyl selenoureas
Musthafa Moideen, Konakanchi Ramaiah, Ganguly Rakesh, Balachandran Chandrasekar, Aoki Shin, Sreekanth Anandaram
Journal of Biomolecular Structure and Dynamics 1778531 (2020) 1-16

Effect of Rapamycin on the Radio-Sensitivity of Cultured Tumor Cells Following Boron Neutron Capture Reaction Tatebe Hitoshi, Masunaga Shin-ichiro, Nishimura Yasumasa
World Journal of Oncology 11(4) (2020) 158-164

Asp isomerization increases aggregation of αcrystallin and decreases its chaperone activity in human lens of various ages
Fujii Noriko, Takata Takumi, Kim Ingu, Morishima Ken, Inoue Rintaro, Magami Kousuke, Matsubara Toshiya, Sugiyama Masaaki, Koide Tamaki
Biochimica et Biophysica Acta (BBA) - Proteins and Proteomics 1868(9) (2020) 140446

N-substitution in isatin thiosemicarbazones decides nuclearity of Cu(II) complexes − Spectroscopic, molecular docking and cytotoxic studies
Haribabu Jebiti, Alajrawy Othman I., Jeyalakshmi Kumaramangalam, Balachandran Chandrasekar, Krishnan Dhanabalan Anantha, Bhuvanesh Nattamai, Aoki Shin, Natarajan Karuppannan, Karvembu Ramasamy
Spectrochimica Acta Part A: Molecular and Biomolecular Spectroscopy 246 (2020) 118963

A use of microgravity for the structural investigation in the space : For a high precision anti-cancer drug design
Yukio Morimoto, Masayuki Kamo, Naoki FURUBAYASHI, Yuki Higashino, Koji Inaka
Radiation biology research communications 55(3) (2020) 197-209 (in Japanese)

A novel soybean protein disulphide isomerase family protein possesses dithiol oxidation activity: identification and characterization of GmPDIL6
Okuda Aya, Matsusaki Motonori, Masuda Taro, Morishima Ken, Sato Nobuhiro, Inoue Rintaro, Sugiyama Masaaki, Urade Reiko
The Journal of Biochemistry 168(4) (2020) 393-405

Glioma Stem-Like Cells Can Be Targeted in Boron Neutron Capture Therapy with Boronophenylalanine
Kondo Natsuko, Hikida Masaki, Nakada Mitsutoshi, Sakurai Yoshinori, Hirata Eishu, Takeno Satoshi, Suzuki Minoru
Cancers (12)10 (2020) 3040

Nuclear Resonance Vibrational Spectroscopic Definition of the Facial Triad FeIV═O Intermediate in Taurine Dioxygenase: Evaluation of Structural Contributions to Hydrogen Atom Abstraction
Srnec Martin, Iyer Shyam R., Dassama Laura M. K., Park Kiyoung, Wong Shaun D., Sutherlin Kyle D., Yoda Yoshitaka, Kobayashi Yasuhiro, Kurokuzu Masayuki, Saito Makina, Seto Makoto, Krebs Carsten, Bollinger J. Martin, Solomon Edward I.
Journal of the American Chemical Society 142(44) (2020) 18886-18896

An attempt to improve the therapeutic effect of boron neutron capture therapy using commonly employed ^{10}B-carriers based on analytical studies on the correlation among quiescent tumor cell characteristics, tumor heterogeneity and cancer stemness
Masunaga Shin-ichiro, Sanada Yu, Tano Keizo, Sakurai Yoshinori, Tanaka Hiroki, Takata Takushi, Suzuki Minoru, Ono Koji
Journal of Radiation Research 61(6) (2020) 876-885

Crystal Structure Analysis of the 20S Proteasome Grown in Space: Comparison between Space and Ground Crystals
Yukio MORIMOTO, Masayuki KAMO, Naoki FURUBAYASHI, Yuuki HIGASHINO, Koji INAKA
International Journal of Microgravity Science and Application 19 (2020) 370404

PV1 Protein from Plasmodium falciparum Exhibits Chaperone-Like Functions and Cooperates with Hsp100s
Hakamada Kazuaki, Nakamura Manami, Midorikawa Rio, Shinohara Kyosuke, Noguchi Keiichi, Nagaoka Hikaru, Takashima Eizo, Morishima Ken, Inoue Rintaro, Sugiyama Masaaki, Kawamoto Akihiro, Yohda Masafumi
International Journal of Molecular Sciences 21(22) (2020) 8616

Synthesis, anticancer and molecular docking studies of new class of benzoisoxazolyl-piperidinyl-1, 2, 3-triazoles
Muniyappan Govindhan, Kathavarayan Subramanian, Balachandran Chandrasekar, Kalliyappan Easwaramoorthi, Mahalingam Sakkarapalayam M., Ajees Abdul Salam Abdul, Aoki Shin, Arumugam Natarajan, Almansour Abdulrahman I.,Suresh Kumar Raju
Journal of King Saud University - Science 32(8) (2020) 3286-3292

Dynamics of proteins with different molecular structures under solution condition
Inoue Rintaro, Oda Takashi, Nakagawa Hiroshi, Tominaga Taiki, Saio Tomohide, Kawakita Yukinobu, Shimizu Masahiro, Okuda Aya, Morishima Ken, Sato Nobuhiro, Urade Reiko, Sato Mamoru, Sugiyama Masaaki
Scientific Reports 10(1) (2020) 21678

Effect of a Lens Protein in Low-Temperature Culture of Novel Immortalized Human Lens Epithelial Cells (iHLEC-NY2)
Yamamoto Naoki, Takeda Shun, Hatsusaka Natsuko, Hiramatsu Noriko, Nagai Noriaki, Deguchi Saori, Nakazawa Yosuke, Takata Takumi, Kodera Sachiko, Hirata Akimasa, Kubo Eri, Sasaki Hiroshi
Cells 9(12) (2020) 2670

Effect of the Electron Density of the Heme Fe Atom on the Nature of Fe−O_2 Bonding in Oxy Myoglobin
Yamamoto Yasuhiko, Hasegawa Kazuyasu, Shibata Tomokazu, Momotake Atsuya, Ogura Takashi, Yanagisawa Sachiko, Neya Saburo, Suzuki Akihiro, Kobayashi Yasuhiro, Saito Makina, Seto Makoto, Ohta Takehiro
Inorganic Chemistry (60)2 (2020) 1021-1027

Protective Effects of p53 Regulatory Agents Against High-LET Radiation-Induced Injury in Mice
Morita Akinori, Wang Bing, Tanaka Kaoru, Katsube Takanori, Murakami Masahiro, Shimokawa Takashi, Nishiyama Yuichi, Ochi Shintaro, Satoh Hidetoshi, Nenoi Mitsuru, Aoki Shin
Frontiers in Public Health 8 (2020) 601124

Elucidation of the mechanism of subunit exchange in αB crystallin oligomers
Inoue Rintaro, Sakamaki Yusuke, Takata Takumi ,Wood Kathleen, Morishima Ken, Sato Nobuhiro, Okuda Aya, Shimizu Masahiro, Urade Reiko, Fujii Noriko, Sugiyama Masaaki
Scientific Reports 11(1) (2021) 2555

Histone variant H2A.B-H2B dimers are spontaneously exchanged with canonical H2A-H2B in the nucleosome
Hirano Rina, Arimura Yasuhiro, Kujirai Tomoya, Shibata Mikihiro, Okuda Aya, Morishima Ken, Inoue Rintaro, Sugiyama Masaaki, Kurumizaka Hitoshi
Communications Biology 4(1) (2021) 191

Recent structural insights into the mechanism of lysozyme hydrolysis
Tanaka Ichiro, Nishinomiya Ryota, Goto Ryosuke, Shimazaki Shun, Chatake Toshiyuki
Acta Crystallographica Section D Structural Biology 77(3) (2021) 288-292

Solution structure of multi-domain protein ER-60 studied by aggregation-free SAXS and coarse-grained-MD simulation
Okuda Aya, Shimizu Masahiro, Morishima Ken, Inoue Rintaro, Sato Nobuhiro, Urade Reiko, Sugiyama Masaaki
Scientific Reports 11(1) (2021) 5655

Proceedings

Analyzing tumor microenvironment and exploiting its characteristics in search of optimizing cancer therapy neutron capture therapy
Akiko Kita, Yukio Morimoto
Proceedings of the 55th KURNS Scientific Meeting Web Meeting 2020 (Jan. 28-29, 2021) 24 (in Japanese)

Optimizing protein ligation reactions: a molecular modeling approach
Yosuke Miyamoto,Ken Morishima, Yasuhiro Yunoki, Masahiro Shimizu,Aya Okuda, Nobuhiro Sato, Rintaro Inoue, Reiko Urade,Hirokazu Yagi,Koichi Kato, Masaaki Sugiyama
Proceedings of the 55th KURNS Scientific Meeting Web Meeting 2020 (Jan. 28-29, 2021) 38 (in Japanese)

Neutron structure analysis of the deuterated denatured/refolded protein crystals
Nobuhiro Sato, Aya Okuda, Masahiro Shimizu, Ken Morishima, Rintaro Inoue, Reiko Urade, Masaaki Sugiyama.
Proceedings of the 55th KURNS Scientific Meeting Web Meeting 2020 (Jan. 28-29, 2021) 42 (in Japanese)

Structural analysis of protein complex in solution under association-discussion equilibrium
Masahiro Shimizu, Aya Okuda, Ken Morishima, Nobuhiro Sato, Rintaro Inoue, Reiko Urade, Masayuki Sugiyama
Proceedings of the 55th KURNS Scientific Meeting Web Meeting 2020 (Jan. 28-29, 2021) 16 (in Japanese)

Preparation of deuterated wheat proteins of contrast-variation SANS measurements
Shin-i-chiro Masunaga, Yu Sanada, Hideko Nagasawa, HIroshi Harada, Ryoichi Hirayama, Satoshi Kasaoka, Ken Nagasaki, Yoshihiro Uto, Hironobu Yasui, Mitsuko Masutani,Kei Nakai, Yoshitaka, Matsumoto
Proceedings of the 55th KURNS Scientific Meeting Web Meeting 2020 (Jan. 28-29, 2021) 13 (in Japanese)

Reviews

”オンコサーミア” (Modulated Electro Hyperthermia [mEHT])の臨床応用に関する最近の知見について
増永慎一郎
Thermal Medicine 36(2) (2020) 46-47 (in Japanese)

Books

放射線治療中でも普通に生活できますか？ がん放射線治療のしくみについておしえてください。放射線治療は,なぜがんに有効なのですか？
増永慎一郎
患者さんと家族のための放射線治療 Q&A 2020 年版 第 2 版
日本放射線腫瘍学会
金原出版株式会社 (2020) (in Japanese)

第 VI 部 60. 溶液散乱法 I: 静的構造解析
杉山正明

現代化学増刊 46: 相分離生物学の全貌
白木賢太郎
東京化学同人 (2020) (in Japanese)

第 VI 部 61. 溶液散乱法 II: 動的構造を中心に
井上倫太郎
現代化学増刊 46: 相分離生物学の全貌
白木賢太郎
東京化学同人 (2020) (in Japanese)

第 VI 部 62. 超遠心分析
守島健
現代化学増刊 46: 相分離生物学の全貌
白木賢太郎
東京化学同人 (2020) (in Japanese)

7. Neutron Capture Therapy

Papers

Boron Neutron Capture Therapy Study of ^{10}B Enriched Nanostructured Boron Carbide Against Cervical Cancer and Glioblastoma Cell Line
Kaur Manjot, Singh Paviter, Meena Ramovatar, Nakagawa Fumiko, Suzuki Minoru, Nakamura Hiroyuki, Kumar Akshay
Journal of Cluster Science 32 (2021) 221-225

Development of Optical-fiber-based Neutron Detector Using Li-glass Scintillator for an Intense Neutron Field
Ishikawa Akihisa, Yamazaki Atsushi, Watanabe Kenichi, Yoshihashi Sachiko,Uritani Akira, Sakurai Yoshinori, Tanaka Hiroki, Ogawara Ryo, Suda Mitsuru, Hamano Tsuyoshi
Sensors and Materials 32(4) (2020) 1489-1495

Reevaluation of CBE value of BPA for hepatocytes
Ono, K., Tanaka, H., Suzuki, M.
Applied Radiation and Isotopes 161 (2020) 109159

Chemical structure of hydrolysates of cereulide and their time course profile
Naka Toshihito, Takaki Yuka, Hattori Yoshihide, Takenaka Hiroshi, Ohta Yoichiro, Kirihata Mitsunori, Tanimori Shinji
Bioorganic & Medicinal Chemistry Letters 30(9) (2020) 127050

Evaluation of a Novel Boron-Containing αd-Mannopyranoside for BNCT
Tsurubuchi Takao, Shirakawa Makoto, Kurosawa Wataru, Matsumoto Kayo, Ubagai Risa, Umishio Hiroshi, Suga Yasuyo, Yamazaki Junko, Arakawa Akihiro, Maruyama Yutaka, Seki Takuya, Shibui Yusuke, Yoshida Fumiyo, Zaboronok Alexander, Suzuki Minoru, Sakurai Yoshinori, Tanaka Hiroki, Nakai Kei, Ishikawa Eiichi, Matsumura Akira
Cells 9(5) (2020) 1277

Synthesis and Evaluation of Dodecaboranethiol Containing Kojic Acid (KA-BSH) as a Novel Agent for Boron Neutron Capture Therapy
Takeuchi Koji, Hattori Yoshihide, Kawabata Shinji, Futamura Gen, Hiramatsu Ryo, Wanibuchi Masahiko, Tanaka Hiroki, Masunaga Shin-ichiro, Ono Koji, Miyatake Shin-Ichi, Kirihata Mitsunori
Cells 9(6) (2020) 1551

Optimization of preparation methods for high loading content and high encapsulation efficiency of BSH into liposomes
Shirakawa Makoto, Nakai Kei, Sato Yuhki, Nakamura Shunji, Harada Mari, Ishihara Kazuki, Yoshida Fumiyo, Matsumura Akira, Tomida Hisao
Applied Radiation and Isotopes 10926 (2020) 109260

Cyclic RGD-Functionalized closo-Dodecaborate Albumin Conjugates as Integrin Targeting Boron Carriers for Neutron Capture Therapy
Kawai Kazuki, Nishimura Kai, Okada Satoshi, Sato Shinichi, Suzuki Minoru, Takata Takushi, Nakamura Hiroyuki
Molecular Pharmaceutics 17(10) (2020) 3740-3747

A study on remotely-changeable moderators in Bonner sphere spectrometer for irradiation-field characterization in boron neutron capture therapy
Shiraishi Sadaaki, Takata Takushi, Tanaka Hiroki, Sakurai Yoshinori
Applied Radiation and Isotopes 163 (2020) 109213

Antibody-Based Receptor Targeting Using an Fc-Binding Peptide-Dodecaborate Conjugate and Macropinocytosis Induction for Boron Neutron Capture Therapy
Nakase Ikuhiko, Aoki Ayako, Sakai Yuriko, Hirase Shiori, Ishimura Miki, Takatani-Nakase Tomoka, Hattori Yoshihide, Kirihata Mitsunori
ACS Omega 5(36) (2020) 22731-22738

Characterization of a real-time neutron detector for boron neutron capture therapy using a thin silicon diode
Takada Masashi, Nunomiya Tomoya, Masuda Akihiko, Matsumoto Tetsuro, Tanaka Hiroki, Nakamura Satoshi, Endo Satoru, Nakamura Masaru, Aoyama Kei, Ueda Osamu, Narita Masataka, Nakamura Takashi
Radiation Measurements 137 (2020) 106381

Deep abscopal response to radiotherapy and anti-PD-1 in an oligometastatic melanoma patient with unfavorable pretreatment immune signature
Watanabe Tsubasa, Firat Elke, Scholber Jutta, Gaedicke Simone, Heinrich Corinne, Luo Ren, Ehrat Nicolas, Multhoff Gabriele, Schmitt-Graeff Annette, Grosu Anca-Ligia, Abdollahi Amir, Hassel Jessica C., von Bubnoff Dagmar, Meiss Frank, Niedermann Gabriele
Cancer Immunology, Immunotherapy 69(9) (2020) 1823-1832

Evaluation of the energy resolution of a prompt gamma-ray imaging detector using $LaBr_3$ (Ce) scintillator and 8 × 8 array MPPC for an animal study of BNCT
Okazaki Keita, Tanaka Hiroki, Takata Takushi, Kawabata Shinji, Akabori Kiyotaka, Sakurai Yoshinori
Applied Radiation and Isotopes 163 (2020) 109214

Single-dose toxicity study by intra-arterial injection of ^{10}BSH entrapped water-in-oil-in-water emulsion for boron neutron capture therapy to hepatocellular carcinoma
Yanagie Hironobu, Yanagawa Masashi, Higuchi Tsuyoshi, Mizumachi Ryouji, Fujihara Mitsuteru, Morishita Yasuyuki, Sakurai Yuriko, Mouri Kikue, Dewi Novriana, Nonaka Yasumasa, Shinohara Atsuko, Matsukawa Takehisa, Kubota Ayano, Yokoyama Kazuhito, Suzuki Minoru, Masunaga Shin-ichiro, Sakurai Yohinori, Tanaka Hiroki, Ono Koji, Yamauchi Haruo, Ono Minoru, Nakajima Jun, Higashi Shushi, Takahashi Hiroyuki
Applied Radiation and Isotopes 163 (2020) 109202

A simulation study on beam property of ^{124}Sb−Be isotope-based neutron for BNCT
Tanaka Kenichi, Kajimoto Tsuyoshi, Sakurai Yoshinori, Bengua Gerard, Endo Satoru
Applied Radiation and Isotopes 164 (2020) 09227

Influence of the particle size of gadolinium-loaded chitosan nanoparticles on their tumor-killing effect in neutron capture therapy in vitro
Andoh Tooru, Nakatani Yugo, Suzuki Minoru, Sakurai Yoshinori, Fujimoto Takuya, Ichikawa Hideki
Applied Radiation and Isotopes 164 (2020) 109270

Boron neutron capture therapy using cyclotron-based epithermal neutron source and borofalan (^{10}B) for recurrent or locally advanced head and neck cancer (JHN002): An open-label phase II trial
Hirose Katsumi, Konno Akiyoshi, Hiratsuka Junichi, Yoshimoto Seiichi, Kato Takahiro, Ono Koji, Otsuki Naoki, Hatazawa Jun, Tanaka Hiroki, Takayama Kanako, Wada Hitoshi, Suzuki Motohisa, Sato Mariko, Yamaguchi Hisashi, Seto Ichiro, Ueki Yuji, Iketani Susumu, Imai Shigeki, Nakamura Tatsuya, Ono Takashi, Endo Hiromasa, Azami Yusuke, Kikuchi Yasuhiro, Murakami Masao,Takai Yoshihiro
Radiotherapy and Oncology 155 (2020) 182-187

Long-term outcome of cutaneous melanoma patients treated with boron neutron capture therapy (BNCT)
Hiratsuka Junichi, Kamitani Nobuhiko,Tanaka Ryo,Tokiya Ryoji,Yoden Eisaku,Sakurai Yosinori,Suzuki Minoru

Journal of Radiation Research 61(6) (2020) 945 -951

Preclinical study of boron neutron capture therapy for bone metastasis using human breast cancer cell lines
Andoh Tooru,Fujimoto Takuya,Satani Ryoichi,Suzuki Minoru,Wada Keijiro,Sudo Tamotsu,Sakurai Yoshinori,Tanaka Hiroki,Takata Takushi,Ichikawa Hideki
Applied Radiation and Isotopes 165 (2020) 109257

Simulation for improved collimation system of gamma-ray telescope system for boron neutron capture therapy at Kyoto University Reactor
Sakurai Y., Takata T., Tanaka H., Suzuki M.
Applied Radiation and Isotopes 165 (2020) 109256

Boron neutron capture therapy for clear cell sarcoma
Fujimoto Takuya, Suzuki Minoru, Sudo Tamotsu, Fujita Ikuo, Sakuma Toshiko, Sakurai Yoshinori, Hirose Takanori, Morishita Masayuki, Takata Takushi, Tamari Yuki, Tanaka Hiroki, Andoh Tooru, Kawamoto Teruya, Hara Hitomi, Fukase Naomasa, Kawakami Yohei, Shigemoto Rika, Matsumoto Tomoyuki, Ichikawa Hideki, Ono Koji, Kuroda Ryosuke, Akisue Toshihiro
Applied Radiation and Isotopes 166 (2020) 109324

Characteristic evaluation of the thermal neutron irradiation field using a 30 MeV cyclotron accelerator for basic research on neutron capture therapy
Tanaka H., Takata T., Watanabe T., Suzuki M., Mitsumoto T., Kawabata S., Masunaga S., Kinashi Y., Sakurai Y., Maruhashi A., Ono K.
Nuclear Instruments and Methods in Physics Research Section A: Accelerators, Spectrometers, Detectors and Associated Equipment 983 (2020) 164533

DEVELOPMENT OF A NEUTRON DOSIMETRY SYSTEM BASED ON DOUBLE SELF-ACTIVATED CSI DETECTORS FOR MEDICAL LINAC ENVIRONMENTS
Hanada Yumika, Nohtomi Akihiro, Fukunaga Junichi, Shioyama Yoshiyuki
Radiation Protection Dosimetry 192(3) (2020) 378-386

Pharmacokinetics of ^{10}B-p-boronophenylalanine (BPA) in the blood and tumors in human patients: A critical review with special reference to tumor-to-blood (T/B) ratios using resected tumor samples
Fukuda Hiroshi, Hiratsuka Junichi
Applied Radiation and Isotopes 166 (2020) 109308

Self-assembling A6K peptide nanotubes as a mercaptoundecahydrododecaborate (BSH) delivery system for boron neutron capture therapy (BNCT)
Michiue Hiroyuki, Kitamatsu Mizuki, Fukunaga Asami, Tsuboi Nobushige, Fujimura Atsushi, Matsushita Hiroaki, Igawa Kazuyo, Kasai Tomonari, Kondo Natsuko, Matsui Hideki, Furuya Shuichi
Journal of Controlled Release 10(330) (2020) 788-796

The Therapeutic Effects of Dodecaborate Containing Boronophenylalanine for Boron Neutron Capture Therapy in a Rat Brain Tumor Model
Fukuo Yusuke, Hattori Yoshihide, Kawabata Shinji, Kashiwagi Hideki, Kanemitsu Takuya, Takeuchi Koji, Futamura Gen, Hiramatsu Ryo, Watanabe Tsubasa, Hu Naonori, Takata Takushi, Tanaka Hiroki, Suzuki Minoru, Miyatake Shin-Ichi, Kirihata Mitsunori, Wanibuchi Masahiko
Biology 9(12) (2020) E437

Development of real-time neutron detectors with different sensitivities to thermal, epithermal, and fast neutrons in BNCT
Matsubayashi Nishiki, Tanaka Hiroki, Takata Takushi, Okazaki Keita, Sakurai Yoshinori, Suzuki Minoru
Radiation Measurements 140 (2021) 106489

Improvement of Water Solubility of Mercaptoundecahydrododecaborate (BSH)-Peptides by Conjugating with Ethylene Glycol Linker and Interaction with Cyclodextrin
Kitamatsu Mizuki, Nakamura-Tachibana Ayaka, Ishikawa Yoshimichi, Michiue Hiroyuki
Processes 9(1) (2021) 167

Non-isotope enriched phenylboronic acid-decorated dual-functional nano-assembles for an actively targeting BNCT drug
Kim Ahram, Suzuki Minoru, Matsumoto Yoshitaka, Fukumitsu Nobuyoshi, Nagasaki Yukio

Biomaterials 268 (2021) 120551

Tumor vasculature-targeted ^{10}B delivery by an Annexin A1-binding peptide boosts effects of boron neutron capture therapy
Yoneyama Tohru, Hatakeyama Shingo, Sutoh-Yoneyama Mihoko, Yoshiya Taku, Uemura Tsuyoshi, Ishizu Takehiro, Suzuki Minoru, Hachinohe Shingo, Ishiyama Shintaro, Nonaka Motohiro, Fukuda Michiko N., Ohyama Chikara
BMC Cancer 21(1) (2021) 72

Construction of Boronophenylalanine-Loaded Biodegradable Periodic Mesoporous Organosilica Nanoparticles for BNCT Cancer Therapy
Tamanoi Fuyuhiko, Chinnathambi Shanmugavel, Laird Mathilde, Komatsu Aoi, Birault Albane, Takata Takushi, Doan Tan Le-Hoang, Mai Ngoc Xuan Dat, Raitano Arthur, Morrison Kendall, Suzuki Minoru, Matsumoto Kotaro
International Journal of Molecular Sciences 22(5) (2021) 2251

Development of a dose distribution shifter to fit inside the collimator of a Boron Neutron Capture Therapy irradiation system to treat superficial tumours
Hu N., Tanaka H., Yoshikawa S., Miyao M., Akita K., Aihara T., Ono K.
Physica Medica 82 (2021) 17-24

Fructose-functionalized polymers to enhance therapeutic potential of p-boronophenylalanine for neutron capture therapy
Nomoto Takahiro, Yao Ying, Inoue Yukiya, Suzuki Minoru, Kanamori Kaito,Takemoto Hiroyasu, Matsui Makoto, Tomoda Keishiro, Nishiyama Nobuhiro
Journal of Controlled Release 332 (2021) 184-193

BNCT for primary synovial sarcoma
Fujimoto Takuya, Suzuki Minoru, Kuratsu Shigeyuki, Fujita Ikuo, Morishita Masayuki, Sudo Tamotsu, Sakuma Toshiko, Nakamatsu Yuta, Sakurai Yoshinori, Takata Takushi, Tamari Yuki, Tanaka Hiroki, Masunaga Shin-ichiro, Kinashi Yuko, Kondo Natsuko, Sakakibara Shunsuke, Igaki Hiroshi, Andoh Tooru, Sakamoto Setsu, Kawamoto Teruya, Watabe Tadashi, Hara Hitomi, Fukase Naomasa, Kawakami Yohei, Matsumoto Tomoyuki, Akisue Toshihiro, Ono Koji, Ichikawa Hideki, Kuroda Ryosuke, Hirose Takanori
Applied Radiation and Isotopes 169 (2021) 109407

Complementary leucine zippering system for effective intracellular delivery of proteins by cell-penetrating peptides Kitamatsu Mizuki, Yuasa Hiroki, Ohtsuki Takashi, Michiue Hiroyuki
Bioorganic & Medicinal Chemistry 33 (2021) 116036

Improving the spatial resolution of a pixelated $LaBr_3$(Ce) scintillator coupled with a multi-pixel photon counter array for boron neutron capture therapy
Okazaki Keita, Tanaka Hiroki, Takata Takushi, Hu Naonori, Mukawa Tetsuya, Sakurai Yoshinori, Suzuki Minoru
Nuclear Instruments and Methods in Physics Research Section A: Accelerators, Spectrometers, Detectors and Associated Equipment 992 (2021) 165026

Quantitative autoradiography in boron neutron capture therapy considering the particle ranges in the samples
Takeno Satoshi, Tanaka Hiroki, Watanabe Tsubasa, Mizowaki Takashi, Suzuki Minoru
Physica Medica 82 (2021) 306-320

Proceedings

Present Status and Boron Nwutron Capture Therapy: Moving from research reactors to in-hospital based accelerator technologies
D.Ridicas, K. Igawa, A. Jalilian, I. Swainson, H. Mavric, O.Belyakov K. KAMITANI, J.A. Osso-Junior, K. Ono, Y. Kiyanagi, H. Nakamura.
RFFM Conference- proceedings Helsinki, Finland (2020)

Development of Absolute Epi-thermal and Fast Neutron Flux Intensity Detectors for BNCT
K.Aoki, S.Tamaki, S.Kusaka, F.Sato, I.Murata
Symposium on Nuclear Data 2020, Saitama, Japan (RIKEN Wako Campus) (Nov. 26-27, 2020)

Investigation of a small-animal PG-SPECT system for basic BNCT research utilizing a TlBr detector
Keita Okazaki, Takushi Takata, Tetsuya Mukawa, Yoshinori Sakurai, Hiroki Tanaka
Proceedings of the 55th KURNS Scientific Meeting Web Meeting 2020 (Jan. 28-29, 2021) 33 (in Japanese)

Research of optimal irradiation method for superficial tumors in a cyclotron-based epithermal neutron source
Yuki Kakimoto, Shin-ichiro Hayashi, Takushi Takata, Hiroki Tanaka, Yoshinori Sakurai
Proceedings of the 55th KURNS Scientific Meeting Web Meeting 2020 (Jan. 28-29, 2021) 23 (in Japanese)

Size distribution of Chlorine(Cl) and Bromine(Br) in the atmosphric aerosols
Akinori Sakurai,TakushiTakata,Yuki Tamari Tsubasa Watanabe, Naonori Hu, Shinji Kawabata, Yoshihiro Kudo, Toshinori Mitsumoto, Nishiki Matyubayashi, Yoshinori Sakurai, Hiroki Tanaka
Proceedings of the 55th KURNS Scientific Meeting Web Meeting 2020 (Jan. 28-29, 2021) 18 (in Japanese)

Study on two- dimensional beam-component discrimination for BNCT using PVA-GTA-I gel dosimetor Hikaru Matsunaga, Yoshinori Sakurai, Takushi Takata, Hiroki Tanaka, Minoru Suzuki
Proceedings of the 55th KURNS Scientific Meeting Web Meeting 2020 (Jan. 28-29, 2021) 20 (in Japanese)

Invention of polyamine derivatives for boron neutron capture Therapy
Akari Matsushita, Mieko Tsuji, Yu Sanada, Tasuku Hirayama, Shinichiro Masunaga, Hideko Nagasawa
Proceedings of the 55th KURNS Scientific Meeting Web Meeting 2020 (Jan. 28-29, 2021) 35 (in Japanese)

Development of real-time neutron detectors for whole body exposure during BNCT
Nishiki Matsubayashi, Takushi Takata, Micihkata Sato, Tadaaki Tsukamoto, Keita Okazaki, Akinori Sasaki Yoshinori Sakurai, Hiroki Tanaka
Proceedings of the 55th KURNS Scientific Meeting Web Meeting 2020 (Jan. 28-29, 2021) 32 (in Japanese)

Development of prompt gamma ray imaging detectors for BNCT
Hiroki Ueda, Tomohiro Tanaka, Minoru Suzuki, Yoshinori Sakurai, Shin Aoki
Proceedings of the 55th KURNS Scientific Meeting Web Meeting 2020 (Jan. 28-29, 2021) 28 (in Japanese)

Improvement of efficiency i dose evaluation of tumor-bearing mice irradiation using KUR heavy water neutron
Taiki Nakamura, Keitaro Hitomi, Mitsuhiro Nogami, Kenichi Watanabe, Takushi Takata, Yoshinori Sakurai, Hiroki Tanaka
Proceedings of the 55th KURNS Scientific Meeting Web Meeting 2020 (Jan. 28-29, 2021) 17 (in Japanese)

Development of new boron carriers for BNCT targeting amino acid transporters
Hiroki Ueda, Tomohiro Tanaka, Minoru Suzuki, Yoshinori Sakurai, Shin Aoki
Proceedings of the 55th KURNS Scientific Meeting Web Meeting 2020 (Jan. 28-29, 2021) 41 (in Japanese)

Invention of polyamine derivatives for boron neutron capture therapy
Takushi Takata, Hiroki Tanaka, Yoshinori Sakurai, Tsubasa Watanabe, Minoru Suzuki
Proceedings of the 55th KURNS Scientific Meeting Web Meeting 2020 (Jan. 28-29, 2021) 34 (in Japanese)

Reviews

「スライム」から発想を得たがん治療―液体のりの主成分が最先端がん治療法の効果を向上させた！―
Nomoto Takahiro
Chemistry 20(5) (2020) 66 71 (in Japanese)

Current status and potential of neutron capture therapy as a new treatment option for malignant soft tissue tumors Andoh Tooru, Ichikawa Hideki, Fujimoto Takuya, Suzuki Minoru
Drug Delivery System 35(2) (2020) 137-145 (in Japanese)

Application for Clinical Guideline Assessment by Fluorescent Measurements of Sensitizer Molecule in Tumor
Miyoshi Norio, Kaneko Sadao, Kitai Ryuhei, Tsutsumi Koutarou, Sakurai Yoshinori, Asayama-Kosaka Sachiko, Inoue Keiji, Okada Shigetoshi
Nippon Laser Igakkaishi 41(2) (2020) 110 118 (in Japanese)

安価な「ポリビニルアルコール」を利用した新たながん治療の可能性
Nomoto Takahiro

MATERIAL STAGE 20(5) (2020) 66 71 (in Japanese)

トピックス「液体のりの主成分ががんの治療効果を飛躍的に向上させる」
Nomoto Takahiro, Nishiyama Nobuhiro
B&I Bioscience and Industry 772 (2020) (in Japanese)

ホウ素中性子捕捉療法(BNCT)の現状と将来展望
Minoru Suzuki
Medical Science Digest 2020 年 11 月臨時増刊号 46 (2020) (in Japanese)

Nursing in boron neutron capture therapy (BNCT): Future prospects
Yuka Yamamoto, Minoru Suzuki
The Journal of Radiological Nursing Society of Japan 8(2) (2020) 69 78 (in Japanese)

展望「ポリビニルアルコールによる BNCT 治療効果向上について」
Nomoto Takahiro, Nishiyama Nobuhiro
Isotope News 772 (2020) (in Japanese)

Boron Neutron Capture Therapy: Next-generation Radiation Therapy That Generates αRays inside Cancer Cell
Horoyuki Nakamura
Drug Delivery System 35(2) (2020) 129-136 (in Japanese)

8. Neutron Radiography and Radiation Application

Papers

Crystal Growth and Scintillation Properties of Carbazole for Neutron Detection
Yamaji Akihiro, Yamato Shinnosuke, Kurosawa Shunsuke, Yoshino Masao, Toyoda Satoshi, Kamada Kei, Yokota Yuui, Sato Hiroki, Ohashi Yuji, Yoshikawa Akira
IEEE Transactions on Nuclear Science 67(6) (2020) 1027-1031

Organomercury Captured by Lyase Overexpressed *Escherichia coli* and Its Evaluation by *In-Cell* Radiometry
Morimoto Yukio, Takamiya Koichi
Advances in Enzyme Research 8(2) (2020) 19-26

プレートフィンチューブ熱交換器での除霜時の融解水挙動
Ryosuke MATSUMOTO, Takuto Makihara, Daisuke Ito, Yasuji Saito
Transactions of the Japan Society of Refrigerating and Air Conditioning Engineers 2020 (2020) C112-1 C112-4 (in Japanese)

In-situ visualization of heavy oil behavior in supercritical water using neutron radiography
Shoji Eita, Kikuchi Takahiro,Yamagiwa Koshiro, Kubo Masaki, Tsukada Takao, Takami Seiichi, Sugimoto Katsumi, Ito Daisuke, Saito Yasushi
Chemical Engineering Science 225 (2020) 115816

9. TRU and Nuclear Chemistry

Papers

Experimental study of the thermoelectric properties of YbH_2
Wang Yunxia, Ohishi Yuji, Kurosaki Ken, Muta Hiroaki
Journal of Alloys and Compounds 821 (2020) 153496

Precise determination of iridium by neutron activation analysis coupled with internal standard method
Miura Tsutomu, Iinuma Yuto, Sekimoto Shun
Journal of Radioanalytical and Nuclear Chemistry 324(3) (2020) 1007-1012

Production of $^{9}Mo/^{99m}Tc$ by photonuclear reaction using a $^{nat}MoO_3$ target
Inagaki Makoto, Sekimoto Shun, Tadokoro Takahiro, Ueno Yuichiro, Kani Yuko, Ohtsuki Tsutomu
Journal of Radioanalytical and Nuclear Chemistry 327(2) (2020) 681-686

Thermodynamic interpretation of zirconium solubility in the presence of hydroxyacetic,3-hydroxypropionic, and 2,3-dihydroxypropanoic acids
T. Kobayashi, P. Wang, T. Sasaki
Journal of Nuclear and Radiochemical Sciences 20 (2020) 20-24

High-pressure synthesis of heavily hole-doped cuprates $Mg_{1-x}Li_xCu_2O_3$ with quasi-one-dimensional structure
Imai Yoshinori, Sasaki Koya, Aoyama Takuya, Shirasaki Kenji, Yamamura Tomoo, Ohgushi Kenya
Physical Review B 101(24) (2020) 245112

Solubility and solid phase of trivalent lanthanide hydroxides and oxides
Md. Moniruzzaman, Taishi Kobayashi, Takayuki Sasaki
Journal of Nuclear and Radiochemical Sciences 20 (2020) 32-42

Transfer Rates of ^{225}Ac to Exhaust Air, Surface, and Waste Water under Chemical Operations
YAMAMURA Tomoo, SHIRASAKI Kenji, KIKUNAGA Hidetoshi, NAGATA Kojiro, ZHANG Zi Jian, WASHIYAMA Kohshin, TOYOSHIMA Atsushi, YOSHIMURA Takashi, SHINOHARA Atsushi
Radiation Safety Management 19 (2020) 35-48

Fast Neutron Capture Reaction Data Measurement of Minor Actinides for Development of Nuclear Transmutation Systems
Katabuchi Tatsuya, Iwamoto Osamu, Hori Jun-ichi, Kimura Atsushi, Iwamoto Nobuyuki, Nakamura Shoji, Shibahara Yuji, Terada Kazushi, Rovira Gerard, Matsuura Shota
EPJ Web of Conferences 239 (2020) 01044

Neutron capture and total cross-section measurements of ^{155}Gd and ^{157}Gd at ANNRI in J-PARC
Kimura Atsushi, Nakamura Shoji, Iwamoto Osamu, Iwamoto Nobuyuki, Harada Hideo, Katabuchi Tatsuya, Terada Kazushi, Hori Jun-ichi, Shibahara Yuji, Fujii Toshiyuki
EPJ Web of Conferences 239 (2020) 01012

Thermal-neutron capture cross sections and resonance integrals of the ^{243}Am(n, γ)^{244g}Am and ^{243}Am(n, γ)$^{244m+g}$Am reactions
Nakamura Shoji, Shibahara Yuji, Endo Shunsuke, Kimura Atsushi
Journal of Nuclear Science and Technology 58 (3) (2020) 1-19

Vertical distribution of ^{90}Sr and ^{137}Cs in soils near the Fukushima Daiichi nuclear power station
Sasaki Takayuki, Matoba Daisuke, Dohi Terumi, Fujiwara Kenso, Kobayashi Taishi, Iijima Kazuki
Journal of Radioanalytical and Nuclear Chemistry 326(1) (2020) 303-314

Design and testing of a W-MoO3 target system for electron linac production of ^{99}Mo/^{99m}Tc
Jang Jaewoong, Kikunaga Hidetoshi, Sekimoto Shun, Inagaki Makoto, Kawakami Tomohiko, Ohtsuki Tsutomu, Kashiwagi Shigeru, Takahashi Ken, Tsukada Kyo, Tatenuma Katsuyoshi, Uesaka Mitsuru
Nuclear Instruments and Methods in Physics Research Section A: Accelerators, Spectrometers, Detectors and Associated Equipment 987 (2021) 164815

Discussion on Translational Research of Drug Product for Targeted Alpha Therapy(Part 5) Report of IAEA Technical Meeting : Latest Trend of α-Nuclides and TAT Drug Products
Tsuneo Yano, Koki Hasegawa, Tomoo Yamamura, Tadashi Watabe, Mitsuaki Tatsumi, Tatsuhiko Sato, Yuichirou Kadonaga, Kazuya Kabayama, Koichi Fukase, Hirabayashi Yoko, Hirofumi Fujii ,Yoshiharu Yonekura
Pharmaceutical and medical device regulatory science 52 (2021) 85-106 (in Japanese)

Proceedings

Study if isotope separation via chemical exchange reaction Ryuta Hazama, Takaaki Yoshimoto, Anawat Rittirong, Yoichi Sakuma, Toshiyuki Fujii, Satoshi Fukutani, Yuji Shibahara
Proceedings of the 55th KURNS Scientific Meeting Web Meeting 2020 (Jan. 28-29, 2021) 31(in Japanese)

RI production for medical applications in Japanese Research Reactors, JRR-3, KUR and future reactor
Tomoo Yamamura
Technical Meeting on State of the Art Research Reactor Based Radioisotope and Radiopharmaceutical Production, Vinna, Austria, WebEX (Mar. 22-23, 2021)

10. Health Physics and Waste Management

Papers

Estimation of dietary ^{14}C dose coefficient using ^{13}C-labelled compound administration analysis
Masuda Tsuyoshi,Yoshioka Toshitada,Takahashi Tomoyuki,Takeda Hiroshi,Hatta Hideo,Matsushita Kensaku,Tako Yasuhiro,Takaku Yuichi,Hisamatsu Shun'ichi
Scientific Reports 10(1) (2020) 8156

Investigation of variations in cobalt and europium concentrations in concrete to prepare for accelerator decommissioning
YoshidaGo, Nishikawa Koichi, Nakamura Hajime, Yashima Hiroshi, Sekimoto Shun, Miura Taichi, Masumoto Kazuyoshi, Toyoda Akihiro, Matsumura Hiroshi
Journal of Radioanalytical and Nuclear Chemistry 325(3) (2020) 801-806

Preliminary Investigation of Pretreatment Methods for Liquid Scintillation Measurements of Environmental Water Samples Using Ion Exchange Resins
NAKASONE Shunya, YOKOYAMA Sumi, TAKAHASHI Tomoyuki, OTA Masakazu, KAKIUCHI Hideki, SUGIHARA Shinji, HIRAO Shigekazu, MOMOSHIMA Noriyuki, TAMARI Toshiya, SHIMA Nagayoshi, ATARASHI-ANDOH Mariko, FUKUTANI Satoshi, ISHIMINE Akinobu, FURUKAWA Masahide, TANAKA Masahiro, AKATA Naofumi
Plasma and Fusion Research 15 (2020) 2405027

Age-related isomerization of Asp in human immunoglobulin G kappa chain
Ha Seongmin, Kinouchi Tadatoshi, Fujii Noriko
Biochimica et Biophysica Acta (BBA) - Proteins and Proteomics 1868(6) (2020) 140410

Monte-Carlo simulations with mathematical phantoms to investigate the effectiveness of a whole-body counter for thyroid measurement
Tani Kotaro, Igarashi Yu, Kim Eunjoo, Iimoto Takeshi, Kurihara Osamu
Radiation Measurements 135 (2020) 106335

Simultaneous and Rapid Detection of Multiple Epimers and Isomers of Aspartyl Residues in Lens Proteins Using an LC-MS-MRM Method
Fujii Noriko, Takata Takumi, Kim Ingu, Matsubara Toshiya
ACS Omega 5(42) (2020) 27626-27632

山間埋立地周辺の地下水流動と水質変動の関係
谷口文紀,藤川陽子,国分宏城,橋本芳,村沢直治,谷口省吾,尾崎博明
土木学会論文集 G 76(4) (2020) 84-97 (in Japanese)

土壌との混合による飛灰からの Cs 溶出率制御の可能性
島田洋子, 米田 稔, 樽岡晃大,米谷達成,福谷 哲,池上麻衣子,颯田尚哉, 菅原大輔
環境放射能除染学会誌 8(4) (2021) 197-205 (in Japanese)

Proceedings

190-CONSCIOUSNESS ANALYSIS ON SAFETY CULTURE IMPROVEMENT IN RADIATION FACILITIES IN JAPAN
Hiromi Koike, Takahiro Koshiba, Akira Kudo, Takeshi Iimoto
International Conference on Radiation Safety: Improving Radiation Protection in Practice Online, IAEA, Vienna (Nov. 9-11, 2020) 317-318

Reviews

不溶性 Cs 粒子の溶解や加熱による変化
高宮幸一
科学 90(11) (2020) 1032-1034 (in Japanese)

Others

Analysis of Latest Activity to Foster Radiation Safety Culture in The Higher Education, Research and Teaching Sector
Hiromi Koike, Takeshi Iimoto
jhps53-webmtg Online (Kindai University) 2020 (in Japanese)

11. Accelerator Physics

Papers

Design and Construction of an Imaging beamline at the Nagoya University Neutron Source
Hirota Katsuya, Awano Shogo, Fujiie Takuhiro, Fukumura Seiso, Hishida Mayu, Ichikawa Go, Imajo Sohei, Itoh Ikuya, Iwashita Yoshihisa, Kitaguchi Masaaki, Kiyanagi Yoshiaki, Kuriyama Yasutoshi, Morikawa Koki, Niinomi Yu-dai, Shimizu Hirohiko M., Tsuchida Kazuki, Tsuchikwa Yusuke, Tsurita Yukio, Uritani Akira, Watanabe Kenichi, Yamagata Yutaka, Yamamoto Nana, Yamazaki Atsushi,Yoshihashi Sachiko, Yoshioka Tamaki
EPJ Web of Conferences 231 (2020) 05002

Bipolar Correction Magnet With Permanent Magnets
Iwashita Yoshihisa, Abe Masashi, Yako Tomoki, Fuwa Yasuhiro, Terunuma Nobuhiro
IEEE Transactions on Applied Superconductivity 30(4) (2020) 1-3

Development of a neutron imaging sensor using INTPIX4-SOI pixelated silicon devices
Kamiya Y., Miyoshi T., Iwase H., Inada T., Mizushima A., Mita Y., Shimazoe K., Tanaka H., Kurachi I., Arai Y. **Nuclear Instruments and Methods in Physics Research Section A: Accelerators, Spectrometers, Detectors and Associated Equipment 979 (2020) 164400**

Beam emittance growth in the proposed gaseous target ERIT ring for muon production
Okita H., Ishi Y., Mori Y.
Nuclear Instruments and Methods in Physics Research Section A: Accelerators, Spectrometers, Detectors and Associated Equipment 982 (2020) 164565

On-line range verification for proton beam therapy using spherical ionoacoustic waves with resonant frequency
Takayanagi Taisuke, Uesaka Tomoki, Nakamura Yuta, Unlu Mehmet Burcin, Kuriyama Yasutoshi, Uesugi Tomonori, Ishi Yoshihiro, Kudo Nobuki, Kobayashi Masanori, Umegaki Kikuo, Tomioka Satoshi, Matsuura Taeko
Scientific Reports 10(1) (2020) 20385

Double differential cross sections of neutron production by 135 and 180 MeV protons on A-150 tissue-equivalent plastic
Kajimoto Tsuyoshi, Tanaka Kenichi, Endo Satoru, Kamada So, Tanaka Hiroki, Takada Masashi, Hamano Tsuyoshi
Nuclear Instruments and Methods in Physics Research Section B: Beam Interactions with Materials and Atoms 487 (2021) 38-44

Measurements of secondary-particle emissions from copper target bombarded with 24-GeV/c protons Takahiro Oyama, Toshiya Sanami, Hiroshi Yashima, Masayuki Hagiwara, Noriaki Nakao, Angelo Infantino Elpida Iliopoulou, Robert Froeschl Stefan Roesler, Tsuyoshi Kajimoto, Eunji Leef, Seiji Nagaguro, Tetsuro Matsumoto, Akihiko Masuda,Yoshitomo Uwamino
Nuclear Instruments and Methods in Physics Research Section A: Accelerators, Spectrometers, Detectors and Associated Equipment 990 (2021) 164977

The synthetic fluorinated tetracarboranylchlorin as a versatile antitumor photoradiosensitizer
Valentina A. Olʹshevskaya, Andrei V.Zaitsev, Albina S.Petrova, Anastasia Yu Arkhipova, Mikhail M.Moisenovich, Alexey A. Kostyukov, Anton E. Egorov, Olga A. Koroleva, Galina V. Golovina, Yulia L.Volodina, Elena V.Kalinina, Vladimir A. Kuzmin, Yoshinori Sakurai, Hiroki Tanaka, Norio Miyoshi, Alexander A.
Shtile Dyes and Pigments 186 (2021) 108993

Proceedings

Recent Experimental Results of the Accelerator Driven System with a Sub-Critical Nuclear Reactor (ADS) Program Y. Ishi, Y. Fuwa, Y. Kuriyama, Y. Mori, H. Okita, K. Suga, T. Uesugi
22nd International Conference on Cyclotrons and their Applications (CYC2019), Cape Town, South Africa (Sep. 22-27, 2020)

Resonant ionoacoustic measurement under clinical dose: A study toward online range verification
T Takayanagi, T Uesaka, Y Nakamura, M B Unlu, Y Kuriyama, T Uesugi, Y Ishi, N Kudo, K Umegaki, T Matsuura
Joint AAPM COMP Virtual Meeting ONLINE (Jul. 12-16, 2020)

Pulsed Proton Beams From An FFA Via Ionoacoustic Measurement
Y Nakamura, T Uesaka, T Takayanagi, M Unlu, Y Kuriyama, Y Ishi, T Uesugi, M Kobayashi, N Kudo, S Tanaka, K Umegaki, T Matsuura Joint
Joint AAPM COMP Virtual Meeting ONLINE (Jul. 12-16, 2020)

12. Other

Papers

Short-term vs long-term reliance: Development of a novel approach for diversity of fuels for electricity in energy security
Kosai Shoki, Unesaki Hironobu
Applied Energy 262 (2020) 114520

Enhancing Thermoelectric Properties of Higher Manganese Silicide (HMS) by Partial Ta Substitution
Parse Nuttawat, Tanusilp Sora-At, Silpawilawan Wanthana, Kurosaki, Ken
Pinitsoontorn, Supree Journal of Electronic Materials 49 (2020) 2726-2733

Quantitative evaluation of security of nuclear energy supply: United States as a case study
Kosai Shoki, Unesaki Hironobu
Energy Strategy Reviews 29 (2020) 100491

Synthesis of Silicon and Higher Manganese Silicide Bulk Nano-composites and Their Thermoelectric Properties Palaporn, Dulyawich; Parse, Nuttawat; Tanusilp, Sora-At; Silpawilawan, Wanthana; Kurosaki, Ken;
Pinitsoontorn, Supree Journal of Electronic Materials 49 (2020) 2920-2927

Realizing Excellent n- and p-Type Niobium-Based Half-Heusler Compounds Based on Thermoelectric Properties and High-Temperature Stability
Silpawilawan, Wanthana; Tanuslip, Sora-at; Chetty, Raju; Ohta, Michihiro; Ohishi, Yuji; Muta, Hiroaki; Kurosaki, Ken
Advanced Electronic Materials 6 (2020) 2000083-1-9

Low temperature heat capacity of $Cs_2Si_4O_9$
Suzuki, Eriko; Nakajima, Kunihisa; Osaka, Masahiko; Ohishi, Yuji; Muta, Hiroaki; Kurosaki, Ken
Journal of Nuclear Science and Technology 57 (2020) 852-857

Synthesis and characterization of bulk Si-Ti nanocomposite and comparisons of approaches for enhanced thermoelectric properties in nanocomposites composed of Si and various metal silicides
Tanusilp, Sora-at; Ohishi, Yuji; Muta, Hiroaki; Kurosaki, Ken
Journal of Applied Physics 128 (2020) 095101-1-8

Synthesis, microstructure, multifunctional properties of mayenite $Ca_{12}Al_{14}O_{33}$ (C12A7) cement and graphene oxide (GO) composites
Sriwong, Chaval; Phrompet, Chaiwat; Tuichai, Wattana; Karaphun, Attaphol; Kurosaki, Ken; Ruttanapun,
Chesta Scientific Reports 11077 (2020) 1-19

Enhancement of Thermoelectric Figure of Merit of p-Type $Nb_{0.9}Ti_{0.1}FeSb$ Half-Heusler Compound by Nanostructuring

Silpawilawan, Wanthana; Tanuslip, Sora-at; Ohishi, Yuji; Muta, Hiroaki; Kurosaki, Ken
Physica Status Solidi (a) 2000419 (2020) 1-5

Liquid Structure of Tantalum under Internal Negative Pressure
K. Katagiri, N. Ozaki, S. Ohmura, B. Albertazzi, Y. Hironaka, Y. Inubushi, K. Ishida, M. Koenig, K. Miyanishi, H. Nakamura, M. Nishikino, T. Okuchi, T. Sato, Y. Seto, K.Shigemori, K. Sueda, Y. Tange, T. Togashi, Y. Umeda, M. Yabashi, T. Yabuuchi, and R. Kodama
Physical Review Letters 126 (2021) 175503

Love-Wave Phase-Velocity Estimation from Array-Based Rotational Motion Microtremor
Yoshida Kunikazu, Uebayashi Hirotoshi
Bulletin of the Seismological Society of America 111 (2021) 121-128

高強度レーザーを用いた惑星物質の衝撃圧縮実験
奥地拓生, 尾崎典雅
レーザー研究 49,1 (2021) 35-39 (in Japanese)

Observation of terahertz coherent edge radiation amplified by infrared free-electron laser oscillations
Sei Norihiro, Sakai Takeshi,Hayakawa Yasushi,Sumitomo Yoske,Nogami Kyoko,Tanaka Toshinari,Hayakawa Ken
Scientific Reports 11(1) (2021) 3433

Reviews

第 4 回国際アナモックスシンポジウム IANAS2019 報告
Yoko Fujikawa
Journal of Environmental Conservation Engineering 49(2) (2020) 63-64 (in Japanese)

中性子集束スーパーミラーのための金属基板の小径ツール研磨
細畠拓也, 竹田真宏, 河合利秀, 山形 豊, 日野正裕, 吉永尚生
機械技術 68 (2020) 52-55 (in Japanese)

原子力災害後の長期汚染地域における放射線量率マッピングシステムの開発
Minoru Tanigaki
日本物理学会誌 75 (2020) 766-769 (in Japanese)

Introduction to Nuclear Security (3)
Takahashi Yoshiyuki, Koizumi Mitsuo
Journal of the Atomic Energy Society of Japan 62(8) (2021) 452-456 (in Japanese)

Issues and recommendations about application of graded approach to research reactors
Uesaka Mitsuru, Yonomoto Taisuke, Mineo Hideaki, Murayama Yoji, Hohara Shinya, Nakajima Ken, Nakatsuka Toru
Journal of the Atomic Energy Society of Japan 63(1) (2021) 73-77 (in Japanese)

新潟県技術委員会による 1F 事故の検証報告
Ken Nakajima
Journal of the Atomic Energy Society of Japan (63)3 (2021) 249-250 (in Japanese)

放射化分析研究のロードマップ
大浦泰嗣, 菊永英寿,高宮幸一,藤暢輔,松江秀明,三浦勉,松尾基之
放射化学 43 (2021) 11-13 (in Japanese)

KURNS Progress Report 2020

Issued in August 2021

Issued by the Institute for Integrated Radiation and Nuclear Science,
Kyoto University
Kumatori-cho, Sennan-gun, Osaka 590-0494 Japan

Tel. +81-72-451-2300
Fax. +81-72-451-2600

In case that corrections are made, an errata will be provided
in the following webpage:
https://www.rri.kyoto-u.ac.jp/PUB/report/PR/ProgRep2020/ProgRep2020.html

Publication Team

ABE Naoya
INOUE, Rintaro (Subchief)
KITAMURA, Yasunori
KONDO Natsuko
MORI, Kazuhiro (Chief)
NAKATANI Maki
NAKAYAMA, Chiyoko
PYEON, Cheol Ho
SAKURAI, Yoshinori (Subchief)
SANO, Hiroaki
TOMINAGA, Yuta
YOKOTA Kaori